

**Development and Implementation of a Battery-Electric
Light-Duty Class 2a Truck including
Hybrid Energy Storage**

By
Phillip J. Kollmeyer

A dissertation submitted in partial fulfillment of
the requirements for the degree of

Doctor of Philosophy
(Electrical Engineering)

at the
UNIVERSITY OF WISCONSIN – MADISON
2015

Date of final oral examination: 12/17/2015

The dissertation is approved by the following members of the Final Oral Committee:

Thomas M. Jahns, Professor, Electrical Engineering
Robert D. Lorenz, Professor, Mechanical Engineering
Bulent Sarlioglu, Assistant Professor, Electrical Engineering
Yehui Han, Assistant Professor, Electrical Engineering
Thomas W. Nehl, Ph.D., Propulsion Systems Research Lab, General Motors

© Copyright by Phillip J. Kollmeyer 2015

All Rights Reserved

Abstract

This dissertation addresses two major related research topics: 1) the design, fabrication, modeling, and experimental testing of a battery-electric light-duty Class 2a truck; and 2) the design and evaluation of a hybrid energy storage system (HESS) for this and other vehicles. The work begins with the determination of the truck's peak power and wheel torque requirements (135kW/4900Nm). An electric traction system is then designed that consists of an interior permanent magnet synchronous machine, two-speed gearbox, three-phase motor drive, and LiFePO₄ battery pack. The battery pack capacity is selected to achieve a driving range similar to the 2011 Nissan Leaf electric vehicle (73 miles).

Next, the demonstrator electric traction system is built and installed in the vehicle, a Ford F150 pickup truck. An extensive set of sensors and data acquisition equipment is installed, and the software is developed to control the vehicle and to log driving data. Detailed loss models of the battery pack, electric traction machine, and motor drive are developed and experimentally verified using the driving data. Many aspects of the truck's performance are investigated, including efficiency differences between the two-gear configuration and the optimal gear selection. These studies provide valuable insights into how to approach the design of an electric truck and other vehicle types as well.

The remainder of the dissertation focuses on the application of battery/ultracapacitor hybrid energy storage systems (HESS) to electric vehicles. First, the electric truck is modeled with the addition of an ultracapacitor pack and a dc/dc converter. Rule-based and optimal battery/ultracapacitor power-split control algorithms are then developed, and the performance improvements achieved for both algorithms with a range of ultracapacitor pack sizes are evaluated for operation at 25°C.

The HESS modeling is then extended to low temperatures, where battery resistance increases substantially. To verify the accuracy of the model-predicted results, a scaled hybrid energy storage system is built and the system is tested for several drive cycles and for two temperatures. The HESS performance is then modeled for three variants of the vehicle design, including the prototype electric truck with a different battery pack, the prototype electric truck with a higher power drivetrain and higher towing capability, and an electric city transit bus. Performance advantages provided by the HESS are demonstrated and verified for these vehicles in several areas including:

longer vehicle range, improved low-temperature operation with lithium-ion batteries, and reduced battery losses and cycling stresses.

Summarizing, this dissertation presents an integrated engineering approach for designing, building, and testing an electric Class 2a truck, a vehicle type that has not been presented in the technical literature before this work. In addition, this dissertation provides a very detailed methodology for properly designing and evaluating hybrid energy storage systems over a wide range of operating conditions. The methodology can be applied to any vehicle type, but it has been applied primarily to Class 2a trucks in this work, illuminating both the advantages and limitations of these specialized energy storage configurations for this application.

Acknowledgements

A project such as this requires help, and patience, from a great number of people. I started this work in January of 2011 and it began with the staff at Orchid International, including the owner Grant Bibby, committing to fund and work collaboratively on this project. I am very thankful to Orchid and the many staff who contributed so much time and effort to make this project a great success. Orchid really went far above and beyond, adding extra resources as needed and committing to not just making this a research vehicle as originally planned, but a show vehicle, which they brought to the 2012 International Electric Vehicle Symposium (EVS26) in Los Angeles and the 2012 International Transportation Electrification Conference (ITEC) in Detroit. The electric truck continues to be a great and well utilized resource for researchers at UW-Madison, and has enabled all of the research in this dissertation, so again, I cannot thank Orchid enough for making this work possible.

I also am very grateful to the Wisconsin Electric Machines and Power Electronics Consortium (WEMPEC) and to my research advisor, Professor Thomas Jahns. I proposed many project ideas to Professor Jahns over the years, and no matter how unrealistic or overambitious they many have seemed to him as a seasoned researcher, he was always very supportive and helped to reign my ideas in. The many other projects we worked on together pale in comparison to the electric truck, which we (*I*) thought would take a year to design and assemble. In actuality it was almost two years from the start of the project until the wheels spun, and to this day, even after 6000 miles of driving the vehicle, the process of working on and improving the truck continue and Professor Jahns continues to be as supportive as ever, committing new students and researchers to the work. So Professor Jahns, although my work at UW-Madison was often arduous, I'm eternally thankful to you for enabling me to do this great body of work presented here, and for being supportive in every way you were able.

Of course with this being a work of such a large scale, many individuals came together to make this project happen. The energy and enthusiasm they contributed is much of what brought this project to fruition, and I am very thankful for all of their contributions which are discussed in the following. The design and fabrication of the electric truck was made possible by the generous support of Orchid International and their staff, who contributed as follows: The electric machine was designed by Will Lamb with the help of consultant Ahmed Elantably. The electric machine

and battery boxes were fabricated and mounted in the vehicle with great effort and attention to detail by Randy Lashbrook and Bill Eisenhuth. Craig Woodard, Keith Cornacchia, Chip Forrest, Dennis Anderson, and Frank Reilly provided the leadership as well as the engineering and manufacturing expertise to manage many aspects the project. Larry Rinehart and Chris Brune of Rinehart Motion Systems helped to perform the dynamometer testing of the machine at their facility. Additionally many UW-Madison students contributed to the project, including visiting graduate student Matthew Henriksen who dedicated several months to fabricating and assembling the truck. UW graduate students James McFarland and Gilsu Choi modeled the traction machine in FEA, and graduate student Larry Juang assisted with the battery testing and evaluation and assembly of the truck. Graduate student Ananth Sridhar also contributed tirelessly, designing and implementing the control system for the dc/dc converter for the hybrid energy research. Additionally many other students at the university helped to design, assemble, and install the subsystems, including Joe Levene, Scott Tovsen, Phil Hart, Kevin Frankforter, Adam Shea, Mark Garrison, Will Plaxico, Jacob Dubie, and graduate Adam Anders as a consultant. The staff of Wempec also contributed greatly, with Raymon Marion placing a million and one orders for equipment for our research and Helene Demont and Jim Sember providing various support and importantly organizing the transfer of ownership of the truck to UW-Madison.

Finally I must thank all of my friends and family who have been very supportive through this long process. To my parents, Bob and Jeanne Kollmeyer, thank you for letting me be a creative, sometimes terror of a kid, taking things apart and doing all sorts of crazy projects around the house. Thank you as well for helping me to get a great education at the University of Wisconsin, education is a truly priceless gift, and for all your love and kindness that have made me who I am. Thanks to my younger brother, Keith, and younger sister, Claire, who managed to get college degrees, get married, and start careers, before I did the same. I want to thank my siblings for not giving me a harder time for being a perennial student. I also want to thank my two best friends, Travis Tennessen and Keith Sorenson, who've been close to me since my undergraduate and who always have an ear for philosophizing about life. And most importantly, I want to thank my partner, Pinar Okumus, who has been with me since before I began this work. Pinar has had amazing patience since she finished her PhD in structural engineering 3 ½ years ago, and she has been so supportive even with my graduation deadline continually seeming to be six months in the future and with her

working through the academic tenure process herself. Pinar is the love of my life, and I could not have done this work without her smile, her laugh, and her encouragement through this whole process.

Phil Kollmeyer

December 18th, 2015

Table of Contents

Index of Figures	xii
Index of Tables	xxvi
Chapter 1	
Introduction.....	1
1.1 Motivation and Background.....	1
1.2 Research Problem Statement.....	3
1.3 Research Objectives and Technical Approach.....	4
1.4 Document Organization	8
Chapter 2 State of the Art	10
2.1 Production Electric Vehicles	10
2.2 Brief Overview of Electric Vehicle Traction System Design and Modeling.....	13
2.3 Introduction & Overview of Hybrid Energy Storage.....	19
2.4 Hybrid Energy Storage Topologies and Power Conversion Topologies	24
2.5 Design & Simulation of Hybrid Energy Storage Systems	30
2.5.1 Electric Vehicle Design and Simulation	30
2.5.2 Hybrid Electric Vehicle Design and Simulation	48
2.6 Power Split Control Strategies	57
2.6.1 Power Split Control for Electric Vehicles.....	58
2.6.2 Power Split Control for Hybrid Electric Vehicles	63
Chapter 3 Traction System Design, Modeling, and Fabrication for Class 2a Electric Truck.....	75
3.1 Introduction	75
3.2 Determination of Power and Energy Storage Requirements	76
3.2.1 IPM Machine Output Power Requirement.....	77
3.2.2 Battery Energy Storage Requirement.....	78
3.3 Energy Storage and Electric Drivetrain Design	82
3.3.1 Battery Pack Design	83

3.3.2	Rinehart Motion Systems Motor Drive Parameters	85
3.3.3	135kW Prototype IPM Machine Design	87
3.4	System Level Design and Data Acquisition & Battery management System Design ...	92
3.5	Conclusion.....	95
Chapter 4 Implementation of Traction System and On the Road Experimental Verification of Electric Truck Model		
4.1	Introduction	97
4.2	Vehicle Systems Design & Fabrication	98
4.2.1	Drivetrain Design	98
4.2.2	Electrical Subsystem and Cabling Design	101
4.2.3	Battery Pack Design	106
4.2.4	Vehicle Software and Touchscreen User Interface	111
4.3	Updated Model Parameters from Completed Vehicle	113
4.3.1	Measured Mass of Vehicle & Estimated Mass Breakdown of Added Components 113	
4.3.2	Inertia of Rotating Drivetrain Components.....	115
4.3.3	Calculation of total vehicle mass and equivalent mass	117
4.3.4	Coast Down Tests Redone with Electric Truck	118
4.3.5	Motor and Drive Loss Modeling w/ Experimental Verification	122
4.3.6	Battery Loss Model	142
4.4	Vehicle Modeling Utilizing Updated Model Parameters from section 4.4.....	149
4.4.1	Constant Speed Performance	151
4.4.2	Drive Cycle Performance	155
4.4.3	Gradeability of Truck	161
4.5	Conclusion.....	165

Chapter 5 Loss Optimization and Ultracapacitor Pack Sizing for Electric Truck with Battery/Ultracapacitor Hybrid Energy Storage.....	167
5.1 Introduction	167
5.2 Battery, Ultracapacitor, DC/DC Converter, and Vehicle Model	169
5.2.1 Battery Pack Model.....	169
5.2.2 Reference Ultracapacitor Pack Design & Model	171
5.2.3 DC/DC Converter Model	172
5.2.4 Comparison of Battery & Ultracapacitor Pack Parameters.....	173
5.3 Analytical Calculation of Minimized HESS Losses	174
5.4 Loss Reduction for a Drive Cycle using HESS with Rule-Based Control.....	179
5.5 Optimizing Battery-Ultracapacitor Power Split Using Dynamic Programming.....	182
5.5.1 Introduction to Dynamic Programming	182
5.5.2 Dynamic Programming versus Rule Based Control	183
5.5.3 Improvements Achieved with Dynamic Programming for Different Drive Cycles and Varied Ultracapacitor Size	183
5.5.4 Improvements Achieved with Dynamic Programming for Low Temperature and High Towing Weight	186
5.6 Experimental Verification	187
5.6.1 Battery Testing	188
5.6.2 Ultracapacitor Testing	189
5.7 Investigation of Other Powersplit Optimization Goals, Effect on Mass of Including HESS Mass, and Increase in Motor Power Capability Achieved with HESS	191
5.7.1 Alternative HESS Powersplit Optimization Goals.....	191
5.7.2 Effect on Vehicle Range of Including HESS Mass.....	194
5.7.3 IPM Traction Machine Increase in Power Capability with HESS	195
5.8 Conclusions	197
Chapter 6 Low Temperature Hybrid Energy Storage System Modeling and Performance	199

6.1	Introduction	199
6.2	Battery Characterization Testing and Modeling for Low Temperatures	200
6.2.1	Low Temperature Testing	200
6.2.2	Low Temperature Butler-Volmer Modeling	209
6.2.3	Electric Truck Battery Pack Power Capability Calculated with Low Temperature Model	214
6.2.4	Implementation of Model in Matlab with Example Results	215
6.3	Ultracapacitor Characterization Testing and Modeling	220
6.3.1	Ultracapacitor Characterization Testing.....	220
6.3.2	Discrete Time Ultracapacitor Modeling.....	225
6.3.3	Ultracapacitor Modeling Example – with Matlab Code	231
6.3.4	Demonstration of proper performance of ultracapacitor model.....	236
6.4	HESS Low Temperature System Modeling and Performance	238
6.4.1	Dynamic programming model format.....	239
6.4.2	Performance for a Single Drive – LA92 at -10°C	242
6.4.3	Summary of performance results for a range of temperatures, dc/dc converter ratings, ultracapacitor pack sizes, and control optimization goals.....	246
6.5	Conclusion.....	253
Chapter 7	Experimental Evaluation of Hybrid Energy Storage System.....	255
7.1	Introduction	255
7.2	DC/DC Converter Design and Experimental Testing	255
7.2.1	Introduction	255
7.2.2	Prototype dc/dc converter design and experimental testing.....	256
7.2.3	Example 400A dc/dc converter design for use in modeling	261
7.2.4	HESS Design with 400A dc/dc converter and Skeleton Ultracapacitor Pack...	264
7.2.5	Summary	267

7.3	Hardware Test Setup	267
7.4	Rules for Rule Based Control.....	271
7.5	Testing Matrix & Test Procedure.....	273
7.6	HESS Efficiency versus Power	276
7.7	Measured Results from Experimental Testing.....	278
7.7.1	Overview of results for a single test case – <i>LA92, 0°C, HESS & battery only</i> .	278
7.7.2	Measured battery temperature for each test case	280
7.7.3	Summary of Measured System Improvements Achieved with HESS	281
7.7.4	Ultracapacitor Pack Contribution to System Energy	285
7.8	Summary of Measured versus Modeled System Performance.....	285
7.8.1	Measured and Modeled Ultracapacitor Voltage for Each Test Case	286
7.8.2	Measured versus Modeled Battery RMS Current	287
7.8.3	Measured versus Modeled Battery Amp-hours for Each Test Case	288
7.8.4	Modeled Reduction in Amp-hours for HESS with $\approx 97\%$ dc/dc converter efficiency.....	290
7.9	Conclusions	292
Chapter 8	HESS Performance for Alternative Vehicle Configurations.....	294
8.1	Introduction	294
8.2	HESS Performance for an Electric Truck with a Panasonic Battery Pack.....	295
8.2.1	Measured Panasonic NCR18650PF Parameters	295
8.2.2	Panasonic Battery Pack Design and Specifications	297
8.2.3	Temperature Dependence of Battery Pack Resistance and Power Capability ..	298
8.2.4	Measured versus Modeled Battery Drive Cycle Performance at 0°C and 25°C	299
8.2.5	Electric Truck Performance with Panasonic Battery Pack and an HESS	301
8.2.6	Comparison to Benefits Achieved with HESS with the CALB Pack	304

8.3	HESS Performance for a City Passenger Bus	305
8.3.1	Electric Bus Drivetrain Specifications	306
8.3.2	Mechanical Model of the Electric Bus	308
8.3.3	Bus Drive Cycles and Modeled Power Profiles	310
8.3.4	Bus Driving Range and Performance Improvements Achieved with HESS	311
8.3.5	Summary of Electric Bus Results	314
8.4	HESS Performance for an Electric Truck with 2015 Model Year Ford F150 Truck Performance Capabilities	314
8.4.1	2015 Model Year Electric Truck Performance Specifications.....	315
8.4.2	Modeled Drive Cycle Power Profiles for No Load and Max GCWR Load	317
8.4.3	Performance Improvement Achieved with HESS.....	318
8.4.4	Summary of 2015 Model Year Performance Electric Truck Results.....	321
8.5	Conclusion.....	322
Chapter 9	Contributions & Future Work	324
9.1	Conclusions	324
9.2	Contributions.....	330
9.2.1	Electric Truck Powertrain Design	330
9.2.2	Electric Truck Powertrain Modeling with On-the-Road Experimental Verification	334
9.2.3	Hybrid Energy Storage System (HESS) Investigation.....	338
9.3	Recommended Future Work	342
References	351
Appendix I	– Modeling of Electric Truck Rotating Inertial Components (by Scott Towsen)	364
Appendix II	- Motor control operating tables for electric machine	376
Appendix III	– Pinouts for Electric Truck Cables and Sockets	384
Appendix IV	– DC/DC Converter Loss Modeling Report	398

Index of Figures

Figure 1.1 Gasoline engine vehicle's distribution of energy [1]	1
Figure 1.2 Electric vehicle's MPG greenhouse gas equivalence to gasoline-powered vehicles based on electric grid emissions [2].....	2
Figure 2.1 2014 model year production electric vehicles and UW-Madison electric truck	11
Figure 2.2 Chevy Spark EV motor power and efficiency [10]	16
Figure 2.3 Chevy Spark EV full vehicle and motor and gearbox CAD drawings [10, 11]	16
Figure 2.4 Tesla Model S EV measured coefficient of drag improvements for blanking of different air vents [12]	17
Figure 2.5 Production intent Tesla Model S aero wheel [13]	17
Figure 2.6 Thermal model of electric vehicle cabin and predicted vehicle range with and without use of AC [14].....	18
Figure 2.7 Example hybrid energy storage system w/ typical ranges of energy/power density...	19
Figure 2.8 Commercial applications of hybrid energy storage [16-19].....	20
Figure 2.9 Battery (BU) and ultracapacitor (UC) hybrid energy storage topologies [21]	21
Figure 2.10 Vehicles which hybrid energy storage can be applied to [1].....	22
Figure 2.11 Energy management control strategies for hybrid electric vehicle or hybrid energy storage applications [1]	23
Figure 2.12 Bidirectional DC/DC converter topologies [96].....	25
Figure 2.13 (a) Cascade buck-boost, (b) Half-Bridge (c) Cúk, and (d) SEPIC/Luo bidirectional dc/dc converters [97].....	27
Figure 2.14 (a) Conventional hard switched and (b) proposed zero voltage switching dc/dc converter [98].....	27
Figure 2.15 Simulated dc/dc converter efficiency with Si IGBT, Si IGBT w/SiC diode hybrid, and all SiC, and converter passive component sizing [100]	28
Figure 2.16 Design of 4-wheeled robot with HESS	32
Figure 2.17 HESS system topology for 4-wheeled robot [22].....	32

Figure 2.18 System loss versus ultracapacitor energy storage for 4-wheeled robot [22]	33
Figure 2.19 Series-parallel reconfigurable HESS topology [25]	35
Figure 2.20 Electric go-kart with hybrid energy storage [26]	35
Figure 2.21 Electric three-wheel single passenger vehicle with hybrid energy storage	37
Figure 2.22 Electric three-wheeled auto rickshaw with battery and solar panel hybrid energy system [28]	38
Figure 2.23 Modeled HESS performance for Fiat Electra [30]	40
Figure 2.24 VW Lupo with simulated HESS for low temperature and 50% aged case [37]	41
Figure 2.25 Proposes HESS drive topology w/ ultracapacitor on drive dc bus [34]	42
Figure 2.26 Proposed HESS drive topology with ultracapacitor connected directly to dc motor terminals [39]	42
Figure 2.27 Passive battery and ultracapacitor HESS with experimental results [32]	43
Figure 2.28 Genovation G2 prototype vehicle and proposed hybrid energy storage drivetrain ...	44
Figure 2.29 Chevy LUV EV conversion with part of HESS ultracapacitor pack and dc/dc converter installed under hood [42]	44
Figure 2.30 Efficiency, range, and acceleration improvements for battery only and HESS Chevy LUV EV [42]	45
Figure 2.31 44T Metro railcar proposed HESS topology and ultracapacitor sizing versus maximum grade [47, 48]	47
Figure 2.32 Topology and sales flyer for passive battery and ultracapacitor hybrid for two wheeled vehicle (\$1 = ₹63) [50]	49
Figure 2.33 Mild hybrid hess topology with experimental data [53]	50
Figure 2.34 Fuel economy improvements for Chevy Equinox mild hybrid with HESS for various dc/dc converter power ratings [57]	51
Figure 2.35 Fuel economy improvements for mild hybrid light duty commercial vehicle with HESS [58]	51
Figure 2.36 Statistical HESS battery and ultracapacitor sizing for example parameters [55]	53

Figure 2.37 Fuel cell vehicle with hybrid energy storage topology and experimental results [52]	53
Figure 2.38 Battery and UC energy rating and system losses vs UC capacity for hybrid bus [61]	54
Figure 2.39 Hybrid bus modeled HESS vs battery only ESS performance for drive cycles [62]	54
Figure 2.40 Fuel cell heavy duty tactical mobility truck with HESS [64]	55
Figure 2.41 Dynamic programming and heuristic normalized battery rms current and losses [65]	59
Figure 2.42 EV hess management framework [66]	59
Figure 2.43 Simulated losses for convex multi-objective control methodology (<i>proposed algorithm</i>) for FTP75 drive cycle [68]	60
Figure 2.44 Frequency based power split control with experimental verification [69]	61
Figure 2.45 Simulated EV vs EV with HESS vehicle performance metrics for four power split strategies [70]	62
Figure 2.46 Idle-stop/start & regenerative braking cycle life test for 36V battery ultracapacitor system for a mild hybrid [77]	65
Figure 2.47 Mild hybrid HESS configuration and simulated performance for a drive cycle [80]	66
Figure 2.48 System topology and truth table control for series hybrid military combat vehicle with HESS [81]	67
Figure 2.49 Series hybrid bus optimized # of ultracapacitor packs to minimize 10 year system cost by extending battery pack life [82]	68
Figure 2.50 Low pass filter and velocity based power split control for hybrid bus [83]	69
Figure 2.51 Calculated minimum losses control results for Parallel HEV and NEDC drive cycle [84]	70
Figure 2.52 Parallel hybrid fuel consumption vs battery rms current for rule based (blue) and optimal (black diamonds) control [87]	71
Figure 2.53 HESS performance improvements for parallel through the road hybrid [89]	72
Figure 2.54 Computationally efficient modified dynamic programming for parallel hybrid vehicle control [90]	73

Figure 2.55 Battery and ultracapacitor pack sizing for fuel cell hybrid bus considering battery aging [93]	74
Figure 3.1 F150 truck with electric powertrain	76
Figure 3.2 Gasoline-powered F150 drag power versus speed derived from coastdown test.....	79
Figure 3.3 CAD drawing of truck drivetrain showing battery pack, motor controller, motor, gearbox & rear differential.....	83
Figure 3.4 Internal resistance of 60Ah-rated Thunder Sky (TS) and CALB lithium batteries estimated with HPPC test.....	84
Figure 3.5 100Ah, 108 cell pack (2.8V/cell min. & 3.6V/cell max) power capability estimated from 60Ah HPPC results	85
Figure 3.6 View of prototype IPM machine on dynamometer	88
Figure 3.7 Experimentally-measured versus FEA-predicted torque for prototype IPM machine	89
Figure 3.8 4.2L ICE versus FEA-predicted traction motor torque & power for 302V dc bus and 450Arms current limit.....	90
Figure 3.9 4.2L ICE versus FEA predicted traction motor torque for 302V dc bus and 450Arms current limit.....	91
Figure 3.10 4.2L ICE versus FEA predicted traction motor power for 302V dc bus and 450Arms current limit.....	91
Figure 3.11 Simplified diagram of electric truck energy storage, drive train, and vehicle controller/data logger	93
Figure 3.12 Battery management board for 12 cells with test pack.....	95
Figure 4.1 Mechanical drivetrain diagram with relevant torques and speeds labeled	99
Figure 4.2 Electric machine, torque sensor and gearbox assembly	100
Figure 4.3 Electrical subsystems and cabling diagram	102
Figure 4.4 Pictures of electric truck subsystems.....	104
Figure 4.5 Additional pictures of electric truck subsystems.....	105
Figure 4.6 Battery pack electrical layout and temperature sensor placement.....	107
Figure 4.7 Pictures of battery module and battery boxes.....	108

Figure 4.8 Battery management board.....	109
Figure 4.9 Pictures of electric truck battery boxes	110
Figure 4.10 User interface screenshot.....	112
Figure 4.11 Truck weigh station document, picture of scale, and measured mass of truck	115
Figure 4.12 Speed versus time for example coast down test	119
Figure 4.13 Road load vs speed for coast down test.....	120
Figure 4.14 Road load aero, viscous, and static components for stock F150 and E-Truck.....	121
Figure 4.15 Comparison of drag power and drag power Wh/mile for a selection of vehicles ...	122
Figure 4.16 I_d / I_q operating points used for drive programming table, with speeds of 100, 2500, 2750... 7000rpm and torques of 0Nm, 20Nm... 360Nm, 390Nm... 450Nm	125
Figure 4.17 Motor phase current and winding losses for points in drive I_d / I_q table.....	126
Figure 4.18 Motor output power limit with 300Vdc bus and 450Arms phase current.....	127
Figure 4.19 Eddy current and hysteresis iron losses for 100Nm machine torque	128
Figure 4.20 FEA calculated motor iron losses versus torque and speed	129
Figure 4.21 Dynamometer measured no load motor losses	130
Figure 4.22 Sum of motor winding and iron losses	130
Figure 4.23 <i>Motor efficiency contour plot</i> (with constant vehicle speed torque vs motor speed for 1 st and 2 nd gear overlaid)	131
Figure 4.24 Motor drive DC bus caps and semiconductors.....	133
Figure 4.25 Motor drive semiconductor losses for varied dc bus and temperature	135
Figure 4.26 Motor drive semiconductor losses for 330Vdc bus and 40°C heat sink	136
Figure 4.27 <i>Motor drive efficiency contour plot for battery parameters: 50% SOC, 25°C</i> (with constant vehicle speed torque vs motor speed for 1 st and 2 nd gear overlaid)	137
Figure 4.28 Sum of motor and drive losses	138
Figure 4.29 <i>Combined motor and drive efficiency contour plot</i> (with constant vehicle speed torque vs motor speed for 1 st and 2 nd gear overlaid)	139

Figure 4.30 Measured vs modeled combined motor and drive losses	140
Figure 4.31 Pulse current test at 25°C & 90% SOC for 100Ah CALB battery	142
Figure 4.32 Measured open-circuit voltage and HPPC resistance LA92 test for CALB SE100AHA LiFePO4 battery cell at 25°C	143
Figure 4.33 Battery pack cable resistance measured from cable voltage drop	144
Figure 4.34 Battery pack losses and efficiency vs output power and SOC	146
Figure 4.35 Operating point for maximum motor output power as battery pack is discharged	148
Figure 4.36 Battery pack losses and efficiency vs output power and SOC	149
Figure 4.37 Block diagram of vehicle model power calculation methodology	150
Figure 4.38 Constant speed driving motor torque and phase current	152
Figure 4.39 Constant speed driving motor and drive efficiency and losses	153
Figure 4.40 Constant speed driving battery energy consumption for 1 st and 2 nd gear	153
Figure 4.41 Constant speed driving range for 1 st and 2 nd gear to 90% DOD	154
Figure 4.42 Model predicted LA92 drive cycle performance using 2 nd gear only	155
Figure 4.43 HWFET drive cycle model calculated vehicle parameters	156
Figure 4.44 Experimental vs model predicted performance for eight drives	160
Figure 4.45 Gravitation force calculation parameters.....	161
Figure 4.46 Truck acceleration rate for various road grades and vehicle loading	163
Figure 4.47 Battery pack power at constant speed of 25mph and 60mph for various road grades and vehicle load	164
Figure 5.1 Hybrid energy storage system evaluated in this study	168
Figure 5.2 Measured open-circuit voltage and HPPC resistance for Standard and LA92 test for CALB SE100AHA LiFePO4 battery cell	170
Figure 5.3 Energy capacities shown as x's for 5 ultracapacitor packs which match truck's kinetic energy at speeds between 29 and 63 mph	171

Figure 5.4 Experimentally-measured capacitance and resistances of 0.8m Ω 650F rated Maxwell K2 series ultracapacitor.....	172
Figure 5.5 Experimentally-measured Toyota Prius dc/dc converter efficiency [95] together with extrapolated 3:1 boost ratio efficiency curve.....	173
Figure 5.6 Ultracapacitor pack discharge resistance and power capability	174
Figure 5.7 Battery pack discharge resistance and power capability	174
Figure 5.8 Ultracapacitor and battery current solution curves for a range of HESS output powers assuming 270V ultracapacitor pack voltage, 3000F cell pack and nominal battery resistance and dc/dc converter efficiency	177
Figure 5.9 Total HESS losses versus battery current for a range of HESS output powers assuming 270V ultracapacitor pack voltage, 3000F cell pack, and nominal battery resistance and dc/dc converter efficiency	177
Figure 5.10 Calculated minimum loss power splits output power for 270Vdc, 200Vdc, and 135Vdc ultracapacitor pack voltage with a 3000F cell pack	178
Figure 5.11 Calculated system efficiency for battery-only and hybrid system for 270Vdc, 200Vdc, and 135Vdc ultracapacitor pack voltages.....	179
Figure 5.12 Calculated battery, ultracapacitor, and total HESS power vs. time for US06 drive cycle using adopted rule-based control	180
Figure 5.13 Calculated vehicle speed and ultracapacitor voltage vs time for the US06 drive cycle, comparing voltage profiles with rule-based and dynamic programming power split control	181
Figure 5.14 Calculated ratio of hybrid ESS to battery-only losses for four drive cycles with 1200F and 3000F ultracapacitor cell packs, comparing rule-based control and dynamic programming cases	183
Figure 5.15 Predicted range improvement achieved with dynamic programming.....	184
Figure 5.16 Predicted reduction of regeneration charge and battery cycles achieved with dynamic programming	185
Figure 5.17 Predicted reduction of battery losses achieved with dynamic programming	185
Figure 5.18 Ultracapacitor cycles and predicted reduction of battery cycles achieved with dynamic programming and scaled for 150k miles of travel	186

Figure 5.19 Predicted reduction in LA92 drive cycle energy consumption vs ratio of battery pack resistance to 25°C battery pack resistance	187
Figure 5.20 Predicted reduction in LA92 drive cycle energy consumption vs mass towed by truck	187
Figure 5.21 Model-predicted vs measured single battery voltage for LA92 cycle.....	189
Figure 5.22 Model-predicted vs measured single ultracapacitor voltage for LA92 drive cycle with HESS current command.....	190
Figure 5.23 Normalized energy storage system loss and range for LA92 drive cycle and three DP powersplit control cost minimization options.....	192
Figure 5.24 Battery RMS current for LA92 drive cycle and three DP powersplit control cost minimization options	193
Figure 5.25 Battery and ultracapacitor cycles for LA92 drive cycle and three DP powersplit control cost minimization options.....	193
Figure 5.26 Improvement in vehicle range achieved with HESS at 25°C for model which <i>does</i> and <i>does not</i> include extra mass due to addition of HESS	195
Figure 5.27 Increase in motor output power capability achieved at 25°C with HESS with 3000F ultracapacitor cells and 400A dc/dc converter.....	196
Figure 6.1 Measured range versus temperature for Nissan Leaf and Chevy Volt electric vehicles [135].....	199
Figure 6.2 Example of combination multiple current magnitude HPPC and LA92 HPPC testing to obtain resistance values utilized for low temperature modeling.....	201
Figure 6.3 Modeled versus measured battery voltage for -10°C case starting with 40Ah discharged	202
Figure 6.4 Methodology for performing multiple current magnitude HPPC resistance test	203
Figure 6.5 Discharge resistance versus HPPC pulse current magnitude for Calb 100Ah LiFePO4 battery at various temperatures	204
Figure 6.6 Charge and discharge pulse resistance at 10°C and 80Ah discharged for Calb 100Ah LiFePO4 battery.....	205
Figure 6.7 Resistance versus HPPC pulse current magnitude for Calb 100Ah LiFePO4 battery with 20Ah discharged	205

Figure 6.8 LA92 HPPC Test for 0°C	207
Figure 6.9 Comparison of open circuit voltage and resistance from HPPC tests	208
Figure 6.10 Open circuit voltage and nominal resistance values for example low temperature battery model calculation	211
Figure 6.11 Nonlinear resistance versus current characteristic, $R_{BV-table}$, for example low temperature battery model calculation	212
Figure 6.12 Maximum discharge current and power limit for example low temperature battery model calculation	213
Figure 6.13 Battery current and resisted calculated for example low temperature battery model calculation	214
Figure 6.14 Truck battery pack discharge and charge power capability calculated from Butler-Volmer model for 2.5V min and 3.6V max cell voltages.....	215
Figure 6.15 Butler-Volmer battery model calculated parameters for Calb cell at 0°C.....	219
Figure 6.16 Example of Butler-Volmer model predicted versus measured results for 0°C LA92 Calb battery test results	220
Figure 6.17 Current pulse waveforms and voltage measurement points for ultracapacitor charge and discharge resistance measurement test	221
Figure 6.18 Method for calculating capacitance from measured ultracapacitor voltage versus charge characteristic.....	222
Figure 6.19 Experimentally measured ultracapacitor discharge resistance and capacitance with 2 nd order polynomial curve fit for Maxwell BMOD165 at 0°C	222
Figure 6.20 Maxwell BMOD165 ultracapacitor discharged resistance versus temperature	223
Figure 6.21 Maxwell BMOD165 ultracapacitor capacitance versus temperature	224
Figure 6.22 Ultracapacitor model discrete time solution overlaid with continuous time solution for one second, 1000A current pulse	226
Figure 6.23 Ultracapacitor model output for current and power command examples	235
Figure 6.24 Ultracapacitor current command waveform repeated 1000 times to demonstrate conservation of charge in model	237

Figure 6.25 Ultracapacitor measured versus modeled results for LA92 drive cycle profile at 0°C	237
Figure 6.26 Ultracapacitor measured versus modeled results for LA92 drive cycle profile at 0°C	238
Figure 6.27 HESS battery amp-hours discharged versus number of iterative runs of DP algorithm for -10°C US06 and UDDS case	241
Figure 6.28 Commanded, HESS, and battery only output power for LA92 drive cycle at -10°C	242
Figure 6.29 HESS ultracapacitor voltage, current, and power for LA92 drive cycle at -10°C...	243
Figure 6.30 HESS ultracapacitor, battery, and total power and ultracapacitor voltage and current for selected portion of LA92 drive cycle at -10°C	244
Figure 6.31 HESS versus battery performance for HESS with 30F/270V ultracapacitor pack and 400A dc/dc converter rating.....	246
Figure 6.32 Battery only and HESS losses for HESS with 30F/270V ultracapacitor pack and 400A dc/dc converter rating.....	247
Figure 6.33 Performance improvements achieved with HESS for HESS with 30F/270V ultracapacitor pack and 400A dc/dc converter rating	248
Figure 6.34 Performance improvements achieved with HESS for a range of ultracapacitor pack energy ratings and a 400A rated dc/dc converter.....	249
Figure 6.35 HESS 5 second power capability at -10°C for 120, 200, and 300Wh of ultracapacitor energy storage	250
Figure 6.36 Performance improvements achieved with HESS for a range of dc/dc converter current rating and 300Wh ultracapacitor pack.....	251
Figure 6.37 HESS power capability at -10°C for 200A and 400A dc/dc converter rating with 300Wh ultracapacitor pack	252
Figure 7.1 Half bridge topology used for.....	257
Figure 7.2 Prototype DC/DC converter with components labeled	258
Figure 7.3 Measured inductance and measured versus modeled loss for prototype inductor	259

Figure 7.4 Modeled versus measured prototype dc/dc converter IGBT half bridge loss and full converter loss	260
Figure 7.5 DC/DC converter efficiency for 80Vdc bus as used in experimental testing and for 350Vdc bus as would be used in vehicle	260
Figure 7.6 Scale drawing of example 400A dc/dc converter	262
Figure 7.7 Example 400A dc/dc converter model calculated loss and efficiency	263
Figure 7.8 Scale drawing of Skeleton ultracapacitor pack with 400A dc/dc converter	265
Figure 7.9 Example 400A dc/dc converter model calculated loss and efficiency	266
Figure 7.10 Block diagram of HESS test setup	268
Figure 7.11 <i>Battery Pack</i> : 80V/100Ah LiFePO ₄ pack (24 series connected cells, 2/9 of truck pack).....	268
Figure 7.12 <i>Ultracapacitor Pack</i> : 48V/165F Maxwell module	268
Figure 7.13 Prototype 200A dc/dc converter	269
Figure 7.14 Measured dc/dc converter efficiency with 80vdc bus for various ultracapacitor pack voltages (V _{uc}).....	271
Figure 7.15 Measured battery and HESS temperature for continuously repeated LA92 drive ..	274
Figure 7.16 UDDS drive cycle speed profile, power calculated for electric truck, experimental testing profile with pauses, and experimentally measured temperature for profile with pauses	275
Figure 7.17 LA92 drive cycle speed profile, power calculated for electric truck, experimental testing profile with pauses, and experimentally measured temperature for profile with pauses	275
Figure 7.18 US06 drive cycle speed profile, power calculated for electric truck, experimental testing profile with pauses, and experimentally measured temperature for profile with pauses	276
Figure 7.19 Battery only and HESS efficiency for scaled system at 25°C, calculated with scaled system parameters in Table 7.10.....	277
Figure 7.20 Drive cycle power distribution and battery only and HESS efficiency for full scale system, calculated with full scale system parameters in Table 7.10, including 89% dc/dc converter efficiency	278
Figure 7.21 HESS battery, ultracapacitor, and total system power for first LA92 0°C drive cycle	279

Figure 7.22 Ultracapacitor current, voltage, and power for first LA92 0°C drive cycle	279
Figure 7.23 Battery voltage for battery only and HESS for first LA92 0°C drive cycle.....	280
Figure 7.24 Commanded, HESS, and battery only power for first LA92 0°C drive cycle.....	280
Figure 7.25 Measured battery temperature for each test case.....	281
Figure 7.26 Experimentally measured amp-hours consumed from battery pack for each test case and model estimated amp-hours for lossless battery only case	282
Figure 7.27 Summary of experimentally measured performance results for battery only and HESS tests.....	283
Figure 7.28 Experimentally measured motoring, regenerative braking, and total energy for all test cases.....	284
Figure 7.29 Experimentally measured distribution of battery and ultracapacitor motoring and regenerative braking energy for each HESS test case	285
Figure 7.30 Measured versus modeled ultracapacitor voltage for each HESS test case	287
Figure 7.31 Measured versus modeled battery RMS current for each test case	288
Figure 7.32 Experimentally measured cell voltage for LA92 25°C battery only test.....	288
Figure 7.33 Measured versus modeled battery amp-hours consumed for each test case	289
Figure 7.34 Modeled HESS versus battery only reduction in battery amp-hours consumed for experimental $\approx 89\%$ efficient dc/dc converter and for modeled $\approx 97\%$ efficient converter	291
Figure 7.35 LA92 and US06 0°C experimentally measured ultracapacitor voltage.....	292
Figure 8.1 Panasonic NCR18650PF LiNiCOMnO ₂ Battery	295
Figure 8.2 Comparison of CALB LiFePO ₄ and Panasonic LiNiCOMnO ₂ Pack Voltage and Resistance	298
Figure 8.3 Truck Panasonic battery pack discharge and charge power capability calculated from Butler-Volmer model	299
Figure 8.4 Measured versus modeled current and voltage for Panasonic NCR18650PF performing LA92 drive cycle power profile at 25°C.....	300
Figure 8.5 Measured versus modeled current and voltage for Panasonic NCR18650PF performing LA92 drive cycle power profile at 0°C.....	301

Figure 8.6 Battery only and HESS range for four drive cycles for electric truck with Panasonic battery pack	302
Figure 8.7 HESS versus battery performance for Panasonic Battery Pack and HESS with 375Wh ultracapacitor pack and 400A dc/dc converter rating	303
Figure 8.8 Battery only and HESS losses for Panasonic Battery Pack and HESS with 375Wh ultracapacitor pack and 400A dc/dc converter rating	304
Figure 8.9 Performance improvements achieved for Panasonic Battery Pack and HESS with 375Wh ultracapacitor pack and 400A dc/dc converter rating	304
Figure 8.10 Two examples of 40' electric buses in production	305
Figure 8.11 Torque and power versus engine speed for Cummins ISL 280 diesel engine [139]	307
Figure 8.12 Comparison of electric truck and electric bus road load power and energy	309
Figure 8.13 Speed and model calculated power profile for three bus drive cycles	310
Figure 8.14 Electric bus range improvement achieved with HESS at 25°C	312
Figure 8.15 Electric bus ESS and battery loss reduction achieved with HESS	312
Figure 8.16 Electric bus improvements in miles driven over battery lifetime with HESS and ultracapacitor cycles over approximate vehicle lifetime of 500k miles	313
Figure 8.17 Ford F150 from 97-03 as used for the prototype electric truck and current model year truck	315
Figure 8.18 Model calculated power profile for HWFET and UDDS drive cycles for 2015 MY Ford F150 electric truck with no load and with max GCWR mass of 17,100lb (7,759kg)	317
Figure 8.19 Model calculated power profile for LA92 and US06 drive cycles for 2015 MY Ford F150 electric truck with no load and with max GCWR mass of 17,100lb (7,759kg)	318
Figure 8.20 Battery only and HESS power for US06 drive cycle for 2015 MY Ford F150 electric truck with max GCWR mass of 17,100lb (7,759kg)	319
Figure 8.21 Battery only and HESS losses versus payload mass 2015 MY Ford F150 electric truck at 25°C	320
Figure 8.22 Range improvement achieved with HESS for 2015 MY Ford F150 electric truck at 25°C	321
Figure 8.23 Range achieved with HESS for 2015 MY Ford F150 electric truck at 25°C	321

Index of Tables

Table 2.1 Specifications for 2014 model year production EVs and UW-Madison electric truck	13
Table 2.2 Nissan Leaf Dynamometer Testing Results [8]	15
Table 2.3 Ford Focus EV Dynamometer Measured versus Modeled Energy Consumption [9] .	15
Table 2.4 CFD Modeled Drag Coefficient for Various Tesla Model S Wheel Designs [13]	17
Table 2.5 Suitable Energy Storage Ratings for Passenger Vehicles Less than 2000kg [1] (reference numbers indicated in table are for references in [1]).....	22
Table 2.6 Comparison of Three Battery and Ultracapacitor HESS System Topologies [94].....	24
Table 2.7 Advantages & Disadvantages of the Power Electronics Topologies shown in the above Figure 2.12 [96]	26
Table 2.8 DC/DC Converter Design Specifications & Resulting Passive Component Sizing [97]	27
Table 2.9 Electric Vehicle Hybrid Energy Storage Projects	31
Table 2.10 HESS and Battery Only Performance of a Scooter/Bicycle Drivetrain [23, 24]	34
Table 2.11 Electric Motorcycle Parameters Used in HESS Modeling [25].....	34
Table 2.12 Hybrid Electric Vehicle Hybrid Energy Storage Projects	48
Table 2.13 Electric Vehicle Power Split Control Projects	58
Table 2.14 Hybrid Electric Vehicle Power Split Control Projects	64
Table 3.1 Estimated Vehicle Mass and Drag Power Coefficients	79
Table 3.2: Component Efficiencies and Accessory Power for Model.....	80
Table 3.3: Predicted Electric F150 Energy Consumption	82
Table 3.4 Prototype IPM Machine Parameters	87
Table 3.5 Accessories Powered Off 12V System	93
Table 3.6 Equipment Powered Off High Voltage System.....	94
Table 3.7 Sensor Specifications	94
Table 4.1 Functional Description of System Cables.....	103

Table 4.2 Battery Cell and Pack Specifications.....	106
Table 4.3 Battery Management Board Specs	109
Table 4.4 Compact-RIO Module Specifications	111
Table 4.5 Measured Mass of Components Removed From Gas Truck.....	113
Table 4.6 Original vs Final Mass Estimate of Components Added to Truck.....	114
Table 4.7 Inertia of Rotating Components as Calculated from Solidworks Models in Appendix I	117
Table 4.8 Vehicle Mass and Inertial Equivalent Mass Parameter Values	118
Table 4.9 Experimentally Determined Drag Power / Road Load Coefficient	121
Table 4.10 Measured Motor Winding Resistance	124
Table 4.11 Rinehart Motion Systems PM150 Motor Drive Specifications	132
Table 4.12 IGBT Specifications	134
Table 4.13 Capacitor Specifications	134
Table 4.14 Semikron Semisel Simulation Settings.....	134
Table 4.15 Measured vs Modeled Motor and Drive Losses for Six Drives	141
Table 4.16 Predicted Electric F150 Energy Consumption.....	157
Table 4.17 Predicted vs Experimentally Measured Energy Consumption.....	159
Table 5.1 Estimated Drag Power Coefficients for Elec. F150 Truck	169
Table 5.2 Battery and Ultracapacitor Pack Specifications.....	174
Table 5.3 Calculated Energy and Power Consumptions for Four Cycles with Battery-Only and HESS Configurations.....	181
Table 5.4 Single Battery Cell Model-Predicted vs Experimental Results for LA92 Drive Cycle for Battery-Only and Hybrid ESS.....	189
Table 5.5 Single Ultracapacitor Model Predicted versus Experimental Energy for LA92 Drive Cycle Scaled for 2p100s Pack.....	190
Table 5.6 HESS Powersplit Control Cost Minimization Options.....	192

Table 5.7 Mass of Ultracapacitor and DC/DC Converter Systems for HESS	194
Table 6.1 Resistance versus HPPC pulse current magnitude for Calb 100Ah LiFePO ₄ battery with 20Ah discharged	206
Table 6.2 LA92 HPPC Resistance and Open Circuit Voltage for Calb 100Ah LiFePO ₄ Battery	209
Table 6.3 Butler-Volmer Model Inputs for Example Calculations.....	210
Table 6.4 Battery Model Implementation in Matlab – <i>Code can be Pasted Directly into a Matlab Script File and Run (ctl+enter)</i>	216
Table 6.5 Ultracapacitor Pack Specifications Provided by Manufacturer	220
Table 6.6 Ultracapacitor Pack Parameters at 25°C, 10°C, and 0°C.....	224
Table 6.7 Ultracapacitor Pack Parameters at -10°C, -20°C, and -30°C.....	225
Table 6.8 Definition of Ultracapacitor model inputs including parameters used in Matlab example	227
Table 6.9 Ultracapacitor Model Implementation in Matlab – <i>Code can be Pasted Directly into a Matlab Script File and Run (ctl+enter)</i>	231
Table 6.10 Ultracapacitor model output for current command case and for power command case where current command power output is used for power command input.....	236
Table 6.11 Definition of control input, cost, and state variable for HESS dynamic programming model.....	239
Table 6.12 Tables of input parameters for dynamic programming model.....	240
Table 6.13 Summary of Battery Only and HESS Performance for LA92 drive cycle at -10°C	245
Table 7.1 Prototype DC/DC Converter Specifications	257
Table 7.2 Example 400A DC/DC Converter Design Specifications	261
Table 7.3 Example 400A DC/DC Component Specifications Including Mass and Volume.....	262
Table 7.4 Example 400A DC/DC converter model calculated loss	263
Table 7.5 Skeleton SCHE3500 Ultracapacitor Pack Parameters [136]	265
Table 7.6 Skeleton ultracapacitor pack and 400A dc/dc converter	266

Table 7.7 Battery Pack Parameters	270
Table 7.8 Ultracapacitor Pack Parameters	270
Table 7.9 DC/DC Converter Specifications	271
Table 7.10 Fixed Parameters for Calculating HESS Discharging Power Split.....	272
Table 7.11 Test Plan for Scaled Battery Pack and Hybrid Energy Storage System	273
Table 7.12 Modeled versus Measured Reduction in Amp-Hours Consumed for HESS versus Battery Only Case	290
Table 8.1 LA92 HPPC Resistance and Open Circuit Voltage for Panasonic NCR18650PF Cell	296
Table 8.2 Resistance versus HPPC pulse current magnitude for Panasonic NCR18650PF battery with 0.58Ah discharged at 10°C and 0°C	296
Table 8.3 Resistance versus HPPC pulse current magnitude for Panasonic NCR18650PF battery with 0.58Ah discharged at -10°C and -20°C	297
Table 8.4 Panasonic and Calb Battery Cell and Pack Specifications for Electric Truck	297
Table 8.5 LA92 Drive Cycle Discharge Measured versus Modeled Amp-hours for.....	301
Table 8.6 Specifications for New Flyer Excelsior 40' Diesel Bus.....	306
Table 8.7 Specifications for Modeled Electric Bus Utilizing Components from Electric Truck	306
Table 8.8 Battery Pack Specifications for Modeled Electric Bus	308
Table 8.9 Electric Bus Road Load Drag Parameters.....	309
Table 8.10 Road Load Coefficients for Fully Loaded Electric Bus	309
Table 8.11 Selected Drive Cycle Parameters for Electric Bus.....	311
Table 8.12 Energy Storage System (ESS) Configurations Modeled for Electric Bus	311
Table 8.13 Comparison of Specifications for 2002 and 2015 Model Year Ford F150 Crew Cab 2-wheel Drive Trucks Configured for Maximum Towing Capability	315
Table 8.14 Specifications for 2015 Model Year Ford F150 Crew Cab 2-wheel Drive Truck Configured for Maximum Towing Capability	316

Table 8.15 Drivetrain Specifications for Electric Version of 2015 Model Year Ford F150 Truck	316
Table 8.16 Mass of 2015 Model Year F150 with Two Prototype IPM Machines and HESS ...	317
Table 8.17 Energy Storage System Configuration for 2015 Model Year F150.....	317

Chapter 1

Introduction

1.1 Motivation and Background

Gasoline- and diesel-powered vehicles have dominated motorized transit for many decades, but for a period in the early 1900s electric cars were competing successfully with the first gasoline-powered vehicles. The electric cars of the early 1900s, with their limited range and power, were eventually overtaken by gasoline cars as their technology improved. The domination of gasoline-powered cars has only recently begun to change, due primarily to major improvements in battery and electric traction system technology. This transition back to electrified technology is largely motivated by the world's limited supply of petroleum, urban air pollution, and serious concerns about the growing impact of greenhouse gas emissions. The transition is also motivated by the inefficiency of gasoline-powered cars, in which as much as 80% of the energy in the liquid fuel ends up as thermal losses, as shown in Figure 1.1.

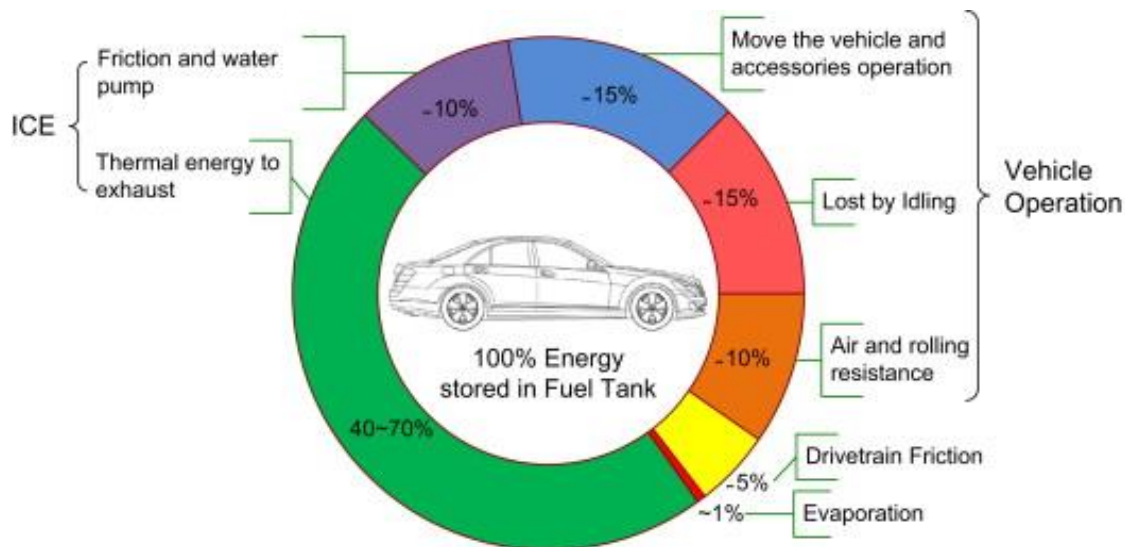


Figure 1.1 Gasoline engine vehicle's distribution of energy [1]

Although plug-in vehicles are vastly superior at converting their electrochemically-stored energy to tractive power, with 80% or more of the electrical energy being converted to mechanical energy, they are still typically powered from the electric grid. Presently, the U.S. electric grid is predominantly powered by fossil fuels, with coal accounting for 45% of electric power generation, natural gas for 24%, and emissions-free sources for 31% (i.e., nuclear, hydro-power, and renewable energy) [2]. The breakdown of sources is reflected in Figure 1.2, which shows that the greenhouse gas emissions of an electric vehicle (EV) driven in Wisconsin are equivalent to that of a gasoline car achieving 40 miles per gallon (MPG), and that in many states EV equivalent emissions are 70MPG or higher. This illustrates that there is already a compelling case for EVs, and that the case will only grow as emissions-free electric generation increases and electric vehicle traction system technology improves.

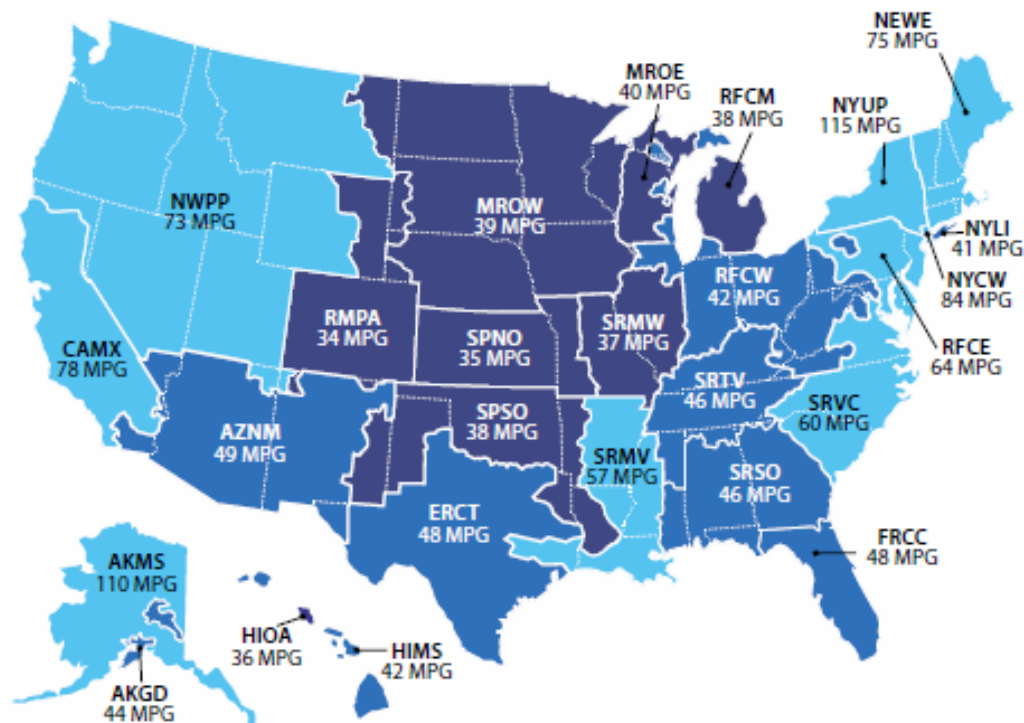


Figure 1.2 Electric vehicle's MPG greenhouse gas equivalence to gasoline-powered vehicles based on electric grid emissions [2]

The greater efficiency of electric traction systems, along with relatively low greenhouse gas emissions and the displacement of liquid transportation fuels with electricity, all motivate the transition to plug-in vehicles, which is already under way with over 375,000 plug-in vehicles sold in the U.S. since December of 2010 [3]. Many new technologies and system designs have enabled this transition.

1.2 Research Problem Statement

Attention in industry as well as academia has been primarily focused on the development of electric traction systems for passenger vehicles. As will be discussed more thoroughly in Chapter 2, there is very little technical literature devoted to the electrification of light-duty Class 2a trucks. Pickup trucks and similar vehicles present special opportunities and challenges that have not been thoroughly discussed in the open literature. This poses a problem for both research and development engineers who are faced with the task of designing one of these vehicles.

One of the very real technical challenges faced by designers of electric traction systems for Class 2a trucks is meeting both the energy and power requirements for the vehicle. Although the challenges associated with achieving both long driving ranges and fast acceleration is a design problem for nearly all passenger vehicles as well, the challenge is even more severe for Class 2a trucks because of the heavier loads that they are expected to carry while still meeting range and acceleration specifications. It is well-known that hybrid energy storage systems represent one of the candidate approaches for meeting both the energy and power requirements. However, here again, there is very limited information available in the technical literature that specifically address HESS applications in Class 2a light-duty trucks (see Chapter 2 for more details).

The work in this dissertation aims to contribute to plug-in vehicle technology by thoroughly documenting the design, modeling, fabrication, and testing processes for the development of a

plug-in electric light-duty Class 2a truck (i.e., pickup truck), and by advancing the state-of-the-art in hybrid energy storage technology that is targeted for this vehicle class.

1.3 Research Objectives and Technical Approach

This dissertation focuses on addressing two research objectives: (1) design and evaluation of an electric traction drive and other electrified subsystems for a Ford F150 pickup truck; and (2) application of a battery and ultracapacitor hybrid energy storage system (HESS) to the electric truck and to other vehicles. This work began in January of 2011 with the task of converting a gas-powered, 2002 model year Ford F150 truck to a fully-functional electric truck. Several design goals were identified for the electric truck conversion, including: 1) achieving power and wheel torque ratings that are similar to those of the gas-powered truck; 2) achieving similar driving range to the 2011 battery-electric Nissan Leaf EV (73 miles); 3) utilization of technology similar to that used in production electric vehicles; and 4) the incorporation of a large number of sensors to make the vehicle a rolling laboratory.

After the design was complete and the traction system was built and installed, the next goal was to develop a detailed electromechanical model of the prototype vehicle, in order to verify it with on-the-road experimental data. An additional goal was to use the developed model to evaluate the application of other technologies to the vehicle, such as hybrid energy storage or alternative motor and battery technologies. Similar work could be performed in the lab, but several million dollars of lab equipment would be needed to test a full-scale traction system as thoroughly as has been done in the truck with a much more modest budget.

Electrifying a Ford F150 offers a unique design challenge because, unlike the available compact and mid-size production electric cars, the truck is much larger and heavier, must be capable of towing, and requires a significantly higher continuous traction system power rating. An additional

unique aspect of the electric research truck compared to production and prototype vehicles is the incorporation of high-accuracy, automated sensors into the traction system, including an in-line torque sensor connected to the machine's rotor shaft. These aspects of the truck make the design process, which is thoroughly documented in this dissertation, particularly interesting and useful to other researchers and vehicle designers. Additionally, because this is the first case of a full-size Class 2a electric truck design appearing in the literature, the documented performance of the vehicle serves as a benchmark for future projects.

The developed electric truck design incorporates many technologies utilized in other EVs including an interior permanent magnet (IPM) synchronous traction machine, a liquid-cooled three-phase regenerative traction inverter drive, a LiFePO_4 battery pack, and a 6kW charger with a J1772 charge port. However, the vehicle also includes one feature that is more unusual for an EV – a two-speed gearbox. The complete traction system is modeled, including a finite element analysis (FEA) model of the traction machine, a loss model of the motor drive, and a state-of-charge-dependent loss model for the battery. This full traction system model is necessary to determine the maximum machine output power, which is a function of the battery pack voltage, as well as to calculate the battery, machine, and drive losses for a drive cycle.

The traction system model accuracy is confirmed using on-the-road data, and traction system efficiency for both gears is modeled for constant speed and for various drive cycles, and optimal gear selection based on traction system efficiency is modeled as well. The developed model, which includes full efficiency maps for the machine and drive, is much more detailed than that which is typically presented in the literature for electric vehicles. It provides significant insights into how much energy is dissipated as machine, drive, and battery pack losses, giving a baseline for how much system efficiency will increase due to an improvement to any of these systems.

As mentioned earlier, one of the additional purposes of designing the electric truck is to use it as a platform for developing new electric vehicle technologies that have potential to significantly improve vehicle performance. In this work, the developed truck is used as a platform for evaluating one proposed technology, hybrid energy storage, which is the combination of two or more energy storage sources. Hybrid energy storage is used to address one of the most common challenges in electric vehicles: designing the battery pack to provide the power, energy, and cycle life needed for the application. By adding an ultracapacitor pack to the battery pack and hybridizing the system, the ultracapacitor pack can be used to provide much of the power needed to accelerate and brake the vehicle, leaving the battery pack to provide the average power drawn by the vehicle. The hybrid energy storage system (HESS) offers many potential benefits over a battery-only system, including: (1) increased vehicle range due to reduced energy storage system losses; (2) reduced battery pack losses resulting in reduced battery heating and aging; (3) reduced battery cycling due to regenerative energy going to the ultracapacitor; (4) increased dc bus voltage leading to increased traction drive output power capability; and (5) greatly improved low-temperature performance due to ultracapacitor's excellent low-temperature characteristics.

While the potential benefits of an HESS are quite compelling, the HESS design benefits must be sufficient to justify the high cost and low energy density of ultracapacitors. To determine just how large the ultracapacitor pack must be to achieve most of the design benefits, the electric truck is modeled both with and without an HESS for several ultracapacitor pack sizes, and the potential system benefits discussed above are presented. The ideal, optimal power split between the battery and ultracapacitor pack is determined using dynamic programming, and it is compared to the power split calculated by a rule-based control which uses an analytical solution of minimized system losses.

A significant effort is also made to investigate HESS performance benefits at low temperatures, for which the battery pack in a typical EV must be heated at the expense of vehicle range in order to maintain sufficient power capability. Low-temperature ultracapacitor and battery models are developed, and the candidate ultracapacitor and battery cells are tested over a wide range of temperatures to provide the model parameters. The HESS performance is then evaluated over a range of temperatures, and several benefits which contribute to improved vehicle performance and range are quantified, including (1) reduced motoring power limiting, (2) improved regenerative braking energy capture, and (3) reduced battery and energy storage system losses.

A scaled hybrid energy storage system is then built to verify the model accuracy and to demonstrate how an actual system, including the dc/dc converter and controls, can be implemented. The scaled HESS consists of an 80V LiFeP₀₄ battery pack made of cells from the electric truck, a 48V, 165F ultracapacitor pack, and a prototype 200A rated dc/dc converter. The scaled HESS is tested by drawing drive cycle power profiles from the HESS unit with battery test equipment that is available in the laboratory. The system is additionally tested at low temperature by placing it in a large thermal chamber.

The final portion of the work demonstrates that the developed HESS modeling methodology is also applicable for variants in vehicle design and type. First, the electric truck is modeled with a different battery pack consisting of Panasonic NCR18650PF LiNiCOMnO₂ cells. Then a heavy-duty electric city transit bus is modeled, and, finally, an electric truck with a much higher drivetrain power rating and higher towing capability is modeled. The modeling methodology can also be adapted for application to hybrid, start/stop, and fuel cell vehicles, but this work has not been carried out in this research program.

1.4 Document Organization

This dissertation is organized into nine chapters, with the first chapter providing the motivation and introduction to the work. Chapter 2 presents a state-of-the-art review that focuses primarily on the state of hybrid energy storage research in the world today, together with a discussion of the more limited technical literature that is devoted to the design, fabrication, and testing of electric vehicles which is relevant to the work in this dissertation on Class 2a trucks.

The electric truck traction system design, including lab testing of the prototype traction motor, a simplified vehicle model, and a preliminary prediction of vehicle range and performance, is presented in Chapter 3. The demonstrator truck, based on the design presented in Chapter 3, is then fabricated and built and the final design is presented in Chapter 4. Detailed machine, drive, and battery loss models are then developed, experimentally verified, added to the vehicle model, and used to develop accurate predictions of vehicle performance which are also presented in Chapter 4.

In Chapter 5 the battery and ultracapacitor hybrid energy storage system model for 25°C is developed for the electric truck and evaluated for several drive cycles and ultracapacitor pack sizes for both rule-based and optimized dynamic programming control. In Chapter 6 a low-temperature battery model that includes the Butler-Volmer effect is developed and a low-temperature ultracapacitor model is also developed. The low-temperature models are then incorporated into the system model, and the HESS low-temperature performance is thoroughly evaluated.

A demonstrator hybrid energy storage system is designed and built in Chapter 7, and the system is tested at 0°C and 25°C. The HESS modeling methodology is then applied for three vehicle design variants in Chapter 8, including a truck with a different battery type, an electric city transit bus, and a truck with a higher power drivetrain.

The work concludes in Chapter 9 with a discussion of the key contributions that have been made to electric vehicle research regarding light-duty electric trucks and hybrid energy storage energy storage systems. Opportunities for future research that builds on the results achieved during this research program are also discussed.

Chapter 2

State of the Art

2.1 Production Electric Vehicles

Electric vehicles were first available in the early 1900s, with models available from Detroit Electric, Baker Electric, and others. These vehicles were early competition for gasoline powered vehicles, but eventually fell out of favor due to the advent of the electric starter and other improvements to gasoline powered vehicles. Electric vehicles did not again become publicly available until the mid-90s, when a California mandate requiring all automakers to sell zero-emissions vehicles resulted in GM developing the purpose built EV1, and with other automakers developing electric versions of their gas powered offerings. These EVs were only available in California, and had somewhat limited range and power performance due to the state of battery, power electronics, and electric motor technology at the time.

California, aided by plug-in vehicle incentives from the U.S. Federal Government, has again helped to usher in a new era of EVs, with strict requirements for automakers to sell plug-in vehicles, with a financial penalty of \$5,000 per vehicle not produced if the required quota is not met. The first vehicles of this new modern era of plug-in vehicles, the Nissan Leaf and Chevy Volt, entered production and became publicly available in December of 2010, and both vehicles have gone on to sell more than 50,000 total in the U.S. Compared to the earlier eras of EVs in the early 1900s and the 1990s, these and other currently available vehicles are remarkably successful, well received vehicles, mostly due to huge improvements in battery and electric traction drive technology, and to large investments by traditional automakers as well as the new electric only automaker, Tesla.

All eleven of the 2014 model year production electric vehicles are shown Figure 2.1, along with the electric truck designed and built for this dissertation. In addition to the pure electric vehicles focused on here, there are many plug-in hybrids available as well, such as the Chevy Volt, Prius plug-in, Ford Focus and C-Max plug-in, and others which all have electric ranges varying from about 10 to 40 miles.



Nissan Leaf



Tesla Model S



Mitsubishi iMIEV



Chevy Spark EV



Smart EV



Ford Focus EV



BMW i3



Fiat 500 EV



Toyota Rav4 EV



Mercedes

B-Class EV



UW-Madison

Electric F150



Honda Fit EV

Figure 2.1 2014 model year production electric vehicles and UW-Madison electric truck

These production electric vehicles have many similarities – they are all relatively small vehicles, they all have a single, fixed gear ratio, their range is between 60 and 90 miles, except for the Rav4 with 100 miles of range and the Tesla's with 200 miles or more of range, as shown in Table 2.1

below. The vehicles also have many technology similarities, all utilizing either permanent magnet or induction machines, silicon IGBT traction drives, and lithium battery packs of various chemistries. When digging deeper into their designs though, there are many technology differences and innovations which truly represent the state of the art of electric vehicle design, and distinguish the designs of several of the vehicles from the competition. A few notable innovations include: (1) the use of carbon fiber reinforced plastic and an aluminum frame to construct the BMW i3, (2) the use by Tesla of the most energy dense available batteries, Panasonic NCR18650 cells, to create a flat battery that sits below the floor of the vehicle and enables much greater range than the competition, and (3) the use of a high torque, low speed bar wound electric machine to increase motor efficiency in the Chevy Spark EV, allowing for a light vehicle with almost as high of performance as the \$15k more expensive BMW i3.

Most of the production electric vehicles also have a power rating of around 100kW, a torque rating around 200Nm, a gear ratio around 10:1, a battery pack with about 20kWh of energy storage, an energy consumption rating of about 100mpge, and a mass of about 3000lb, as shown Table 2.1. There are of course many outliers, which illustrate the range of vehicle capabilities available. The electric truck's capabilities are also outlined in Table 2.1, and it is shown to be unique from the production vehicles in several ways: it has higher power than all but the Tesla's, it is the only vehicle with two gears – which was necessary to achieve sufficient wheel torque for towing, it is the heaviest vehicle due to its large size and heavy traction system, it's machine has higher torque than all but the Chevy Spark EV, and it has higher wheel torque - the product of motor torque and gear ratio – than any of the other vehicles. The truck also has some similarities, with a similar predicted range to many of the production EVs, and a battery pack which is not too much larger than that in most of the EVs, but much smaller than the Tesla's battery pack.

Table 2.1 Specifications for 2014 model year production EVs and UW-Madison electric truck

Manufacturer/ Model	Power/Torque	Gear Ratio	Battery (kWh)	Range (miles)	MPGe (comb)	MSRP	Curb Wt (lb)
Mitsubishi iMIEV	49kW/196Nm	7.07	16	62	112	\$23k	2,579
Smart EV	55kW/130Nm	9.92	17.6	68	107	\$25k	2,094
Honda Fit EV	92kW/256Nm	8.06	20	82	118	\$37k	3,252
Chevy Spark EV	97kW/542Nm	3.17	21	82	119	\$27k	2,989
BMW i3	132kW/250Nm		22	81	124	\$41k	2,799
Ford Focus	106kW/250Nm	7.82	23	76	105	\$29k	3,640
Fiat 500EV	83kW/199Nm	9.59	24	87	116	\$32k	2,980
Nissan Leaf	80kW/254Nm	7.94	24	84	114	\$29k	3,256
Mercedes B-Class EV	132kW/340Nm	-	28	87	84	\$41k	3,900
UW-Madison Electric F150	135kW/460Nm	10.65/ 3.55	35	88*	78*	\$∞	5,940
Toyota Rav4 EV	114kW/370Nm	9.73	41.8	103	76	\$50k	4,032
Tesla Model S (60kWh)	225kW/430Nm	9.73	60	208	95	\$70k	4,464
Tesla Model S (85kWh)	270kW/441Nm	9.73	85	265	89	\$80k	4,647

*Range & MPGe for electric truck are calculated directly from HWFET & UDDS, rather than from the 5-cycle EPA test as is done for all production automobiles, 5-cycle numbers would likely be 10-20% lower

2.2 Brief Overview of Electric Vehicle Traction System Design and Modeling

Vehicle modeling is necessary to determine the power and energy required for a drive cycle. A vehicle model consists of a balance between the force provided by the traction system and the mechanical forces acting on the vehicle – primarily aerodynamic, tire drag, and acceleration forces. Additionally the model must account for traction system losses, power to heat and cool the vehicle, and accessory system power. With a well done vehicle and traction system model, the vehicle's fuel economy and vehicle performance can be accurately predicted.

Vehicle modeling has been used extensively in the literature, and is commonly taught in courses using texts such as *Theory of Ground Vehicles*, which was referenced regularly for the work

presented in this dissertation [4]. Several examples of work utilizing vehicle modeling are presented in this subsection, but a more thorough discussion of vehicle modeling and design is provided in work which precedes this dissertation - a master's thesis on the modeling of a Corbin Sparrow electric vehicle [5]. The vehicle modeling examples provided here illustrate the scope of how vehicle modeling can be used to predict vehicle performance, to corroborate a model with experimental data, to predict benefits of aerodynamic improvements, and to predict the effect of climate control on vehicle range.

There are several examples of work on modeling vehicles and experimentally verify their performance, as is done for the electric truck in Chapter 3 and Chapter 4 of this dissertation. Ukaew develops a model of a small electric pickup truck, with assumptions of constant motor and drive efficiency, and models some basic vehicle performance metrics [6]. De Gennaro et al forgo vehicle modeling and perform extensive dynamometer testing on an electric vehicle with very similar specifications to the Mitsubishi iMIEV, showing the vehicle range, drivetrain efficiency, and effect of air conditioning on range for several different drive cycles [7]. Dynamometer and on the road testing is performed by Idaho National Labs for a Nissan Leaf electric vehicle, and a large selection of performance results are provided, including UDDS, HWFET, and US06 range for several different temperatures and energy consumption for constant speed as shown in Table 2.2 [8].

In the most thorough work in this area, Lee et al of Argonne National Labs develop a detailed model of a Ford Focus electric vehicle from experimental test data collected on a vehicle dynamometer [9]. Several different drive cycles are then performed on the dynamometer, and the vehicle model is shown to predict vehicle energy consumption very accurately, with an error of 4.2% or less as shown in Table 2.3. This Ford Focus EV modeling and testing effort demonstrates

that with a vehicle model similar to that developed in Chapter 4 of this dissertation it is possible to estimate vehicle performance with a high level of accuracy.

Table 2.2 Nissan Leaf Dynamometer Testing Results [8]

<u>Cycle Results¹⁰</u>			
	72 °F	20 °F	95 °F + 850 W/m ²
UDDS (Cold Start)	211.7 Wh/mi	458.7 Wh/mi	293.5 Wh/mi
UDDS	201.4 Wh/mi	369.1 Wh/mi	274.5 Wh/mi
HWFET	240.8 Wh/mi	349.9 Wh/mi	272.1 Wh/mi
US06	321.6 Wh/mi	425.7 Wh/mi	359.8 Wh/mi
SC03	N/A	N/A	289.3 Wh/mi
City Range	110.9 miles	US06 Range	68.2 miles
Highway Range	92.7 miles		

Energy Consumption at Steady-State Speed, 0% Grade

10 mph	133.4 Wh/mi	50 mph	236.0 Wh/mi
20 mph	147.1 Wh/mi	60 mph	285.4 Wh/mi
30 mph	168.0 Wh/mi	70 mph	343.8 Wh/mi
40 mph	197.6 Wh/mi	80 mph	397.8 Wh/mi

Table 2.3 Ford Focus EV Dynamometer Measured versus Modeled Energy Consumption [9]

<u>Test Results</u>			<u>Autonomie Simulation</u>		
Driving Cycle	Test #	Electric Consumption [DC Wh/mile]	Electric Consumption [DC Wh/mile]	Discrepancy to Test Results	Initial SOC (Estimated)
WOT X 4	57	353	344	-2.3%	95.1%
UDDS #1	70	178	172	-3.4%	94.8%
UDDS #2	72	168	172	+2.1%	80.7%
UDDS #3	77	166	172	+3.5%	40.8%
UDDS #4	79	166	172	+3.7%	25.2%
HWY #1	71	200	199	-0.5%	89.6%
HWY #2	78	196	199	+1.8%	34.9%
US06 #1	73	282	270	-4.2%	75.3%
US06 #2	76	278	270	-2.8%	50.3%
SSS #1	75	209	213	+2.1%	66.6%
SSS #2	80	210	213	+1.8%	19.1%

In papers from General Motors by Hawkins and Schieffer et al, the design of the Chevy Spark EV drivetrain is thoroughly documented, and vehicle modeling is utilized to show in Figure 2.2 that the city range of the vehicle can be increased by about 5 miles if a 3.87:1 gear ratio were used in place of the 3.17:1 gear ratio utilized in the production vehicle [10, 11]. The Chevy Spark drivetrain is unique compared to other production EVs because it was designed with a high-torque low-speed electric motor, with a 3.17:1 gear ratio rather than an 8:1 or greater ratio as used in other production EVs. This design choice was made to reduce motor losses at higher speeds and increase vehicle range, as is discussed in [10]. The motor efficiency is shown in Figure 2.2 to be greater than 92% over much of the operating range, and the unique coaxial motor and gearbox system which connects directly to the vehicle front axle is illustrated in Figure 2.3. The level of system design detail presented is unusual for a production vehicle, and gives a lot of insight into how to design a high efficiency, torque and power dense electric drive system.

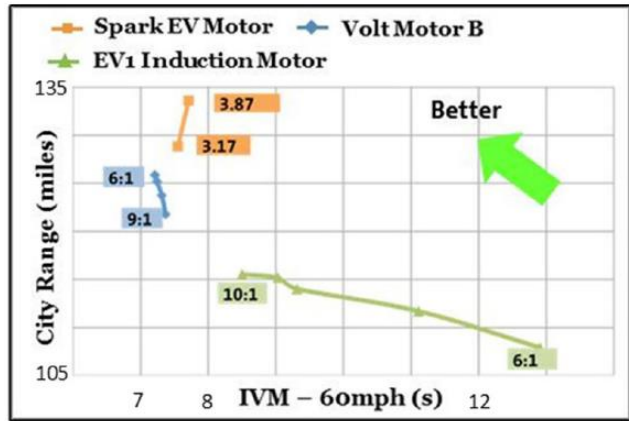


Figure 2.2 Chevy Spark EV motor power and efficiency [10]

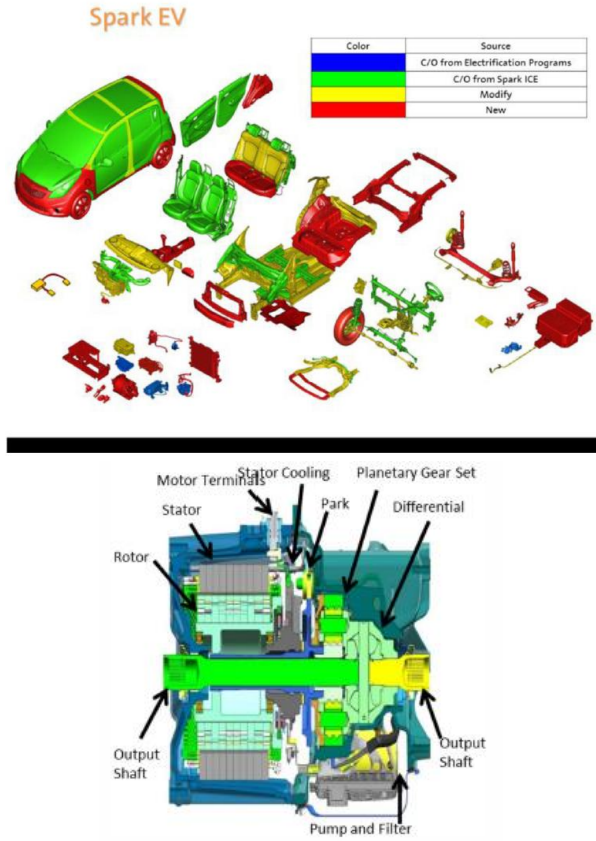


Figure 2.3 Chevy Spark EV full vehicle and motor and gearbox CAD drawings [10, 11]

Another work by Palin and D’Hooge et al of Tesla documents the process of modeling the Model S’s aerodynamic drag in a computational fluid dynamics program and experimentally verifying the model with a full size foam and steel model vehicle in a wind tunnel [12, 13]. Several design variations which reduced drag were investigated, and the effect of the various front grill air vents on the vehicle drag was investigated as well and is shown in Figure 2.4, which shows that the air vents are responsible for about 8% of the total aerodynamic drag coefficient of 0.247. An aerodynamic wheel set was also developed was also designed and is shown in Table 2.4 to reduce the aerodynamic drag a further 9% to 0.225. The production intent aerodynamic wheel, which was available for a period of time as an option for the Model S, is shown in Figure 2.5.

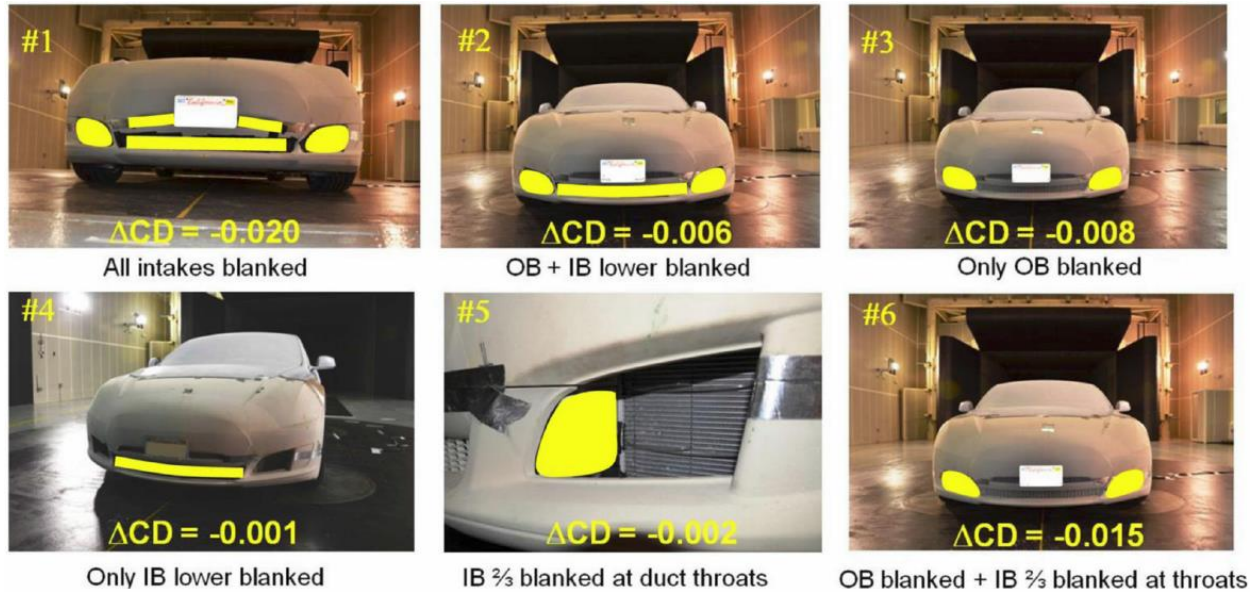


Figure 2.4 Tesla Model S EV measured coefficient of drag improvements for blanking of different air vents [12]

Table 2.4 CFD Modeled Drag Coefficient for Various Tesla Model S Wheel Designs [13]

Wheel Style	Translational Drag (C_D)	Rotational Moment (N-m)	Rotational Drag (C_D)	Total Drag (C_D)
Standard 19"	0.227	10.1	0.020	0.247
Standard 21"	0.244	6.3	0.013	0.257
Concept 1	0.238	4.7	0.009	0.247
Concept 2	0.236	5.1	0.010	0.246
Concept 3	0.223	4.6	0.009	0.232
Parametric Optimized	0.214	3.6	0.007	0.221
Production Intent	0.217	4.1	0.008	0.225



Figure 2.5 Production intent Tesla Model S aero wheel [13]

One additional important modeling topic is the effect of the climate control system on vehicle range. Due to the relatively low power needed to maintain constant speed in EV, typically in the range of 10 – 20kW, the climate control system, which can draw up to 5-6kW, has a large effect on vehicle range. Samadani et al develop a thermal model of an electric vehicle cabin and a model of the cooling system, and use a full electric vehicle model to show that using the air conditioning

reduces vehicle range for the highway drive cycle from about 115km to 80km, as shown in Figure 2.6 [14]. Gao of Ford Motor Company also developed a climate control model for an electric vehicle to examine how the climate control system effects vehicle range prediction algorithms [15]. These studies on climate control power consumption illustrate that a climate control model is necessary to fully characterize the performance of an electric vehicle.

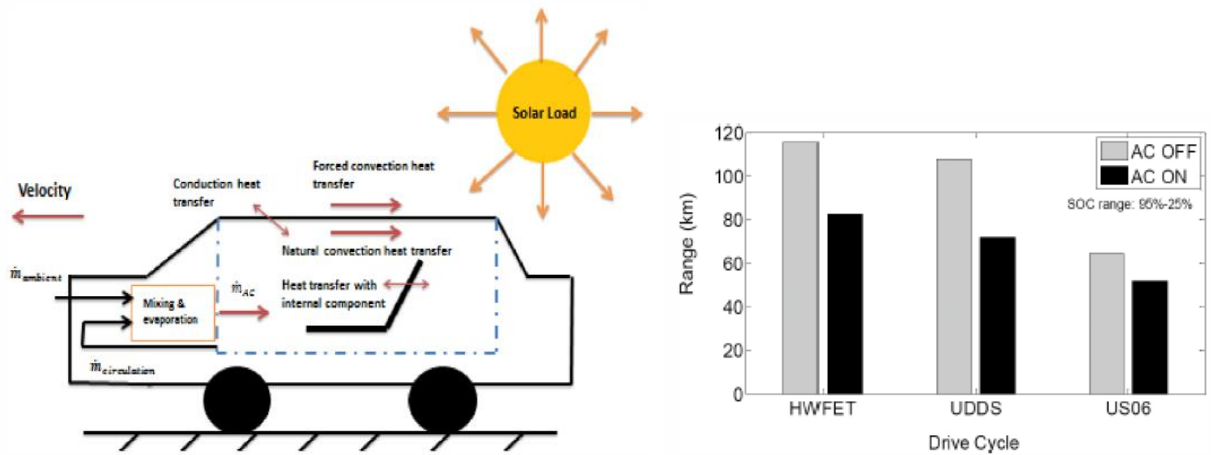


Figure 2.6 Thermal model of electric vehicle cabin and predicted vehicle range with and without use of AC [14]

2.3 Introduction & Overview of Hybrid Energy Storage

Hybrid energy storage is the concept of combining two or more energy sources with the goal of creating an improved energy storage system design. Typically a power dense and an energy dense storage source would be combined, such as an energy battery combined with a power battery, a flywheel, or an ultracapacitor pack. Often a power converter is utilized to control the power flow from one or more of the energy storages, as illustrated in Figure 2.7, which outlines the components and energy/power densities used in a typical battery and ultracapacitor hybrid energy storage system.

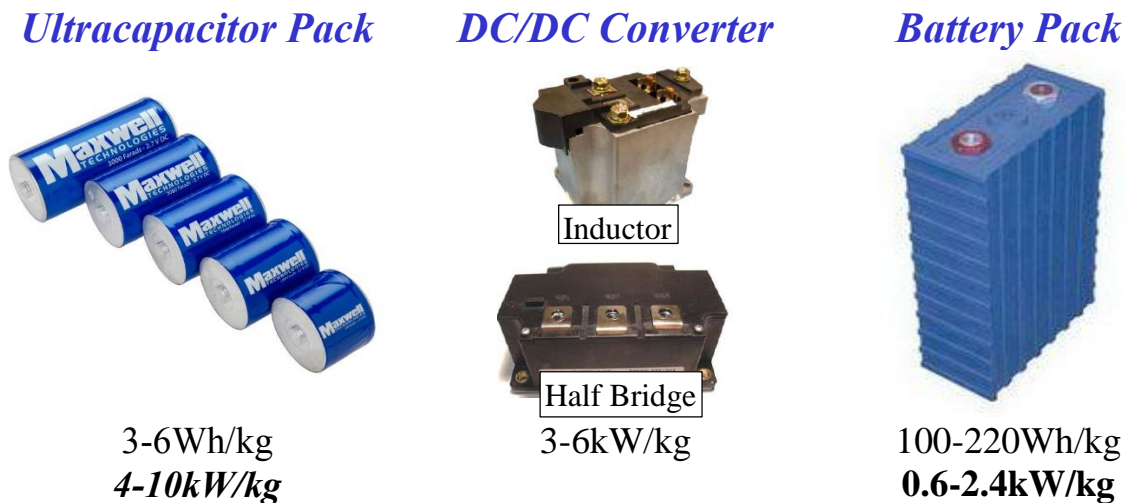


Figure 2.7 Example hybrid energy storage system w/ typical ranges of energy/power density

Hybrid energy storage has been actively studied as a concept for use in vehicles for more than a decade, is just starting to see some commercial applications, such as Peugeot's e-HDi micro-hybrid system introduced in 2010 [16, 17], the Lamborghini Aventador's micro-hybrid system [18], and the Philadelphia Transit System's off board regenerative braking system [19], all of which are shown below in Figure 2.8. The Peugeot and Lamborghini both utilize a lead acid battery and small ultracapacitor pack, with the 5V/600F ultracapacitor pack in the Peugeot application storing just 4Wh. Peugeot engineers state that utilizing the ultracapacitor pack to aid

in engine starting has allowed them to downsize from a 100Ah to a 70Ah lead acid battery, saving room under the hood of the vehicle while reducing vehicle weight and improving starting performance [16]. The Philadelphia Transit application will supplement a 1.5MW rated lithium battery installation with a large ultracapacitor installation to improve the battery pack's ability to capture regeneration power from the trains as well as to improve the system's ability to provide frequency regulation services to the local grid [19].



Figure 2.8 Commercial applications of hybrid energy storage [16-19]

Several review papers [1, 20, 21] examine different energy storage components, the variety of electrified vehicle, hybrid energy, and power electronics topologies, as well as the different types of energy management strategies. A summary of the various battery and ultracapacitor hybrid energy storage topologies is shown in Figure 2.9, where (a) has a passive connection of the two energy storage sources to the dc bus of the drive, (b) and (c) have a partially decoupled connection to the dc bus, and (f) – (g) have fully decoupled connections from the dc bus. A discussion of power topologies as well as some of the benefits of different hybrid energy storage topologies is

provided in section 2.4, and the topology shown in (c) is chosen for the electric truck application developed in this study.

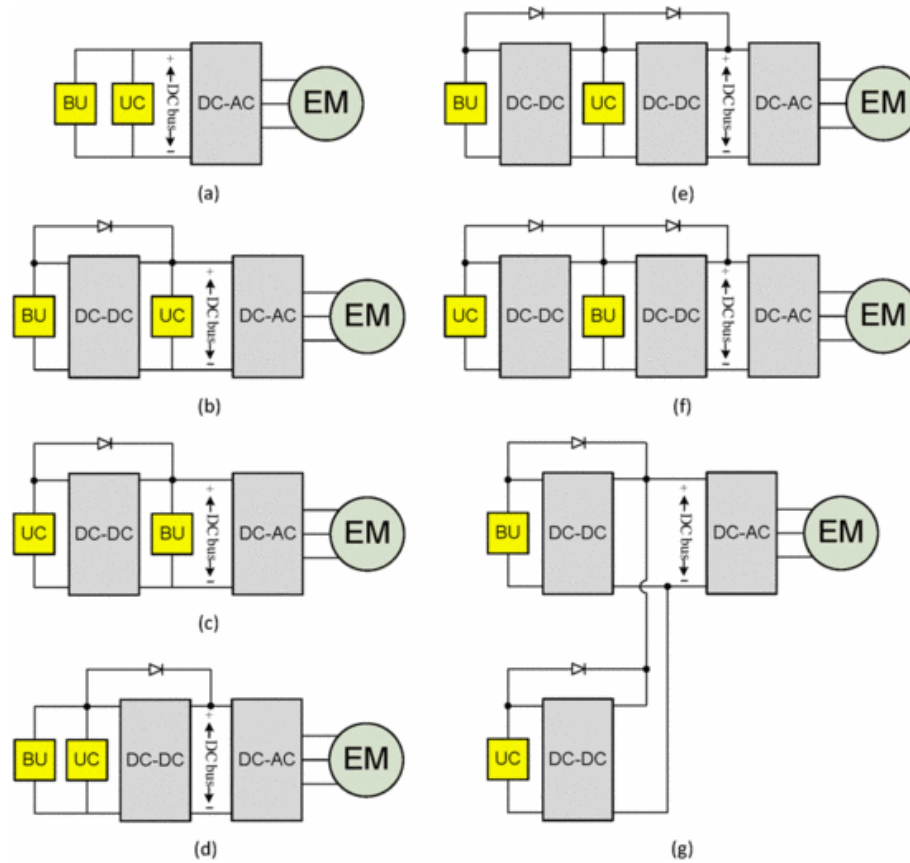


Figure 2.9 Battery (BU) and ultracapacitor (UC) hybrid energy storage topologies [21]

Hybrid energy storage can be utilized in any vehicle which utilizes energy storage, including hybrid electric vehicles, electric vehicles, and fuel cell vehicles with energy storage, all of which are shown in Figure 2.10 below. Hybrid energy storage can even be used to improve starting performance of traditional gas powered non-hybrid and micro-hybrid vehicles, as is done in the Peugeot and Lamborghini vehicles discussed earlier. Many research projects have focused on applying hybrid energy storage to these different types of vehicle powertrain topologies, as well as to many different types of vehicles ranging from motorcycles to three-wheeled auto rickshaws,

passenger vehicles, buses, and metro railcars [22-64]. The variety of research projects, some of which have been experimentally verified on the road, are outlined in section 2.5.

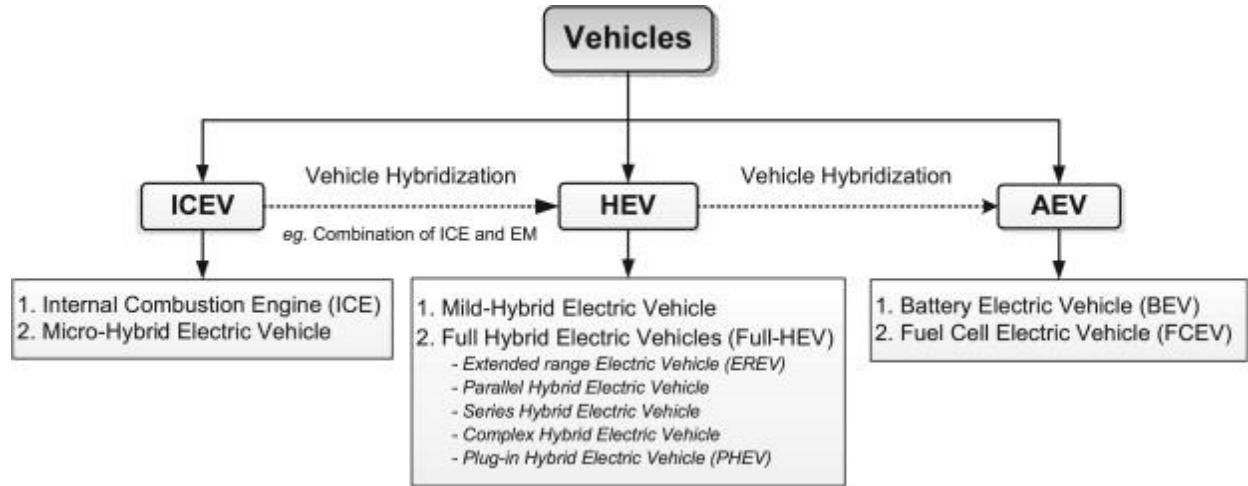


Figure 2.10 Vehicles which hybrid energy storage can be applied to [1]

The approximate amount of battery and/or ultracapacitor energy storage required for different vehicle powertrain configurations as determined by Tie in [1] is shown in Table 2.5. The ultracapacitor packs, which are presumably designed to replace the battery in micro, mild, and full-HEVs and to complement the battery in the EV, is sized from a modest 30Wh for the micro hybrid, up to a large 300Wh pack for the EV. Assuming a typical ultracapacitor energy density of 5Wh/kg, the cells for the proposed EV ultracapacitor pack would weigh a total of 60kg, a significant added mass for the vehicle, which requires that sizing of the ultracapacitor be carefully considered.

Table 2.5 Suitable Energy Storage Ratings for Passenger Vehicles Less than 2000kg [1]
(reference numbers indicated in table are for references in [1])

Class of HEV[19]	System voltage (V)	Battery (kWh)	UC		Fuel cell		EM or integrated starter-generator (ISG) (kW)
			Energy (W h)	Peak power (kW)	Energy (kWh)	Peak power (kW)	
Conventional ICE	12	–	–	–	–	–	–
Micro-HEV	12–42	0.02–0.05	30	6	–	–	3–5
Mild-HEV[13]	150–200	0.125–1.2	100–150	35	–	–	7–12
Full-HEV [20]	200–350	1.4–4.0	100–200	–	–	–	40
PHEV[21,22]	300–500	6.0–20.0	100–200	28–45	–	–	30–70
AEV[22]	300–500	20.0–40.0	300	28–45	150–200	50–100	50–100

Energy management strategies, which are used to determine the amount of power each energy source supplies, are discussed in detail in review papers [1] and [21]. There are two general types of energy management strategies: rule based and optimization approaches, as shown Figure 2.11 below. Rule based controls choose power based on some set of rules, which may for example split power in a fixed manner, based on frequency, or based on an analytical calculation of maximum efficiency, while optimization based approaches aim to optimize an objective such as minimized system losses. There is a large body of work developing, evaluating, and comparing these different rule based and optimization approaches [65-93], which is examined here in section 2.6. Additionally a deterministic rule-based control method and a global optimization approach utilizing dynamic programming are implemented for the electric truck application studied for this project, with the details for these control methods described in sections 5.4 and 5.5.

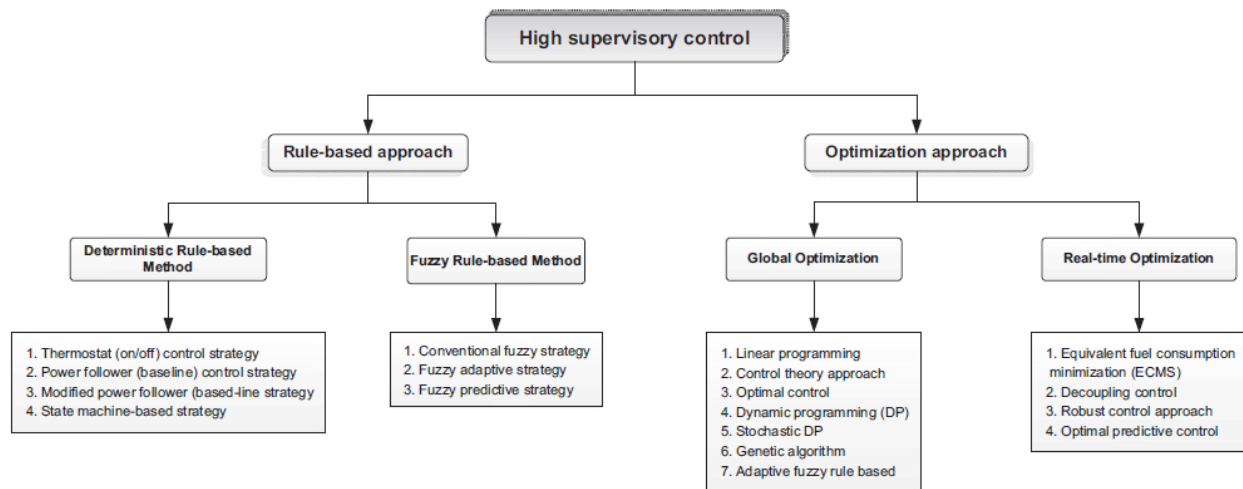


Figure 2.11 Energy management control strategies for hybrid electric vehicle or hybrid energy storage applications [1]

2.4 Hybrid Energy Storage Topologies and Power Conversion Topologies

Although the concept of hybrid energy storage - combining two energy storage sources - is simple, the implementation can be achieved in a huge variety of ways. The differences between systems include variations in system topology, types of energy sources, energy source voltage and power level, and dc/dc converter topology and components.

2.4.1.1 Hybrid Energy Storage Topologies

Seven different topologies which utilize none, one, or two dc/dc converters are outlined above in Figure 2.9, and the choice of which topology to use depends on the application and system design goals. Although the topologies shown in Figure 2.9 are for a battery and ultracapacitor pack, these sources could be substituted for a fuel cell, a flywheel, or power or energy battery packs. Additionally, many of the topologies shown in Figure 2.9 are actually utilized in the vehicles and projects examined in the following section 2.5.

Miller and Sartorelli examine several battery and ultracapacitor HESS system topologies, and they conclude that connecting a lower voltage ultracapacitor pack to the battery through a dc/dc converter and connecting the battery directly to the motor drive, topology (c) in Figure 2.9,

Table 2.6 Comparison of Three Battery and Ultracapacitor HESS System Topologies [94]

Architecture	Robustness	Cost	Performance	Overall
Up Convert	Fewer, large UC cells, few conn's High input current to converter Stable dc link	1 Lower voltage semiconductor	1 Converter operates only when needed High bandwidth control	+
Down Convert	More, smaller UC cells, more conn's Lower input current Stable dc link	0 high voltage semiconductor	1 Converter operates only when needed High bandwidth control	0 Too many interconnects, voltage management, higher voltage UC system
Converter on Batt	More, smaller UC cells, more conn's Highly dynamic dc link voltage Difficult Inverter PWM control	-1 Converter operational 100% of time Thermal concerns	0 Converter fault cannot be tolerated Higher thermal burden	- Requires ultra-robust converter and high performance inverter controller and higher current inverter switch

performs best on the metrics of robustness, cost, and performance as shown in Table 2.6 [94]. Miller and Sartorelli's conclusion is largely qualitative though and applies mostly to passenger EVs, so more analysis should be performed to determine the best solution for a specific application.

2.4.1.2 Power Converter Topologies

For HESS topologies which require a dc/dc converter, the converter specifications and power electronics topology must be chosen as well. The most common dc/dc converter topology utilized in high power automotive applications is a non-isolated half bridge bidirectional buck/boost converter, as used in the Toyota Prius to boost the 200V hybrid battery pack voltage to the motor drive dc bus voltage [95]. Many power electronics topologies can be utilized for this application though, including the SEPIC/Luo, CUK, and the isolated converters shown in Figure 2.12, as well as multiphase half bridge converters which help to reduce the inductor size.

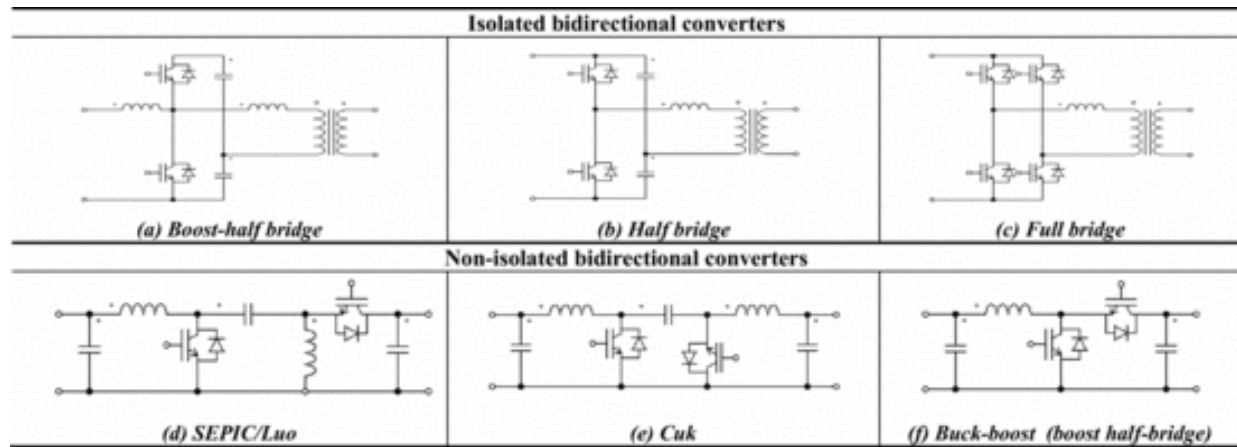


Figure 2.12 Bidirectional DC/DC converter topologies [96]

Al-Sheikh provides a qualitative analysis of the different dc/dc converters which are shown in Figure 2.12 above in Table 2.7 below, and concludes that the main advantage of isolated topologies is that they allow higher voltage conversion ratios, and that the half bridge buck boost topology offers the most advantages of the three non-isolated topologies considered [96]. Since the isolated topologies suffer from higher mass and cost, as well as typically lower efficiency, hybrid energy

storage systems typically utilize an ultracapacitor pack with similar voltage to the battery pack, resulting in a low conversion ratio and no need for the higher boost ratios that can be achieved with isolated topologies.

Table 2.7 Advantages & Disadvantages of the Power Electronics Topologies shown in the above Figure 2.12 [96]

Isolated topologies (a), (b), (c)	
<i>Advantages</i>	<i>Disadvantages</i>
Galvanic isolation; higher voltage conversion ratios	Bulky, heavy, and costly magnetic core; higher EMI; higher voltage stresses across switches
Non-isolated topology (d)	
<i>Advantages</i>	<i>Disadvantages</i>
Lower transfer capacitor voltage rating	Two larger inductors; discontinuous output current; large output capacitor; higher switch/diode voltage ratings
Non-isolated topology (e)	
<i>Advantages</i>	<i>Disadvantages</i>
Reduced input/output current ripples	Two larger inductors; higher transfer capacitor voltage rating; higher switch/diode voltage ratings
Non-isolated topology (f)	
<i>Advantages</i>	<i>Disadvantages</i>
One smaller inductor; no transfer capacitor; lower switch/diode voltage ratings; lower switching/conduction losses	Discontinuous output current

Schupbach and Balda go far beyond the qualitative analysis provided by Al-Sheikh in [96] by going through the design process for 75kW Cuk, Sepic/Luo, and half-bridge bidirectional converters. Each converter is designed to output 75kW, have an input (ultracapacitor) voltage of 150-300V, output (battery) voltage of 300V, and have equivalent inductor current and capacitor voltage ripple, as shown in Table 2.8 below for the topologies given in Figure 2.13. To achieve the design specifications, the half-bridge converter requires a 30uH inductor, while the Cúk and SEPIC/Luo both require two 100uH inductors. The half bridge converter does require more capacitance than the Cúk converter, but the authors conclude the half bridge converter is a better

choice because it requires less inductance and requires a 600A / 600V IGBTs rather than the 900A / 1200V IGBTs required by both the Cúk and SEPIC/Luo [97].

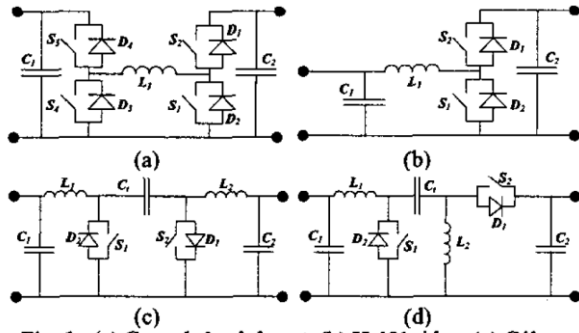


Fig. 1 (a) Cascade buck-boost, (b) Half-bridge, (c) Cúk, and (d) SEPIC/Luo converters.

Figure 2.13 (a) Cascade buck-boost, (b) Half-Bridge (c) Cúk, and (d) SEPIC/Luo bidirectional dc/dc converters [97]

Table 2.8 DC/DC Converter Design Specifications & Resulting Passive Component Sizing [97]

Parameter	Value
Maximum continuous output power, P_o	75 kW
Rated output voltage, V_o	300 V
Continuous DC input voltage range, V_i	150 – 300 V
Maximum output voltage ripple, ΔV_o	5 %
Maximum input voltage ripple, ΔV_i	5 %
Maximum inductor current ripple ratio, r_L	30 %
Maximum transfer capacitor voltage ripple ratio, r_C	30 %
Switching frequency, f_{sw}	20 kHz

Converter	Half-bridge	Cúk	SEPIC/Luo
Inductor, L_1	29.6 μ H	100 μ H	100 μ H
Inductor, L_2	--	100 μ H	100 μ H
Input capacitor, C_1	105.4 μ F	31.2 μ F	31.2 μ F
Output capacitor, C_2	417.0 μ F	31.2 μ F	555.0 μ F
Transfer capacitor, C_t	--	61.7 μ F	61.7 μ F

Schupbach and Balda's analysis is detailed enough that it can safely be concluded that the half-bridge dc/dc converter is a better choice than the Cúk and SEPIC/Luo converters, but other many other converter topologies are available which may perform better. For example, the author's in [98] design and test a bidirectional zero voltage switching converter topology as shown in Figure 2.14, which should perform with higher efficiency than an equivalent hard switched design but

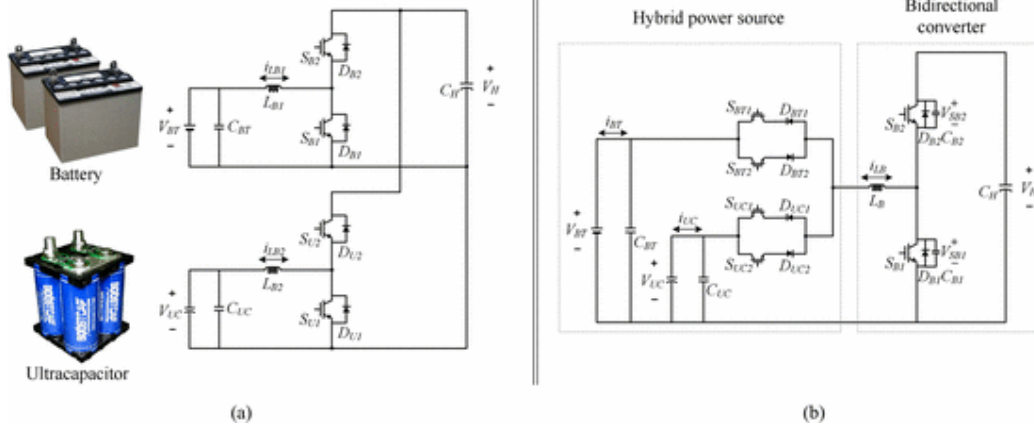


Figure 2.14 (a) Conventional hard switched and (b) proposed zero voltage switching dc/dc converter [98]

requires some additional components.

DC/DC converter efficiency and performance metrics can also be improved by utilizing next generation power semiconductor technologies, such as GaN and SiC, in place of silicon IGBTs or Mosfets. Han et al propose replacing conventional silicon IGBTs in a half bridge bidirectional dc/dc converter with SiC switches and diodes, allowing for greatly increased switching frequencies and reduced passive component sizes [99, 100]. The simulated results in Figure 2.15 show that for a 20kHz switching frequency an all SiC dc/dc converter has about half the losses of the equivalent Si converter and that at 100kHz the passive component size reduces by about $\frac{1}{2}$ and the SiC converter is still more efficient than the Si converter is at 20kHz.

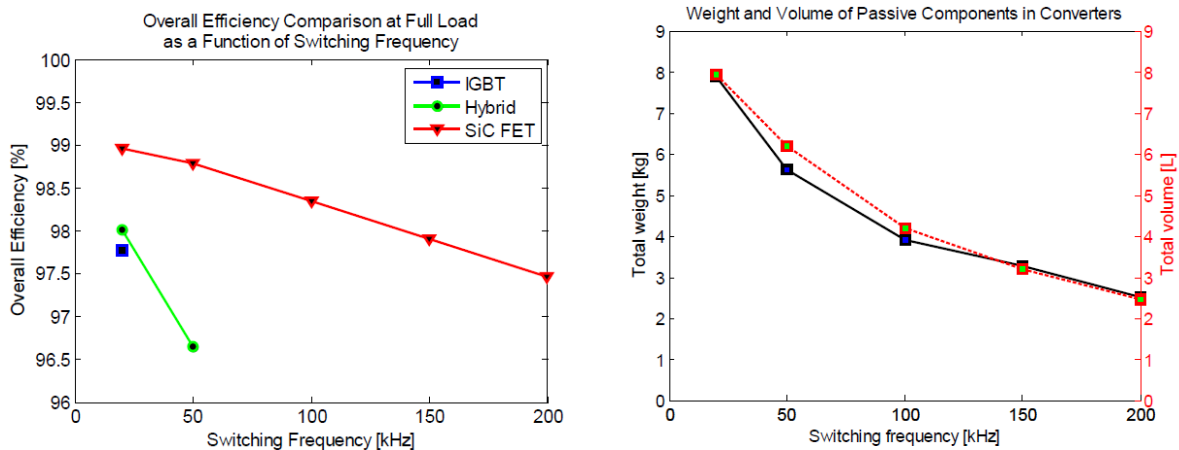


Figure 2.15 Simulated dc/dc converter efficiency with Si IGBT, Si IGBT w/SiC diode hybrid, and all SiC, and converter passive component sizing [100]

Several other studies examine slight variations in power electronics topologies and variations in the voltage of the energy storage components. Kumar and Ikkurti propose a unique low voltage system which includes a battery with a unidirectional dc/dc converter and an ultracapacitor pack with a bidirectional dc/dc converter which directly drive a brushed permanent magnet dc motor. They claim the system has the benefit of fewer semiconductor devices and better regenerative braking capabilities, and they provide a detailed state space model and simulation of the power

electronics and motor system [101]. Li and Liu propose a triple half bridge bidirectional converter which utilizes a transformer to boost low voltage battery and ultracapacitor pack voltages to a high voltage motor drive dc bus with a fuel cell [102], and Karimi et al compare the power converter efficiency of systems with low voltage battery packs and either low voltage motors or high voltage motors with a dc/dc converter [103]. Each of these studies gives some insight into the tradeoffs of low voltage and higher voltage systems and of alternative system topologies, and can be used as a starting point to determining the best power electronics and system voltage design for an application.

The prior papers shown here focus on system and power electronics topologies, but do not focus specifically on the current or voltage regulator design for these dc/dc converters. Jung, Wang, and Hu provide a very detailed control system design for a two dc/dc converter HESS which takes into account cross coupling between the inverters and focuses on achieving robust current and voltage tracking and on handling the transition between the two energy sources [104]. Further examination of similarly detailed controls papers would aid in the design of current and voltage regulators for any of the considered HESS and dc/dc converter topologies.

2.5 Design & Simulation of Hybrid Energy Storage Systems

There are many projects which have focused primarily on hybrid energy storage system design for electric [22-48] and hybrid electric [49-64] vehicles. These projects range in size from small autonomous robots up to passenger buses and metro rail cars, and they examine many different battery and other energy storage types as well as a variety of HESS topologies. A variety of conclusions can be drawn from these projects, which are discussed in 2.5.1 and 2.5.2.

2.5.1 Electric Vehicle Design and Simulation

Hybrid energy storage has been considered for electric vehicles since at least 2003, but there has been a large growth in the number of projects since 2010, as shown in Table 2.9 which outlines all of the electric vehicle hybrid energy storage projects identified for this review. Seven of these projects examine hybrid energy storage for small vehicles such as motorcycles and rickshaws, ten projects focus on light duty vehicles – the focus of the work in this dissertation, and another six focus on heavy duty vehicles. Each of these projects is discussed in the following subsections, with a focus on the most significant results and how they may apply to hybrid energy storage design for light duty electric vehicles.

Table 2.9 Electric Vehicle Hybrid Energy Storage Projects

Vehicle Type	Vehicle Description	University/Company	Year
4-wheeled robot	Prototype [22]	ETH Zurich	2010
Light Electric Vehicle – scooters, bicycles, etc.	Not Specified, but tested with 500W Lab Test System [23, 24]	Purdue & University of Toronto, Canada	2013
Motorcycle	Not specified [25]	McMaster Univ., Canada	2012
Go-Kart	Kart Mini Chassis [26]	Univ. of Campinas, Campinas, Brazil	2013
Single Passenger 3-Wheeler	Prototype [27]	Univ. of Maryland and Yildiz - Istanbul, Turkey	2012
3-Wheeled Auto Rickshaw	Generic Auto Rickshaw [28]	Dhaka Univ. of Eng. & Technol., Dhaka, Bangladesh	2014
Unspecified Light Electric Vehicle	Prototype / Made up Specs [29]	Indian Institute of Technology Delhi, India	2012
Light Duty Passenger Vehicles	Fiat Electra [30]	Univ. of Manchester & Univ. of Sheffield, UK	2005
	Maruti 800 (designed for, but implemented in lab) [31]	S V National Institute of Technology, Surat, India.	2010
	Fictional parameters, bench tested [32]	Ind. Technol. Res. Inst., Hsinchu, Taiwan	2010
	Chrysler Pacifica [33] (proposed)	Univ. of Waterloo, Canada	2011
	Not Specified [34]	PSNACET, Dindigul, India	2012
	Honda Accord [35, 36]	Illinois Inst. of Technol., Chicago, IL	2012
	VW Lupo [37]	Warsaw Polytechnic, Poland	2012
	Genovation G2 Prototype [38]	Genovation and University of Maryland	2013
	Not Specified [39]	REVA Inst. of Technol. & Manage., Bangalore, India	2013
Light Duty Class 1 Truck	1997 Chevy LUV Crew Cab Truck [40-42]	Pontifical Catholic University of Chile	2006-2010
1.2 ton Railed Vehicle	Prototype Linear Motor Railed Vehicle [43]	Inst. for Power Electron. & Electr. Drives, Paderborn Univ., Germany	2005
Military Vehicle	None specified [44]	Texas A&M University	2003
15 ton Garbage Truck	PVI Puncher [45]	French Inst. of Sci. & Technol. for Transp., France	2011
Electric Railed Passenger Tram	Scaled parameters [46]	Dept. of Electr. Eng., Hanyang Univ., Seoul, South Korea	2009
44 ton Metro Railcar	Budapest Metro Railway [47, 48]	Szechenyi Univ., Gyor, Hungary	2013

2.5.1.1 Small Vehicles

4-Wheeled Robot

A small four wheeled-robot built by Mariethoz and Barrade, as shown in Figure 2.16, incorporated an ultracapacitor pack as well as a battery pack with the goal of improving system

efficiency [22]. This is the smallest example of a vehicle with hybrid energy storage, and it is surprising there would be system advantages in such a light weight system.

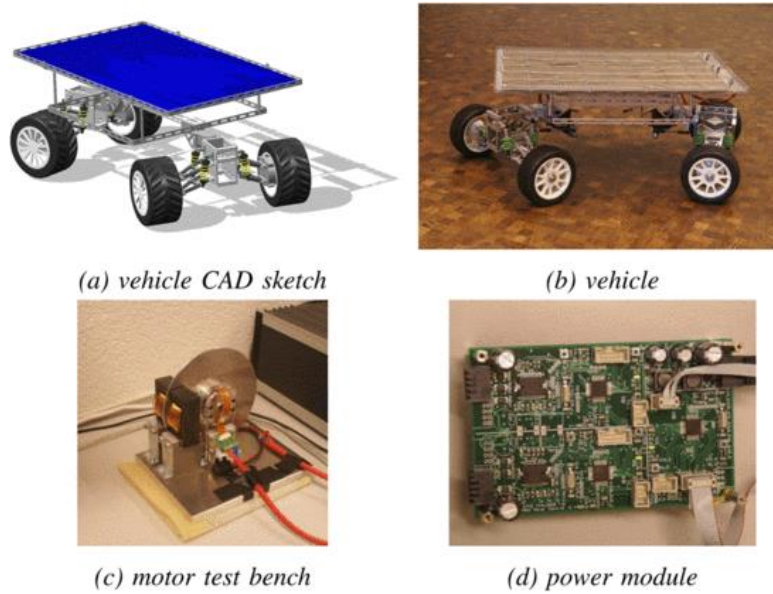


Figure 2.16 Design of 4-wheeled robot with HESS

The system topology is illustrated in Figure 2.17, and includes a solar panel to charge the energy storage, two wheel motors with drives, and a hybrid energy storage system consisting of an ultracapacitor and battery pack both connected through dc/dc converters.

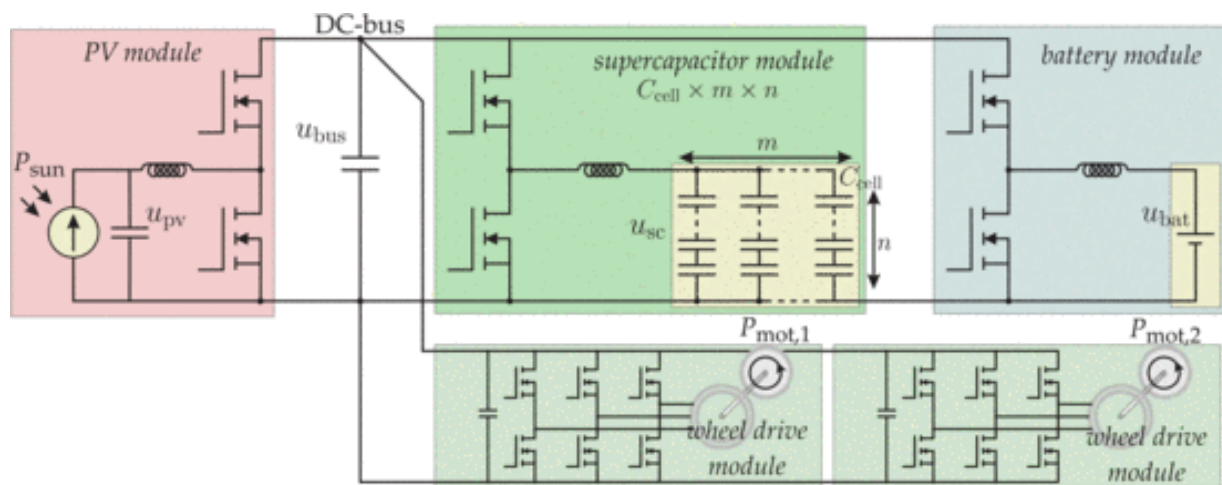


Figure 2.17 HESS system topology for 4-wheeled robot [22]

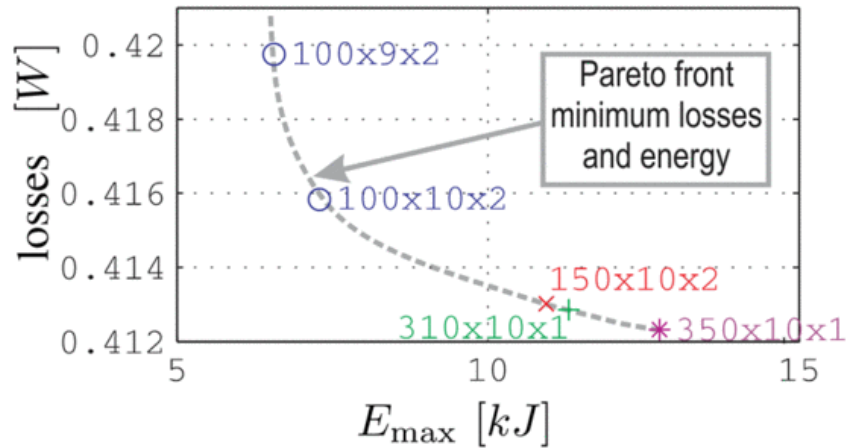


Figure 2.18 System loss versus ultracapacitor energy storage for 4-wheeled robot [22]

primarily on loss modeling of the system components and sizing the ultracapacitor pack with a tradeoff between losses and ultracapacitor size for a worst case driving cycle, as illustrated in Figure 2.18. A design methodology is demonstrated, and it is concluded that system losses can be reduced with the ultracapacitor pack, but it is unclear if the system is really any better than the battery only system.

Scooters, Bicycles Etc.

A battery and ultracapacitor HESS with two dc/dc converters was designed for an electric bicycle or small scooter application in [23, 24]. The drivetrain draws a peak of 500W, and the HESS utilizes a 5.3Ah, 43.3V, 268mΩ battery and a 34F, 27V, 48mΩ ultracapacitor. The authors built a bench top version of the system, developed an optimal power flow algorithm, and achieved a more than 10% reduction in battery energy consumption for a drive cycle, as shown in Table 2.10. Further examination of the results though shows that the reduction in energy consumption is not due an improvement in the energy storage system efficiency, but due to an improvement in the ability of the system to capture regenerative braking energy with the HESS. If the battery was

able to capture the regenerative braking energy in Test #1, the battery only system would have performed better.

Table 2.10 HESS and Battery Only Performance of a Scooter/Bicycle Drivetrain [23, 24]

Energy Quantity	Test #1 Battery Only	Test #2 HESS	Units
Total Battery Energy Used	69.1	61.9	Wh
Drive-Cycle Energy (Sink)	98.0	103.3	Wh
Drive-Cycle Energy (Sourced)	-42.8	-42.4	Wh
Battery /and U-cap Loss	2.30	4.47	Wh
DC-DC Converter Loss	2.67	4.60	Wh
Braking Loss	18.7	2.3	Wh
Average Power Loss	10.5	3.8	W

Motorcycle

Chia-Hao and Emadi propose a novel reconfigurable hybrid energy storage system topology which is designed and modeled for an electric motorcycle, with specifications as given Table 2.11. [25]. The main concept is to design a topology which can connect the battery and ultracapacitor packs either in series or parallel, and to take advantage of this flexibility to improve the system performance. The series parallel connection can be made either with switches or a power electronics converter, as shown Figure 2.18. A power electronics topology is developed which can make the series parallel connection. The system is modeled and some basic simulation results are provided, showing the system is functional. More work is needed to demonstrate what, if any, improvements to overall system performance could be achieved with this topology.

Table 2.11 Electric Motorcycle Parameters Used in HESS Modeling [25]

Powertrain Structure	Pure electric, single speed reduction
Electric Motor	Permanent magnet brushless DC (EMRAX Liquid Cooled)
Electric Motor Power	35kW continuous, 60kW Peak @ 3,000 rpm
Motor Drive	Piktronik SAC41
Energy Storage	Li-ion Polymer PQ5400, 255.3V, 10.8Ah
Motorbike Weight	110kg without driver

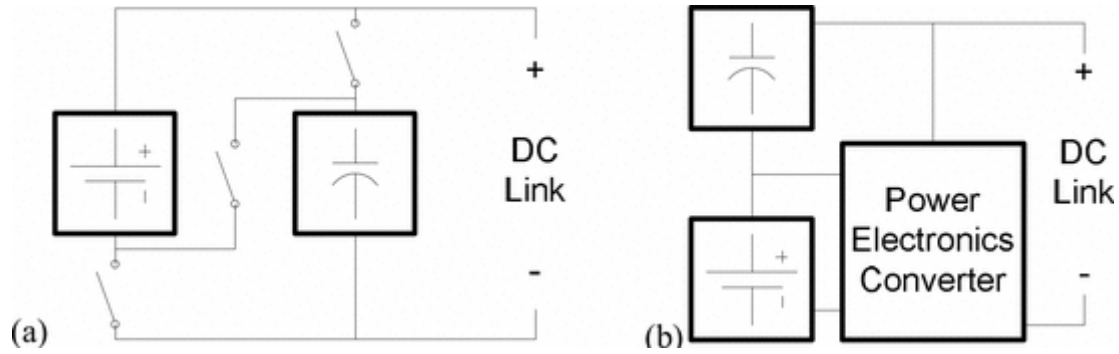
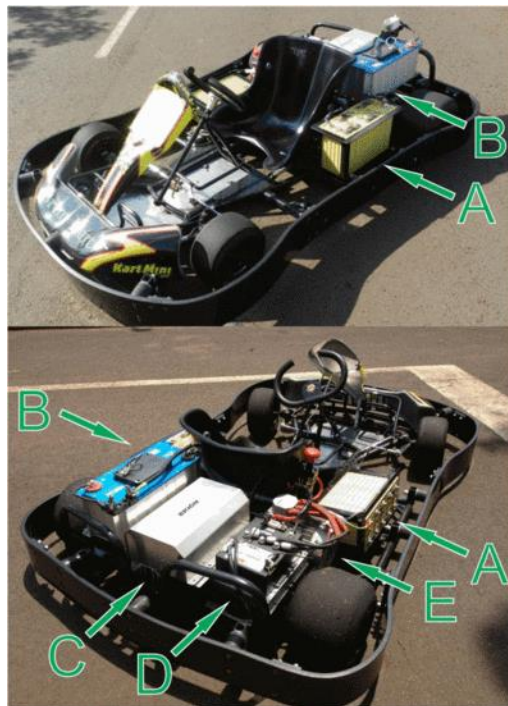


Figure 2.19 Series-parallel reconfigurable HESS topology [25]

Go-Kart

Avelino et al designed and built a hybrid energy storage system for an electric go-kart, as shown in Figure 2.17 [26]. The HESS consists of a 3.2kWh, 32V, 100Ah LiFePO₄ battery pack, a 52Wh, 48V Maxwell ultracapacitor pack, and a custom build dc/dc converter. There is a bidirectional dc/dc converter for both the battery and ultracapacitor pack, which boosts voltage up to the 84Vdc bus rating of the 5kW motor drive. Experimental data from a lap driven on a go-kart track shows



Motor	
Type	AC, induction, 3-phase
Rated Power	5 kW
Nominal Voltage (at the DC-link)	84 V
Manufacturer/Model	FIMEA / N20
Inverter	
Nominal Input Voltage	84 V
Peak input current	300 A
Frequency range	Up to 200Hz
Manufacturer/Model	ZAPI/AC-2
Battery	
Type	Lithium (LiFePO ₄)
Cell configuration (Series/Parallel)	10S/1P
Nominal Voltage	32 V
Operational Voltage	28 V ~ 40 V
Nominal Capacity	100 Ah
Weight	35 kg
Model	TS-LFP100AHA
Cell Manufacturer	Winston Batteries
Ultracapacitor	
Rated Capacitance	165 F
Rated Voltage	48 V
Manufacturer	Maxwell Technologies

Figure 2.20 Electric go-kart with hybrid energy storage [26]

that the power split controls are typically able to limit the power drawn from the battery to 2.5kW, reducing the losses in the battery pack.

The main conclusion is that the system is functional and was demonstrated, but no comparison was made to a battery only system. Due to the very low resistance of the battery pack (similar cells as used in the truck) and the low current draw an efficiency analysis of the system would likely show that it would be more efficient with no ultracapacitor pack. However, the system would enable the use of a high energy density, higher resistance battery pack, which would reduce the vehicle mass or allow more energy storage on board.

Single Passenger Three-Wheeler

Application of a hybrid energy storage system to a prototype single passenger three wheeled vehicle is examined by Ugur et al in [27]. The vehicle, shown in Figure 2.21, has several similarities to the go-kart discussed previously, including a relatively low drivetrain power of 7kW and the use of a 52Wh, 48V Maxwell ultracapacitor pack. However this vehicle utilizes a 1.6kWh, 48V, 33Ah, lead acid battery pack which will likely benefit from the hybrid energy storage system due to its higher resistance.

This vehicle also has a second unique feature, the use of a cascaded bidirectional buck boost converter connected between the ultracapacitor pack and the battery. The cascaded converter allows the ultracapacitor voltage to cross over and be greater than or less than the battery voltage. This allows more flexibility of system voltages, but will reduce the converter efficiency compared to a non-cascade buck boost converter. The focus of the project was to build and experimentally test the system, and it was shown that their power split algorithm utilized the ultracapacitor pack to reduce the battery pack power. While the power split algorithm was shown to be nominally functional, again in this work there was no comparison between battery only and HESS

performance, although due to the higher resistance of a small lead acid battery pack it is likely some system efficiency and range benefits would be achieved.

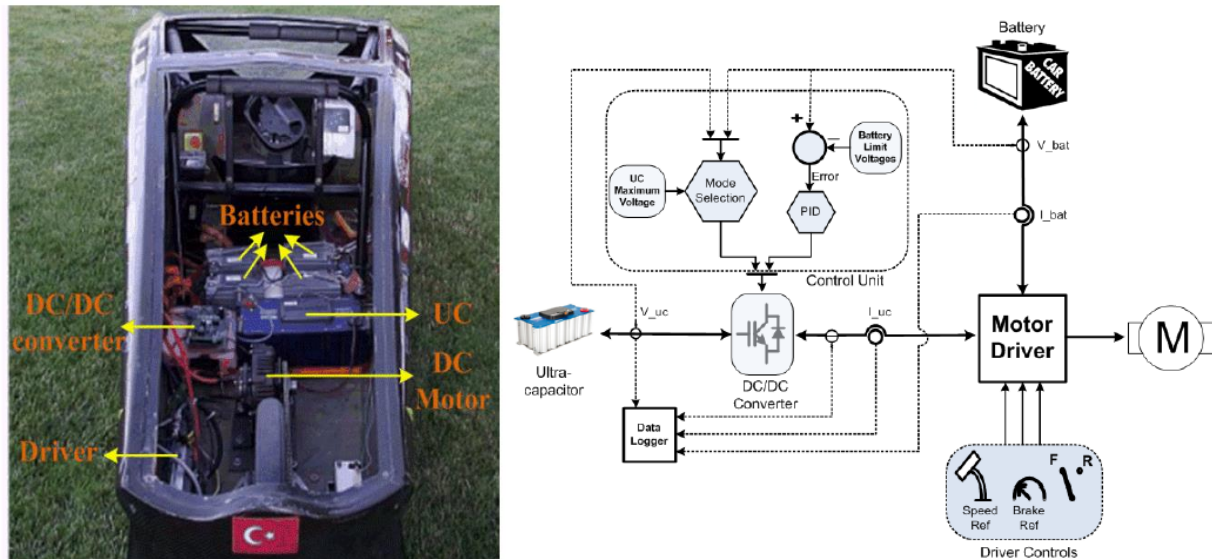


Figure 2.21 Electric three-wheel single passenger vehicle with hybrid energy storage

3-Wheeled Auto Rickshaw

The 3-wheeled, electric auto rickshaw examined by Shaha and Uddin, is used in their home country of Bangladesh as a taxi for transit of up to 6 passengers. The vehicle weighs about 350kg unloaded, and is outfitted with a 7.2kWh, 60V, 120Ah lead acid battery pack, which tends to degrade rather quickly due it typically being used to cover more than 100km per day. Due to the quick degradation of the battery packs, often less than 1 year of good service, and unsafe conditions created by the poorly performing batteries, such as the driver turning off the headlight at night to increase range, there is a strong desire to improve the performance of the system to make it more functional and economical for the taxi drivers.

Shaha and Uddin propose adding a 280W solar panel to the roof of the vehicle as shown in the system diagram of Figure 2.22, to hybridize the vehicle. An extensive, detailed analysis is performed to characterize just how much this will improve the vehicle's performance and the profit

earned by the taxi drivers, the results of which are shown in the table of Figure 2.22. This is not a hybrid energy storage system, as is discussed for the other vehicles in this section, but a hybrid energy system, in which two energy sources are used – the battery pack and solar panel. While this is a little outside the scope of this project, the excellent and practical analysis performed in the paper, and the unique application, make it worth considering as a model for how to analyze the value of hybrid energy storage systems.

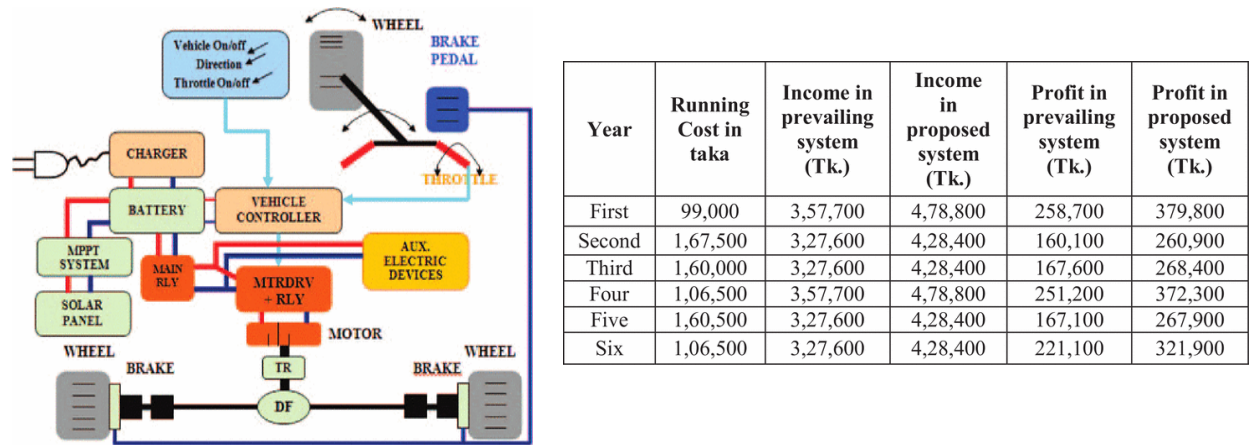


Figure 2.22 Electric three-wheeled auto rickshaw with battery and solar panel hybrid energy system [28]

Unspecified Light Electric Vehicle

Bobba and Rajagopal design a hybrid energy storage system for a small 175kg electric vehicle with a brushless dc motor which draws several kW at peak vehicle loading [29]. The hybrid energy storage system consists of a 960Wh, 48V, 56mΩ lead acid battery pack connected to the motor drive and an 8.3Wh, 32V, 7.2mΩ ultracapacitor pack connected to a 1kW bidirectional dc/dc converter. A detailed system model is developed and some simple simulations are performed, but no definitive conclusions about the performance of the system, or the benefits versus a battery only system are presented. With the relatively high resistance of the chosen battery though, it is likely the ultracapacitor pack would reduce system losses and improve range a meaningful amount.

2.5.1.2 **Light Duty Automobiles**

The small electric vehicles presented in the prior section apply to more niche applications, while light duty automobiles are used for the vast majority of transit in many countries, including the United States. Essentially all passenger vehicles - cars, minivans, SUVs, pickup trucks, etc. - are classified as light duty vehicles, while larger vehicles such as delivery trucks, buses, and semis are classified as medium or heavy duty vehicles. This section will examine two classes of vehicles – light duty passenger vehicles, mostly cars, and light duty class 1 trucks, one weight classification lower than the class 2a Ford F150 truck used in this study.

Light Duty Passenger Vehicles

There have been many projects looking at the use of hybrid energy storage in light duty passenger vehicles. Most projects design systems for an actual production vehicle, but most of these projects are simulation only, with only a few testing scaled hardware in the lab. This differs compared to small vehicles in the previous section, where many projects have actually verified the performance of the hardware through testing in a vehicle. The lack of full scale testing is likely due to the challenge associated with the building and fine tuning of a functional, on the road vehicle.

Several simulation based projects are noteworthy. First Mikkelsen and Lambert modeled the drivetrain for a proposed Chrysler Pacifica EV [33]. A battery only, energy battery and ultracapacitor HESS, and energy battery and power battery HESS for ranges of approximately 140km, 200km, and 300km were modeled. The vehicle was then simulated for different drive cycles, and the resulting range and energy consumed by different subsystems was presented, giving insight into the pros and cons of each solution. Shah et al design an HESS for a Maruti 800 passenger car, which is considered the most influential vehicle in India [31]. The small 800kg car, with a maximum electric motor power of 27kW is powered by a 6.2kWh, 156V lead acid battery

pack and a 52Wh, 48V ultracapacitor pack with a dc/dc converter for the battery and ultracapacitor pack. Again no hardware is built, but some simulation of the vehicle is performed to demonstrate the performance of their relatively simple proposed control solution.

Schoefield et al model a Fiat Electra EV in [30]. They consider as a baseline a 15.1kWh, 216V, 70Ah, lead acid battery pack with a 217Wh ultracapacitor pack, with the battery pack connected directly to the motor drive and the ultracapacitor pack connected via a dc/dc converter. A detailed model of the vehicle and energy storage components is developed based off experimental testing in a prior project, and battery only versus battery and ultracapacitor cases with equivalent mass are modeled and the results are shown in Figure 2.23. Schoefield et al show that a vehicle with a smaller battery pack, 70Ah versus 80.7Ah, paired with an ultracapacitor pack can actually travel further, 84.5km versus 68.6km, on the ECE15 drive cycle. Even though this study was published in 2005, it remains one of the more definitive studies characterizing HESS performance in a vehicle.

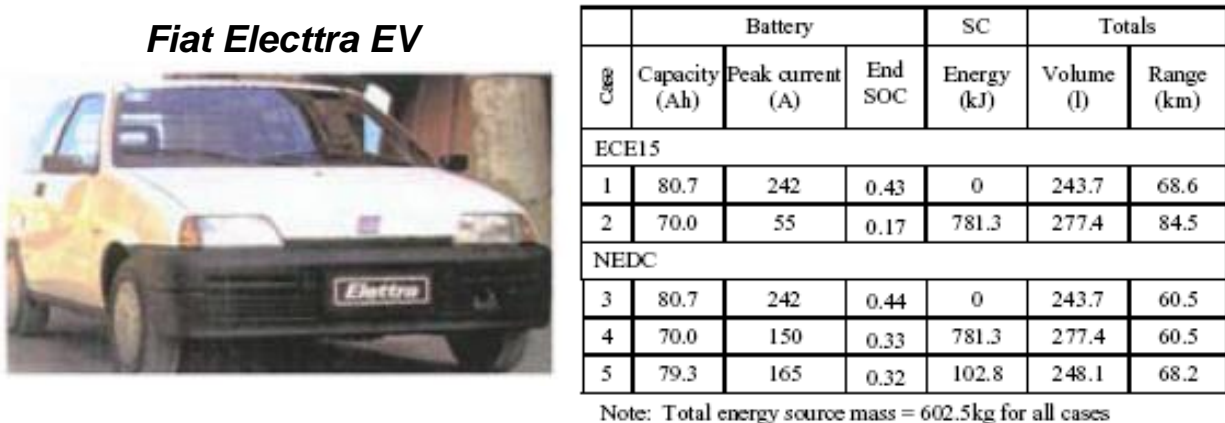


Figure 2.23 Modeled HESS performance for Fiat Electra [30]

Michalczuk et al model an electric, 1100kg, VW Lupo with a more modern battery pack than used in the Fiat Electra project discussed above [37]. The Lupo is modeled with a 9.1kWh, 125m Ω (est.), 165V, 110kg, 55Ah LiFEPO₄ battery pack paired with an 81Wh, 14m Ω 105V,

14.5kg ultracapacitor pack. The ultracapacitor pack is connected to the battery pack through a dc/dc converter, which efficiency is modeled for but current and power limits are not specified. The battery and ultracapacitor models are developed entirely from data provided by the manufacturer, and the modeling results for the ECE15 drive cycle show a 5% increase in range at 35°C and a 54% increase in range at -5°C, as shown in Figure 2.24. The modeling results also show that HESS losses decrease modestly, by about a factor of 1/3, at higher temperatures, and by a factor of two or three at lower temperatures. Additionally the authors make some assumptions about how an aged cell's parameters will evolve, and that the HESS system provides even more benefit for these aged conditions. With experimental results included to confirm their modeling, the presented results would make a strong case for hybridizing the proposed vehicle.

New Battery & Ultracapacitor Cells						Parameters for 50% Aging					
		ECE15		Real cycle				ECE15		Real cycle	
		Battery	Hybrid	Battery	Hybrid			Battery	Hybrid	Battery	Hybrid
35°C	Range	116.01	122.22	94.44	100.14	35°C	Range	103.5	107.63	80.88	86.05
	Power losses	3.51%	2.38%	4.51%	3.25%		Power losses	4.58%	2.74%	5.84%	3.85%
25°C	Range	114.97	121.19	92.98	99.2	25°C	Range	101.43	106.59	80.28	85.41
	Power losses	3.77%	2.70%	4.86%	3.66%		Power losses	4.93%	2.82%	6.04%	3.98%
10°C	Range	102.48	115.99	80.9	92.99	10°C	Range	84.79	101.41	65.35	79.82
	Power losses	6.19%	2.97%	7.82%	4.24%		Power losses	8.52%	3.53%	9.80%	5.17%
0°C	Range	88.95	112.86	75.7	90.63	0°C	Range	43.15	98.2	---	75.7
	Power losses	7.93%	3.26%	10.40%	4.88%		Power losses	10.53%	4.23%	---	5.99%
-5°C	Range	71.25	109.77	65.35	87.81	-5°C	Range	---	95.19	---	70.93
	Power losses	8.95%	3.61%	11.04%	5.30%		Power losses	---	4.39%	---	6.54%

Figure 2.24 VW Lupo with simulated HESS for low temperature and 50% aged case [37]

Two somewhat unique HESS configurations are designed and simulated in [34] and [39]. Neenu and Muthukumaran outline five different HESS topologies in [34], and then select the topology shown in Figure 2.25. The topology is identical to that proposed earlier in [35], where an ultracapacitor pack is connected directly to the motor drive and the battery is connected to the motor drive via a dc/dc converter. This configuration is chosen to enable the use of a lower power dc/dc converter because only the average battery power must be provided with the converter. This

topology however requires a large bus voltage swing to fully utilize the ultracapacitor packs, and the simple modeling performed for a generic vehicle does not quantify the benefits of the system. Misal and Divakar propose another interesting topology in [39], in which an ultracapacitor pack is connected directly to a dc motor and the battery pack is connected via a dc/dc converter, as shown in Figure 2.26. A cursory modeling exercise is performed and some qualitative results are presented, but the topology is likely not to be beneficial due to the ultracapacitor being fully discharged at zero speed, therefore not allowing the ultracapacitor pack to help with acceleration from a stop.

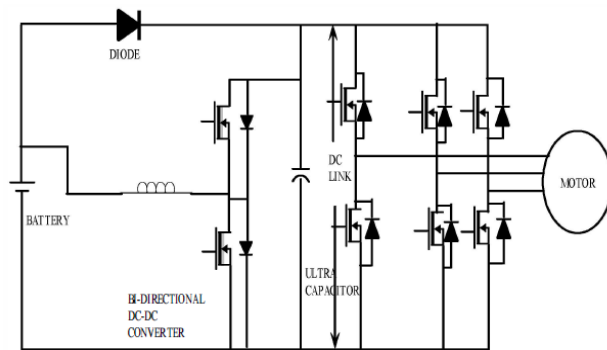


Figure 2.25 Proposes HESS drive topology w/ ultracapacitor on drive dc bus [34]

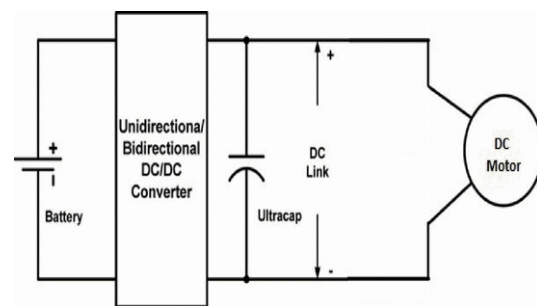


Figure 2.26 Proposed HESS drive topology with ultracapacitor connected directly to dc motor terminals [39]

There are also two light duty vehicle projects in which scaled hardware was tested to help verify the performance of the proposed systems. Wu et al modeled a passive lithium battery and ultracapacitor hybrid energy storage system, performed an optimization process which varies the ratio of battery to ultracapacitor to meet the vehicle requirements, and then built and tested a scaled version of the system as shown in Figure 2.27 [32]. The pricing and energy storage parameters used in their model are now outdated, and they only got as far as qualitatively verifying their model and graphically demonstrating the performance, but by actually testing the system they do show that their model was relatively accurate.

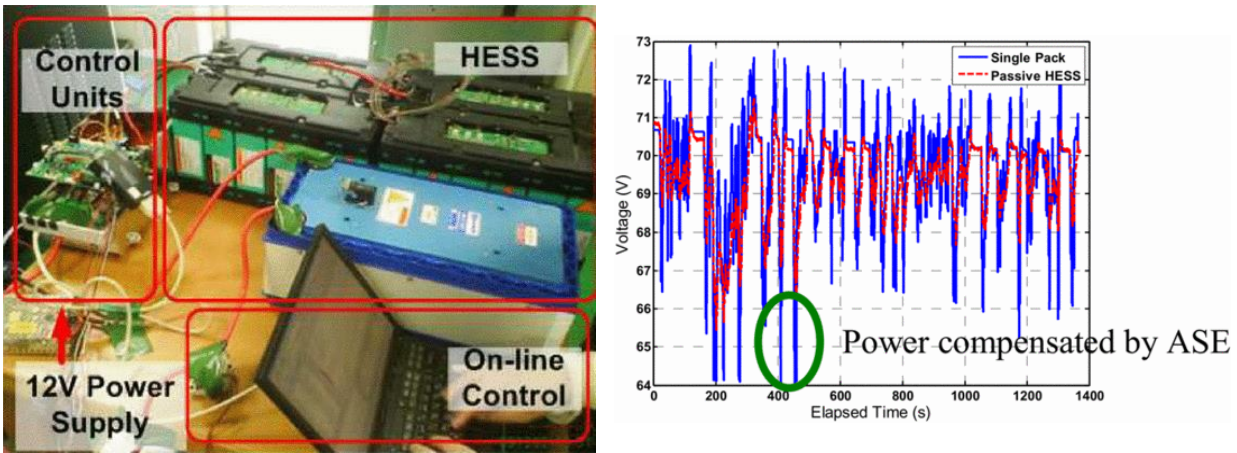


Figure 2.27 Passive battery and ultracapacitor HESS with experimental results [32]

The second light duty vehicle modeling project with scaled experimental verification, performed by Cao and Emadi, models a 1740kg Honda Accord EV with a 75kW motor, a 380Wh 400V ultracapacitor pack, and a 31kWh, 173V Ni-MH battery pack [35, 36]. The HESS is configured the same as in Figure 2.25, and the dc/dc converter is rated for 12kW. A scaled down system with a 12V battery and 32V ultracapacitor pack is tested in the lab, and the experimental results verify the functionality of the converter topology. This topology does suffer from requiring an oversized motor drive which can provide sufficient power over a wide voltage range, and more work is needed to prove this topology is beneficial from a system design standpoint.

One startup company, Genovation, has also considered a hybrid energy storage drivetrain for their proposed G2 Sedan, as shown Figure 2.28 [38]. The proposed hybrid energy storage drivetrain, also shown Figure 2.28, consists of two motor and drive systems with an equal power rating, with one connected to an ultracapacitor pack and the other connected to a battery pack, and the two energy storage sources connected with a dc/dc converter. While this proposed topology is unique, no details or argument is made in the published paper as to why this is a preferable solution. One clear disadvantage is that as the vehicle accelerates the ultracapacitor pack will discharge and reduce in voltage, reducing the power capability of the propulsion converter

connected to it. It may have some advantages when decelerating due to the ability to put regen energy directly from the motor drive into the ultracapacitor pack, but a significant amount of system design work is needed to characterize the advantages, if any, of this system.

Genovation G2 Prototype

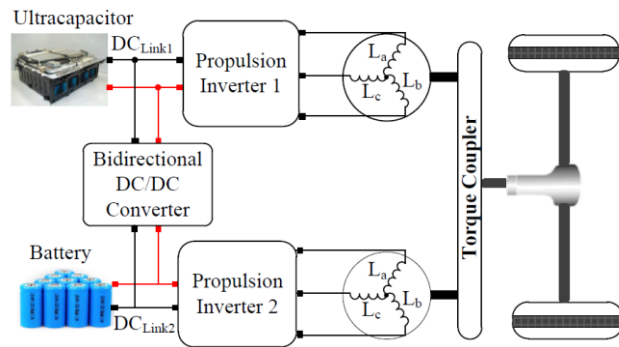


Figure 2.28 Genovation G2 prototype vehicle and proposed hybrid energy storage drivetrain

Light Duty Class 1 Truck

The only light duty vehicle project in which an HESS was installed on an actual electric vehicle was performed by Dixon et al in Chile [40-42]. A 1700kg Chevy LUV crew cab truck, shown in Figure 2.29, was first converted to an electric research vehicle with a 53kW peak traction motor and a 28.2kWh, 37.5kW peak, ZEBRA battery. The electric truck was then converted to a hybrid energy storage vehicle by adding a custom built 45kW dc/dc converter which controls power flow between a 250Wh, 300Vdc ultracapacitor pack and the battery pack.

Chevy LUV EV Conversion

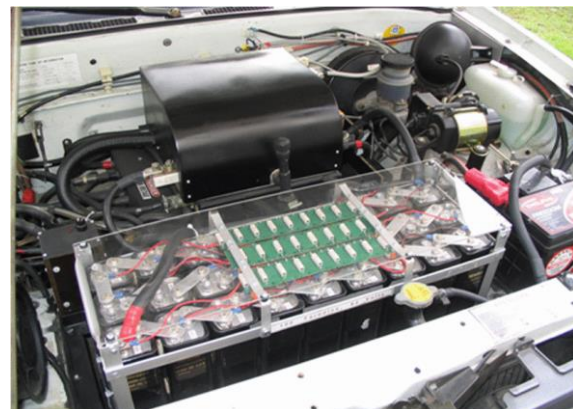


Figure 2.29 Chevy LUV EV conversion with part of HESS ultracapacitor pack and dc/dc converter installed under hood [42]

The vehicle is a perfect candidate for hybrid energy storage because the ZEBRA battery pack's resistance is so high that it cannot provide the peak motor drive output power. The HESS topology, and the experimental testing results, are outlined in Figure 2.30. With the addition of the HESS the vehicle was shown to accelerate from 0-80km/h 38.5% faster due to the increased motor output power achieved with the HESS, and the range was shown to increase 10.7% on a fast track and 16.7% on a slow track due mostly to reduced losses in the battery pack. Additionally the energy consumption was shown to be reduced by 8.3% on the slow track and 18.4% on the fast track. These testing results show that for this case, where the battery has high resistance relative to the power it must provide and where the vehicle is relatively heavy, that the HESS can improve vehicle range, energy consumption, and acceleration metrics by 10% - 20% or more. Additionally the authors' state that based on the experimental results an ultracapacitor pack which is 1/3 the size, about 80Wh, could provide the same performance benefits to the vehicle. A test is also performed with a lead acid battery pack with less resistance than the XEBRA pack, and efficiency

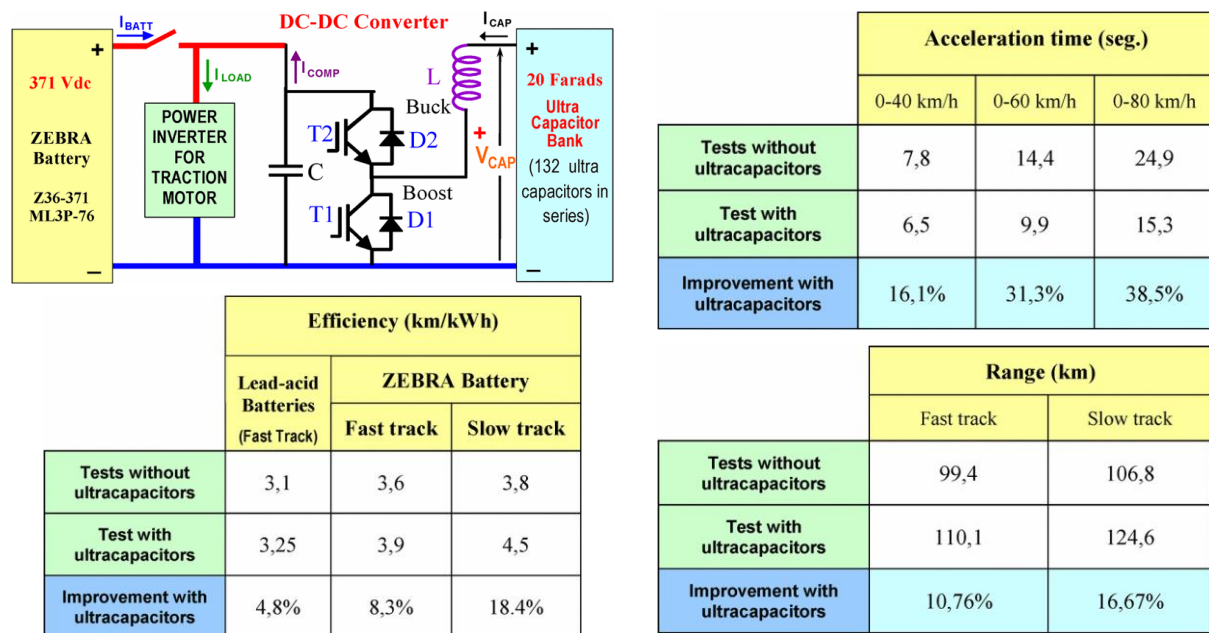


Figure 2.30 Efficiency, range, and acceleration improvements for battery only and HESS Chevy LUV EV [42]

is improved by 4.8% - similar to some of the modeled improvements shown in Chapter 5 of this dissertation.

2.5.1.3 *Heavy Duty Vehicles*

Hybrid energy storage systems have been examined for a variety of heavy duty electric vehicles, including a scaled down rail car, a garbage truck, a 44t metro rail and others. Li et al design and built an HESS for a 3.2m long, 1200kg rail car powered with a doubly fed linear motor[43]. The rail car is powered with a 2.4kWh, 360V NiMH battery and a 35.6Wh, 42V ultracapacitor pack connected to the battery pack via an isolated buck / boost converter. The authors develop discrete optimization methods with the goal of controlling the power split between the battery and ultracapacitor pack to increase system efficiency and decrease aging, and they present some simulation and experimental results demonstrating the system performance.

In another project, Gao et al model and describe the performance of various combinations of batteries, ultracapacitors, and flywheels for application in military vehicles [44]. In a more recent project, Butterbach et al create a detailed, experimentally based model based on experimental test of a 20 ton electric garbage truck power by a 90kW traction motor and a very large 137kWh, 528V, 240Ah, 88m Ω lead acid battery pack. The author's state the lead acid battery pack cannot be used for regenerative braking above 85% SOC, so a 1.5kWh, 540V, 70m Ω ultracapacitor pack and dc/dc converter is added to allow regenerative braking in this region. The modeling shows the addition of the ultracapacitor pack reduces energy consumption for a daily garbage pickup route by about 19%, enabling the battery pack to be downsized.

Two studies also look at passenger rail vehicles. Lee et al perform a very interesting analysis in [46] where they create a detailed model of the mechanical dynamics of a scaled version of a railed streetcar which is powered by a battery and ultracapacitor HESS. The most compelling part

of the study is that they test their model with a hardware in the loop (HIL) system which consists of a motor representing the tram's traction drive which is coupled to a second motor representing the loads on the vehicle. This test setup would be particularly useful for evaluating the traction drive controls, and if it were not a scaled down system it would also be useful for evaluating the traction motor and drive's performance in a simulated real world environment. Szenasy performs an extensive modeling and optimal energy storage sizing study for a 44 ton metro rail car with 200kW total of traction power provided by overhead catenary lines [47, 48]. The addition of a battery and ultracapacitor HESS is proposed to capture the regenerative braking energy that would otherwise be dissipated as heat in a resistor bank. The optimization study shows that as long as the maximum grade is less than 20%, a 22.5kWh lithium battery paired with a 112Wh, 1F, 900V ultracapacitor pack will be sufficient for the application.

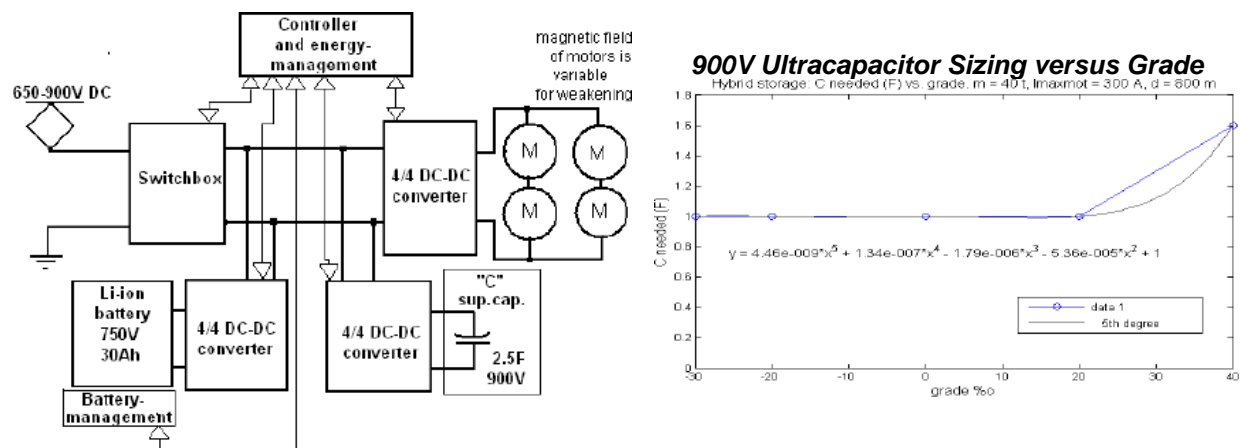


Figure 2.31 44T Metro railcar proposed HESS topology and ultracapacitor sizing versus maximum grade [47, 48]

2.5.2 **Hybrid Electric Vehicle** Design and Simulation

Hybrid electric vehicles, which typically utilize a gas or diesel engine, one or more electric motors, and a battery pack for energy storage, are potentially a good candidate for hybrid energy storage since their small battery packs tend to see high power and frequent swings in state of charge. An HEV though typically requires mostly power, and only a small amount of energy storage, meaning the combination of an energy dense and power dense source may not be too beneficial, except for specific applications which require a lot of energy storage or have other specialized requirements. The most studied applications are mild and micro hybrids and heavy duty vehicles such as busses and military trucks, although as shown in Table 2.12 a range of other applications are studied as well.

Table 2.12 Hybrid Electric Vehicle Hybrid Energy Storage Projects

Vehicle Type	Vehicle Description	University/Company	Year
Single Passenger Race Car	Formula SAE Hybrid Vehicle [49]	Illinois Inst. of Technol., Chicago, IL, USA	2011
Motorcycle (hybrid starter battery)	Honda Activa or Other Two Wheeled Vehicles (exp. tests on vehicle) [50]	Chheda Electricals & Electronics Pvt. Ltd, India	2009
Light Duty Passenger Vehicle	Ford Explorer [51]	University of Alberta, Canada	2003
	Fiat 600 (exp in lab) [52]	University ROMA TRE, Rome, Italy	2004
	None specified (exp. test in lab) [53]	Ohio Northern University & University of Toledo	2006
	BJUT-SHEV [54]	Beijing Univ. of Technol., China	2010
	Toyota PHEV [55]	Illinois Institute of Technology, Chicago, IL	2010
	None provided [56]	Southeast Univ., Nanjing, China	2011
	Chevy Equinox [57]	General Motors	2011
Light Duty Commercial Vehicle (mild hybrid)	Non specified [58]	AVL Powertrain UK & Ford	2009
12 ton Military Truck	Prototype Series Hybrid [59]	University of Franche-Comte, France	2006
Passenger Bus	First Automobile Works (FAW) Parallel Hybrid Bus [60]	Harbin Inst. of Technol., China	2008
Passenger Bus	15 ton bus [61]	Jilin University, China	2014
Passenger Bus	18 ton bus [62]	Univ. of Tehran, Tehran, Iran	2011
20 ton Hybrid Excavator	Prototype [63]	Zhejiang Univ., Hangzhou, China	2013
30 ton Military Truck (w/ fuel cell)	Hybrid 8x8 Military Truck [64]	Cranfield University, UK	2013

2.5.2.1 Small Vehicles

Nielsen and Emadi propose an HESS for a Formula Hybrid competition vehicle which consists of a 2.5kWh, 74V lithium battery in parallel with a 105Wh, 96V ultracapacitor pack [49]. The authors model the system for different events, and show that the HESS is predicted to perform better than the battery only or ultracapacitor only alternatives. Chheda and Vernekar designed and prototyped a passively connected sealed lead acid battery and ultracapacitor hybrid designed to replace conventional starter batteries in two wheeled moped and motorcycles [50]. They thoroughly document the design, commercial application, and performance details, and claim that the hybrid battery solution will have a lower cost of ownership over time because the flooded lead acid starter battery, which is claimed to require replacement every 2-3 years, can be downsized to 1/3 of its original rating and replaced with a sealed battery, reducing replacement costs by 1/3 due to the reduced battery energy rating. The provided experimental data shows that the hybrid system, detailed in Figure 2.32, performs similarly to the battery only system even though the battery has been downsized by 1/3. The product is actually available for purchase from local auto

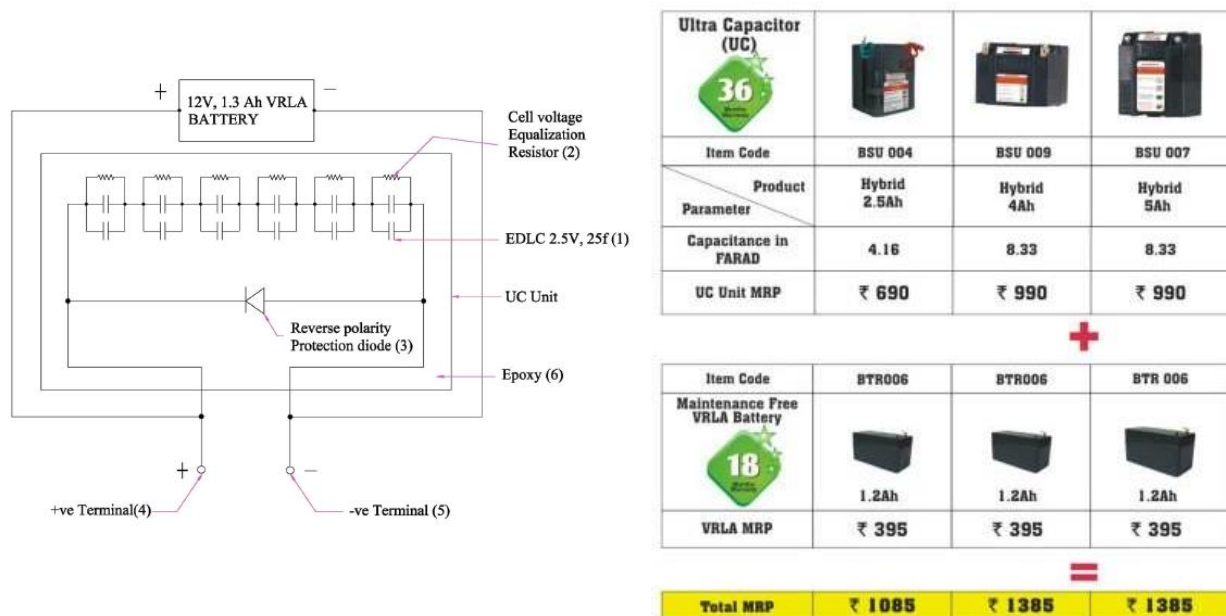


Figure 2.32 Topology and sales flyer for passive battery and ultracapacitor hybrid for two wheeled vehicle (\$1 = ₹63) [50]

parts suppliers in India, and as shown in Figure 2.32 costs a total of ₹1385 Indian Rupees (\$22) for the 5Ah version, which is sized for a typical small motorcycle.

2.5.2.2 Light Duty Vehicles

Mild Hybrids

Three light duty vehicle projects examine the use of lead acid battery and ultracapacitor hybrid energy storage for low voltage mild hybrid electric vehicles [53, 57, 58]. Mild hybrids are an attractive application for HESS's because just a lead acid battery is typically not sufficient for gasoline start stop and mild regenerative braking capabilities. The combination of two energy sources, which could also include a lithium ion battery, allows the system to distribute the responsibilities of providing engine cranking power, accessory power, and electric traction assist power. Steinecker et al develop a mild hybrid system which utilizes an ultracapacitor pack for engine starting and regenerative braking so the lead acid battery SOC can be maintained around 100%, significantly increasing battery lifetime [53]. The system consists of a 24V lead acid battery paired with a 26Wh, 45V ultracapacitor pack which is normally connected to the motor drive, as shown in Figure 2.32. An experimental version of the system was built and tested in the lab, and ultracapacitor current and voltage and battery current for a 300A charge / discharge pulse are provided to demonstrate functionality, also shown in Figure 2.32.

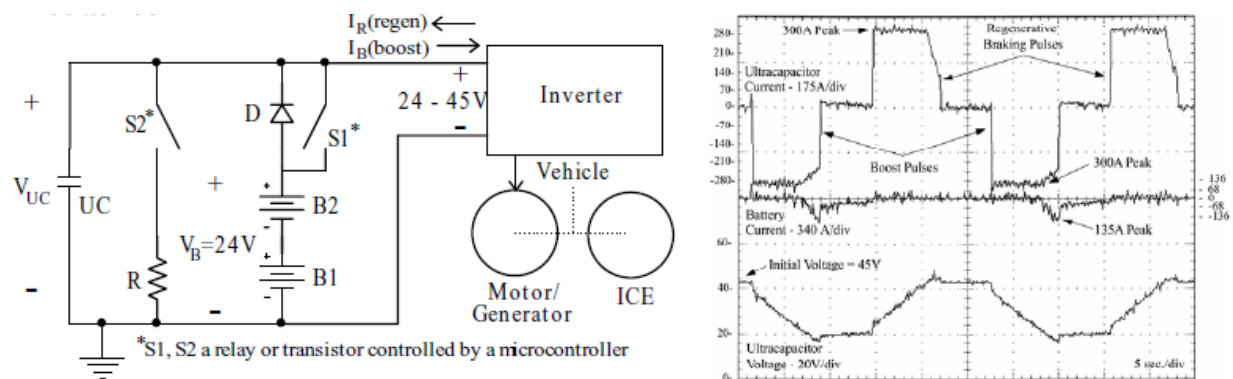


Figure 2.33 Mild hybrid hess topology with experimental data [53]

Gopalakrishnan et al from General Motors designed a mild hybrid system and modeled its performance for a Chevy Equinox compact SUV [57]. The system essentially uses the alternator to charge a small ultracapacitor pack via a 1.0 to 1.5kW dc/dc converter when the vehicle is decelerating. Three ultracapacitor packs are considered - an 8.8Wh, 36F, 42V pack, 4.4Wh, 18F, 42V pack, and 6.8Wh, 150F, 18V pack – and the modeled fuel economy improvements are shown to be between 0.23 and 0.42 mpg, as shown in Figure 2.34. Presumably these relatively modest fuel economy improvements prevented this mild hybrid system from entering production since the publication of this work in 2011.

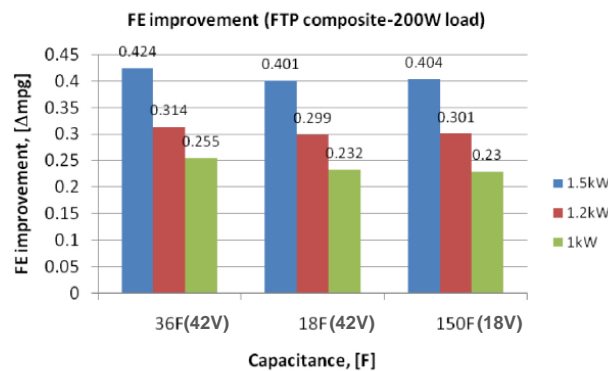


Figure 2.34 Fuel economy improvements for Chevy Equinox mild hybrid with HESS for various dc/dc converter power ratings [57]

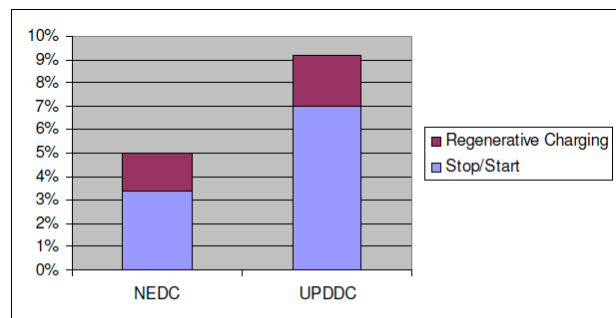


Figure 2.35 Fuel economy improvements for mild hybrid light duty commercial vehicle with HESS [58]

Gao et al from AVL Powertrain and Ford Motor company develop a belt-driven integrated starter generator system and model its performance for a light duty commercial delivery vehicle [58]. The system consists of a 4kW clawpole synchronous starter/generator and motor drive whose dc output is connected directly to a 20Wh, 200F, 27V ultracapacitor pack. The ultracapacitor pack is connected via a bidirectional 1.5kW dc/dc converter to a 12V lead acid battery, which provides power to the vehicle's accessory loads. This topology utilizes the ultracapacitor pack to start the engine, and can utilize both the battery and ultracapacitor pack to store regenerative braking energy. The system achieves significant fuel economy improvements of 5% for the NEDC cycle

and 9.2% for the urban parcel delivery UPDDC cycle. This system is able to perform better than that proposed by General Motors because of the greater amount of ultracapacitor energy storage, ability to charge the ultracapacitor at 4kW, and the start stop capability, but due to the BISG's greater complexity and cost it may not be preferable to the GM system.

Full Hybrids

Several projects consider also consider hybrid energy storage systems for gasoline electric full hybrid vehicles, which have greater power and regenerative braking capabilities than their mild HEV counterparts. Bond et al lay out the basics for a battery and ultracapacitor hybrid energy storage system for a Ford Explorer SUV planned to be converted to a full hybrid for the 2003 FutureTruck competition [51]. Jianmin and Min provide a basic design and some simulation of an HESS consisting of a 48.6Wh, 54V ultracapacitor pack and a 3.2kWh, 53.2V battery pack to be utilized in their university's BJUT-SHEV test vehicle, which appears to be a passenger van [54]. Ding et al propose a series hybrid architecture with an unusual double stator generator and a battery ultracapacitor hybrid energy storage system, but the system design is almost entirely conceptual and more is clearly needed to prove the merits of the topology [56]. None of these three projects go as far as to quantify the performance of the proposed systems, and provide little insight into design considerations leaving it unclear if an HESS is a good solution for full HEVs.

One final paper which discusses the application of hybrid energy storage to a full HEV focuses entirely on statistical lifetime modeling and system design. The statistical model considers variation in component parameters, and sizes the system for various levels of certainty of the statistical lifetime estimate, as shown in Figure 2.36. The paper is very heavily focused on the statistical analysis, but if the methodology is sound it could be useful for system component sizing if the proper component variability information was available.

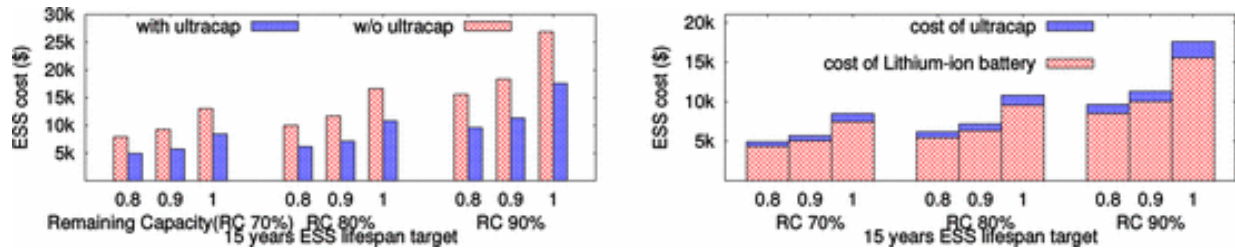


Figure 2.36 Statistical HESS battery and ultracapacitor sizing for example parameters [55]

Fuel Cell Hybrids

One project examined here designs an HESS for a fuel cell vehicle. Napoli et al design a 35kW, 216V electric traction system for a Fiat 600 passenger car, which is powered by a 19.2kW, 200V fuel cell, an 11.2kW, 168V battery pack, and a 28kW, 140V ultracapacitor pack, each connected to the motor drive via a separate dc/dc converter, as shown in Figure 2.37 [52]. Detailed parameters of each subsystem are not provided, but a vehicle control strategy is developed and experimental results for a drive cycle applied to a laboratory test system are also given in Figure 2.37.

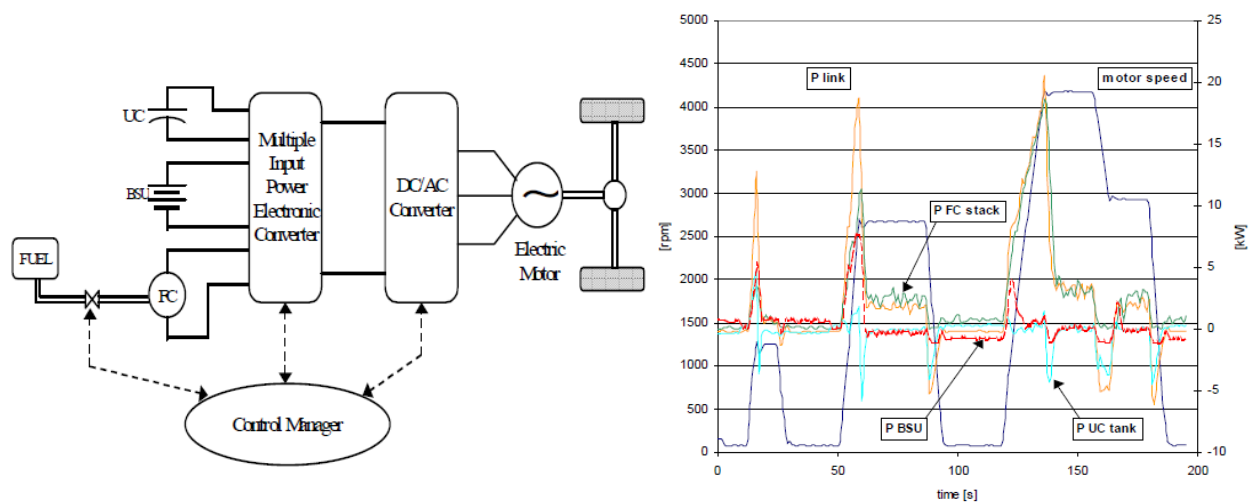


Figure 2.37 Fuel cell vehicle with hybrid energy storage topology and experimental results [52]

2.5.2.3 Heavy Duty Vehicles

Hybrid energy storage has been considered for several types of heavy duty hybrid electric vehicles, including passenger buses, excavating equipment, and military vehicles. Three bus

projects have considered utilizing an HESS, and each proposes a slightly different powertrain configuration [60-62]. Wang et al consider a battery and ultracapacitor hybrid energy storage system for an electric bus manufactured by FAW automotive of China, but only give a high level conceptual description of the system design and performance, and provide no system parameters or details [60]. Xiaodong et al develop a very detailed methodology for design and control of an HEV with a hybrid energy storage system, and show in Figure 2.38 the tradeoff between battery and ultracapacitor size and system losses for a 15 ton bus [61]. In a more application oriented project, Tehrani et al design an HESS for an 18 ton series hybrid electric with two 85kW, 530Nm, 650Vdc bus traction motors. The HESS consists of a 25kWh, 620V LiPo battery pack and a 350Wh, 630Vdc ultracapacitor pack which is connected to the battery pack via a dc/dc converter with an unspecified power rating. The bus performance was modeled for pure electric mode only, and the results as given in Figure 2.39 show that for drive cycles with heavy regenerative braking, such as the *Manhattan* and *New York* cycles, the bus with an HESS, rather than just a battery pack, is capable of recuperating about 40-50% more regenerative braking energy, resulting in improved fuel economy [62].

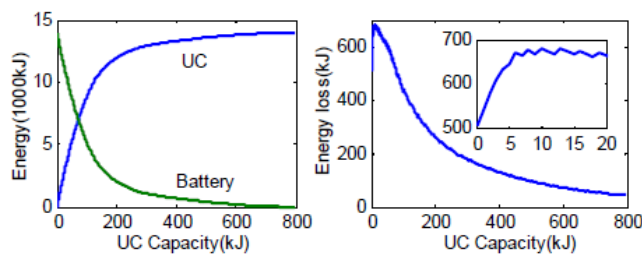


Figure 2.38 Battery and UC energy rating and system losses vs UC capacity for hybrid bus [61]

Driving Cycles	Teh2	Teh1	Manhattan	New York	Test
BRP HESS (kWh)	-0.01	-0.0066	-0.312	-0.154	0
BRP ESS (kWh)	-0.28	-0.0072	-1.278	-0.825	0
BRP Variation (%)	97.74	7.93	75.59	81.31	0
Available Negative Energy (kWh)	-2.17	-0.21	-3.53	-2.56	-0.30
Percentage of Regenerative Energy (HESS) (%)	99.71	96.87	91.16	93.99	100
Percentage of Regenerative Energy (ESS) (%)	87.00	96.60	63.77	67.85	100
Percentage of Regenerative Energy Improvement (%)	14.62	0.28	42.94	38.53	0

Figure 2.39 Hybrid bus modeled HESS vs battery only ESS performance for drive cycles [62]

Wang et al propose utilizing a hybrid energy storage system in a 20 ton class parallel hybrid excavator, which is powered by a 118kW, 560Nm Mitsubishi diesel engine [63]. The authors develop an efficiency model of the diesel engine and the prototype 60kW, 320Nm IPM motor, which is connected directly to the drive shaft of the diesel engine. The system aims to improve the excavator's efficiency by operating at more efficient operating points of the diesel engine. The HESS, which consists of a 485Wh, 437V ultracapacitor pack connected directly to the motor drive dc bus and a 10.8kWh, 270Vdc NiMH battery pack connected to the dc bus via a dc/dc converter, is used to smooth the diesel engine power and allow more efficient operation of the system. No efficiency improvement results are provided, but the authors state that a prototype system has been built in the lab which will be used to fully characterize the system performance.

Felix et al propose a battery ultracapacitor hybrid energy storage system for a 31 ton 8x8 heavy duty military truck, as shown in Figure 2.40. The system consists of four 75kW, 1000Nm traction motors, two 150kW fuel cells, a 17.6kWh battery pack, and a 500Wh (est.), 500V ultracapacitor pack, and the paper focuses on developing and demonstrating a state machine and fuzzy logic controller for the vehicle [64]. Additionally Kadri et al consider utilizing hybrid energy sources in a military truck with four 30kW wheel motors, two 80kW ICEs with generators, and a

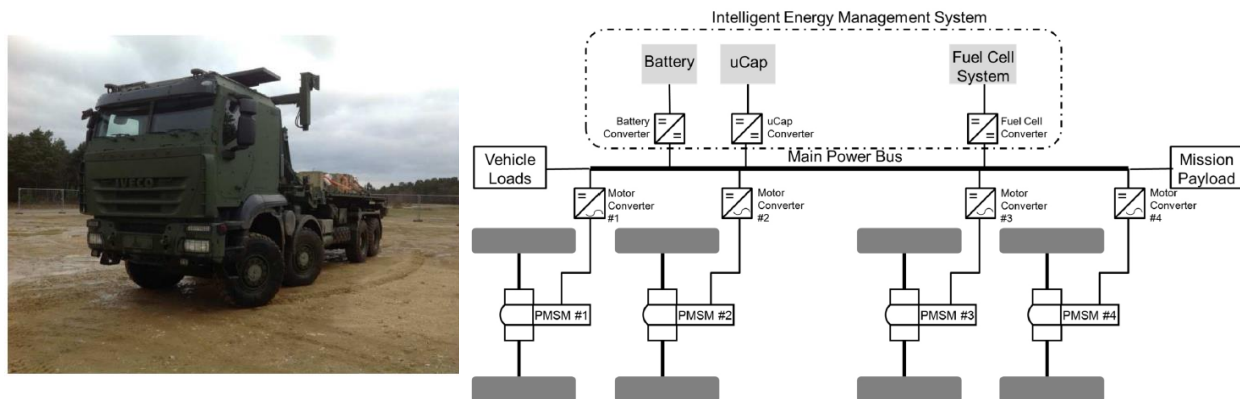


Figure 2.40 Fuel cell heavy duty tactical mobility truck with HESS [64]

battery pack [59]. While this is not a hybrid energy storage system it does have some similar challenges due to the multiplicity of energy sources and the desire to optimize their performance.

In summary, hybrid energy storage has been proposed for several different types of heavy duty vehicles, but the system efficiency, cost, and other improvements that may be achievable have not been well documented. Heavy duty vehicles, due to their high mass and dynamic cycles, are likely a good application for an HESS though, suggesting further work in this area would help to identify the best applications.

2.6 Power Split Control Strategies

While the vehicle type, powertrain, and HESS configuration will play a big role in determining the performance of a hybrid energy storage system, the performance benefits achieved will ultimately be dictated by how the vehicle controls the split in power between the two energy sources, which is referred to as *power split control*. The most common goal of the power split algorithm is to minimize energy storage system losses, however other goals such as minimizing battery rms current and battery losses and minimizing battery aging are common as well.

When utilizing an ultracapacitor pack, controlling the power split is not very straightforward due to the small amount of stored energy available in ultracapacitors. Due to the cost, mass, and volume of ultracapacitors, the goal is typically to use as small of an ultracapacitor pack as possible, making it very difficult to keep the ultracapacitor pack charged at a level which provides maximum system performance. Power split control is typically focused on developing methods to control ultracapacitor SOC in a way which minimizes system losses.

For any vehicle with an HESS, it is possible to determine the ideal, optimized power split if the entire drive cycle is known ahead of time. Dynamic programming, an optimization method which is discussed in more detail in section 5.5, is often used to calculate the optimal power split based on a model of the vehicle and a cost function which is the value to be minimized and is typically either HESS losses or battery rms current. The optimal solution cannot be achieved without perfect future knowledge of the drive cycle, so many heuristic or rule based controls and predictive optimization techniques have been developed and are discussed in the following sections. Power split controls for EVs are discussed in 2.6.1 and [65-76], and power split controls for HEVs are discussed in 2.6.2 and [77-93].

2.6.1 Power Split Control for Electric Vehicles

A variety of power split control methods have been developed and evaluated for EVs, as outlined in Table 2.13. Rule based control methods have been developed which are similar to the rule based control developed in Chapter 5, dynamic programming has been utilized to minimize system losses as is also done in Chapter 5, and self-optimization techniques have been employed which are beyond the scope of the work in this dissertation. The power split work is organized by the HESS topology, but for the most part the methods developed could be applied to many different HESS topologies.

Table 2.13 Electric Vehicle Power Split Control Projects

Topology	Control Type	University/ Company	Experimental Verification	Year
Batt/UC w/ <u>only UC</u> dc/dc converter	Offline Dynamic Programming & Online Rule Based <i>Min. Battery RMS or System Losses</i>	IFP New Energy, Rueil-Malmaison, France [65]	No	2011
	Optimization – <i>Min. System Losses</i>	Seoul Nat. Univ., South Korea [66]	No	2013
	Sliding Mode Current Control w/ UC <i>Current Reference and Output Voltage Reference</i>	American University of Sharjah, UAE [67]	No	2014
	Convex Multi-objective Optimization – <i>Min. Power Variation & Losses</i>	Seoul National University, Korea [68]	No	2014
Batt/UC w/ <u>batt & UC</u> dc/dc converters	Frequency Based w/ UC <i>Voltage Reference</i>	Univ. of Campinas, Brazil [69]	Yes – Lab	2009
	Rule Based Strategies compared: (1) <i>Source Resistance</i> (2) <i>Vehicle Acceleration</i> (3) <i>Filtration</i> (4) <i>Variable saturation current</i>	Univ. Lille Nord de France, France [70]	No	2010
	Optimization w/ 3 objective functions: (1) <i>Min. battery current</i> (2) <i>Min. change of batt. Current</i> (3) <i>Track UC Voltage Reference</i>	Seoul Nat. Univ., South Korea [71]	No	2012
	Inversion Based Control w/ <i>Frequency Based or Switching Power Split Control</i>	Univ. Lille Nord de France, France [72, 73]	Yes - Lab	2013
	Multi-objective Self Optimization <i>Min. Losses & Max. Power Reserves</i>	Univ. of Paderborn, Germany [74, 75]	Yes - Lab	2013
Solar/Batt/UC	Rule Based Control	Xi'an Jiaotong Univ., Xi'an, China [76]	Yes - Lab	2011

Battery & Ultracapacitor HESS - dc/dc Converter for Battery Only

Several projects develop and evaluate methods for power split control for battery and ultracapacitor HESS's which just have a dc/dc converter for the battery [65]. Malaize and Tona develop a rule based, heuristic control with the goal of either minimizing the battery rms current, thereby reducing battery aging, or minimizing system losses, resulting in improved vehicle range. The rule based control is evaluated by modeling a transit shuttle with an HESS for a non-standard drive cycle, and comparing the rule based results to optimal results achieved with dynamic programming, as shown in Figure 2.41. The heuristic control is shown to only have 10% higher rms current than the optimal DP solution, and 7% more losses than the DP solution. While this suggests the heuristic works well, no data is given for the vehicle or energy storage components, and a non-standard drive cycle is evaluated so it's difficult to generalize the meaning of these results.

control strategy	I_{rms}/I_{rms}^*	I_{losses}/I_{losses}^*
stress minimization via DP	100%	152%
stress minimization via heuristics	110%	141%
losses minimization via DP	155%	100%
losses minimization via heuristics	188%	107%

Figure 2.41 Dynamic programming and heuristic normalized battery rms current and losses [65]

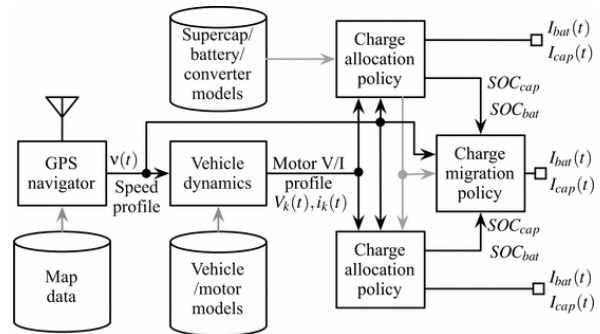


Figure 2.42 EV hess management framework [66]

Another project develops an HESS loss minimizing optimization algorithm and management framework, as shown in Figure 2.42 [66]. A 1560kg, Nissan Leaf EV is modeled with a dc/dc converter and a 600Wh, 540V, 100kg ultracapacitor pack and the algorithm is shown to achieve a 19.4% reduction in system energy consumption for a single acceleration. While a 19.4% improvement sounds very promising, the ultracapacitor pack size is very unrealistic and an

unrealistic, best case high-power high-loss scenario was chosen to evaluate the algorithm, rather than a typical drive cycle.

Dhaouadi et al give a very good description of the development of a sliding mode current control which has the battery provide the low frequency power and the ultracapacitor provide the high frequency power [67]. This control method will have the effect of having the ultracapacitor provide acceleration power and the battery pack provide the constant speed road load power. Choi et al develop a convex multi-objective optimization methodology which, while not requiring any future information, minimizes power variation & losses [68]. They apply the optimization algorithm to a passenger vehicle model taken from another paper, and compare their proposed algorithm to a rule based and fuzzy logic algorithm and an algorithm which sets ultracapacitor voltage based on speed, and show the proposed algorithm reduces losses more than all but the fuzzy logic algorithm.

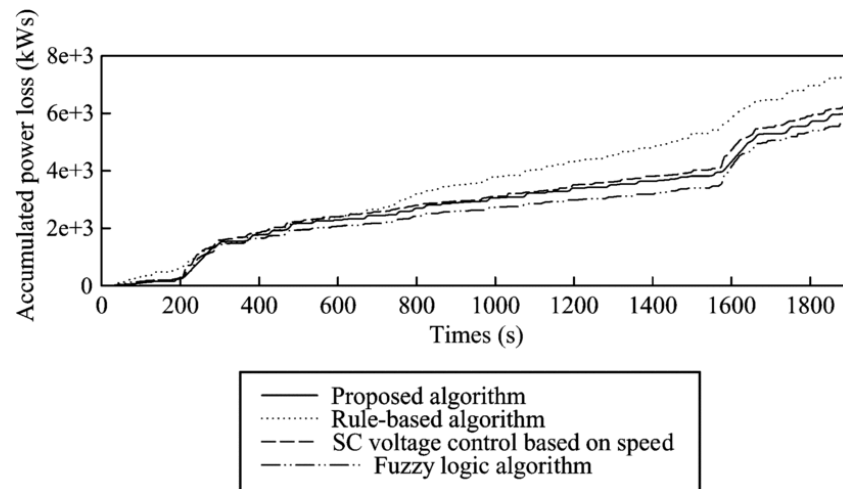


Figure 2.43 Simulated losses for convex multi-objective control methodology (*proposed algorithm*) for FTP75 drive cycle [68]

Battery & Ultracapacitor HESS - dc/dc Converter for Battery & Ultracapacitor

There are also several projects which develop power split controls for HESS's with a dc/dc converter for both the battery and ultracapacitor pack. Most of the power split control strategies

could however, with some modification, be applied to a one or two dc/dc converter systems, so all the presented control strategies can be considered when seeking a solution for an application.

Garcia et al develop a frequency based power split and power electronics control strategy, and show in Figure 2.44 the frequency response for both sources with a crossover frequency of about 0.1Hz [69]. To prove that the proposed control strategy functions properly in a real system with power electronics and a battery and ultracapacitor pack, they test the system with a 144V, 2.2Ah lead acid battery pack a 210V 30F ultracapacitor pack, and Figure 2.44 shows the experimental magnitude and phase response aligns well with the simulated response.

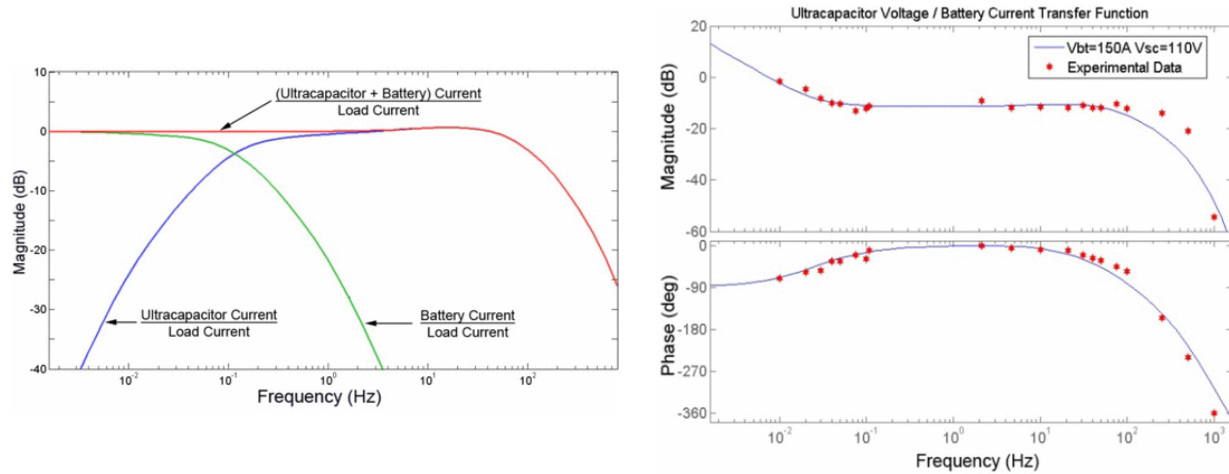
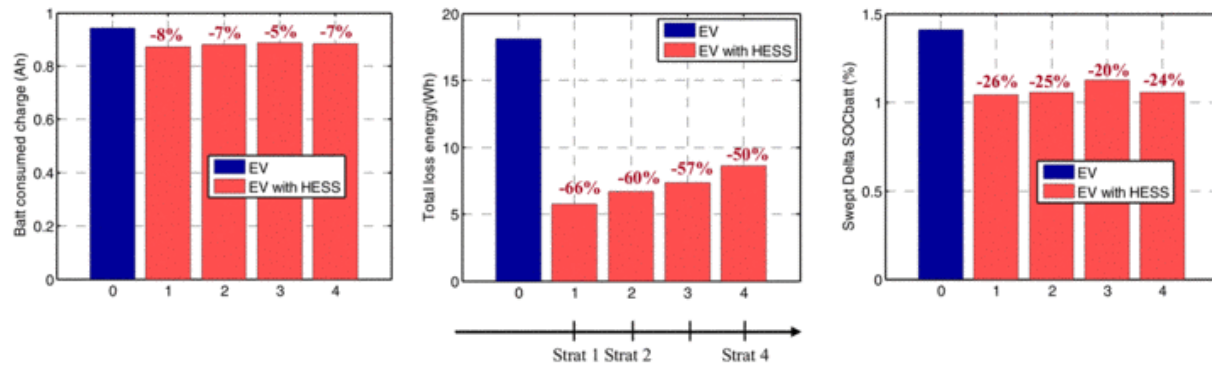


Figure 2.44 Frequency based power split control with experimental verification [69]

Allègre et al focus on different, non-optimized, strategies for commanding power split between the battery and ultracapacitor pack [70]. The authors consider four strategies – (1) source resistance, (2) vehicle acceleration, (3) filtration, and (4) variable saturation current – and model vehicle performance for each one. The source resistance strategies aims to calculate a minimized system loss power split at each time point based on a system model, which has some similarities to the work presented in Chapter 5 in this dissertation. The acceleration strategy utilizes the ultracapacitors to apply acceleration power, and the filtration strategy utilizes the battery pack for low frequencies and the ultracapacitor for high frequencies, similar as what's done above in [69].

The saturation strategy has batteries supply all the current up to a certain level, and then has the ultracapacitors provide power above that level. The selected results for the ECE urban driving cycle in Figure 2.45 show that strategy 1, the source resistance solution, results in the greatest reduction in energy consumed from the battery, losses, and swept SOC, and is therefore the best solution for this drive cycle.



Strat 1: Source resistance **Strat 2:** Vehicle acceleration **Strat 3:** Filtration **Strat 4:** Variable Saturation Current

Figure 2.45 Simulated EV vs EV with HESS vehicle performance metrics for four power split strategies [70]

Choi and Seo focus on developing an online optimized power split strategy which minimizes battery current and change of battery current, and tracks an ultracapacitor reference voltage, but don't show quite enough results to illustrate the performance and benefits of the proposed control [71]. Allegre et al in another work apply energetic macroscopic representation, a method of modeling electromechanical systems, to an electric vehicle with an HESS and create an inversion based control for the system based off the modeling [72, 73]. The inversion based controller is shown in lab experiments to work for two different power split methods, and the authors state that the developed control strategy has been implemented on an electric bus.

Romaus et al develop an online multi-objective self-optimization control method, which bases the power split off of a system model and learning from past drive cycles [74, 75]. This is the most advanced of the power split strategies investigated here, a comparison of this strategy to

others presented here would likely provide some interesting insights. The control strategy aims to minimize losses and maximum system power capability reserve. The authors evaluate the control strategy for a modeled Mini Cooper EV with a 9.2kWh (est), 200kg NiMH battery pack and a 222Wh, 54kg ultracapacitor pack, and they compare different control strategy weightings and self-optimization methods.

Solar w/ Battery & Ultracapacitor HESS

For the final electric vehicle project examined, Wu et al develop an energy management strategy for a solar car powered by a solar panel, battery pack, and supercapacitor [76]. The system consists of a solar panel connected to the battery pack through a maximum power point tracking (MPPT) boost converter, a 2.9kWh battery pack connected directly to a 3.8kW motor drive system, and a 6.7Wh ultracapacitor pack connected to the battery pack through a dc/dc converter. A rule based system control strategy is developed and is shown experimentally in the lab to be functional, providing a good example of how to control an HESS in a solar vehicle.

2.6.2 Power Split Control for Hybrid Electric Vehicles

Many different power split methods have also been developed for hybrid electric vehicles, as outlined in Table 2.14. The methods developed for mild hybrids are somewhat unique, due to the low voltage, distinct system requirements, and use of lead acid batteries, but the remainder of the power split methods have similarities to those presented for EVs. Several projects stand out as taking a unique approach though, with [82] and [93] utilizing a battery life model to control power split and size the HESS components, and with [87], which is arguably the best paper on power split control, comparing a heuristic and optimal control in a very thorough fashion which includes a parametric study which varies eight system parameters.

Table 2.14 Hybrid Electric Vehicle Power Split Control Projects

Topology	Control Type	University/Company	Exp. Test	Year
Mild HEV w/ Lead Acid Battery & Ultracapacitor	Parallel Connection of Battery & Ultracapacitor – w/ SOC management	Hanyang Univ., Korea & Korea Auto. Tech. Inst. [77]	Yes – Lab w/ cycle life	2006
	Battery & Ultracapacitor SOC Control – control via parallel connection w/switch	Hanyang & Ulsan Univ., Korea & Korea Auto. Tech. Inst. [78]	Yes - Lab	2007
	Ultracapacitor SOC Compensation - control via parallel connection w/switch	Korea Univ., Hanyang Univ., Korea & Korea Auto. Tech. Inst. [79]	Yes - Lab	2009
	Rule Based Predictive Energy Management System	Tata Motors [80]	Yes – Lab	2014
Series HEV w/ Batt/UC w/ UC dc/dc converter	Mode & Switch Based Control w/ <i>Truth Tables</i>	Harbin Inst. of Technol., China [81]	No	2008
	Dynamic Programming w/ <i>goal to minimize LiFePO₄ battery capacity loss per drive</i>	University of Tehran, Iran [82]	No	2013
Parallel HEV w/ Batt/UC w/ UC dc/dc converter	Low Pass Filter w/ <i>Velocity Based UC Voltage Control</i>	Harbin Inst. of Technol., Harbin, China [83] (for FAW hybrid electric bus)	No	2009
	Three Strategies Compared: (1) Battery Current Threshold, (2) Minimize Losses, (3) UC Velocity Based Volt. Target	Univ. Muenchen, Munich, Germany [84]	No	2009
	Calculated minimum loss w/ Velocity Based UC Voltage Control	Florida State, Florida A&M, & Pusan Nat. Univ., South Korea [85, 86]	Yes - Lab	2010-2011
	Comparison of Rule Based w/ <i>Low Pass Filter & Optimal Control min.</i>	French Institute of Sciences and Tech. for Transport and Valeo [87]	No	2013
Parallel HEV, two topology options	Various Simple Controls Examined	Illinois Inst. of Technol., Chicago, IL [88]	No	2006
Parallel Through the Road HEV	Rule Based Control, Model Predictive Control, & Dynamic Programming Control	University of Surrey, Guildford, UK [89]	No	2014
Parallel HEV w/ Battery Only	Dynamic Programming – <i>Comp. of Conventional, Local Linear, & Spline</i>	Chalmers University of Technology, Goteborg, Sweden [90]	No	2014
Fuel Cell/UC both w/ dc/dc converters	Nonlinear Controller w/ <i>UC Current reference and Output Voltage Reference</i>	Ibn Tofail University, Morocco [91, 92]	No	2012-2014
Fuel Cell w/ Batt/UC w/ UC dc/dc converter	Convex Optimization w/ <i>ultracapacitor sizing with goal of optimizing battery service life</i>	Chalmers University of Technology, Sweden [93]	No	2014

Mild Hybrids

There are several projects which consider hybrid energy storage for mild hybrids, most of which were performed at Hanyang University in Korea. In the first of these projects Lee et al utilize a 36V, 20Ah lead acid battery connected in parallel with a 45V, 77Wh ultracapacitor pack in a 42V mild hybrid application [77]. The motivation for the work was the proposed switch to 42V, rather than 12V, low voltage systems in vehicles, which has since been abandoned. However mild hybrids with 12V and 48V power systems are currently under greater consideration, and this work may apply to such systems. The authors test the lead acid battery and ultracapacitor system thoroughly in the lab, demonstrating improved performance for high current pulses that would be seen during regenerative braking and engine starting, and perform a start-stop / regenerative braking cycle life test up to 200k cycles, and show that the system capacity only decreases by 5% and the resistance only increases by 8%, as shown in Figure 2.46 below.

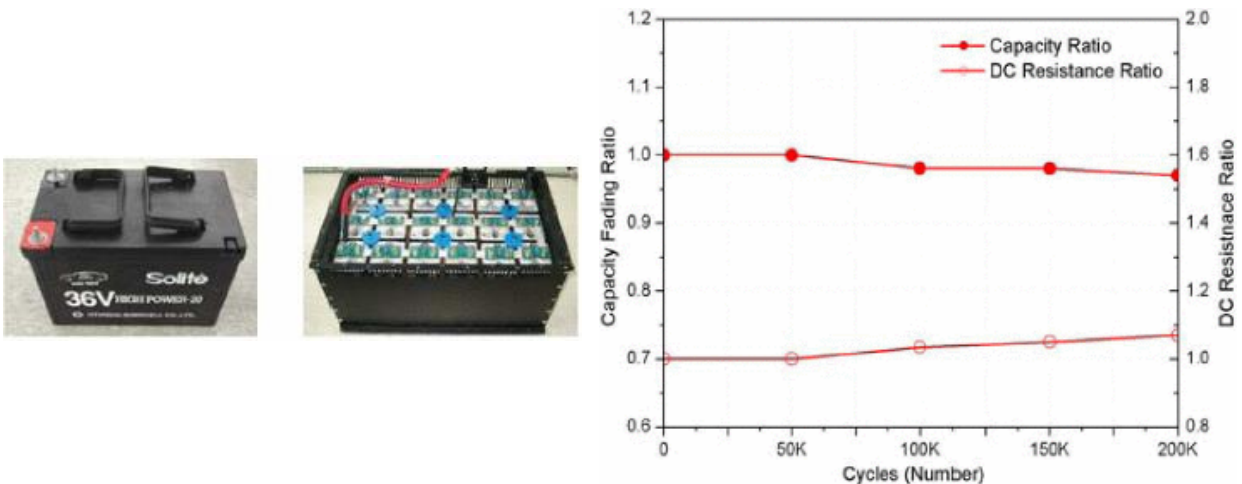


Figure 2.46 Idle-stop/start & regenerative braking cycle life test for 36V battery ultracapacitor system for a mild hybrid [77]

In a continuation of the work discussed above, Lee et al improve the performance of the system by reducing the ultracapacitor pack size to 17Wh/45V, and by connecting the ultracapacitor pack directly to the vehicle's integrated starter generator. A switch is also added to break the parallel

connection of the battery and ultracapacitor pack, enabling improved system efficiency and reduced cycles on the battery pack [78]. In another related project from Korea University which uses the same mild hybrid system, Song et al develop an ultracapacitor state of charge estimation methodology [79]. The ultracapacitor SOC is calculated through a combination of Ah counting and correction based on the measured voltage of the device, including adjustments for different temperatures. The SOC estimation method is then shown experimentally, with a 2% accurate current sensor and 0.5% accurate voltage sensor, to estimate ultracapacitor SOC nearly as well as is calculated with a 0.05% accurate current sensor and Ah counting. This work is especially valuable because it demonstrates how to achieve a good estimate of a critical system parameter using lower accuracy, cheap automotive grade sensors.

In the final project to examine hybrid energy storage for a mild hybrid, Kulkarni et al develop and test an energy management strategy for a mild hybrid, as shown in Figure 2.47, with a 5kW traction motor (est.), a 1.5kWh, 48V, 40m Ω lead acid battery and a 35V, 14.6Wh, 7m Ω ultracapacitor pack [80]. The ultracapacitor power flow is controlled by a dc/dc converter, and the goal of the developed control algorithm is to keep the ultracapacitor pack charged enough to

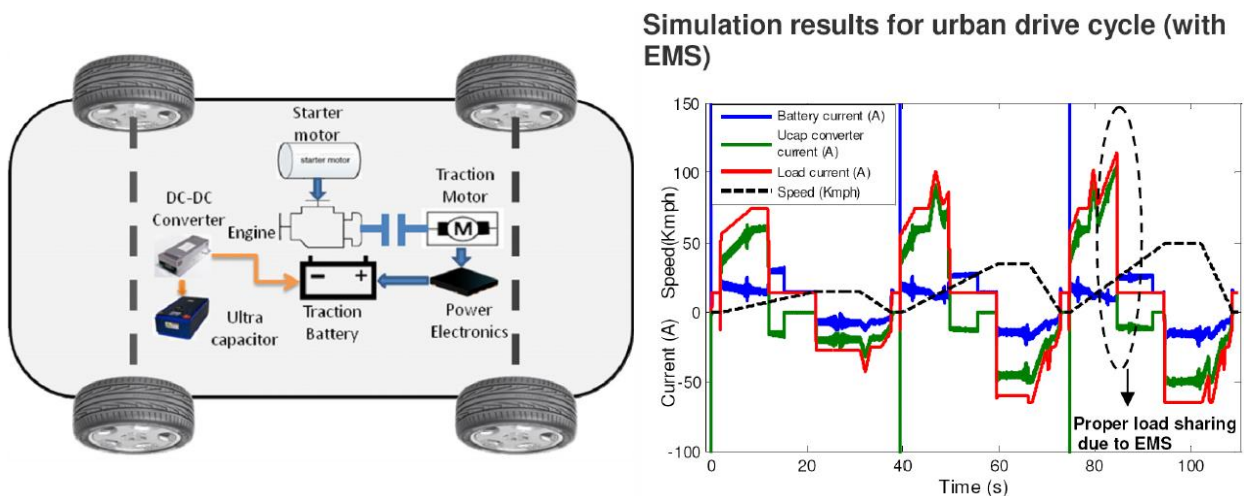


Figure 2.47 Mild hybrid HESS configuration and simulated performance for a drive cycle [80]

contribute to vehicle acceleration. The algorithm calculates charge to add to the ultracapacitor pack based on calculated ultracapacitor and dc/dc converter losses, which if not accounted for would result in slowly depleting ultracapacitor voltage. The simulated controller results for a drive cycle are shown in Figure 2.47, and experimental results from a lab test system are included in the paper as well.

Series Hybrid – w/ Battery and Ultracapacitor HESS w/ Ultracapacitor dc/dc converter

There are two papers which work specifically on series hybrid system and control design, and both provide some interesting insights. Shu-mei et al design a control strategy for a 16 ton, 100kW series hybrid combat vehicle with a 283Wh, 400V ultracapacitor connected directly to the motor and generator dc bus and a 28kWh, 300V battery pack connected via a dc/dc converter, as shown in Figure 2.48. To control the system a very functional approach is taken, which identifies different operating states, such as start, normal, and brake as given in Figure 2.48, and defines how the system will operate in each state and simulates that performance. This paper deals with some of the more practical aspects of creating a functional system, which are necessary to consider when implementing an HESS in a hybrid vehicle.

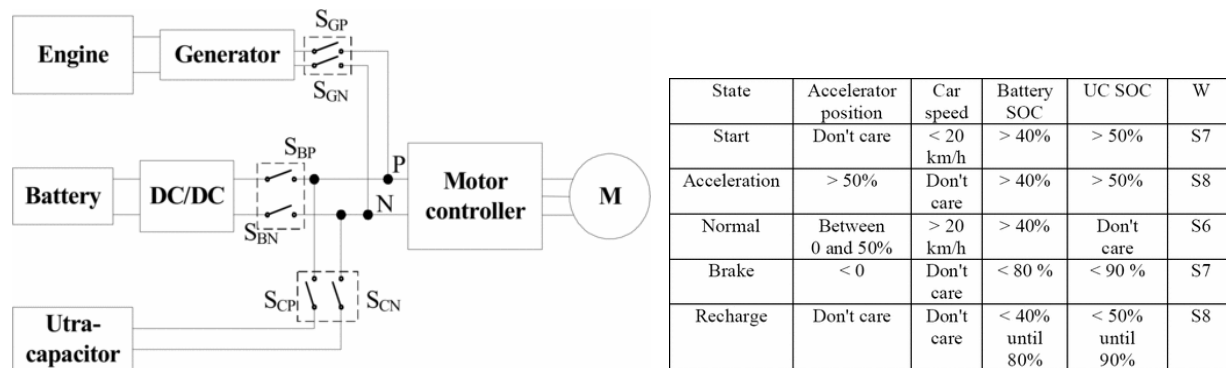
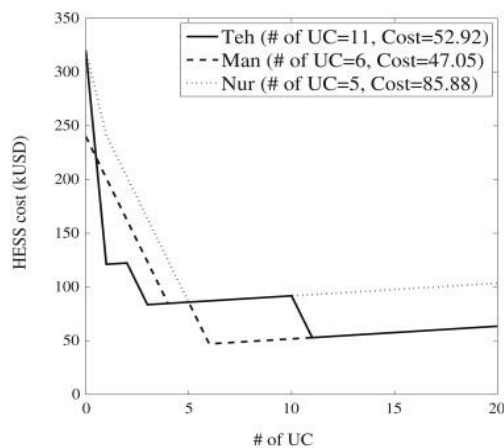


Figure 2.48 System topology and truth table control for series hybrid military combat vehicle with HESS [81]

In the second paper to address series hybrid HESS design, Masih-Tehrani et al do an excellent job of sizing battery and ultracapacitor packs for an 18 ton bus based on predicted cycle life and lifetime cost, and develop an optimum energy management system as well [82]. The bus is outfitted with a 24kWh, 614V LiFePO₄ battery pack, and the authors utilize the results of an experimental cycle life study in which temperature, current, and DOD are varied [105] to estimate how many times the battery pack will need to be replaced over ten years of service life. Dynamic programming is used in a very clever way, to control the power split to minimize battery aging for a drive cycle.

The system cost is then optimized by adding a varied number of 54Wh ultracapacitor modules, which are connected through a dc/dc converter. The number of ultracapacitor modules which results in a minimized 10 year system cost (due to reduced number of replacement battery packs) is then calculated for different drive cycles and shown in Figure 2.49. The addition of ultracapacitor modules is shown to result in a very significant cost saving of several \$100k, but this large savings is mostly due to an assumed battery cost of \$1500/kWh, which is about 3-5 times what the battery pack would likely cost today. Even so, the methodology presented is



Effects of ESS hybridization.

Performances	Tehran	Manhattan	Nuremberg
# of UC	11	6	5
Cost improvement (%)	83.46	80.40	73.16
Fuel consumption improvement (%)	41.74	29.68	26.85

Figure 2.49 Series hybrid bus optimized # of ultracapacitor packs to minimize 10 year system cost by extending battery pack life [82]

applicable with different component costs, and it is likely there would still be a cost benefit to adding ultracapacitor packs even with the lower battery price.

Parallel Hybrid – w/ Battery and Ultracapacitor HESS w/ Ultracapacitor dc/dc converter

There are several different projects that develop power split control strategies and apply them to parallel HEVs. Haifang et al continue their work proposed in [60] on the FAW parallel hybrid bus and model it with an 8.1kWh, 300V NiMH battery pack and a 281Wh, 300V ultracapacitor. They then design a power split control which utilizes a lower pass filter and a velocity based ultracapacitor SOC command, as illustrated in Figure 2.50. The system is modeled both with and without the ultracapacitor pack for two drive cycles, and the HESS is shown in Figure 2.50 to reduce the battery's peak and rms current significantly.

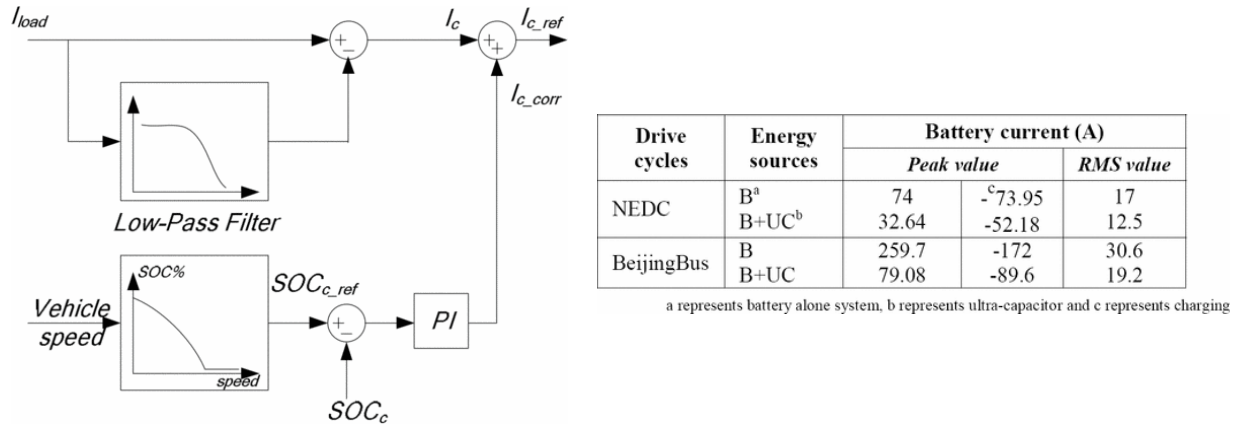


Figure 2.50 Low pass filter and velocity based power split control for hybrid bus [83]

Kohler et al develop and evaluate three power split strategies for a parallel HEV [84]. The first strategy considered is a battery current threshold strategy, where the ultracapacitor provides all current above a certain threshold. The second strategy analytically calculates the minimized loss power split at each operating point, as is done in Chapter 5 of this dissertation, and the resulting state of charge and accumulated losses for an NEDC drive cycle are shown in Figure 2.51 below. This method has the disadvantage of not controlling ultracapacitor SOC, so a third method that

utilizes a vehicle velocity based voltage target is developed and evaluated as well, which the authors conclude is the best of the three options.

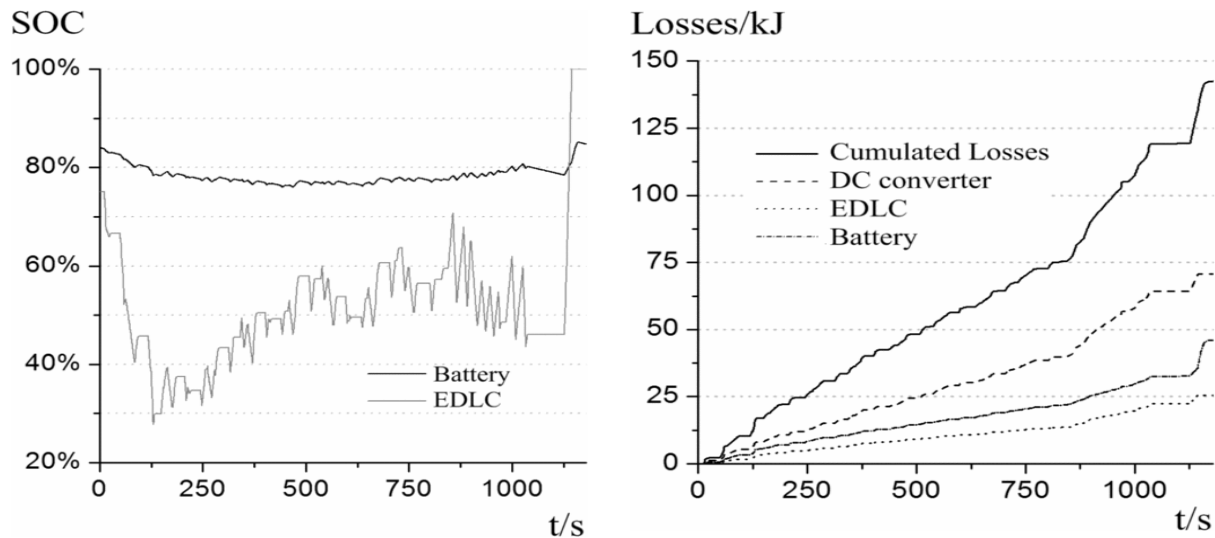


Figure 2.51 Calculated minimum losses control results for Parallel HEV and NEDC drive cycle [84]

Vinot and Trigui, in what is arguably the best paper on hybrid energy storage for HEVs, provide a very detailed design and model of a parallel HEV with lead acid battery and ultracapacitor hybrid energy storage [87]. The authors then develop and compare a rule based low pass filter control and an optimal control which performs a weighted minimization of battery rms current and fuel consumption. Additionally a parametric study is performed in which eight system parameters, including hybrid system power, SOC thresholds, and low pass filter frequency, are varied. In Figure 2.52, the fuel consumption versus battery rms current is shown for the NEDC drive cycle for all of the rule based parametric study solutions the NEDC drive cycle. The results show that the rule based solution can achieve fuel economy within 3% of the optimal solution, and that lower battery rms current can be traded for slightly higher vehicle fuel consumption. This methodology could be used to characterize the battery rms current and electrical energy consumption tradeoffs

for an electric vehicle with hybrid energy storage, and likewise to evaluate rule based versus optimal control in an EV.

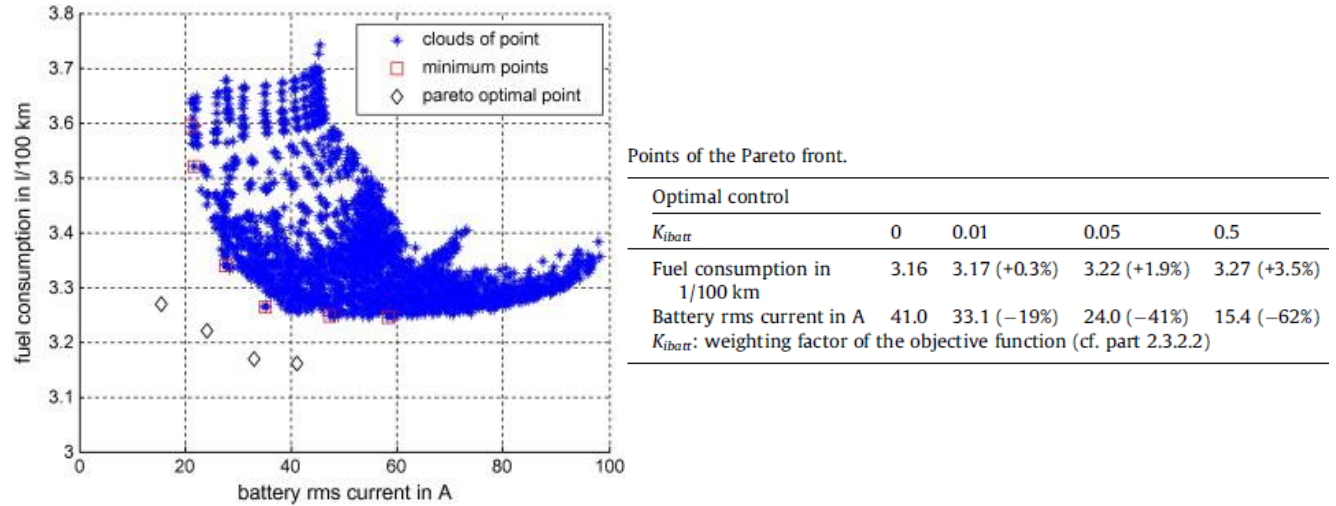


Figure 2.52 Parallel hybrid fuel consumption vs battery rms current for rule based (blue) and optimal (black diamonds) control [87]

Wang et al develop a power split control method for a PHEV which calculates the minimum loss power split at each operating point and controls ultracapacitor voltage based on velocity, similar to the third method evaluated in [84] and the rule based method evaluated in Chapter 5 of this dissertation [85, 86]. The authors also go through a process of minimizing the HESS system mass and losses by varying the ultracapacitor pack size, and perform an experimental test, demonstrating the developed control systems' performance for a single drive cycle.

Parallel Hybrid – variations on topology

Several projects also examine a few different topology variations of the typical parallel hybrid vehicle with an HESS. Lukic et al compare three HESS topologies for a parallel hybrid: (1) passive parallel connection of battery and ultracapacitor packs, (2) ultracapacitor pack with a dc/dc converter, and (3) both battery and ultracapacitor pack with a dc/dc converter [88]. They conclude that the passive solution requires more ultracapacitors to perform as well as active topologies, and

that the ultracapacitor pack can be shrunk even further with future knowledge of the drive cycle, which is similar to the conclusion reached in Chapter 5 of this dissertation.

Santucci et al model a through the road parallel hybrid with an 18kWh, 300V LiPo battery pack and a 570Wh, 300V, 104kg ultracapacitor pack connected to the battery pack via a dc/dc converter [89]. The authors develop several power split controls, including a rule based (RB), model predictive control (MPC), and dynamic programming (DP) control. The goal of the controls is to increase the cycle life of the battery by reducing battery maximum and rms current, and the results of the three controls are shown in Figure 2.53 below. All three control methods are shown to greatly reduce battery rms current and to increase battery lifetime. These results should not be extrapolated to apply to other situations though, since the ultracapacitor pack needed to achieve this performance is unrealistically large (104kg) and the life increase is predicted using an adapted cycle life methodology which likely doesn't accurately represent this cell chemistry and its application in a vehicle.

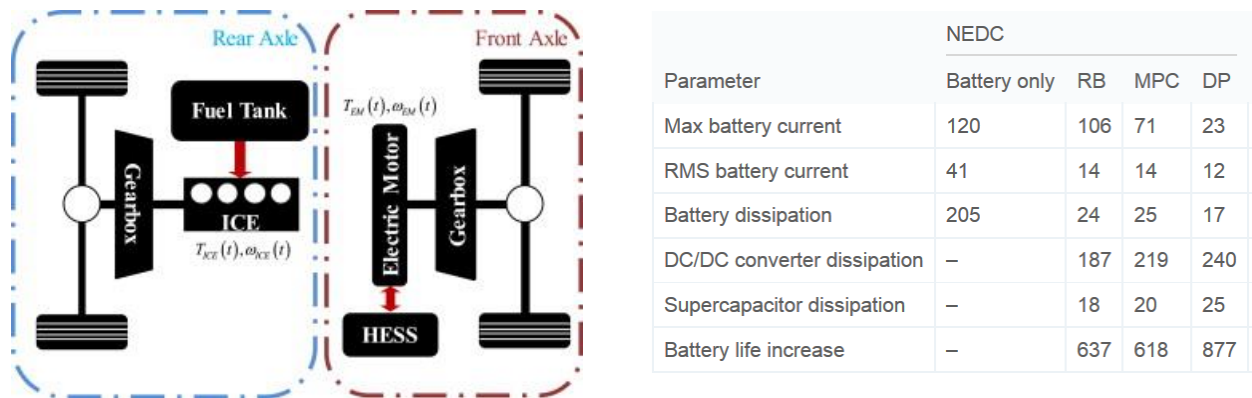


Figure 2.53 HESS performance improvements for parallel through the road hybrid [89]

Larson et al develop several methods to reduce the computational requirements of dynamic programming, which has been used to calculate the optimal power split for many of projects discussed in this chapter [90]. The methods utilize an analytical vehicle system model to calculate

a local approximation of the solution, resulting in computation time being reduced up to a factor of 100, as shown in Figure 2.54, which the authors claim is sufficient to allow a vehicle ECU run the proposed algorithm. The methodology is developed for calculating gas engine and electric motor power split for a PHEV, but could potentially be applied to a system with hybrid energy storage as well. The authors do however state that algorithm will not work as well for systems with a small energy buffer, so the method may not work well for systems with a small ultracapacitor pack.

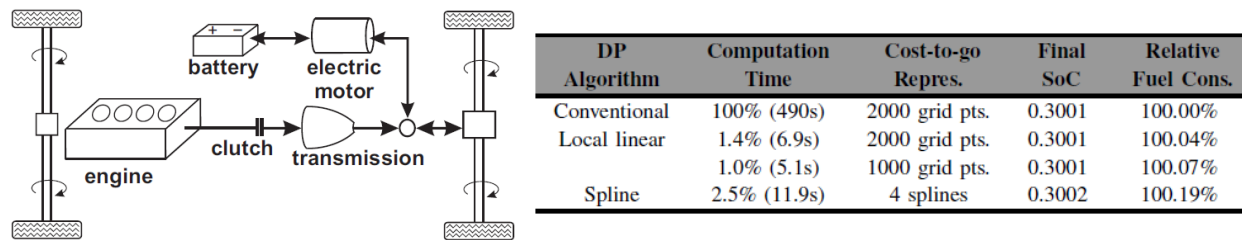


Figure 2.54 Computationally efficient modified dynamic programming for parallel hybrid vehicle control [90]

Fuel Cell Hybrid

Only a two projects are examined which consider power split methods for fuel cell hybrid vehicles. In the first, Fadil et al exam a vehicle which only utilizes a fuel cell and an ultracapacitor both with dc/dc converters, and does not actually utilize hybrid energy storage [91, 92]. This work is notable because of the global state space power electronics system model and Lyapunov controller which is developed, and may be applicable to modeling or control of power electronics in an HESS.

In the second project, Hu et al consider a hybrid energy storage system for a fuel cell bus with a 220kW traction system and a 100kW fuel cell. The focus is on sizing both the battery and ultracapacitor pack based to reduce the number of necessary battery replacements by utilizing a state of health model based on the results in [105], and is similar to the work performed in [82] for

a diesel powered series hybrid bus. One difference between this work and that in [82] is that both battery pack size and ultracapacitor pack size are varied to achieve the optimal solution, as shown below in Figure 2.55. This figure also shows that when considering state of health, the optimal battery size shrinks slightly and the ultracapacitor size increases by a factor of five. This methodology, which utilizes a convex optimization power split control could likely be applied to other vehicle topologies with an HESS.

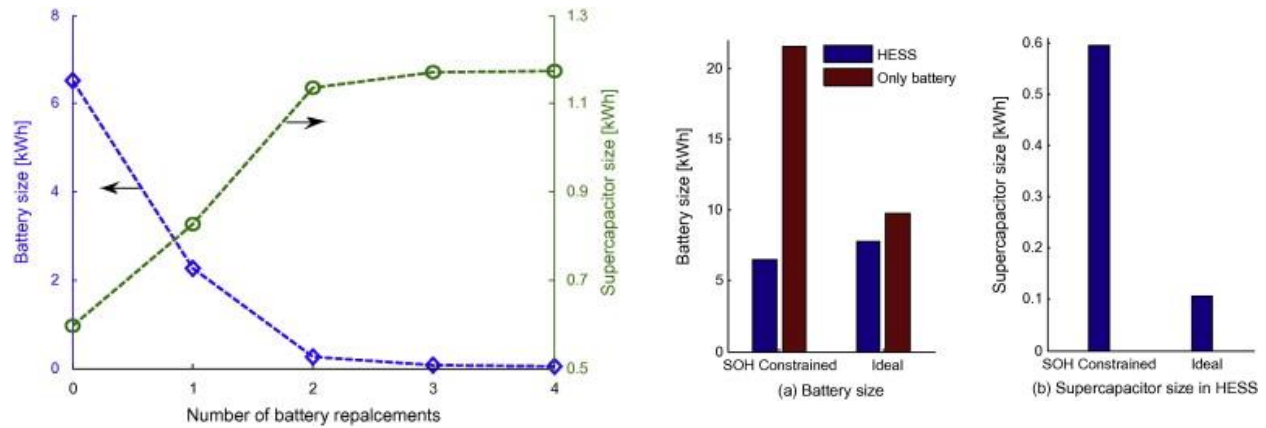


Figure 2.55 Battery and ultracapacitor pack sizing for fuel cell hybrid bus considering battery aging [93]

Chapter 3

Traction System Design, Modeling, and Fabrication for Class 2a Electric Truck

3.1 Introduction

The goal of this project is to design and install an electric powertrain into a Ford F150 truck, as shown in Figure 3.1 below. The system will provide similar power and performance to the 2002 model year stock truck with a 4.2L V6, 150kW (peak) gasoline engine. The electric truck will be heavily instrumented with data acquisition equipment including a torque sensor mounted between electric traction motor and gearbox shafts. The data provided by this instrumentation will be used to develop and evaluate a detailed electromechanical model of the vehicle, as well as enabling the evaluation of alternative motor, motor drive, and energy storage systems in the future.

Many companies have used the Ford F150 as a platform for developing electric and hybrid electric vehicle drive trains. Protean has an electric F150 prototype with in-wheel motors, Enova has an electric F150 prototype, HEVT has a plug in-hybrid F150 prototype, and AltE and Quantum Technologies offer retrofitting of F150s with plug-in hybrid drivetrain systems [106-110]. Each F150 truck project has a similar aim – to reduce fuel consumption, greenhouse gas emissions, and the total cost of ownership of light-duty work trucks.

This electric truck project outlines the design process for a Ford F150 electric truck that has many similarities to the production-oriented vehicles. Insights are provided on how to design an electric drivetrain for a light-duty truck as well as providing data on the electrical energy consumption of the vehicle. Additionally, this project builds on other projects to design, model, and experimentally verify electric vehicle and electric vehicle component performance [111-118].



Figure 3.1 F150 truck with electric powertrain

The process of choosing the vehicle power and range goals, choosing a battery pack that can meet the power and energy demands, and designing a prototype interior permanent magnet (IPM) machine that can provide sufficient power is described. The IPM machine performance is experimentally verified, and the system-level vehicle design, data acquisition, and battery management systems are described, documenting one method for designing and building a research-oriented electric vehicle.

3.2 Determination of Power and Energy Storage Requirements

The IPM machine output power requirement is first developed from the power rating of the gas powered truck. Then the energy consumption of the truck for several Department of Energy (DOE) drive cycles is estimated from a simple model developed with experimentally determined mass and drag power.

3.2.1 IPM Machine Output Power Requirement

The 2002 model year Ford F150 truck to be fitted with the prototype electric traction system was offered originally with three gasoline engine options: a 4.2L V6, a 4.6L V8, and 5.4L V8, providing peak power values of 150kW, 172kW, and 193kW, respectively, at the engine's output shaft [119]. The goal for this project is to develop an IPM machine based drive system that can provide 135kW at the shaft of the machine, 10% less power output power than the 4.2L V6. Although the IPM machine will have less power output than the 4.2L V6 engine, similar performance is expected to be achieved by utilizing an Integrated Electric (IE) Drives transmission in place of the stock automatic transmission. The IE Drives transmission is rated for greater than 95% efficiency, which should reduce drivetrain mechanical losses significantly below the observed losses of 22% between the gas engine and rear wheels in 2011 model year Ford trucks [120, 121].

The 2002 model year F150 engines were chosen as a benchmark because the 135kW power range is seen as being reasonably achievable with available battery and motor drive technology. Since 2002, significant advances have been made in gasoline engine performance. As a result, 2011 model year Ford light-duty trucks have much higher output power, ranging from 225kW to 307kW. It was ultimately decided that the engineering effort and costs involved in the development of a battery pack, motor, and electric drive that can achieve this higher level of performance was not justifiable or necessary in order to accomplish the primary objective of developing a prototype electric vehicle that can be used as a productive research platform for exploring new components and subsystems.

3.2.2 Battery Energy Storage Requirement

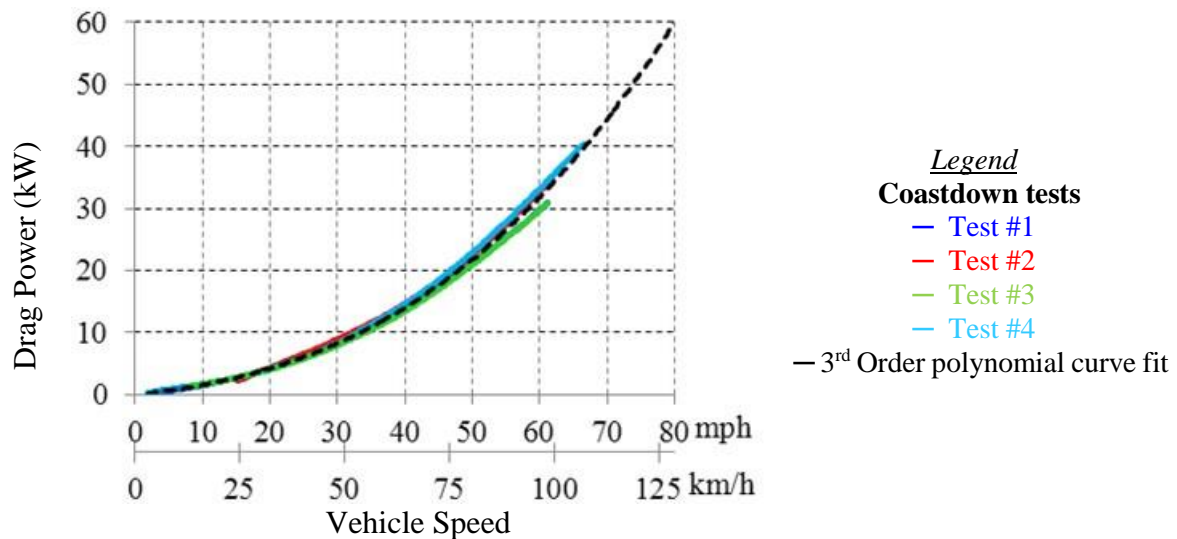
The current generation of mid-priced electric vehicles, e.g. - the Nissan Leaf, Mitsubishi i-MiEV, Ford Focus EV, and Honda Fit EV, typically have a range between about 80 and 160 km [122]. This range is considered to be sufficient for daily use around a metropolitan area, and fast charging stations are being strategically placed between cities to allow these vehicles to travel longer distances. A similar goal of approx. 80 to 160 km range will be adopted for this electric truck. A simple vehicle model is necessary to estimate how much battery energy is required to achieve this range goal.

A simplified model for the vehicle's mechanical and electric drive systems has been adapted from the electromechanical model of a Corbin Sparrow electric vehicle presented in [116]. The vehicle model consists of two major parts - the mechanical forces acting on the vehicle and the electric drivetrain model. To determine the mechanical forces acting on the vehicle, the vehicle mass, rotational inertia, and drag power as a function of speed must be determined. The vehicle mass prior to electrification was measured to be 2250kg. The vehicle mass is expected to increase by approx. 10% due to electrification of the vehicle, so a vehicle mass of 2475kg together with a driver and gear mass of 100kg has been used for the model. The rotational inertia of the wheels and drivetrain is considered to increase the effective mass of the vehicle by approx. 5%, similar to that observed in [116], resulting in an equivalent mass of 2700kg, shown in Table 3.1.

Table 3.1 Estimated Vehicle Mass and Drag Power Coefficients

Total estimated vehicle mass w/ 100kg driver + gear mass		m_{veh}	2575 kg
Total estimated vehicle mass plus effective inertial mass		m_{veh-eq}	2700 kg
Drag Power Coefficient	z_3	z_2	z_1
Value	0.551 $W/(m/s)^3$	20.3 $W/(m/s)^2$	245.8 $W/(m/s)$

The mechanical drag power component used in the model was estimated by performing four coast-down tests with the truck in neutral gear position. The testing and analysis procedure described in [116] was used. The drag power test results presented in Figure 3.2 show that approx. 32kW is required to maintain a speed of 100km/h. The drag power estimate is likely high, however, due to drag in the transmission while in neutral. The actual drag power for the electric vehicle will likely be significantly less, so the results of this simple model are considered to be a conservative estimate.

**Figure 3.2** Gasoline-powered F150 drag power versus speed derived from coastdown test

The total mechanical power acting on the vehicle for a given speed and acceleration can then be calculated as the sum of the acceleration power, gravitational power, and drag power, as shown in

(3.1), where gravitational power is assumed to be zero due to the absence of elevation change in the DOE test cycles.

$$P_{mot-mech} = P_{accel} + P_{grav}^0 + P_{drag-tot} \quad (3.1)$$

Next, the acceleration power is calculated using the equivalent mass, and the drag power is calculated using the drag power coefficients provided in Table 3.1.

$$P_{mot-mech} = m_{veh-eq} a_{veh} v_{veh} + z_3 v_{veh}^3 + z_2 v_{veh}^2 + z_1 v_{veh} \quad (3.2)$$

where v_{veh} is the velocity in m/s and a_{veh} is the acceleration in m/s^2 . The truck's electromechanical drive system provides the power, as calculated with (3.2), to accelerate the vehicle and overcome frictional drag forces. For use in this simple model, the average efficiencies of the motor, motor controller, and battery for charge or discharge is assumed to be 94%, 94%, and 95%, respectively. The accessory power is assumed to be constant at 1kW, listed in Table 3.2.

Table 3.2: Component Efficiencies and Accessory Power for Model

Motor efficiency	η_{mot}	94%
Motor controller efficiency	$\eta_{mot-cont}$	94%
Battery charge/discharge efficiency	η_{batt}	95%
Accessory power	P_{acc}	1000W

The motor controller's dc input power is calculated as the ratio of the motor's mechanical output power to the product of the motor and motor controller efficiency for motoring mode and as the product of the motor's mechanical input power, motor efficiency, and motor controller efficiency for regeneration mode, as shown in (3.3). This calculation assumes that only motor regeneration is used to brake the vehicle, neglecting the fact that some of the kinetic energy available for regeneration will be dissipated in the mechanical braking system.

$$P_{mc-in} = \begin{cases} \frac{P_{mot-mech}}{\eta_{mot} \eta_{mc}}; & \text{motoring: } P_{mot-mech} > 0 \\ P_{mot-mech} \eta_{mot} \eta_{mc}; & \text{regen: } P_{mot-mech} < 0 \end{cases} \quad (3.3)$$

The battery output power is calculated as the sum of the motor controller input power and accessory power in (3.4).

$$P_{batt-out} = P_{mc-in} + P_{acc} \quad (3.4)$$

Since the battery output power only describes how much power is extracted from the battery terminals, it neglects the battery internal resistive losses that must also be accounted for to determine how much internal battery energy storage is necessary. To account for these losses, the internal battery power, $P_{batt-int}$, is calculated in (3.5) for battery discharging as the battery output power divided by the battery efficiency, and, for battery charging, as the product of the battery input power and battery efficiency.

$$P_{batt-int} = \begin{cases} \frac{P_{batt-out}}{\eta_{batt}}; & \text{discharge: } P_{batt-out} > 0 \\ P_{batt-out} \eta_{batt}; & \text{charge: } P_{batt-out} < 0 \end{cases} \quad (3.5)$$

The energy consumption per km drawn from the internal stored energy of the batteries (in Wh/km) as well as the total battery energy storage (in kWh) necessary to drive 80 and 160 km is then calculated for this simple model, as shown in Table 3.3. Depending on the driving speed/cycle, the model predicts that between 18.3 and 37.2 kWh of energy storage is required to travel 80 km, and between 36.6 and 74.5 kWh is necessary to travel 160 km. Therefore, to achieve the desired minimum of 80 km range for most driving conditions, 30 to 40 kWh of battery energy storage will be necessary. However, since it is expected the drag power measurement is too high, the energy consumption predictions of the simple model are likely conservative.

Table 3.3: Predicted Electric F150 Energy Consumption

Drive Cycle or Constant Speed	Energy per km (mi)	Energy per 80km(50mi)	Energy per 160km(100mi)
Urban (UDDS)	292 Wh/km (470 Wh/mi)	23.5 kWh	47.0 kWh
Highway (HWFET)	347 Wh/km (559 Wh/mi)	27.9 kWh	55.9 kWh
Aggressive (US06)	463 Wh/km (745 Wh/mi)	37.2 kWh	74.5 kWh
50km/h (31mph)	227 Wh/km (366 Wh/mi)	18.3 kWh	36.6 kWh
110km/h (68mph)	459 Wh/km (739 Wh/mi)	37.0 kWh	73.9 kWh

3.3 Energy Storage and Electric Drivetrain Design

Section 3.2 presented calculations estimating that between 30 and 40kWh of battery energy storage and an output power of 135kW from the IPM machine are necessary to achieve the range and power goals. The energy storage system consists of a lithium battery pack combined with the electric drivetrain consisting of the motor controller, IPM motor, transmission, and rear differential gearing to form an inter-dependent system.

This section first establishes the desired battery pack voltage. This is followed by a discussion of a motor design that can produce 135kW output power using the bus voltage that is available when the battery is under peak load. The motor power delivered to the wheels using the IE Drives gearbox is then compared to the stock truck's power delivery to the wheels. The mechanical layout of the drivetrain components is illustrated in Figure 3.3, a CAD drawing of the truck's drivetrain system. In addition, the battery charger, controller box, touch panel, frame rails, and other subsystem components are shown in the figure.

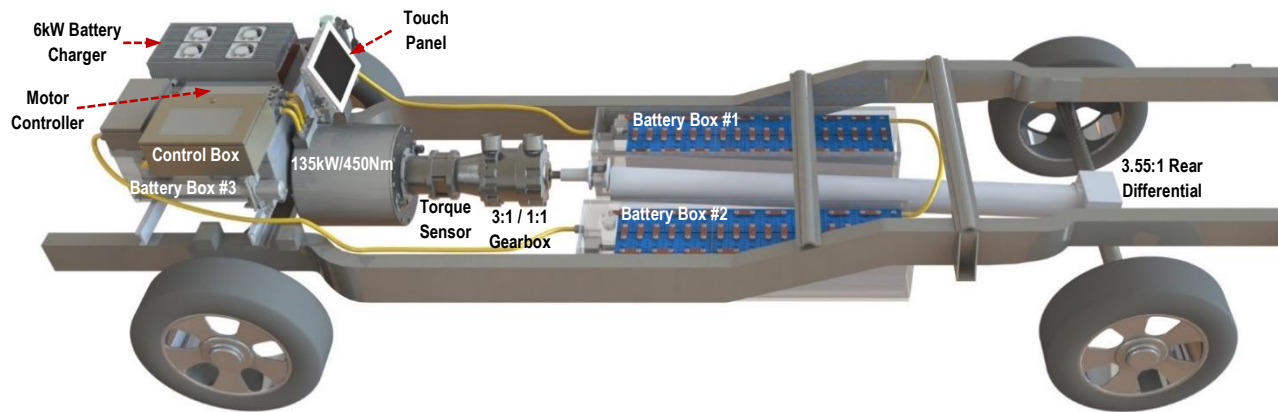


Figure 3.3 CAD drawing of truck drivetrain showing battery pack, motor controller, motor, gearbox & rear differential

3.3.1 Battery Pack Design

The voltage ratings of vehicle battery packs for electrified vehicles are typically in the range of 300V to 350V dc. Higher battery pack voltage ratings have some benefits attributed to reductions of the motor current magnitudes. However they require more battery management hardware for voltage sensing and balancing and higher power semiconductor voltage ratings for the power electronic converters. Additionally, most commercially-available automotive motor drives, dc/dc converters, battery chargers, and fluid heaters are only rated for input voltages up to approx. 400Vdc, making designing for a higher bus voltage difficult. As a result, the battery pack bus voltage was chosen to be approx. 350Vdc, enabling the use of standardized automotive parts and equipment.

Lithium-iron-phosphate (LiFePO_4) batteries from two companies, CALB and Thunder Sky, were evaluated for this project. These batteries offer several desirable features. They are relatively affordable in small quantities (approx. \$400/kWh), easy to interconnect (via bolt-on terminals), convenient to purchase from several EV parts retailers, and they have been applied to many other custom EV projects [123]. To achieve the desired energy storage capacity of 30-40kWh, a 35kWh

battery pack consisting of 108 series-connected 3.3V nominal, 100Ah cells from CALB and Thunder Sky cells was considered.

To be able to deliver 135kW at the IPM machine rotor shaft, the 35kWh battery pack must supply the required accessory power, motor output power, as well as the motor and motor controller losses, summing to 155kW total for motor and motor controller efficiency of 94% and 2kW of accessory power. To ensure that the battery can deliver 155kW, the power capability of the batteries was experimentally measured at 25°C for 60Ah cells using the high-power pulse characterization (HPPC) test that was developed by the US Advanced Battery Consortium (USABC). Figure 3.4 shows that the 60Ah Thunder Sky cell exhibited approx. 50% higher charge and discharge resistances than the CALB battery.

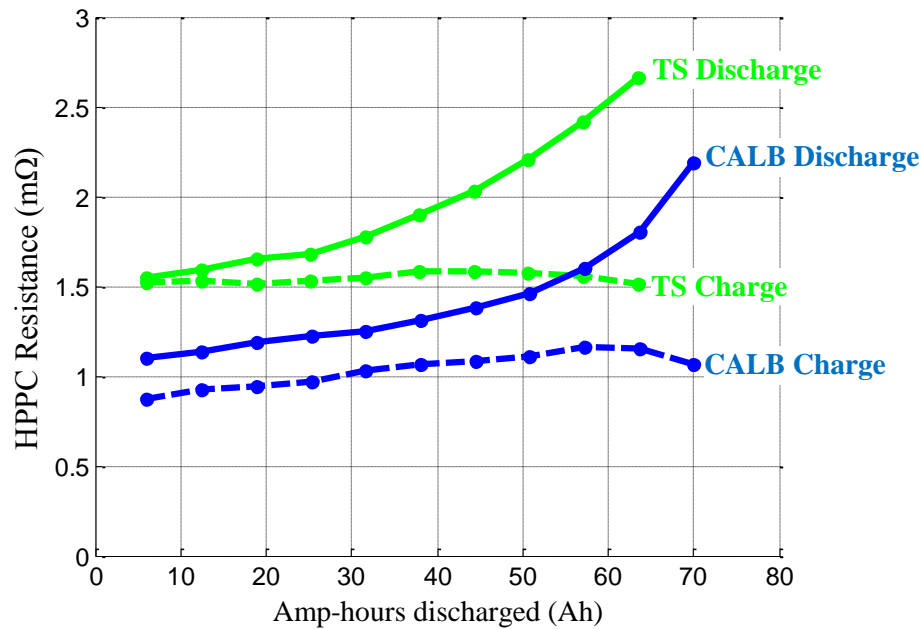


Figure 3.4 Internal resistance of 60Ah-rated Thunder Sky (TS) and CALB lithium batteries estimated with HPPC test

The power capability of the proposed battery pack with 108 100Ah cells for 2.8V/cell minimum has been estimated using a cell resistance value that was scaled linearly from the measured the

single 60Ah cell resistance. The estimated pack power capability is given in Figure 3.5, which shows that the Thunder Sky battery can supply 155kW only until the discharged energy reaches 38Ah, while the CALB battery can supply 155kW until a much higher discharge energy of nearly 90Ah is removed. Only the CALB battery meets the power requirements for the truck, and it has therefore been chosen for the project.

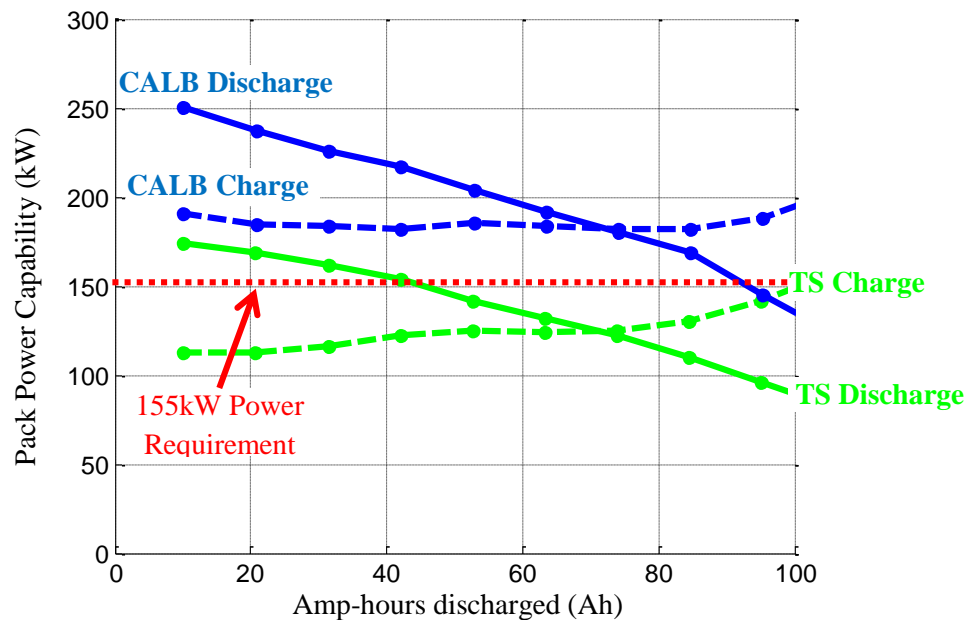


Figure 3.5 100Ah, 108 cell pack (2.8V/cell min. & 3.6V/cell max) power capability estimated from 60Ah HPPC results

3.3.2 Rinehart Motion Systems Motor Drive Parameters

A Rinehart Motion Systems PM150DX motor drive, rated for 450Arms (continuous) motor phase current and a 360Vdc bus, was chosen for the F150 vehicle drivetrain. To achieve the 135kW motor output power goal, the motor must be able to deliver 135kW with the dc bus voltage of 302V that is available with a minimum battery cell voltage of 2.8V/cell. Ideally, with no motor drive losses and a modulation index of 1.15, the maximum modulation index achievable with space

vector pulse-width modulation (SVPWM), the motor drive can provide peak line-to-line voltage equal to the dc bus voltage, so the rms value of this voltage can be expressed as:

$$V_{\phi ll-rms} = V_{dc} / \sqrt{2} \quad (3.6)$$

Due to the voltage overhead necessary for stable control system operation and the voltage drop of the semiconductors, the achievable line-to-line voltage is reduced to about 95% of ideal. Taking this factor into account, the achievable line-to-line voltage is calculated to be 203Vrms for a 302Vdc bus:

$$V_{\phi ll-rms} = 0.95 * V_{dc} / \sqrt{2} = 203Vrms \quad (3.7)$$

The primary design goal for the motor drive is to deliver sufficient kVA to the machine so that it can produce 135kW of mechanical output power with 203Vrms line-to-line voltage and 450Arms phase current. The outlook is promising, since the motor drive can deliver 158kVA with a 302Vdc bus, calculated as follows:

$$S_{mc-out} = \sqrt{3} V_{\phi ll-rms} I_{\phi-rms} \quad (3.8)$$

The motor controller's output kVA is consumed by the combination of machine reactive power, machine losses, and the mechanical output power. A realistic motor will have efficiency and power factor values of 0.95 or less at peak power, reducing the maximum machine mechanical output power well below the ideal of 158kW. For example, a 95% efficient motor with 0.90 power factor will deliver 135kW of mechanical power with 158kVA delivered to the machine stator terminals.

3.3.3 135kW Prototype IPM Machine Design

In addition to the constraint of providing 135kW with 203V_{rms} line-to-line voltage and 450Arms phase current, the prototype machine was designed for air cooling with distributed stator windings and conventional random-wound wire coils for the stator windings. The maximum machine speed was set at 7000r/min.

Due to the high torque requirement, a larger-diameter shorter-stack machine was selected as a starting point for the design. *Infolytica's MotorSolve* software combined with the designer's past experience were used to iteratively develop a machine that meets the design specifications. Subsequently, a 2-dimensional finite element analysis (FEA) model of the final design was developed using *Infolytica's Magnet* software. The final machine, described in Table 3.4 and shown in Figure 3.6, is an 8-pole, 72-slot, IPM machine with single-layer rotor magnets and stator windings short-pitched by one slot to achieve more sinusoidal back-EMF waveforms.

Table 3.4 Prototype IPM Machine Parameters

# of Slots	72	# of Poles	8
Stator O.D.	410 mm	Air Gap Length	1.5 mm
Stator I.D.	248 mm	Rotor I.D.	142 mm
Stack Length	150 mm	Copper Fill Factor	48%
Stator Iron	55.7 kg	Rotor Iron	28.2 kg
Copper Mass	45.5 kg	Magnet Mass	3.6 kg
Total Active Material Mass	133 kg	Total Est. Machine Assembly Mass	243kg
Iron Type	M-15 29 Ga	Magnet Type	NdFeB 38/23
Peak Current	450 Arms	Magnet layout	Single layer chevron
Current Density	3.4 A/mm ²		

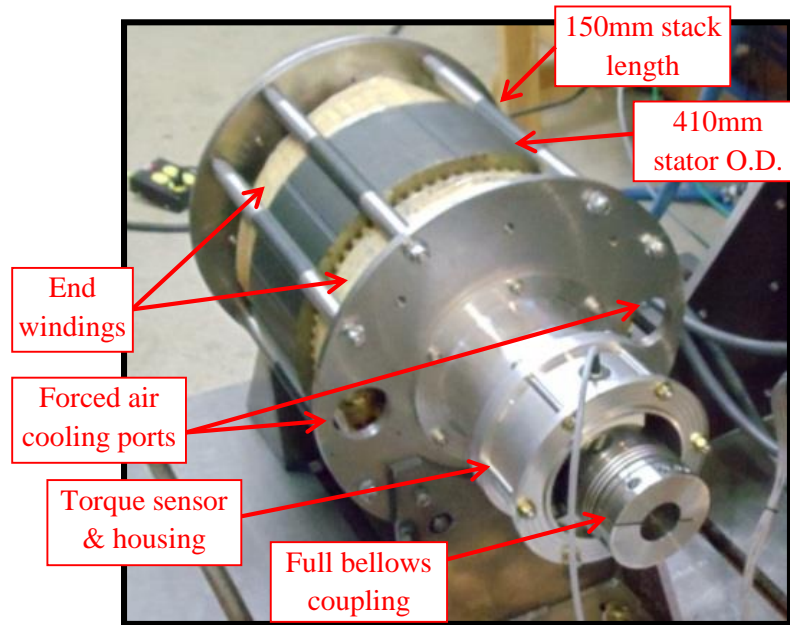


Figure 3.6 View of prototype IPM machine on dynamometer

The prototype machine was tested up to the full rated current at 500r/min, and the torque was measured with an in-line HBM T22 torque sensor. The original FEA model utilized the iron and magnet properties provided in the *Infolytica* software package, yielding a rated machine torque prediction of 489Nm. Figure 3.7 shows that the machine was measured to produce only 460Nm of torque at 450Arms, approx. 6% less than predicted with the original FEA model.

One pragmatic approach for improving the match between the FEA-predicted and measured torque curves is to modify the magnet remanent flux density B_r and coercive force H_c values until the error between the predicted and measured torque curves is minimized. The results of using this heuristic adjustment of B_r and H_c are plotted in Figure 3.7, demonstrating much better agreement with the measured torque curve. Other factors in the analysis that could be enhanced in order to improve the agreement between measured and predicted performance characteristics include the incorporation of machine end effects. The predicted machine and vehicle performance

curves provided in Figure 3.8 to Figure 3.10 use the machine model with the adjusted value of B_r and H_c .

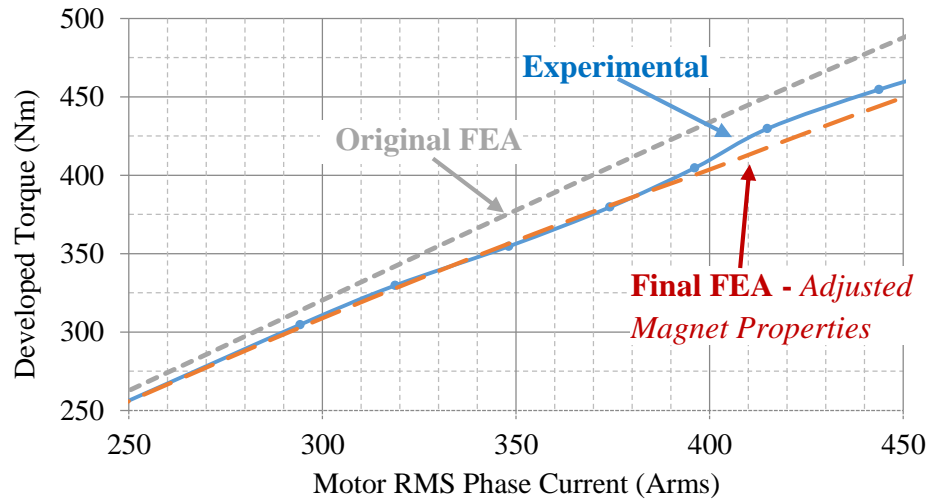


Figure 3.7 Experimentally-measured versus FEA-predicted torque for prototype IPM machine

To provide an idea of how the electric motor will perform compared to the baseline gasoline engine, the FEA-predicted electric machine torque and power curves are compared in Figure 3.8 to the predicted 4.2L internal combustion engine (ICE) torque and power curves, which were derived from Ford's peak torque and power specifications for the 4.2L ICE and the torque-speed curve for a similar ICE. The electric machine produces more accelerating torque and power than the 4.2L ICE until the speed reaches 4000r/min. The ICE's relatively flat torque-speed curve results in a peak power of 150kW occurring at 4800r/min. In contrast, the electric machine's relatively flat power vs. speed curve at elevated speeds results in approx. constant power above 2800r/min, and a peak power of 135kW at 4000r/min.

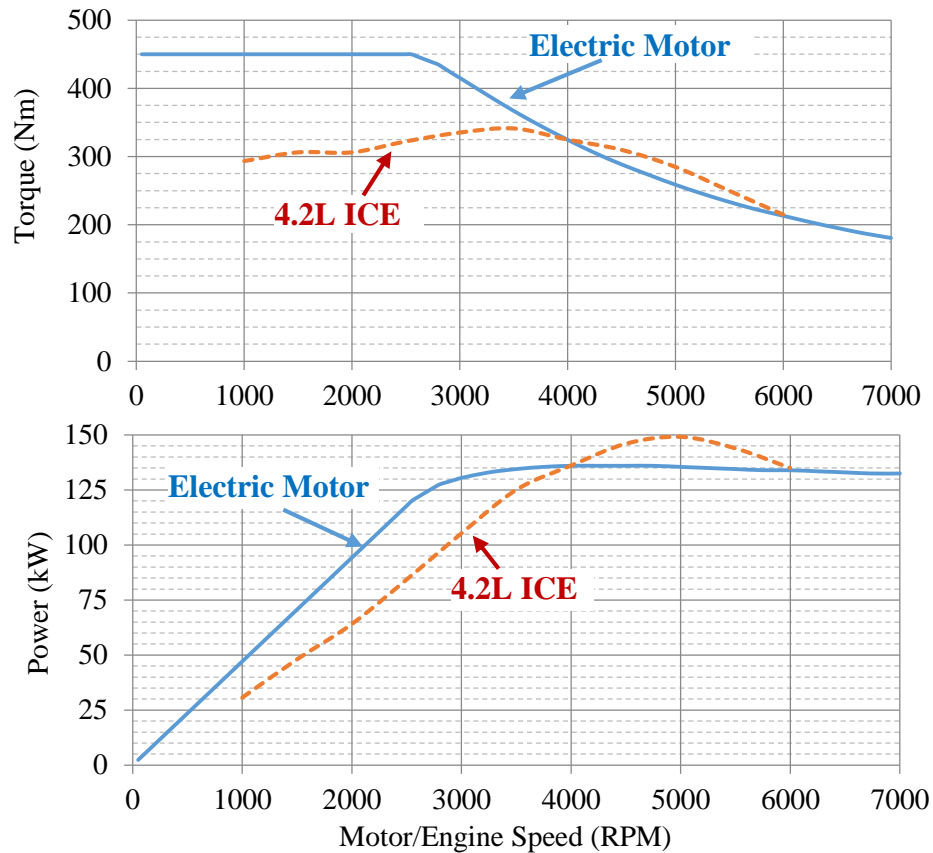


Figure 3.8 4.2L ICE versus FEA-predicted traction motor torque & power for 302V dc bus and 450Arms current limit

The torque and power curves for the ICE and IPM machine give the impression the IPM machine will provide superior performance compared to the ICE in the vehicle. However, this can be misleading since it is the power delivered to the wheels, rather than to the machine shaft, that will dictate which performs best. Both the electric drive and ICE have the same drivetrain architecture: the motor or engine shaft delivers power to a multi-speed gearbox, spinning a driveshaft connected to a differential gearbox at the rear wheels that reduces the driveshaft speed by a factor of 3.55:1.

The ICE truck utilizes either a 5-speed manual transmission or 4-speed automatic transmission, and the latter will be considered here. The four-speed automatic transmission has a 2.3:1 torque converter, which multiplies the torque from zero speed up until the vehicle speed reaches approx. 20mph with an engine speed of 2500r/min, as shown in Figure 3.9. This figure also shows the

torque delivered to the wheels for each gear. The electric drivetrain uses a more efficient and much smaller and lighter two-speed IE Drives gearbox with a 3:1 and 1:1 gear ratio, which allows the IPM machine to deliver torque values of 4800Nm and 1600Nm to the wheels, also shown in Figure 3.9. The ICE drivetrain can be observed to deliver the same or more torque than the electric counterpart except for low speed up to approx. 30mph.

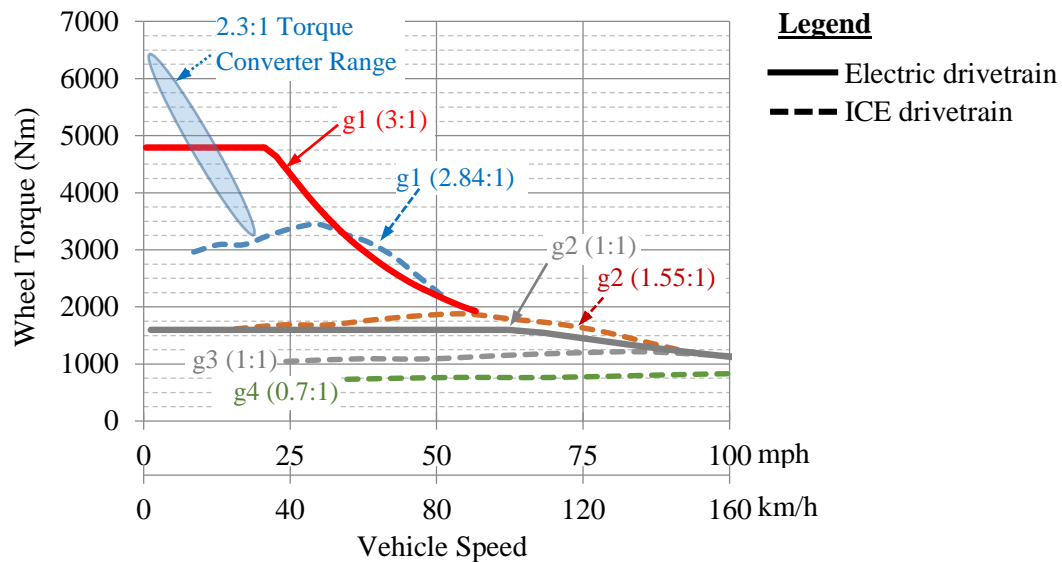


Figure 3.9 4.2L ICE versus FEA predicted traction motor torque for 302V dc bus and 450Arms current limit

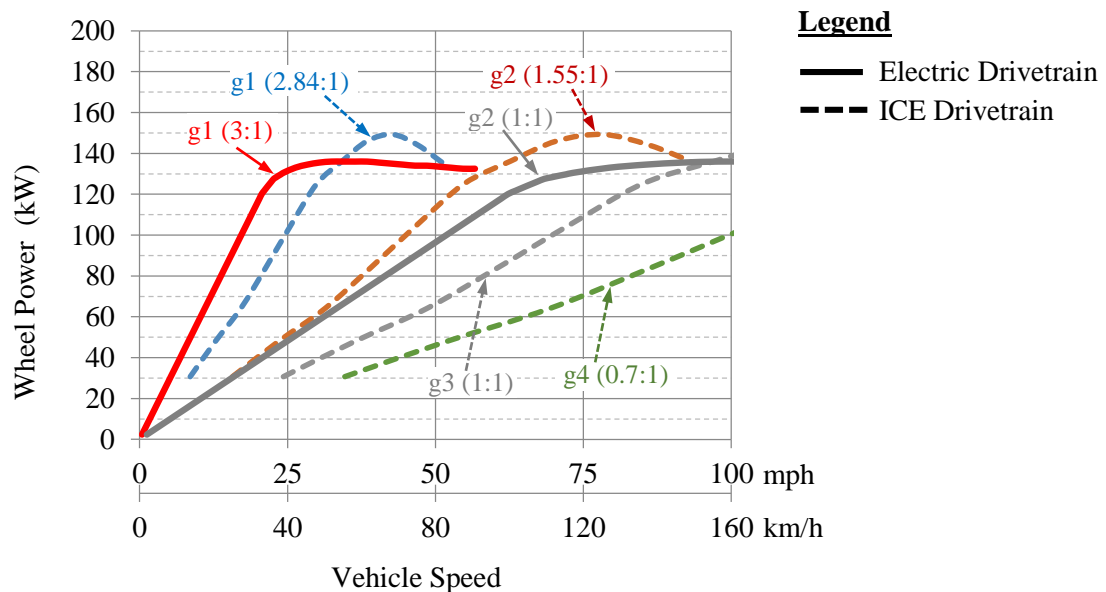


Figure 3.10 4.2L ICE versus FEA predicted traction motor power for 302V dc bus and 450Arms current limit

The amount of power each drivetrain can deliver to the wheels is shown in Figure 3.10, which illustrates how the ICE drivetrain uses the combination of 1st and 2nd gear to achieve an operating envelope that approaches peak power above approx. 50km/hr (30mph), and how the electric drivetrain utilizes these two gears to accomplish the same objective above 42km/hr (25mph). The 3rd and 4th gears that are available in the ICE drivetrain make it possible for the engine to operate nearer to its optimum conditions for high fuel economy at high speeds. One of the advantages of the electric drive is that the electric machine's power capability and efficiency are not as sensitive to speed as the IC engine, making it more practical to eliminate the 3rd and 4th gears.

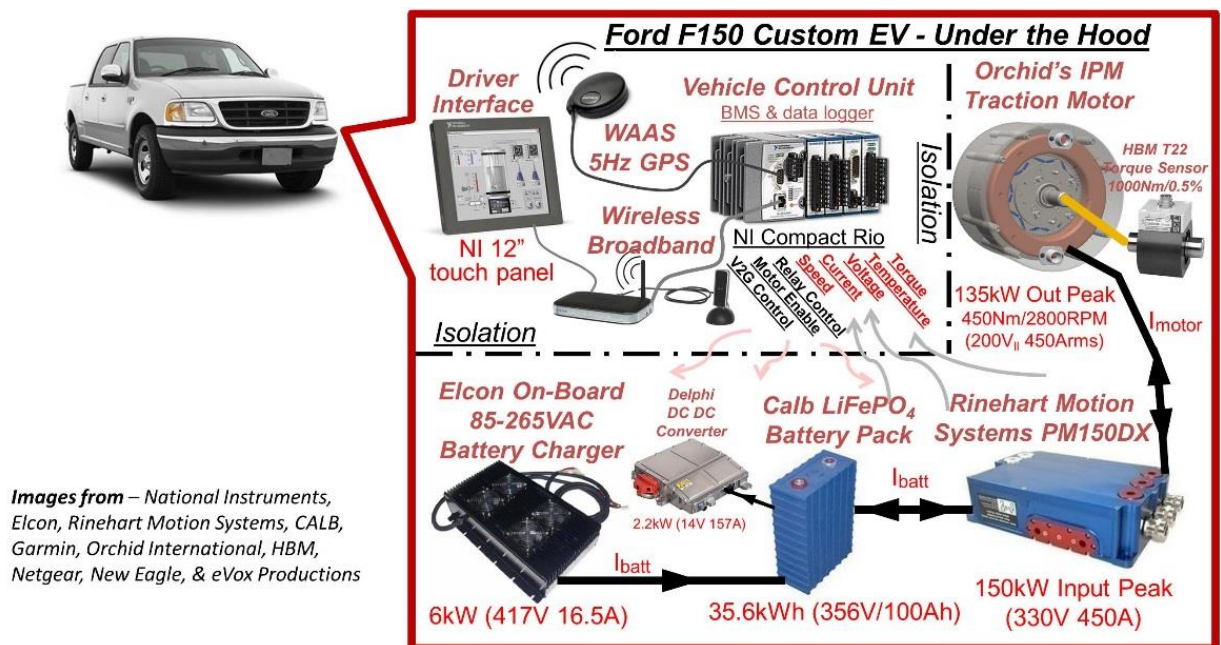
3.4 System Level Design and Data Acquisition & Battery management

System Design

Converting the truck to electric drive requires the replacement of many subsystems that would typically be powered or provided by the internal combustion engine. The electric replacements for the power steering pump, brake vacuum pump, radiator fan, and vehicle cab heater, as well as the dc/dc converter which provides 12V from the high voltage battery pack, are listed below in Table 3.5 and Table 3.6. The maximum current consumption of each of the 12V accessory systems, including the air compressor for the gearbox, battery pack and motor cooling fans, control and data logging equipment, and stock truck systems is listed and summed in Table 3.5 as well, showing that a peak current of 183.4A is required. Because the maximum current consumption is greater than the current that can be provided by the 2.2kW Delphi dc/dc converter, a 12V 65Ahr AGM lead acid battery is used to buffer the 12V electrical system.

Table 3.5 Accessories Powered Off 12V System

Device	Manufacturer / Model	Current Requirement
Brake Vacuum Pump	MES-DEA 70/6E2	5A
Power Steering Pump	Blue Turn Power Steering Pump	30A
Coolant Pump	Bosch PAD Pump	1A
Radiator Fan & Controller	Flex-a-lite 390 & 31165	6.5A
Compressor for Gearbox Shifting	ARB CKMA12	13A
Motor Cooling Fan	San Ace 120 CR Type	7.2A
Battery Cooling Fans (3)	San Ace 120 CR Type	21.6A
Data Logging & Control	Various	20A
Stock truck equipment	(est. peak current)	80A
Total Peak Current:		184.3A

**Figure 3.11** Simplified diagram of electric truck energy storage, drive train, and vehicle controller/data logger

The data acquisition system and user interface that are integrated with the electromechanical drivetrain system are outlined in the functional system diagram shown in Figure 3.11, along with the electromechanical drivetrain components and the 6kW battery charger which is powered via a

standard J1772 socket. A National Instruments Compact Rio 533MHz real-time controller with FPGA and modules providing two CAN communication lines, 40 analog inputs, and 80 digital I/O channels is used to measure system parameters, control relays and vehicle subsystems, and provide information to the user through a 12-inch touch panel.

Table 3.6 Equipment Powered Off High Voltage System

Device	<i>Manufacturer / Model</i>	<i>Current Requirement</i>
Cabin heat fluid heater	<i>MES-DEA RM4</i>	15A
dc/dc converter	<i>Delphi U2C 2.2kW</i>	8A
Motor controller	<i>Rinehart PM150DX</i>	450A
Total Peak Current:		473A

The vehicle is instrumented with dozens of sensors, many of which are listed in Table 3.7. The signals sensed allow the logging of all key parameters including battery cell voltage, battery pack power, motor controller input and output power, battery charger input and output power, motor torque and speed, GPS position, and accessory power. The temperatures of most system components and nine locations in the motor stator windings are measured as well.

Table 3.7 Sensor Specifications

Sensed Signals	<i>Manufacturer / Model</i>	<i>Range & Accuracy</i>
Motor phase & motor controller input current	<i>LEM LF 505s</i>	700A / 0.6%
Motor phase, battery pack, and charger AC voltage	<i>LEM LV 25-P/SP2</i>	500V / 0.8%
dc/dc converter, charger, and accessory currents	<i>LEM HAL 50-S</i>	150A / 1%
Battery cell voltage	<i>Maxim 11068</i>	5V / 0.25%
Battery and other subsystems temperature	<i>Texas Instruments TMP175</i>	-40 to 125°C / +/-2.0°C
Motor temperature	<i>Minco PW & PS element RTDs</i>	-50 to 200°C / 0.12% @ 0°C
GPS position	<i>Garmin GPS 18x-5Hz</i>	3m accuracy
Torque sensor	<i>HBM T22</i>	1000Nm / 0.5%

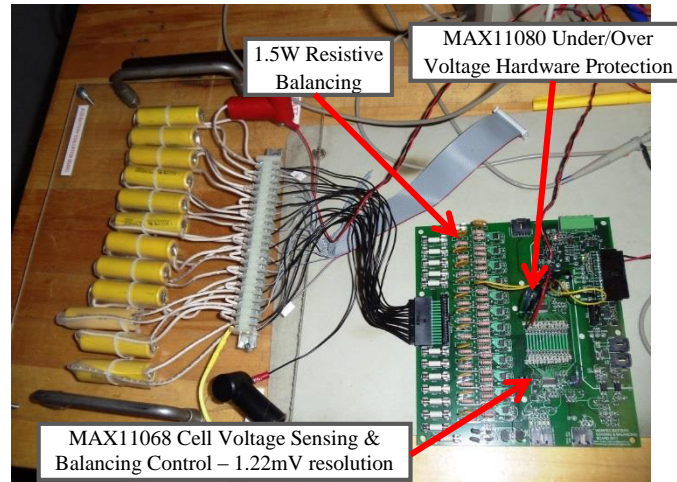


Figure 3.12 Battery management board for 12 cells with test pack

The main component of the battery management system (BMS) is a custom-designed BMS board, shown in Figure 3.12. The BMS board measures the cell voltages and balances up to 12 cells with a MAX11068 battery monitoring chip that communicates with the Compact Rio on an isolated digital I2C bus. The BMS board also contains a MAX11080 chip which provides hardware-programmable over- and under- voltage protection, and an interface for connecting up to 27 TMP175 temperature sensing chips for measuring battery temperatures. The Compact Rio serves as the master controller for the battery management system, and provides protection against under-voltage and over-voltage, over-current, over-temperature, and excessive discharge. The Compact Rio also controls the battery charger, battery box cooling fan speed and battery charger, and has the ability to shut off the entire system, including itself, if the battery is at risk of becoming over-discharged.

3.5 Conclusion

This chapter has described the development of an electric drivetrain that is being retrofitted into a Ford F150 truck with the objective of delivering similar performance to the stock vehicle. Key design issues associated with development of an electric replacement for a light-duty truck's

gasoline engine have been presented, highlighting some of the advantages and disadvantages of the electric drive compared to the conventional ICE drivetrain. This work has shown that the lithium battery pack is capable of providing sufficient power and range for this application, and test results verify that the prototype IPM machine meets the desired performance criteria.

Suitable electric replacements for the stock truck's brake vacuum pump, power steering pump, alternator, and cabin heater have been presented. The performance of the resulting electric drivetrain will be evaluated in more detail using both analysis and experimental verification in the following chapter.

Chapter 4

Implementation of Traction System and On the Road Experimental Verification of Electric Truck Model

4.1 Introduction

Chapter 3 only went as far as designing the electric truck drivetrain with a simplified model, and building and testing the traction motor. The vehicle was conceptually designed at this point and most of the subsystem components were selected, but there was not yet an actual plan for how to interconnect, mount, and control all the vehicle systems. This chapter first focuses on documenting the full design and assembly of the prototype electric truck, including the traction drive system, electrical subsystems, cabling, battery pack, battery management system, vehicle controller, and software. Because of the large number of sensors integrated into the vehicle, the design is in many ways more complex than a production electric vehicle. Additionally, because the vehicle is designed to work on the road in all types of weather conditions, significant effort was required to develop a waterproof, sturdy, and reliable system.

With the full truck designed and built, the next step is to update and improve the simplified model developed in Chapter 3, so the range and performance of the prototype vehicle can be accurately predicted. The electric truck mass is measured, the inertia of rotating components is modeled, coast down tests are performed again, the motor and drive losses are modeled and experimentally verified over their full operating range, and a battery loss model is developed. All of these aspects are then incorporated into a much more detailed version of the truck model, greatly improving upon the simple constant motor, drive, and battery efficiency assumptions used for the design process of the truck.

The improved vehicle model is then used to predict the performance of the electric truck for several different conditions. The constant speed energy consumption and range are predicted for 1st and 2nd gear, drive cycle energy consumption for 1st, 2nd, or optimal gear selection is predicted, and the gradeability of the truck for a range of vehicle loading is modeled. The energy consumption for several real drives is also compared to the model predicted energy consumption to illustrate the model's performance and to highlight environmental factors the model does not account for.

4.2 Vehicle Systems Design & Fabrication

4.2.1 Drivetrain Design

The drivetrain consists of a traction motor, torque sensor, gear box, drive shaft, and rear differential as illustrated in Figure 4.1 below. The motor torque, maximum speed, and gear ratios were selected with the goal of matching the stock truck's torque at the wheel's and constant power speed range as described earlier in 3.3.3. Figure 4.1 is provided to give further clarity to the flow of power through the drivetrain and for the purpose of defining some of the parameters which will be utilized in the forthcoming modeling. The parameters defined in the figure include wheel torque and speed, T_{wh} & ω_{wh} , gear box gear ratios, N_{gb} , N_{g1} , & N_{g2} , driveshaft torque and speed, T_{DS} & ω_{DS} , rear differential gear ratio, N_{diff} , wheel torque and speed, T_{DS} & ω_{DS} , and wheel radius and force, r_{wh} & F_{wh} .

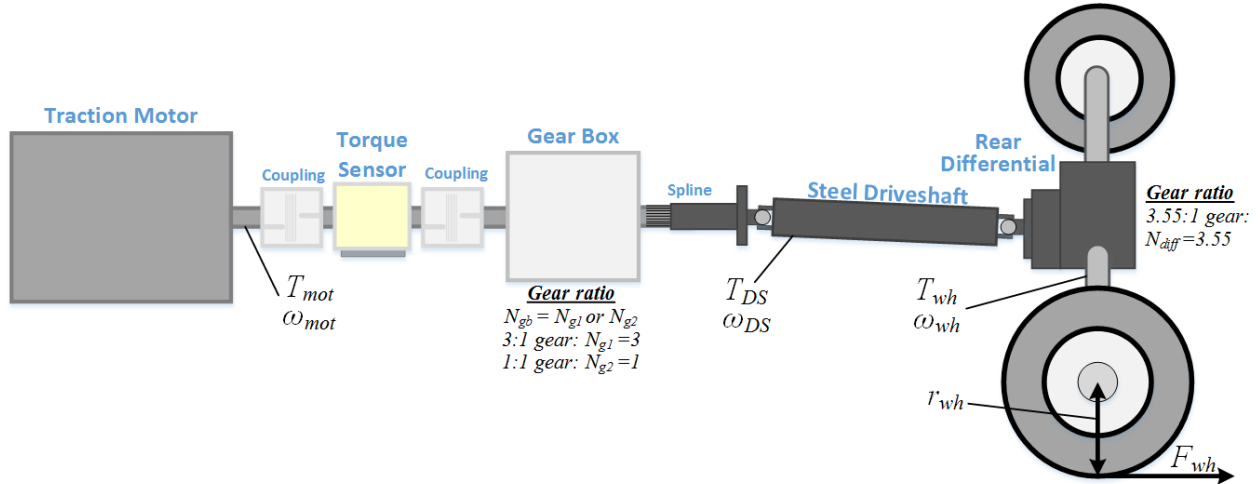


Figure 4.1 Mechanical drivetrain diagram with relevant torques and speeds labeled

The gear box and rear differential both reduce the motor speed, so wheel torque is the multiple of the gear ratios and the motor torque, and wheel speed is motor speed divided by the gear ratios, as shown in (4.1) and (4.2) below.

$$T_{wh} = N_{gb} N_{diff} T_{mot} \quad (4.1)$$

$$\omega_{wh} = \frac{\omega_{mot}}{N_{gb} N_{diff}} \quad (4.2)$$

The wheel force acting on the driving surface is then calculated as the wheel torque divided by the radius of the wheel as follows in (4.3), where the wheel radius as determined from the experimentally measured wheel circumference is given in (4.4).

$$F_{wh} = \frac{T_{wh}}{r_{wh}} \quad (4.3)$$

$$r_{wh} = 0.371m \quad (4.4)$$

The final assembly of the motor, torque sensor, and gearbox is shown below in Figure 4.2. The IPM traction machine is assembled in a housing with two steel structural faceplates which hold the rotor bearing and which the stator is mounted to via long bolts sheathed in cylindrical spacers.

A power coated black cylindrical cover bridges between the two faceplates, and there is a ½” spacing between the stator o.d. and the cover allowing air to be blown through the housing for cooling. The 3/0 AWG three phase leads exit the top of the machine through the aluminum cable glands visible in the image.

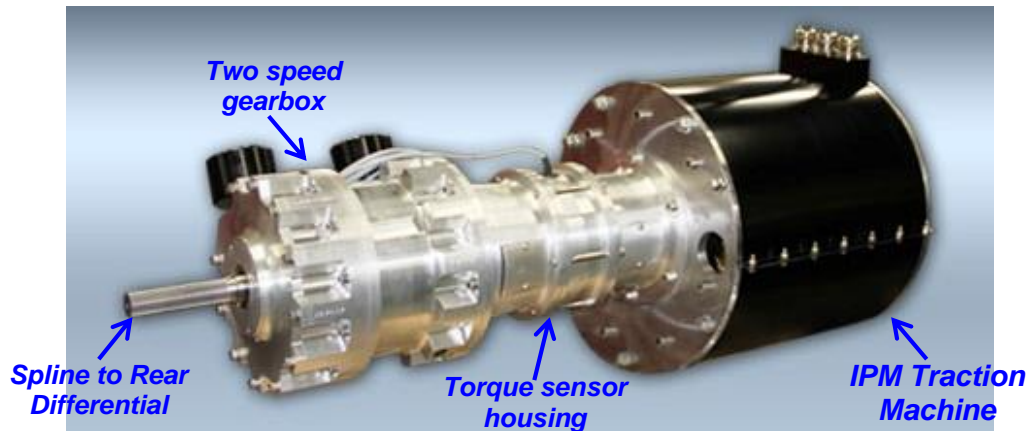


Figure 4.2 Electric machine, torque sensor and gearbox assembly

The torque sensor is housed in a machined aluminum structural housing, and the sensing cable is seen in coming out the top of the housing in the image. The round shafts of the motor, torque sensor, and gearbox are connected by two full bellows couplings which help allow smooth operation even with any angular or linear offset between the devices.

The aluminum gearbox mounts directly to the torque sensor housing, and has pneumatic shifting. When pressurized air is applied to the black pressure valves on top of the gearbox, the clutch for either gear 1 or gear 2 is closed. The gearbox clutch is very fast acting, and locks the input shaft to the output shaft very quickly, resulting in a large torque transient and shuddering felt throughout the vehicle if the input and output shaft speed are not precisely matched. For this reason, gear shifting is currently only done when the vehicle is not moving, but the eventual goal is to have automated shifting while the vehicle is moving.

4.2.2 Electrical Subsystem and Cabling Design

While the electromechanical drivetrain provides the traction force to move the vehicle, it is only one of many, many systems required to make the vehicle operational and able to perform its role as an advanced data collection tool. The subsystems which were originally powered via the gas engine – the alternator, power steering pump, brake vacuum, and cabin heater – must all be replaced with electrically powered equivalents. Additionally many of the vehicle system control services originally performed by the engine control unit (ECU) must be performed by a new control system. Furthermore many of the vehicle subsystems require cooling, either via variable or fixed speed fan, or via pumped oil or coolant and a radiator. All of these added vehicle subsystems, and the control box which houses the control system, are shown in Figure 4.3.

A few highlights of the systems are also provided below:

- **Equipment in truck cab:**
 1. 5Hz Garmin WAAS GPS
 2. Wireless router with option for wireless broadband
 3. 12" industrial touch screen
 4. System power on button, forward reverse knob, e-stop, and ignition switch
- **Cooling:**
 1. **Motor:** 300CFM variable speed fan w/ filter box
 2. **Rear Battery Boxes:** 300CFM variable speed fans
 3. **Front Battery Box:** Dual 150CFM variable speed fans
 4. **Gear Box:** 11L/min oil cooling with radiator w/ 325CFM fixed speed fan
 5. **Drive & DC/DC Converter:** 15L/min coolant with radiator w/ 785CFM fixed speed fan
- **Gear Box Air Compressor** set to 70psi with 1.4L accumulator
- **4kW Cabin Fluid Heater** – Pumps heated coolant through stock cabin heat exchanger
- **Brake and Accelerator Pedal Position Sensors** 0-5V, interfaced with motor drive
- **12V Distribution Box:** with relays and current sensors for each subsystem
- **Emergency Stop:** Shuts off high voltage power by opening battery pack contactors
- **Bender Isolation Sensor:** In *HV V/I Sensing & Distribution* box, senses isolation between high voltage system and vehicle chassis
- **J1772 Charging Socket:** 30A/240Vac rated, vehicle controls charging rate based on plug proximity sensor and pwm current limit signal from charger

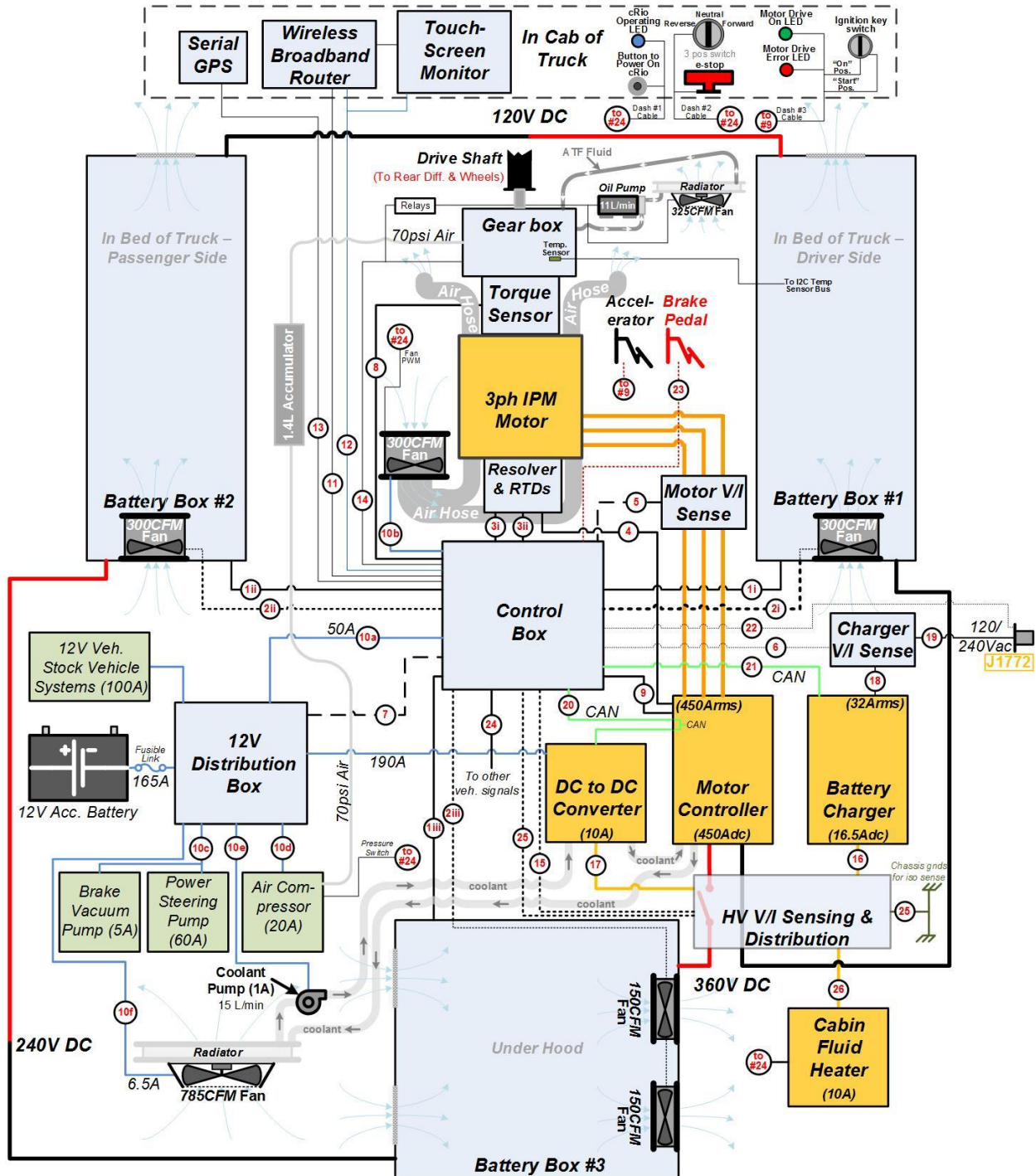


Figure 4.3 Electrical subsystems and cabling diagram

Additionally each cable, all of which are waterproof twist-on industrial automation cables, is shown and labeled with a number in Figure 4.3. Each of these 37 cables, with a total of 294 individual conductors, are described in Table 4.1 and the pinouts will be in Appendix III.

Table 4.1 Functional Description of System Cables

Cable #	Cable From	Cable To	# of pins	Signal Type
1i	Control Box	Battery Box #1	19	BMS & Temp Sensor
2i			12	Fan & Contactor
1ii		Battery Box #2	19	BMS & Temp Sensor
2ii			12	Fan & Contactor
1iii		Battery Box #3	19	BMS & Temp Sensor
2iii			12	Fan & Contactor
3i		Motor	12	RTD Temp Sensors
3ii		Motor	12	RTD Temp Sensors
4	Motor	Motor Controller	10	Resolver
5	Control Box	Motor V/I Sense Box	12	3ph AC V/I Sense
6		Charger V/I Sense Box	6	1ph AC V/I Sense
7		12V Dist. Box	28	V/I Sense & Relays
8		Torque Sensor	12	Power & Signal
9		Motor Controller	28	12V Power & Signal
10a		12V Dist. Box	6	12V Power (50A)
10b		Motor Fan	2	12V Power (9A)
10c	12V Dist. Box	Brake Vacuum & Power Steering	6	12V Power (65A)
10d		Air Compressor	2	12V Power (20A)
10e		Coolant Pump	2	12V Power (1A)
10f		Radiator Fan	2	12V Power (6.5A)
11	Control Box	Wireless Router	6	Ethernet
12		Router & Touchscreen	4	24V & 5V Power
13		GPS	8	5V power & serial
14		Gear box	5	Gear shift signals
15		HV Dist. & Sense Box	12	DC V/I sense signals
16	Battery Charger		2	350V Power (16.5A)
17	DC/DC Converter		2	350V Power (10A)
18	Battery Charger		3	120/240Vac Power (32A)
19	Battery Charger	J1772 Socket	3	120/240Vac Power (32A)
20	Control Box	Motor Controller & DC/DC Converter	3	CAN signal (no power)
21		Battery Charger	3	CAN Signal (no power)
22		J1772 Socket	3	J1772 Prox. & Pilot
23		Brake Pedal Sensor	3	Analog position signal
24		To Other Signals	12	Signal & low power
25		HV Dist. & Sense Box	6	Isolation sense signals
26	Cabin Fluid Heater		2	350V Power (10A)
27	Chassis Grounds		3	Iso. Sense Chassis Grounds

To give further insight into how the truck is mechanically assembled, several images of the truck are provided in Figure 4.4. The radiator for cooling the motor drive and dc/dc converter is visible in the picture with the front grill of the truck removed. The radiator is a little less than half the size of the original, so the passenger side grill opening is covered with black painted sheet metal and the dc/dc converter is located on the back side of it. Under the hood, one of three battery boxes is mounted where the engine originally resided, as illustrated in the CAD drawing in Figure 3.3, and the charger, motor drive, control box, and high voltage dc distribution box (not visible) are mounted directly to the top of the battery box. The brake vacuum pump and power steering pump are mounted to a vehicle frame cross member beneath the front battery box, and the 12V battery, cabin coolant heater, 12V distribution box, air compressor, accelerator position sensor,

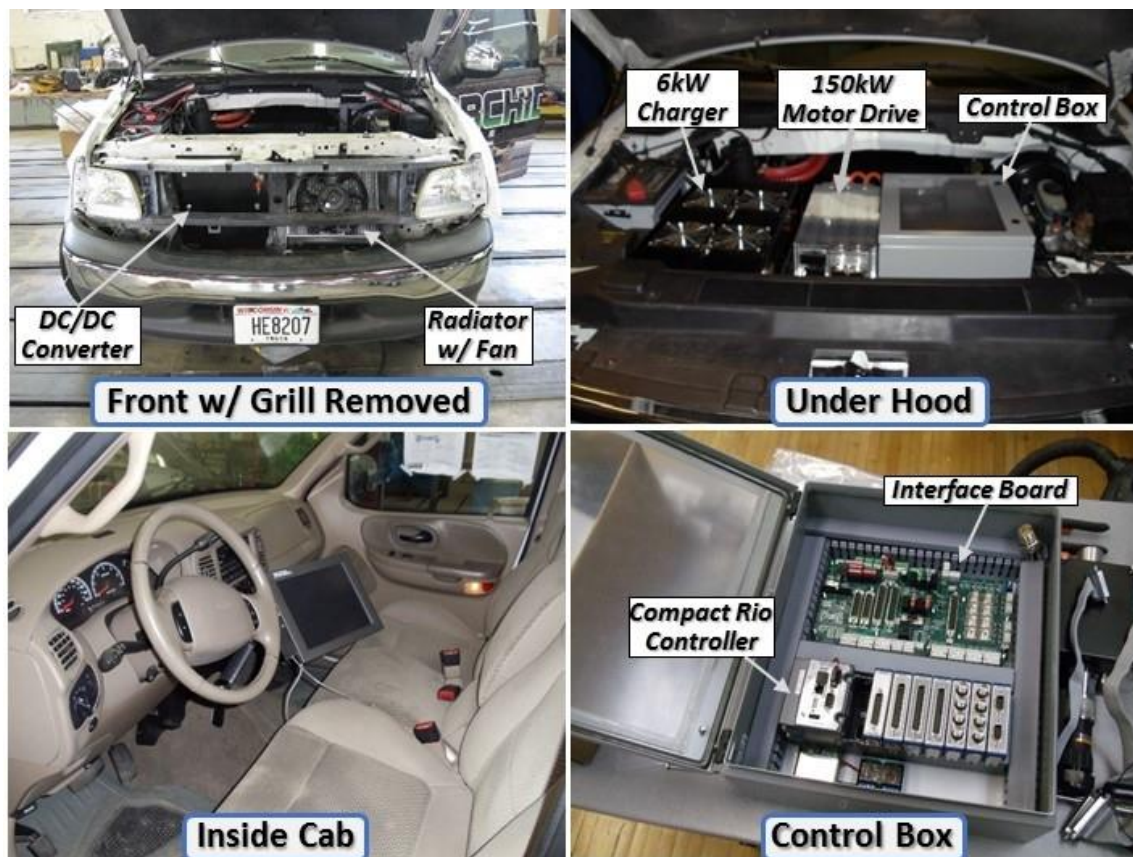


Figure 4.4 Pictures of electric truck subsystems

and coolant pump, are all mounted in visible locations under the hood. For the picture inside the cab the touchscreen is visible, and the National Instruments Compact Rio and custom designed interface board are shown in the control box as well.

Additional pictures of the subsystems are shown in Figure 4.9 below, with the GPS mounted on the ceiling in the rear of the cab and the wireless router mounted in a compartment behind the rear driver's side seat. The control box with some of the cables connected is shown, and the J1772 socket, which is in place of the gas fill cap, is shown as well. The interior of several of the voltage and current sensing boxes are also shown, illustrating the current and voltage sensor placement for all the boxes as well as the fuse and contactor placement in the high voltage dc distribution and sensing box. The 2.2kW dc/dc converter, which is normally concealed by the front battery box, and the very small I2C temperature sensor boards used in the battery pack are also shown.

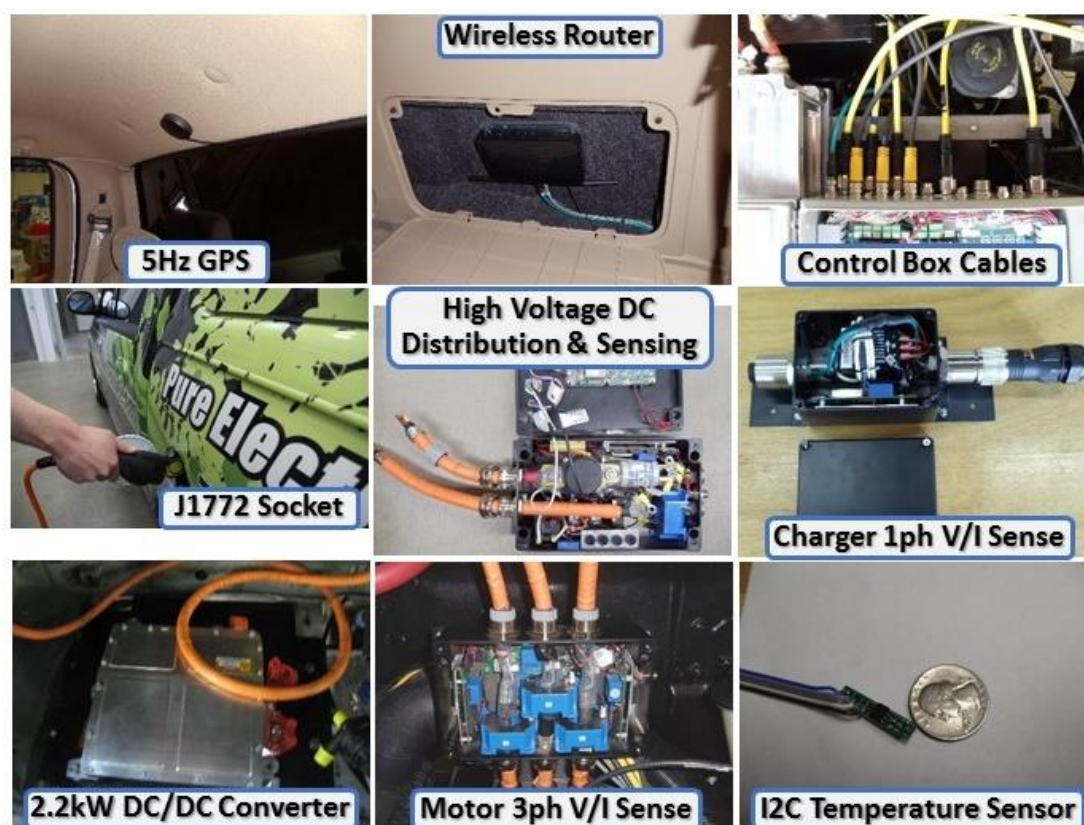


Figure 4.5 Additional pictures of electric truck subsystems

The vehicle subsystems are outlined above, giving a basic idea of the function of each system, how it is connected, and where it is located in the vehicle.

4.2.3 Battery Pack Design

The battery pack and management system was custom designed specifically for the truck, and is assembled from individual battery cells, raw materials, custom printed circuit boards, and electrical components. The pack consists of 108 series connected 100Ah CALB LiFePO₄ battery cells, providing a nominal pack voltage of 356V, mass of 345kg, and 35.6kWh of energy storage, as outlined in Table 4.2. The battery cells are built placed in three boxes, one under the hood and two which were designed to be mounted beneath the bed of the truck, but are currently mounted in the bed. Each box contains 36 series connected batteries, as shown in Figure 4.6, and an electrical contactor to break battery current in the case of a fault and to allow the high voltage to be disconnected for maintenance. Additionally there is a fuse in battery box 2 to break current in case of a short in the battery pack, and to supply power to the motor drive there is a contactor, pre-charge circuit, and fuse in the high voltage dc distribution box, as is also shown in Figure 4.6.

Table 4.2 Battery Cell and Pack Specifications

	Parameter	Cell	Pack
# of cells in series	N_{b-cell}	-	108
Open Circuit Voltage	V_{ocv} or V_b	3.3Vdc	356.4Vdc
Amp-hours	Ah_b	100Ah	100Ah
Nominal Resistance	R_b	1.1m Ω	119m Ω
Mass	m_b	3.2kg	345.6kg
Energy Storage	E_b	330Wh	35.6kWh

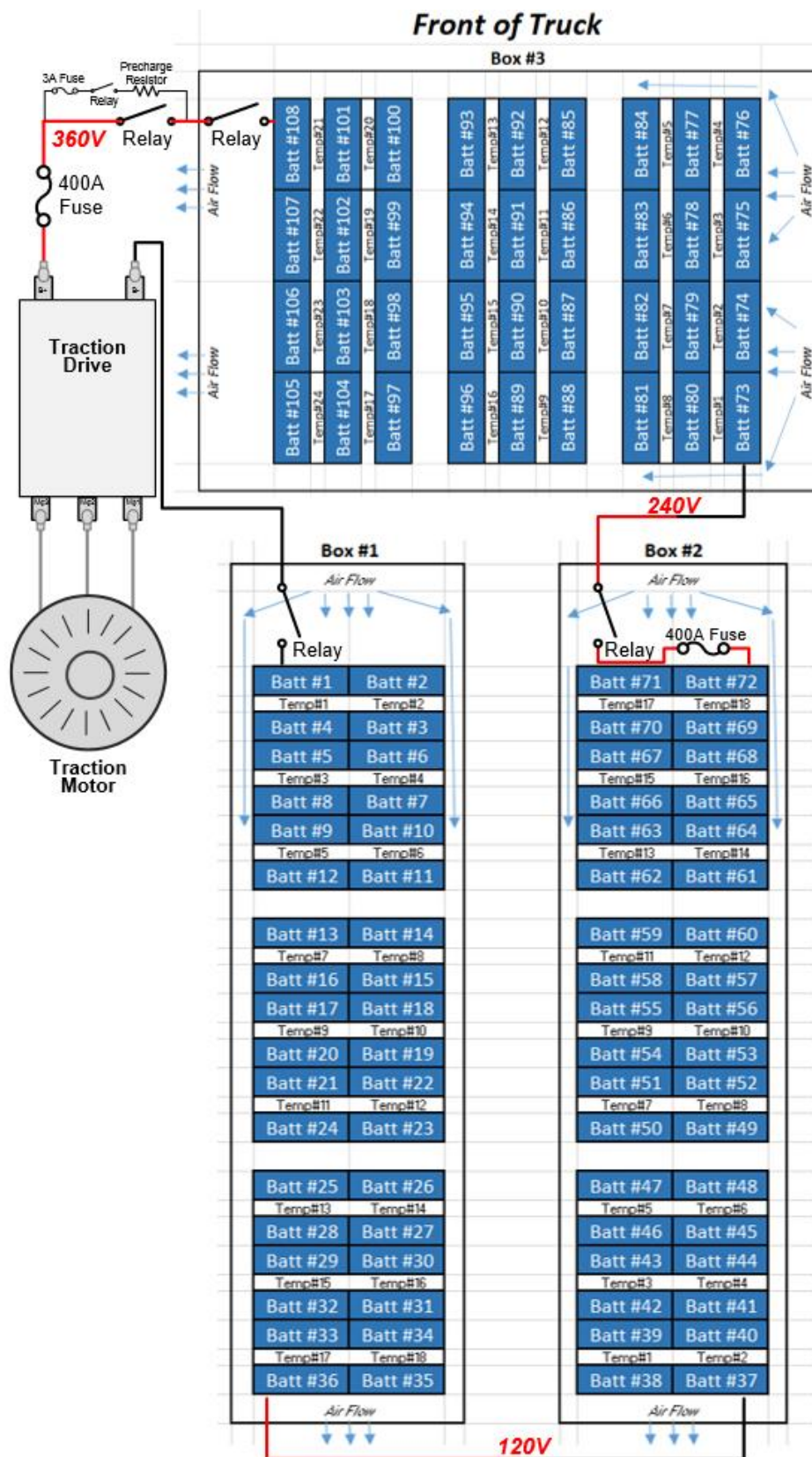


Figure 4.6 Battery pack electrical layout and temperature sensor placement

The battery pack is built in modules of 12 cells, as shown in Figure 4.7 below. Each pack of 12 batteries sits on an aluminum tray with a sheet of neoprene, which allows for slight differences in height between the battery cells and some shock and vibration isolation. An aluminum plate is placed on both ends of the module, and the module is strapped with heavy duty nylon strapping material, providing the force on the ends of the batteries which is needed to keep their plastic cases from expanding while charging. Plastic strapping is also used to add two handles on each module, making it easier to place them in the powder coated steel battery boxes.

The battery cells are connected with custom designed and milled nickel coated copper bus bars, which are covered with heat shrink for electrical insulation and have a tapped screw for connecting the battery voltage sensing wire. Three modules are placed in each battery box and are centered in the proper place with plastic spaces around the bottom edges and held down by plastic stand offs on the top of the batteries which make contact with the top of the battery boxes when they are in place. Additionally the battery packs are air cooled, and have about 1 inch of spacing around the battery pack to allow the flow of air.

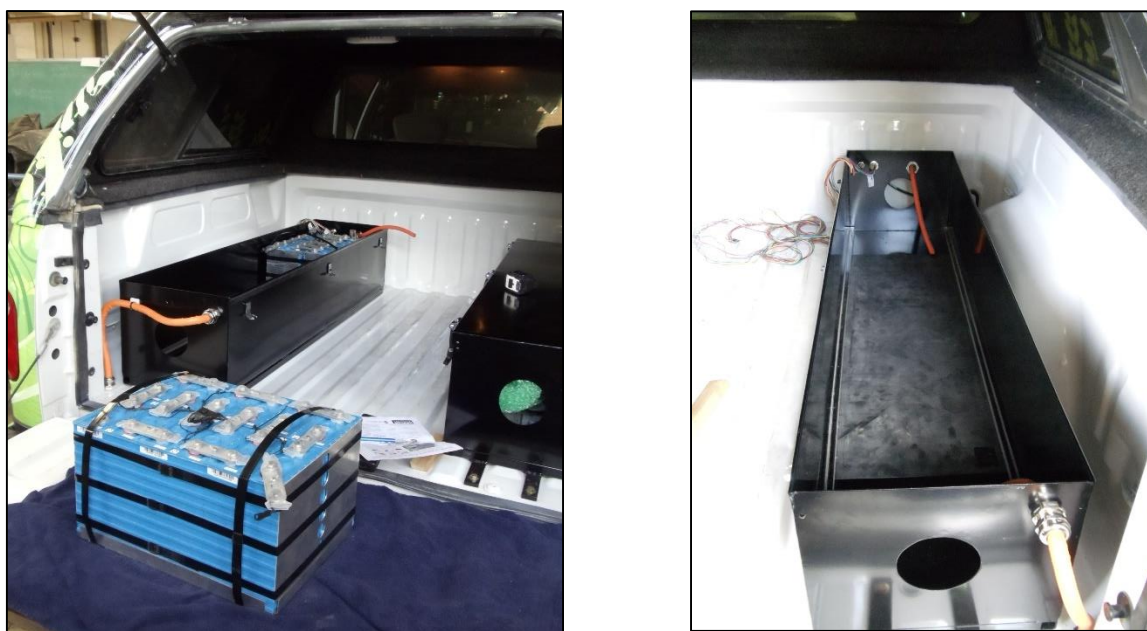


Figure 4.7 Pictures of battery module and battery boxes

Each module of 12 batteries also has a custom designed, conformal coated battery management board, which is shown in Figure 4.8. The battery management board uses the now discontinued Max11068 battery management IC to measure the 12 cell voltages and to short a resistor across individual cells for balancing. The Maxim chips were chosen primarily because they were the only chip available at the time, but also because of their relatively good resolution, 1.22mV, and because of their ability to take time aligned measurements at a higher frequency - 25Hz or more - than available commercial products. The board also has a Max11080 IC for hardware cell under and overvoltage protection, an I2C communication isolation chip, and a temperature sensor chip and sensor interface for up to 27 total temperature sensors.

The BMS boards daisy chain, so there is one master board in each battery box and two slave boards. Each box is also outfitted with an array of temperature sensors placed between the cells, as illustrated and numbered for reference in Figure 4.6 above. A selection of the BMS performance specifications are provided in Table 4.3.

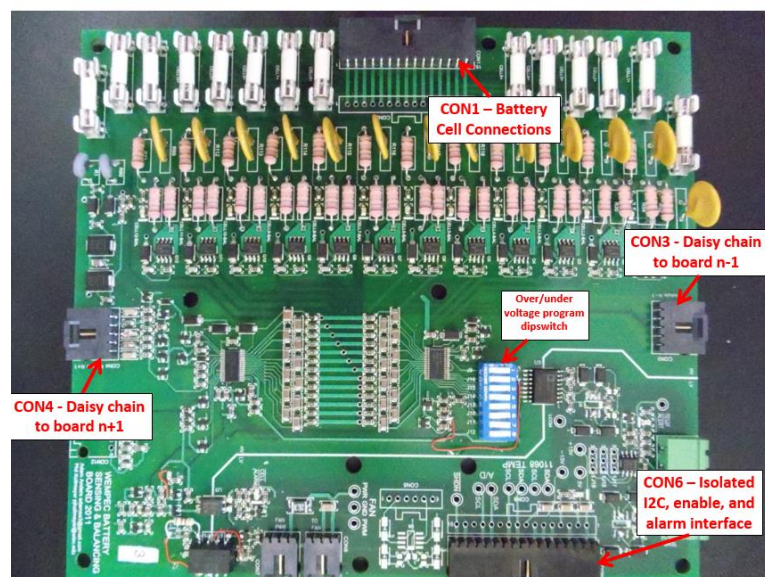


Figure 4.8 Battery management board

Table 4.3 Battery Management Board Specs

# of cells	12
Max Cell Voltage	5V
Voltage Resolution	1.22mV
Voltage Accuracy	0.25%
Sampling Frequency	25Hz
Resistive Balancing	0.7W
I2C Frequency	50kHz
I2C Isolation	2000V
600V Fusing	3.15A
Temperature	-40 to 105°C
Shutdown Mode Current	1μA

The fully assembled front battery box is shown Figure 4.9, with the battery management boards covered with an insulating plastic sheet and mounted to each module, and with yellow Gigavac contactor visible in the bottom right hand corner. A steel cover is placed on top of the box, and the charger, motor drive, and control box mount to the cover. One of the rear battery boxes is also shown without the battery management boards mounted in place.

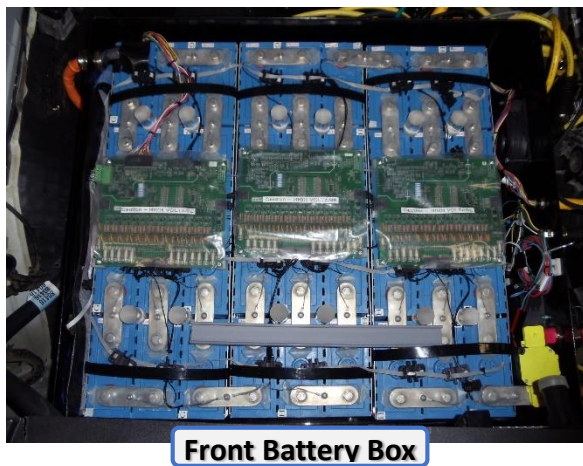


Figure 4.9 Pictures of electric truck battery boxes

In summary the design and assembly of the electric truck's battery pack was outlined in the subsection. The battery pack was designed as a system to sturdily hold the batteries in place, provide air cooling, and measure battery voltages and temperatures. The battery pack has structurally performed very well over the first 4000 miles of operation, but there are some electrical noise issues with the BMS. The front battery box BMS signals are quite noisy when the motor drive is enabled. This is likely due to common mode motor current flowing through capacitive paths and through the structure of the motor and vehicle, and some EMI reduction methods are planned to be applied to the system to reduce the resulting electrical noise.

4.2.4 Vehicle Software and Touchscreen User Interface

The vehicle is controlled and data logging is performed by LabVIEW software running on a National Instruments Compact-RIO (cRIO) system, as shown on page 104 in Figure 4.4. The cRIO consists of a real time controller with a 533MHz processor, an FPGA, a serial and Ethernet port, and eight modules for digital and analog IO and CAN communication, as outlined in Table 4.4. The cRIO is paired with a custom designed interface board, also shown in Figure 4.4, which provides the filtering, relay drivers, power supply, I2C drivers, and many other functions necessary to interface with the sensors, subsystems, and BMS boards in the truck.

Table 4.4 Compact-RIO Module Specifications

<i>Module #</i>	<i>Part #</i>	<i>Type</i>	<i># of Channels</i>	<i>Max Frequency</i>	<i>Purpose</i>
1	9401	DIO	8	10MHz	BMS I2C
2	9401	DIO	8	10MHz	Fan PWM Control
3	9403	DIO	32	140kHz	Temp Sensor I2C & Relay Control
4	9477	DO	32	125kHz	Relay Control
5	9205	AI	32	200kHz	Voltage/Current Sensing
6	9215	AI	4	100kHz	Motor & Battery Current Sensing
7	9215	AI	4	100kHz	Motor & Battery Voltage Sensing
8	9853	CAN	2	1MHz	Motor drive, dc/dc, charger communication

The cRIO's main purpose is to control all the vehicle systems necessary to make the vehicle operate. To power on the vehicle, the cRIO must first be powered on by pressing a *power on* button to the left of the steering wheel. The cRIO boots, and powers on the high voltage system, dc/dc converter, and touchscreen user interface. When the key is then turned to the ignition position, the cRIO software starts logging a new driving data log file and powers on the brake vacuum pump, power steering pump, air compressor, and motor drive and puts the truck into second gear by default. The various system cooling fans are only turned on temperature thresholds

are exceeded and the fan speed is increased as temperature increases. When the key is turned to the off position, the cRIO software enters an idle state, and will enter a charging state automatically when the truck is plugged in.

A screenshot of the default user interface screen is shown below in Figure 4.10. The stock dashboard no longer functions, so the touchscreen provides all of the critical driving data, including the vehicle speed, gear, amp-hours discharged from the battery, motor power, motor torque, battery current, battery pack and cell voltage, and important subsystem temperatures. Additionally there is a warning indicator in the bottom right hand corner, which provides many different temperature and battery voltage related warnings to the driver. The software also has many features in addition to those described here which can be explored when driving the truck or modifying the software.

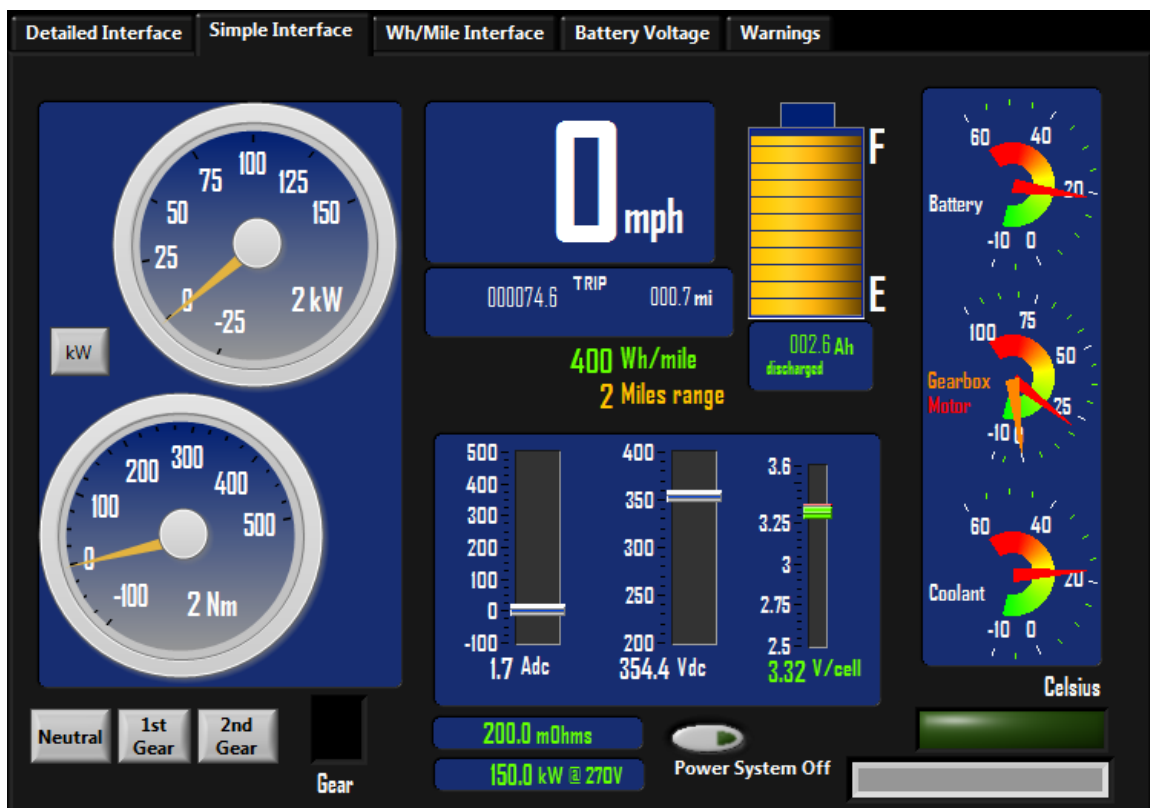


Figure 4.10 User interface screenshot

4.3 Updated Model Parameters from Completed Vehicle

4.3.1 Measured Mass of Vehicle & Estimated Mass Breakdown of Added Components

The stock truck's mass, prior to conversion to electric, was measured to be 2245kg with a full tank of gas. A total of 515kg of components were removed from the truck, as documented in Table 4.5 below, which shows that the majority of the removed mass was that of the internal combustion engine and accompanying transmission.

Table 4.5 Measured Mass of Components Removed From Gas Truck

Components Removed From Trucks	Measured Mass of Components
I.C.E. and Transmission	317 kg
Scrap fuel lines, AC system, heat shield guards, motor mounts, etc.	33 kg
Exhaust System	41 kg
Fuel Tank, Radiator, Starter Motor and Alternator	55 kg
Full Tank of Gasoline	70 kg
Total Mass Removed	515 kg
Original Mass of Truck	2245 kg
Mass with Components Removed	1729 kg

Ideally the electric traction system would weigh no more than the gas system, but with just the battery pack cells weighing 356kg, or 70% of the mass of the removed components, it would be a great challenge to avoid exceeding the mass of the stock vehicle. Initial estimates suggested the electrified truck would actually weigh about 200kg more than the original truck, a large but tolerable increase. Much of the expected mass increase would be due to the massive 200kg plus prototype IPM machine, as is shown in the “*Original Mass Estimate*” column of Table 4.6 below.

However after the electrification process was completed and acceleration tests were performed, it became clear the actual truck mass must be considerably greater than originally predicted. To determine the actual mass, the completed vehicle was driven to a truck weigh station outside

Madison. The measured mass was 2704kg, as shown in Figure 4.11, 459kg greater than the original truck and 246kg greater than predicted.

Table 4.6 Original vs Final Mass Estimate of Components Added to Truck

Components Added	Original Mass Estimate	Final Mass Estimate
IPM Motor	227 kg	272 kg
Two speed transmission - Dry Weight	36 kg	36 kg
Torque sensor and housing	-	27 kg
Steel mounting hardware	-	27 kg
Battery Pack - Calb	356 kg	356 kg
Gearbox cooling system	-	11 kg
Electrical wiring and touchscreen	-	45 kg
Fluids	-	9 kg
Battery pack boxes	45 kg	45 kg
Control system box and equipment	16 kg	18 kg
Elcon Battery Charger	20 kg	20 kg
Motor Controller	18 kg	11 kg
Heater/Brake Vacuum Pump/Power Steering Pump/Compressor	9 kg	23 kg
Other Added Mass	-	73 kg
Total Mass Added:	728 kg	984 kg
Final Truck Mass:	2457 kg	2704 kg
Difference from Original Truck:	+213 kg	+459 kg

Examination of the updated mass estimate in Table 4.6 shows that much of the difference is likely due to the mass of some equipment being greater than originally predicted and due to equipment which was not accounted for in the original estimate. This large increase in mass will result in slower acceleration times, somewhat increased energy consumption, and a reduction in the rated payload of the vehicle. However in daily driving the mass increase is not particularly noticeable, and may actually improve the dynamics and handling because the style of leaf spring suspension utilized for the truck's rear axle typically has a more damped response when loaded.

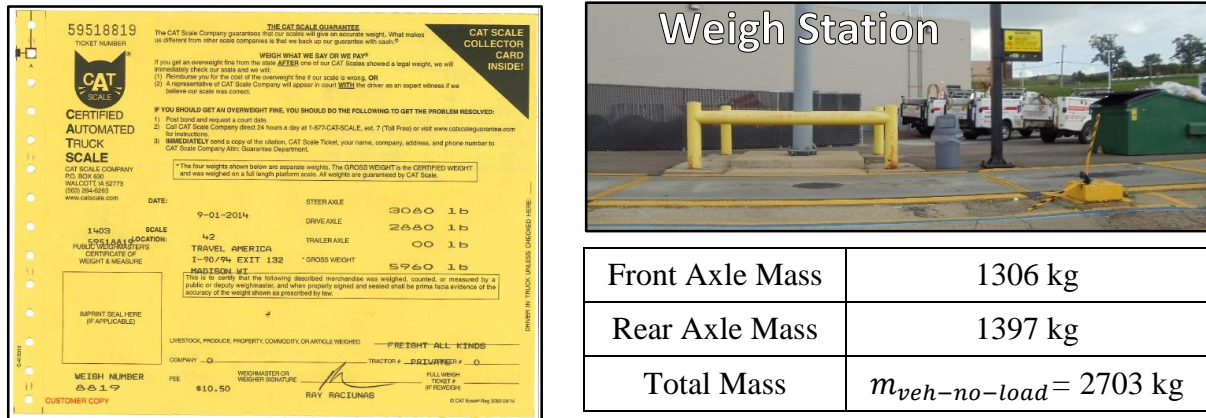


Figure 4.11 Truck weigh station document, picture of scale, and measured mass of truck

4.3.2 Inertia of Rotating Drivetrain Components

The rotational inertia of the drivetrain components, like the vehicle's mass, has a significant impact on the rate of acceleration of the vehicle. In a typical internal combustion vehicle the rotational inertia of the wheels, brakes, driveshafts, gears, engine components, etc. will typically have the effect of increasing the effective mass of the vehicle by about 2-5%. In an electric vehicle with a high speed machine, a high rotor inertia may add a much larger effective mass to the vehicle than would typically be seen for an internal combustion engine vehicle. This requires care to be taken when designing the rotor, aiming to minimize inertia by reducing rotor diameter and rotor mass, or by developing a higher torque lower speed machine which requires a lesser gear ratio.

The effective mass of the rotational components is defined as the rotational inertia translated to the linear reference frame. The practical meaning of this is that if you were to pull the vehicle and accelerate it, it would feel as if it were so much heavier due to the acceleration of the rotational components. The effective mass is a function of the rotational inertia of the component, the gear ratio between that component and the wheel, and the radius of the wheel, as shown in (4.5). The effective mass increases linearly with increased inertia, and with the square of the gear ratio and the inverse square of the wheel radius.

$$m_{eq} = J_{comp} \left(\frac{Gear\ Ratio}{r_{wh}} \right)^2 \quad (4.5)$$

To demonstrate this calculation the equivalent mass of the rotor, which has a rotational inertia of $0.419kgm^2$ as determined by a Solidworks CAD model, is calculated as follows for first gear in (4.6).

$$m_{eq-rotor} = J_{rotor} \left(\frac{N_{g1}N_{diff}}{r_{wh}} \right)^2 = 0.419kgm^2 \left(\frac{3 \times 3.55}{0.371m} \right)^2 = 345.4kg \quad (4.6)$$

The resulting equivalent mass of 345.4kg is equivalent to about 15% of the vehicle's mass, showing clearly that rotor inertia can have a large effect on the vehicle's performance. This calculation, which was not performed as part of the design process of the traction machine for this project, should always be performed to allow inertia to be considered fully in the design process. It should also be noted that the traction machine used for this project is quite large due to the requirement of air cooling, and should not be considered a typical automotive traction machine.

The same calculation process as shown above was performed for each rotating component of the vehicle, and the results of the calculation are shown in Table 4.7 below and full documentation of the process is included in Appendix I. These calculations show that the sum of the equivalent mass of all of the rotating components other than the rotor is a comparatively insignificant 15-20kg, and that in second gear the equivalent mass of the motor rotor is reduced by a factor of $1/3^2$ to only 38.3kg. The small impact of the rotating inertias other than the rotor inertia also suggests that they could typically be neglected in the vehicle design process with little effect to the vehicle performance.

Table 4.7 Inertia of Rotating Components as Calculated from Solidworks Models in Appendix I

Part	Mass (kg)	Inertia (kg m ² *10 ⁻³)	Total Gear Ratio	Equivalent Mass (kg)	
				1 st Gear	2 nd Gear
Motor Rotor	57.04	419.2	10.65:1 (1 st) 3.55:1 (2 nd)	344.8	38.3
Torque Sensor	2	0.352		0.3	0.03
Gear Box – Input Gear	4.54	5.76		4.7	0.5
Gear Box – Output Gear	6.8	6.21	3.55:1	0.6	
Drive Shaft	14.03	29.1		2.7	
Differential – Input Gear	5	8.16		0.8	
Differential–Output Gear	5	3.45	1:1	0.03	
Rear Axle	22.7	39.3		0.3	
Tire & Rim	30.2	1200		8.8	
Front Brake Disc	7.20	84.6		0.6	
Rear Brake Disc	9.84	139		1.0	
				1 st Gear	2 nd Gear
Total Equiv. Mass:				392.7 kg	81.8 kg
Percentage of Vehicle Mass:				14.5%	3.0%

4.3.3 Calculation of total vehicle mass and equivalent mass

The total vehicle mass, as calculated in (4.7), is the mass of the unloaded vehicle as measured in 4.3.1, $m_{veh-no-load}$, and the sum of the passenger, gear, and trailer mass, m_{load} . The vehicle equivalent mass, which should be used for acceleration calculations, is calculated in (4.8) as the sum of the loaded vehicle mass, m_{veh} , and the equivalent inertial mass, m_{J-eq} .

$$m_{veh} = m_{veh-no-load} + m_{load} \quad (4.7)$$

$$m_{veh-eq} = m_{veh} + m_{J-eq} \quad (4.8)$$

The equivalent inertial mass is defined for gears 1 and 2 in (4.9). Parameter values for the masses and equivalent masses are summarized in Table 4.8, where the load mass is assumed to 100kg by default unless stated otherwise, as is done in future sections examining towing and gradeability for a range of loads.

$$m_{J-eq} = \begin{cases} m_{J-eq-g1}, & \text{gear 1} \\ m_{J-eq-g2}, & \text{gear 2} \end{cases} \quad (4.9)$$

Table 4.8 Vehicle Mass and Inertial Equivalent Mass Parameter Values

Mass of unloaded vehicle	m_{veh}	2703 kg
Passenger and gear load	m_{load}	100kg default or as defined
Gear 1 inertial equivalent mass	$m_{J-eq-g1}$	392.7 kg
Gear 2 inertial equivalent mass	$m_{J-eq-g2}$	81.8 kg

4.3.4 Coast Down Tests Redone with Electric Truck

The coast down tests are performed to determine what is commonly referred to as the road load of the vehicle. The road load consists of the aerodynamic drag, bearing friction, electric motor friction and windage losses, unloaded tire and gearbox losses, and any other frictional forces acting to slow the vehicle down. The road load, ideally, is the power at a given speed the electric traction machine must provide to maintain a constant velocity on a flat surface. There are some tire and gearbox losses which are a function of torque though, and which unless accounted for in the model (they are not accounted for yet in this study) will result in some model error, roughly in the range of 2-5% error. Modeling of these torque dependent tire and gearbox losses is presently beyond the scope of this study, but is important for obtaining the highest levels of accuracy.

The coast down tests were performed on a 1 mile stretch of Seminole Highway south of Lacy Rd outside of Madison, WI. This is the flattest stretch of 55mph road near Madison, only varying a few feet in elevation over 1 mile. The test was performed 5 times in each direction on a 70 degree Fahrenheit evening with negligible wind, and the test was performed by accelerating to 60mph in second gear, disabling the motor drive, and coasting down to zero or until the end of the flat stretch of road was reached. The speed versus time for one coast down, as given in Figure

4.12 below, shows that about 70 seconds are needed to coast from about 65mph to 30mph and that the flat stretch of road is not long enough to coast down to zero. Several of the coast downs were instead performed from about 40mph down to 0mph and the data was combined to account for this issue.

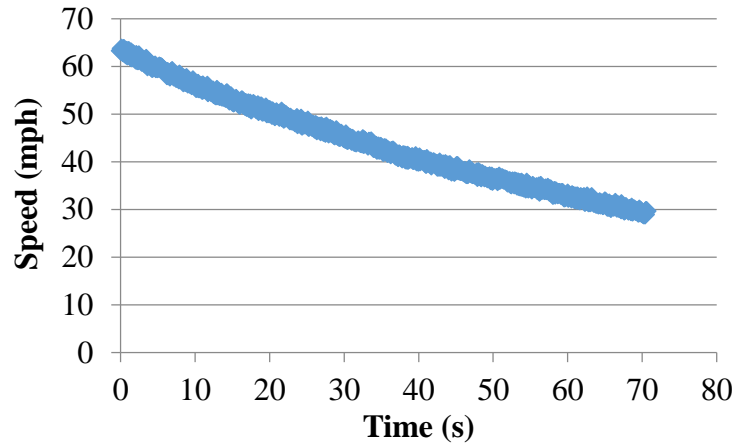


Figure 4.12 Speed versus time for example coast down test

To calculate the coast down power from the coast downs, acceleration as well as velocity is needed. Acceleration is determined by first fitting a cubic polynomial to the coast down velocity data, such as that in Figure 4.12, and then differentiating the velocity to obtain acceleration, as shown in (4.10) and (4.11), where a , b , c , and d are the curve fit coefficients and t is time.

$$v_{veh} = at^3 + bt^2 + ct + d \quad (4.10)$$

$$a_{veh} = \frac{dv_{veh}}{dt} = 3at^2 + 2bt + c \quad (4.11)$$

The coast down power is then calculated using the vehicle's equivalent mass, the acceleration obtained via curve fitting the coast down velocity curve, and measured velocity as follows in (4.12). The electric F150 and stock gas F150 road load power are then shown to be very similar

in Figure 4.14, where the stock gas F150 road load parameters are obtained from the EPA's *Annual Certification Test Results & Data* database [124].

$$P_{acc} = m_{veh-eq} a_{veh} v_{veh} \quad (4.12)$$

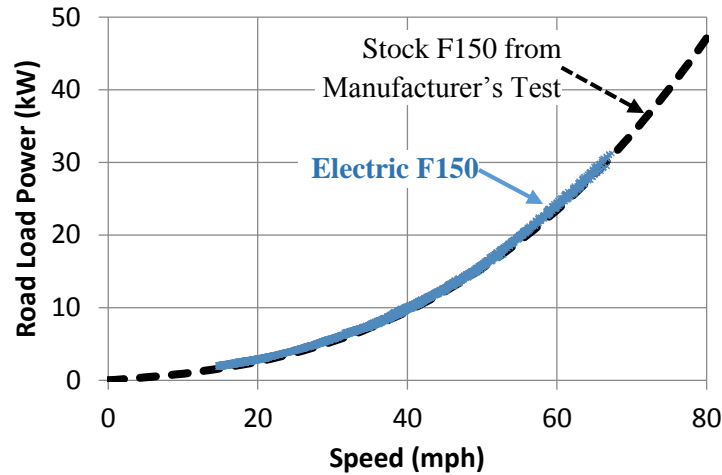


Figure 4.13 Road load vs speed for coast down test

It is actually rather surprising though that the electric and gas vehicle road load are so similar because the electric vehicle has several differences from the gas vehicle which will affect road load including: (1) 459kg of additional mass, (2) a topper on the truck bed, (3) low rolling resistance tires, and (4) a two speed planetary gearbox. Theoretically, the additional mass should increase the viscous, speed dependent portion of drag, while the low rolling resistance tires and planetary gearbox should decrease the viscous drag. Additionally the truck bed topper should increase aerodynamic drag due to the sharper angle at the rear vehicle.

The breakdown of the individual drag components in Figure 4.14 below is in line with this explanation, with aero drag being higher for the electric truck and viscous drag being lower, presumably due to reduced gearbox and tire losses. However this breakdown of drag components should not be taken too seriously unless more coast down tests, preferably with a longer flat road surface, were performed to confirm the consistency of the breakdown of the drag components.

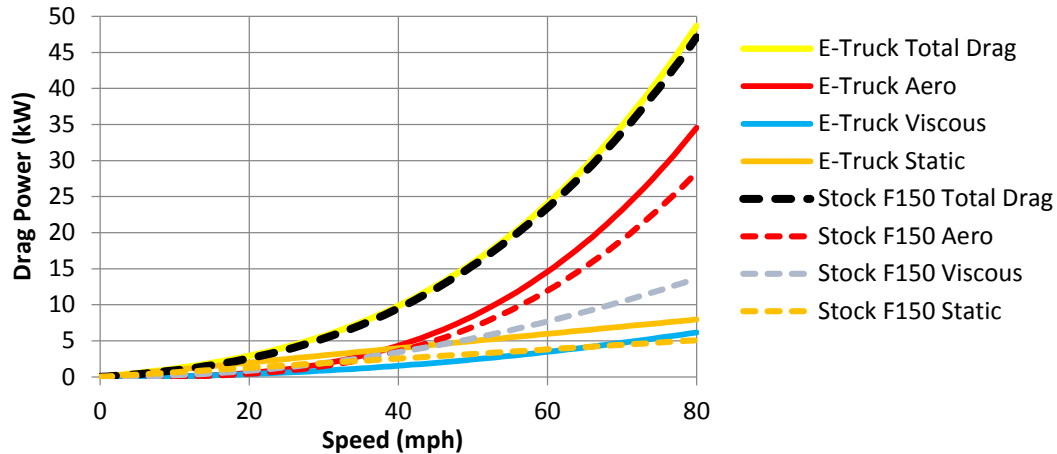


Figure 4.14 Road load aero, viscous, and static components for stock F150 and E-Truck

The road load parameters are then determined by fitting a third order polynomial to the road load power versus speed curve. The coefficients are given below in the SI units used in the calculations in this study, and in the English units commonly used by the EPA and automakers.

Table 4.9 Experimentally Determined Drag Power / Road Load Coefficient

Drag Power Coefficient	z_3	z_2	z_1
Value	0.7194 W/(m/s) ³	6.189 W/(m/s) ²	210.8 W/(m/s)
Road Load Coefficient	A	B	C
Value	0.03480 lbf	0.4319 lbf/mph	50.40 lbf/mph ²

When travelling at a constant speed on level ground, the vehicle's traction system must supply power equivalent to the road load. This road load consumes the large majority of the energy produced by the traction system, and is therefore a very useful metric to compare different vehicles. The road load for a 2013 F150, 2002 F150 (the vehicle studied here), 2015 Toyota Tacoma midsize pickup truck, Tesla Model S electric vehicle, and Toyota Prius hybrid are all shown in Figure 4.15 below. The energy per mile figure shows that the F150s require about 400Wh/mile to maintain 60mph, while the Model S and the Prius require about 200Wh/mile and the midsize Tacoma pickup requires about 280Wh/mile. This difference in energy consumption translates to the Tesla and

Prius being able to travel about twice as far with the same amount of energy supplied by the drivetrain, and to the Tacoma being able travel about 40% farther.

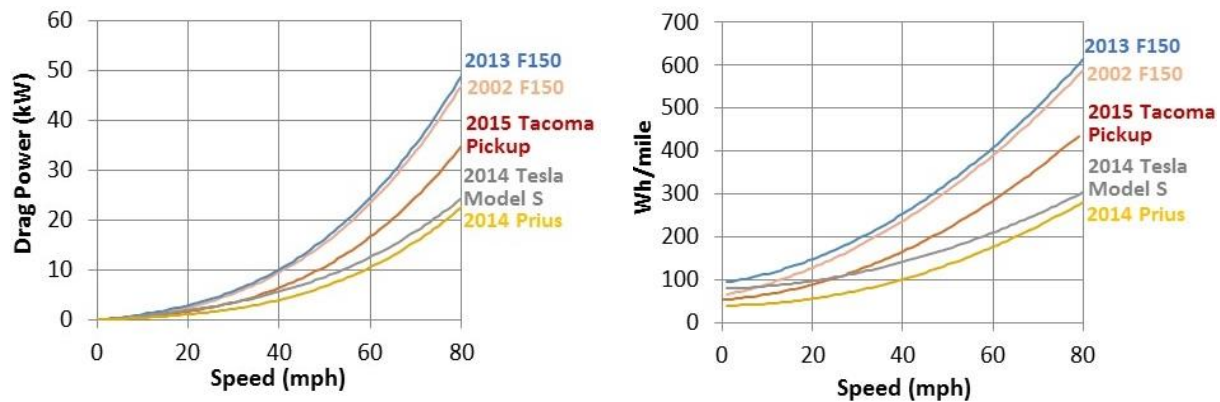


Figure 4.15 Comparison of drag power and drag power Wh/mile for a selection of vehicles

The 2015 Tacoma pickup has followed the trend in pickup trucks to have ever increasing towing and payload capabilities, and actually has similar capabilities to the 2002 model year F150 even though it is a mid-size truck. This suggests that if similar performance capabilities to our existing pickup were desired, the 2015 Tacoma could be converted to an electric vehicle and have an approximately 40% greater range with the same amount of energy storage, a huge benefit since the since the energy storage is one of the most costly and heavy systems on the vehicle. This conclusion can be applied generally to any EV design though, a more aerodynamic chassis with lower road load will directly translate to a reduction in battery pack size for a desired range.

4.3.5 Motor and Drive Loss Modeling w/ Experimental Verification

The traction motor and motor drive system losses contribute significantly to the energy consumption of an electric vehicle, typically consuming anywhere from 5% to 20% of the total energy required for a drive cycle. Many machine and power electronics design methods can be used to minimize the traction system losses. Two of the design choices for this project, the choice to design an air rather than liquid cooled traction machine and to utilize a two speed gearbox, has

resulted in higher efficiencies than would be achieved with a typical EV traction system. These choices were not made for efficiency purposes though, air cooling was chosen to make the traction machine easier to design and fabricate and a two, rather than single, speed gearbox was chosen to achieve the required torque at the wheels for a truck application.

While these two design choices do improve system efficiency, the air cooled motor is impractical due to its very large size. The gearbox though, as shown in the following subsections, can be utilized to significantly improve system efficiency. All production EVs to date, except for the early Tesla Roadster's and the brand new BMW I8 plug-in hybrid, utilize a single speed gearbox. Judging from the results shown here though it seems likely two-speed gearboxes will be considered for future electrified vehicle designs.

i. **Motor Losses**

The electric machine is very efficient, primarily resulting from the choice to build a forced air cooled machine. Air cooling, compared to oil spray or water jacket cooling, is not very effective at removing heat and therefore requires that the current density in the machine's windings is kept low. Liquid cooled hybrid and EV traction machines typically have current densities ranging from $10 - 20\text{A/mm}^2$, while air cooled industrial machines have current densities ranging from $3 - 4\text{A/mm}^2$, resulting in about $1/10^{\text{th}}$ the loss density in air versus liquid cooled machine windings. While lower current density has the benefit of higher machine efficiency, it has the downside of requiring many times more copper to provide the same amp-turns of flux, which ultimately results in a much larger machine. Air cooling was chosen for this project because of a lack of experience in oil cooled machine design, and because the larger air cooled machine could be tolerated in a truck application.

The losses in the machine are primarily hysteresis and eddy current losses in the rotor and stator iron, and ohmic losses in the stator windings. There are magnet losses, but they are very small due to segmentation of the magnets and due to a lack of rotor harmonics resulting from the use of distributed, rather than concentrated, windings. There are also friction and windage losses, but these losses cannot be directly measured with the existing rotor. The magnets in the rotor cause iron losses even when no current is flowing in the stator winding, and these iron losses create a torque in addition to the friction and windage torque. A dummy rotor with no magnets inserted would be necessary to directly measure friction and windage losses. In lab testing of the machine up to 2000rpm friction and windage losses could not be distinguished from iron losses, so friction and windage losses will therefore be neglected.

The machine's winding resistance was measured after the machine was installed in the vehicle, and was measured at the motor controller so the phase leads and connection resistance are included in the resistance measurement. The voltage drop across the winding was measured with about 7A of current flowing through winding, and the voltage and current measurement that resistance was calculated with was made with two Fluke multimeters. The mean winding phase resistance was calculated to be approximately 2.21mΩ at 45°C, resulting in only about 1.4kW of losses at the maximum phase current of 450Arms as calculated in (4.18).

Table 4.10 Measured Motor Winding Resistance

Machine Temperature	12 °C
Phase A to B Resistance	3.89 mΩ
Phase B to C Resistance	3.91 mΩ
Phase C to A Resistance	3.96 mΩ
Mean Phase Resistance at 12°C	1.96 mΩ
Mean Phase Resistance at 45°C (calculated)	$R_{ph} = 2.21 \text{ m}\Omega$

$$P_{I^2R-loss} = 3I_{ph}^2 R_{ph} \quad (4.13)$$

The winding losses over the machine's whole operating space are calculated by using the I_d / I_q current table used by the motor drive to control the machine. The I_d / I_q table for maximum torque per amp and maximum power operating points was determined using the Infolytica Magnet FEA model, which was adjusted to be more accurate based on machine back emf and torque measurements as described in 3.3.3. Each I_d / I_q pair which is used in the control table in the drive is shown below in Figure 4.16.

There is a limited amount of space available for the table in the drive hardware, about 20x20 points, so only a select number of torque and speed points are used in the table. The I_d / I_q command is constant for a given torque in the constant torque operating range, so there are only points at low speed, 100RPM, and at the edge of the constant torque operating range, 2500RPM. The speed points are then spaced evenly beyond 2500RPM, and the drive software interpolates between the operating points. There is also a second table used by the drive for negative regenerative torque points, the values of which are given in Appendix II.

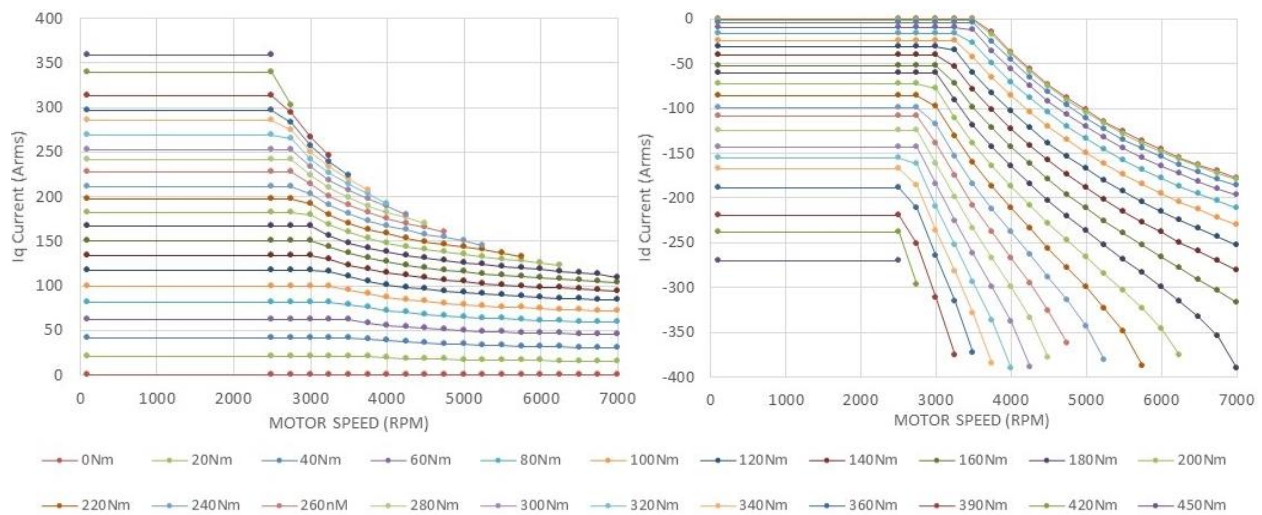


Figure 4.16 I_d / I_q operating points used for drive programming table, with speeds of 100, 2500, 2750... 7000rpm and torques of 0Nm, 20Nm... 360Nm, 390Nm... 450Nm

The copper losses are then calculated directly from the phase current for each operating, using (4.13) and the resistance for 45°C given in **Table 4.10**, and are shown along with the phase current in Figure 4.17 below. The phase current plot shows that the phase current does not reach its maximum of 450Arms for each motor torque. This is due to the resolution of control table used by the drive, which is in steps of 20Nm or 30Nm and steps of 250RPM above 2500RPM.

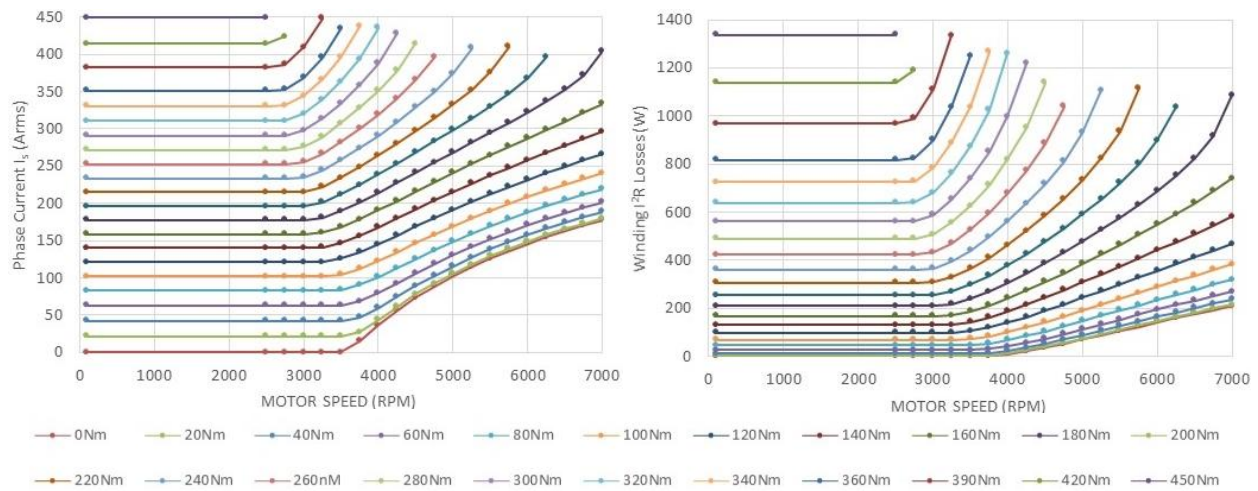


Figure 4.17 Motor phase current and winding losses for points in drive I_d / I_q table

The control table power limit is also up to 10kW less than actual motor power limit, as shown in Figure 4.18 below, due to the resolution of the control table. The control system in the motor drive may account for this though, by still utilizing full current at the power limit edge. Full power tests of the motor have been inconclusive, due to the bus voltage drooping below 300V. With the battery fully charged and the battery temperature above 25°C the voltage should stay above 300V, but this test was not performed before the onset of cold weather. This plot does show though that motor output power peaks at 136kW and remains above 130kW from 3000RPM to 7000RPM.

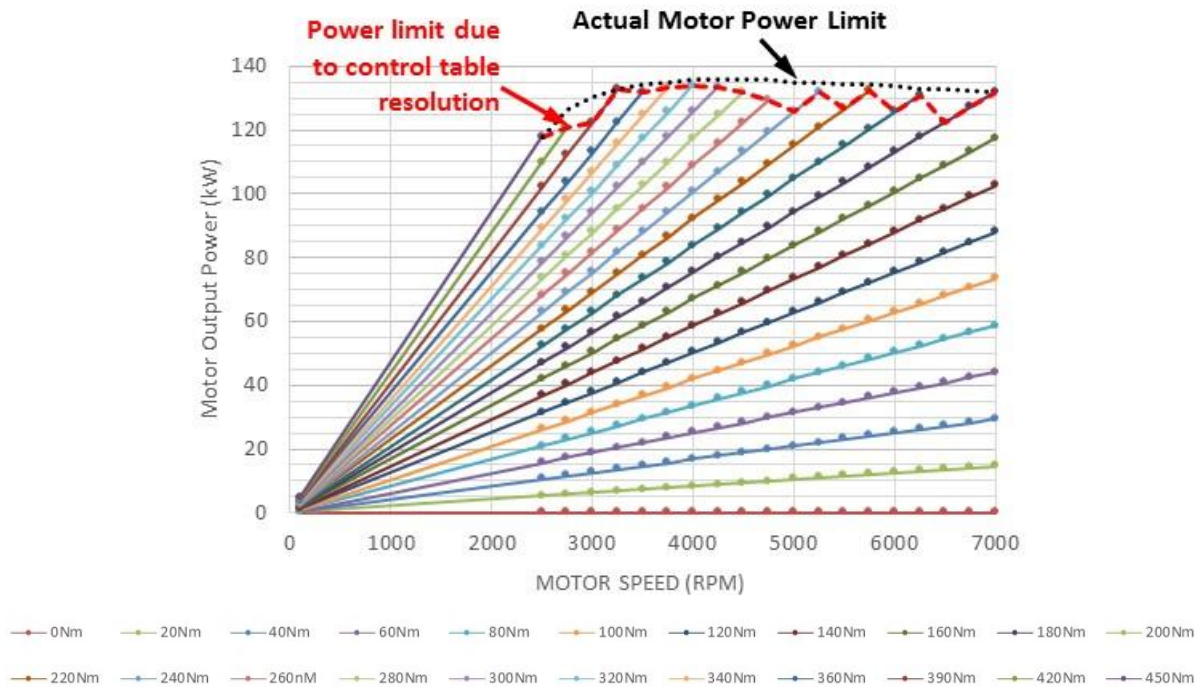


Figure 4.18 Motor output power limit with 300Vdc bus and 450Arms phase current

The electric machine's iron losses were determined using an Infolytica Magnet model of the machine which was developed in [125]. Iron losses consist of two primary components, eddy current and hysteresis losses. Eddy current losses are from current induced in the iron cross section due to Faraday's law and the time varying magnetic field in the iron. The losses are proportional to electrical frequency squared and the magnetic flux density squared, as shown in (4.14) below. Hysteresis losses are due to the energy needed to reverse the polarity of the magnetic dipoles in the iron, and is proportional to electrical frequency and magnetic flux density squared. The magnetic flux density is due to both the permanent magnetic and electromagnet flux, so there will be iron losses even when no current is provided to the machine. Figure 4.27 shows the machine's iron losses for a torque of 100Nm, and illustrates that at lower speeds hysteresis losses are dominant and that eddy current losses become more dominant as machine speed increases due to the speed squared relation of the losses.

$$P_{eddy} \propto f_{elec}^2 B^2 \quad (4.14)$$

$$P_{hyst} \propto f_{elec} B^2 \quad (4.15)$$

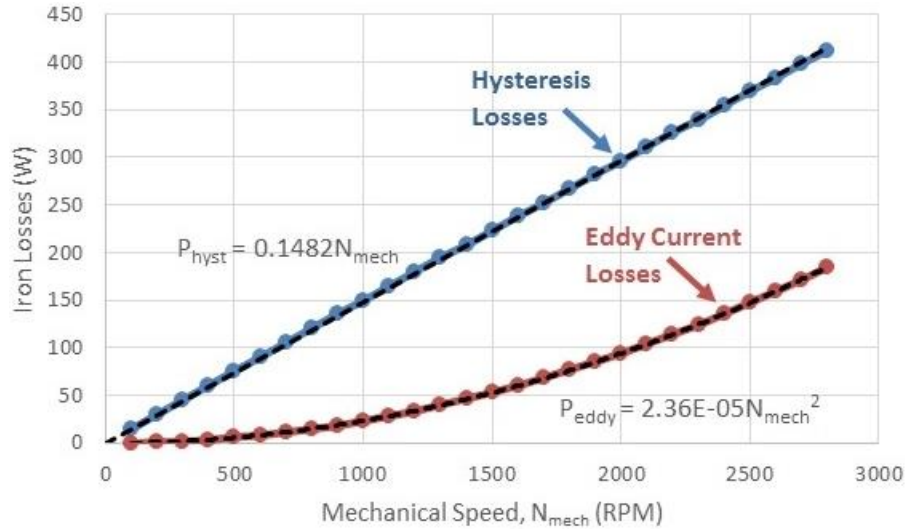


Figure 4.19 Eddy current and hysteresis iron losses for 100Nm machine torque

The iron losses for the full operating space of the machine, which are used for all of the following motor and system efficiency calculations, are shown in Figure 4.20 below. The figure shows that iron losses increase with increased torque, and that the no load iron losses at higher speeds are significant.

The large majority of the machine losses are due to iron and copper losses, however there are several other loss mechanisms which are not incorporated into the loss model, including magnet losses, increased AC winding losses due to skin and proximity effects, PWM losses, and friction and windage losses. These losses are neglected for various reasons. Magnet losses were neglected because they are small due to the use of a distributed winding machine with a high winding factor and the use of segmented magnets, and were calculated to be a maximum of 7W.

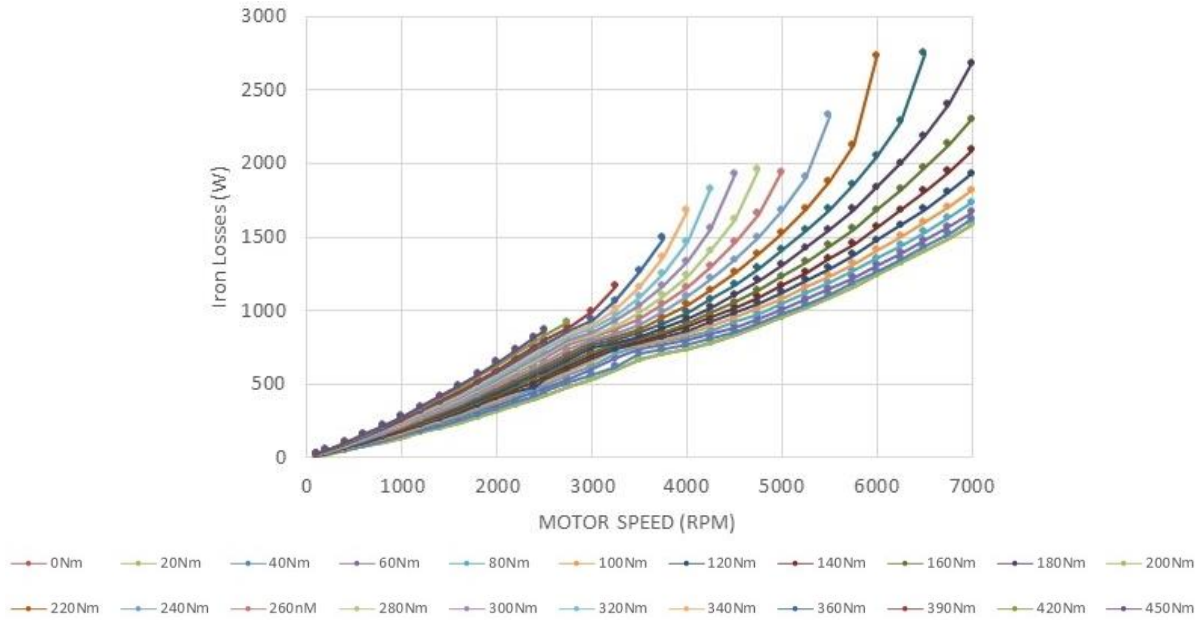


Figure 4.20 FEA calculated motor iron losses versus torque and speed

The AC winding losses were neglected because they are expected to be relatively small for the machine for two reasons – the maximum electrical frequency is not that high and the skin depth is several times greater than the winding wire diameter at the maximum electrical frequency of 466Hz. There may still be significant extra winding losses due to proximity effects, but the modeling of these losses is considered beyond the scope of this project. PWM losses are neglected because the iron loss properties are not known for frequencies this high, additional winding losses due to current ripple are likely small, and because it was suggested by a knowledgeable machine designer that the overall PWM losses will likely only result 5% or less additional losses.

Friction and windage losses, which are likely somewhat significant, were neglected because of a lack of a method to measure them. The no load machine losses were measured before the motor was installed in the truck by spinning the motor on a dynamometer and measuring the torque. The measured losses, shown below in Figure 4.27, align well with the FEA calculated iron losses, but the test was not able to be carried out at a high enough speed to differentiate between iron losses and friction and windage losses. The last two measured points, around 1900RPM and 2000RPM,

do suggest that some additional losses due to friction and windage are becoming evident, but without further testing these results are inconclusive and friction and windage losses are therefore neglected.

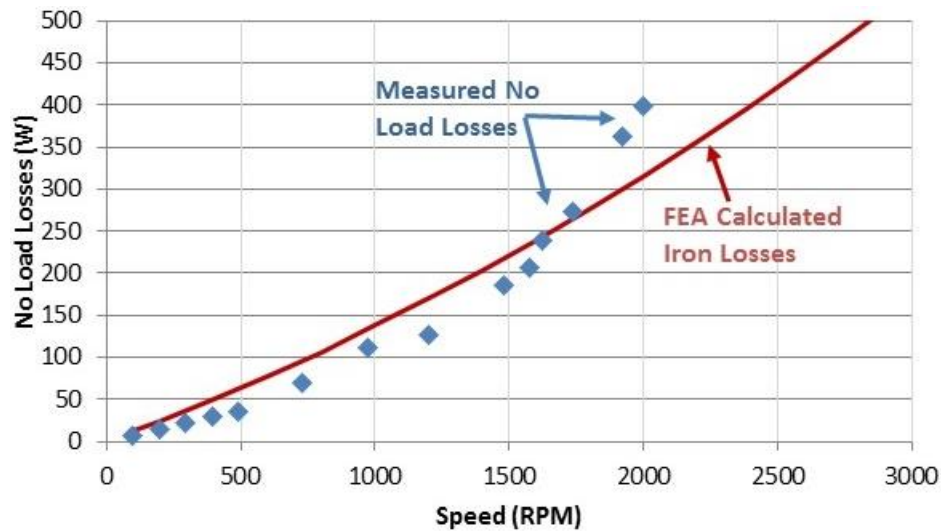


Figure 4.21 Dynamometer measured no load motor losses

The total machine losses are therefore considered to be the sum of the iron losses and copper losses, which is shown in Figure 4.22 below. The total losses vary from 0 to 1.4kW at low speed

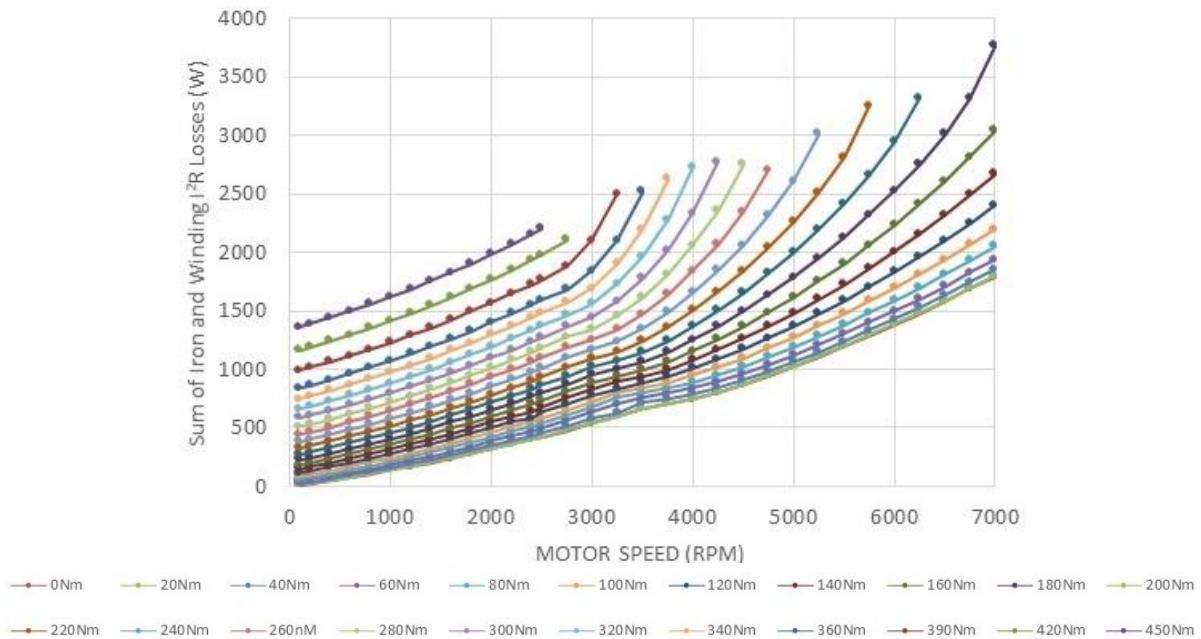


Figure 4.22 Sum of motor winding and iron losses

up to 1.8kW to 3.8kW at peak speed, which are quite low losses considering the machine's peak power is 135kW.

The machine's efficiency is calculated as machine output power divided by the sum of machine output power and losses, and is shown in Figure 4.31 below. The machine's efficiency is above 95% throughout most of the operating range, with the exception of high torque low speed points where copper losses dominate and low torque points where iron losses dominate. The torque speed curve for constant speed operation in gear 1 & 2, taken from Figure 4.38, is also overlaid on the efficiency contour plot. Due to the dominance of iron losses at higher speeds the machine is significantly more efficient in gear 2 for constant speed vehicle operation, with about 97% efficiency in gear 2 at 50mph and 90% efficiency in gear 1. This suggests that gear shifting should be based on system efficiency as well as torque and speed requirements, and this topic will be further explored in the coming sections. Overall, the machine's efficiency is excellent and could likely only be marginally improved with a more optimized design.

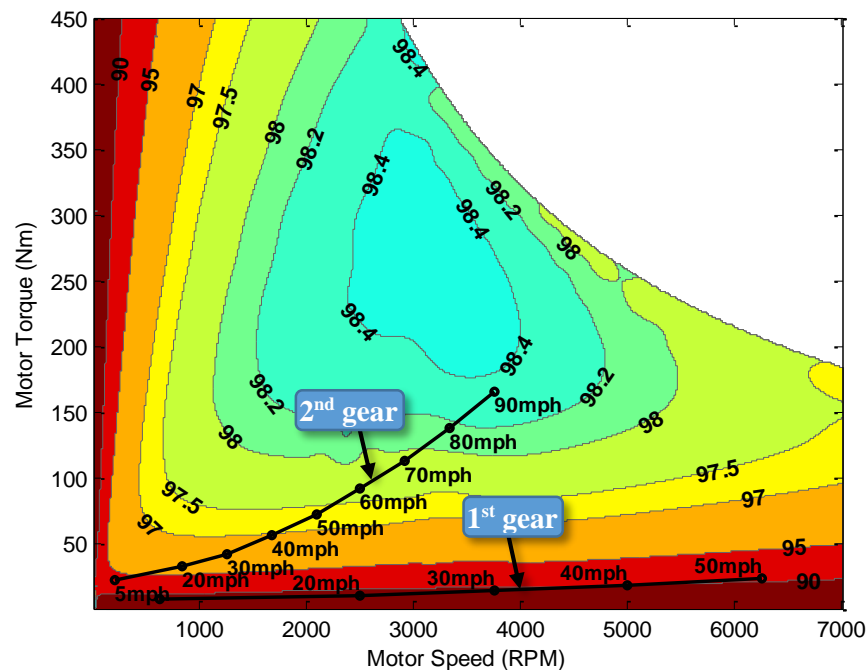


Figure 4.23 *Motor efficiency contour plot* (with constant vehicle speed torque vs motor speed for 1st and 2nd gear overlaid)

ii. Motor Drive Losses

The motor drive in the truck converts the battery pack's dc voltage to a current controlled three phase AC voltage source to power the motor. The motor drive, designed and manufactured by Rinehart Motion Systems and described in Table 4.11 below, can operate with up to a 360Vdc bus voltage and is rated for 450Arms continuous, which is sufficient to supply approximately 158kVA to the motor with a 302Vdc bus as derived in 3.3.2.

Table 4.11 Rinehart Motion Systems PM150 Motor Drive Specifications

Model Number	PM150DX
Switching Frequency	12kHz
Motor Phase Current	450Arms (cont. & peak)
Maximum Bus Voltage	360Vdc*
Coolant Temperature Range (no derating)	-40 to 80°C
Coolant Flow Rate	8 – 12 lpm
Dimensions (mm)	314 x 200 x 87 (5.5l)
Weight	10.7kg
Power Density @ 350Vdc	17kVA/kg 33kVA/l
Price (quantity 1)	\$8,900

**operated to 390V during regenerative braking, may slightly reduce reliability of unit according to Larry Rinehart, designer of the drive*

The motor drive offers a very high power density of 17kVA/kg and 33kVA/l, which scales to 12.6kW/kg and 24.7kW/l for our peak motor output power of 135kW. The Rinehart drive, as used in our application, nearly meets the U.S. Department of Energy's 2020 power density goal of 14.1kW/kg and greatly exceeds the goal of 13.4kW/l [126]. The Rinehart drive achieves this phenomenal power density by utilizing the latest generation 900A peak SKiM power module from Semikron and high performance AVX film capacitors, shown in Figure 4.24 below. The power module and capacitors are mounted on a custom made friction stir welded copper fin cooling plate, which is very effective at removing heat from the system. Additionally compact, custom designed

gate drive and control circuit boards are utilized, further helping to achieve the drive's very small mass and volume.

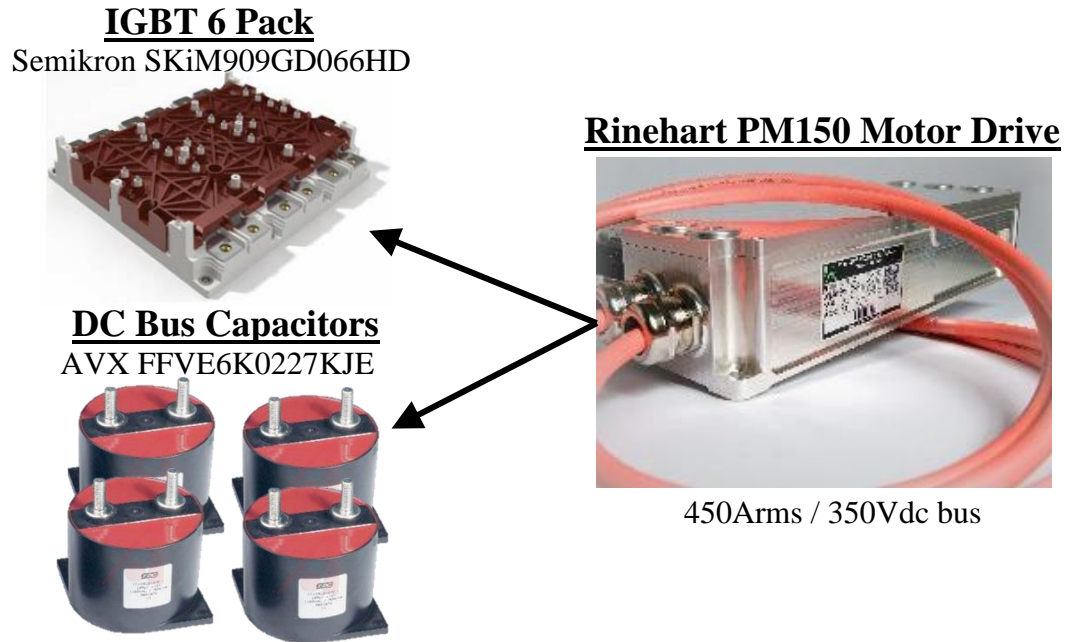


Figure 4.24 Motor drive DC bus caps and semiconductors

The IGBT power module is rated for 600Vdc maximum voltage and 900A maximum current, and contributes about 1kg of mass, 0.8l of volume, and \$1,000 of cost to the power converter, as documented in Table 4.12 below. The four capacitors contribute about the double the volume as the IGBT module contributes, a total of 2kg and 1.6l as shown in Table 4.13, but at a cost of \$76.75 each contribute substantially less cost. This shows that improvements in film capacitor design will contribute more to the reduction of drive volume and mass than improvements in semiconductors.

Table 4.12 IGBT Specifications

Manufacturer	Semikron
Part Number	SKiM909GD066HD
Max Voltage	600Vdc
Max Current	900A peak
$V_{CE(sat)}$ @ $I_C = 900A$	1.45V typ.
V_{diode} @ $I_{diode} = 900A$	1.5V typ.
di/dt_{on}	5100A/ μ s
di/dt_{off}	9000A/ μ s
Inductance, L_{CE}	10nH typ.
Junction Temperature	150°C max usable
Dimensions (mm)	150 x 160 x 34.3 (0.8l)
Mass	1042g
Price (quant. 20)	\$926.58 each

Table 4.13 Capacitor Specifications

Manufacturer	AVX
Part Number	FFVE6K0227KJE
Quantity Used	4 in parallel
Capacitance	220uF
Max Voltage	600Vdc
Ripple Current	100Arms max
Resistance at 12kHz	1.3m Ω
Inductance	40nH
Temperature	-40 to 105°C
Dimensions (mm)	85(diam.) 64(ht.) (0.4l)
Mass	500g
Price (quant. 1000)	\$76.75 each

The motor drive losses consist almost entirely of semiconductor losses, although capacitor and bus bar losses contribute an extra few percent to the total losses. The semiconductor losses were modeled utilizing Semikron's Semisel simulation tool, which is available for free use on Semikron's website. Semisel calculates the semiconductor losses by utilizing parameters available on the IGBT module datasheet with relatively standard methods for calculating switching and conduction losses, as described in their documentation. The inputs used for modeling the losses include module part number, switching frequency of the drive, bus voltage, calculation method, correction factors, and heat sink type and temperature, all shown in Table 4.14 below.

Table 4.14 Semikron Semisel Simulation Settings

IGBT Module	SKiM909GD066HD
Switching Frequency	12kHz
Bus Voltage	330Vdc
Calculation Method	Use Typical Values
Correction Factors	1 (no correction)
Heat sink type	Fixed temperature
Heat sink temperature	40°C

Fixed heat sink temperature was chosen because the heat sink temperature has been observed to reach a maximum of 40°C on the hottest days and a fixed bus voltage of 330Vdc was chosen

because this is the typical average bus voltage for a drive. Heat sink temperature and bus voltage have a significant effect on the semiconductor losses. At peak output current if bus voltage droops from 330V down 250V, losses will be reduced by about 20%, and if heat sink temperature is reduced from 40°C to -10°C losses will also be reduced about 20%, as shown in Figure 4.25. At -10°C and 250Vdc, maximum current losses are reduced to 2475W, a full 30% reduction from the losses at nominal bus voltage and heat sink temperature. Although it is recognized that bus voltage and temperature do have a significant impact on losses, at this stage in the project only the change in losses with respect to bus voltage will be considered. The losses were found to consistently change 0.24% per volt, irrespective of the output current, and the losses are adjusted in the model accordingly as the bus voltage changes.

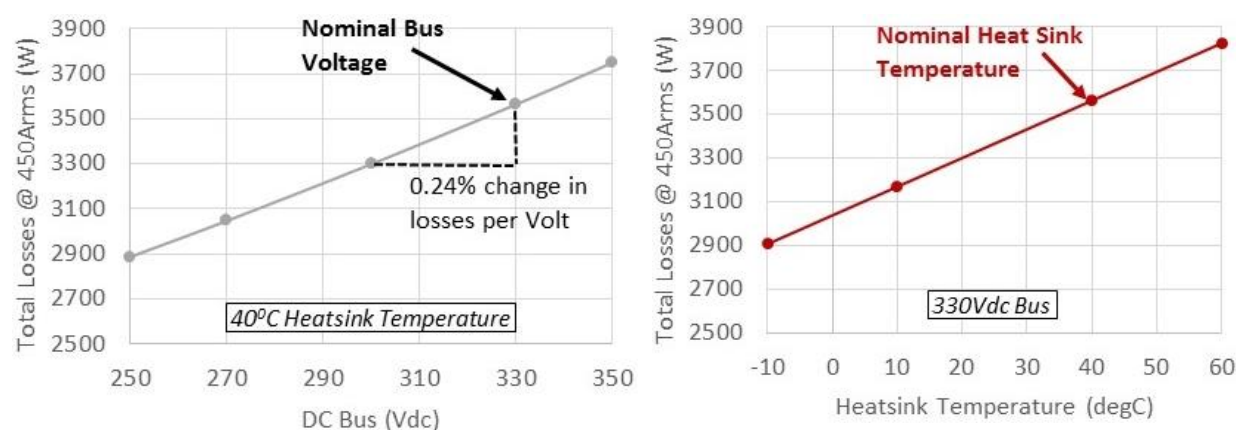


Figure 4.25 Motor drive semiconductor losses for varied dc bus and temperature

The motor drive losses for the nominal parameters as given in Table 4.14 are shown in Figure 4.26 below. The losses increase from about 500W at 75Arms phase current to 3.6kW at 450Arms phase current. The losses increase approximately linearly because the diode and IGBT voltage drop are largely independent of current and because switching losses are proportional to switching current. As voltage is increased from 10V to 200V line to line, the modulation index increases and current flows through the IGBT for more of the switching period. As a result diode conduction

losses decrease and IGBT conduction losses increase as output voltage increases, but total losses are very similar, as shown in Figure 4.26, due to similar voltage drop for both devices.

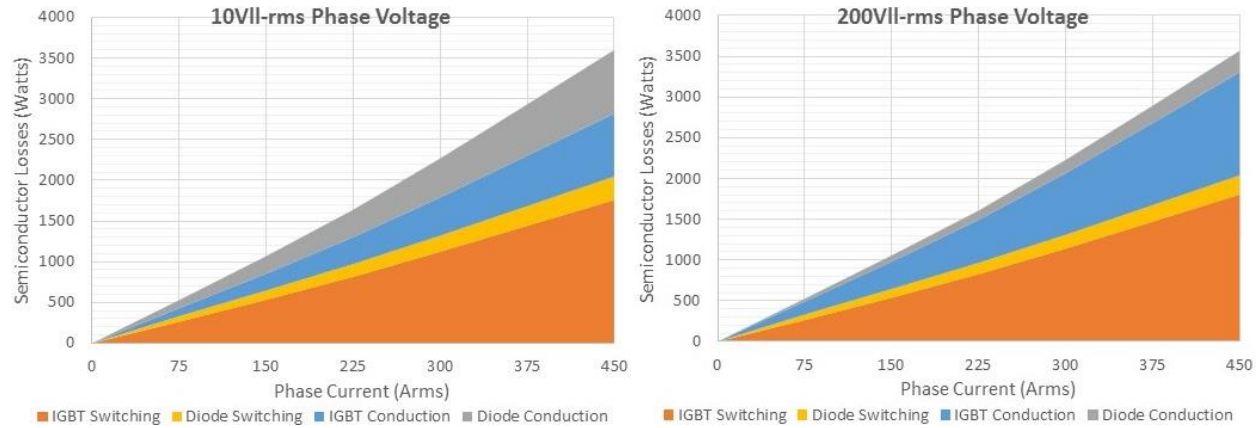


Figure 4.26 Motor drive semiconductor losses for 330Vdc bus and 40°C heat sink

There are also losses in the motor drive bus bars and in the capacitors. The bus bars are quite large though, so even conservatively assuming 0.3mΩ dc side resistance the losses at 500Adc only amount a relatively inconsequential 75W. Capacitor losses are also quite small. The dc link capacitor bank will see a maximum approximately equal to the maximum output current, 450Arms. This current will divide between the four capacitors, which have 1.3mΩ resistance each, and contribute an additional total of 63W to the drive losses, which similar to the bus bar losses is relatively inconsequential and will be ignored at this point.

The motor drive efficiency is then calculated using the 200Vll-rms losses shown in Figure 4.26. The losses are adjusted 0.24% per volt, as shown in Figure 4.25, based on the battery pack voltage calculated from the battery pack model in 4.3.6 for 50% SOC and 25°C. The resulting motor drive efficiency contour plot, given in Figure 4.27, shows that motor drive efficiency is greater than 97% over much of the operating space of the drive, and that motor drive efficiency for constant speed operation is somewhat greater in 1st gear for speeds up to about 30mph.

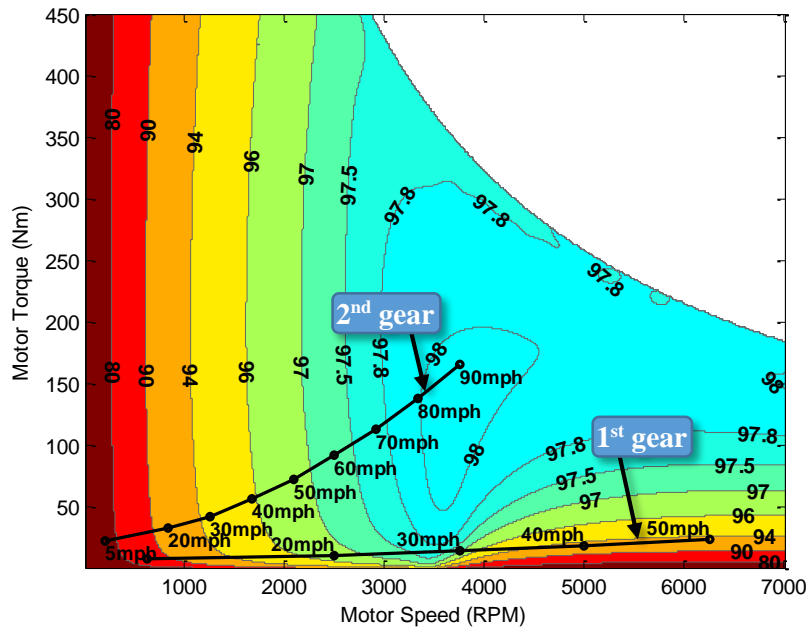


Figure 4.27 *Motor drive efficiency contour plot for battery parameters: 50% SOC, 25°C*
(with constant vehicle speed torque vs motor speed for 1st and 2nd gear overlaid)

iii. Combined Motor and Drive Losses with Experimental Verification

While the segregated motor and drive losses give insight into the efficiency of each subcomponent, the combined efficiency of the two systems will ultimately determine the energy consumption from the battery pack. The sum of the motor and drive losses given in i and ii are shown in Figure 4.28 below. The losses vary from less than 1kW at low torque and low speed and up to 5 to 7kW at peak system torque and power.

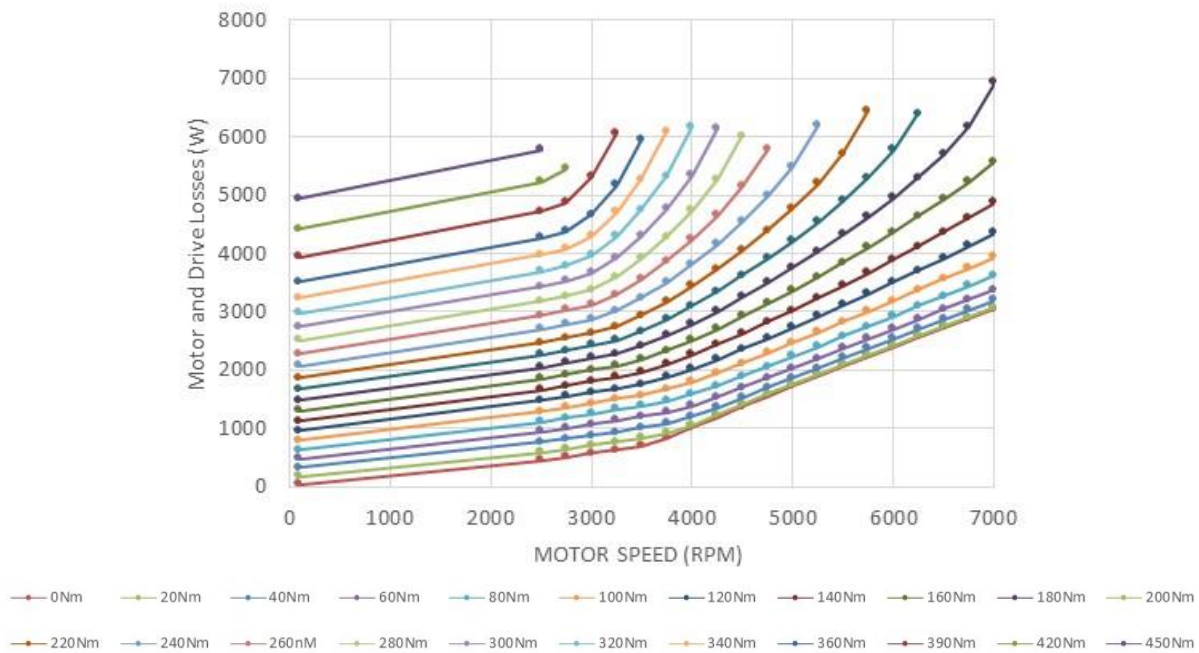


Figure 4.28 Sum of motor and drive losses

The combined motor and drive efficiency contour plot for the whole operating space of the motor is then shown below in Figure 4.29. The combined efficiency of the motor and drive is greater than 92% for most of the operating space, with peak efficiency above 96.3%. The efficiency for constant speed driving is also shown to be substantially greater in 2nd gear, with efficiency in 1st gear never exceeding 90%. The difference in efficiency for the two gears suggests that significant improvements in system energy consumption can be made by selecting the more efficient of the gears based on the operating point. Vehicle range and system efficiency for both gears and an optimal selection of gears is examined in detail in sections 4.4.1 and 4.4.2.

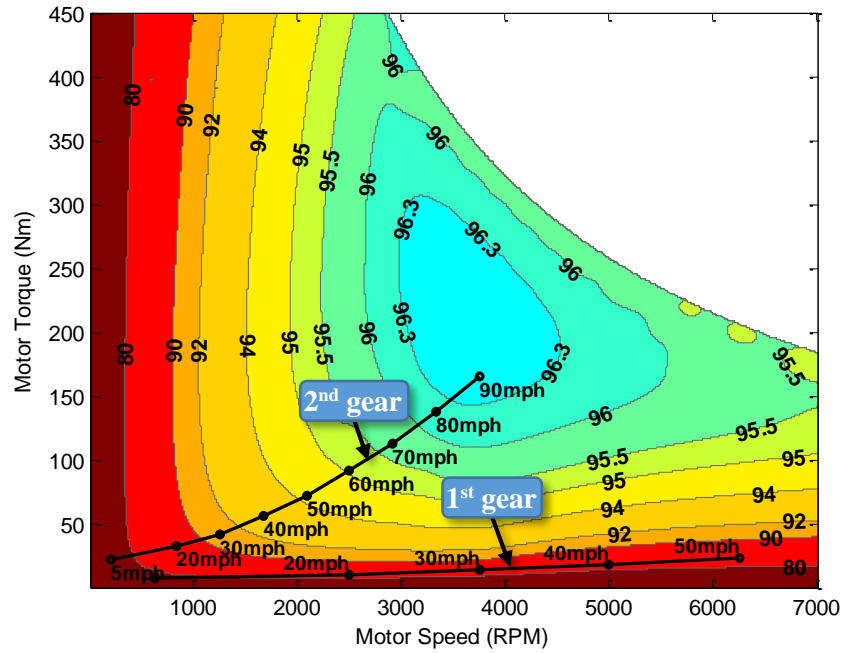


Figure 4.29 *Combined motor and drive efficiency contour plot* (with constant vehicle speed torque vs motor speed for 1st and 2nd gear overlaid)

To confirm that the loss model is correct, measured losses during a truck drive are compared to model predicted losses. The losses are measured by measuring the battery input voltage, V_b , drive input current, I_{drive} , motor speed, ω_m , and motor torque, T_m , and calculating the difference between the input and output power, as done in (4.16).

$$P_{mot \& drive-loss} = \begin{cases} V_b I_{drive} - T_m \omega_m, & T_m > 0 \text{ (Motoring)} \\ T_m \omega_m - V_b I_{drive}, & T_m < 0 \text{ (Generating)} \end{cases} \quad (4.16)$$

All the parameters in (4.16) except T_m are directly measured with sensors in the vehicle. Because the losses are calculated from dynamic data, the motor rotor acceleration torque must be accounted for by adding it to the measured motor torque, as shown in (4.17), where the acceleration torque is calculated as the product of the rotor inertia, J_{rotor} , and the rotor acceleration α_m .

$$T_m = T_{m-meas} + J_{rotor} \alpha_m \quad (4.17)$$

Because the motor's HBM T22 torque sensor offset is rated to drift up to 0.5% of full range per 10°C (5Nm per 10°C), to accurately measure the losses the torque sensor must be re-zeroed occasionally as the drive train heats up. To provide the best possible data, the truck was driven for about a half hour to warm the motor up to 40°C, the torque sensor was re-zeroed, and then the truck was driven for another 22.6 miles over a wide range of torque and speed. The truck was only driven in 2nd gear to improve the quality of the data, but a similar test could be performed in 1st gear to get data up to 4000rpm, the maximum rotor speed for the current version of the rotor.

All of the resulting motor and drive loss data points are shown below in Figure 4.30, along with the predicted motor and drive losses over the range of motor speeds experienced in the drive. There is very good alignment between the measured and model predicted losses at low speeds, as shown by the curve fit of the measured data in Figure 4.30.

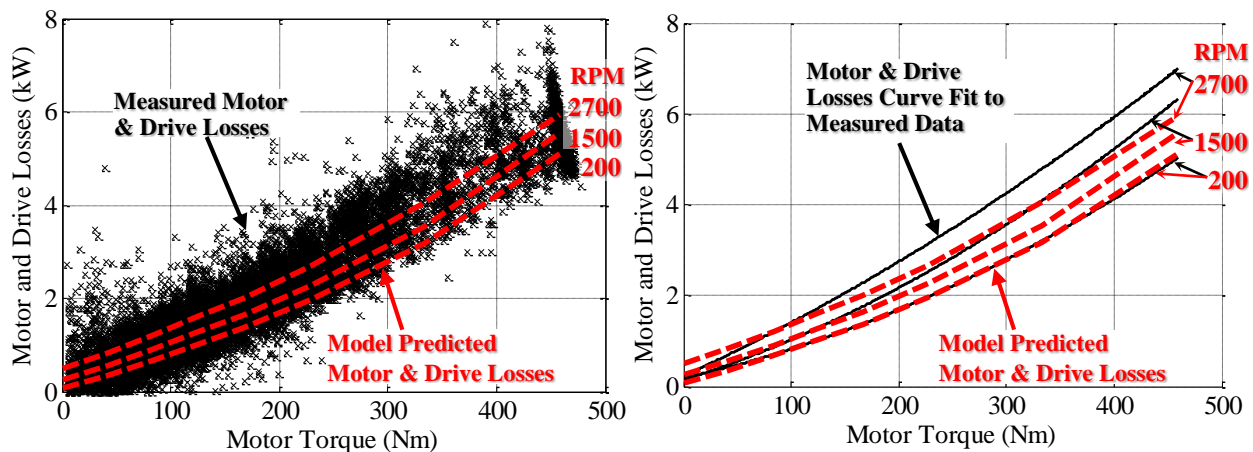


Figure 4.30 Measured vs modeled combined motor and drive losses

As motor speed increases there begins to be some differentiation between measured and modeled losses, with about 1kW difference at maximum torque. The difference is likely partly due to model error and partly due to measurement error. The loss sources not accounted for in the model include motor friction and windage, motor PWM related losses, motor winding proximity losses, and drive capacitor and bus bar losses, and may add up to several hundred watts at higher

speeds. Additionally, torque and voltage offset will also have a large affect, with just 1Nm of offset resulting in a 232W error at 2700RPM, and 1V of voltage offset resulting in a 500W error at the peak battery pack current of 500A. Considering the significant amount of error that is introduced by small offsets, and that these measurements were made on public roads in 10°C ambient temperature, the close alignment of measured and modeled results is actually quite impressive.

To further illustrate the accuracy of the motor and drive model several long drives were analyzed. The measured and model predicted losses for these drives are shown in Table 4.15 below. For drives #1 and #2, in which the torque sensor was periodically manually re-zeroed as the motor and torque sensor warm up, the measured and modeled losses were very close, within 5.3% or 2.1 Wh/mile of each other. Considering that the total energy consumption was greater than 400Wh/mile for both drives, a 2.1Wh/mile error only represents an error of 0.5% of total drive energy.

Table 4.15 Measured vs Modeled Motor and Drive Losses for Six Drives

	Torque offset re-zeroed		Torque offset not re-zeroed			
Parameter	Drive #1	Drive #2	Drive #3	Drive #4	Drive #5	Drive #6
Date / Time	10/23/14 9:31PM	11/4/14 10:00PM	10/17/14 6:28PM	10/19/14 10:07PM	10/25/14 9:47AM	10/26/14 5:58PM
Drive Length	31.5 mi	29.4 mi	48.6 mi	46.4 mi	35.1 mi	28.1 mi
Energy Consumption	412.4 Wh/mi	461.9 Wh/mi	470.0 Wh/mi	445.4 Wh/mi	409.1 Wh/mi	412.9 Wh/mi
Measured Motor & Drive Losses	39.4 Wh/mi	46.5 Wh/mi	23.3 Wh/mi	29.2 Wh/mi	28.6 Wh/mi	29.9 Wh/mi
Modeled Motor & Drive Losses	37.3 Wh/mi	44.8 Wh/mi	29.2 Wh/mi	36.2 Wh/mi	27.6 Wh/mi	34.7 Wh/mi
Error	-5.3%	-3.6%	+25.3%	+24.0%	-3.5%	+16.1%

Much higher error, up to 25%, was witnessed for the drives where the torque sensor was not re-zeroed. The measured losses are consistently less than the model predicted error, which is almost

certainly due to the torque sensor offset drifting upward with increasing temperature, resulting in the system measuring more torque than is actually produced and therefore measuring less losses.

In summary, the model is shown to be very close to measured results up to a motor speed of 2700RPM. Differences between measured and modeled loss of up to about 1kW are witnessed, but over a whole drive cycle the model estimates losses to within 5% of measured losses, a very commendable result considering the challenge of measuring drivetrain losses in a moving vehicle.

4.3.6 Battery Loss Model

Battery losses are due to ohmic losses in the conductive terminals and current collector plates in the anode and the cathode, as well as due to electrochemical loss mechanisms. The battery terminal voltage drops in response to a current pulse, and continues to decrease with a capacitor like discharge response, as shown in Figure 4.31 below. For the 200A ten second current discharge pulse shown, the battery voltage drops about 170mV instantaneously, and drops an additional 30mV after ten seconds due to the aforementioned capacitor like discharge.

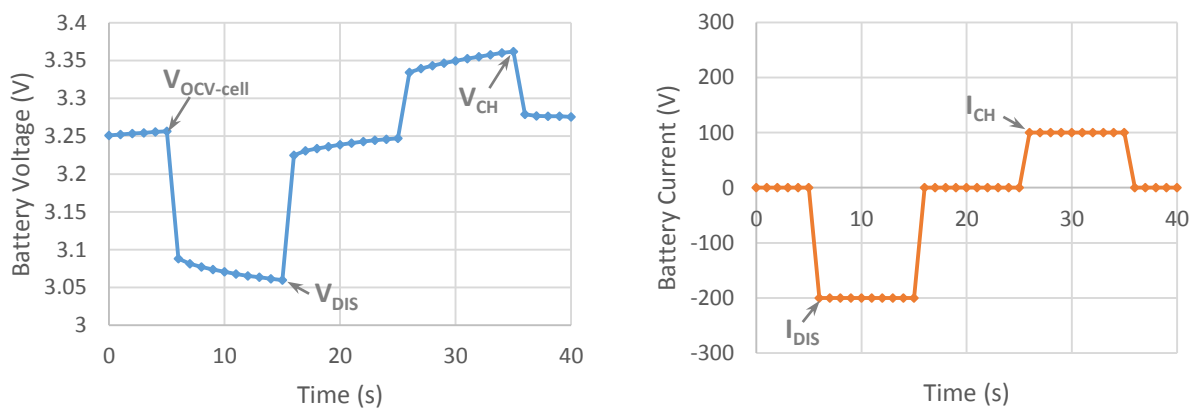


Figure 4.31 Pulse current test at 25°C & 90% SOC for 100Ah CALB battery

The pulsed discharge and charge current test shown in Figure 4.31 is commonly referred to as the hybrid pulsed power characterization (HPPC) test. The HPPC charge and discharge resistances

are calculated from the pulse test by taking the difference of the open circuit voltage, $V_{OCV-cell}$, and the voltage after 10 seconds of discharging, V_{dis} , and dividing by the discharge current I_{dis} , as shown below in (4.18) and (4.19) for the charge case.

$$R_{b-dis} = \frac{V_{ocv-cell} - V_{dis}}{I_{dis}} \quad (4.18)$$

$$R_{b-ch} = \frac{V_{ocv-cell} - V_{ch}}{I_{ch}} \quad (4.19)$$

The open circuit voltage and charge and discharge resistance as a function of battery SOC for a single CALB 100Ah cell is shown in Figure 4.32 below for an HPPC test performed during an LA92 drive cycle discharge of the battery. The battery is then modeled simply as an open circuit voltage in series with a resistance, which provides a good approximation of battery performance.

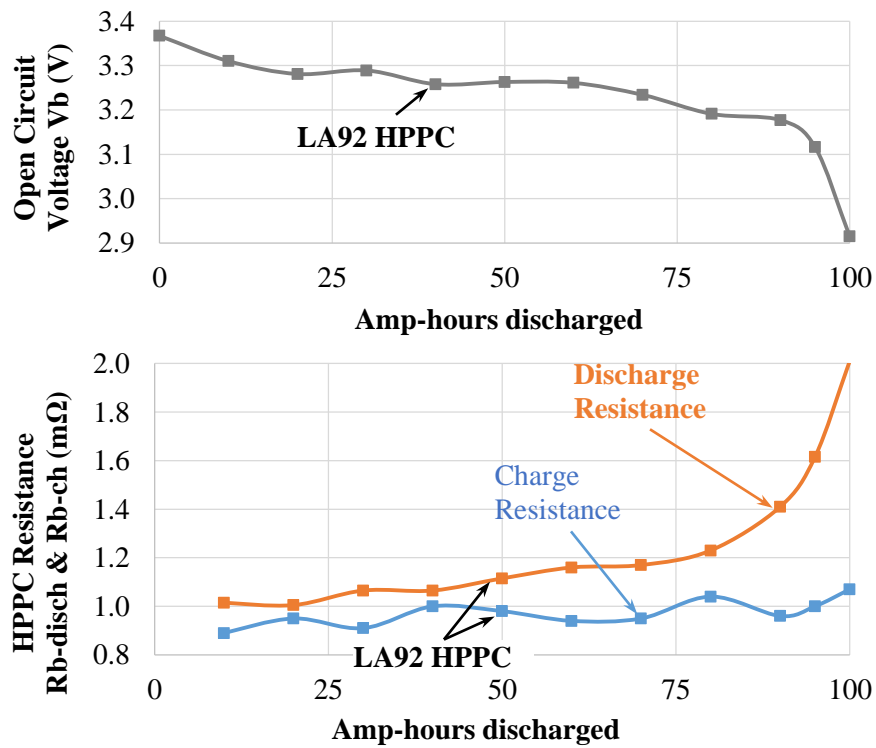


Figure 4.32 Measured open-circuit voltage and HPPC resistance LA92 test for CALB SE100AHA LiFePO4 battery cell at 25°C

This simplified model does neglect several characteristics of the battery though, including reduced resistance at higher currents, the time constant aspect of the discharge, and any temperature effects. A more sophisticated model which includes some of these effects is developed in Chapter 6, but for the analysis presented in this chapter just this model will be used.

The battery pack resistance consists of the sum of the battery cell resistances and the bus bar and cable resistance. The bus bar and cable resistance, R_{b-bus} , is calculated from the slope of the measured battery pack current versus voltage drop across the cabling, as shown in Figure 4.33.

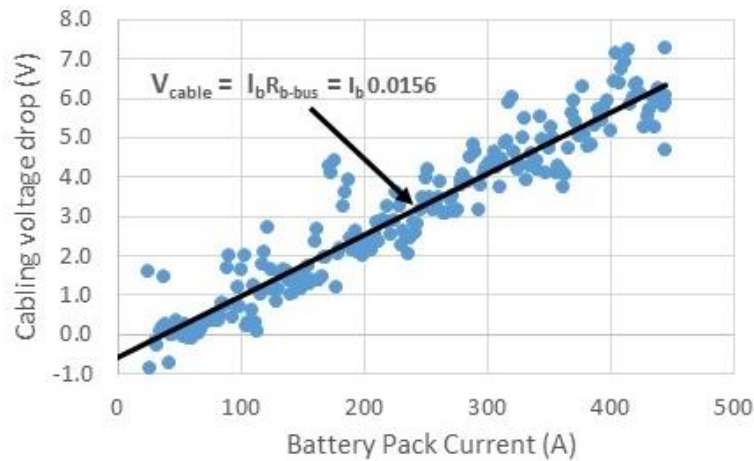


Figure 4.33 Battery pack cable resistance measured from cable voltage drop

The measured bus and cable resistance of $15.6\text{m}\Omega$, given in (4.20), does neglect the resistance of the individual bus bars connecting cells, since bus voltage drop is calculated from the difference of the measured pack voltage at cable terminals and the sum of the measured cell voltages. Cell voltages are measured from the center point of the connecting bus bars and therefore include the bus bar voltage drop in the measurement. Each bus bar is predicted to have a resistance of only about $0.02\text{m}\Omega$ though, so there is likely only about $2.2\text{m}\Omega$ of resistance which is unaccounted for in the pack.

$$R_{b-bus} = 15.6m\Omega \quad (4.20)$$

The open circuit voltage and charge and discharge resistance for a single cell, along with the bus resistance, can now be used to calculate the battery pack resistance, R_b , as is done in (4.43) for charging and discharging, where $N_{b-cells}$ is the number of battery pack cells. The battery pack open circuit voltage, V_{ocv} , is then calculated from the cell open circuit voltage in (4.22) and the battery output voltage, V_b , and battery output power, P_b , is calculated from the circuit model in (4.44) and (4.24). The battery pack current, I_b , for a given battery pack power, P_B , is calculated using the quadratic formula in (4.25).

$$R_b = \begin{cases} N_{b-cells}R_{b-disch} + R_{b-bus}, & I_b > 0 \text{ (discharging)} \\ N_{b-cells}R_{b-ch} + R_{b-bus}, & I_b \leq 0 \text{ (charging)} \end{cases} \quad (4.21)$$

$$V_{ocv} = N_{b-cells}V_{ocv-cell} \quad (4.22)$$

$$V_b = V_{ocv} - I_b R_b \quad (4.23)$$

$$P_b = V_b I_b \quad (4.24)$$

$$I_b = \frac{V_{ocv} \pm \sqrt{V_{ocv}^2 - 4P_b R_b}}{2R_b} \quad (4.25)$$

The maximum battery pack charge and discharge power can also be calculated from the HPPC results. The power limits are a function of battery pack voltage limits, which are calculated from the cell voltage limits in (4.26) and (4.27). The power limit, P_{b-lim} , is then calculated in (4.28).

$$V_{b-min} = 2.5 \text{ V/cell} \times 108 \text{ cells} = 270V \quad (4.26)$$

$$V_{b-\max} = 3.6 \text{ V/cell} \times 108 \text{ cells} = 388.8\text{V} \quad (4.27)$$

$$P_{b-\lim} = \begin{cases} V_{b-\min} \frac{V_{ocv} - V_{b-\min}}{R_b}, & (\text{discharging}) \\ V_{b-\max} \frac{V_{b-\max} - V_{ocv}}{R_b}, & (\text{charging}) \end{cases} \quad (4.28)$$

The pack open circuit voltage, which varies from 360V when fully charged to 343V at 90% DOD, is given Figure 4.36 along with the pack charge and discharge resistance. The calculated discharge power limit, also shown Figure 4.36, varies from 190kW down to 120kW at 90% SOC. Since the design goal was to provide 135kW of motor power output, this suggests that the motor output will be reduced as the battery pack reaches low discharge states. The charge power limit is only around 80kW over most of the range, but this is acceptable since braking is generally slower than acceleration and extra braking power can be provided by the stock mechanical brakes.

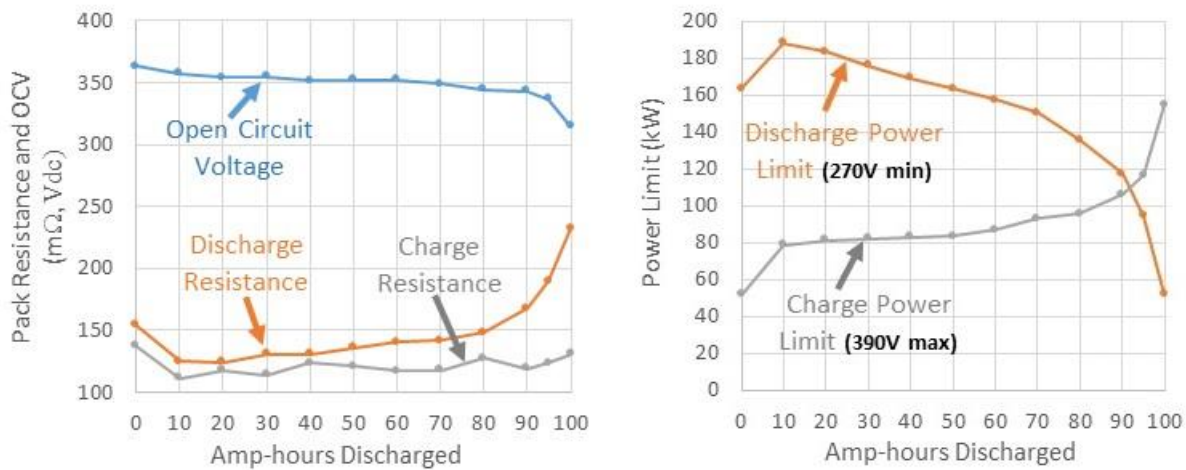


Figure 4.34 Battery pack losses and efficiency vs output power and SOC

To determine the exact power the motor can output at a given state of charge the voltage where the battery power limit and motor output power limit meet must be determined. The motor output power limit, $P_{\text{mot-max}}$, is about 135kW with a 302Vdc bus, and decreases approximately linearly

with reduced battery voltage as shown in (4.29). The max system power which can be drawn from the battery pack, P_{\max} , is then calculated as the sum of the maximum motor power, the maximum motor and drive losses (6kW), and the accessory power (1kW), in (4.30). Finally the maximum power drawn from the battery is calculated as either P_{\max} when the motor drive output power is the limiting factor or as the battery power limit P_{b-lim} when the battery power limit is the limiting factor.

$$P_{\text{mot-max}} \approx V_b \frac{135kW}{302Vdc} \quad (4.29)$$

$$P_{\max} = P_{\text{mot-max}} + P_{\text{mot \& drive loss max}} + P_{\text{acc}} \quad (4.30)$$

$$P_{b-\max} = \begin{cases} P_{\max}, & P_{\max} < P_{b-lim} \text{ (limited by motor drive power)} \\ P_{b-lim}, & P_{\max} > P_{b-lim} \text{ (limited by battery power)} \end{cases} \quad (4.31)$$

To illustrate the intersection of the battery and system power limits, the maximum system power limit as a function of battery voltage is overlaid with the battery power limit versus SOC and the battery pack output voltage Figure 4.35. For battery SOC greater than 20% the maximum system power points are limited by the motor drive, and for lower SOC's the maximum system power is limited by the battery voltage. The maximum motor output power limit is also shown in Figure 4.35 to have a maximum of just under 135kW and to reduce to 123kW when 80Ah are discharged from the battery pack. This is slightly below the design goal of 135kW, and suggests that a lower resistance battery pack, or the addition of an ultracapacitor pack as is examined in Chapter 5, is needed to achieve 135kW of motor output power over a wide range of battery SOC.

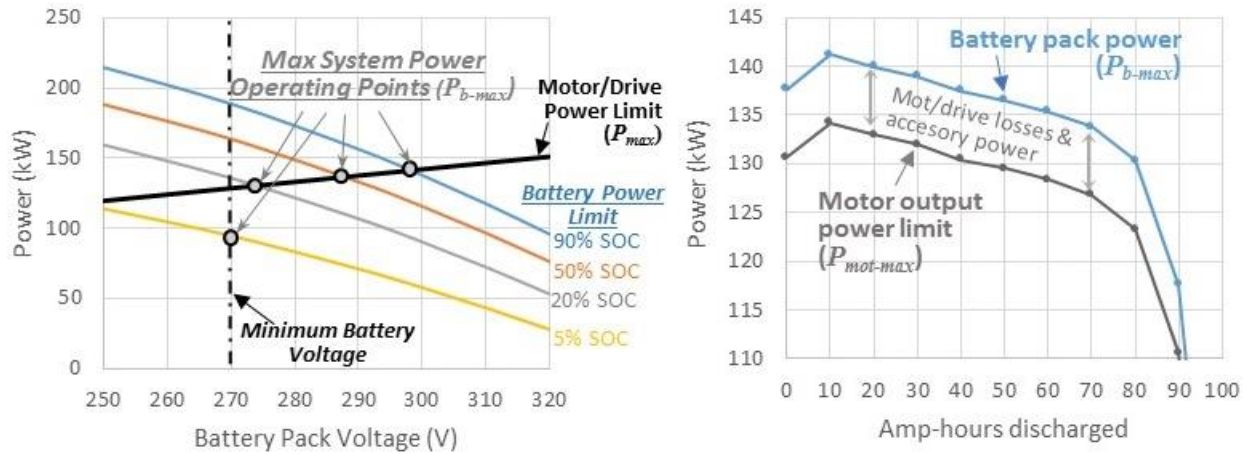


Figure 4.35 Operating point for maximum motor output power as battery pack is discharged

The battery pack parameters presented above are used to calculate battery pack losses, which are used in the following section to calculate how much of the battery energy goes to losses for a given drive cycle. The battery, P_{b-loss} , loss is calculate as the I^2R loss in the battery pack resistance in (4.32), and the battery efficiency, η_b , is calculated as the battery output power over the sum of the battery output power and battery loss in (4.33).

$$P_{b-loss} = I_b^2 R_b \quad (4.32)$$

$$\eta_b = \frac{P_b}{P_b + P_{b-loss}} \quad (4.33)$$

The battery pack losses versus power are shown in Figure 4.36 to increase from a few kW at 50kW of output power to 30kW or greater at 150kW of output power. The battery pack efficiency is also shown to be quite high, greater than 95% for 30kW of output power or less, the most common operating region of the battery pack.

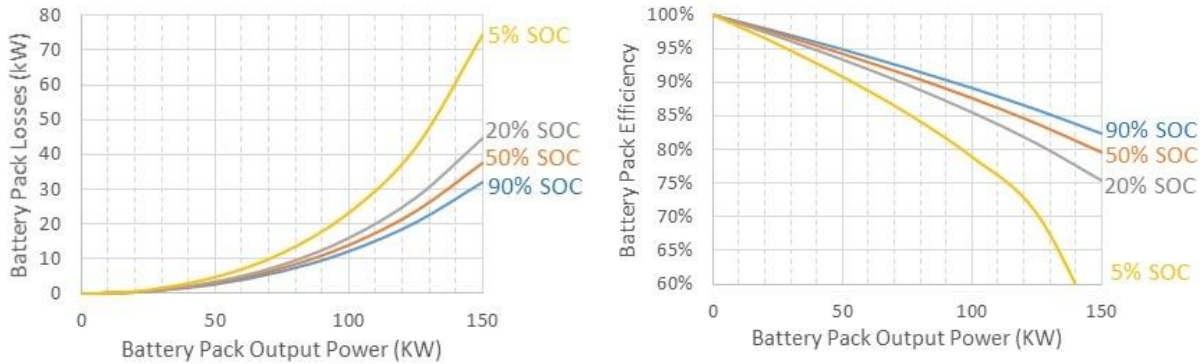


Figure 4.36 Battery pack losses and efficiency vs output power and SOC

The simple battery model presented is actually quite accurate, and is shown in Table 5.4 to estimate the amp hours consumed from the battery for the LA92 drive cycle with an accuracy of 0.1%. This model will only work well though when temperature of the battery pack is tightly controlled, as can be done in a thermal chamber in the lab. As the battery pack temperature increases in the vehicle during a typical drive cycle the resistance will change, requiring additional thermal and temperature dependent battery modeling to accurately determine performance. However temperature changes of only 5 to 10°C have been witnessed for typical drives, so the model will be relatively accurate for drives on starting with a vehicle temperature around 25°C.

Additionally this simplified battery model will not work well for low temperatures because at low temperatures battery resistance is a function of battery current due to the Butler-Volmer effect. An improved battery model which includes the Butler-Volmer effect will be utilized in the future work.

4.4 Vehicle Modeling Utilizing Updated Model Parameters from section 4.4

In this section the vehicle model with the updated parameters given in section 4.4 is used to estimate the electric truck's constant speed and drive cycle performance, 0-30mph and 0-60mph acceleration, and gradeability. The internal battery power required for each of these cases is

calculated as the sum of the battery loss, accessory power, drive loss, motor loss, and motor mechanical power, as is shown in Figure 4.39. This model includes accurate estimates of the mechanical power required to follow a speed profile and of all the subsystem losses, and will therefore provide a very accurate estimate of battery energy required for a specific drive.

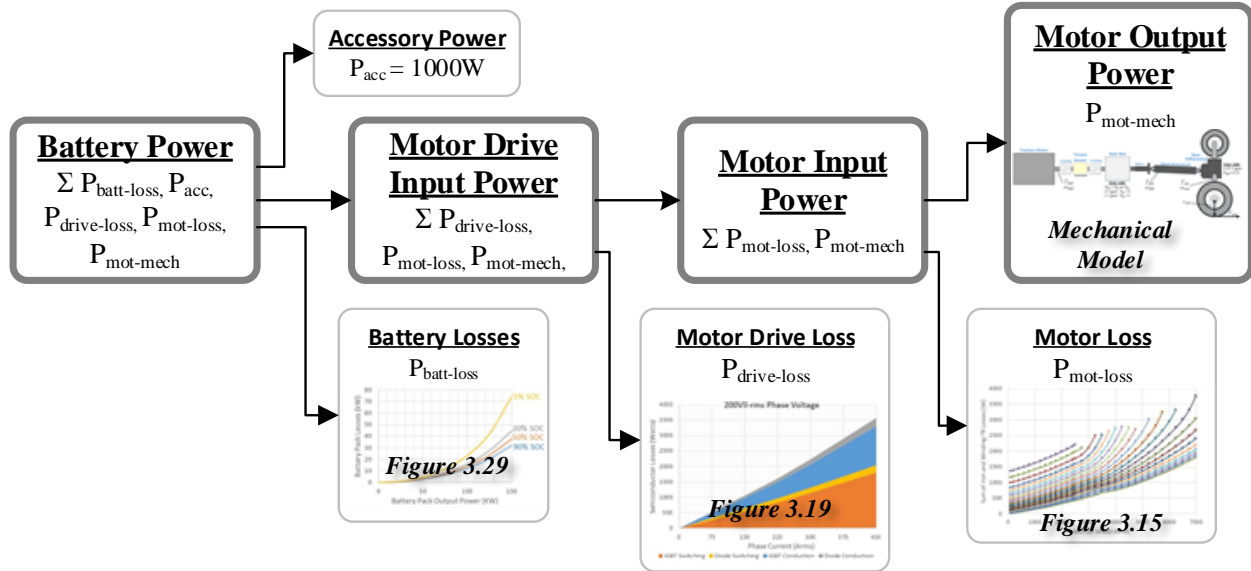


Figure 4.37 Block diagram of vehicle model power calculation methodology

As time progresses, the model integrates amp-hours of charge removed from the battery and updates the battery parameters on a step by step basis. Battery losses are calculated using (4.25) and (4.32) for the battery output power, as calculated in (4.34). The amp-hours discharged from the battery, Ah , are calculated using (4.36), where the battery internal power, P_{b-int} , calculated with (4.35).

$$P_b = P_{acc} + P_{drive-loss} + P_{mot-loss} + P_{mot-mech} \quad (4.34)$$

$$P_{b-int} = V_{ocv} I_b = P_{b-loss} + P_b \quad (4.35)$$

$$Ah = \int \frac{P_{batt-int}}{V_{ocv}} dt = \int I_b dt \quad (4.36)$$

4.4.1 Constant Speed Performance

The constant speed energy consumption of a vehicle is one of the most powerful metrics for describing vehicle performance because vehicles spend much of their time at constant speed. The energy consumption at higher speeds is especially important for an EV because EVs tend to be limited by their range on the highway. A sophisticated analysis will provide insight into range at different speeds and to the benefits of driving slower.

To calculate the constant speed performance first the motor output power necessary to maintain a given speed is calculated from the coast down test results with equation (3.2). Next, so both gears can be considered, the motor rotational speed and torque for each vehicle velocity of interest is calculated in (4.37) and (4.38).

$$\omega_m = \begin{cases} N_{g1} N_{diff} \frac{V_{veh}}{r_{wh}}, & \text{Gear 1} \\ N_{g2} N_{diff} \frac{V_{veh}}{r_{wh}}, & \text{Gear 2} \end{cases} \quad (4.37)$$

$$T_m = P_{mot-mech} / \omega_m \quad (4.38)$$

The calculated torque for each gear is shown Figure 4.38, and is observed to reach a peak of about 25Nm in gear 1 at 55mph and 120Nm at 70mph in gear 2. The phase current for both machines is also shown in Figure 4.38. For speeds below the corner speed of the motor the current in gear 1 is about 1/3 the current in gear 2, resulting in significantly lower winding and semiconductor losses in gear 1 below the corner speed. Beyond the corner speed though the motor

current starts to increase drastically, resulting in gear 1 having greater phase current, and therefore greater winding and semiconductor losses than gear 2 beyond 35mph.

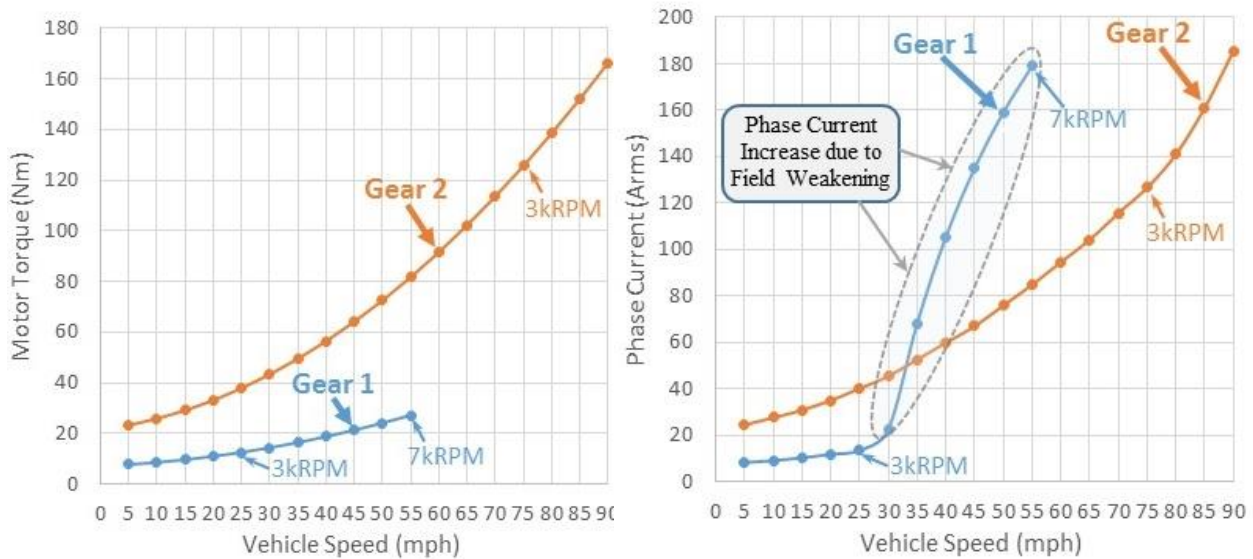
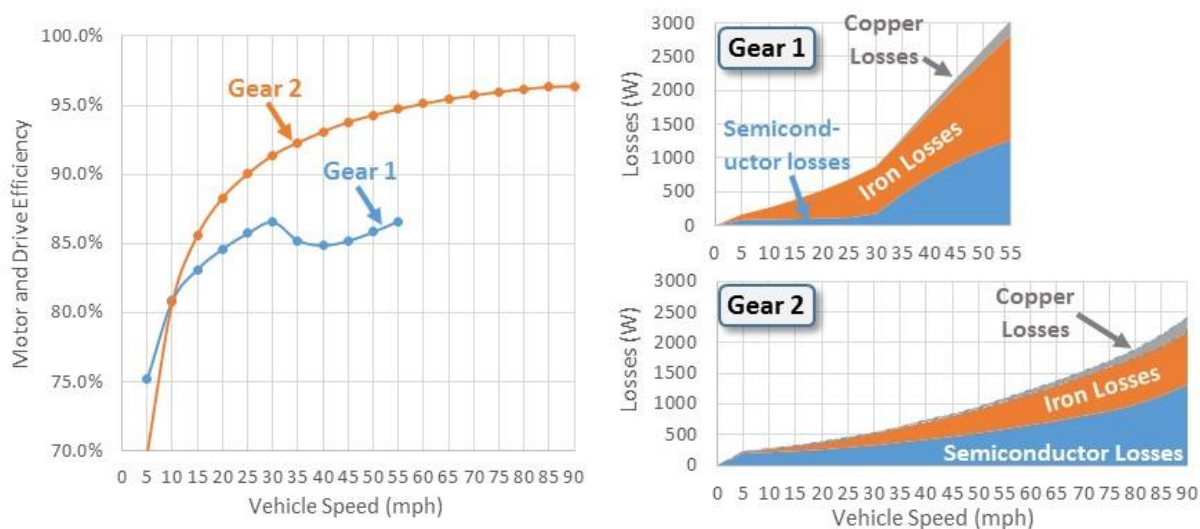


Figure 4.38 Constant speed driving motor torque and phase current

Next, using the methodology described in Figure 4.37, the motor and drive losses and resulting motor and drive efficiency are calculated for each operating speed examined - 5mph to 90mph in 5mph steps. In Figure 4.39 it is shown that the combined motor and drive efficiency for gear 1 reaches 85% by 20mph, and remains relatively constant up to 55mph, the peak speed in gear 1. Gear 2 is shown to be more efficient than gear one for all speeds above 10mph, with greater than 90% efficiency above 25mph and greater than 95% efficiency above 65mph. Gear 2 is more efficient than gear 1 due to the lower iron losses in gear 2 and due to field weakening current required in gear 1, as is also shown in Figure 4.39.



The energy consumption per mile neglecting battery losses is then calculated from the model, and is shown in Figure 4.40 to vary from around 250Wh/mi at lower speeds up to 400Wh/mi at 55mph and 500Wh/mi or greater at expressway speeds. The Nissan Leaf's constant speed energy consumption, as measured by the U.S. DOE, is also overlaid with the electric truck's predicted consumption [8]. The electric truck's constant speed energy consumption is about 50% greater than the Leaf, and the truck also has about 50% more energy storage than the leaf, so the two vehicles are likely to have similar range.

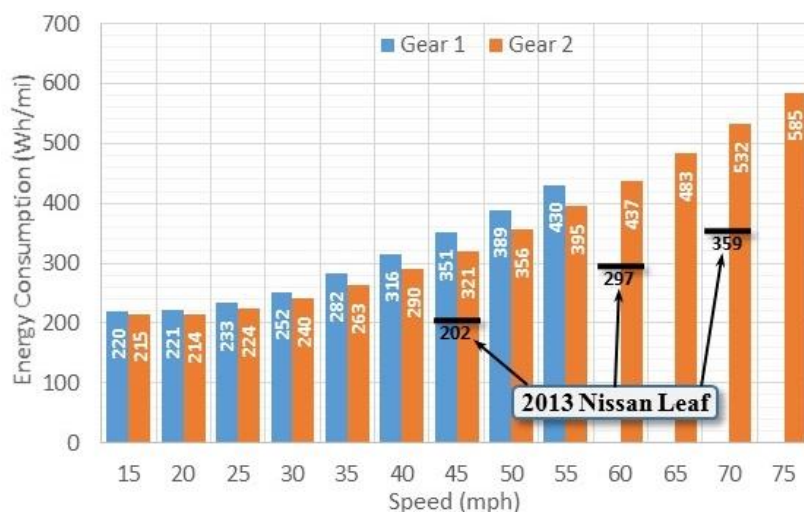


Figure 4.40 Constant speed driving battery energy consumption for 1st and 2nd gear

The difference in efficiency between the two gears has a substantial effect on the range of the vehicle. The constant speed range, including battery pack losses, is calculated for 90% battery DOD and shown in Figure 4.41. The results show that constant speed range in gear 2 is as much as 8.8 miles greater than the constant speed range in gear 1, an increase in range of almost 10%. Additionally the truck is shown to have slightly greater range than the Leaf for the three speed cases tested. This is due to the Leaf only having a useable battery capacity of about 18.5kWh for these tests, while the truck had a useable battery capacity of about 30kWh, 62% more than the leaf.

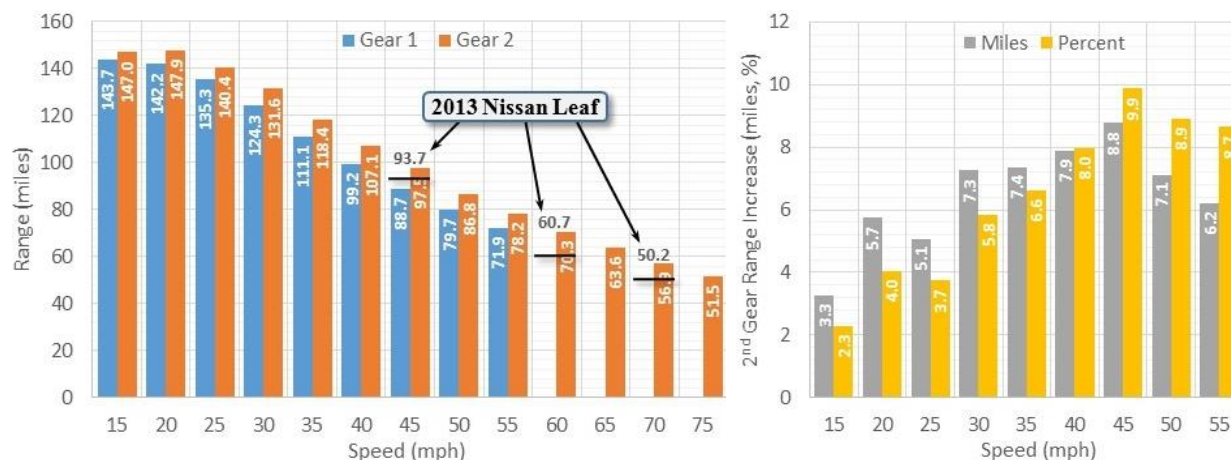


Figure 4.41 Constant speed driving range for 1st and 2nd gear to 90% DOD

In summary this analysis shows that there are significant differences in efficiency between the two gears, so effort should be made to select the most efficient gear for a particular operating point. Additionally the truck was shown to have a range of 56 miles at 70mph and 70 miles at 60mph, which proves that there is significant range benefits to driving slower. The truck was also shown to consume about 50% more energy per mile than the Nissan Leaf, and to have slightly more range than the Nissan Leaf at highway speed. One goal of the project was to have similar range to typical production electric vehicles, this section shows that this objective was achieved.

4.4.2 Drive Cycle Performance

The drive cycle performance for the four most common drive cycles, the urban (UDDS), highway (HWFET), LA92, and aggressive US06 are calculated in this section. The drive cycle energy consumption and range is calculated by inputting the drive cycle speed profile into the vehicle model and repeating the drive cycle until either 90Ah is discharged from the battery or the battery can no longer supply sufficient power for the drive cycle. The LA92 drive cycle, which is representative of higher speed, mid acceleration driving, is used as an example to describe the testing results. The LA92 speed profile, and the model predicted power, gear motor torque, and motor and drive losses for a single drive cycle operating in 2nd gear only are shown in Figure 4.42.

The drive cycle is quite mild, peaking at about 60mph and never exceeding 50kW or the motor torque limit of 460Nm, and the motor and drive losses are typically around 1kW. The battery pack parameters for the whole drive cycle until the 90Ah discharge limit is reached are also shown. Due to the relatively low power of the drive cycle, the battery current is not seen to increase significantly as the battery is discharged, as would be witnessed for a more aggressive drive cycle.

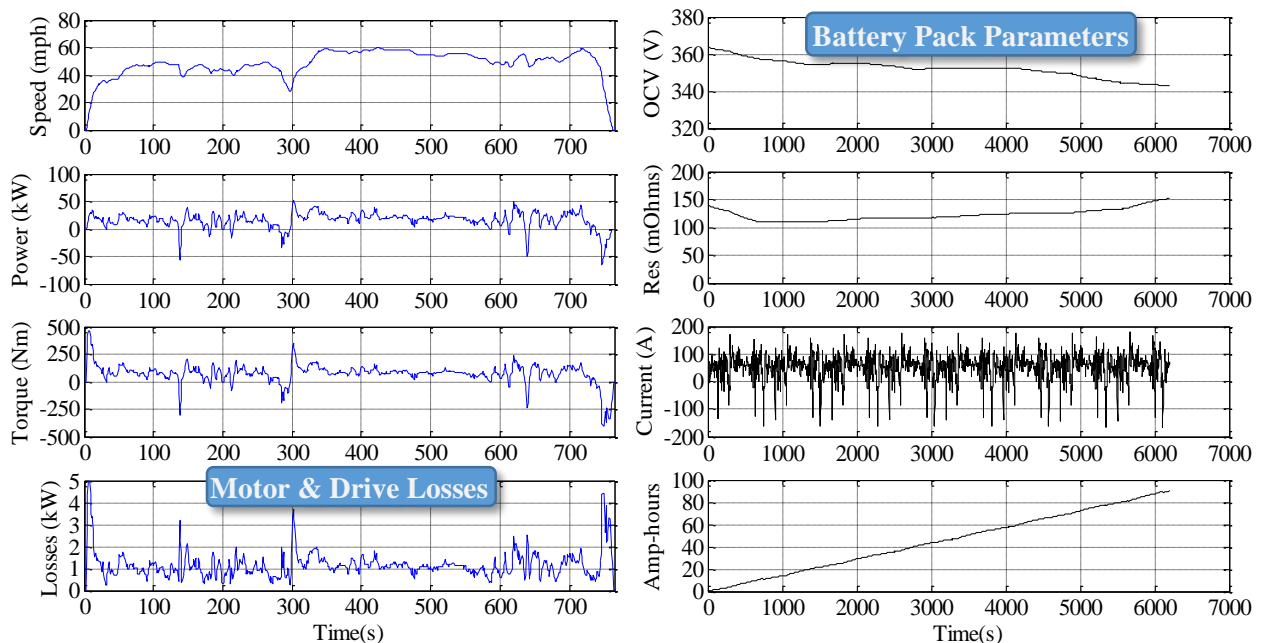


Figure 4.42 Model predicted LA92 drive cycle performance using 2nd gear only

While the truck can drive the HWFET cycle in 2nd gear, there are likely some efficiency benefits to changing gears, and for the more aggressive drive cycles both gears are necessary to provide sufficient and speed range. To evaluate the truck's performance utilizing both gears, the motor torque and speed, and the resulting motor and drive losses are calculated for both gears. Additionally the ranges over which a given gear can't be used, due to either being out of the motor's torque or speed range, are calculated. Then the gear is selected which results in the least motor and drive losses, and the losses as the selected gear for the HWFET drive cycle are shown below in Figure 4.43.

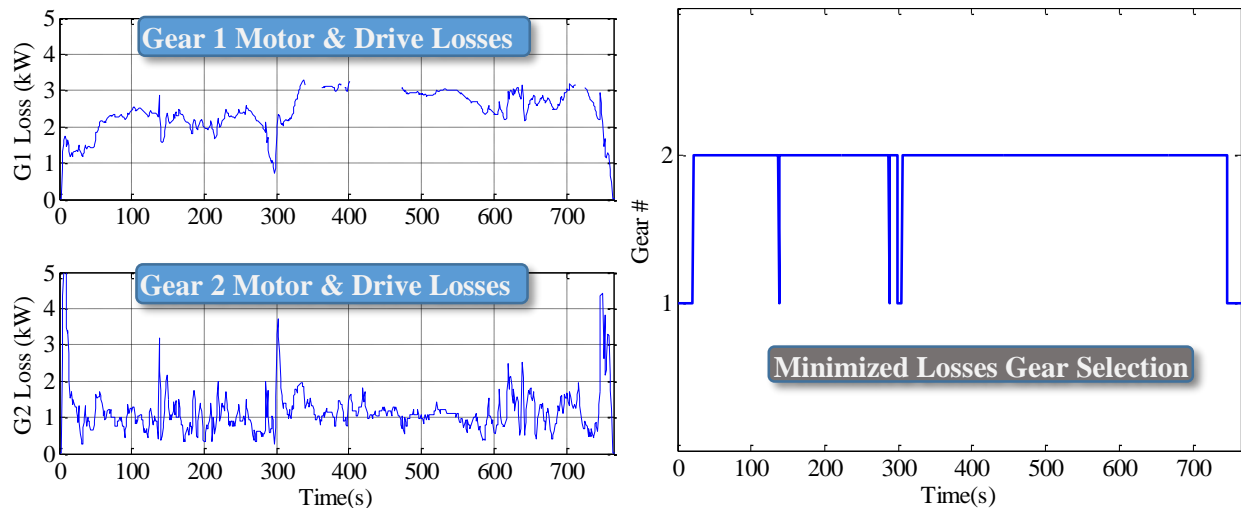


Figure 4.43 HWFET drive cycle model calculated vehicle parameters

For HWFET, gear two is mostly used because much of the drive cycle is relatively constant speed, high speed driving. Gear 1 is chosen for the higher acceleration points. For the more aggressive LA92 and US06 drive cycles, much more gear shifting is witnessed, which is actually an issue with this simplified approach of choosing the most efficient gear. In practice, it takes a finite amount of time to change gears, likely at least 300ms for the configuration in the truck (automated gear shifting has not yet been added as a feature).

The time to change gears, in addition to the losses incurred changing gears due to accelerating and decelerating the rotor, and noise and vibration concerns will limit how often the gears can and should be changed in practice. The simplified analysis here will give a rough idea of the efficiency, but a more sophisticated analysis accounting for these other limitations is necessary to accurately determine real world performance. Dynamic programming, which is utilized in Chapter 5, could be used as a tool to find the optimum gear selection while accounting for these other factors. This more accurate modeling is not considered a high priority though because it will likely only change the results by a few percent.

The resulting model predicted performance for the four drive cycles is shown Table 4.16. The truck is shown to have a range with optimal gear shifting of 92 miles for UDDS and 83 miles for HWFET, the two less aggressive drive cycles, and 74 miles for LA92 and 56 miles for US06, the two more aggressive drive cycles. Based on experience driving the truck, it is possible to achieve the UDDS and HWFET range, but the LA92 drive cycle, consuming 395Wh/mi, is most representative of typical energy consumption and range.

Table 4.16 Predicted Electric F150 Energy Consumption

Drive Cycle	Gear	90% DOD		Motor & Drive Efficiency			Losses (Wh/mi)		Range Reduction
		Wh/mi	Range (mi)	Motoring	Generating	Combined	Mot & Drive	Battery	
UDDS	1st Gear	336	90	92%	92%	92%	49	15	-1.6%
	2nd Gear	353	87	90%	83%	88%	69	14	-6.7%
	Opt. Gear	331	92	94%	93%	94%	38	15	-
HWFET	1st Gear	401	77	88%	89%	88%	52	13	-8.1%
	2nd Gear	372	83	94%	91%	94%	24	11	-0.5%
	Opt. Gear	370	83	95%	94%	95%	23	11	-
LA92	1st Gear	-	-	-	-	-	-	-	-
	2nd Gear	-	-	-	-	-	-	-	-
	Opt. Gear	395	74	95%	94%	95%	42	31	-
US06	1st Gear	-	-	-	-	-	-	-	-
	2nd Gear	-	-	-	-	-	-	-	-
	Opt. Gear	509	56	96%	95%	95%	36	53	-

Table 4.16 also shows that the combined motor and drive efficiency is 94% or greater for all of the drive cycles when utilizing optimal gearing. This is a very impressive number, considering that a representative from a major auto manufacturer stated, off that record, that they were very proud to achieve a battery to wheels drivetrain efficiency of 92%. The efficiency calculation for the truck does neglect gearbox losses, but with a more efficient gearing system it is conceivable that the truck could also achieve 92% drivetrain efficiency. The truck's efficiency achievement though likely represents the upper limit of achievable efficiency with mature technologies because the efficiency is largely achieved by having a very low current density in the machine windings and by having a two-speed gearbox, which is uncommon. The battery losses are also shown to be relatively low, about 3-4% of total drive energy for UDDS and HWFET and up to 10% of total drive energy for LA92 and US06.

To illustrate the ability of the model to predict energy consumption for a real world drive, the drive cycle energy was predicted using the model for eight higher speed drives, with drive length varying from 27 to 54 miles. The velocity of the drive was used as the input to the model in Figure 4.37, and the mechanical power and motor and drive losses were then calculated for each modeled drive, and the measured accessory power was used rather than the 1000W assumption typically used in the model. Elevation data was not incorporated into the model at this point, introducing some error in the model.

The resulting predicted versus measured energy consumption is shown below in Table 4.17. For five of the eight drives the experimental results are very close to the measured results, within +/-7%. For the remaining drives the error is quite large, with model error between 17% and 24%. This error is likely mostly due to environmental variables not included in the model: drive #7 had significant headwinds the whole time (20-30mph) and drive #4 had significant tailwinds the whole

time (20-30mph), as shown in Figure 4.44, and for drive #2 a large vehicle was tailed for much of the drive, reducing aerodynamic drag.

Table 4.17 Predicted vs Experimentally Measured Energy Consumption

Drive #	Avg Speed (mph)	Distance (miles)	Energy (Wh/mile)		Model Error	
			<i>Predicted</i>	<i>Measured</i>	<i>Percent</i>	<i>Wh/mi</i>
1	39	28	397	413	-4%	16
2	53	27	433	379	14%	-54
3	53	27	424	451	-6%	26
4	52	47	454	366	24%	-88
5	45	35	439	409	7%	-30
6	47	47	425	452	-6%	27
7	46	49	391	470	-17%	79
8	45	54	388	418	-7%	30
Mean	48 <i>mph</i>	39 <i>miles</i>	419 <i>Wh/mi</i>	420 <i>Wh/mi</i>	1%	1 <i>Wh/mi</i>

The experimental versus model predicted energy consumption is shown in Figure 4.44 to illustrate the range of energy consumption for these drives. The model predicts energy consumption varying from about 390Wh/mile to 460Wh/mile, while in practice a larger range is witnessed, from 340 to 470Wh/mile. While the estimate is close for several of the drives, its likely there would be many outliers over a large set of drives due to wind, temperature, and road conditions. A study of a large set of drives could be performed in the future to determine the variability in performance and opportunities to improve model performance.

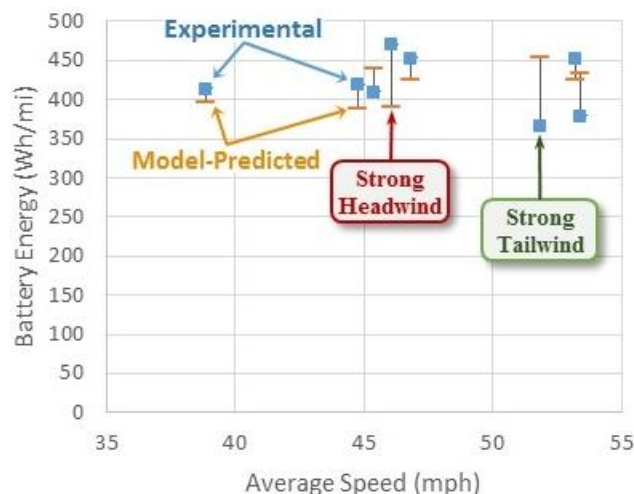


Figure 4.44 Experimental vs model predicted performance for eight drives

In summary a methodology for calculating the energy consumption and range for drive cycles has been introduced, and it shows the truck's range will vary from 56 to 92 miles based on the drive cycle. Additionally the model was shown to predict energy consumption relatively accurately for a selection of experimentally performed drives. The drive cycle calculations were not converted to the standard 5-cycle EPA testing results, which are used to officially determine the range and energy consumption of an electric vehicle. There is a standardized methodology for converting UDDS and HWFET results to 5-cycle, but the methodology was designed for gas vehicles and has been observed to under predict range and mpg_e for electric vehicles. The 5-cycle would be performed, but the required tests involve cold and hot weather and cabin heating and cooling, which our model does not currently account for. It may be useful though to develop a method of calculating 5-cycle results for future comparisons to production vehicles, such as the Nissan Leaf.

4.4.3 Gradeability of Truck

Gradeability is the ability of a vehicle to climb a specific grade, or steepness of road. There are two important aspects of gradeability: (1) the ability to accelerate from a stop, and (2) the ability to maintain a specific speed on a road grade. Road grades may be as steep as 30% for a driveway or a very steep section of city road, but are typically 6% or less for an expressway and not more than 10 or 15% for a highway. Vehicles must be designed with sufficient wheel torque and engine power to handle this range of grades. Trucks are a particular challenge because they are designed to carry and tow significant payloads, which will proportionally increase their torque and power requirements. The electric truck was designed to have about the same wheel torque and power as the gas powered truck with a 4.2L V6, so it should therefore have similar performance on grade. This section goes through the process of calculating the acceleration rate from a stop and power to maintain a given speed at various road grades.

The first step to calculating a vehicles' performance on a specific road grade is to calculate the gravitation force acting on the vehicle. The gravitational force parallel to the ground is the product of the sine of the angle of the road, α , the mass of the vehicle, and the gravitational force constant, as illustrated in Figure 4.45 and calculated in (4.41). Additionally in (4.39) and (4.40) the road angle is calculated from the grade, which is defined as the ratio of the rise over run of the road.

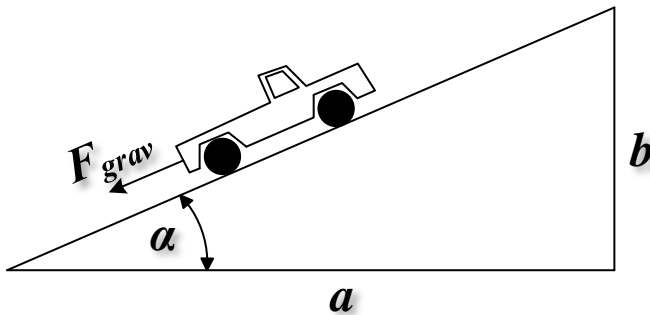


Figure 4.45 Gravitation force calculation parameters

$$\%grade = 100 \times \frac{b}{a} \quad (4.39)$$

$$\alpha = \tan^{-1} \left(\frac{\%grade}{100} \right) \quad (4.40)$$

$$F_{grav} = \sin(\alpha) m_{veh} g \quad (4.41)$$

The next step is to calculate the vehicles rate of acceleration from a stop. The acceleration of the vehicle is calculated as the wheel force provided to the road by the drive train as calculated in (4.41), minus the gravitational force acting on the vehicle as calculated in (4.41), divided by the equivalent mass of the vehicle, as shown in (4.42).

$$a_{veh} = \frac{F_{wh} - F_{grav}}{m_{veh-eq}} \quad (4.42)$$

To provide more direct insight into the effect of the vehicle parameters and road grade on the rate of acceleration, the calculations for wheel and gravitational force are substituted into equation (4.42) in (4.43) below. This shows that vehicle acceleration can be increased by increasing the gear ratios or motor torque, and it can be decreased by increasing the wheel radius, road grade, or the vehicle mass.

$$a_{veh} = \frac{\frac{N_{gb}N_{diff}T_{mot}}{r_{wh}} - \sin\left(\tan^{-1}\frac{\%grade}{100}\right)m_{veh}g}{m_{veh-eq}} \quad (4.43)$$

The resulting acceleration versus road grade for vehicle loading, m_{load} , of 250kg, 1000kg, 2000kg, and 3000kg, is shown in Figure 4.46 below. In first gear with a 250kg load the truck is capable of accelerating at 3.7m/s^2 (0.38g) on a flat road surface, and is still able to accelerate at 1.5m/s^2 at a 30% road grade, the grade of the steepest roads and driveways. With a heavy load of 3000kg the truck will not be able to accelerate at all on a 30% grade, but will be able to accelerate from 0-10km/h in about 8s at a 20% grade as is also shown in Figure 4.46. In gear two, which has 1/3 the wheel torque of gear 1, acceleration is only 1.25m/s^2 at 0% grade and 250kg of vehicle loading, and for grades above 10% the vehicle will accelerate very slowly or not at all. The truck has mostly just been driven in gear 2, and the gradeability limit is regularly noticed when stopped on a steep hill, resulting in little or no acceleration and necessitating a quick change to first gear!

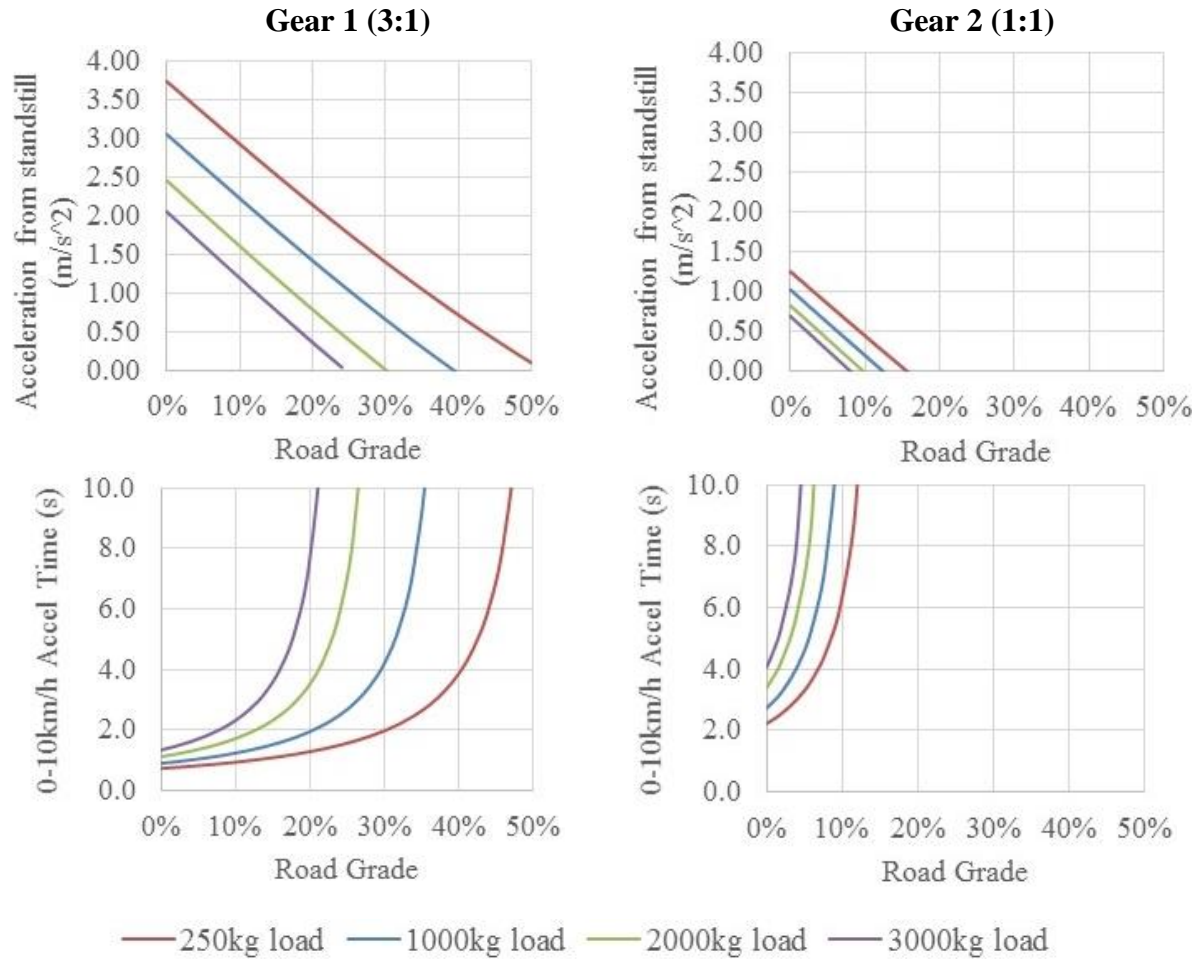


Figure 4.46 Truck acceleration rate for various road grades and vehicle loading

The third step to understanding the vehicle's performance at grade is to calculate the mechanical power required to maintain a constant speed at a specific grade. The maximum available motor power will limit the speed at which the vehicle can travel on steep grades. The gravitational power for a given grade is calculated as the product of the gravitational force, F_{grav} , and the vehicle's velocity in (4.44).

$$P_{grav} = F_{grav} v_{veh} \quad (4.44)$$

The total mechanical power the vehicle's motor must provide then is the sum of gravitational and road load power, and is shown for 25mph and 60mph for a selection of grades and vehicle

loads in Figure 4.47 below. The motor's maximum power rating of 135kW is shown to be sufficient to maintain 60mph at a 6% road grade, where 70.4kW is required for a 250kg load and 113.6kW is required for a 3000kg load. The significant constant power required to maintain 60mph on a 6% road grade with a heavy load shows that the motor, drive, and battery pack will need to be designed such that they can handle a high power rating for a significant period of time. In the electric truck the motor and motor drive should be capable of providing this power continuously, with the battery pack being the limiting factor.

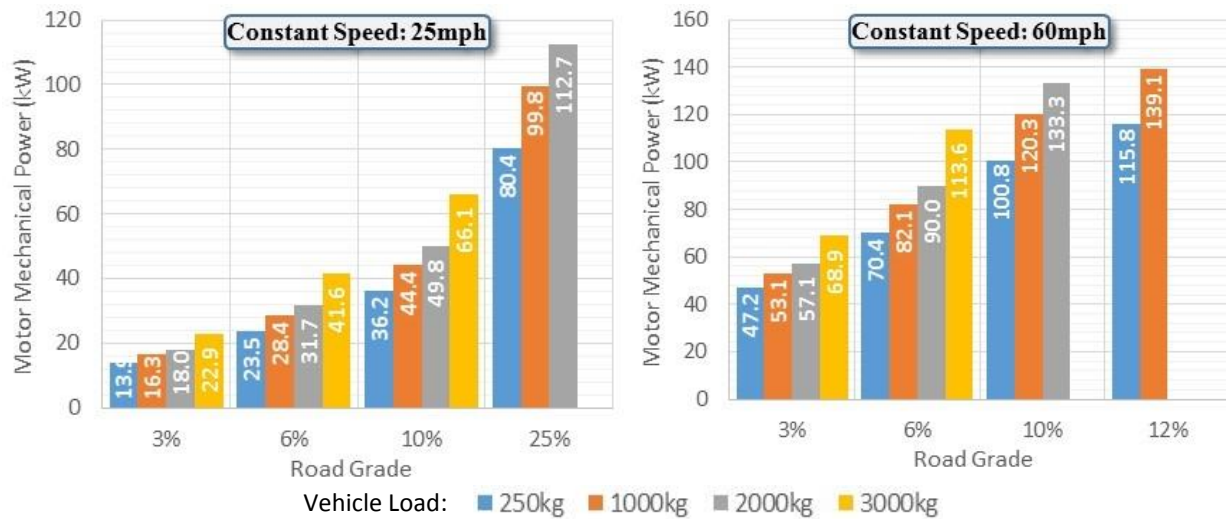


Figure 4.47 Battery pack power at constant speed of 25mph and 60mph for various road grades and vehicle load

Another observation from Figure 4.47 is that the vehicle can maintain a speed of 25mph on a 25% grade with up to 2000kg of load, which should be sufficient for even the most demanding environments. The truck is also capable of maintaining 60mph at a 12% grade with lower loading.

In summary, in first gear the truck is capable of accelerating from a stop at very steep grades, 20% when heavily loaded and up to more than 40% when lightly loaded. The truck is also capable of maintaining lower 25mph at a 25% grade and 60mph at a 12% grade if the truck is not too heavily loaded. Driving up steep grades at high speed, for more than several minutes, will likely

push the battery pack temperature too high, and require reduced speeds to maintain a safe battery temperature. Additional work could be performed to determine the continuous power capabilities of the battery, motor drive, and motor, which would determine the gradeability limitations of the truck.

4.5 Conclusion

In this chapter the final design of the prototype truck was presented along with an updated and improved vehicle model and modeled and experimental driving results. The fully assembled truck was shown to weigh 2704kg, 459kg more than the original gasoline powered truck and 250kg more than originally predicted. The inertia of the rotating components was modeled, and it was shown that the rotor inertia had the largest impact on the vehicles performance, adding 345kg of equivalent mass to the truck in 1st gear and 38kg in 2nd gear. The coast down tests were performed again, and the electric truck's road load was shown to be very similar to the gasoline powered truck's road load as specified by the manufacturer.

Motor and drive loss models were also developed, showing that over much of the operating space the motor efficiency exceeds 97%, the drive efficiency exceeds 96%, and the combined motor and drive efficiency exceeds 94%. The loss model was also shown to be quite accurate at predicting losses for real drives, with measured versus predicted losses being within about 5%. A battery loss model is also developed, showing that battery efficiency is typically about 95% or higher at 25°C for power less than 50kW. Additionally, the battery model is combined with the motor and drive loss model to show that the motor's output power decreases from 134kW at 90% SOC, to 123kW at 20% SOC, and to 110kW at 10% SOC.

The updated model is then used to predict the trucks on the road performance, and it is shown that for constant speed operation motor and drive efficiency is significantly higher in 2nd gear than

in 1st gear, primarily due to the 3x higher speed in 1st gear resulting in increased iron and motor drive losses. The efficiency difference between the two gears is shown to be quite significant, with up to 9.9% or 8.8 miles more range in second gear. The truck is also shown to have similar constant speed range to the Nissan Leaf, with 97.9 miles range at 45mph and 70.3 miles range at 60mph, and to consume 321Wh/mi at 45mph and 437Wh/mi at 60mph, which is about 50% more energy per mile than the Nissan Leaf.

The truck's drive cycle performance is also modeled, and it's shown that gear choice also has a significant effect for drive cycles, with an optimal selection of gears improving range up to 6.7% for UDDS and up to 8.1% for HWFET. Additionally, with optimal gear selection the truck is shown to have a range of 92 miles for UDDS, 83 miles for HWFET, 74 miles for LA92, and 56 miles for US06. The model predicted and measured energy consumption are compared for several real drives, and the model error is shown to be 7% or less for many of the drives. The model error is as high as 24% though, which is likely due mostly to high wind speeds but also due to the model not currently incorporating altitude and the assumption of perfect regenerative braking. The truck is also shown to be able to handle steep grades, up to about 20% with 3000kg of load. The truck is also shown to require high power at high speeds on steep grades, 114kW at 60mph on a 6% grade for example, showing that the drivetrain must have a high continuous power rating than a lighter electric vehicle not designed for towing.

In summary, the full truck design is presented and the electric drive system is shown to be very efficient. The truck is shown to have similar range to a Nissan Leaf, and to consume about 50% more energy per mile than a Nissan Leaf. The model is shown to be quite accurate at predicting drivetrain losses, but to be not quite as accurate for predicting energy required for an actual drive since wind speed and altitude are not currently accounted for in the model.

Chapter 5

Loss Optimization and Ultracapacitor Pack Sizing for Electric Truck with Battery/Ultracapacitor Hybrid Energy Storage

5.1 Introduction

Electric and plug-in hybrid electric vehicles (EVs and PHEVs) typically utilize a single high-voltage battery pack for energy storage. It is desirable for this battery pack to have high energy density so that sufficient range can be achieved with a small pack, and this battery pack must be capable of providing enough power to adequately propel the vehicle. A typical EV battery pack must provide current up to five times the amp-hour rating (5C), and up to 10-12C for a PHEV. The necessity to provide such high currents makes it necessary to use more power-oriented, less energy-dense cells.

The concept of hybrid energy storage – utilizing multiple energy sources for the vehicle, one energy-dense and one power-dense source, for example – has been proposed to improve the system design of electrified vehicles and allow the use of battery cells that are more optimized for energy density. Hybrid energy storage may also help to reduce the cost per kW for the energy storage system (ESS), improve ESS performance at cold temperatures, and increase the usable battery state-of-charge (SOC) window [127]. In addition, the battery cooling requirements can be reduced, and peak currents can be potentially reduced resulting in increased battery cycle life.

There are many possible configurations for hybrid energy storage systems (HESS) [20]. One popular hybrid energy storage configuration, consisting of the combination of an energy-dense battery pack and a power-dense ultracapacitor connected to the battery pack through a dc/dc converter, is modeled and analyzed for electric vehicles in [29, 94] and is examined in this chapter using the configuration shown in Figure 5.1. Reduction in ESS energy consumption for a light

electric vehicle with hybrid energy storage is demonstrated in [24], and a method for optimizing the ultracapacitor pack size for electric vehicles is presented in [86]. Dynamic programming is utilized in [128] to evaluate different ultracapacitor pack sizes for a gasoline hybrid electric vehicle with an ultracapacitor pack instead of a battery pack.

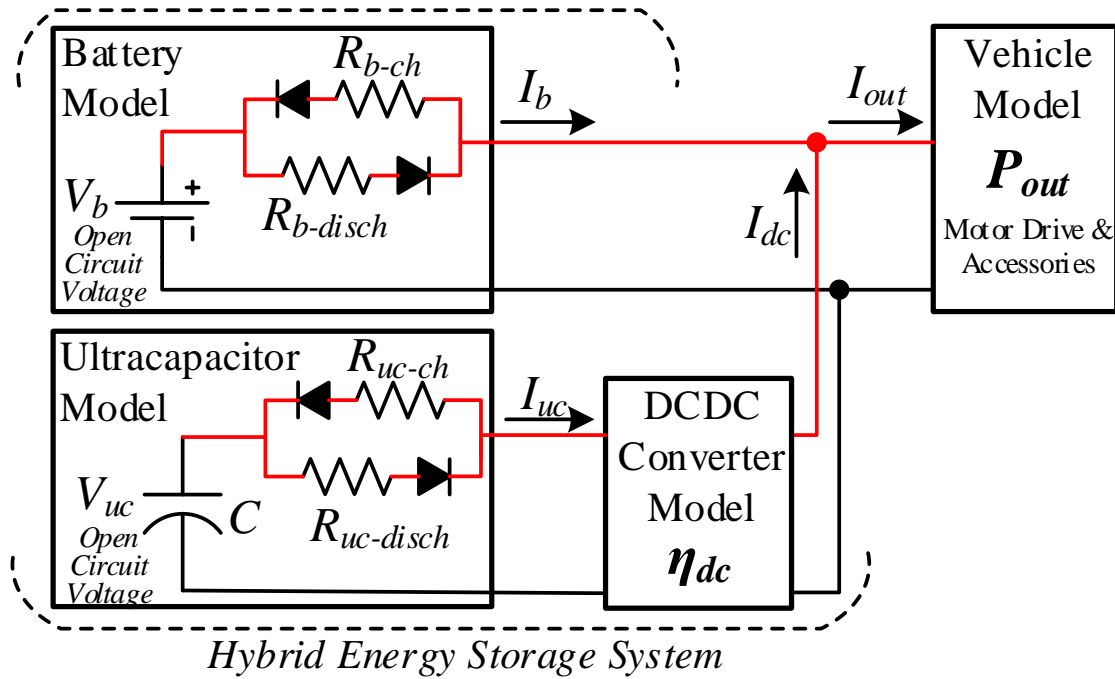


Figure 5.1 Hybrid energy storage system evaluated in this study

The purpose of this paper is to apply dynamic programming to evaluate the reduction in energy storage losses that can be achieved by introducing ultracapacitor packs of varying sizes into an electrified vehicle for different drive cycles. An analytical solution for the power split between the battery and ultracapacitor pack that minimizes the losses is developed, making it possible to evaluate the resulting efficiency improvement for a specific operating point. A rule-based control algorithm is developed which uses the analytical minimum loss solution to control the power split between the battery and ultracapacitor pack and is evaluated for different drive cycles. Optimization via dynamic programming is then introduced to improve on the rule-based control result and calculate the power split which minimizes system losses for various drive cycles and

ultracapacitor pack sizes, showing the maximum efficiency improvement that can be achieved for a given ultracapacitor pack size. Finally, confidence in the model and model results is strengthened by experimentally testing a single battery and ultracapacitor of the same types that are used in the analytical studies of the full hybrid energy storage system.

5.2 Battery, Ultracapacitor, DC/DC Converter, and Vehicle Model

The hybrid energy storage system is designed for a Ford F150 electric research vehicle, although the methodology developed can be applied to any electric vehicle and, with some modifications, to hybrid-electric vehicles as well. The simplified electromechanical model of the electric truck is used, which utilizes the parameters given in Table 3.1 and Table 3.2 of section 3.2. Equations (3.1) – (3.4) are used to calculate the electric power profile provided by the energy storage system for different drive cycles. The only change to the model parameters given in Chapter 3 is the drag power coefficients, which have been updated to the values in Table 5.1 that are derived from a newly performed coast-down test. These values of coast down coefficients are only utilized in Chapter 5 though, with the final coast down coefficients presented in **Table 4.9** utilized in Chapter 4 and utilized in any future work.

Table 5.1 Estimated Drag Power Coefficients for Elec. F150 Truck

Drag Power Coefficient	z_3	z_2	z_1
Value	0.694 W/(m/s) ³	10.04 W/(m/s) ²	107.6 W/(m/s)

5.2.1 Battery Pack Model

The battery pack in the electric truck consists of 108 series connected 100Ah 3.2V LiFePO₄ cells, model SE100AHA, manufactured by CALB [129]. The battery pack is modeled as an open-circuit voltage source, V_b (notation is V_{ocv} in Chapter 4) in series with a charge and discharge

resistance, R_{b-ch} and $R_{b-disch}$, as shown in Figure 5.1. The open-circuit voltage and resistance parameters were measured for a single 100Ah Calb cell using the high-power pulse characterization (HPPC) test developed by the US Advanced Battery Consortium (USABC). The HPPC test was performed at 25°C with a 10-second 400A discharge and 200A charge pulse with 0, 10... 90, 95, and 100Ah discharged from the battery, and the results are labeled as *Standard HPPC* and shown below in Figure 5.2.

When it was found that the standard HPPC test delivered parameters that over-predicted that battery losses in a drive cycle, a modified version of the HPPC test was adopted. The modified test is performed by discharging the battery 10Ah with the LA92 drive cycle, pausing for 60 seconds to determine a pseudo-open-circuit voltage, applying a 10-second 200A discharge pulse,

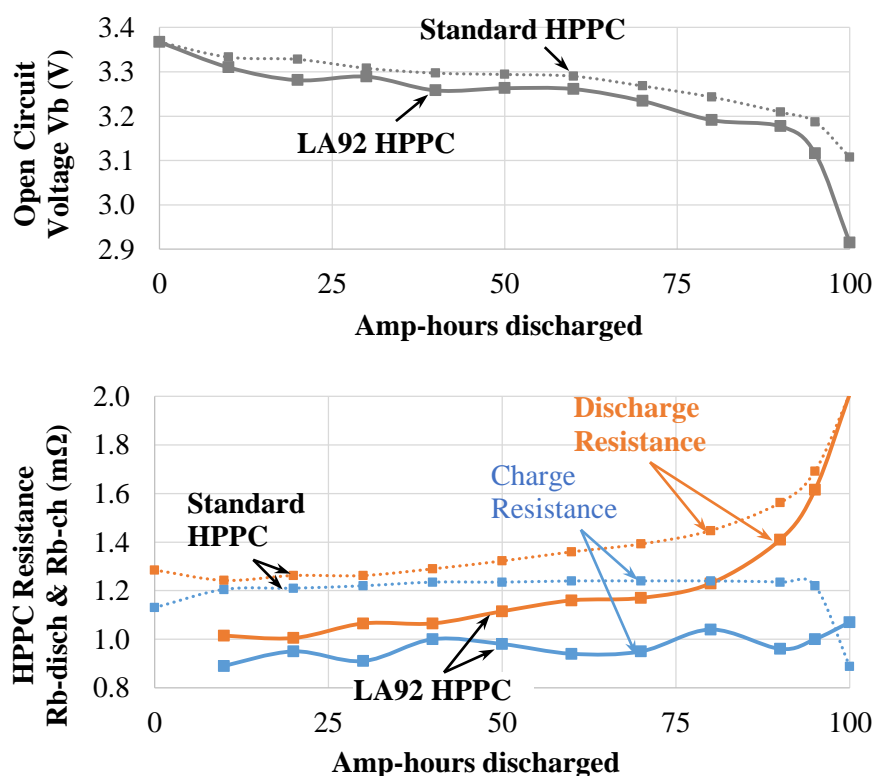


Figure 5.2 Measured open-circuit voltage and HPPC resistance for Standard and LA92 test for CALB SE100AHA LiFePO₄ battery cell

and then applying a 10 second 100A charge pulse. The results, referred to as *LA92 HPPC* in Figure 5.2, are used in a lookup table with cubic interpolation in the model so that the battery parameters are updated continuously as the pack is discharged.

5.2.2 Reference Ultracapacitor Pack Design & Model

The reference ultracapacitor packs were chosen to consist of 100 series-connected Maxwell 650F, 1200F, 1500F, 2000F, or 3000F ultracapacitor cells, and the largest 3000F pack was sized to have about the same energy capacity as the truck's kinetic energy at 60mph, as illustrated in Figure 5.3 [130]. The 3000F pack is sized with the goal of significantly reducing battery pack losses by having the ultracapacitor pack provide nearly all of the acceleration and regeneration kinetic energy. The smaller packs, which can only provide a smaller portion of the kinetic energy, are considered as well to determine how the benefits of the HESS scale, and to determine if the rather large 51kg, 40L 3000F pack is necessary.

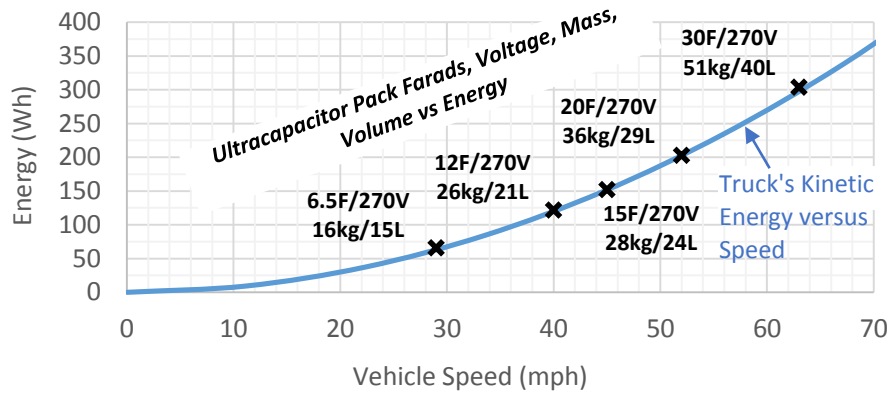


Figure 5.3 Energy capacities shown as x's for 5 ultracapacitor packs which match truck's kinetic energy at speeds between 29 and 63 mph

The capacitance C , and charge and discharge resistances R_{uc-ch} and $R_{uc-disch}$ that were identified in the ultracapacitor model in Figure 5.1 have been experimentally measured for a single ultracapacitor of the type selected for this investigation, the Maxwell BCAP0650 ultracapacitor

rated at 650F, 2.7V and 0.8m Ω . The results are shown in Figure 5.4. The capacitance was measured by discharging the ultracapacitor at 2.5A and calculating $C = Q/\Delta V$ at discrete voltage steps. The resistance was measured with 50A 0.5-second charge and discharge pulses at discrete voltage steps using an adaptation of the methodology described in the Maxwell datasheet [130]. The measurements are used in the model in a lookup table with cubic interpolation so that the ultracapacitor parameters are also continuously updated as the pack is charged and discharged. The 650F results are scaled as a function of the ratio of the data sheet parameters for the other capacitance values.

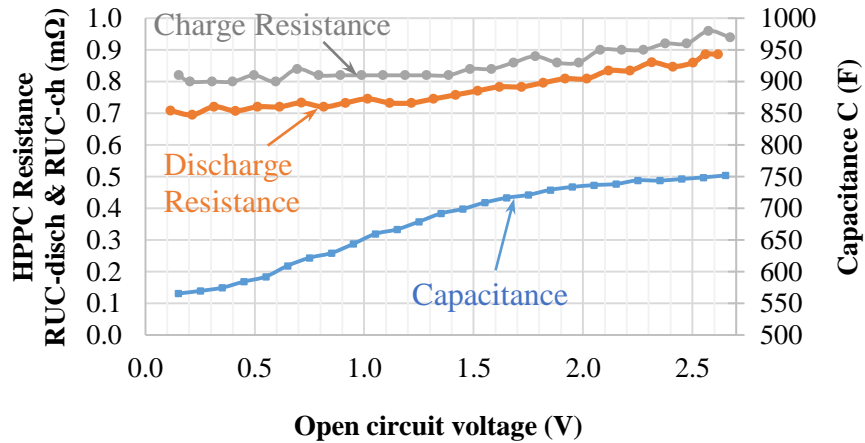


Figure 5.4 Experimentally-measured capacitance and resistances of 0.8m Ω 650F rated Maxwell K2 series ultracapacitor

5.2.3 DC/DC Converter Model

The bidirectional dc/dc converter is used to transfer power between the ultracapacitor pack that has voltage ranging from 135V-270V, and the battery pack that has voltage ranging from 270V to 395V. The boost ratio varies from 1:1 to 3:1, depending on the respective pack voltages. The boost ratio and voltage ranges are somewhat similar to those of the 20kW dc/dc boost converter in the 2004 model year Toyota Prius, which boosts from a 200V battery pack to the motor drives' dc bus which varies between 200V and 650V.

The measured efficiency of the Toyota Prius 20kW dc/dc converter, shown in Figure 5.5, varies from approx. 97% to 98.5% [95]. These values have been used to model the dc/dc converter efficiency for this study because the converter is similar to that required for our application, and it is quite efficient while being sufficiently affordable to be used in a mass-produced vehicle. The efficiency, modeled as a function of boost ratio and low-side/ultracapacitor current, is incorporated into the model as a 2d lookup table, but is scaled for two converters giving a peak ultracapacitor current of 200A. The lookup table uses efficiency points from 4th-order polynomial curve-fits of the experimental data and the extrapolated 3:1 boost ratio curve-fit that are shown in Figure 5.5.

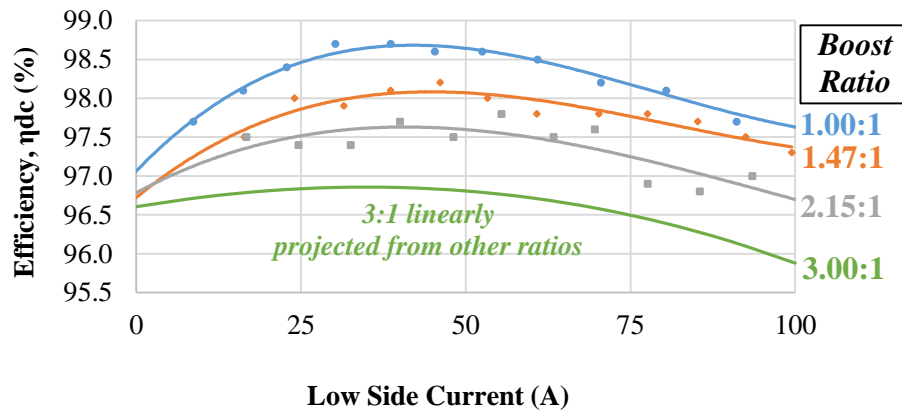


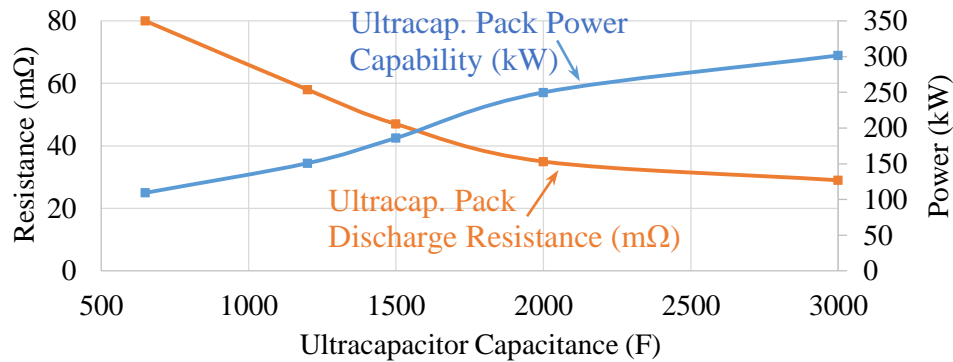
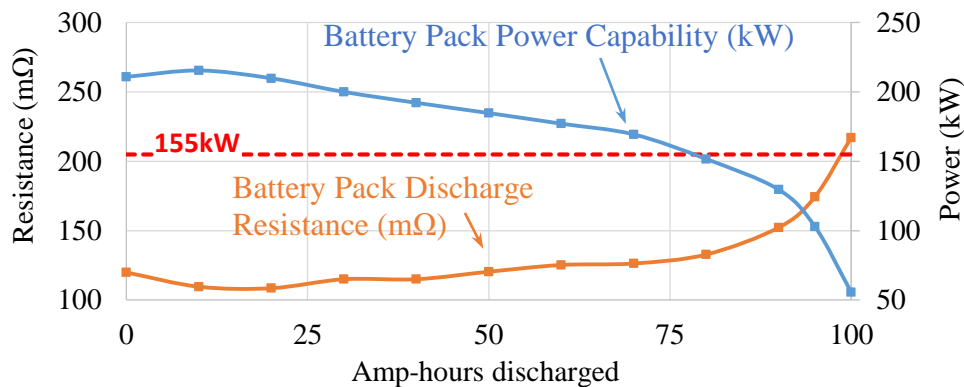
Figure 5.5 Experimentally-measured Toyota Prius dc/dc converter efficiency [95] together with extrapolated 3:1 boost ratio efficiency curve

5.2.4 Comparison of Battery & Ultracapacitor Pack Parameters

The resistance and discharge power capability characteristics for the single cells have been scaled for the number of series-connected cells in the battery and ultracapacitor packs, given in Table 5.2, and is shown in Figure 5.6 and Figure 5.7. Comparison of the figures shows that even the smallest 650F ultracapacitor pack has less resistance than the battery. The ultracapacitor pack power capability ranges from 100kW to 300kW, and is sufficient to complement the battery pack's 50kW to 215kW power capability in order to help maintain a system power capability higher than the drivetrain's peak requirement of 155kW.

Table 5.2 Battery and Ultracapacitor Pack Specifications

	Battery Pack	Ultracap. Pack
# of cells in series	108	100
Pack Voltage	350Vdc	270Vdc
Pack Resistance	115mΩ	29mΩ to 80mΩ
Pack Mass	346kg	16kg to 51kg
Pack Energy Storage	35kWh	66Wh to 304Wh

**Figure 5.6** Ultracapacitor pack discharge resistance and power capability**Figure 5.7** Battery pack discharge resistance and power capability

5.3 Analytical Calculation of Minimized HESS Losses

There are many ways the split of power between the battery and ultracapacitor packs could be controlled, such as to minimize the battery rms current or regenerative braking energy to the battery. One of the most beneficial methods is to minimize the total system losses, thereby

increasing vehicle range. The total HESS losses are a function of how the power demand is split between the battery and ultracapacitor pack (referred to henceforth as the *power split*).

To determine the analytical solution for the minimized losses, the loss equation must be made a function of a single variable – battery current is chosen in this case – and then differentiated with respect to that variable. To solve for losses as a function of battery current, the first step is to calculate the ultracapacitor current I_{uc} as a function of the battery current I_b and HESS output power P_{out} . The HESS output power is equal to the sum of the battery output power and dc/dc converter output power, as shown in (5.1) for the ultracapacitor discharging case. To solve for the ultracapacitor current as a function of battery current and output power, referred to as $I_{uc}(I_b, P_{out})$, the equations for ultracapacitor and battery output power (5.4) and (5.5) are substituted into (5.1) where ultracapacitor and battery resistance R_{uc} and R_b are equal to either the charge or discharge resistance as shown in (5.2) and (5.3). Equation (5.1) is then solved for ultracapacitor current and the result is given in (5.6).

$$P_{out} = P_{b-out} + \eta_{dc}P_{uc-out} \quad (5.1)$$

$$R_{uc} = \begin{cases} R_{uc-disch}, & I_{uc} > 0 \text{ (discharging)} \\ R_{uc-ch}, & I_{uc} \leq 0 \text{ (charging)} \end{cases} \quad (5.2)$$

$$R_b = \begin{cases} R_{b-disch}, & I_b > 0 \text{ (discharging)} \\ R_{b-ch}, & I_b \leq 0 \text{ (charging)} \end{cases} \quad (5.3)$$

$$P_{uc-out} = (V_{uc} - I_{uc}R_{uc})I_{uc} \quad (5.4)$$

$$P_{b-out} = (V_b - I_bR_b)I_b \quad (5.5)$$

$$I_{uc}(I_b, P_{out}) = \frac{-\sqrt{\eta_{dc}(4R_{uc}V_bI_b + \eta_{dc}V_{uc}^2 - 4P_{out}R_{uc} - 4R_bR_{uc}I_b^2)} - V_{uc}\eta_{dc}}{2R_{uc}\eta_{dc}} \quad (5.6)$$

The next step to calculate the analytical solution for the power split for minimum losses is to calculate the losses for each HESS component as a function of battery current and output power.

The ultracapacitor and battery losses for the models shown in Figure 5.1 are purely ohmic and are calculated using (5.7) and (5.8). The dc/dc converter losses are calculated in (5.9) where the ultracapacitor output power, $P_{uc-out}(I_b, P_{out})$, is calculated as a function of I_b and P_{out} by substituting (5.6) into (5.4).

$$P_{uc-losses} = I_{uc}^2 R_{uc} \quad (5.7)$$

$$P_{b-losses} = I_b^2 R_b \quad (5.8)$$

$$P_{dc-losses} = \begin{cases} (1 - \eta_{dc})P_{uc-out}(I_b, P_{out}), & I_{uc} > 0 \\ \frac{P_{uc-out}(I_b, P_{out})}{(1 - \eta_{dc})}, & I_{uc} \leq 0 \end{cases} \quad (5.9)$$

The final step to derive the analytical solution for the minimum loss operating point is to differentiate the sum of the losses with respect to I_b , as shown in (5.10). The differentiated result is then set equal to 0 and solved for I_b , as shown for the ultracapacitor discharge case in (5.11), which gives the battery current that will result in the minimum total HESS losses for a given operating point.

$$\frac{dP_{losses}}{dI_b} = \frac{d}{dI_b} (P_{uc-losses} + P_{b-losses} + P_{dc-losses}) \quad (5.10)$$

$$I_b = \frac{\left(R_b V_b V_{uc}^2 + \eta_{dc} R_{uc} V_b^3 - V_b \sqrt{(\eta_{dc} (R_{uc} \eta_{dc} V_b^2 + R_b V_{uc}^2) (R_{uc} V_b^2 + R_b \eta_{dc} V_{uc}^2 - 4P_{out} R_b R_{uc}))} \right)}{2(R_b^2 V_{uc}^2 + \eta_{dc} R_{uc} R_b V_b^2)} \quad (5.11)$$

Figure 5.8 and Figure 5.9 show the spectrum of battery and ultracapacitor currents for a given HESS output power. The calculated lines labeled “Minimum HESS losses” identify the unique power split for each output power that minimizes the system losses. The results indicate that the hybrid system can substantially reduce losses for high power cases.

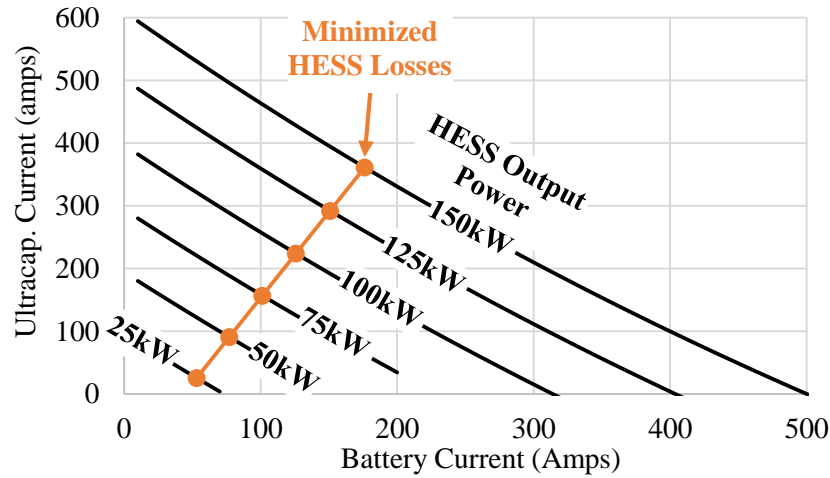


Figure 5.8 Ultracapacitor and battery current solution curves for a range of HESS output powers assuming 270V ultracapacitor pack voltage, 3000F cell pack and nominal battery resistance and dc/dc converter efficiency

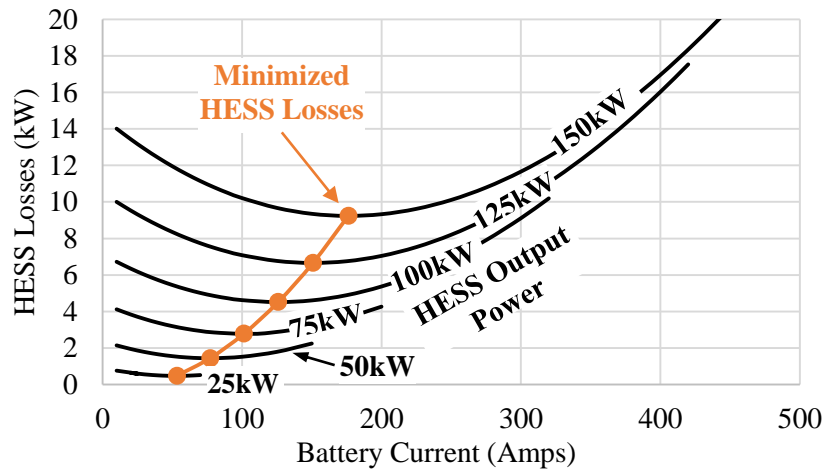


Figure 5.9 Total HESS losses versus battery current for a range of HESS output powers assuming 270V ultracapacitor pack voltage, 3000F cell pack, and nominal battery resistance and dc/dc converter efficiency

The minimum-loss battery and ultracapacitor power as a function of HESS output power and ultracapacitor voltage is then calculated using the prior equations for the 3000F pack, and is plotted below in Figure 5.10. There are two important observations about the power split: (i) When the HESS power is low enough (12kW or less, in this case), the efficiency is maximized by not

utilizing the ultracapacitor pack at all due to the dc/dc converter losses; and (ii) For lower ultracapacitor voltages, more ultracapacitor current is required for a given power resulting in more losses and, therefore, less utilization of the ultracapacitor pack.

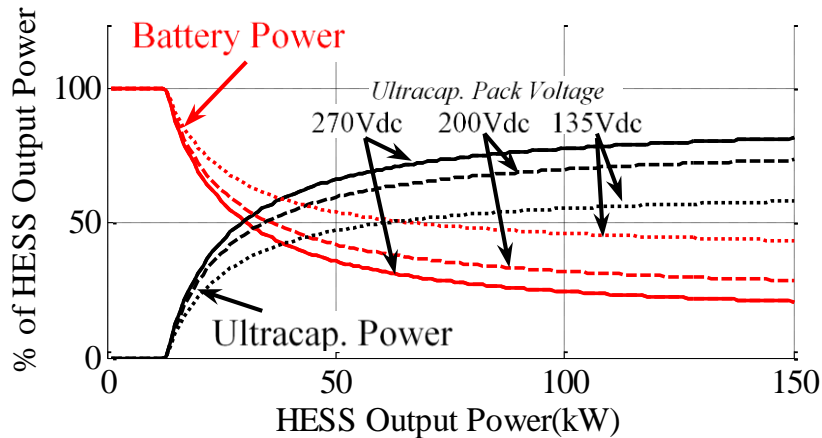


Figure 5.10 Calculated minimum loss power splits output power for 270Vdc, 200Vdc, and 135Vdc ultracapacitor pack voltage with a 3000F cell pack

Figure 5.11 shows that the hybrid system with the 3000F cell pack has much greater efficiency than the battery-only system for all output power values above 12kW, with the hybrid system achieving an efficiency of 91% to 95% at 150kW compared to 78% for the battery-only system at the same power. However, this large improvement does not necessarily translate into large efficiency gains for the vehicle, since the vehicle usually draws much less than peak power and the ultracapacitor state-of-charge (SOC) must be managed. The calculated vehicle efficiency improvements for actual drive cycles will be presented in the following sections.

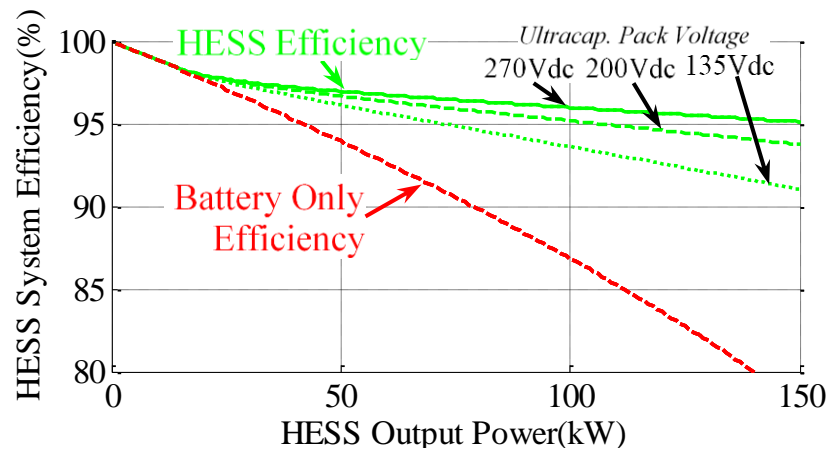


Figure 5.11 Calculated system efficiency for battery-only and hybrid system for 270Vdc, 200Vdc, and 135Vdc ultracapacitor pack voltages

5.4 Loss Reduction for a Drive Cycle using HESS with Rule-Based Control

To examine the benefits of hybrid energy storage during normal driving situations, the energy consumption for the aggressive US06 drive cycle has been modeled for the battery-only and HESS vehicle. To keep the ultracapacitor state-of-charge within its prescribed range and to help maximize efficiency, several rules have been adopted to determine the power split between the battery and ultracapacitor, as follows:

1. If the vehicle acceleration is greater than 1 mph/s and the ultracapacitor voltage is above its minimum value, then:
 - Use the maximum efficiency power split calculated using (5.11)
2. If the vehicle is decelerating at greater than 1 mph/s and the ultracapacitor voltage is below its maximum value, then:
 - Direct all of the deceleration power to the ultracapacitor pack.
3. If the vehicle is accelerating or decelerating at a rate less than 1 mph/s, then
 - Slowly charge/discharge the ultracapacitor at a rate of 15C where C is the ultracapacitor's Ah rating to the target ultracapacitor state-of-charge (SOC), where the target SOC is fully-charged at zero speed and fully-discharged at 80mph, scaled by the vehicle inertial energy between 0 and 80mph.

The first rule uses the ultracapacitor to help accelerate the vehicle by using the minimum-loss power split calculated in Section 5.3. The second rule helps to keep the ultracapacitor sufficiently charged by providing it with all of the regeneration energy, and the third rule keeps the ultracapacitor SOC at a level that will allow the vehicle to utilize the ultracapacitor when accelerating or braking.

The battery, ultracapacitor, and total ESS power achieved for the US06 drive cycle while using the above rules with a 1Hz sample rate for the model are shown in Figure 5.12. The vehicle speed and ultracapacitor voltage for the drive cycle are provided in Figure 5.13. Inspection of these figures shows that the proposed algorithm maintains the ultracapacitor voltage within the prescribed limits, insuring that the ultracapacitor can provide power to accelerate and decelerate the vehicle at all times during the drive cycle.

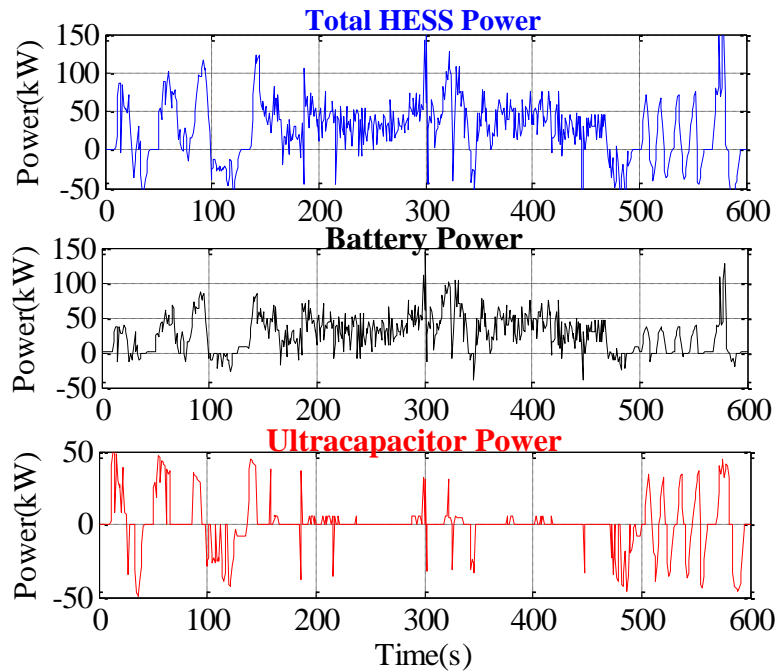


Figure 5.12 Calculated battery, ultracapacitor, and total HESS power vs. time for US06 drive cycle using adopted rule-based control

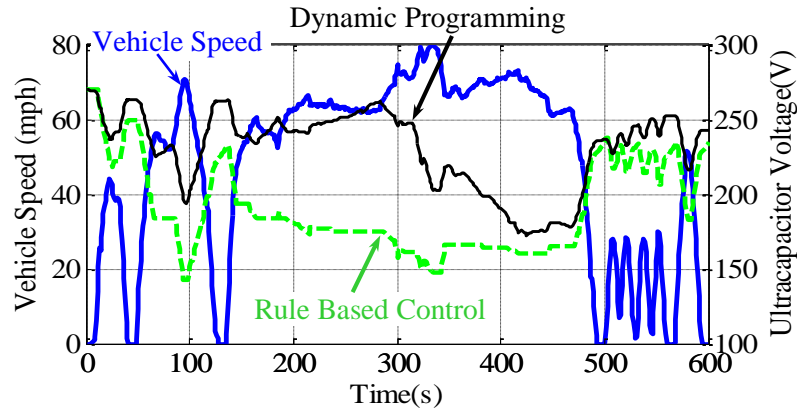


Figure 5.13 Calculated vehicle speed and ultracapacitor voltage vs time for the US06 drive cycle, comparing voltage profiles with rule-based and dynamic programming power split control

In addition to regulating the ultracapacitor pack's SOC, the control algorithm also achieves a 21.2% reduction in ESS losses and 1.9% reduction in energy consumption for the US06 drive cycle compared to the battery-only case, as shown in Table 5.3. The less aggressive UDDS and HWFET cycles' energy consumption is relatively unaffected, while the energy consumption for the more aggressive LA92 and US06 cycles is reduced by 1 to 2%. Considering that the ultracapacitor pack used to achieve this modest reduction in energy consumption is large (40L and 51kg) and likely quite expensive even for automotive quantities, it is desirable to explore how much the ultracapacitor pack can be downsized while still receiving as much of the benefits as possible.

Table 5.3 Calculated Energy and Power Consumptions for Four Cycles with Battery-Only and HESS Configurations

Drive Cycle	Energy Consumption (Wh/mile)			Total ESS Losses (Wh/mile)		
	Battery Only	Hybrid ESS	Wh/mile Reduction	Battery Only	Hybrid ESS	Wh/mile Reduction
Urban (UDDS)	331	331	-0.2%	12.7	13.2	-4.1%
Highway (HWFET)	393	393	0.1%	11.7	11.4	1.9%
Unified (LA92)	433	429	0.9%	27.7	23.7	14.3%
Supplemental (US06)	601	590	1.9%	54.6	43.0	21.2%

5.5 Optimizing Battery-Ultracapacitor Power Split Using Dynamic Programming

5.5.1 Introduction to Dynamic Programming

Section 5.3 demonstrated that the minimum-loss power split can be calculated analytically for a specific HESS output power and ultracapacitor voltage operating point. However, to minimize losses for an entire drive cycle, it is necessary to control the power split between the battery and ultracapacitor so that the power split at each time instant takes into account the future needs of the vehicle.

The control rules proposed in section 5.4 are effective at reducing the ESS losses for a drive but are not sufficient to guarantee that losses are minimized for the entire drive cycle. To accomplish this objective, an optimization technique, dynamic programming, has been utilized to minimize the sum of the battery, ultracapacitor, and dc/dc converter losses for any specified drive cycle. The optimization, which requires advance knowledge of the entire drive cycle, determines the best performance that can be achieved with an online control algorithm, such as the predictive algorithm proposed in [24]. The dynamic programming techniques developed by Sundström and Guzzella in [131] and made available as an open-source MATLAB function [132] are used.

The dynamic programming function in [131] is utilized with the vehicle model that includes the battery, ultracapacitor, and dc/dc converter models described in section 5.2. A 1Hz time step is adopted and the search continues until it finds the minimum-loss solution for a given drive cycle. The ultracapacitor voltage for the US06 drive cycle resulting from the dynamic programming and rule-based control cases are compared in Figure 5.13 for the 3000F ultracapacitor cell case. The general characteristics of the results for the two cases are similar, but the dynamic programming algorithm uses the ultracapacitor energy at different points of the drive cycle compared to the rule-based control.

5.5.2 Dynamic Programming versus Rule Based Control

Figure 5.14 compares the loss reduction achieved with dynamic programming and rule-based control for enough repetitions of the specified drive cycle to fully discharge the battery pack. It illustrates that, with the optimized result achieved via *dynamic programming*, a 1200F ultracapacitor cell pack can provide approximately the same amount of loss reduction that is achieved with a 3000F ultracapacitor cell pack controlled with *rule-based control*. The improved loss reduction achieved with dynamic programming shows that an optimized online control system is very important to achieving the best performance for a given ultracapacitor pack. Additionally, the results in Figure 5.14 show that the loss reduction achieved with the relatively small 1200F/58mΩ ultracapacitor cell pack (26kg/21L) is significant.

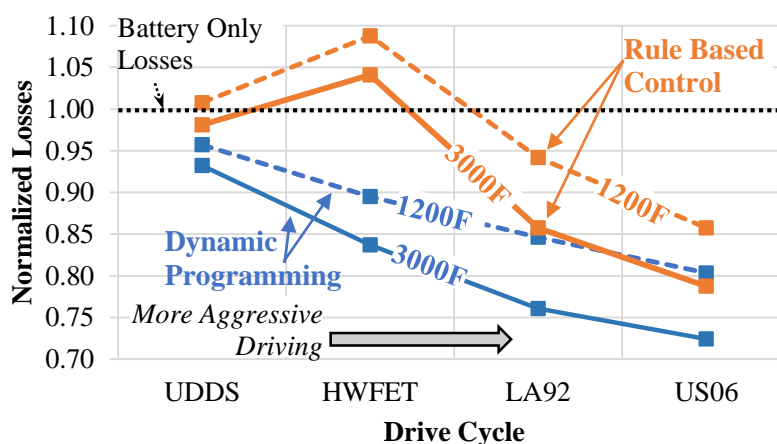


Figure 5.14 Calculated ratio of hybrid ESS to battery-only losses for four drive cycles with 1200F and 3000F ultracapacitor cell packs, comparing rule-based control and dynamic programming cases

5.5.3 Improvements Achieved with Dynamic Programming for Different Drive Cycles and Varied Ultracapacitor Size

To explore the range of system improvements achieved with the hybrid energy storage system and minimized loss dynamic programming control, the system is modeled for a full discharge of the vehicle's battery pack by repeating the specified drive cycle and solving for the minimum loss

power split. The results shown in Figure 5.15 to Figure 5.18 illustrate several benefits of the system. Figure 5.15 shows that a relatively modest range increase of up to 1.5 miles or 2.5% can be achieved. Figure 5.16 shows that, because some of the regenerative braking energy is directed to the ultracapacitor, the regeneration charge to the battery is reduced. As a result, the energy circulated through the battery is reduced, reducing battery cycles up to 15%. Figure 5.17 shows that battery losses are reduced by more than 30% for most drive cycles with the 1500F pack. Figure 5.18 shows that when battery and ultracapacitor cycles for a single discharge of the battery pack are scaled to 150k miles of travel, ultracapacitor cycles are well below their one million cycle rating and battery cycles are reduced significantly.

Additionally, the figures show that doubling the cell capacitance from 1500F to 3000F tends to only improve the performance metrics by approx. 25%, suggesting that a smaller pack consisting of 1500F cells can provide the majority of the performance benefits.

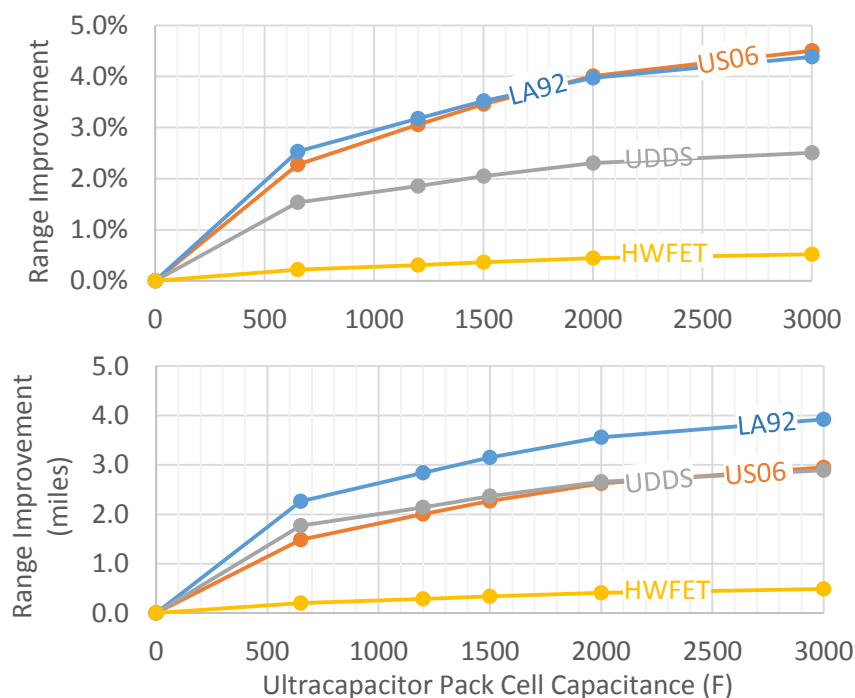


Figure 5.15 Predicted range improvement achieved with dynamic programming

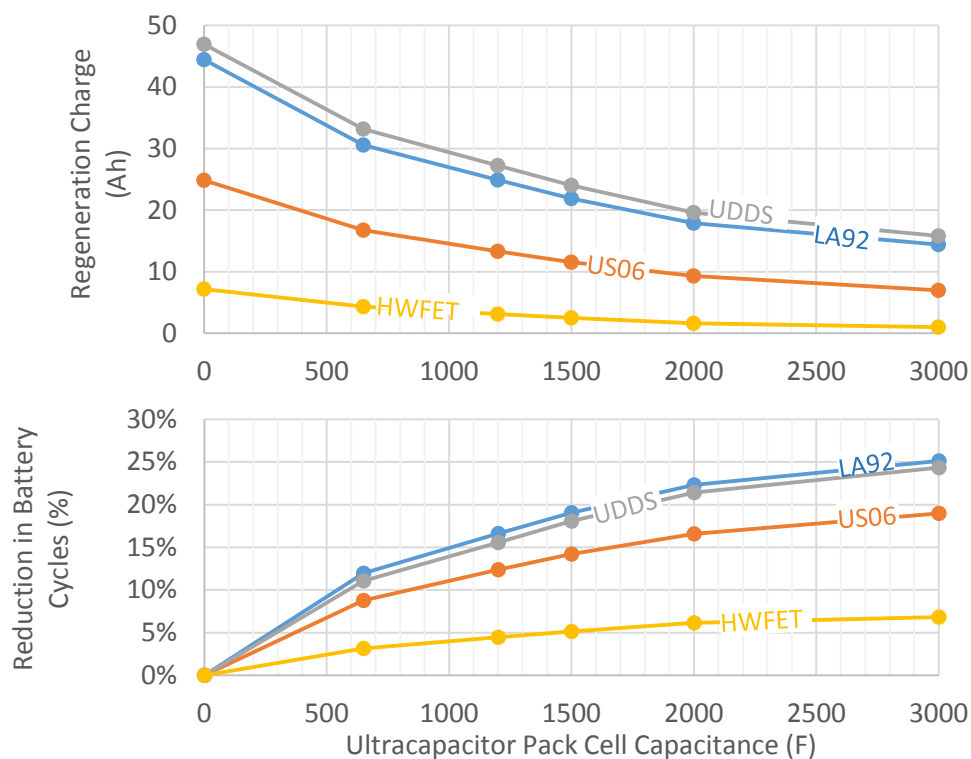


Figure 5.16 Predicted reduction of regeneration charge and battery cycles achieved with dynamic programming

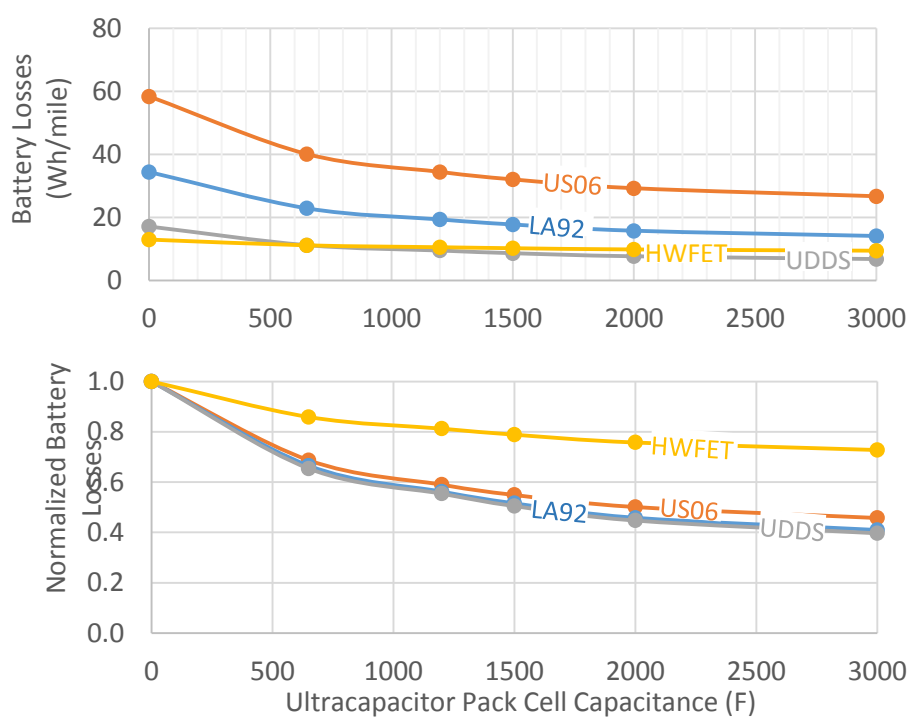


Figure 5.17 Predicted reduction of battery losses achieved with dynamic programming

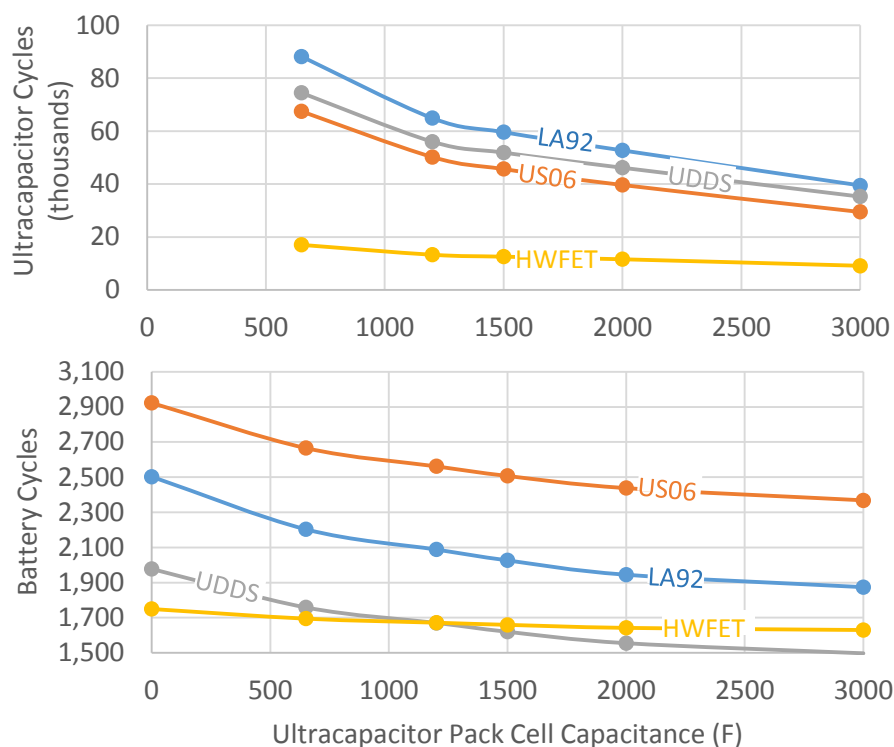


Figure 5.18 Ultracapacitor cycles and predicted reduction of battery cycles achieved with dynamic programming and scaled for 150k miles of travel

5.5.4 Improvements Achieved with Dynamic Programming for Low Temperature and High Towing Weight

The hybrid energy storage system will increase the system efficiency more when the battery resistance is higher, due to low temperatures or aging, for example, and when the rms power drawn by the vehicle is higher due to increased vehicle mass resulting in greater acceleration power or due to more aggressive driving. To examine the effects of reduced temperature, the LA92 dynamic programming controlled drive cycle was repeated for battery resistance equal to 1.5, 2, 2.5, and 3 times the battery resistance at 25°C. Figure 5.19 shows that the energy consumption of the vehicle is reduced significantly as battery resistance increases, with a 6-10% increase in range with 3 times the battery resistance, which is similar to the battery resistance at -5°C.

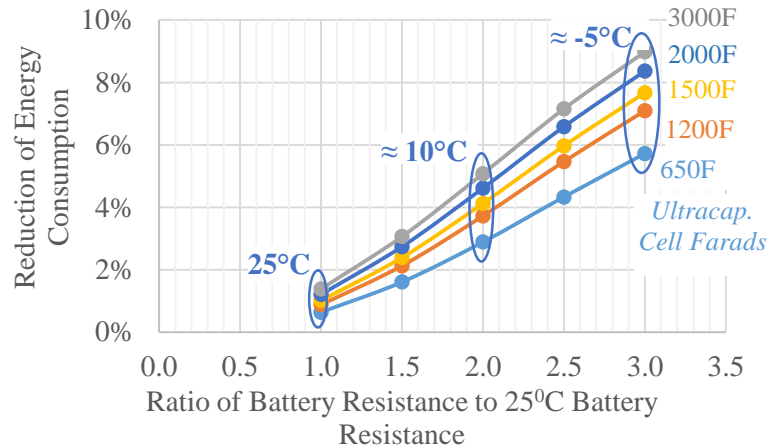


Figure 5.19 Predicted reduction in LA92 drive cycle energy consumption vs ratio of battery pack resistance to 25°C battery pack resistance

To examine the effects of increased rms power, the vehicle was also modeled for the LA92 drive cycle with a towing mass of 1000, 2000, and 3000kg. The hybrid energy storage system is shown in Figure 5.20 to reduce the energy consumption 3% to 5.5% with a 3000kg load.

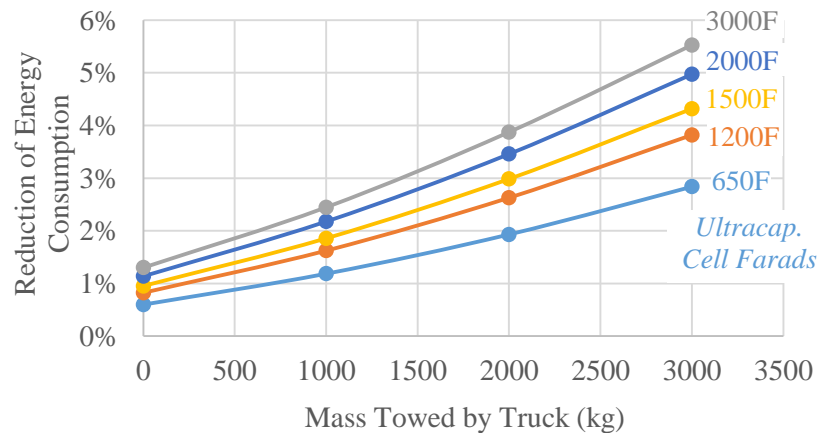


Figure 5.20 Predicted reduction in LA92 drive cycle energy consumption vs mass towed by truck

5.6 Experimental Verification

The model results were experimentally verified by using a Digatron Firing Circuits Universal Battery Tester to apply drive cycles calculated using the model with dynamic programming control to a single battery and a single ultracapacitor placed in a 25°C thermal chamber [133]. The two main criteria required to prove that the model and experiment agree are: (1) The amp-hours

experimentally discharged from the battery are similar to the amp-hours predicted, and the difference in amp-hours between the battery-only and battery-hybrid case is similar to the model prediction; and (2) The ultracapacitor provides similar energy and has similar losses to the model prediction.

Experimental testing was performed for a drive cycle consisting of eight LA92 drive cycles for a total driving distance of 78.5 miles. The drive cycle was performed for the battery-only case and hybrid energy storage case assuming a 2-parallel, 100-series connected 650F ultracapacitor pack in the model. The ultracapacitor pack considered in the model is similar to the 1200F cell pack modeled in previous sections, but instead utilizes two parallel 650F ultracapacitor cells because they were available for testing.

5.6.1 Battery Testing

The single battery cell was tested by commanding the cycler to apply the drive cycle power profiles to the battery. The power profiles are scaled for a single battery and have a 1Hz sample rate that is the same as the sample rate used for the dynamic programming simulation. Figure 5.21 shows that the measured and model-predicted voltage for a single battery cell are similar, while Table 5.4 compares the predicted and experimental results for the full drive cycles. The model is shown to perform very well, predicting the amp-hours drawn from the single battery within 0.1%, and predicting the reduction in amp-hours drawn from the single battery for the hybrid case within 5%. The model under-predicts the charging amp-hours by approximately 0.6%, and would have more error if used for modeling the battery at lower temperatures due to the increased impact of nonlinear resistance described by the Butler-Volmer equation [134].

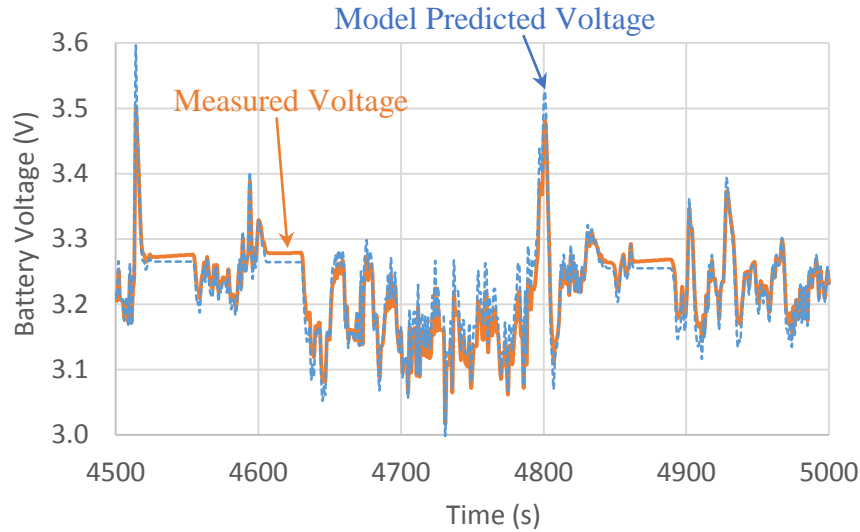


Figure 5.21 Model-predicted vs measured single battery voltage for LA92 cycle

Table 5.4 Single Battery Cell Model-Predicted vs Experimental Results for LA92 Drive Cycle for Battery-Only and Hybrid ESS

	Battery Only			Hybrid ESS		
	<i>Pred.</i>	<i>Exp.</i>	<i>Error</i>	<i>Pred.</i>	<i>Exp.</i>	<i>Error</i>
Amp-hours discharged	129.26	129.41	0.1%	112.84	113.08	0.2%
Amp-hours charged	-32.55	-32.75	0.6%	-17.27	-17.38	0.6%
Amp-hours total	96.71	96.66	-0.1%	95.57	95.70	0.1%
Output Energy Scaled for Full Pack kWh	31.80	31.82	0.1%	32.20	32.20	0.0%

	<i>Pred.</i>	<i>Exp.</i>	<i>Error</i>
Hybrid ESS Reduction of Charge Consumed from Single Battery	1.14Ah	1.09Ah	-5%

5.6.2 Ultracapacitor Testing

The ultracapacitor model was evaluated by commanding the cyclers to draw the 1Hz sample rate drive cycle current profile, scaled for a single ultracapacitor, from a single 650F ultracapacitor. The current profile was drawn from the ultracapacitor to insure the ultracapacitor stayed within its specified voltage range. If the power profile were used, any model error would result in the voltage drifting up or down through the drive cycle. Figure 5.22 shows that measured and model-predicted

voltage are very close, suggesting the model is an accurate representation of the ultracapacitor. The experimental results for the drive cycle current profile are scaled for the full 2p/100s pack and presented in Table 5.5. The scaled test results show that the charge and discharge energy values are very close to the predicted values. Although the predicted ultracapacitor losses are off by 40%, this only represents an error of 0.7Wh/mi, and the error may be partially attributable to the measurement.

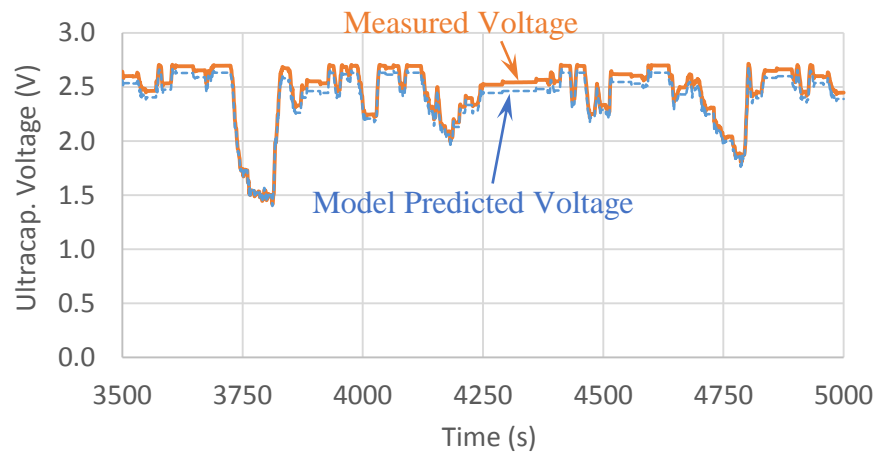


Figure 5.22 Model-predicted vs measured single ultracapacitor voltage for LA92 drive cycle with HESS current command

Table 5.5 Single Ultracapacitor Model Predicted versus Experimental Energy for LA92 Drive Cycle Scaled for 2p100s Pack

Ultracapacitor (scaled for 2p100s pack)			
	<i>Predicted</i>	<i>Experimental</i>	<i>Error</i>
Discharge Energy	5.56 kWh	5.56 kWh	0.0%
Charge Energy	-5.70 kWh	-5.76 kWh	1.0%
Total Losses	0.14 kWh	0.20 kWh	39.6%
Losses per Mile	1.8 Wh/mi	2.5 Wh/mi	0.7 Wh/mi
Efficiency	97.5%	96.5%	-1.0%

5.7 Investigation of Other Powersplit Optimization Goals, Effect on Mass of Including HESS Mass, and Increase in Motor Power Capability Achieved with HESS

Several interesting mini topics regarding HESS performance are investigated in this subsection. First, two alternative battery / ultracapacitor powersplit optimization goals, minimizing battery rms current and minimizing battery cycles, are investigated. The HESS performance for these goals is compared to performance for the minimization of system losses, which is the goal used for all other cases in this dissertation. Then the HESS mass is included in the system model and compared to the modeled results where HESS mass is neglected, as has been done in most cases in this dissertation. Finally an extra benefit of the HESS, an increase in motor power capability due to higher battery voltage under load, is described and quantified.

5.7.1 Alternative HESS Powersplit Optimization Goals

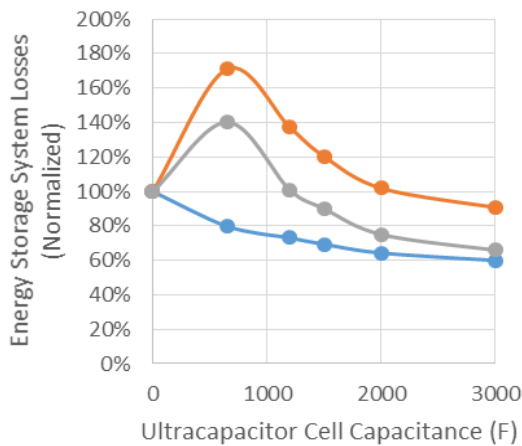
For all the other cases in this chapter, as well as the rest of the dissertation, the dynamic programming power split control optimization algorithm has been utilized to minimize system losses and to minimize any error between the commanded and actual HESS output power. Minimizing the commanded power error ensures that at low temperatures for example, when the battery pack cannot supply the commanded power, the control system will if possible utilize the ultracapacitor to provide the extra power. While it is always desirable to have the system provide the commanded power, the powersplit can be controlled to minimize or maximize any other vehicle parameter as desired. Two alternative values are minimized in this section, including minimizing the battery rms current and minimizing battery cycles, which essentially directs as much of the regenerative braking energy to the ultracapacitor pack as possible. Both of these optimization goals, which are listed as option 2 and 3 in Table 5.6 below, will help reduce battery

aging, the first by reducing battery losses and the second by reducing the microcycles provided by the battery for regenerative braking.

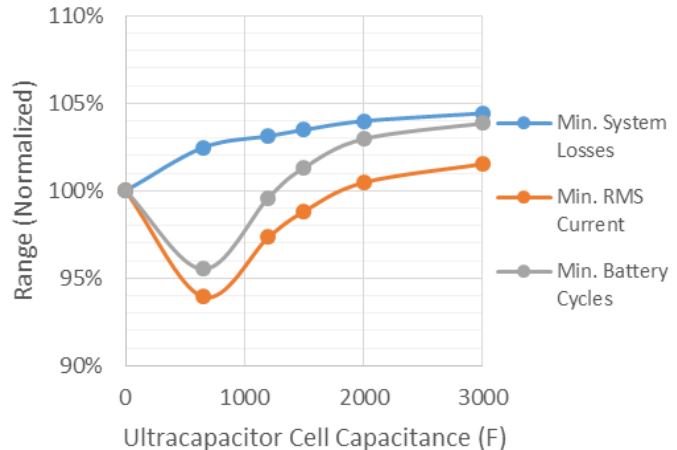
Table 5.6 HESS Powersplit Control Cost Minimization Options

Values to minimize:	
Used for All Options:	HESS discharge power limiting (<i>output power < commanded power</i>)
Option 1 – Min. System Losses:	Sum of battery, ultracapacitor, and dc/dc converter losses
Option 2 – Min. RMS Current:	Battery RMS current
Option 3 – Min. Battery Cycles:	Battery cycles

The dynamic programming algorithm was run for a range of ultracapacitor pack sizes for the US06 and LA92 drive cycles at 25°C, and because the results were similar for both drive cycles just the LA92 results are provided here. First the energy storage system losses, the sum of the battery, dc/dc converter, and ultracapacitor losses, and the normalized range are shown in Figure 5.23 below. As is expected, for the goal of minimizing system losses the energy storage system losses are decreased below the losses for the battery only case (0F), resulting in up to a 4.5% increase in range. For the other two cases though, minimizing battery rms current and cycles, the



(a) Normalized energy storage system loss



(b) Normalized vehicle driving range

Figure 5.23 Normalized energy storage system loss and range for LA92 drive cycle and three DP powersplit control cost minimization options

energy storage system losses are actually increased above the battery only losses for several of the ultracapacitor values, resulting in decreased range. For a driving case in which range is not an issue, a loss in range may be an acceptable tradeoff for reducing battery wear.

The battery RMS current is then shown in Figure 5.24 below to be decreased by about an additional 10 Arms when for the minimizing RMS current case, resulting in a further 20% reduction in battery losses. The battery cycles are also minimized the most for the minimizing battery cycles case, as is shown in Figure 5.25 (a), with about 10% fewer battery cycles occurring than for the

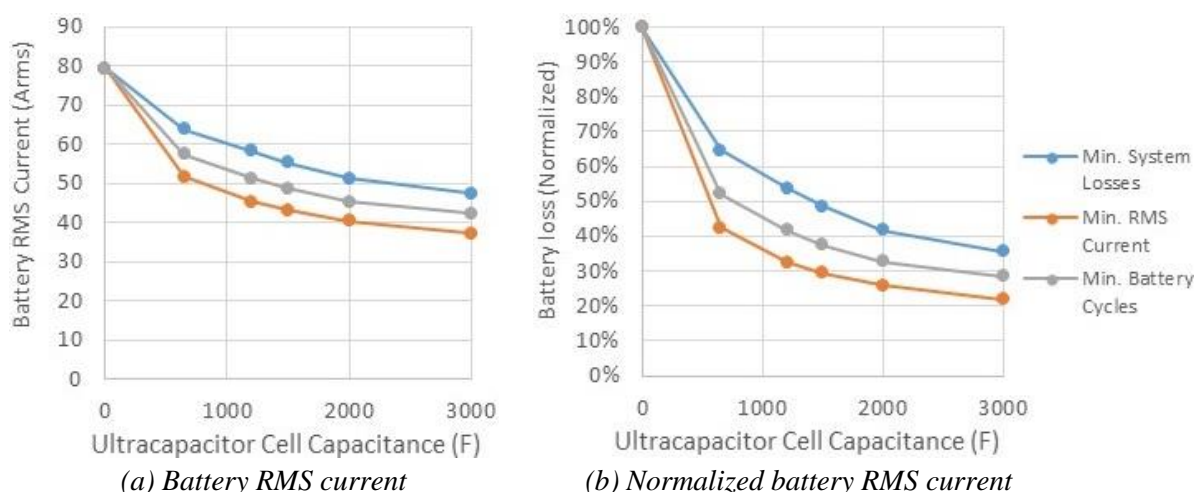


Figure 5.24 Battery RMS current for LA92 drive cycle and three DP powersplit control cost minimization options

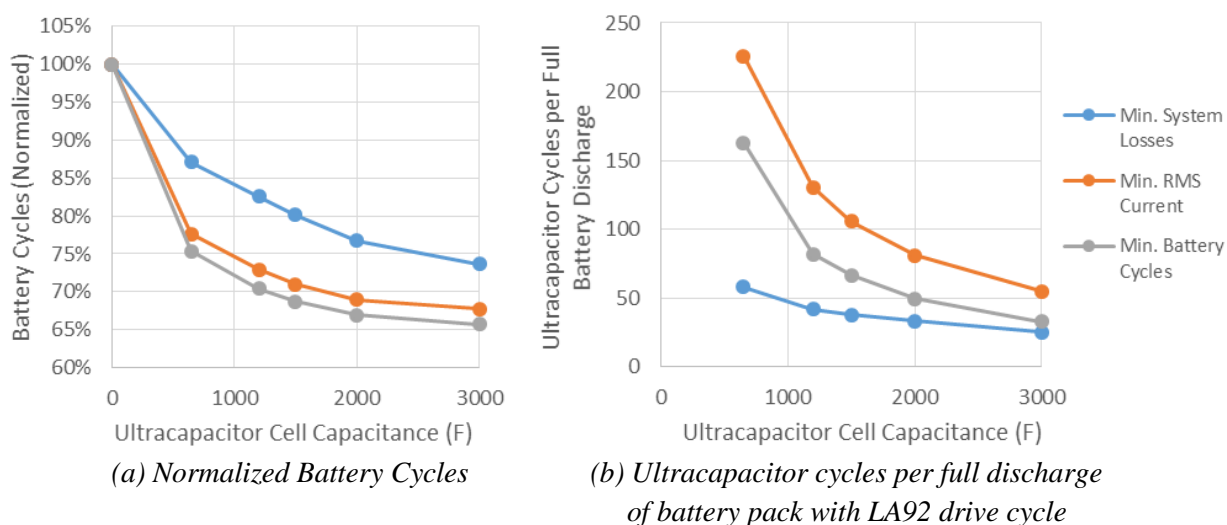


Figure 5.25 Battery and ultracapacitor cycles for LA92 drive cycle and three DP powersplit control cost minimization options

minimizing system losses cases. And finally, as might be expected, significantly more ultracapacitor cycles are shown (Figure 5.25 (b)) to occur for the cases of minimizing rms current and battery cycling, which both transfer energy throughput to the ultracapacitor at the expense of system efficiency. These three cases highlight the tradeoffs between each minimization option, and suggest that a hybrid approach or a change in minimization goals as a function of driving style, drive length, or battery temperature, may be appropriate.

5.7.2 Effect on Vehicle Range of Including HESS Mass

One factor which was neglected in this chapter is the effect of the HESS mass on vehicle range. The estimated mass of the additional equipment needed for the HESS, the ultracapacitor and dc/dc converter, ranges from 35.4kg to 77.4kg as specified in Table 5.7, and will increase the vehicle's total mass 1.5-3%. This increase in mass will result in greater energy consumption from the battery pack, primarily due to increased losses in the motor, drive, and battery pack when accelerating and decelerating.

Table 5.7 Mass of Ultracapacitor and DC/DC Converter Systems for HESS

	<i>Ultracapacitor Cell Capacitance</i>				
	<i>650F</i>	<i>1200F</i>	<i>1500F</i>	<i>2000F</i>	<i>3000F</i>
Total Ultracapacitor Cell Mass (100 series connected cells)	16kg	26kg	28kg	36kg	51kg
DC/DC Converter Mass (400A rated converter)	13.5kg	13.5kg	13.5kg	13.5kg	13.5kg
Housing and Subcomponent Mass Allowing (20% of dc/dc and ultracapacitor cell mass)	5.9kg	7.9kg	8.3kg	9.9kg	12.9kg
Total Ultracapacitor & DC/DC Converter System Mass	35.4kg	47.4kg	49.8kg	59.4kg	77.4kg

To quantify the additional losses, the vehicle was modeled both with and without the additional HESS mass, and the results are shown in Figure 5.26 below. The inclusion of the HESS mass

results in as much as a 0.5% reduction in range, which does negate some of the benefits of the system. The general trends in performance improvement still hold true though, and the effect on range will be proportionally less for lower temperatures, when towing a heavy trailer, or for heavier vehicles such as the transit bus which will be modeled in a later chapter. Since the HESS mass was not included for the majority of the calculations included in this dissertation, it can just be assumed that there will be about a 0.5% reduction in range improvement when HESS mass is accounted for.

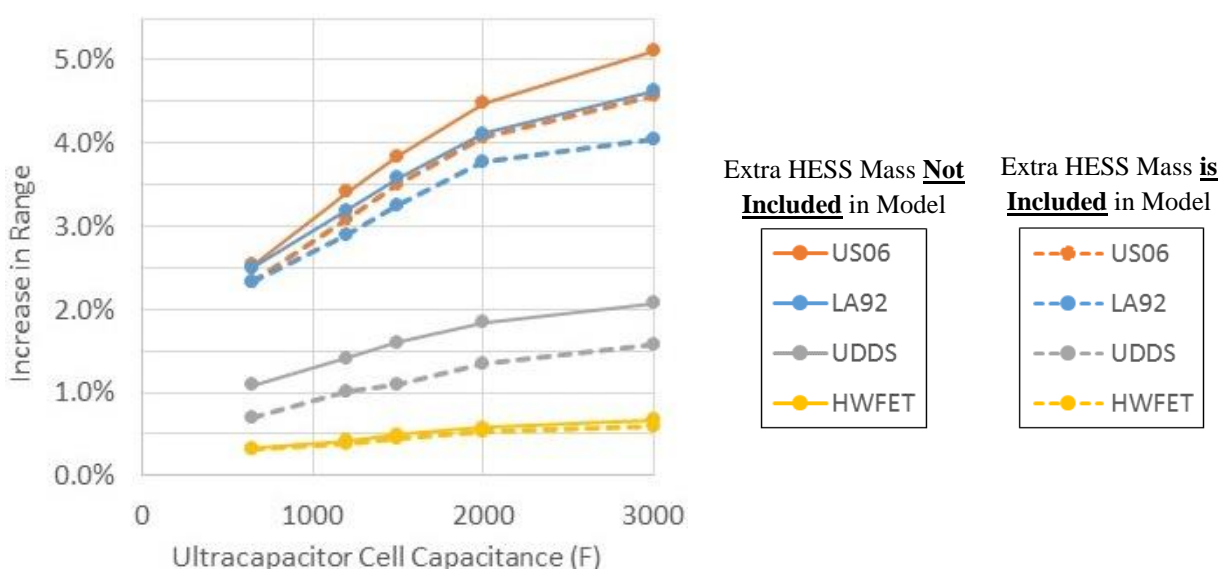


Figure 5.26 Improvement in vehicle range achieved with HESS at 25°C for model which *does* and *does not* include extra mass due to addition of HESS

5.7.3 IPM Traction Machine Increase in Power Capability with HESS

One incidental benefit of the HESS is an increase in the IPM traction machine's power capability. Because the battery pack power is supplemented with power from the ultracapacitor pack, the battery pack voltage can be higher for a given energy storage system output power. The battery only and HESS case power, assuming an HESS with a 3000F ultracapacitor cells and a 400A dc/dc converter, is shown versus battery terminal voltage in Figure 5.27 (a) below. With

the HESS, the same power can be output with a 30V or more increase in battery terminal voltage. Because the motor's output power capability is a function of the ac voltage magnitude the drive can supply, a higher battery (dc bus) voltage translate to higher motor output power capability.

The motor power capability increases approximately linearly with an increase in dc bus voltage, as is defined in equation (4.29). The motor and drive power capability is overlaid in grey in Figure 5.27 (a), showing that with just the battery pack the motor can provide a maximum of 131kW with 50Ah discharged from the battery pack, while with the HESS the motor can provide 146kW at this point. This same methodology was used to determine the motor power capability over the full discharge range of the battery, and the motor power capability is shown Figure 5.27 (b) to be increased by about 10% over most of the discharge range of the battery, with the HESS allowing nearly rated power to be supplied by the drivetrain until the full 100Ah of capacity is used from the battery pack. The HESS will boost the motor power capability proportionally even more for low temperatures and as the battery ages and resistance increases, providing a further benefit to the overall vehicle drivetrain performance.

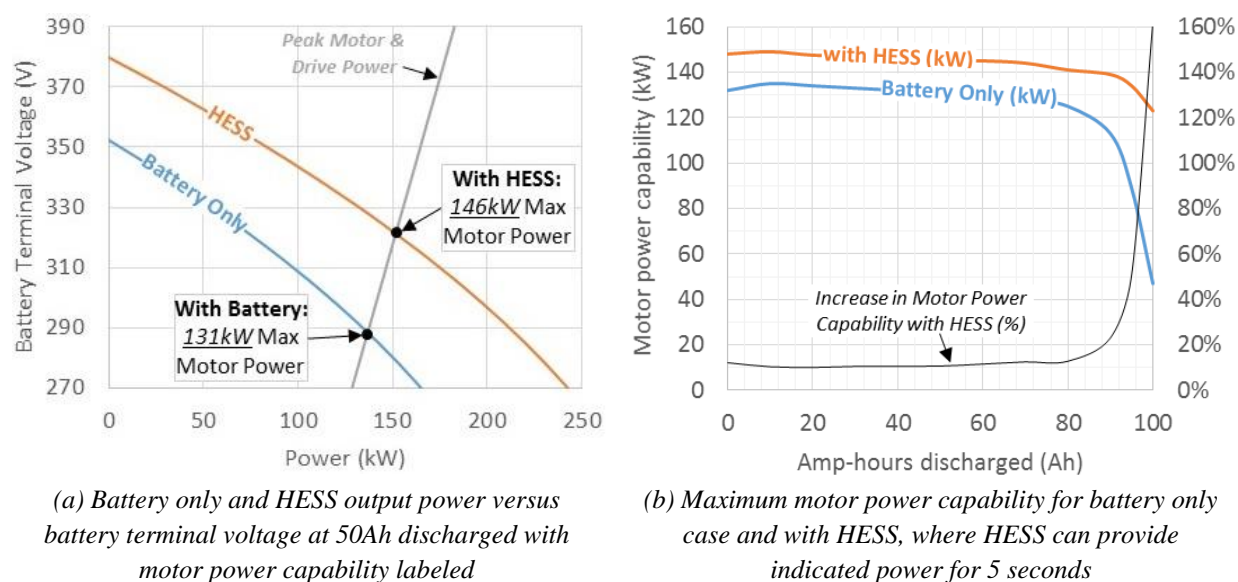


Figure 5.27 Increase in motor output power capability achieved at 25°C with HESS with 3000F ultracapacitor cells and 400A dc/dc converter

5.8 Conclusions

The results of this investigation have highlighted the importance of the choice of power split control algorithm for determining ESS loss reduction that can be achieved by using a hybrid battery/ultracapacitor energy storage system in an electrified vehicle. For a HESS consisting of a battery pack, ultracapacitor pack, and dc/dc converter, it was first shown that there is a unique power split between the battery and ultracapacitor pack that will result in minimum ESS losses. Next, a rule-based control algorithm was introduced that uses the minimum-loss algorithm to manage the power split during a drive cycle, demonstrating that significant loss reductions can be achieved. This led to the introduction of dynamic programming that further improved the results by finding the minimum-loss power split solution for an entire drive cycle.

The results achieved with dynamic programming are very promising, showing that the ESS energy consumption can be reduced up to 2% at room temperature with a relatively small 150Wh 28kg/24L ultracapacitor pack. The study results have also highlighted the increased benefits provided by the HESS configuration at low battery temperatures and for towing heavy loads.

It is important to recognize that the dynamic programming control requires prior knowledge of the whole drive cycle. Consequently, the results achieved with dynamic programming represent the upper bound of the benefits that can be achieved in a real vehicle in which the control system can only rely on an estimate of the future drive profile. It is expected that a control system can be developed that would perform better than the proposed rule-based control that delivers approximately 75% of the improvement predicted with dynamic programming for the US06 drive cycle. However, it cannot be expected to reach the same improvement level as the dynamic programming solution presented in this chapter.

The battery and ultracapacitor models that were used to generate the estimates of improved system performance with dynamic programming control were also experimentally shown to be very accurate by comparing the model-predicted and measured battery charge and ultracapacitor energy for the LA92 drive cycle. In the final subsection, several topics are covered which give more insight into the performance of the HESS. First the powersplit is calculated using dynamic programming for three different optimization goals, demonstrating that battery rms current and battery cycles can be minimized with the HESS at the expense of system efficiency, which is reduced for both cases. The effect of the HESS mass on vehicle range is then shown to be relatively minimal, reducing range by no more than 0.5%, and finally the HESS is shown to boost the motor power capability about 10% over the battery only case.

Chapter 6

Low Temperature Hybrid Energy Storage System Modeling and Performance

6.1 Introduction

At low temperatures the resistance of lithium batteries increases substantially, substantially reducing their power capability and increasing losses. Additionally for many lithium chemistries lithium plating, an irreversible plating of lithium metal in the battery, may occur when charging at low temperature. Lithium batteries are therefore often not rated to charge at low temperatures, preventing the capture of regenerative braking energy. For electric vehicle applications these poor characteristics combine to result in reduced range and power limiting at low temperatures. Battery pre-heating while the vehicle is parked, or heating once it is being driven, is typically employed to minimize this poor performance at low temperatures, but even so electric range is reduced at low temperature as much as $\frac{1}{3}$ for the Nissan electric vehicle and as much as $\frac{1}{2}$ for the Chevy Volt plug-in hybrid, as shown in Figure 6.1 below.

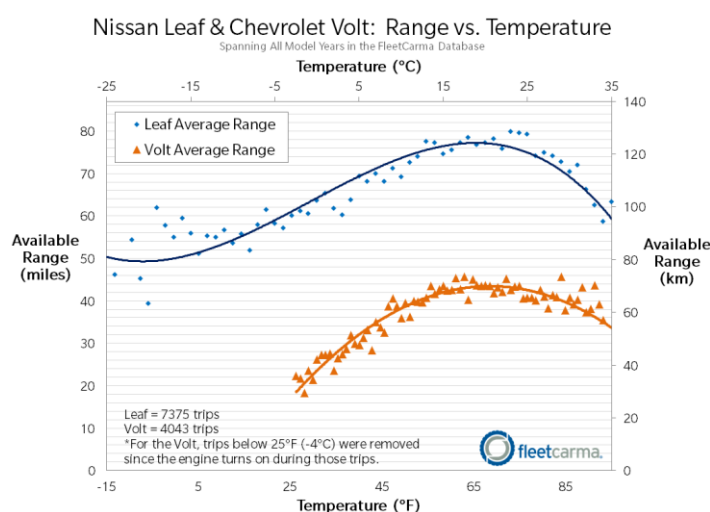


Figure 6.1 Measured range versus temperature for Nissan Leaf and Chevy Volt electric vehicles [135]

Because of the poor characteristics of lithium batteries at low temperatures, the addition of a second energy storage source which is less effected by temperature, such as the ultracapacitors utilized in this work, is very appealing. The work in this section extends the hybrid energy storage system modeling presented in Chapter 5 to low temperatures. The ultracapacitor and battery pack are both tested over a wide range of temperatures, and low temperature models are developed for both and the methodology is presented in detail to ensure it can be utilized by other researchers. Additionally, because lithium battery resistance is a nonlinear function of current at low temperatures due to the Butler Volmer effect, a specially developed Butler-Volmer battery model is developed and incorporated into the system model as well. The low temperature model is then utilized to characterize the performance benefits achieved with the HESS at low temperature, and a range of results are shown. Finally the system's performance is also examined in detail for three cases of battery power limiting: mild, medium, and severe, highlighting some unusual performance aspects which occur under severe power limiting.

6.2 Battery Characterization Testing and Modeling for Low Temperatures

6.2.1 Low Temperature Testing

The goal of the low temperature battery testing is to collect the measurements necessary for a battery model which includes the nonlinear battery resistance described by the Butler-Volmer equation. Two tests, both based off the HPPC test, were found to be necessary. The first test, a multiple current magnitude HPPC test, was utilized to capture the battery's nonlinear resistance versus current magnitude characteristic which is more prominent at low temperatures. The second test is equivalent to the LA92 HPPC test utilized in Chapter 5, and is used to capture the pseudo open circuit voltage and resistance during an LA92 drive cycle. The results of these two tests are combined, as illustrated in Figure 6.2 below, with the multiple current magnitude HPPC test

providing the shape of the nonlinear resistance curve and with the LA92 HPPC test providing the open circuit voltage and the nominal resistance for the model. Both tests are performed at -20, -10, 0, and 10°C, and the methodology for performing the tests along with the test results are provided in the following two subsections.

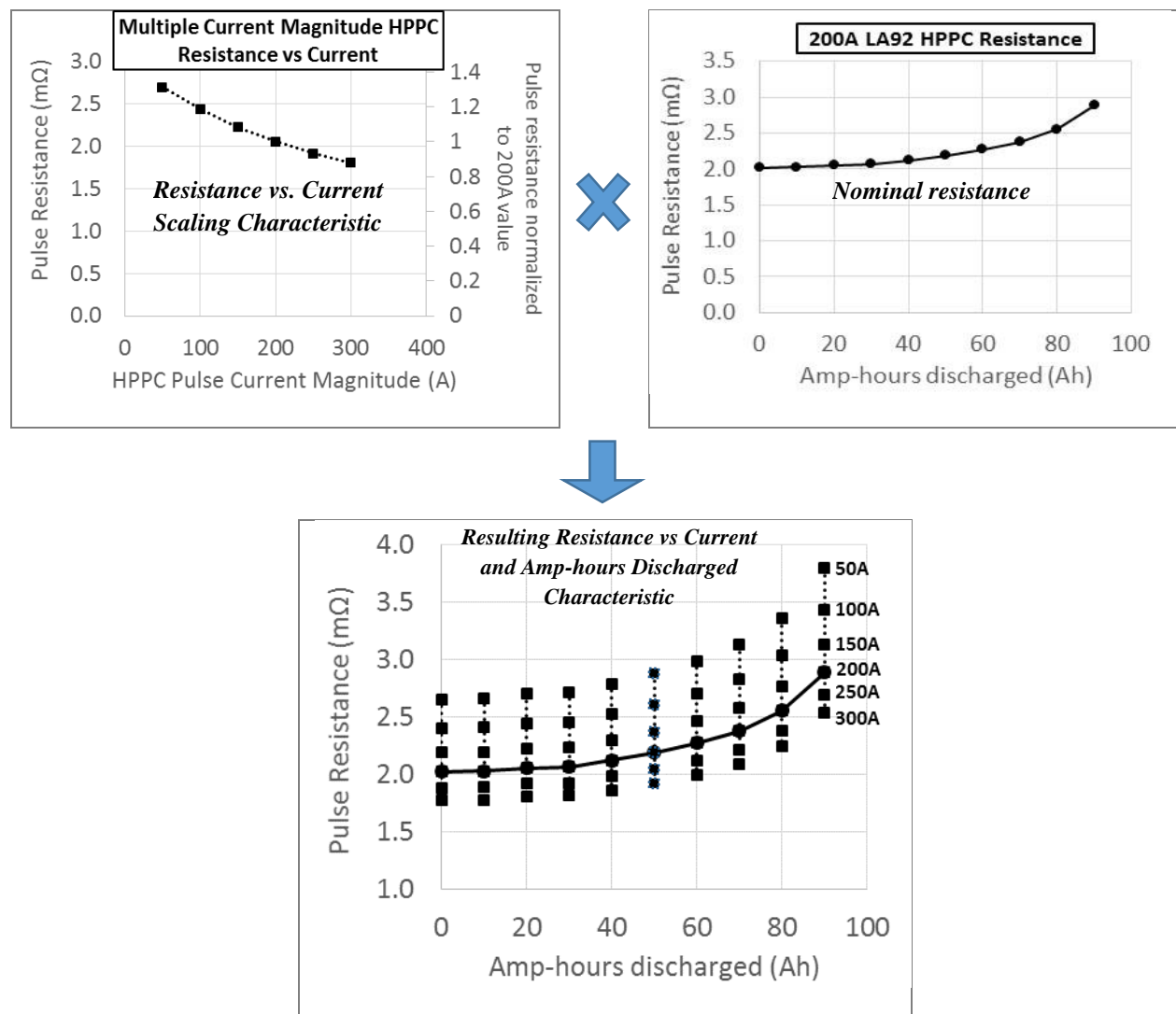
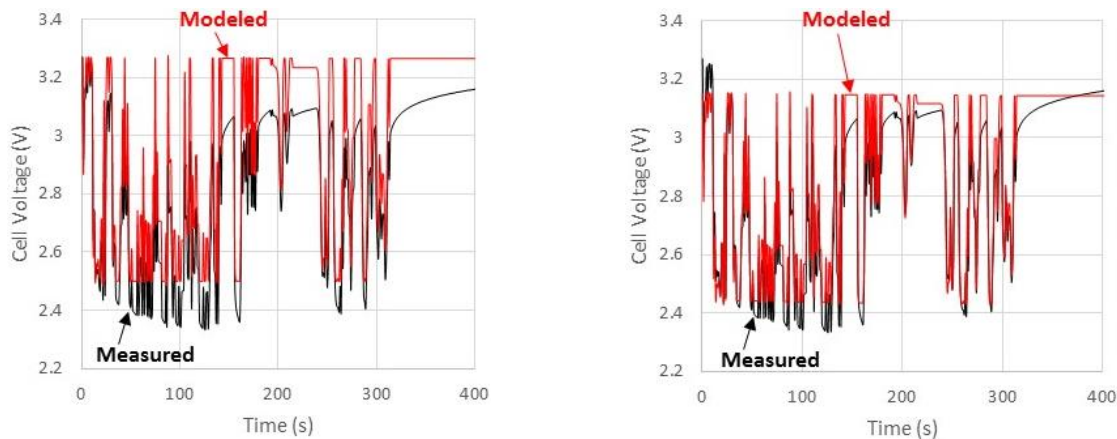


Figure 6.2 Example of combination multiple current magnitude HPPC and LA92 HPPC testing to obtain resistance values utilized for low temperature modeling

To illustrate the necessity of utilizing the LA92 HPPC test results, the measured versus modeled battery voltage for a drive cycle at -10°C is shown below in Figure 6.3 for a model which utilizes

the OCV and nominal resistance from the LA92 HPPC test and a model which utilizes the OCV and resistance from just the multiple current magnitude HPPC test. The modeled and measured voltage is visibly much more similar for the model with the LA92 HPPC values, which is primarily due to the OCV from the LA92 HPPC test being lower, as will be discussed further in the following section on the LA92 testing.



(a) Model Utilizing Multiple Current Magnitude HPPC OCV and Resistance

(b) Model Utilizing LA92 HPPC OCV and Nominal Resistance

Figure 6.3 Modeled versus measured battery voltage for -10°C case starting with 40Ah discharged

6.2.1.1 Multiple Current Magnitude HPPC Test

For the multiple current magnitude HPPC test a series of ten second long current pulses of varying magnitude are applied to the battery, and the resistance is calculated from the results for each current value. Figure 6.4 shows the current pulses applied to the battery for the 0°C test, ranging from 50A to 300A in steps of 50A. There is a one hour pause prior to the application of the current pulses and a 12 minute pause between each current pulse, and the resistance is calculated as a function of the open circuit voltage (the voltage immediately prior to the current pulse), the voltage at the end of the 10 second pulse, and the applied current, as is also shown in Figure 6.4 below.

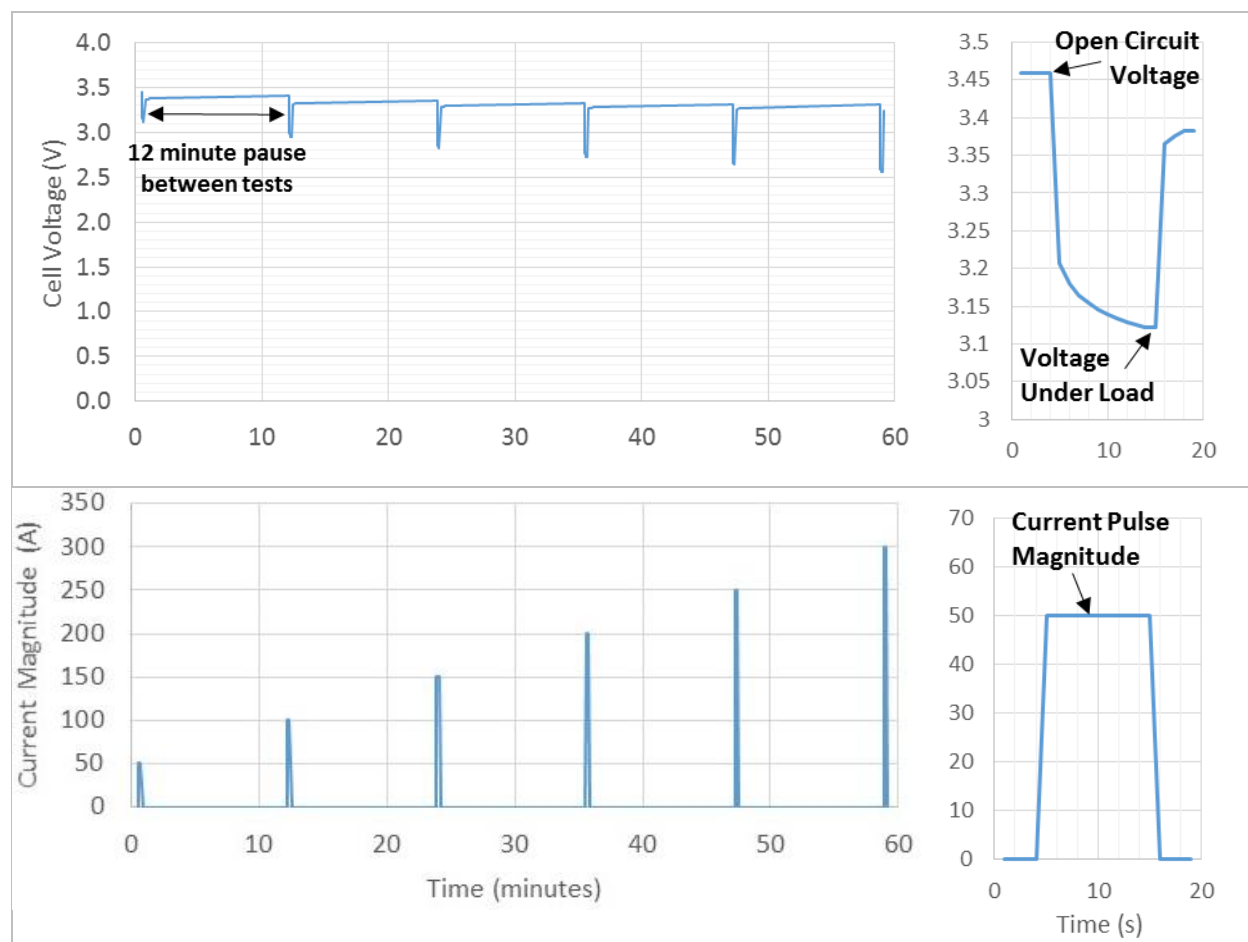


Figure 6.4 Methodology for performing multiple current magnitude HPPC resistance test

The series of pulse currents are applied to the battery in increments of 10% of capacity, 10Ah for the 100Ah battery tested here, to show how the resistance varies both as a function of state of charge and current amplitude. The experimental test results for each temperature, as given in Figure 6.5 below, clearly show that discharge resistance is a nonlinear function of a current, which as mentioned previously is described by the Butler-Volmer equation. The results also show that the nonlinear resistance is more prominent at lower temperatures and that, with the exception of the fully charged 0Ah discharged case, the shape of the resistance versus current curve changes very little with state of charge, a desirable characteristic that allows the use of a more simplified model. The multiple pulse current test was also performed for *charge* current pulses for 10°C and

0°C and the shape of charge and discharge resistance versus current magnitude curves were found to be similar, as shown in Figure 6.6, allowing the discharge curve shape to be used for the charging case as well.

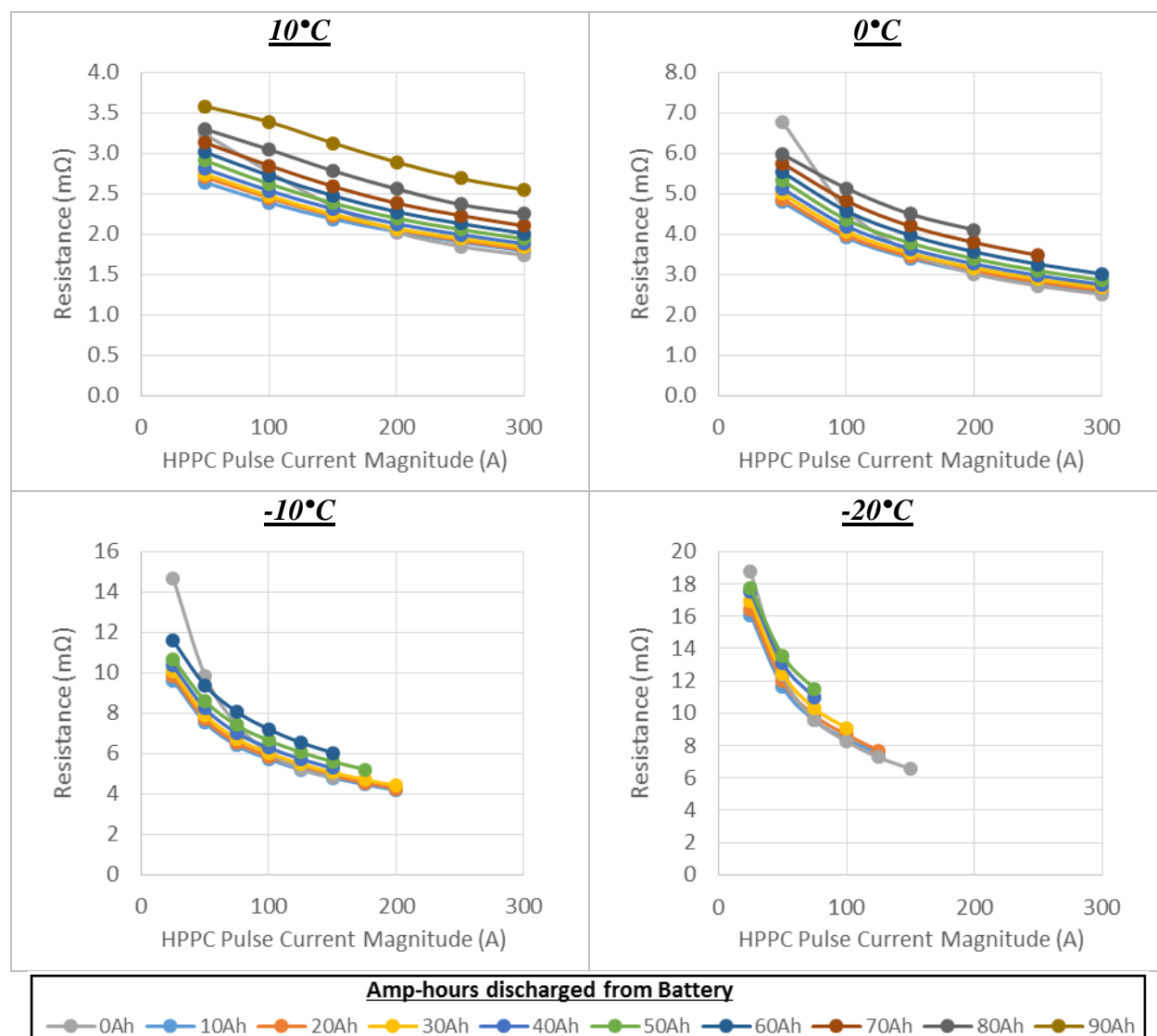


Figure 6.5 Discharge resistance versus HPPC pulse current magnitude for Calb 100Ah LiFePO4 battery at various temperatures

Because the shape of the non-linear resistance curve is relatively unaffected by state of charge, as demonstrated in Figure 6.5, the model as shown in Figure 6.2 is implemented with only a single

curve shape used to attenuate the resistance as a function of current. The 20Ah discharged case was chosen to provide the resistance versus current curve shape, and the resistance and normalized resistance curve for each temperature is overlaid below in Figure 6.7. The figure clearly shows that the Butler-Volmer effect is much greater at lower temperatures, with for example the 100A resistance being reduced by 10% at 10°C and by 28%, almost triple the amount, at -20°C.

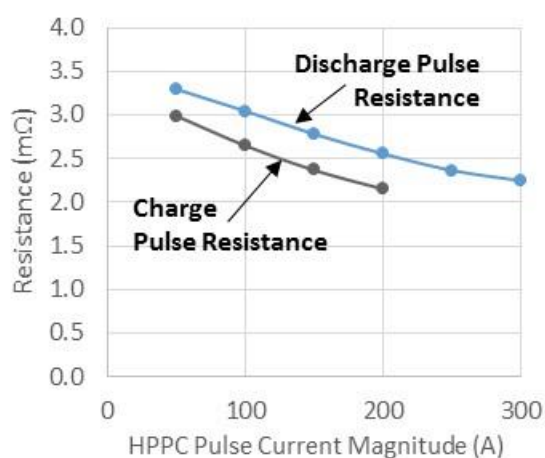


Figure 6.6 Charge and discharge pulse resistance at 10°C and 80Ah discharged for Calb 100Ah LiFePO4 battery

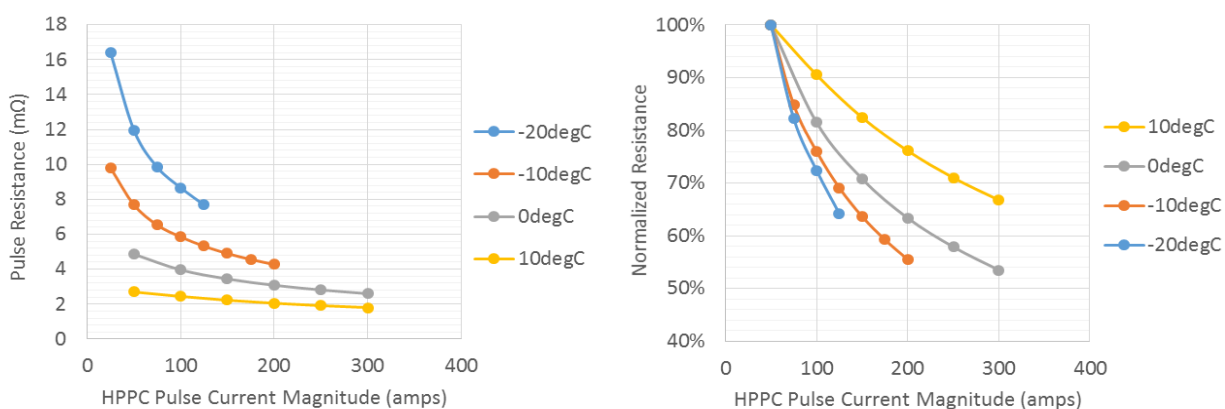


Figure 6.7 Resistance versus HPPC pulse current magnitude for Calb 100Ah LiFePO4 battery with 20Ah discharged

Additionally the resistance and normalized resistance versus battery current values for the 20Ah discharged case, which will be used in the modeling, are given in Table 6.1 below. Due to

the higher resistance at the lower temperatures, the current is limited by the minimum voltage rating of the battery to 200A at -10°C and 125A at -20°C .

Table 6.1 Resistance versus HPPC pulse current magnitude for Calb 100Ah LiFePO4 battery with 20Ah discharged

10°C

<i>Battery Current</i>	50 A	100 A	150 A	200 A	250 A	300 A
<i>Resistance ($R_{batt-BV}$)</i>	2.70 m Ω	2.44 m Ω	2.23 m Ω	2.06 m Ω	1.92 m Ω	1.80 m Ω
<i>Resistance Normalized to 200A (BV_{scale})</i>	1.31	1.19	1.08	1.00	0.93	0.88

0°C

<i>Battery Current</i>	50 A	100 A	150 A	200 A	250 A	300 A
<i>Resistance ($R_{batt-BV}$)</i>	4.86 m Ω	3.96 m Ω	3.45 m Ω	3.08 m Ω	2.82 m Ω	2.60 m Ω
<i>Resistance Normalized to 200A (BV_{scale})</i>	1.58	1.29	1.12	1.00	0.91	0.84

-10°C

<i>Battery Current</i>	25 A	50 A	75 A	100 A	125 A	150 A	175 A	200 A
<i>Resistance ($R_{batt-BV}$)</i>	9.81 m Ω	7.70 m Ω	6.53 m Ω	5.85 m Ω	5.32 m Ω	4.90 m Ω	4.56 m Ω	4.27 m Ω
<i>Resistance Normalized to 100A (BV_{scale})</i>	1.68	1.32	1.12	1.00	0.91	0.84	0.78	0.73

-20°C

<i>Battery Current</i>	25 A	50 A	75 A	100 A	125 A
<i>Resistance ($R_{batt-BV}$)</i>	16.4 m Ω	12.0 m Ω	9.9 m Ω	8.7 m Ω	7.7 m Ω
<i>Resistance Normalized to 50A (BV_{scale})</i>	1.37	1.00	0.82	0.72	0.64

6.2.1.2 LA92 HPPC Test

The second test, the LA92 HPPC Test, is used to get the open circuit voltage and the nominal resistance for the battery model, where the nominal resistance is scaled in the model as a function of current using the multiple current magnitude HPPC test results presented in the prior section. The two tests are distinguished by the conditions which occur prior to the test pulse: for the multiple current pulse HPPC test there is an hour pause prior to the test pulses, while for the LA92

HPPC test the test pulses are preceded by a 60 second pause following an LA92 drive cycle discharge profile, as shown in Figure 6.8 below. The main effect of performing the discharge pulse immediately following a drive cycle is that the open circuit voltage is lower due to diffusion effects in the battery.

The diffusion effects result in a long time constant which can be seen in the 60 second pause in Figure 6.8. The effect of the time constant is captured in the lower open circuit voltage of the LA92 HPPC test, but it could also be captured as a capacitance as has been done in prior work. Capturing the time constant as a capacitance would likely increase the accuracy of the modeling, but it would add a second state to the dynamic programming optimization (ultracapacitor voltage is only state currently), increasing the time to execute by N^2 . Therefore the simplified model is greatly preferred because the model already takes about 30 minutes to execute for a four hour drive.

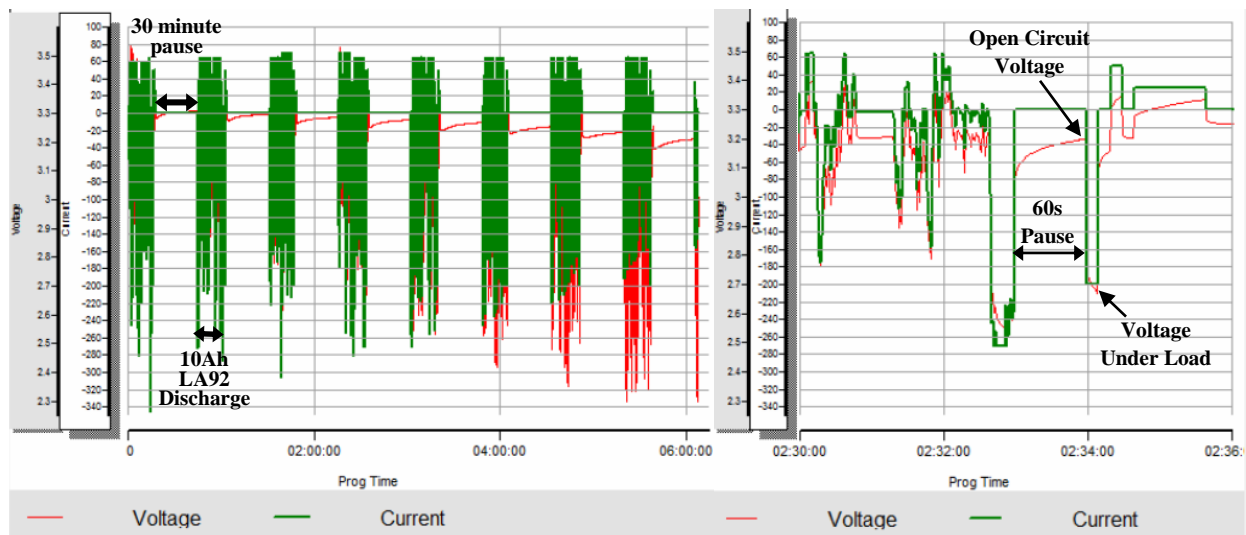


Figure 6.8 LA92 HPPC Test for 0°C

The open circuit voltage measurements from the LA92 and the multiple current magnitude HPPC tests are shown below in Figure 6.9. Because the battery is discharging, diffusion results in

a lower open circuit voltage measurement for the LA92 HPPC test, with open circuit voltage being substantially less for low temperatures, indicating that temperature has a severe effect on the CALB LiFePO₄ battery. The LA92 HPPC resistance, also shown in Figure 6.9, is performed for different pulse current magnitudes ranging from 50A to 200A depending on temperature, such that the battery is capable of providing the current pulse to a relatively deep depth of discharge.

The parameters which will be used in the low temperature model, as shown in Figure 6.9, are also provided in Table 6.2 below, along with the 25°C parameters, so that they can be utilized by others who wish to model and evaluate this battery for their application.

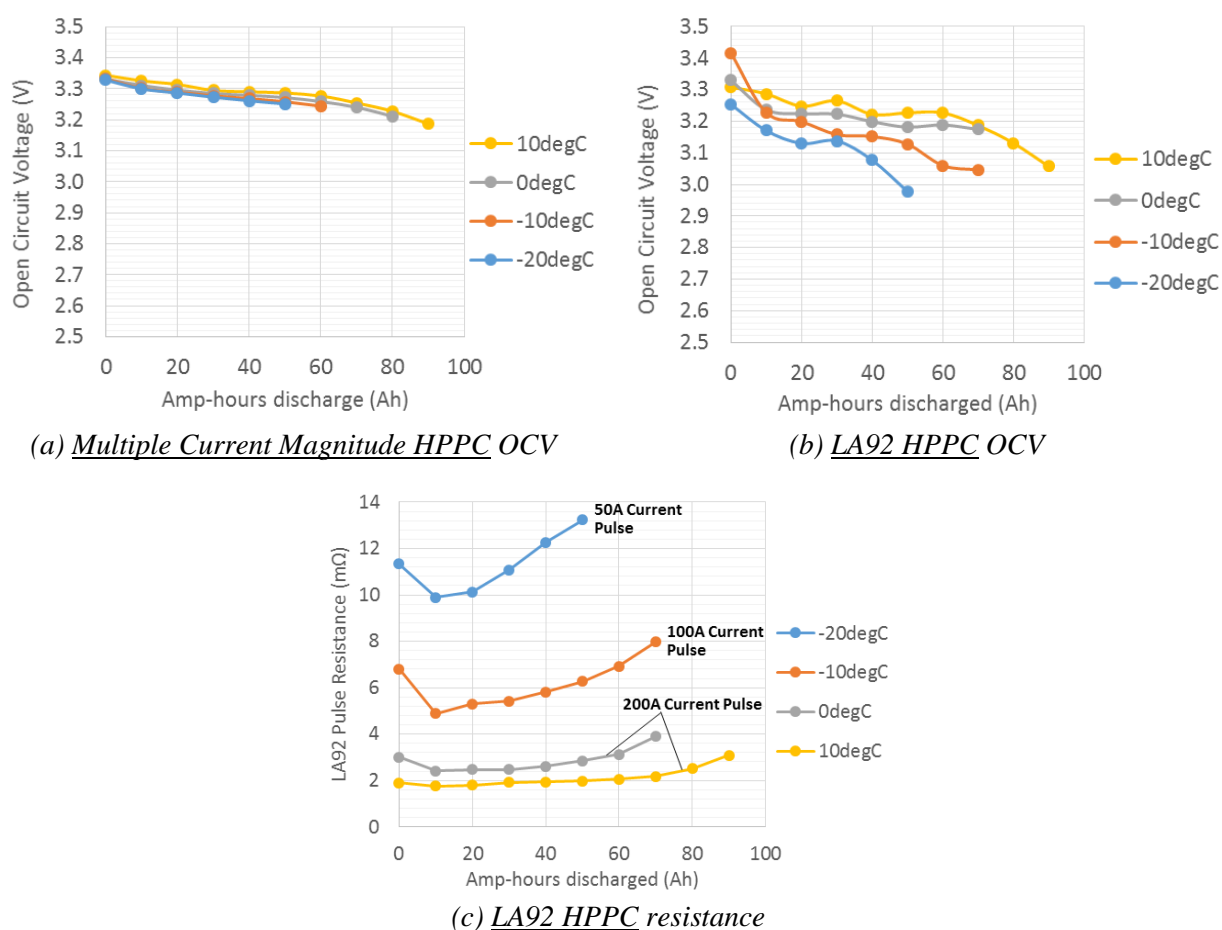


Figure 6.9 Comparison of open circuit voltage and resistance from HPPC tests

Table 6.2 LA92 HPPC Resistance and Open Circuit Voltage for Calb 100Ah LiFePO₄ Battery**25°C**

<i>Ah discharged</i>	0 Ah	10 Ah	20 Ah	30 Ah	40 Ah	50 Ah	60 Ah	70 Ah	80 Ah	90 Ah	95 Ah	100 Ah
<i>OCV</i>	3.367 V	3.31 V	3.281 V	3.289 V	3.258 V	3.263 V	3.261 V	3.234 V	3.191 V	3.177 V	3.116 V	2.915 V
<i>R_{batt-dis}</i>	1.29mΩ	1.02mΩ	1.01mΩ	1.07mΩ	1.07mΩ	1.12mΩ	1.16mΩ	1.17mΩ	1.23mΩ	1.41mΩ	1.62mΩ	2.01mΩ
<i>R_{batt-ch}</i>	1.13mΩ	0.89mΩ	0.95mΩ	0.91mΩ	1.00mΩ	0.98mΩ	0.94mΩ	0.95mΩ	1.04mΩ	0.96mΩ	1.00mΩ	1.07mΩ

10°C

<i>Ah discharged</i>	0 Ah	10 Ah	20 Ah	30 Ah	40 Ah	50 Ah	60 Ah	70 Ah	80 Ah	90 Ah
<i>OCV</i>	3.308 V	3.287 V	3.248 V	3.265 V	3.222 V	3.227 V	3.227 V	3.187 V	3.131 V	3.057 V
<i>R_{batt-dis}</i>	1.9 mΩ	1.8 mΩ	1.8 mΩ	1.9 mΩ	1.9 mΩ	2.0 mΩ	2.1 mΩ	2.2 mΩ	2.5 mΩ	3.1 mΩ
<i>R_{batt-ch}</i>	2.2 mΩ	2.0 mΩ	2.1 mΩ	2.1 mΩ	2.3 mΩ	2.3 mΩ	2.2 mΩ	2.2 mΩ	2.1 mΩ	2.3 mΩ

0°C

<i>Ah discharged</i>	0 Ah	10 Ah	20 Ah	30 Ah	40 Ah	50 Ah	60 Ah	70 Ah
<i>OCV</i>	3.330 V	3.240 V	3.225 V	3.223 V	3.200 V	3.182 V	3.189 V	3.174 V
<i>R_{batt-dis}</i>	3.0 mΩ	2.4 mΩ	2.5 mΩ	2.5 mΩ	2.7 mΩ	2.9 mΩ	3.1 mΩ	3.9 mΩ
<i>R_{batt-ch}</i>	3.0 mΩ	3.0 mΩ	3.0 mΩ	3.1 mΩ	3.3 mΩ	3.3 mΩ	2.6 mΩ	2.5 mΩ

-10°C

<i>Ah discharged</i>	0 Ah	10 Ah	20 Ah	30 Ah	40 Ah	50 Ah	60 Ah	70 Ah
<i>OCV</i>	3.417 V	3.228 V	3.200 V	3.158 V	3.152 V	3.128 V	3.060 V	3.046 V
<i>R_{batt-dis}</i>	6.8 mΩ	4.9 mΩ	5.3 mΩ	5.4 mΩ	5.8 mΩ	6.3 mΩ	6.9 mΩ	8.0 mΩ

-20°C

<i>Ah discharged</i>	0 Ah	10 Ah	20 Ah	30 Ah	40 Ah	50 Ah
<i>OCV</i>	3.254 V	3.171 V	3.13 V	3.138 V	3.077 V	2.978 V
<i>R_{batt-dis}</i>	11.3 mΩ	9.9 mΩ	10.1 mΩ	11.1 mΩ	12.3 mΩ	13.2 mΩ

6.2.2 Low Temperature Butler-Volmer Modeling

The low temperature battery model takes the same simple form, consisting of an open circuit voltage in series with a resistor, as was utilized in Chapter 5 and presented in Figure 5.1. To extend the model to low temperature, the resistance, which was just a function of SOC of the battery in Chapter 5, is now also a nonlinear function of current amplitude. The purpose of the battery model is to estimate the battery current and terminal voltage for a commanded battery output power. Previously the battery current and terminal voltage could be calculate analytically, directly as a function of the linear circuit model. Due to the non-linear current dependent resistance at low

temperatures, the battery current and output voltage must be solved in a different way. A polynomial, power, or natural log curve could for example be fitted to the resistance versus current curve, and an analytical solution for the non-linear model could be utilized. For the purposes of how the model will be used here though, in a Matlab model of the vehicle and a dynamic programming optimization model, there is little benefit to utilizing an analytical model. A computationally efficient table based model will therefore be utilized, in which the nonlinear battery resistance is determined from a lookup table with linear interpolation between points.

The full process of utilizing the model is described in full in the following steps, and a Matlab script with example calculations is provided as well. First the inputs to the model are declared, then the open circuit voltage and resistance are determined, followed by calculation of the maximum power capability of the battery, limitation of the power command to be less than the maximum power capability, and calculation of the current for the given power command.

Step 1: Declare Model Inputs

The first step is to declare the model inputs, which consist of the power command, the state of charge of the battery, voltage limits, and the temperature dependent battery parameters. The

Table 6.3 Butler-Volmer Model Inputs for Example Calculations

Symbol	Description	Value for Example Calculations
P_{b-cmd}	Battery Power Command	225 W
Ah	Amp-hours discharged from battery	33 Ah
V_{b-min}	Minimum battery voltage limit	2.5 V
V_{b-max}	Maximum battery voltage limit	3.6 V
Ah_{table}	Ah points corresponding with OCV_{table} & $R_{nom-table}$	-10°C Ah points in Table 6.2
OCV_{table}	Table of OCV points	-10°C LA92 OCV points in Table 6.2
$R_{nom-table}$	Table of resistance points	-10°C LA92 resistance points in Table 6.2
$I_{BV-table}$	Current points corresponding with $BV_{scale-table}$	-10°C current points in Table 6.1
$BV_{scale-table}$	Table of Butler-Volmer resistance scaling coefficients	-10°C normalized resistance points in Table 6.1

Step 2: Lookup Open Circuit Voltage and Nominal Resistance

The battery's state of charge dependent parameters, open circuit voltage and nominal resistance, are defined in the LA92 HPPC parameters of Table 6.2. Because the measurements are only taken at fixed intervals, the values must be interpolated between measurements. Linear interpolation is used, and the linear interpolation function, which uses the same syntax as the Matlab linear interpolation function, is defined in (6.1). The function finds the location of input x in x_{table} using linear interpolation, and outputs the corresponding y value from y_{table} . The open circuit voltage, OCV , and nominal resistance, R_{nom} , are looked up using (6.2), (6.3), where Ah_{table} , OCV_{table} , and $R_{nom-table}$ are defined in Table 6.3 above. The open circuit voltage and nominal resistance values for the example calculation, with -10°C temperature and 33Ah discharged, are shown in Figure 6.10.

$$y = \text{interp1}(x_{table}, y_{table}, x, 'linear') \quad (6.1)$$

$$OCV = \text{interp1}(Ah_{table}, OCV_{table}, Ah, 'linear') \quad (6.2)$$

$$R_{nom} = \text{interp1}(Ah_{table}, R_{nom-table}, Ah, 'linear') \quad (6.3)$$

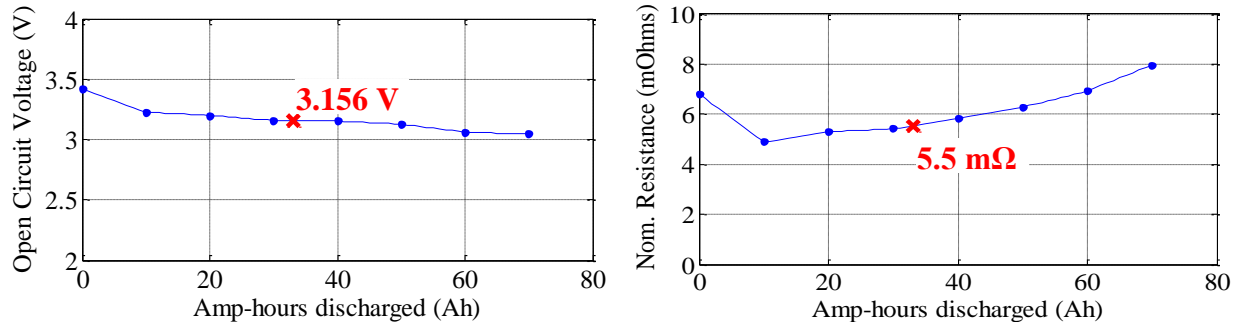


Figure 6.10 Open circuit voltage and nominal resistance values for example low temperature battery model calculation

Step 3: Calculate Nonlinear Resistance Curve

The nonlinear resistance curve the product of the nominal resistance measured with the LA92 HPPC test, R_{nom} , and the nonlinear Butler-Volmer equation scaling table, $BV_{scale-table}$, as is

described in Figure 6.2 above and defined (6.4) in below. The resulting battery current versus resistance curve for the example -10°C temperature and 33Ah discharged case is then given in Figure 6.11, and will be utilized in the following steps to find the battery current corresponding to the power command.

$$R_{BV-table} = R_{nom}BV_{scale-table} \quad (6.4)$$

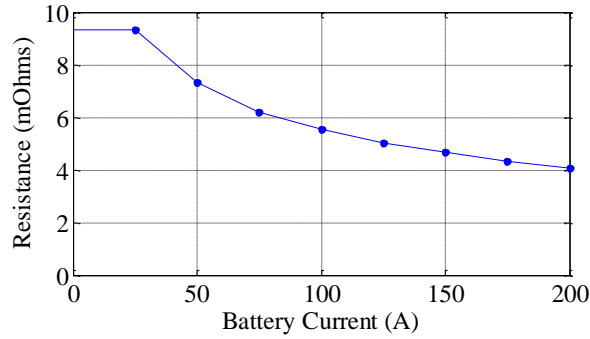


Figure 6.11 Nonlinear resistance versus current characteristic, $R_{BV-table}$, for example low temperature battery model calculation

Step 4: Calculate Maximum Battery Power Limit

One important function of the battery model is to limit the battery output power such that the battery's voltage limits are not exceeded. For a battery model with linear resistance, as is typically used for room temperature cases, the power limit can be calculated directly. Due to the nonlinear resistance though, a few extra steps are required to calculate the power limit. First a table of battery output voltage versus current values, as defined in $I_{BV-table}$, is calculated in (6.5), and the corresponding output power for each current value is calculated in (6.6).

$$V_{b-table} = OCV - I_{BV-table} R_{BV-table} \quad (6.5)$$

$$P_{b-table} = V_{batt-table} I_{BV-table} \quad (6.6)$$

The maximum output power and current for the minimum voltage value, V_{b-min} , is then looked up from the output voltage, power, and current tables in (6.7) and (6.8), and the maximum values are overlaid with the voltage and power tables in Figure 6.12 for the example model values.

$$P_{b-max} = \text{interp1}(V_{b-table}, P_{b-table}, V_{b-min}, 'linear') \quad (6.7)$$

$$I_{b-max} = \text{interp1}(V_{b-table}, I_{b-table}, V_{b-min}, 'linear') \quad (6.8)$$

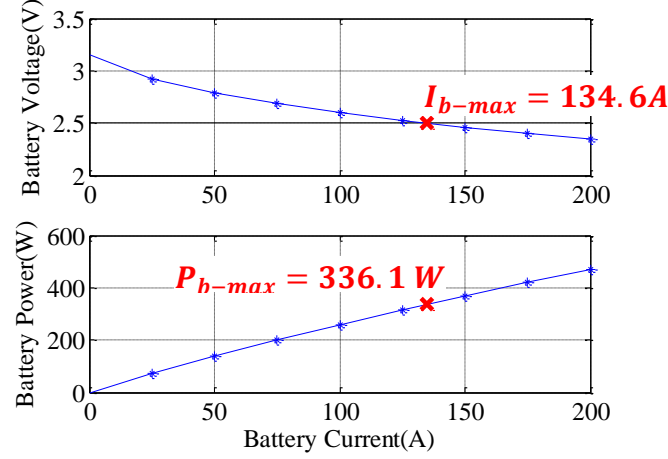


Figure 6.12 Maximum discharge current and power limit for example low temperature battery model calculation

The power command, P_{b-cmd} , is then limited in (6.9) to the maximum power capability from (6.7) above.

$$P_{b-cmd} = \begin{cases} P_{b-cmd} > P_{b-max}, P_{b-max} \\ P_{b-cmd} < P_{b-max}, P_{b-cmd} \end{cases} \quad (6.9)$$

Step 5: Model Output - Lookup Battery Current and Resistance

The final step is to lookup the battery current and resistance for the commanded power, which was defined as 225W for this example case. The battery current, I_b , is looked up as a function of battery power command in (6.10) and the battery resistance at that current is looked up in (6.11).

$$I_b = \text{interp1}(P_{b-table}, I_{b-table}, P_{b-cmd}, 'linear') \quad (6.10)$$

$$R_{b-at-max} = \text{interp1}(I_{b-table}, R_{BV-table}, I_b, 'linear') \quad (6.11)$$

For the 225W example case, the model predicts a current of 84.9A and a resistance of 5.94mΩ, as shown in Figure 6.13, and a battery terminal voltage of 2.65V. To calculate battery performance

for a drive cycle, this model is implemented in a loop, with battery amp-hours updated each iteration.

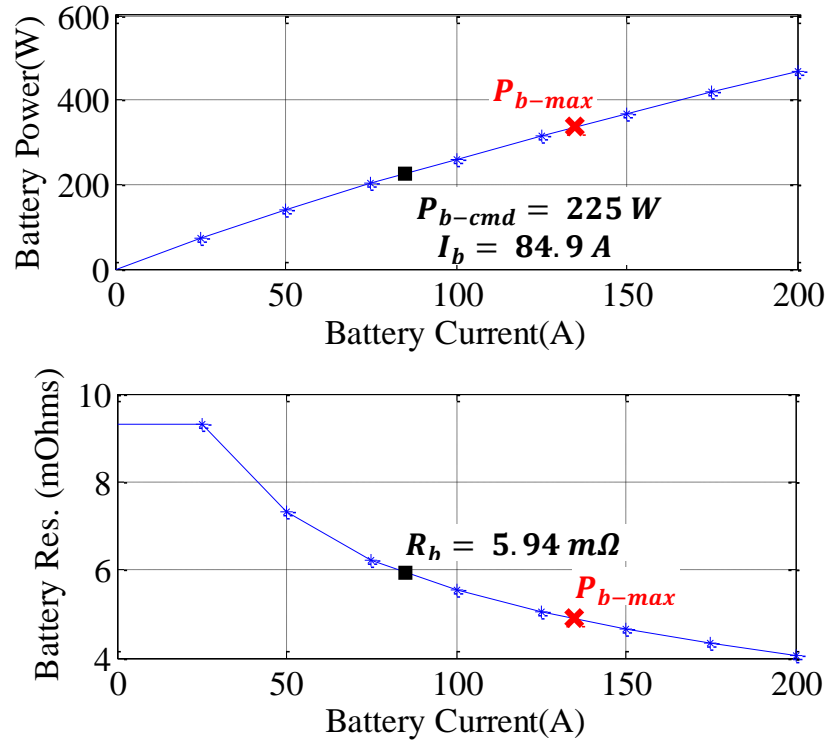


Figure 6.13 Battery current and resisted calculated for example low temperature battery model calculation

6.2.3 Electric Truck Battery Pack Power Capability Calculated with Low Temperature Model

An additional application of the model presented above is to calculate the power capability of the battery for temperature, over the full range of SOC. The charge and discharge power capability are calculated using the model parameters in Table 6.1 and Table 6.2, for 108 series connected cells as utilized in the electric truck, is given below in Figure 6.1, showing that battery power capability is strongly effected by temperature. The truck drivetrain is rated for 150kW, and about 50kW is required to drive mildly (UDDS and HWFET) and 100kW to drive moderately (LA92), so the truck's performance is significantly limited at temperatures of 0°C or less. The charge power capability is observed to be somewhat less effected by temperature, but the truck's Calb

LiFePO₄ batteries are not rated to charge at temperature below 0°C, so no regenerative braking energy be captured by the battery at these low temperatures.

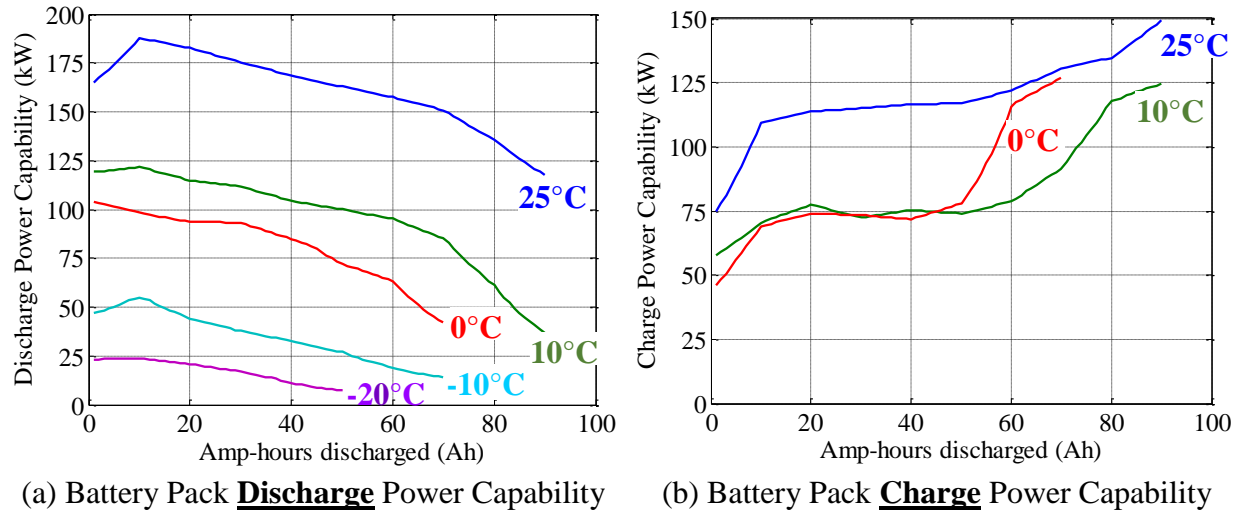


Figure 6.14 Truck battery pack discharge and charge power capability calculated from Butler-Volmer model for 2.5V min and 3.6V max cell voltages

6.2.4 Implementation of Model in Matlab with Example Results

While the model is described in detail in the prior section, implementing the model in a computationally efficient and mathematically correct fashion is not trivial. To enable easy adoption of this low temperature battery model by other researchers, a standalone version of the model was developed in Matlab and the code is provided in Table 6.4 below. The code functions exactly as the model presented above, with some minor differences in implementation, and the code also includes the battery charging case and an option for a current command input, rather than a power command input. The parameter tables for 0°C with nonlinear Butler-Volmer equation resistance and for 25°C with linear resistance are included, and the parameter tables above for other temperatures, or parameters for other batteries, can easily be added. To try the code simply copy it from the document, paste it into a Matlab script page, and run the code with *ctrl+enter*. The

code in its existing form or in a modified form, such as implemented as a Matlab function, can be used by any other researchers, a reference of this work as the source is requested.

Table 6.4 Battery Model Implementation in Matlab – *Code can be Pasted Directly into a Matlab Script File and Run (ctl+enter)*

```

%*****%
% Step 1 Declare Battery Pack Parameters
N_series=1; %Number of series connected cells
V_batt_max=3.6*N_series; %Maximum pack voltage
V_batt_min=2.5*N_series; %Minimum pack voltage

%Choose battery case: 0degC w/ Butler Volmer or 25degC w/ fixed resistances
switch '0degC'
case '0degC'
    %Amp-hours which OCV and resistance data corresponds with
    Ah_table=[0 10 20 30 40 50 60 70 80];
    % Parameters for Calb 100Ah Battery at 0degC, LA92 HPPC w/ 1h pauses
    %Open circuit voltage
    V_ocv_table= [3.33 3.24 3.225 3.223 3.200 3.182...
                  3.189 3.174 3.067]*N_series;
    %Discharge resistance for 10sec, 200A pulse
    R_batt_dis_table= [3.0 2.42 2.49 2.49 2.65 2.88...
                      3.13 3.90 5.61]/1000*N_series;
    %Charge resistance for 10sec, 50A pulse
    R_batt_ch_table = [3.04 3.04 3.05 3.08 3.31 3.30...
                      2.59 2.46 2.4]/1000*N_series;
    %Current points associated with BV resistance scale points
    BV_Ibatt_array = [0 50 100 150 200 ...
                     250 300];
    %Create mirrored negative current points
    BV_Ibatt_array=[fliplr(-BV_Ibatt_array) BV_Ibatt_array(2:end)];
    %Declare resistance scaling array to account for Butler Volmer Effect
    %Normalized to 200A discharge point
    BV_Rbatt_dis_scale=[1.58 1.58 1.29 1.12 1.00 0.91...
                       0.84];
    %Create mirrored Rbatt scale for negative current points
    BV_Rbatt_dis_scale=[fliplr(BV_Rbatt_dis_scale) BV_Rbatt_dis_scale(2:end)];
    %Use same BV curve as for discharge, but scale for 50A charge pulse point
    BV_Rbatt_ch_scale = BV_Rbatt_dis_scale/1.58;

case '25degC'
    %Amp-hours which OCV and resistance data corresponds with
    Ah_table=[0 10 20 30 40 50 60 70 80 90 95 100];
    % Parameters for Calb 100Ah Battery at 0degC, LA92 HPPC w/ 1h pauses
    %Open circuit voltage
    V_ocv_table = [3.367 3.31 3.281 3.289 3.258 3.263 ...
                  3.261 3.234 3.191 3.177 3.116 2.915]*N_series;
    %Charge and Discharge Resistances
    R_batt_dis_table = [1.29 1.02 1.01 1.07 1.07 1.12 ...
                       1.16 1.17 1.23 1.41 1.62 2.01]/1000*N_series;
    R_batt_ch_table = [1.13 0.89 0.95 0.91 1.00 0.98 ...
                      0.94 0.95 1.04 0.96 1.00 1.07]/1000*N_series;

```

```

%Set Butler Volmer scaling arrays such that resistances are fixed and not
%a function of current
BV_Ibatt_array=[-1 0 1];
BV_Rbatt_dis_scale=[1 1 1];BV_Rbatt_ch_scale=[1 1 1];
end

%*****%
% Step 2 Declare battery power array
P_batt_command=true; %true for power command, false for current command
if P_batt_command == true %Power command case
    %Example power waveform
    P_batt_cmd = [0*ones(1,300) 25*ones(1,300) 50*ones(1,300)...
        75*ones(1,300) 100*ones(1,300) 0*ones(1,300) -100*ones(1,300)...
        -75*ones(1,300) -50*ones(1,300) -25*ones(1,300) 0*ones(1,300)]'*10;
    I_batt_cmd = P_batt_cmd; %initialize I_batt_cmd
else %Current command case
    %Example current waveform:
    I_batt_cmd = [0*ones(1,300) 100*ones(1,300) 200*ones(1,300)...
        300*ones(1,300) 400*ones(1,300) 0*ones(1,300) -400*ones(1,300)...
        -300*ones(1,300) -200*ones(1,300) -100*ones(1,300) 0*ones(1,300)]';
    P_batt_cmd = I_batt_cmd; %initialize P_batt_cmd
end
delta_T = 1; %step time in seconds
Ah_starting_point = 0; %Ah, set to 0 to start with fully charged battery

%*****%
% Step 3
%Apply power or current command to battery model and calculate results
%Preallocate values to zero arrays
Ah_batt=0*P_batt_cmd; R_batt_ch=0*P_batt_cmd; R_batt_dis=0*P_batt_cmd;
R_batt=0*P_batt_cmd; V_OCV= 0*P_batt_cmd; R_batt_nom=0*P_batt_cmd;
I_batt=0*P_batt_cmd; P_batt=0*P_batt_cmd;

for i=1:length(P_batt_cmd)
    %Calculate Ah
    if i==1
        Ah_batt(i)=Ah_starting_point;
    else
        Ah_batt(i)=Ah_batt(i-1)+I_batt(i-1)*delta_T/3600;
    end

    %Lookup open circuit battery voltage and nominal battery resistance
    V_OCV(i)=interp1(Ah_table,V_ocv_table,Ah_batt(i),'linear','extrap');
    R_batt_nom(i)=interp1(Ah_table,(P_batt_cmd(i)>=0).*R_batt_dis_table+...
        (P_batt_cmd(i)<0).*R_batt_ch_table,Ah_batt(i),'linear','extrap');

    %Declare BV array for either charge or discharge case
    Rbatt_BV_array = ((P_batt_cmd(i)>=0)*BV_Rbatt_dis_scale + ...
        (P_batt_cmd(i)<0)*BV_Rbatt_ch_scale)*R_batt_nom(i);

    %Calculate max charge or discharge current
    Vbatt_array=V_OCV(i)-BV_Ibatt_array.*Rbatt_BV_array;
    if P_batt_cmd(i)>=0 %Discharging case
        Ibatt_max=interp1(Vbatt_array,BV_Ibatt_array,V_batt_min,...
            'linear','extrap');
    end
end

```

```

else %Charging case
    Ibatt_max=interp1(Vbatt_array,BV_Ibatt_array,V_batt_max,...
                    'linear','extrap');
end

%Create Rbatt, Ibatt, and Pbatt arrays over useable power range
%Array in 1A steps so model works well with low current rated batteries
Ibatt_array = (P_batt_cmd(i)>=0)*[0:1:ceil(Ibatt_max-1) Ibatt_max]+...
    (P_batt_cmd(i)<0)*[Ibatt_max floor(Ibatt_max+1):1:0];
Rbatt_array = interp1(BV_Ibatt_array,Rbatt_BV_array,Ibatt_array,...
    'linear',min(Rbatt_BV_array));
Pbatt_array = (V_OCV(i)-Ibatt_array.*Rbatt_array).*Ibatt_array;

if P_batt_command==true %Power command input
    %Look up battery current
    I_batt(i)=interp1(Pbatt_array,Ibatt_array,P_batt_cmd(i),...
        'linear',(P_batt_cmd(i)>=0)*max(Ibatt_array)...
        +(P_batt_cmd(i)<0)*min(Ibatt_array));
    %Look up Butler Volmer battery resistance
    R_batt(i)=interp1(Ibatt_array,Rbatt_array,I_batt(i),'linear',...
        min(Rbatt_BV_array));
    %Calculate output power
    P_batt(i) = (V_OCV(i)-I_batt(i)*R_batt(i))*I_batt(i);
else %Current command input
    %Look up battery power
    P_batt(i)=interp1(Ibatt_array,Pbatt_array,I_batt_cmd(i),...
        'linear',(P_batt_cmd(i)>=0)*max(Pbatt_array)...
        +(P_batt_cmd(i)<0)*min(Pbatt_array));
    %Look up Butler Volmer battery resistance
    R_batt(i)=interp1(Pbatt_array,Rbatt_array,P_batt(i),...
        'linear',min(Rbatt_BV_array));
    %Calculate output power
    I_batt(i)=(V_OCV(i)-(V_OCV(i)^2-4*P_batt(i))*...
        R_batt(i))^0.5)/(2*R_batt(i));
end
end
%Calculate battery terminal voltage
V_batt_out=V_OCV-I_batt.*R_batt;

%*****%
% Step 4 - Plot Results
figure
if P_batt_command ==true
    subplot(4,1,3); plot(P_batt_cmd,'r')
else
    subplot(4,1,2); plot(I_batt_cmd,'r')
end
hold on
subplot(4,1,1); plot(V_batt_min*ones(length(V_batt_out),1),'k'); hold on
subplot(4,1,1); plot(V_batt_max*ones(length(V_batt_out),1),'k'); hold on
subplot(4,1,1); plot(V_batt_out); ylabel('Voltage(V)'); grid on
subplot(4,1,1); plot(V_batt_max,':k');
subplot(4,1,2); plot(I_batt); ylabel('Current(A)'); grid on
subplot(4,1,3); plot(P_batt); ylabel('Power(W)'); grid on
subplot(4,1,4);plot(cumtrapz(I_batt)/3600),ylabel('Amp-hours(Ah)');grid on;
if P_batt_command ==true

```

```

subplot(4,1,3); legend('Command','Output')
else
subplot(4,1,2); legend('Command','Output')
end

```

The example model code provided in Table 6.4 also contains an example power and current command profile. When run, the model code will automatically produce the following plots given in Figure 6.15, which show the model predicted battery voltage, current, power, and amp-hours for current and power profiles. The plots show that the model limits battery output power or current to be less than the commanded value when the upper or lower voltage limits are reached.

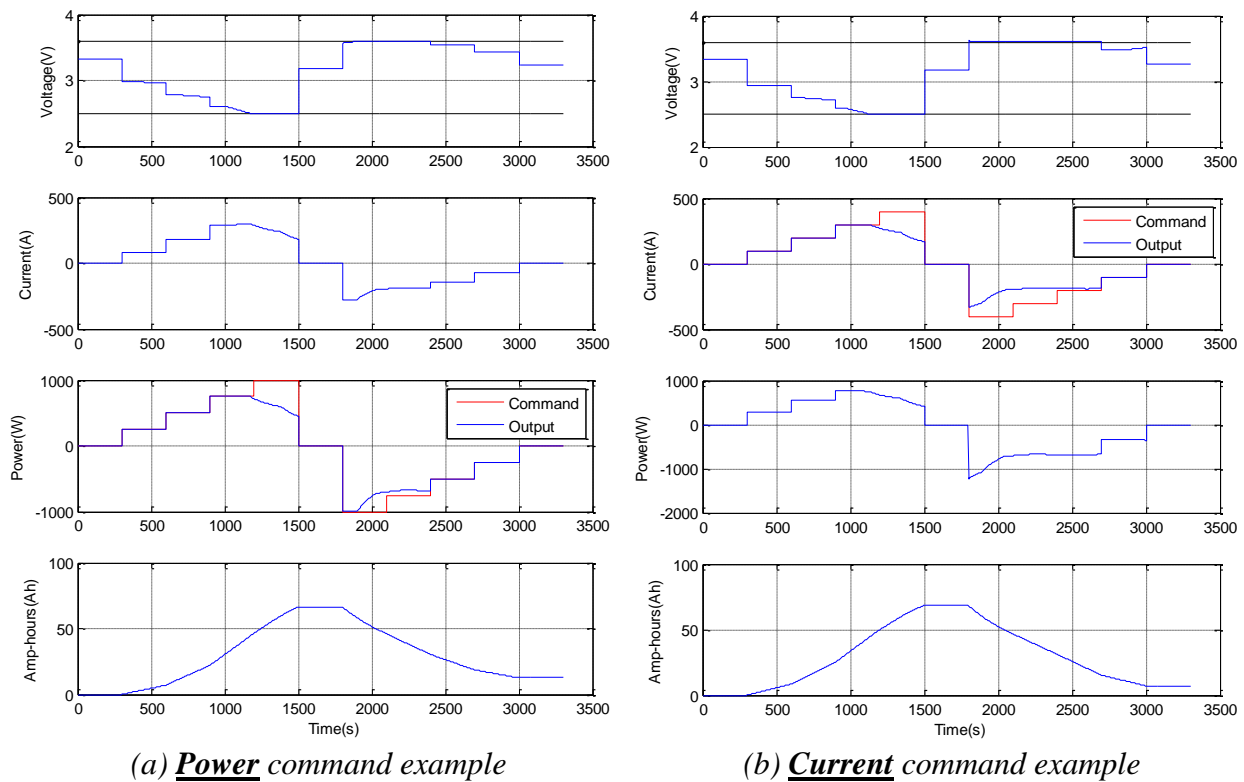


Figure 6.15 Butler-Volmer battery model calculated parameters for Calb cell at 0°C

One further example of the model's use is provided in Figure 6.16 below, where the measured battery output current and voltage for an LA92 drive cycle at 0°C is overlaid on the model predicted battery current and voltage. The measured and model predicted values align well, showing qualitatively that the presented model is functional and performs well under these circumstances.

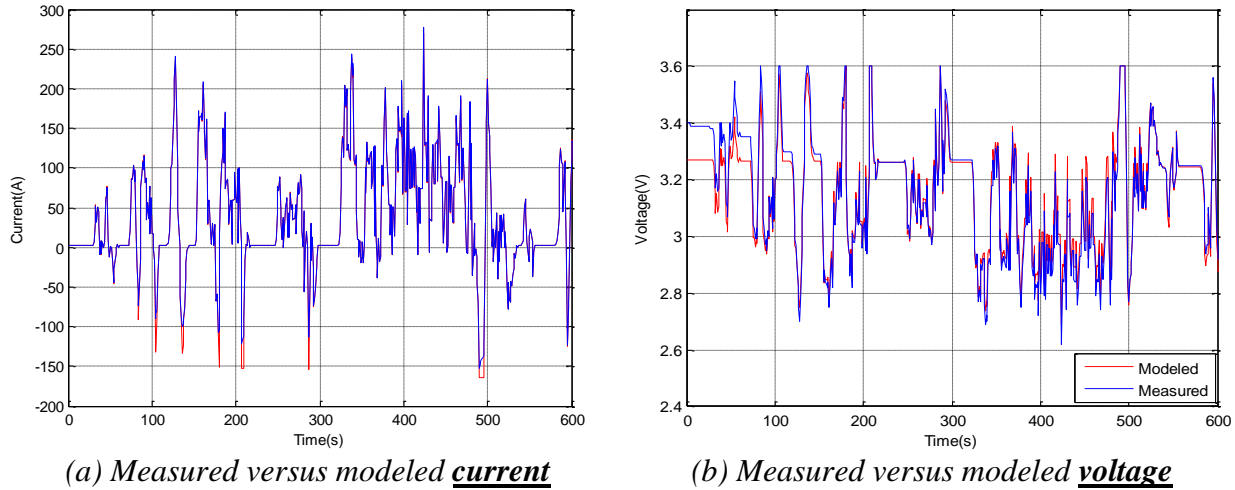


Figure 6.16 Example of Butler-Volmer model predicted versus measured results for 0°C LA92 Calb battery test results

6.3 Ultracapacitor Characterization Testing and Modeling

6.3.1 Ultracapacitor Characterization Testing

Ultracapacitors have two important parameters associated with their performance, capacitance and series resistance, both of which are a function of the open circuit voltage and the temperature of the ultracapacitor. A single ultracapacitor pack is tested in this section, a 48V Maxwell pack rated to have capacitance of 165F and series resistance of 6.3m Ω , as specified in Table 6.5 below. The pack is tested to confirm the manufacturer's capacitance and resistance specifications, as well as to determine how the parameters vary with open circuit voltage and temperature.

Table 6.5 Ultracapacitor Pack Specifications Provided by Manufacturer

Manufacturer / Model	Maxwell / BMOD0165 P048
# of cells in series	18
Capacitance	3000F (cell) / 165F (pack)
Maximum Voltage	48V (2.67V/cell)
Nominal Energy	53 Wh
Series Resistance	6.3m Ω @ 25°C
Mass	13.5 kg
Volume	12.7 liters

Series resistance is measured by applying a charge or discharge current pulse to the ultracapacitor, measuring the voltage at the end of the pulse, and then measuring the open circuit voltage 5 seconds following the pulse, as shown in Figure 6.17 below. The charge and discharge resistance are then calculated from the measurements in (6.12) and (6.13). For the Maxwell ultracapacitor module tested here, a charge and discharge pulse current of 200A was used and the tests were performed in increments of approximately 2V.

$$R_{uc-discharge} = \frac{OCV - V_{dis}}{I_{dis}} \quad (6.12)$$

$$R_{uc-charge} = \frac{OCV - V_{ch}}{I_{ch}} \quad (6.13)$$

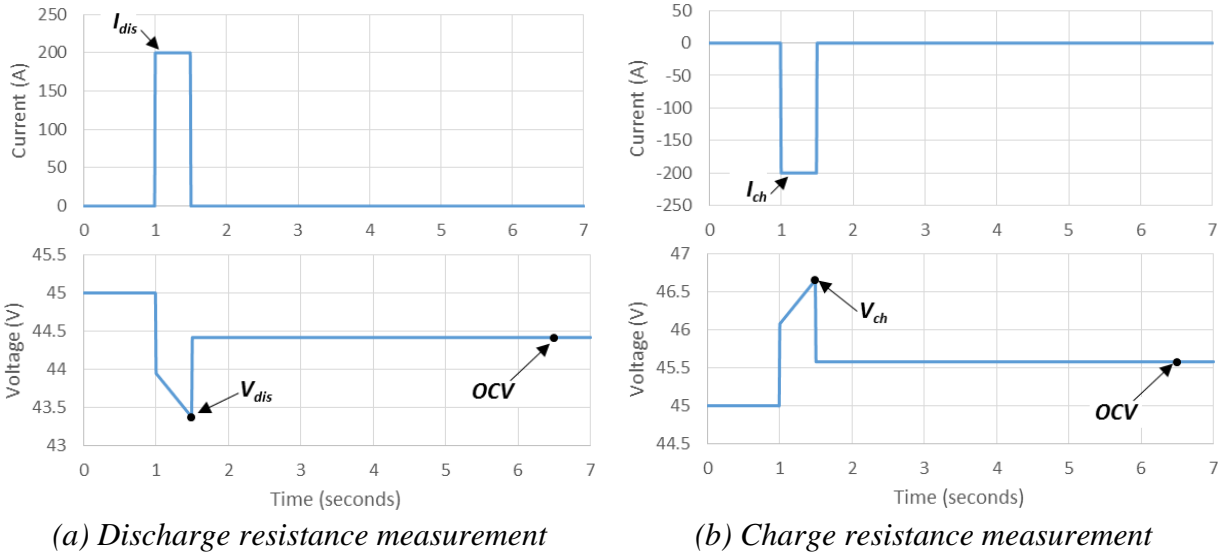


Figure 6.17 Current pulse waveforms and voltage measurement points for ultracapacitor charge and discharge resistance measurement test

The ultracapacitor capacitance is measured by slowly discharging the ultracapacitor, at about a 5C or 10 minute discharge rate equivalent, and calculating the capacitance as the change in charge divided by the change in voltage, $C = \Delta Q / \Delta V_{uc}$, as is illustrated in Figure 6.18 below. For the 48V, 165F ultracapacitor module tested, a discharging rate of 10A was used and the ultracapacitor

capacitance was calculated in steps of 2V, providing sufficient resolution to show the capacitance changes as a function of open circuit voltage.

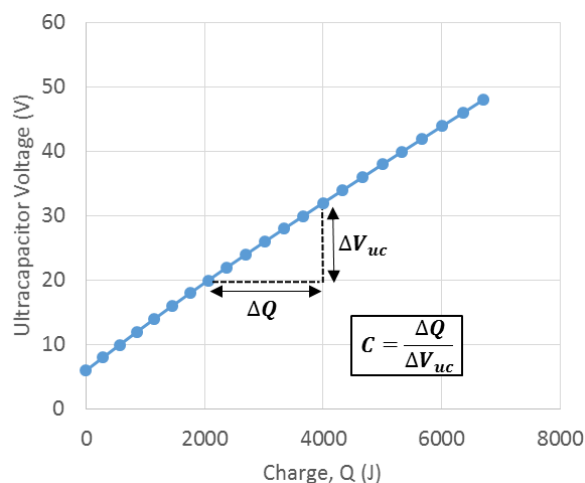


Figure 6.18 Method for calculating capacitance from measured ultracapacitor voltage versus charge characteristic

The charge and discharge resistance and capacitance tests were performed in steps of 2V over the full range of the ultracapacitor's open circuit voltage range, and the discharge resistance and capacitance results for the 0°C case are shown in Figure 6.19 below. The resistance is pretty consistent, varying by only about 0.5mΩ (10%) over the range of state of charge, while the

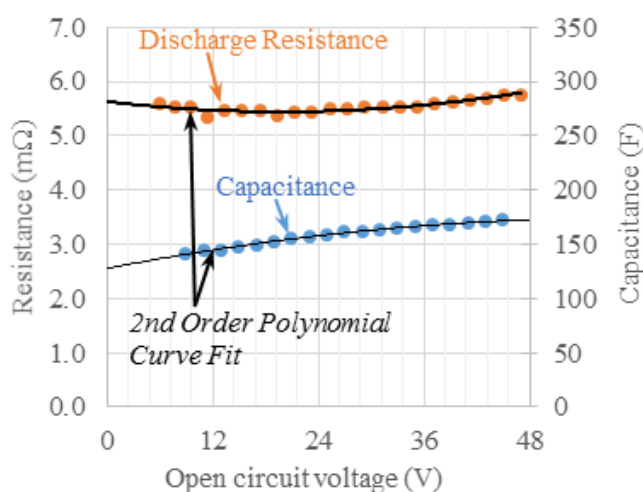


Figure 6.19 Experimentally measured ultracapacitor discharge resistance and capacitance with 2nd order polynomial curve fit for Maxwell BMOD165 at 0°C

capacitance varies by a somewhat greater amount, increasing from 140F at 10V by about 20% to 170F at 45F. Because the measurements are not performed at exact voltage intervals, and because the measurements cannot be performed at the minimum and maximum voltage ratings without exceeding those ratings, a 2nd order polynomial is fit to the measured results, as is also shown in Figure 6.19, and the parameter tables used by the model are derived from the polynomial curve fit.

The capacitance and resistance tests were performed over a wide range of temperatures, at -30°C, -20°C, -10°C, 0°C, 10°C, and 25°C. The resistance is shown in Figure 6.20 to be only mildly effected by temperature, with resistance increasing by only 30% when temperature is lowered from 25°C to -30°C. This change in resistance is much less than what was observed for the LiFePO₄ battery, which had resistance increase by ten-fold when temperature was reduced from 25°C to -20°C, showing that ultracapacitor's are much better suited for providing power in low temperature applications. The measured capacitance, shown in Figure 6.21, is only negligibly affected by temperature, meaning that the ultracapacitor will be able to provide approximately the same amount of energy at low temperatures as at warmer temperatures.

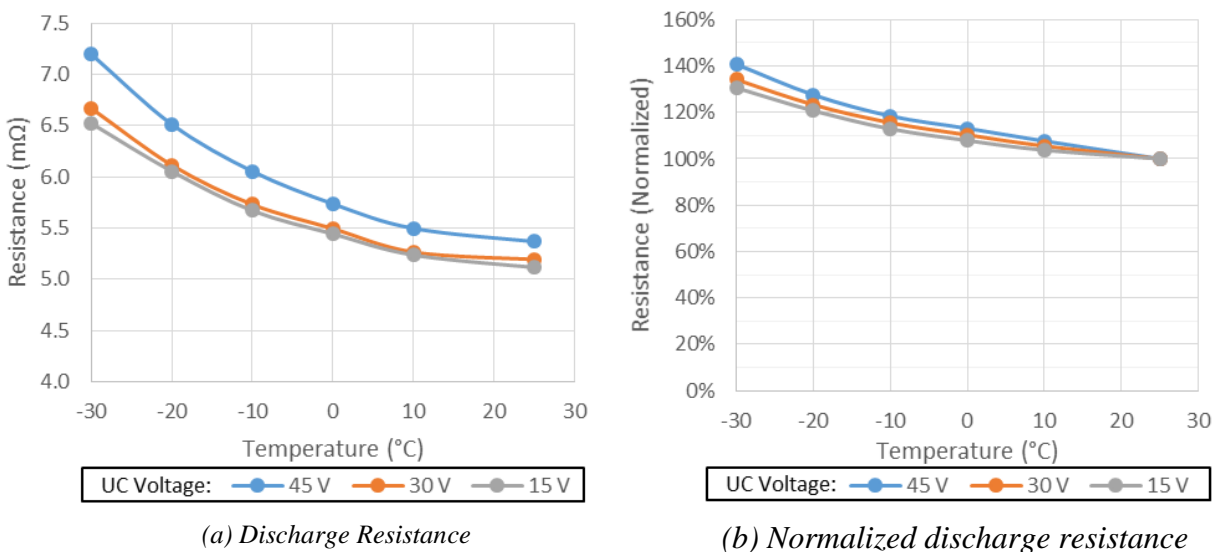


Figure 6.20 Maxwell BMOD165 ultracapacitor discharged resistance versus temperature

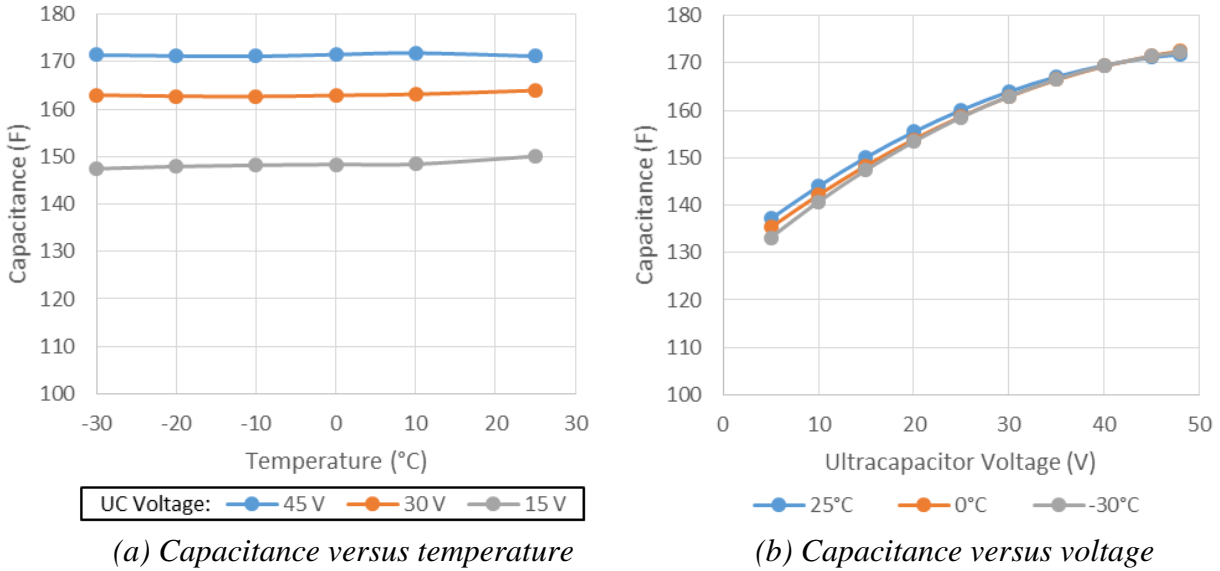


Figure 6.21 Maxwell BMOD165 ultracapacitor capacitance versus temperature

The measured charge and discharge resistance and capacitance is provided for each temperature as a function of the ultracapacitor's open circuit voltage in Table 6.6 and Table 6.7 below. These parameter tables are utilized directly in the model presented in the following subsections, and are provided so that they can be utilized by other researchers as desired.

Table 6.6 Ultracapacitor Pack Parameters at 25°C, 10°C, and 0°C

25°C Pack Temperature

OCV	0	2.5	5	10	15	20	25	30	35	40	45	48
$R_{UC-charge} (m\Omega)$	5.01	5.00	4.99	4.97	4.97	4.99	5.02	5.07	5.13	5.20	5.29	5.35
$R_{UC-discharge} (m\Omega)$	5.07	5.05	5.03	5.00	4.99	4.98	4.99	5.00	5.03	5.07	5.13	5.16
$C_{Farads} (F)$	130	133	137	144	150	155	160	164	167	170	171	172

10°C Pack Temperature

OCV	0	2.5	5	10	15	20	25	30	35	40	45	48
$R_{UC-charge} (m\Omega)$	5.24	5.22	5.20	5.18	5.17	5.19	5.22	5.27	5.33	5.42	5.52	5.59
$R_{UC-discharge} (m\Omega)$	5.41	5.37	5.33	5.27	5.24	5.22	5.23	5.27	5.32	5.40	5.50	5.57
$C_{Farads} (F)$	128	131	135	142	148	154	159	163	167	170	172	173

0°C Pack Temperature

OCV	0	2.5	5	10	15	20	25	30	35	40	45	48
$R_{UC-charge} (m\Omega)$	5.42	5.41	5.39	5.38	5.38	5.40	5.44	5.51	5.58	5.68	5.80	5.88
$R_{UC-discharge} (m\Omega)$	5.58	5.55	5.51	5.47	5.44	5.44	5.46	5.50	5.55	5.64	5.74	5.81
$C_{Farads} (F)$	128	132	135	142	148	154	159	163	166	169	172	173

Table 6.7 Ultracapacitor Pack Parameters at -10°C, -20°C, and -30°C**-10°C Pack Temperature**

OCV	0	2.5	5	10	15	20	25	30	35	40	45	48
$R_{UC-charge} (m\Omega)$	5.67	5.65	5.64	5.62	5.63	5.66	5.70	5.77	5.85	5.95	6.07	6.16
$R_{UC-discharge} (m\Omega)$	5.88	5.82	5.78	5.71	5.67	5.66	5.68	5.73	5.81	5.92	6.06	6.15
$C_{Farads} (F)$	128	132	135	142	148	154	159	163	166	169	171	172

-20°C Pack Temperature

OCV	0	2.5	5	10	15	20	25	30	35	40	45	48
$R_{UC-charge} (m\Omega)$	6.13	6.10	6.07	6.03	6.02	6.04	6.08	6.15	6.26	6.38	6.54	6.65
$R_{UC-discharge} (m\Omega)$	6.33	6.26	6.20	6.11	6.06	6.04	6.06	6.11	6.21	6.34	6.51	6.63
$C_{Farads} (F)$	127	131	135	142	148	154	159	163	166	169	171	172

-30°C Pack Temperature

OCV	0	2.5	5	10	15	20	25	30	35	40	45	48
$R_{UC-charge} (m\Omega)$	6.66	6.61	6.57	6.52	6.51	6.54	6.60	6.70	6.83	7.01	7.22	7.36
$R_{UC-discharge} (m\Omega)$	6.76	6.69	6.64	6.56	6.52	6.53	6.58	6.67	6.80	6.98	7.20	7.35
$C_{Farads} (F)$	125	129	133	141	147	153	159	163	167	169	171	172

6.3.2 Discrete Time Ultracapacitor Modeling

The battery model presented in the prior section was not described, or defined, in terms of time domain because the battery parameters are essentially static, meaning the parameters change only a very small amount in a single time step of the model and that any discretization effects can therefore be ignored. Because the ultracapacitor pack's stored energy is so small though, one of the key parameters, the open circuit voltage, changes very quickly for large currents, about 2.5V/s for a current of 400A for example. A small time step, or even a continuous time modeling tool such as Simulink could be used to eliminate the effects of discretization. The HESS dynamic programming optimization model takes about one minute per 2000 sample points to execute though, so an accurate discrete time model is a necessity for fast computation. A discrete time model, which includes open circuit voltage dependent resistance and capacitance values, is developed in this section and a Matlab script in which the model is implemented is included.

6.3.2.1 Demonstration of discrete time model characteristics

To illustrate how the developed discrete-time model and a continuous-time model compare, the model predicted results are given in Figure 6.22 below for a 1000A, 1 second current pulse applied to the Maxwell ultracapacitor pack with a discrete-time model time step of 1 second. The discrete-time model points shown in the figure illustrate many aspects of the model, including: (1) the capacitance and resistance values are calculated at the center of the time step, such that the average parameter values are used for calculating the model outputs, (2) the output power is calculated at the center of the voltage step, such the average power is output by the model, (3) the output voltage is calculated at the end of the time step, allowing the model to ensure voltage limits are not exceeded at any point during the time step, and (4) the open circuit voltage is also calculated half way through the time step, ($n+0.5$), and is utilized for calculations in the model. Figure 6.22 also

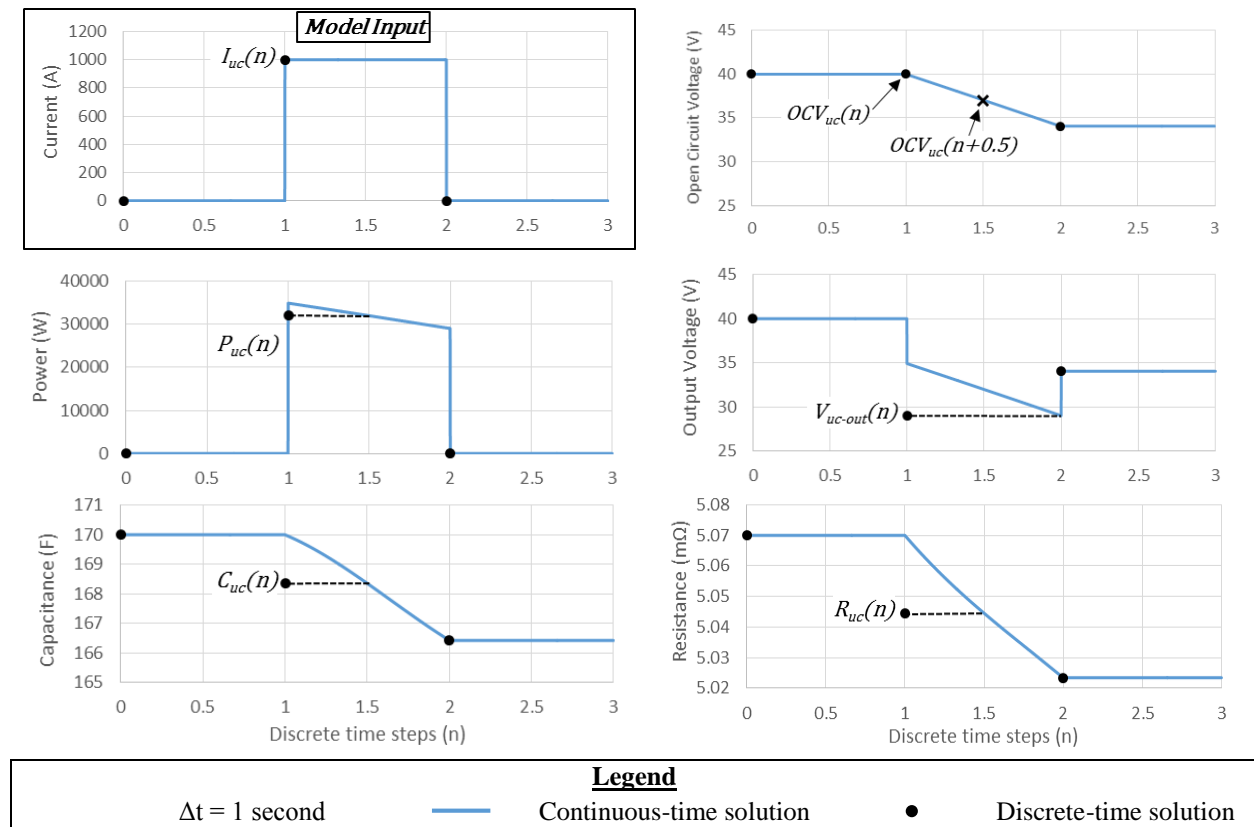


Figure 6.22 Ultracapacitor model discrete time solution overlaid with continuous time solution for one second, 1000A current pulse

shows that the discrete time model solution is in fact equal to the continuous time model solution because the model values are equal at time step $n=2$.

6.3.2.2 Declare Model Inputs

The model inputs include the measured ultracapacitor parameters, as collected in the prior section for a 48V Maxwell ultracapacitor module, the initial ultracapacitor voltage, ultracapacitor terminal voltage limits, the discrete-time step period, and either a current or power command, as is shown in Table 6.8 below. The model's mathematical equations, which utilize the defined model inputs, are developed in the next subsection and the model is then implemented in Matlab code and demonstrated using the parameters defined in Table 6.8.

Table 6.8 Definition of Ultracapacitor model inputs including parameters used in Matlab example

Symbol	Description	Parameters Used in Matlab Example
I_{uc-cmd} or P_{uc-cmd}	Ultracapacitor Current or Power Command	Array of points in code
$OCV_{uc}(1)$	Ultracapacitor open circuit voltage at initial time step	45 V
V_{uc-min}	Minimum ultracapacitor voltage limit	15 V
V_{uc-max}	Maximum ultracapacitor voltage limit	45 V
OCV_{table}	Table of OCV points	Voltage points in Table 6.6 & Table 6.7
$R_{uc-table}$	Table of resistance points	Discharge or charge resistance points in Table 6.6 & Table 6.7
C_{table}	Table of capacitance points	Capacitance points in Table 6.6 & Table 6.7
Δt	Period of discrete time steps	1 second

6.3.2.3 Discrete-time model equations

The discrete-time model equations are presented and described in this subsection for the discharging, current command case. The charging case and power command case utilize the same methodology as developed here, and are included in the example Matlab code. The discrete-time model solution consists of calculating the open circuit voltage value for the current time step,

iteratively calculating of the maximum current limit and limiting the current command to that value, iterative calculating of the capacitance and open circuit voltage values, and finally calculating the resistance, output power, and output voltage, as is done in steps 1-5 below. The series of steps is then repeated for each time step, $1:N$, where N is the total number of current or power command input points.

Step 1 – Calculate current open circuit value

For the first time step, $n=1$, the open circuit voltage parameter should be set to the initial value. The open circuit voltage for the current time step, $OCV_{uc}(n)$, is the sum of the prior value of voltage and the change in voltage calculated by solving the charge relationship for a capacitor, $Q=CV$, for voltage, and substituting $I\Delta t$ for Q , as shown in (6.14).

$$OCV_{uc}(n) = OCV_{uc}(n-1) + \frac{I_{uc}(n-1)\Delta t}{C_{uc}(n-1)} \quad (6.14)$$

Step 2 – Iteratively maximum current limit

The maximum charge or discharge current is defined as the current which will result in a terminal voltage at the end of the time step which is equal to the minimum or maximum voltage limit. Two factors contribute to the value of the terminal voltage at the end of the time step, the change in open circuit voltage over the time step and the resistive voltage drop, both of which are included in the calculation of the maximum discharge current in (6.19).

There are several steps required to get the final calculation of the discharge current limit. First, the capacitance, resistance, and open circuit voltage parameters for the calculation must be initialized, as is done in (6.15), (6.16), and (6.17), using lookup tables as was demonstrated in the battery modeling section. The parameters are initialized to their instantaneous values at time step n . Their correct value, defined as the value at the center of the time step as shown in Figure 6.22,

must be determined in an iterative fashion because the capacitance and open circuit voltage at $n+0.5$ parameters are interdependent.

$$C_{uc-lim}(n) = \text{interp1}(OCV_{UC-table}, C_{table}, OCV_{uc}(n), 'linear') \quad (6.15)$$

$$R_{uc-lim}(n) = \text{interp1}(OCV_{UC-table}, R_{UC-table}, OCV_{uc}(n), 'linear') \quad (6.16)$$

$$OCV_{uc-lim}(n + 0.5) = OCV_{uc}(n) \quad (6.17)$$

$$OCV_{uc-old} = 0 \quad (6.18)$$

The interdependence of these parameters is made clear in (6.21) where $OCV_{uc-lim}(n + 0.5)$ is a function of $C_{uc-lim}(n)$ and in (6.22) where $C_{uc-lim}(n)$ is a function of $OCV_{uc-lim}(n + 0.5)$. While there are two equations and two unknowns in a sense, one of the *equations* is a lookup table and is therefore not easily solvable as a system of equations. The solution is instead achieved by simply iterating the series of calculations in (6.19) to (6.23) until the prior and current OCV values are within 10^{-4} , as represented with the while loop surrounding the equations. Only 3-5 iterations are typically needed, so this is a computationally efficient solution. Following the calculation of maximum current value, $I_{UC-dis-max}(n)$, the current command is limited to that value in (6.24).

while $(OCV_{uc-lim}(n + 0.5) - OCV_{uc-old}) > 10^{-4}$

$$I_{UC-dis-max}(n) = \frac{OCV_{uc}(n) - V_{uc-min}}{R_{uc-lim}(n) + \frac{\Delta t}{C_{uc-lim}(n)}} \quad (6.19)$$

$$OCV_{uc-old} = OCV_{uc-lim}(n + 0.5) \quad (6.20)$$

$$OCV_{uc-lim}(n + 0.5) = OCV_{uc}(n) - \frac{I_{uc-dis-max}(n)(\Delta t/2)}{C_{uc-lim}(n)} \quad (6.21)$$

$$C_{uc-lim}(n + 0.5) = \text{interp1}(OCV_{UC-table}, C_{table}, OCV_{uc-lim}(n + 0.5), 'linear') \quad (6.22)$$

$$R_{uc-lim}(n) = \text{interp1}(OCV_{UC-table}, R_{uc-table}, OCV_{uc-lim}(n + 0.5), 'linear') \quad (6.23)$$

End

$$I_{uc-cmd}(n) = \begin{cases} I_{uc-cmd}(n) > I_{uc-dis-max}(n), I_{uc-dis-max}(n) \\ I_{uc-cmd}(n) < I_{uc-dis-max}(n), I_{uc-cmd}(n) \end{cases} \quad (6.24)$$

Step 3 – Iteratively calculate open circuit voltage at $n+0.5$ and capacitance value for current command

In the prior step the open circuit voltage at $n+0.5$ and the capacitance were calculated for the maximum discharge current case. In this step the values will be calculated for the actual current command. An iterative solution is also required, for the same reasons described in Step 2. First the capacitance value is initialized to the instantaneous value at the beginning of the time step in (6.25), and then the open circuit voltage at $n + 0.5$ is calculated with the initialized capacitance value in (6.26). Then the final capacitance and OCV values are determined by repeatedly calculating (6.28) through (6.30) until the current and prior OCV value, $OCV_{uc}(n + 0.5)$, are within 10^{-4} .

$$C_{uc}(n) = interp1(OCV_{UC-table}, C_{table}, OCV_{uc}(n), 'linear') \quad (6.25)$$

$$OCV_{uc}(n + 0.5) = OCV_{uc}(n) - \frac{I_{uc-cmd}(n)(\Delta t/2)}{C_{UC}(n)} \quad (6.26)$$

$$OCV_{uc-old} = 0 \quad (6.27)$$

while $(OCV_{uc}(n + 0.5) - OCV_{uc-old}) < 10^{-4}$

$$C_{UC}(n) = interp1(OCV_{UC-table}, C_{table}, OCV_{uc}(n + 0.5), 'linear') \quad (6.28)$$

$$OCV_{uc-old} = OCV_{uc}(n + 0.5) \quad (6.29)$$

$$OCV_{uc}(n + 0.5) = OCV_{uc}(n) - \frac{I_{uc-cmd}(n)(\Delta t/2)}{C_{UC}(n)} \quad (6.30)$$

end

Step 4 – Calculate resistance and power:

The average resistance over the time step is calculated in (6.31) by looking up the resistance value at the open circuit voltage at the center of the time step, $OCV_{uc}(n + 0.5)$. The average power

value is then calculated in (6.32), also using the OCV at the center of the time step.

$$R_{uc}(n) = \text{interp1}(\text{OCV}_{UC\text{-table}}, R_{uc\text{-table}}, \text{OCV}_{uc}(n + 0.5), 'linear') \quad (6.31)$$

$$P_{uc}(n) = (\text{OCV}_{uc}(n + 0.5) - I_{uc\text{-cmd}}(n)R_{uc}(n))I_{uc\text{-cmd}}(n) \quad (6.32)$$

Step 5 – Calculate output voltage at end of step, shows min/max values

The last value to calculate is the output voltage at the end of the time step, which is equal to the open circuit voltage at the beginning of the time step, $\text{OCV}_{uc}(n)$, minus the resistive voltage drop and the change in voltage due to the change of state of charge, as shown in (6.33).

$$V_{uc\text{-out}}(n) = \text{OCV}_{uc}(n) - I_{uc\text{-cmd}}(n)R_{uc}(n) - \frac{I_{uc\text{-cmd}}(n)\Delta t}{C_{UC}(n)} \quad (6.33)$$

6.3.3 Ultracapacitor Modeling Example – with Matlab Code

The discrete time model presented in the prior section was implemented in Matlab and is provided in Table 6.9 below. The equations were only provided for the discharge, current command case, but the model is implemented to allow both charging and discharging and a current or power command. The code includes the 25°C ultracapacitor pack parameters and an example current and power profile, and can be run by simply cutting and pasting the code into a Matlab script. The code is efficient, calculating 350 time steps per second on an Intel Core I5 processor, allowing several hour long profiles to be evaluated in less than a minute when a discrete-time step of one second is used. This code in its existing form or in a modified form, such as implemented as a Matlab function, may also be used by any other researchers, a reference of this work as the source is requested.

Table 6.9 Ultracapacitor Model Implementation in Matlab – *Code can be Pasted Directly into a Matlab Script File and Run (ctl+enter)*

```
%Ultracapacitor Model Example
%*****%
%Step 1 - Define Ultracapacitor Parameters
%Ultracapacitor Type: Maxwell BMOD165, 48V/165F/6.5mOhm, 25degC Model
```

```

%Open circuit voltage corresponding with each test point
OCV_table = [0 2.5 5 10 15 20 ...
             25 30 35 40 45 48];

%Charge resistance as a function of open circuit voltage
R_UC_charge_table = [5.01 5.00 4.99 4.97 4.97 4.99...
                    5.02 5.07 5.13 5.20 5.29 5.35]/1000;

%Discharge resistance as a function of open circuit voltage
R_UC_discharge_table = [5.07 5.05 5.03 5.00 4.99 4.98...
                      4.99 5.00 5.03 5.07 5.13 5.16]/1000;

%Calculated ultracapacitor farads as a function of open circuit voltage
Farads_table = [130 133 137 144 150 155 ...
               160 164 167 170 171 172 ];

%Declare minimum, maximum, and initial ultracapacitor pack voltage
V_uc_min=15;
V_uc_max=45; OCV_uc_init=45;

%*****%
%Step 2 - Define Test Profile - Positive Current/Power is Discharging
P_uc_command = true;
delta_T=1; %Model time step in seconds
if P_uc_command == true
    %Profile for power command example - same as current command output
    %power demonstrates model calculates power and current correctly
    P_UC_cmd = [0 250 500 1000 2000 1000 500 250 0 -250 -500 -1000 ...
               -2000 -1000 -500 -250 -0]*40;
    l=length(P_UC_cmd);cmd=P_UC_cmd;
else
    %Profile for current command example
    I_UC_cmd = [0 250 500 1000 2000 1000 500 250 0 -250 -500 -1000 ...
               -2000 -1000 -500 -250 -0];
    l=length(I_UC_cmd);cmd=I_UC_cmd;
end
%*****%
%Step 3 - Implement and run ultracapacitor model
%Preallocate variables to zero arrays
OCV_uc=zeros(l,1);
R_UC=zeros(l,1); I_UC=zeros(l,1); OCV_uc_t_half=zeros(l,1);
UC_farads=zeros(l,1); P_UC=zeros(l,1);UC_farads_lim=zeros(l,1);
OCV_uc_t_half_lim=zeros(l,1); P_UC_cmd_lim=zeros(l,1);R_UC_lim=zeros(l,1);

%Model calculations for current command input
for n=1:l
    if n>1
        %Calculate ultracapacitor open circuit voltage for current time
        %step using farads at center of last time step - prevents
        %discretization effects
        OCV_uc(n)=-I_UC(n-1)*(delta_T)/UC_farads(n-1)+OCV_uc(n-1);
    else
        OCV_uc(n)=OCV_uc_init; %Set to initial ultracap voltage value
    end
    %Choose R_UC table value based on whether charging or discharging
    R_UC_table = (cmd(n)>=0).*R_UC_discharge_table+...
                (cmd(n)<0).*R_UC_charge_table;
    %Calculate min/max UC current and power to stay within OCV limits
    if cmd(n)>0
        %Calculate discharge current and powerlimit

```

```

UC_farads_lim(n)=interp1(OCV_table, Farads_table, OCV_uc(n), 'spline', ...
    'extrap');
OCV_uc_t_half_lim(n)=OCV_uc(n);
R_UC_lim(n)=interp1(OCV_table, R_UC_table, OCV_uc_t_half_lim(n) ...
    , 'spline', 'extrap');
OCV_uc_old=0;
while abs(OCV_uc_t_half_lim(n)-OCV_uc_old)> 10^-4
    I_UC_max=(OCV_uc(n)-V_uc_min)/(R_UC_lim(n)+delta_T/ ...
        UC_farads_lim(n));
    OCV_uc_old=OCV_uc_t_half_lim(n);
    OCV_uc_t_half_lim(n)=-I_UC_max*(delta_T/2)/UC_farads_lim(n) ...
        +OCV_uc(n);
    UC_farads_lim(n)=interp1(OCV_table, Farads_table, ...
        OCV_uc_t_half_lim(n), 'spline', 'extrap');
    R_UC_lim(n)=interp1(OCV_table, R_UC_table, OCV_uc_t_half_lim(n) ...
        , 'spline', 'extrap');
end
P_UC_max = (OCV_uc_t_half_lim(n)-I_UC_max.*R_UC_lim(n)).*I_UC_max;
P_UC_min = -10^12; I_UC_min = -10^10; %set to small values for disch case
else
    %Calculate charge current and power limit
    UC_farads_lim(n)=interp1(OCV_table, Farads_table, OCV_uc(n), 'spline', ...
        'extrap');
    OCV_uc_t_half_lim(n)=OCV_uc(n);
    R_UC_lim(n)=interp1(OCV_table, R_UC_table, ...
        OCV_uc_t_half_lim(n), 'spline', 'extrap');
    OCV_uc_old=0;
    while abs(OCV_uc_t_half_lim(n)-OCV_uc_old)> 10^-5
        I_UC_min=(OCV_uc(n)-V_uc_max)/(R_UC_lim(n)+delta_T/ ...
            UC_farads_lim(n));
        OCV_uc_old=OCV_uc_t_half_lim(n);
        OCV_uc_t_half_lim(n)=-I_UC_min*(delta_T/2)/UC_farads_lim(n) ...
            +OCV_uc(n);
        UC_farads_lim(n)=interp1(OCV_table, Farads_table, ...
            OCV_uc_t_half_lim(n), 'spline', 'extrap');
        R_UC_lim(n)=interp1(OCV_table, R_UC_discharge_table, ...
            OCV_uc_t_half_lim(n), 'spline', 'extrap');
    end
    P_UC_min = (OCV_uc_t_half_lim(n)-I_UC_min.*R_UC_lim(n)).*I_UC_min;
    P_UC_max = 10^12; I_UC_max = 10^10; %set to large values for charge case
end

if P_uc_command == true %Power command case
    %Limit power command between min and max values
    P_UC_cmd_lim(n)=and(P_UC_cmd(n)<P_UC_max, P_UC_cmd(n)>P_UC_min) ...
        *P_UC_cmd(n)+(P_UC_cmd(n)>P_UC_max)*P_UC_max + ...
        (P_UC_cmd(n)<P_UC_min)*P_UC_min;
    R_UC(n)= interp1(OCV_table, R_UC_table, ...
        OCV_uc(n), 'spline', 'extrap');
    %Precalculate ultracapacitor current and init other parameters
    I_UC(n)=(OCV_uc(n)-(OCV_uc(n)^2-4*P_UC_cmd_lim(n)*R_UC(n))^0.5)/...
        (2*R_UC(n));
    I_UC_old = 10^10; %set to large value initially
    UC_farads(n)=interp1(OCV_table, Farads_table, OCV_uc(n), 'spline', ...
        'extrap');
    %Calculate approx. open circuit voltage halfway through time step

```

```

    OCV_uc_t_half(n)=-I_UC(n)*(delta_T/2)/UC_farads(n)+OCV_uc(n);
    while abs(I_UC(n)-I_UC_old)>10^-4 %stop when I_UC is consistent
        %Recalculate ultracapacitor current at center of time step
        I_UC_old=I_UC(n);
        I_UC(n)=(OCV_uc_t_half(n)-(OCV_uc_t_half(n)^2-4*P_UC_cmd_lim(n)*...
            R_UC(n))^0.5)/(2*R_UC(n));
        %Calculate open circuit voltage halfway through time step
        OCV_uc_t_half(n)=-I_UC(n)*(delta_T/2)/UC_farads(n)+OCV_uc(n);
        % Look up farads at center of time step
        UC_farads(n)=interp1(OCV_table,Farads_table,...
            OCV_uc_t_half(n),'spline','extrap');
        % Look up resistance at center of time step
        R_UC(n)=interp1(OCV_table,R_UC_discharge_table,...
            OCV_uc_t_half(n),'spline','extrap');
    end
else %Current command case
    %Limit current command between min and max values
    I_UC(n)=and(I_UC_cmd(n)<I_UC_max,I_UC_cmd(n)>I_UC_min)*...
        I_UC_cmd(n)+(I_UC_cmd(n)>I_UC_max)*I_UC_max + ...
        (I_UC_cmd(n)<I_UC_min)*I_UC_min;
    %Calculate approx. open circuit voltage halfway through time step
    UC_farads(n)=interp1(OCV_table,Farads_table,OCV_uc(n),'spline',...
        'extrap');
    OCV_uc_t_half(n)=-I_UC(n)*(delta_T/2)/UC_farads(n)+OCV_uc(n);
    OCV_uc_old=10^10; %initialize to large value

    while abs(OCV_uc_t_half(n)-OCV_uc_old)>10^-4 %stop when OCV consistent
        % Look up farads at center of time step
        UC_farads(n)=interp1(OCV_table,Farads_table,OCV_uc_t_half(n),...
            'spline','extrap');
        %Calculate open circuit voltage halfway through time step
        OCV_uc_old=OCV_uc_t_half(n);
        OCV_uc_t_half(n)=-I_UC(n)*(delta_T/2)/UC_farads(n)+OCV_uc(n);
    end
    R_UC(n)=interp1(OCV_table,R_UC_discharge_table,OCV_uc_t_half(n),...
        'spline','extrap');
end

%Calculate average ultracapacitor power by using
%voltage value halfway through time step
P_UC(n)=( OCV_uc_t_half(n)-I_UC(n).*R_UC(n)).*I_UC(n);
end
%Calculate output voltage at end of step, captures min/max value
V_uc_out=OCV_uc-I_UC.*R_UC-I_UC.*delta_T/UC_farads;

%*****%
%Step 4 - Plot results
figure
subplot(3,1,1); plot(V_uc_min*ones(length(OCV_uc),1),'k'); hold on
hold on
subplot(3,1,1); plot(V_uc_max*ones(length(OCV_uc),1),'k'); hold on
subplot(3,1,1); plot(V_uc_out,'.-r')
subplot(3,1,1); plot(OCV_uc,'.-'); ylabel('Voltage(V)'); grid on
legend('min','max','Output','Open circuit')
if P_uc_command == true
    subplot(3,1,3); plot(P_UC_cmd/1000,'.-r')
else

```

```

subplot(3,1,2); plot(I_UC_cmd, '.-r')
end
hold on
subplot(3,1,2); plot(I_UC, '.-'); ylabel('Current(A)'); grid on
subplot(3,1,3); plot(P_UC/1000, '.-'); ylabel('Power(kW)'); grid on
if P_uc_command ==true
    subplot(3,1,3); legend('Command', 'Output')
else
    subplot(3,1,2); legend('Command', 'Output')
end

```

The Matlab model results are given in Figure 6.23 for an example current and power command waveform, which are included in the example code above so these results can be easily recreated by the reader. For the current command case, the ultracapacitor voltage is initialized to 45V, then current command is stepped from 250A, to 500A, to 1000A, and then to 2000A at 5 seconds. The 2000A current point would result in a voltage below the 15V minimum voltage setpoint declared in Table 6.8 and in the code, so the current is set to the value which will result in a 15V output voltage, V_{uc-out} . The current remains limited for the rest of the discharge points and then hits the upper limit again when charged and for the power command example, demonstrating the model's that the model properly limits the output current/power of the ultracapacitor.

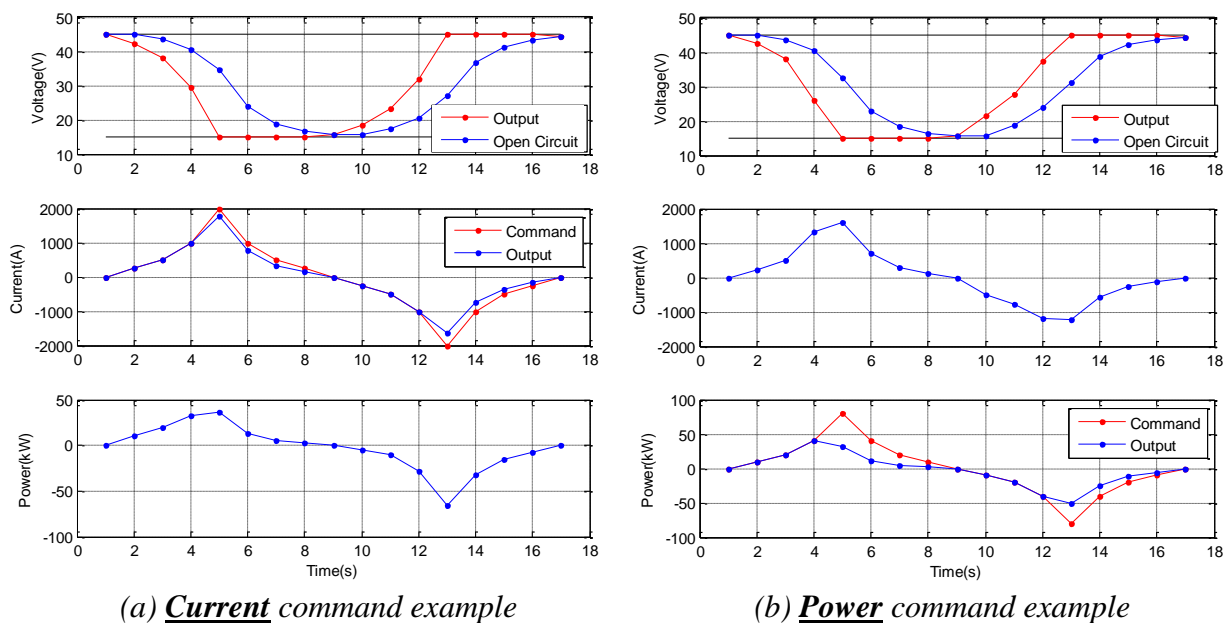


Figure 6.23 Ultracapacitor model output for current and power command examples

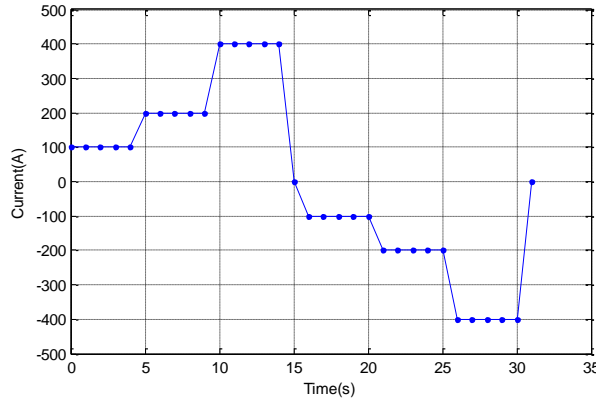
6.3.4 Demonstration of proper performance of ultracapacitor model

To illustrate that the power and the current command case function identically, the power and voltage output for an eight second current command profile is given in Table 6.10. The output power from the current command case is then used as the input for the power command case, and the output voltage and current values are shown to be equal, confirming the math and implementation are correct.

Table 6.10 Ultracapacitor model output for current command case and for power command case where current command power output is used for power command input

Time	Current Command Case			Power Command Case		
	I_{uc-cmd}	P_{uc}	V_{uc-out}	P_{uc-cmd}	I_{uc}	V_{uc-out}
0	0	0.0	45.00	0.0	0.00	45.00
1	200	8678.1	42.81	8678.1	200.00	42.81
2	400	16247.0	39.45	16247.0	400.00	39.45
3	600	22007.8	34.91	22007.8	600.00	34.91
4	0	-7911.2	40.15	-7911.2	-200.00	40.15
5	-200	-12461.7	42.42	-12461.7	-300.00	42.42
6	-300	-17644.1	45.28	-17644.1	-400.00	45.28
7	-400	0.0	43.25	0.0	0.00	43.25

One of the most important characteristics of the ultracapacitor model is that charge is conserved, meaning that coulombs are neither created nor absorbed by the ultracapacitor. A discrete-model which is not formed correctly will consume or create amp-hours, creating an extra energy source in the system, a highly undesirable model characteristic, one which was observed in this work prior to developing a proper model. To demonstrate that this discrete-time model is formed properly, a charge balanced current command waveform, which is shown in Figure 6.24 and results in a swing of about 50% of open circuit voltage, is applied to the modeled ultracapacitor 1000 times. After 1000 cycles the final ultracapacitor has only drifted 7.7mV (0.017%), demonstrating that the model is formed properly and does not create or consume charge.



Initial OCV_{uc}	45.0000 V
OCV_{uc} after repeating current waveform 1000 times	44.9923 V
Change in Voltage	7.7mV

Figure 6.24 Ultracapacitor current command waveform repeated 1000 times to demonstrate conservation of charge in model

A final check on the model's performance is to ensure that the modeled and measured results align well. The 48V Maxwell ultracapacitor was placed in a thermal chamber at 0°C and a 2.5 hour long current profile, representative of what the ultracapacitor would supply for an LA92 drive cycle, was applied to the ultracapacitor with the labs Digatron test equipment. The measured current was then used as the input to the ultracapacitor model, and resulting modeled and measured voltage along with the current are shown in Figure 6.25. One issue that is clearly evident is that the modeled ultracapacitor voltage is drifting upward over time, which is due to the integrated current command, plotted in amp-hours in Figure 6.26, drifting slowly upward over time. This

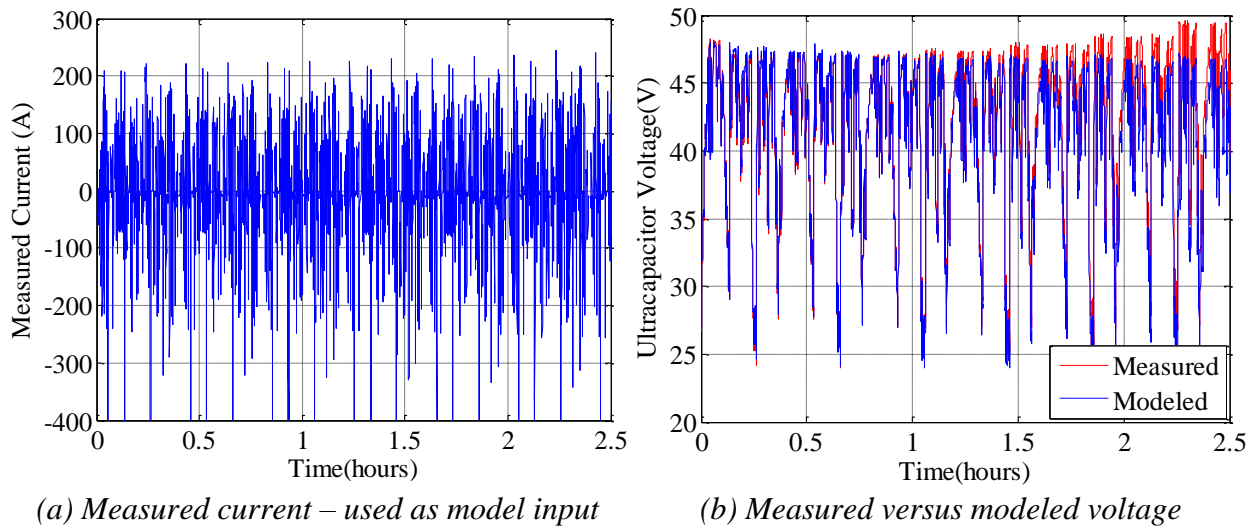


Figure 6.25 Ultracapacitor measured versus modeled results for LA92 drive cycle profile at 0°C

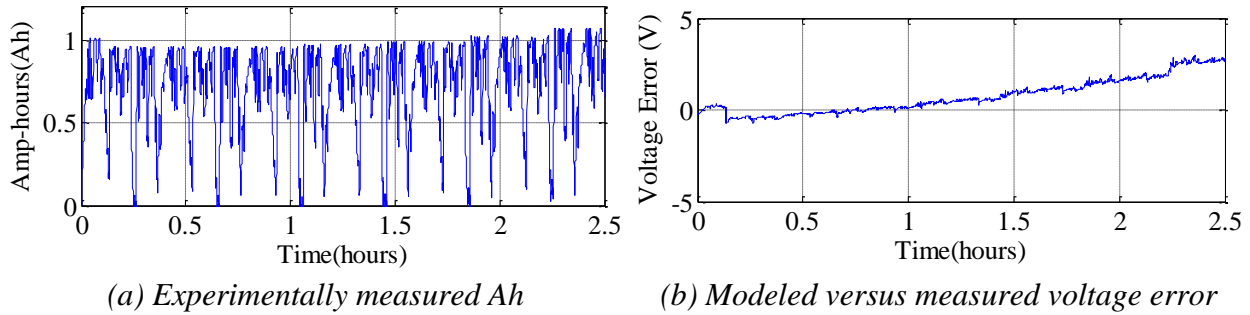


Figure 6.26 Ultracapacitor measured versus modeled results for LA92 drive cycle profile at 0°C

drift is almost certainly mostly due to measurement error. Over the 2.5 hour test the drift is about 100mAh, which would result from an average current measurement offset of just 40mA, which is just 0.01% of the 400A rating of the test channel, and is well within the accuracy rating of the equipment. The actual ultracapacitor pack may also consume some amp-hours, as the rated maximum leakage current of the ultracapacitors is several 5.2mA and the pack contains internal resistive balancing which turns on in the case of a cell voltage exceeding a limit. The voltage error plot of Figure 6.26 shows that the measured versus modeled voltage error, when neglecting the long term drift, is very small, indicating the model predicts output voltage well independent of current magnitude and open circuit voltage.

6.4 HESS Low Temperature System Modeling and Performance

To allow evaluation of the vehicle and HESS performance at low temperatures, the low temperature battery and ultracapacitor models are incorporated into the vehicle and HESS models developed in Chapters 4 and 5. For the battery only case, the Butler-Volmer battery model is simply used in place of the linear battery model used in the prior modeling. For the HESS cases, the Butler-Volmer battery model and the ultracapacitor model with low temperature data are incorporated in the dynamic programming (DP) model, and the way the DP model is utilized is modified in a few ways as is documented in the following section 6.4.1. The low temperature

dynamic programming model is then utilized in sections B, C, and D to examine the low temperature performance for a single drive cycle and temperature, for a range of drive cycles, temperatures, and system parameters, and for an example system proposed for implementation in the vehicle.

6.4.1 Dynamic programming model format

The theory behind the dynamic programming model, as well as additional details regarding its application to the HESS modeling is provided in Chapter 5. Further details are provided in this section to explain how the model is used for low temperature applications and to define the inputs and outputs of the optimal control function. The dynamic programming function utilized was developed by Sundstrom and Guzzela of ETH Zurich, and is described in full in [131]. The dynamic programming function is used to determine the control trajectory which will minimize the cost of a single-state system, where the system is the battery / ultracapacitor hybrid energy storage system, the single-state is the ultracapacitor voltage, the control variable is the ultracapacitor current, and the cost is motor power limiting and the HESS losses or other parameters, as described in Table 6.11. The DP algorithm first solves the HESS model for a grid of control and state variable points at each drive cycle time step. The algorithm

Table 6.11 Definition of control input, cost, and state variable for HESS dynamic programming model

Variable	Description of Variable	
Control function inp.U{1} (input)	Ultracapacitor Current	Minimum: - Current Rating Maximum: + Current Rating # of points in grid: 201
Cost trajectory C[64]	Cost – value to minimize through selection of control function trajectory	All cases: Motoring power limiting (goal: supply commanded output power) Options: (1) HESS losses (default) (2) Battery RMS current (3) Battery cycles
State variable X[64] (output)	Ultracapacitor Voltage	Minimum: 10V Maximum: 270V # of points in grid: 80

then searches through the grid of solutions to find the optimal control trajectory which minimizes the cost, and returns the resulting state variable trajectory and user defined outputs.

The DP model also has additional time dependent, but control and state variable independent inputs, as defined in Table 6.12. The most important input is the HESS power command, $\text{inp.W}\{1\}$, which is the power required by the vehicle for a given drive cycle, as determined from the vehicle model. The DP model calculates the battery power for each time step as a function of the control input (ultracapacitor current), state variable (ultracapacitor voltage), and dc/dc converter efficiency. If due to battery power limiting the HESS cannot provide the HESS power command, the cost function will be penalized pushing the DP algorithm to find a solution path with less power limiting.

Table 6.12 Tables of input parameters for dynamic programming model

Parameter	Parameter Description	Value or Source
$\text{Inp.T}\{s\}$	Time Step of Problem	1 second
$\text{inp.W}\{1\}$	HESS Power Command	Vehicle Model
$\text{inp.W}\{2\}$	Battery Open Circuit Voltage	1 st run of DPM model: <i>Parameters output by battery only model</i> 2 nd run of DPM model: <i>Parameters output by 1st run of DPM model</i>
$\text{inp.W}\{3\}$	Battery Discharge Resistance	
$\text{inp.W}\{4\}$	Battery Charge Resistance	
$\text{inp.W}\{5\}$	Battery Temperature (for selecting Butler-Volmer scaling curve)	Selected Temperature
$\text{inp.W}\{6\}$	Minimum Battery Voltage	270V (for electric truck)
$\text{inp.W}\{7\}$	Maximum Battery Voltage	389V (for electric truck)
$\text{inp.W}\{8\}$	Ultracapacitor type (selects ultracapacitor specs in case structure in function for DPM)	Select based on temperature and ultracapacitor size

The battery input parameters $\text{inp.W}\{2\}$ – $\text{inp.W}\{4\}$ are significant as well because a simplification has been made - the battery parameters are implemented as a function of time in the DP model, rather than as a function of battery state of charge - such that ultracapacitor voltage is the only state variable. While the battery SOC could be implemented as a second state variable,

the time to solve the control problem would increase from N to N^2 , where N is the number of drive cycle time steps. Because the battery parameters change slowly with battery SOC, an alternative approximate solution method was developed in lieu of the 2 state problem, described as follows:

Process to run DP

1. **Run vehicle model:** Determine power versus time requirement for drive cycle
2. **Run battery model:** Determine battery only case parameters for drive cycle power profile
3. **Run DP model 1st time:** Use drive cycle power profile and battery parameters from battery model in 2.
4. **Run DP model 2nd time:** Use drive cycle power profile and updated battery parameters calculated from 1st time DP model Ah trajectory in 3.

The process to run the DP model, as described above, starts with executing the vehicle model to determine the power versus time requirement. Then the battery model is used to determine the battery parameters versus time for the battery only case, and these parameters are used as the inputs for the 1st run of the DP model. For the 2nd run of the DP model an iterative approach is utilized, the battery parameters input to the model are calculated from the 1st run of the DP model. This requires only $2N$ time to get a solution which is relatively accurate, as is demonstrated in Figure 6.27, where the battery amp-hours discharge estimated by the model is with 0.5% and 0.05% of the final value in the second iteration for the US06 and UDDS drive cycles respectively. This calculation was performed for two of the worst cases, -10°C UDDS, where the difference between

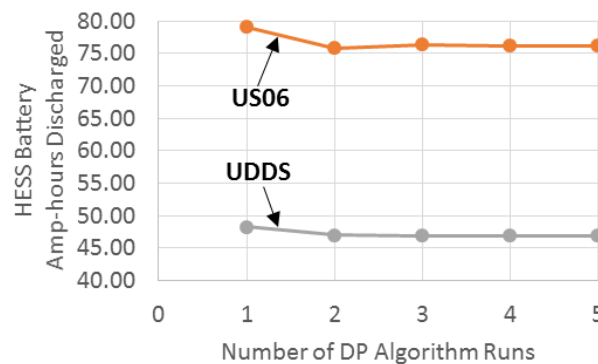


Figure 6.27 HESS battery amp-hours discharged versus number of iterative runs of DP algorithm for -10°C US06 and UDDS case

the battery only and HESS amp-hours is more than 30%, and -10°C US06, where there is heavy power limiting, and therefore represents the largest error that is likely to be encountered. This accuracy is considered sufficient for the work here, but more iterations could be performed to increase the accuracy, with iterations continuing until two successive value are within a set bound for example.

6.4.2 Performance for a Single Drive – LA92 at -10°C

The performance of the HESS is first examined for the electric truck for an LA92 drive cycle at -10°C with a 30F/270V ultracapacitor pack and 400A rated dc/dc converter. To illustrate just how much the HESS improves the performance, the commanded drive cycle power is shown with the battery only and HESS power in Figure 6.28 below. The battery power, in red, is heavily limited due to the low temperature (see Figure 6.14), meaning that the vehicle cannot provide sufficient power to actually follow the drive cycle. The HESS, which can provide as much as 300Wh of energy and 100kW of additional power, is able to prevent any motoring power limiting

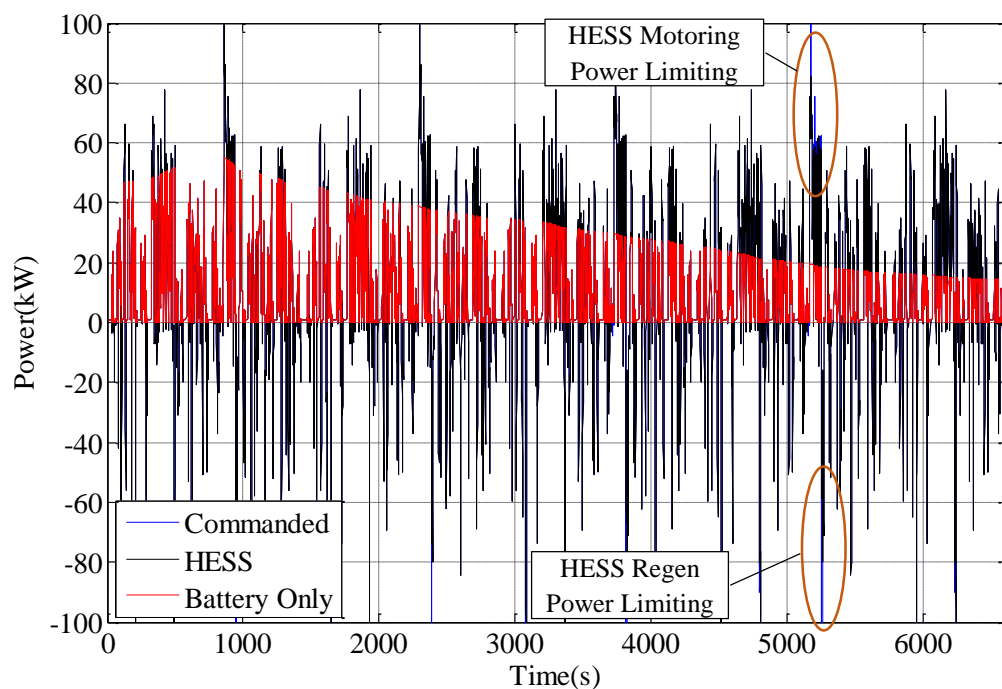


Figure 6.28 Commanded, HESS, and battery only output power for LA92 drive cycle at -10°C

from occurring until more than 5000 seconds into the drive cycle. The battery is also not rated to charge below 0°C , so no regenerative braking energy (negative power in figure) is captured for the battery only case, while almost all of the regenerative braking energy is captured for the HESS case, as can also be observed in Figure 6.28.

The ultracapacitor pack voltage, current, and power for the drive cycle is given in Figure 6.29, showing that much of the range of ultracapacitor voltage is used, but that the maximum dc/dc converter current rating of 400A is rarely utilized. The HESS performance is therefore more limited by the available energy than the converter power rating, which can be observed specifically around 5200 seconds, where the ultracapacitor discharges to a low voltage and the system is unable to provide the commanded motoring energy, as is noted in Figure 6.28. A larger ultracapacitor pack could be utilized, but this is undesirable due to the cost and size of the pack. A smaller pack even than has been modeled here is preferable, so battery heating may have to be considered as an alternative to prevent power limiting.

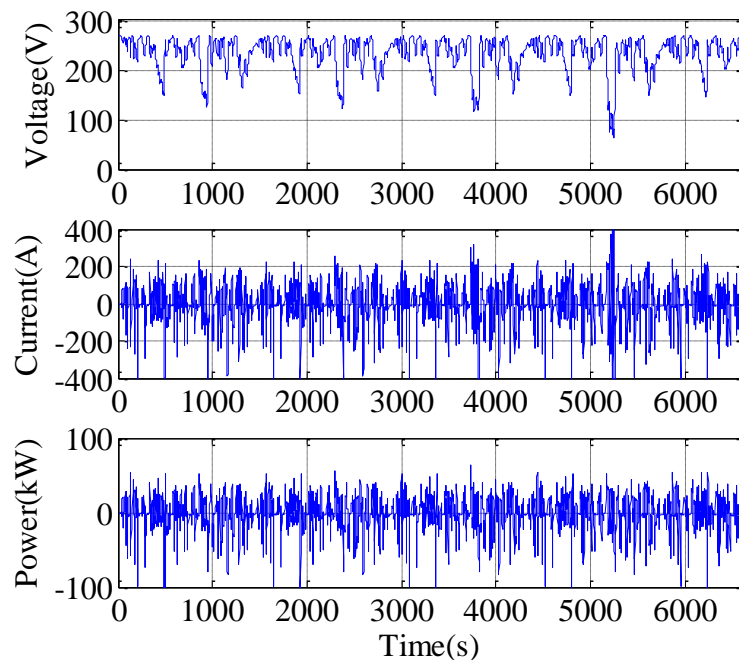


Figure 6.29 HESS ultracapacitor voltage, current, and power for LA92 drive cycle at -10°C

To provide more insight into how power is split between the battery and ultracapacitor, the HESS ultracapacitor, battery, and total power, along with ultracapacitor voltage and current, are shown in Figure 6.30 for a section of the drive cycle. The ultracapacitor starts out fully charged, and for the large power pulse starting around 2300 seconds the battery provides its maximum power capability and the ultracapacitor provides the remaining power. The ultracapacitor continues to supplement battery power until the regenerative braking power pulse around 2375 seconds, where all the regenerative power is consumed by the ultracapacitor pack replenishing it back to a full state of charge.

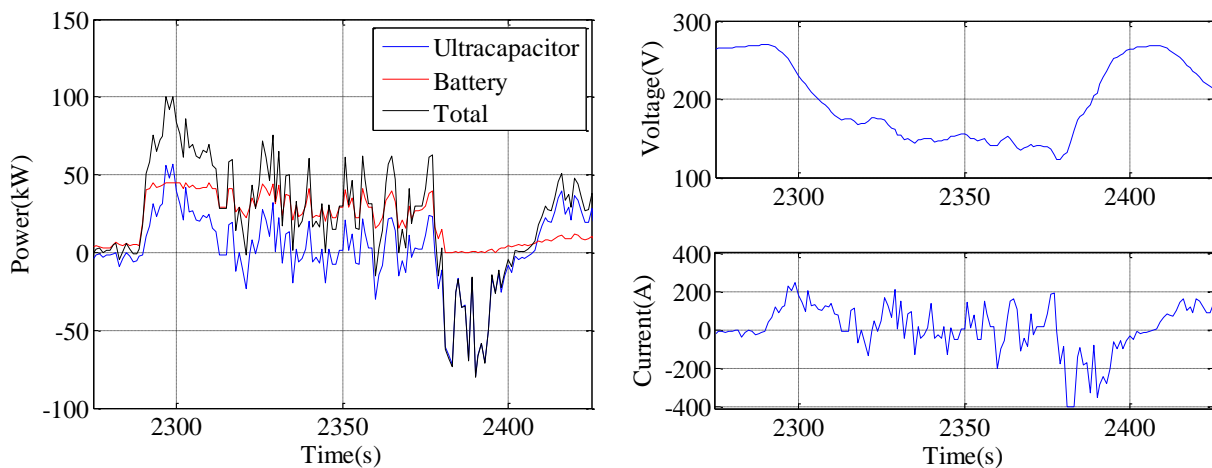


Figure 6.30 HESS ultracapacitor, battery, and total power and ultracapacitor voltage and current for selected portion of LA92 drive cycle at -10°C

The summary of battery only versus HESS performance, given in Table 6.13, shows that the HESS improves the performance of the system in several ways, including reducing the amp-hours consumed from the battery by 19.6% while at the same time increasing the motoring energy supplied by 25.8%. Two factors contribute to making the HESS able to supply more motoring energy with fewer amp-hours drawn from the battery. First, the sum of the HESS losses (battery, ultracapacitor, and dc/dc converter) is only 1,738 W, 23.3% less than the battery only case's 2,267 W of battery losses. Second, the HESS is able to absorb a large majority of the regenerative

braking energy, 194.6 Wh/mi, which is equivalent to returning about 35% of the motoring energy back to the energy storage system.

Table 6.13 Summary of Battery Only and HESS Performance for LA92 drive cycle at -10°C

Parameter	Battery Only	HESS	Difference
Battery Loss	2,267 W	1,279 W	-43.6%
Ultracapacitor Loss	-	273 W	-
DC/DC Converter Loss	-	186 W	-
Total ESS Loss Power	2,267 W	1,738W	-23.3%
Amp-hours Discharged	70.0 Ah	56.3 Ah	-19.6%
Motoring Energy Supplied	442 Wh/mi	556 Wh/mi	+25.8%
Regen Energy Absorbed	0 Wh/mi	194.6 Wh/mi	+∞%
ESS Total Output Energy (Sum Motoring and Regen Energy)	442 Wh/mi	361.8 Wh/mi	-18.1%

It is also desirable to have a parameter which describes how much range is improved by adding the HESS. Because the power output for the battery only case is so limited though, the simple comparison of amp-hours discharged for the commanded drive cycle as shown in Table 6.13 is not sufficient to describe how much range is improved. To provide an estimate of how much range is improved with the HESS, the ratio of motoring energy per battery amp-hour discharged for the HESS and battery only case is compared, as defined in (6.33) which shows range is improved by approximately 56% for this drive cycle and temperature.

$$\begin{aligned}
 \text{Approx. Increase in Range} &= \frac{\left(\frac{\text{HESS Motoring Energy}}{\text{HESS Ah}} \right)}{\left(\frac{\text{Battery Only Motoring Energy}}{\text{Battery Only Ah}} \right)} - 1 & (6.34) \\
 &= \frac{\left(\frac{556 \text{ Wh/mi}}{56.3 \text{ Ah}} \right)}{\left(\frac{442 \text{ Wh/mi}}{70 \text{ Ah}} \right)} - 1 = 56\%
 \end{aligned}$$

6.4.3 Summary of performance results for a range of temperatures, dc/dc converter ratings, ultracapacitor pack sizes, and control optimization goals

6.4.3.1 Example HESS with 400A dc/dc converter and 30F/270V Maxwell Ultracapacitor Pack

To illustrate how the battery only and HESS system performance compare over a wide range of operating parameters, the battery only and HESS model were used to estimate performance for temperatures ranging from -20°C to 25°C and for the HWFET, UDDS, LA92, and US06 drive cycles, which cover a range of mild to aggressive city and highway driving. The first group of results, in Figure 6.31 below, compares the energy provided by each system and the improvement in range achieved with the HESS. Ideally the system would be able to provide the full commanded

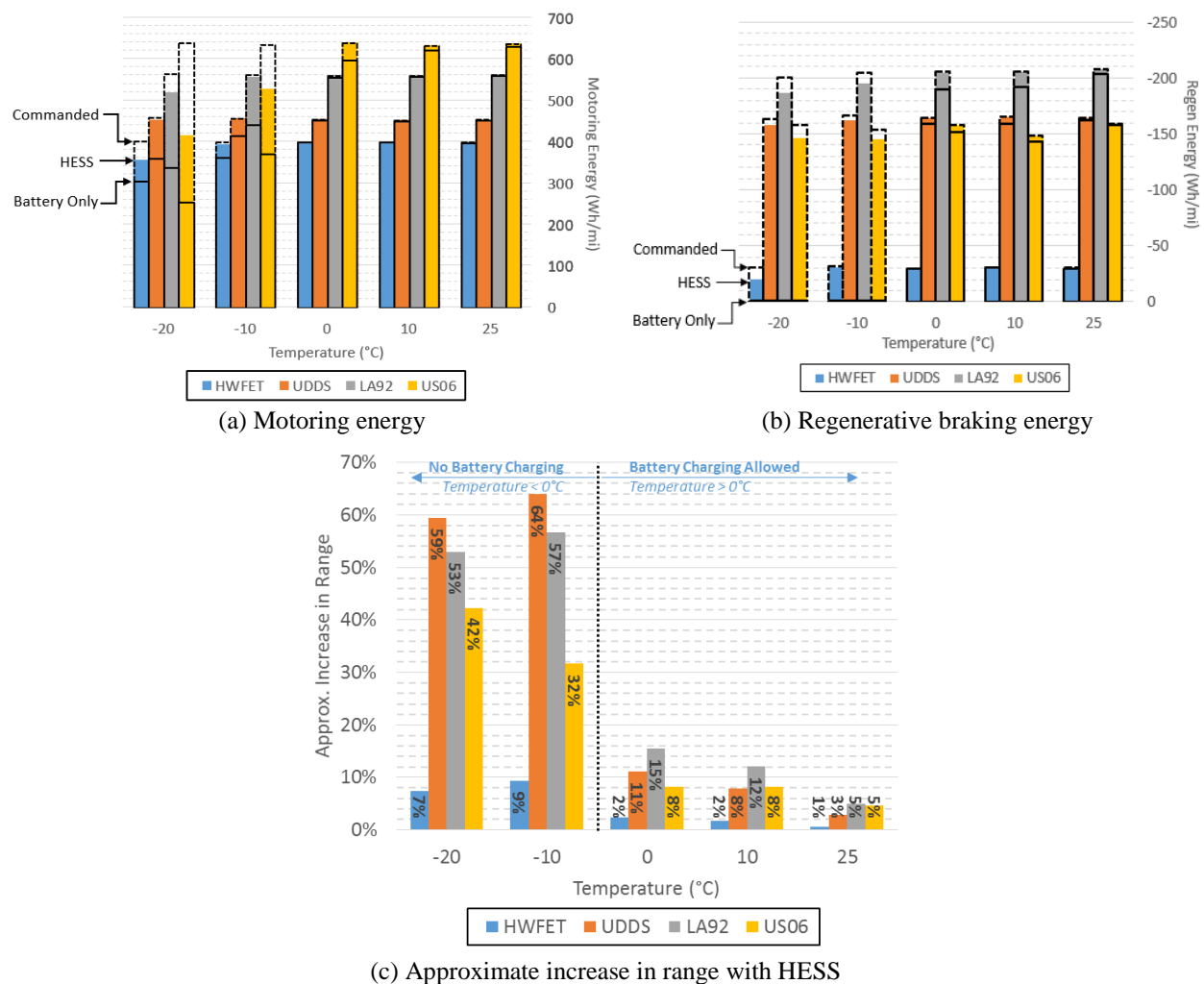


Figure 6.31 HESS versus battery performance for HESS with 30F/270V ultracapacitor pack and 400A dc/dc converter rating

motoring energy under all circumstances, but figure (a) shows that for temperatures below 0°C there is substantial power limiting for the battery only case. The HESS is able to improve substantially upon the battery only system, but there is still some power limiting for the US06 drive cycle at -10°C and for all of the drive cycles at -20°C.

Figure 6.32 (b) shows that the HESS is able to capture the large majority of the regenerative braking energy under all circumstances. The largest improvement in regenerative braking energy capture occurs below 0°C where the battery is not rated to receive any charge power, contributing to an increase in range of between 7 and 64% at these temperatures as shown in sub figure (c). Sub figure (c) also shows that the HESS improves vehicle range by approximately 1 to 15% for temperatures 0°C and above, an improvement achieved primarily through a reduction in energy storage system losses which are shown Figure 6.32. The distribution of the HESS losses are also given in Figure 6.32, showing that the majority of the losses are battery losses and a smaller portion are ultracapacitor and dc/dc converter losses, a result of the very low resistance of the ultracapacitor pack and the very high efficiency of the dc/dc converter.

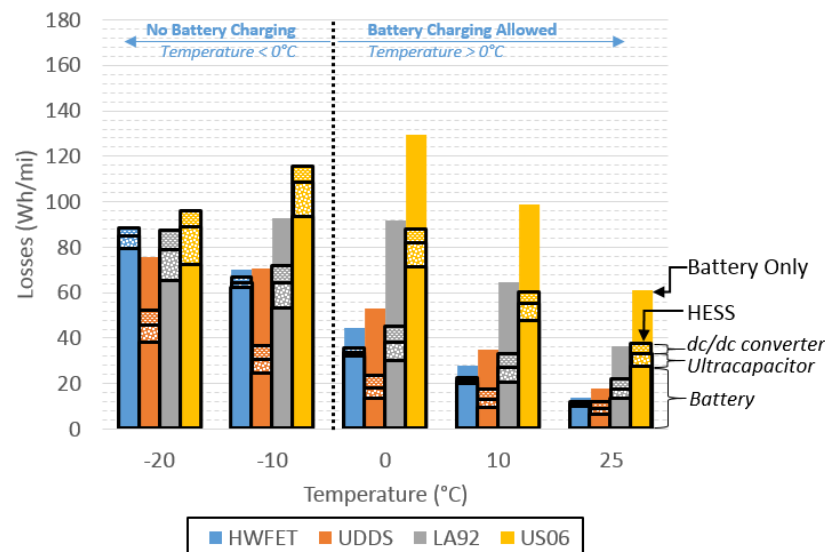


Figure 6.32 Battery only and HESS losses for HESS with 30F/270V ultracapacitor pack and 400A dc/dc converter rating

The prior discussion in this subsection focused on improvements in system performance achieved with the HESS, specifically improvements in range and power delivery, which affect the driver's immediate experience of the vehicle. The HESS has several ancillary effects on the battery pack as well, which should result in reduced battery aging. One effect is reducing the number of cycles provided by the battery, which is achieved by providing many of the acceleration and braking microcycles with the ultracapacitor pack. Figure 6.33 (a) shows that the total battery cycles are reduced substantially, between 8 and 35% at 0°C and above. Additionally Figure 6.33 (b) shows that the battery losses are reduced substantially, between about 20% and 70% for most cases, resulting in reduced temperature rise and presumably reduced aging as well.

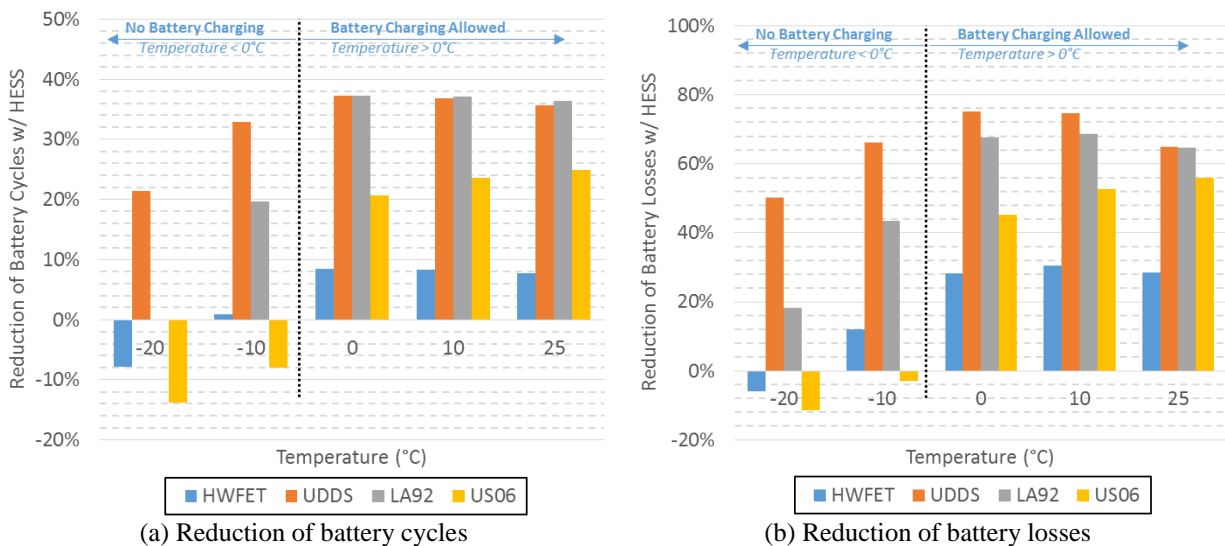


Figure 6.33 Performance improvements achieved with HESS for HESS with 30F/270V ultracapacitor pack and 400A dc/dc converter rating

In summary, the modeling shows that the HESS provides very substantial benefits in range and power delivery at low temperatures, enabling the vehicle to drive much farther and be much more capable. Importantly though, this modeling does neglect any self-heating of the battery pack, which will be significant in practice. For the 0°C LA92 case for example, the pack temperature

was shown to rise about 10°C per hour of driving, meaning that for very short drives the performance improvements achieved with the HESS will be similar to that predicted by the model, and for longer drives the temperature will rise and the contribution of the HESS will reduce accordingly. The HESS does enable the vehicle to be driven at these low temperatures though, by boosting the power capability of the system, and will substantially increase range, especially for short drives.

6.4.3.2 Effect of varied ultracapacitor pack energy storage rating

In the prior subsection the results for an HESS with a 30F, 270V ultracapacitor pack and a 400A dc/dc converter were presented. This ultracapacitor pack is rather large and heavy though, 40L and 51kg as shown in Figure 5.3, so it is desirable to utilize a smaller pack

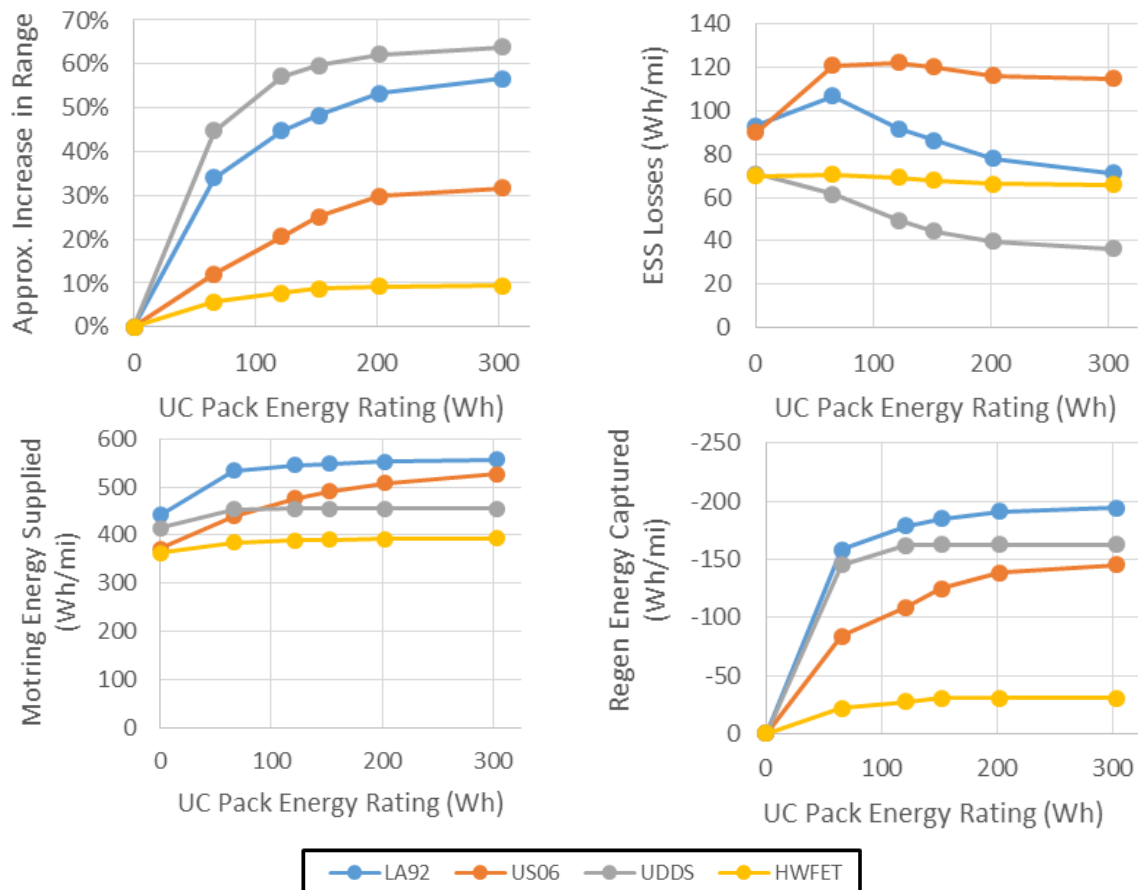
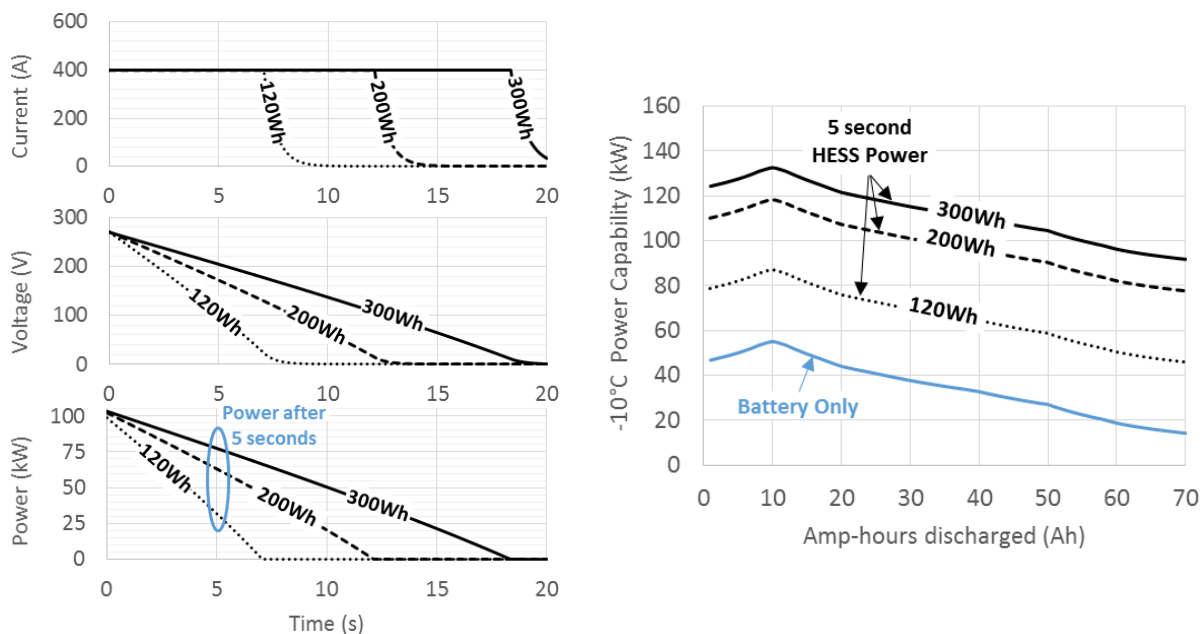


Figure 6.34 Performance improvements achieved with HESS for a range of ultracapacitor pack energy ratings and a 400A rated dc/dc converter

if possible. To demonstrate how HESS performance is effected by ultracapacitor pack size, the system was modeled for the LA92 drive cycle at -10°C for the full range of ultracapacitor pack sizes shown in Figure 5.3, from 6.5F/66Wh to 30F/304Wh, and the selected results are shown in Figure 6.34. As the ultracapacitor energy rating is increased, the range, supplied motoring energy, and captured regen energy are all shown to increase significantly.

The further improvements achieved beyond 120Wh of ultracapacitor energy appear relatively modest though, suggesting that there may not be much benefit in going to a larger size ultracapacitor pack. One key factor is not considered in these results though: the system HESS power capability is a strong function of the ultracapacitor pack energy storage rating. The ultracapacitor output power versus time for a 400A discharge current is shown Figure 6.35 for a 120Wh, 200Wh, and 300Wh ultracapacitor pack. This shows that the 120Wh pack cannot provide power for a very long period of time, with power decreasing to about 30kW after 5 seconds, while



(a) Ultracapacitor pack current, voltage, and power for 400amp discharge (b) Battery only and HESS power capability as a function of ultracapacitor energy storage

Figure 6.35 HESS 5 second power capability at -10°C for 120, 200, and 300Wh of ultracapacitor energy storage

63kW and 77kW are provided by the 200Wh and 300Wh packs after 5 seconds. The result is that at low temperatures a small ultracapacitor pack will not be able to greatly improve power capability, as is illustrated in subfigure (b) of Figure 6.35. Because the truck's drivetrain can draw up to 150kW peak, and because a 0-60mph acceleration at full power would take about 11 seconds, it is highly desirable to have a larger ultracapacitor pack. If necessary a smaller pack can be utilized though, resulting in a loss of power capability but retaining most of the range and power delivery improvements.

6.4.3.3 Effect of varied dc/dc converter current rating

For the prior sections a dc/dc converter low side current rating of 400A was utilized. In this section, the HESS is modeled with a range of dc/dc converter current ratings to provide insight into how high of a current rating is necessary. The modeled results, given in Figure 6.36 below,

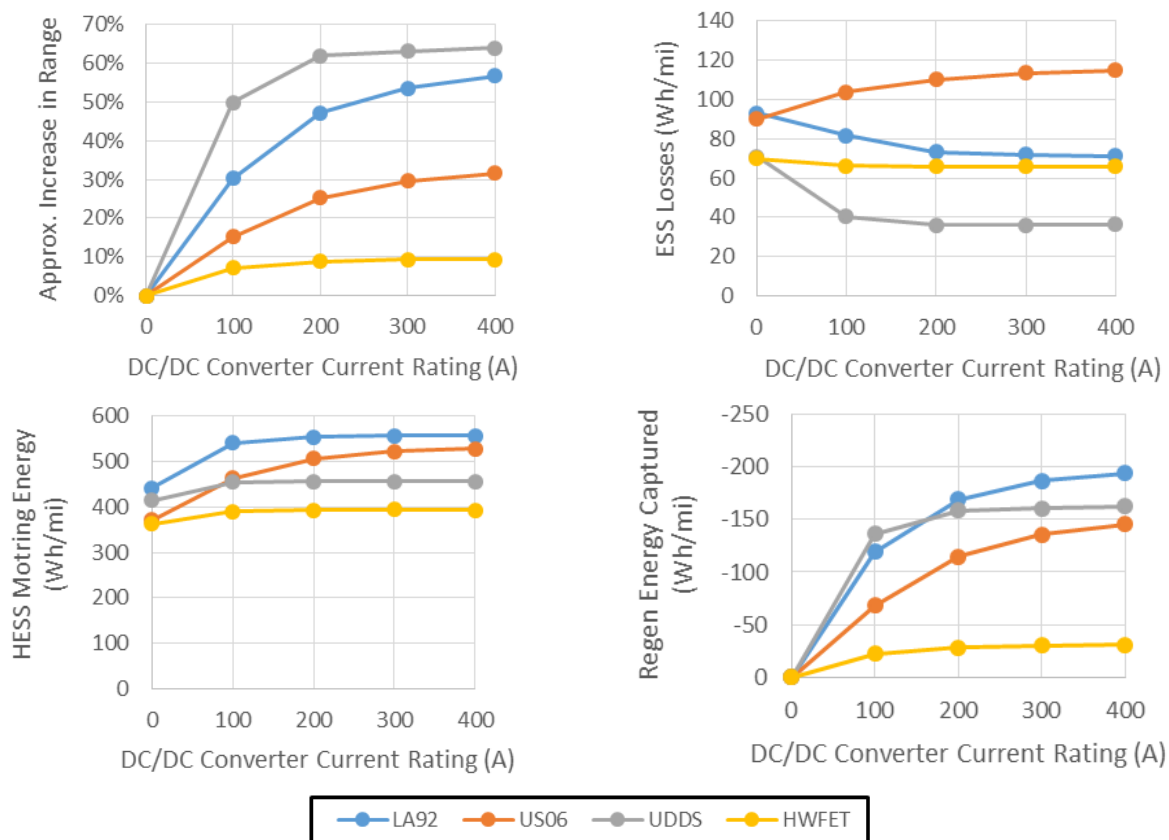
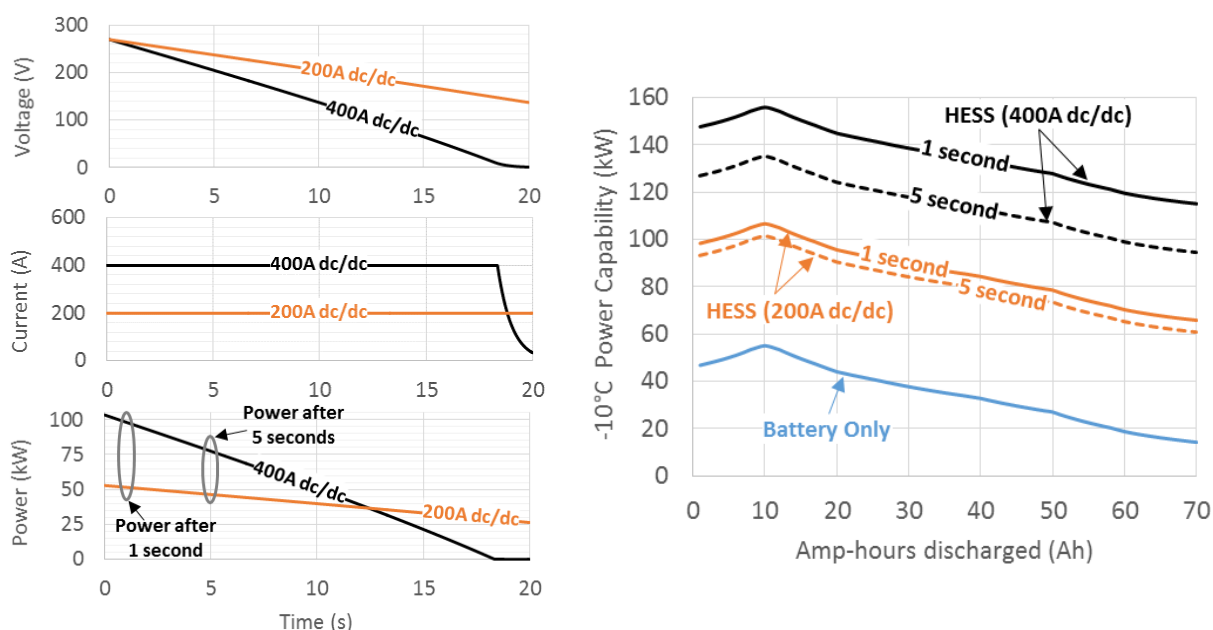


Figure 6.36 Performance improvements achieved with HESS for a range of dc/dc converter current rating and 300Wh ultracapacitor pack

show that half or more of the performance improvements are achieved with just 100A of dc/dc converter current rating, and the improvements achieved beyond a 200A rating are not as significant. A lower dc/dc converter current rating will directly reduce the maximum power the ultracapacitor pack can contribute to the system though, as is shown in Figure 6.37.



(a) Ultracapacitor pack current, voltage, and power for 200A and 400A discharge (b) Battery only and HESS power capability as a function of discharge power time

Figure 6.37 HESS power capability at -10°C for 200A and 400A dc/dc converter rating with 300Wh ultracapacitor pack

With a 400A rated converter, a peak of 100kW can be provided by the converter, which increases power capability at -10°C from 50kW or less with the battery only system to greater than 100kW for power pulses as long as 5 seconds with the HESS, as is shown in Figure 6.37 (b). With a 200A converter only half the peak power can be provided, reducing the HESS's ability to maintain power capability at low temperatures. In summary, the dc/dc converter should have a high enough current rating that most of the range improvements are achieved and that the system can provide sufficient power for the application. In the case of the truck, a current rating of 400A is sufficient that there will not be excessive power limiting, even at very low temperatures.

6.5 Conclusion

The tools required to model a hybrid energy storage system at low temperatures were developed in this chapter and used to thoroughly analyze low temperature performance of the electric truck with an HESS. First one of the Calb LiFePO_4 battery cells from the truck was tested over a wide range of temperatures, and the battery was shown to have many times greater resistance at low temperature and to exhibit non-linear current dependent resistance, as described by the Butler-Volmer equation, at low temperatures as well. A lookup based battery model was then developed which captures the low battery's low temperature characteristics, and the model estimated and measured voltage for an LA92 drive cycle at 0°C were shown to align well.

Next a Maxwell ultracapacitor pack was tested at temperatures as low as -30°C , and it was shown that resistance only increase a very small amount, about 30%, at very low temperatures. A discrete time ultracapacitor model was then derived which allows for large model time steps, such as the 1 second time step used in this study, without any discretization effects. Modeled and experimental results were then compared, and the model was shown to capture the ultracapacitor performance well, but there was some voltage estimation drift which occurred over time that was shown to be likely due to a small offset of the measured current.

The developed models were next incorporated into the HESS model, and the model was used to evaluate the performance of the electric truck with and without the HESS at temperatures ranging from -20°C to 25°C . Driving range is shown to be increased as much as 50% or more at temperatures below 0°C , where the battery is not rated to receive charging power. The HESS is also shown to substantially increase the discharge power capability beyond that of the battery pack, and to reduce battery losses between 25% and 80% for most drive cycles. Finally it is shown that

most loss reduction can be achieved with a small ultracapacitor pack and dc/dc converter, but a larger ultracapacitor pack and converter are necessary to significantly increase power capability.

Chapter 7

Experimental Evaluation of Hybrid Energy Storage System

7.1 Introduction

First the prototype dc/dc converter designed and built for the experimental system is presented, and an example higher current rated converter is designed and paired with an ultracapacitor pack for use in modeling performed in Chapter 8. Then the prototype converter is utilized in an experimental hybrid energy storage system (HESS), consisting of an 80V/100Ah LiFePO₄ battery pack, 48V/165F ultracapacitor pack, and the 200A rated prototype dc/dc converter. The HESS is connected to a 100V/500A Digatron bidirectional battery test system, and the Digatron system is used to draw drive cycle power profiles from the HESS. The HESS is tested with model calculated drive cycle power profiles for the electric F150, with the power scaled by 2/9ths because only two of the nine battery modules in the truck are tested in this scaled system. The HESS is tested for three drive cycles, the UDDS, LA92, and US06 cycles, and is tested at two temperatures, 0°C and 25°C. The measured performance results for each HESS test case are compared to the battery only performance results, and the measured and model calculated results are compared as well.

7.2 DC/DC Converter Design and Experimental Testing

7.2.1 Introduction

The dc/dc converter is of key importance in the HESS system design for several reasons. First, the efficiency of the converter must be very high (>97%), such that the combined efficiency of the converter and ultracapacitor pack is higher than the efficiency of the battery pack. Second the converter's power rating must be high enough to perform the functions desired of the HESS. If

the converter will be used to substantially boost the energy storage system's power capability beyond that of just the battery, as is examined in the following chapters, a dc/dc converter power rating which is half or more of the system power capability may be necessary. Third, the converter must regulate ultracapacitor current quickly and accurately, so that the power split command is followed, and the converter control must operate from 0V up to the rated ultracapacitor voltage and it must regulate the ultracapacitor voltage such that the rated voltage is not exceeded.

In this section a prototype 200A rated dc/dc converter is presented, which is highly efficient and has a controller with the prior described attributes. Then, because a higher power converter is desired for applications which are modeled in the following chapters, a 400A dc/dc converter design is presented as well, and is paired in the final subsection with a high performance ultracapacitor pack from a relatively new ultracapacitor manufacturer, Skeleton Technologies.

7.2.2 Prototype dc/dc converter design and experimental testing

A prototype dc/dc converter was designed and built in the lab to enable the testing of a scaled version of the hybrid energy storage systems modeled in this dissertation. The converter topology is a non-isolated, bidirectional buck-boost half bridge converter as is shown Figure 7.1. This topology has been shown by prior research to be one of the most efficient and power dense topologies, as is discussed briefly in Appendix IV, and is the topology used in the Toyota Prius. The prototype converter, although it is only used up to about 80Vdc in the testing here, is designed to operate up to 400V at +/-200Adc, and has a 5kHz switching frequency, 170 μ H inductor, 2400mF bus capacitor, and a nominal efficiency of 89% with an 80Vdc bus, as is specified in Table 7.2.

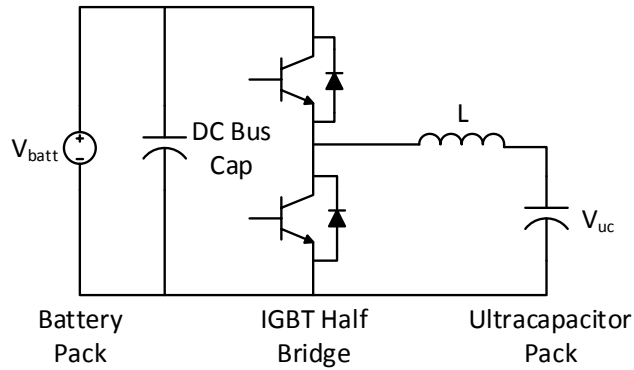


Figure 7.1 Half bridge topology used for dc/dc converter

Table 7.1 Prototype DC/DC Converter Specifications

Topology	Half Bridge Bidirectional Buck/Boost
Switching Frequency	5kHz
DC Bus Voltage Rating	400V maximum (80V used in experiments)
Current Rating	+/-200Adc
Current Rise Time	100ms from 0A 10ms otherwise
Nominal Efficiency	89% (80Vdc bus)
Inductor	170 μ H / 2.4m Ω (at 10kHz, Agilent 4263B)
Bus Capacitance	2400mF
IGBT Module	Semikron 600V/400A Skiip Module

The converter was built on a panel, as is shown in Figure 7.2, and while due to its large it is not ideal for testing in a real automotive application, it could be placed in the bed of the truck and connected to the truck battery pack and an ultracapacitor pack for future testing work. The converter is controlled using a dSPACE system and the controls, which were designed and implemented by graduate student Ananth Sridhar as an independent study project, are thoroughly documented in Appendix V. The converter utilizes 200A rated LEM LA-205s current sensors and 500V rated LEM LV-25P voltage sensors for the feedback control, and additionally has 0.01% accurate LEM IT-700s Ultrastab current sensors built in for performing high accuracy efficiency measurements with a Yokogawa WT-1600 power analyzer, as was done for the measurements described and presented in the following figures.

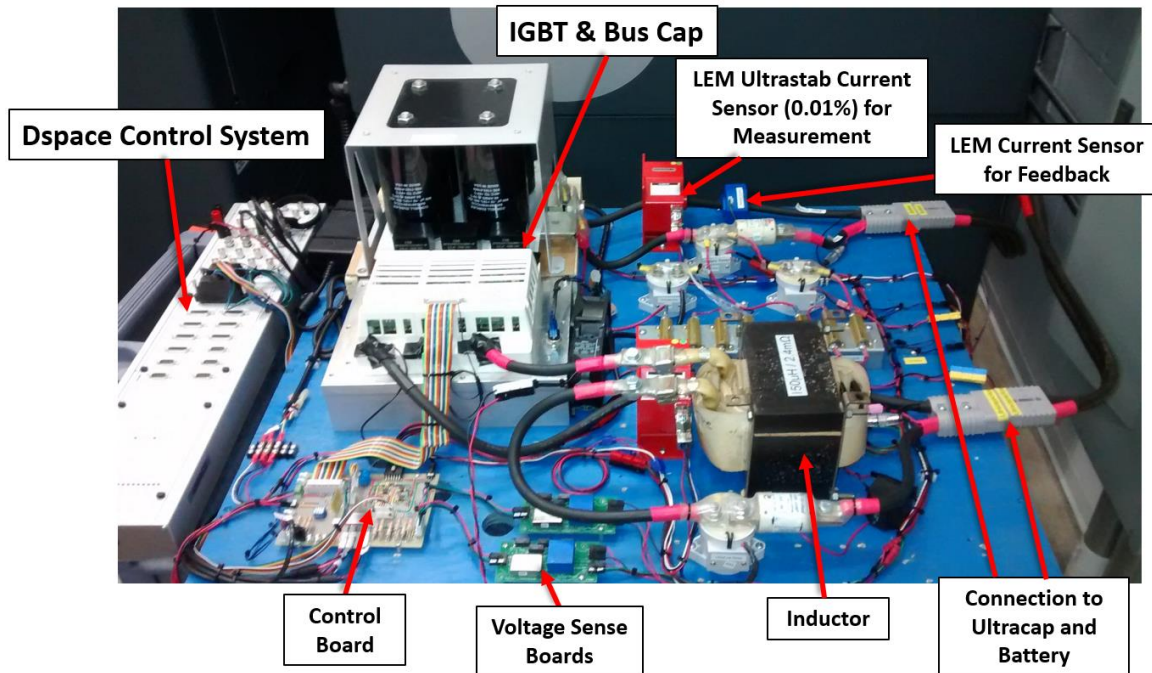


Figure 7.2 Prototype DC/DC converter with components labeled

The large majority of the losses in the system occur in the inductor and the IGBT, so to confirm the efficiency model of the converter is correct the losses of both are measured and compared to the modeled values. The inductor is a very large, 13kg, gapped E core, laminated steel inductor with heavy gage copper windings, as can be seen in Figure 7.2 above. While this 170 μ H inductor was not design specifically for this high dc offset current application, it is an excellent match, and is only mildly saturated with 295A of dc offset current, as is shown in the measured inductance versus current characteristic in Figure 7.3 (a). Due to the low voltage of the system the dc ripple current is quite small (<25A) and iron loss is small enough that it can be neglected. As a result the inductor loss can be modeled simply as a series resistance, which was measured to be 2.4m Ω at 10kHz with an Agilent LCR meter. To confirm that the resistance measured with the LCR meter accurately captures the inductor losses, the inductor loss was measured at five currents ranging from 25 to 200Adc while the converter was operating, and the modeled and measured losses were very close, as shown in Figure 7.3 (b), confirming the accuracy of the loss model.

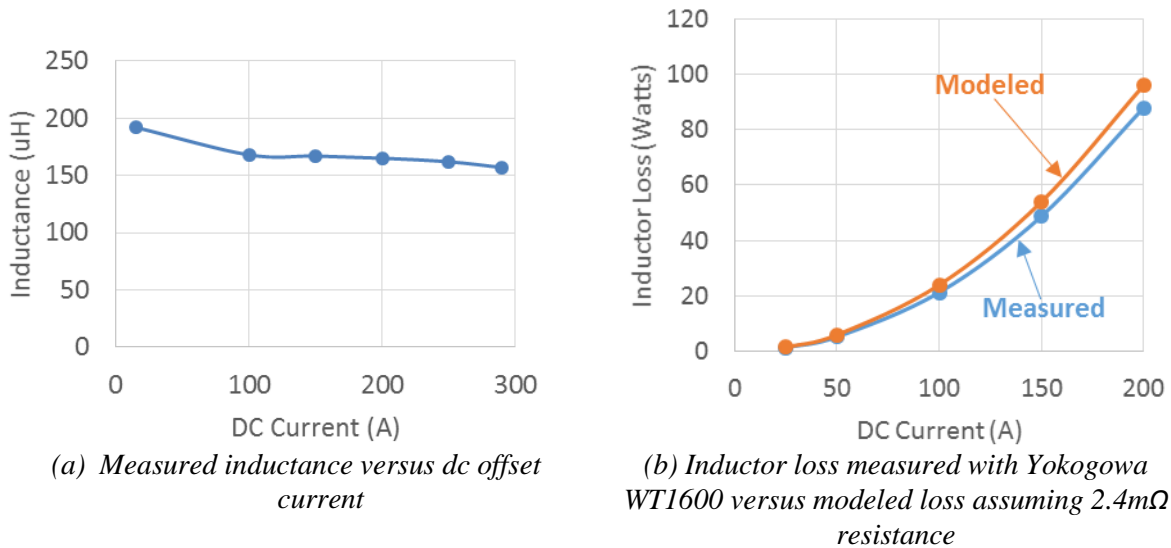
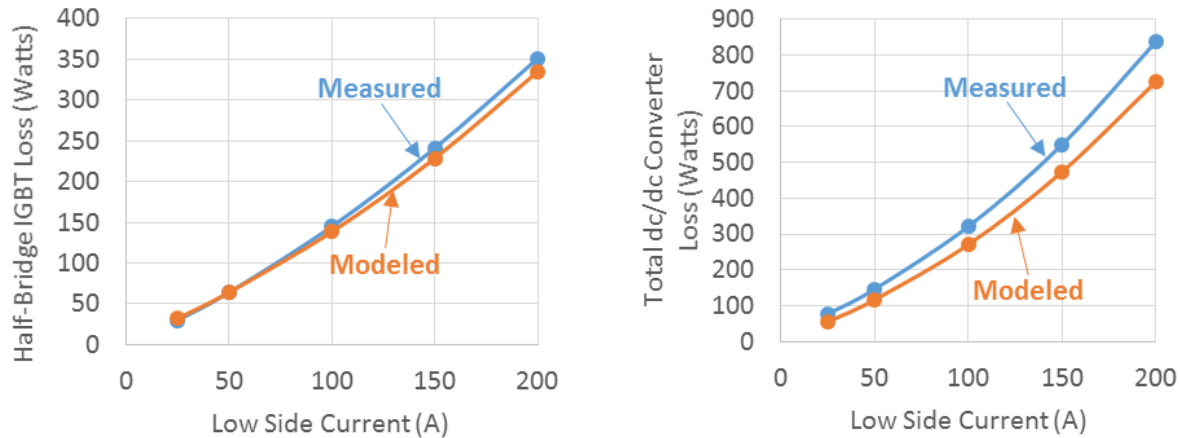


Figure 7.3 Measured inductance and measured versus modeled loss for prototype inductor

The Semikron IGBT module losses were calculated using the modeling methodology, involving Semikron's Semisel modeling tool, as was used in Chapter 4 to model the motor drive semiconductor loss. The Semikron IGBT losses were then measured while the converter was operating using a Yokogawa WT1600 power analyzer with LEM Ultrastab current sensors, and the measured versus modeled losses are shown in Figure 7.4 (a) below to be very close, with 351W of losses measured at 200A and 335W predicted by the model. Additionally the full input to output converter losses were measured, which consists of the half bridge losses, an additional diode loss due to a Semikron module protection feature requiring the ultracapacitor return current to be fed through another phase leg of the inverter module, the inductor loss, and the cabling, contactor, fuse, and capacitor loss. The measured versus modeled loss, where only the inductor and semiconductor losses are modeled, is shown Figure 7.4 (b), and the error is only about 15%, which is respectable considering all the cabling, contactor, and fuse resistance is neglected.

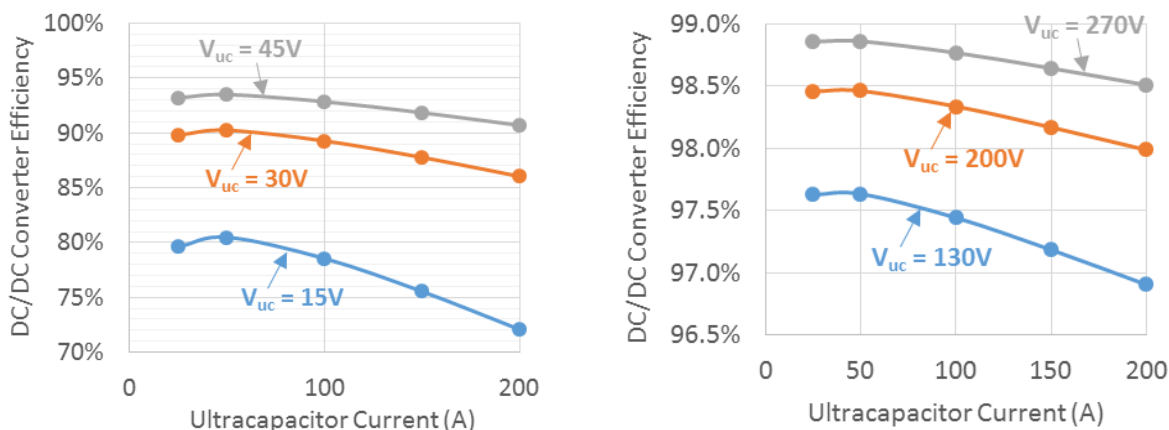


(b) Measured Semikron SKM600GB066D IGBT half-bridge loss with 80V dc bus

(b) DC/DC converter input to output terminal loss

Figure 7.4 Modeled versus measured prototype dc/dc converter IGBT half bridge loss and full converter loss

The measured dc/dc converter losses shown Figure 7.4 (b) are then used to calculate the dc/dc converter efficiency for the full range of ultracapacitor voltages used in the experimental testing, and the efficiency is shown in Figure 7.5 (a) to range from 90-94%, 86-90%, and 72-81% for 15, 30, and 45V ultracapacitor voltage respectively. This efficiency is quite low, less than the >97% efficiency which is desired, but this is due to using 600V rated semiconductors for an 80V application. At 350V the converter efficiency is much higher, modeled to range from 97-98.7%, as shown in Figure 7.5 (b).



(a) DC/DC converter efficiency calculated with measured losses for 80Vdc bus

(b) DC/DC converter efficiency calculated from model for 350Vdc bus

Figure 7.5 DC/DC converter efficiency for 80Vdc bus as used in experimental testing and for 350Vdc bus as would be used in vehicle

7.2.3 Example 400A dc/dc converter design for use in modeling

The prototype 200A dc/dc converter designed and built in the prior subsection shows that the semiconductor and inductor modeling methodology are accurate and demonstrates a functional design. A 400A rated dc/dc converter design is desired for use in the modeling in the following sections though, as well as to provide a more accurate idea of the mass, volume, and efficiency of such a converter. An example 400A rated converter was therefore designed, and the converter has a 12kHz switching frequency, 400V maximum dc bus voltage rating, +/-400A current rating, efficiency between 97-99%, an inductor with 3m Ω resistance and 193 μ H, 480 μ F of bus capacitors, and a 600V/600A Semikron IGBT half bridge, as is specified in Table 7.2.

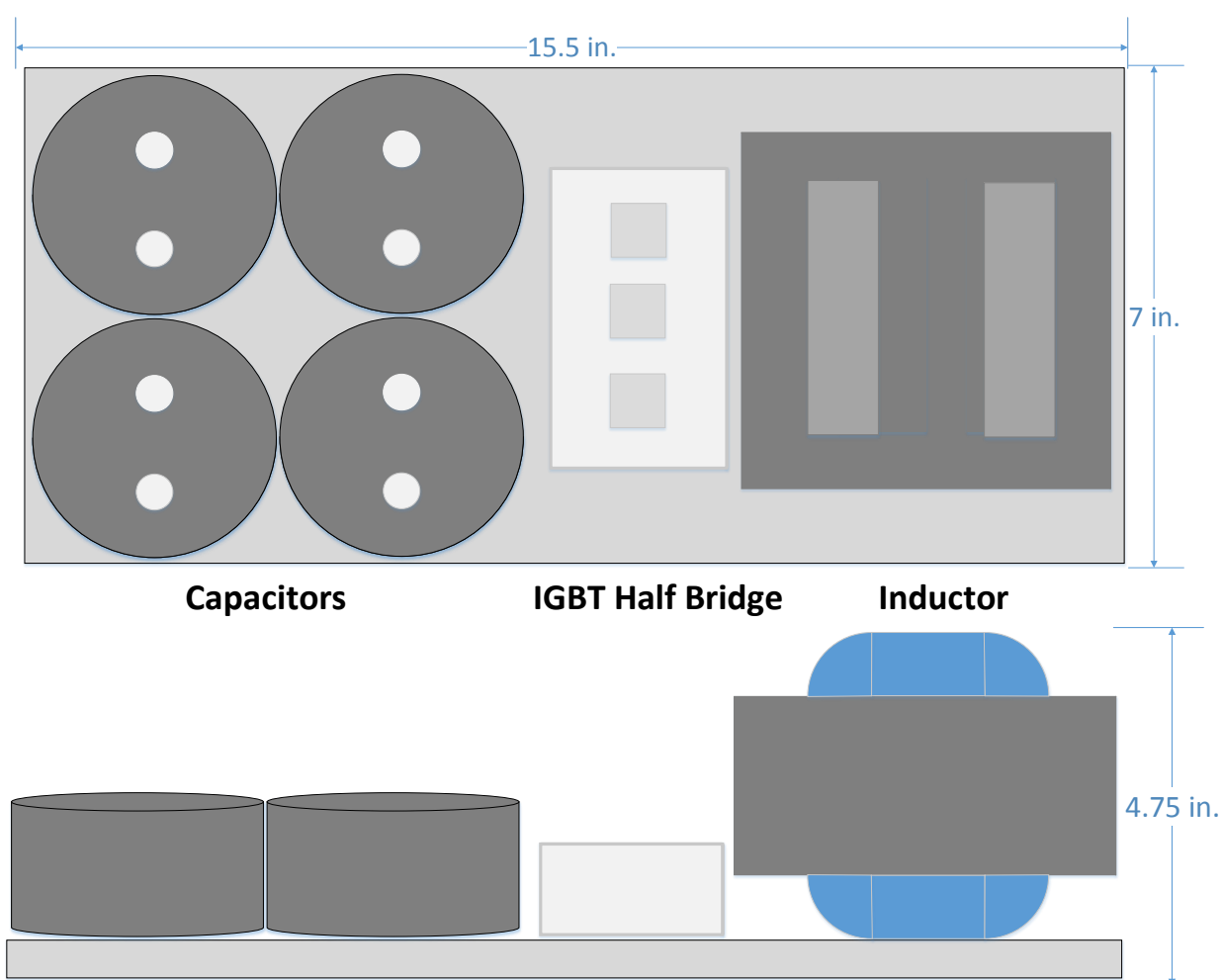
Table 7.2 Example 400A DC/DC Converter Design Specifications

Topology	Half Bridge Bidirectional Buck/Boost
Switching Frequency	12kHz
DC Bus Voltage Rating	400V maximum
Current Rating	+/-400Adc
Efficiency	97% - 99% (350Vdc bus)
Inductor	193 μ H @ 440Adc / 3.0m Ω
Bus Capacitance	480 μ F / 0.15m Ω
IGBT Module	Semikron 600V/600A

The components utilized in the inverter, as well as their mass and volume, are given in Table 7.3 below, showing that the converter components would weigh a total of about 13.5kg and take up 3.3L of volume, achieving a very respectable power density. The Semikron IGBT and the AVX bus capacitors are selected to be able to provide the rated current continuously, and there may be some opportunity to use fewer bus capacitors if the dc/dc converter were collocated with the inverter, although more research into any possible design advantages would have to be performed. The inductor was designed using 4 Hitachi Powerlite C cores in an E configuration,

Table 7.3 Example 400A DC/DC Component Specifications Including Mass and Volume

Component	Description	Mass	Volume
IGBT Half Bridge	Semikron SKM600GB066D	0.325 kg	0.20 L
DC Bus Capacitors	AVX FFVE4I0127K (Quantity 4)	1.2 kg	0.76 L
Inductor Cores	Hitachi Powerlite AMCC-250 (Quantity 4)	4.4 kg	Estimated inductor volume: 1.4 L
Inductor Copper	Approx. 24ft 1AWG magnet wire	3.3 kg	
Heatsink, bus bars, sensors, etc.	-	3 kg	1 L
Total:		13.5 kg	3.3 L

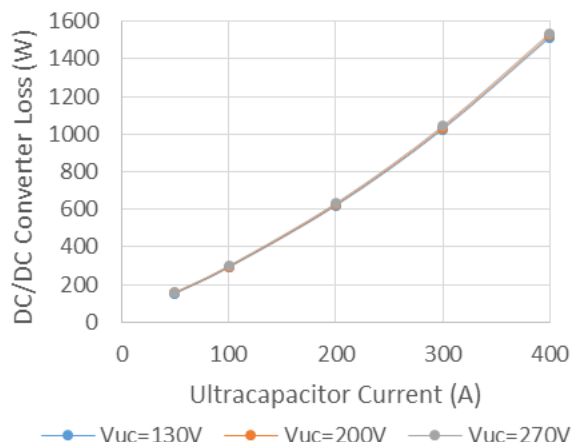
**Figure 7.6** Scale drawing of example 400A dc/dc converter

with a 6mm gap and 27 turns of 1 AWG equivalent magnet wire, providing 193 μ H at 440A, the peak current (dc + ripple) the inductor would be exposed to. Additionally a scale drawing of the converter components laid out on a heatsink is provided in Figure 7.6 above, giving a physical idea of the size of the converter and each component.

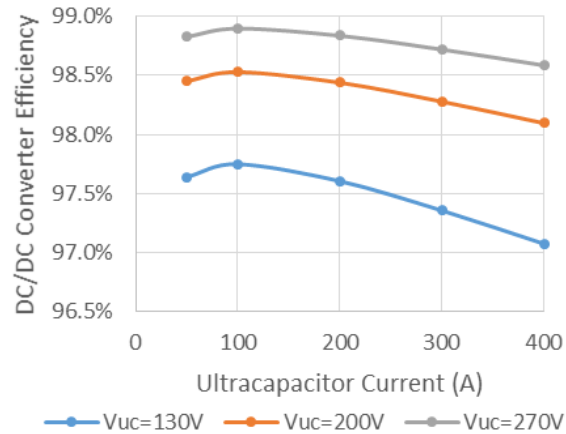
The loss of each component of the converter was calculated and given in Table 7.4 for currents ranging from 50 to 400A. The IGBT and diode losses of the half bridge are responsible for about 2/3 of the loss, with inductor resistive loss being responsible for much of the remainder. The model predicted losses were also calculated for several ultracapacitor voltages, but the losses are shown in Figure 7.7 (a) to be almost entirely independent of ultracapacitor voltage. The efficiency

Table 7.4 Example 400A DC/DC converter model calculated loss

Ultracapacitor Current	IGBT/ Diode Loss	Inductor Resistive Loss	Inductor Iron Loss	Capacitor Loss	Total Loss
50 A	136 W	8 W	15 W	0 W	159 W
100 A	252 W	30 W	15 W	2 W	299 W
200 A	489 W	121 W	15 W	6 W	631 W
300 A	742 W	271 W	15 W	14 W	1042 W
400 A	1014 W	482 W	15 W	24 W	1535 W



(a) Total dc/dc converter loss for 350Vdc bus



(b) Model calculated DC/DC converter efficiency for 350Vdc bus

Figure 7.7 Example 400A dc/dc converter model calculated loss and efficiency

for a range of ultracapacitor voltages was also calculated, and is shown Figure 7.7 (b) to range from 97-98.8%. The values presented here are utilized for modeling in the following chapters, and are considered to be representative of efficiency which could be achieved in an actual application.

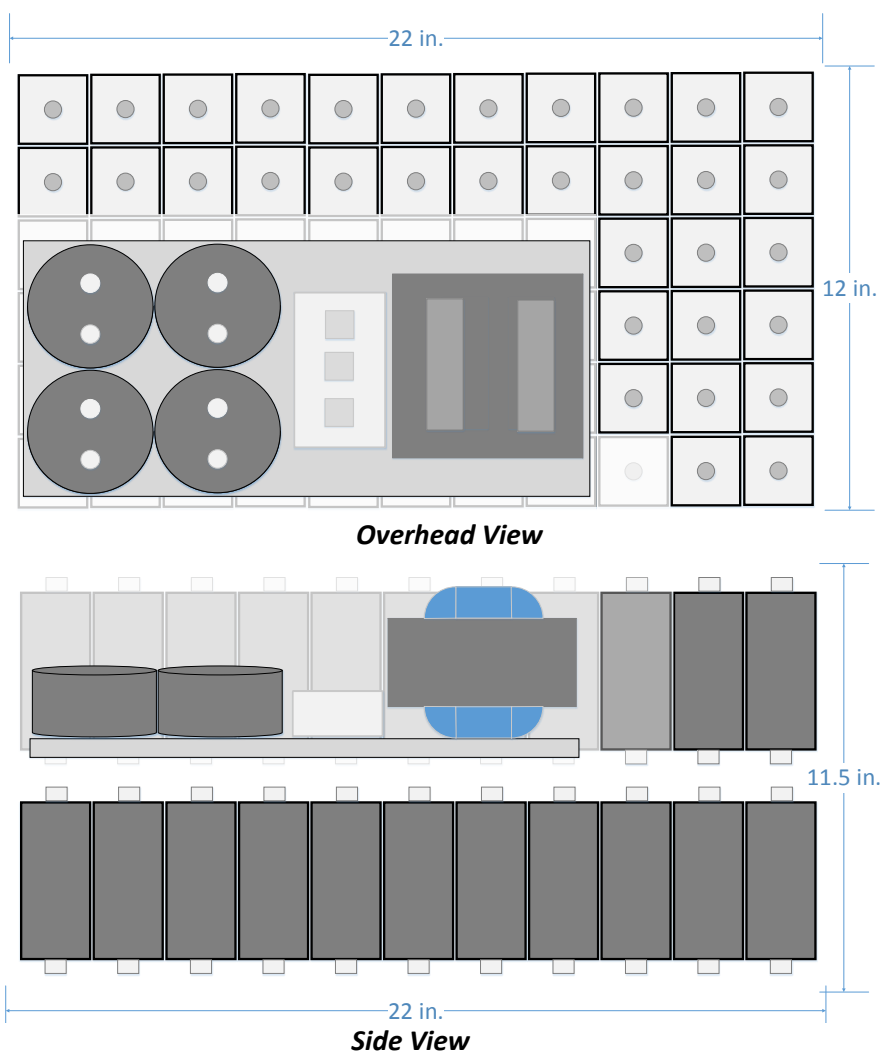
7.2.4 HESS Design with 400A dc/dc converter and Skeleton Ultracapacitor Pack

Only Maxwell ultracapacitors have been considered so far, and for a pack consisting of 100 series connected cells their mass and volume is quite large, ranging from 16-51kg and 15-40L as is shown in Figure 5.3. Another manufacturer of ultracapacitors, Skeleton Technologies, has developed ultracapacitors which utilize graphene and have significantly higher gravimetric and volumetric energy density than the Maxwell ultracapacitors. An example Skeleton ultracapacitor pack design will be utilized in the following chapters which consists of 95 series connected 2.85V 3500F cells, with a pack resistance of only 19m Ω and a total of 375Wh of energy storage, as is shown in Table 7.5. Additionally the 375Wh of Skeleton cells have a mass of 37kg and a volume of 27L, which is substantially less than the 51kg mass and 40L volume of a 300Wh pack consisting of 100 series connected 3000F Maxwell cells.

Because the Skeleton cells are of a prismatic rather than cylindrical design they also pack very well, allowing the 375Wh skeleton pack to be packaged with the 400Adc/dc converter in a 22" x 12" x 11 1/2", as is shown in Figure 7.8. This system is small enough that such a system could easily be fit in a larger application like a full size truck, and for applications such as a compact car a system maybe half this size could provide similar performance benefits.

Table 7.5 Skeleton SCHE3500 Ultracapacitor Pack Parameters [136]

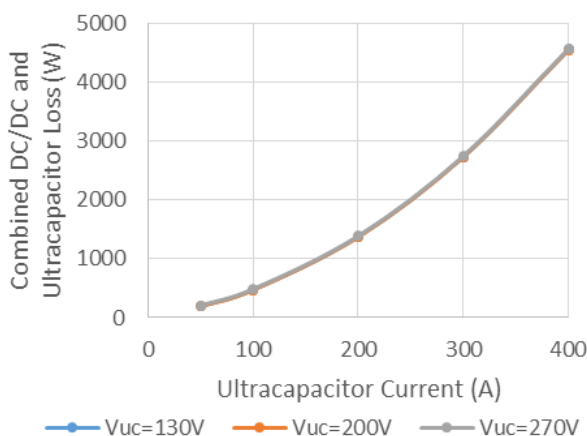
	<i>Cell</i>	<i>Pack</i>
# of cells in series	-	95
Max Voltage	2.85V	271V
Capacitance	3500F	37F
Resistance	0.2m Ω	19m Ω
Mass	0.39kg	37kg
Volume	0.28L	27L
Energy Storage	3.9Wh	375Wh
Price (\$0.005/Farad)	\$17.50	\$1,663

**Figure 7.8** Scale drawing of Skeleton ultracapacitor pack with 400A dc/dc converter

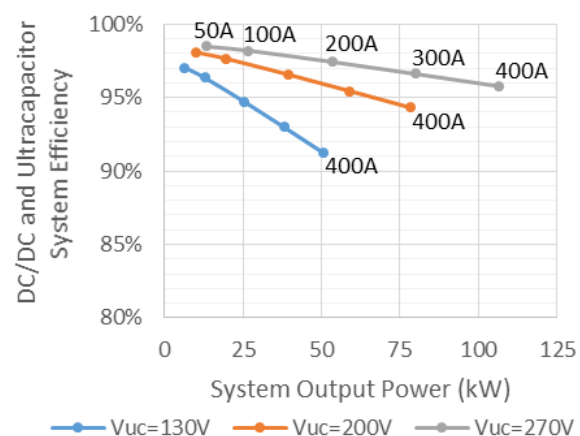
The Skeleton ultracapacitor and 400A dc/dc converter system has a total volume of 50L and a component mass of 40.5kg, as is shown in Table 7.6. The losses of the system, the sum of the ultracapacitor and dc/dc converter losses, peak at about 4.5kW, as is shown in Figure 7.9 (a) and the system efficiency is shown to range from 91 to 97.5% efficiency in Figure 7.9 (b). Overall this is a very efficient and power dense system, giving hope that with the right application and price of materials, a hybrid energy storage system could actually result in an overall improvement in an energy storage system design for a vehicle. To examine how this energy storage system performs in various applications, it will be utilized in Chapter 8, for an application of an electric truck with a Panasonic battery pack, an electric bus, and an electric truck with 2015 model year performance capabilities.

Table 7.6 Skeleton ultracapacitor pack and 400A dc/dc converter system specifications

Volume	50L
Mass of Components	50.5kg
System Efficiency	91-98%
DC/DC Converter Current	+/-400A
Battery Side Voltage	270-400V
Ultracapacitor Side Voltage	0-270V
Ultracapacitor Energy Storage	375Wh



(a) Ultracapacitor and dc/dc converter system loss for 350Vdc bus



(b) Ultracapacitor and dc/dc converter system efficiency for 350Vdc bus

Figure 7.9 Example 400A dc/dc converter model calculated loss and efficiency

7.2.5 Summary

In this subsection the $\pm 200\text{A}$ rated prototype dc/dc converter design utilized for the experimental testing in this chapter is first presented, and is shown experimentally and through modeling to have an efficiency ranging from 72-94% with an 80Vdc bus. Then an example $\pm 400\text{A}$ dc/dc converter is designed, which will be utilized in the system model in the following chapters. The converter is shown through modeling to have an efficiency ranging from 97-99%, and a component mass of approximately 13.5kg. Finally the 400A dc/dc converter is combined with a 375Wh Skeleton ultracapacitor pack, to create a compact 100kW peak hybrid energy storage system, which will be utilized in the modeling in the scaling chapter, Chapter 8.

7.3 Hardware Test Setup

The interconnection between the battery pack, ultracapacitor pack, dc/dc converter, and Digatron test system is shown in the block diagram in Figure 7.10. The dc/dc converter current command is a function of the measured Digatron system current, and is determined using a rule based power split control as described in section 7.4. The hardware setup is used to test the HESS as well as to test just the battery pack by disconnecting the dc/dc converter and ultracapacitor pack.

The battery pack tested consists of the first two 12 cell modules of the truck pack. The modules were removed from the truck and placed in a 32 cubic foot thermal chamber, as shown below in Figure 7.11. Each of the 24 cell voltages are measured with cell voltage measurement channels of the Digatron test system, and the Digatron is set to halt the test if any cell voltage is less than 2.3V or greater than 3.8V. Additionally four thermocouples, which are also measured by the Digatron system, were added to each 12 cell modules, and the thermocouple in the warmest location (sandwiched in the center face between two batteries) is considered to be the measured temperature for all of the tests.

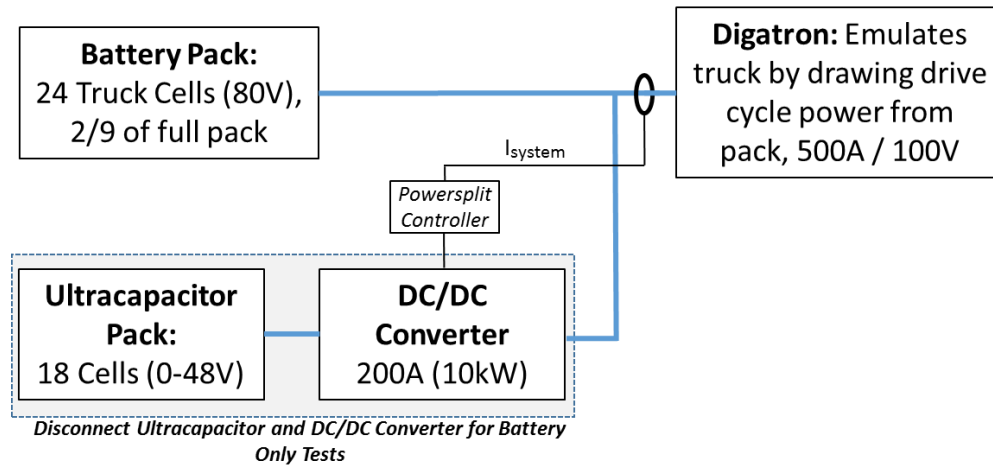


Figure 7.10 Block diagram of HESS test setup

The 48V Maxwell ultracapacitor pack is also placed in the thermal chamber, directly behind the battery pack as shown in Figure 7.12. The Maxwell pack has internal voltage sensing, and pulls an output signal low if any cell voltage is greater than 2.8V. The overvoltage output is used to open a Kilovac contactor, which is also shown in Figure 7.12. The ultracapacitor pack temperature is also measured at the case of the pack, but due to the very low losses of the ultracapacitor pack the pack temperature is relatively constant.

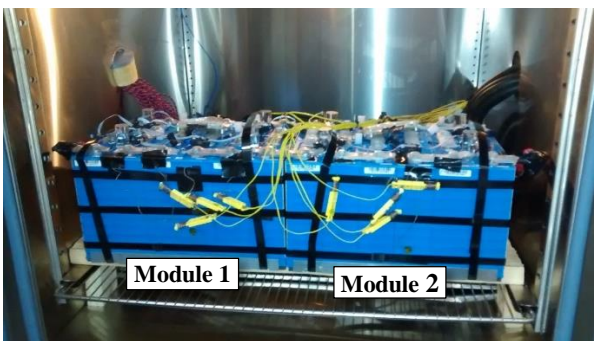


Figure 7.11 *Battery Pack*: 80V/100Ah LiFePO4 pack (24 series connected cells, 2/9 of truck pack)



Figure 7.12 *Ultracapacitor Pack*: 48V/165F Maxwell module

The prototype 200A dc/dc converter was placed on a cart directly in front of the thermal chamber, as shown in Figure 7.13. The dc/dc converter was connected to the ultracapacitor and battery packs via two sets of 2/0awg cables, visible in the right of the picture. The dc/dc converter also has a current sensor placed directly in the thermal chamber which is used to measure the Digatron system current. The dc/dc converter is controlled with a dspace DS1103 real time control system and a specially designed current regulator and control system. The prototype converter and control system will be described in more detail in a separate section or chapter of the dissertation.

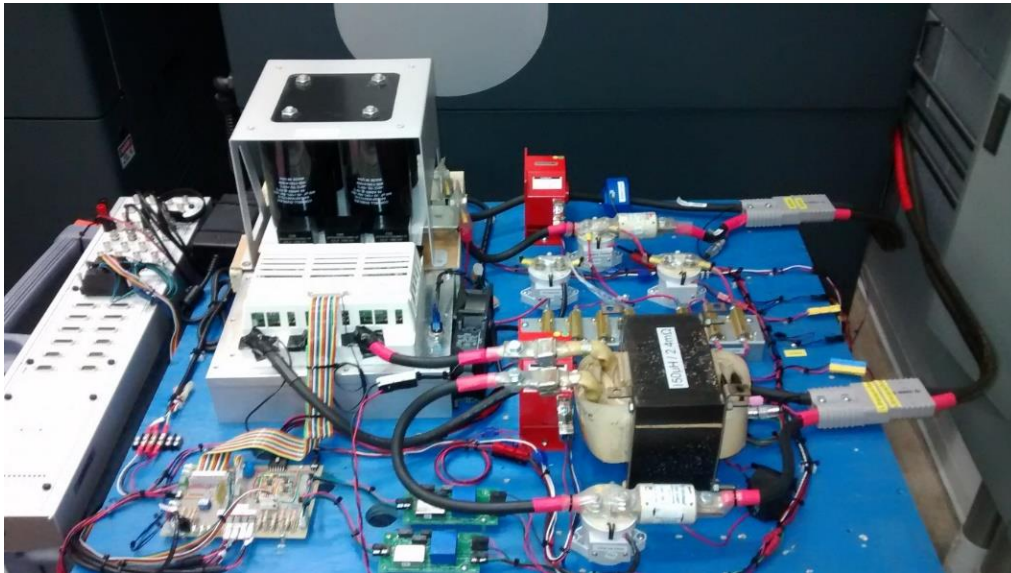


Figure 7.13 Prototype 200A dc/dc converter

The parameters for the battery pack and ultracapacitor pack are given in Table 7.7 and Table 6.5 below. The battery pack stores a significant amount of energy, 7.68kWh, but has a relative high resistance ranging from 31m Ω at 25°C to 70m Ω at 0°C, making it a good match for the ultracapacitor pack which stores a very small amount of energy, 53Wh, but has a very low resistance of about 5m Ω , which is relatively unaffected by temperature. For the tests the battery pack voltage is held by the Digatron equipment to a maximum of 86.4V and a minimum of 60V

and the ultracapacitor pack voltage is held by the dc/dc converter control software to a maximum of 45V and a minimum of 15V.

Table 7.7 Battery Pack Parameters

# of series cells	24
Amp-hours per cell	100Ah
Nominal Voltage	76.8V (3.2V/cell)
Nominal Energy	7.68 kWh
Maximum Voltage	86.4V (3.6V/cell)
Minimum Voltage	60V (2.5V/cell)
Nominal Resistance	31m Ω @ 25°C 70m Ω @ 0°C
Mass	77 kg
Volume	49 liters

Table 7.8 Ultracapacitor Pack Parameters

# of cells	18
Farads per cell	3000F
Maximum Voltage	48V (2.67V/cell) (45V max set for test)
Nominal Energy	53 Wh
Minimum Voltage	0V (15V min set for test)
Nominal Resistance	5.1m Ω @ 25°C 5.6m Ω @ 0°C
Mass	13.5 kg
Volume	12.7 liters

The prototype dc/dc converter is designed to work with the full scale truck battery pack, which has a nominal voltage of 350Vdc. The converter uses a half bridge bidirectional buck/boost topology, and is rated for +/-200Adc continuous, as specified in Table 7.9 below. Because the converter's losses are mostly a function of current, as documented in the section/chapter on the dc/dc converter design, the converter is quite inefficient at the lower voltages used for the experiment. The measured converter efficiency ranges from a low of 81% at 200Adc with a 22V ultracapacitor pack voltage to a high of 93.5% at 50Adc with a 44V ultracapacitor pack voltage, as illustrated in Figure 7.14. With a 200V ultracapacitor pack voltage, the losses would be reduced approximately proportionally and efficiencies higher than 97% would result.

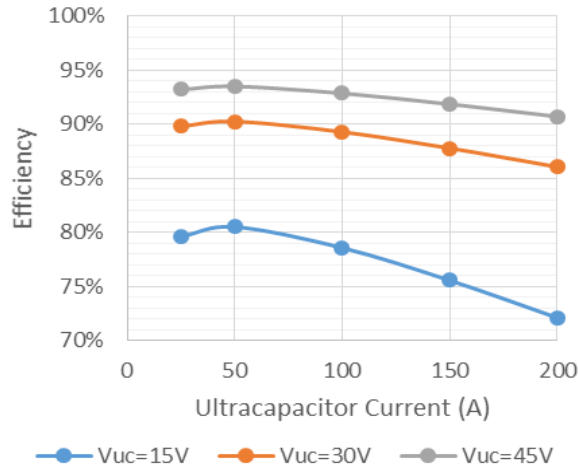


Figure 7.14 Measured dc/dc converter efficiency with 80Vdc bus for various ultracapacitor pack voltages (V_{uc})

Table 7.9 DC/DC Converter Specifications

Topology	Half Bridge Bidirectional Buck/Boost
Switching Frequency	5kHz
DC Bus Voltage Rating	400V maximum
Current Rating	+/-200Adc
Current Rise Time	100ms from 0A 10ms otherwise
Nominal Efficiency	89% (80Vdc bus)
Inductor	170μH / 2.4mΩ
Bus Capacitance	2400mF
IGBT Module	Semikron 600V/400A Skiip Module

7.4 Rules for Rule Based Control

The primary goal of the HESS in the experimental testing is to reduce the energy storage system losses, thereby increasing the range of the vehicle. To reduce the system losses two control rules are adopted, one for the discharging case and one for the charging case:

1. **HESS Discharging:** The calculated maximum efficiency power split is used to determine the ultracapacitor current command (*see Chapter 5*). **Note:** Other speed based rules are not utilized for the experimental test setup because the Digatron system cannot provide a speed reference as a vehicle would.
2. **HESS Charging:** 80% of the charge power is directed to the ultracapacitor.

The charging case is relatively straightforward. First the energy storage system current, $I_{sys-meas}$, is measured as shown Figure 7.10. Then the system power, $P_{out-meas}$, is calculated from the measured current and measured battery pack voltage, V_{b-meas} , as shown in (7.1). Then the ultracapacitor current command, I_{UC}^* , is calculated in (7.2) as a function of the measured output power, measured ultracapacitor current $V_{uc-meas}$, and the nominal dc/dc converter efficiency η_{dc-nom} such that the ultracapacitor outputs approximately 80% of the measured charging power.

I_{UC}^* is then used as the current command for the dc/dc converter, and the ultracapacitor will charge as long as the ultracapacitor voltage remains below the limit of 45V, as specified in Table 6.5.

$$P_{out-meas} = V_{b-meas} I_{sys-meas} \quad (7.1)$$

$$I_{UC}^* = \frac{0.8 \times P_{out-meas}}{V_{uc-meas}} \eta_{dc-nom} \quad (7.2)$$

To calculate the current command for the HESS discharging case the optimal power split equation, equation 5.11 in Chapter 5, is utilized. Because the dc/dc converter control system, which includes the power split control, does not have knowledge of the present values of the battery and ultracapacitor pack parameters, fixed nominal values are used to calculate the power split, as given in Table 7.10. The power split equation (5.11) is given below for reference as well, while the whole calculation process is described in Chapter 5.

Table 7.10 Fixed Parameters for Calculating HESS Discharging Power Split

	Parameter	Full Scale Battery Pack	2/9 Scaled for Experiment
DC/DC Converter Efficiency	η_{dc}	89%	89%
Ultracapacitor Pack Resistance	R_{uc}	29m Ω	6.5m Ω
Battery Pack Open Circuit Voltage	V_b	345V	76.8V
Battery Pack Resistance	R_b (25°C)	140m Ω	31m Ω
	R_b (0°C)	315m Ω	70m Ω
Output Power	P_{out}	-	$P_{out-meas}$

Maximum efficiency power split calculation from Chapter 5:

$$I_b = \frac{\left(R_b V_b V_{uc}^2 + \eta_{dc} R_{uc} V_b^3 - V_b \sqrt{\left(\eta_{dc} (R_{uc} \eta_{dc} V_b^2 + R_b V_{uc}^2) (R_{uc} V_b^2 + R_b \eta_{dc} V_{uc}^2 - 4 P_{out} R_b R_{uc}) \right)} \right)}{2 (R_b^2 V_{uc}^2 + \eta_{dc} R_{uc} R_b V_b^2)} \quad (5.11)$$

7.5 Testing Matrix & Test Procedure

To fully evaluate the performance of the hybrid energy storage system a matrix of tests was designed, as shown in Table 7.11 below. The test matrix includes a range of three drive cycles: (1) the urban UDDS cycle with low speeds and mild acceleration, (2) the LA92 drive cycle with higher speeds and more aggressive acceleration, and (3) the US06 cycle with high speeds and very aggressive acceleration. This range of drive cycles are considered to cover the full spectrum from mild to aggressive drive cycles. The test matrix also includes tests at room temperature, 25°C, to give typical performance in warm weather as well as at 0°C to give typical performance at cold temperatures. Finally the matrix also has each test being performed with only the battery pack as well as with the HESS – consisting of the battery pack with the ultracapacitor pack and dc/dc converter, allowing the battery pack and HESS performance to be directly compared. As shown in Table 7.11, the matrix then consists of three drive cycles, two temperatures, and two energy storage system cases, for a total of 12 tests.

Table 7.11 Test Plan for Scaled Battery Pack and Hybrid Energy Storage System

Drive Cycle	0°C		25°C	
	Battery Only	HESS	Battery Only	HESS
UDDS (urban)	Test #1	Test #2	Test #3	Test #4
LA92 (most typical)	Test #5	Test #6	Test #7	Test #8
US06 (aggressive)	Test #9	Test #10	Test #11	Test #12

Because the rule based power split control and the energy storage system model both assume a constant battery temperature, and therefore a constant nominal battery resistance, an important goal of the experimental testing is to keep the battery temperature as constant as possible. Keeping the temperature constant is a challenge though because a significant amount of losses are generated in the battery pack, especially at 0°C where the resistance of the pack is quite high. To illustrate

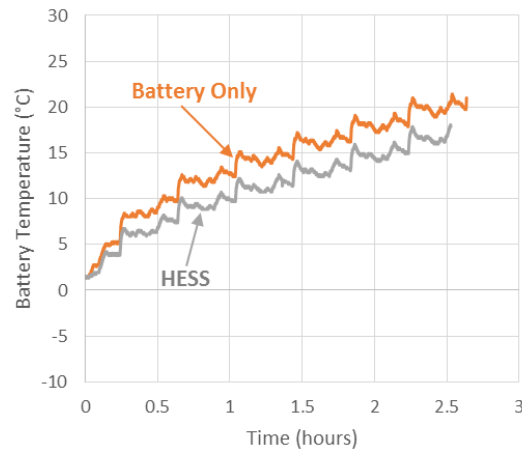


Figure 7.15 Measured battery and HESS temperature for continuously repeated LA92 drive cycles with 0°C ambient temperature and no pauses

just how much heat is generated, the LA92 drive cycle test, with the drive cycle repeating until a single cell voltage reached a lower limit, was performed at 0°C. The battery pack quickly heated up, reaching 10°C after 30 minutes and 20°C by the end of the test, as shown in Figure 7.15 above.

Two changes were made to the test procedure to ensure that battery pack temperature would remain relatively constant. The first change was adding one hour pauses to the test procedure to allow the battery pack to cool. For the UDDS drive cycle a single drive cycle was applied to the energy storage system, followed by a one hour pause and then repeated until the termination of the test, as shown in Figure 7.16. For the LA92 and US06 drive cycles, which have higher power and therefore higher losses than the UDDS cycle, the drive cycle was split into two sections and a one hour pause was performed after each section and repeated as shown in Figure 7.17 and Figure 7.18.

The second change made to keep battery temperature more constant was to utilize the thermal chamber's *product temperature control* feature. For *product temperature control*, a temperature sensor is fixed to the device under test, the battery pack in this case, and the thermal chamber regulates the chamber temperature to keep the device under test at constant temperature. The temperature sensor was placed between two batteries at the center of the pack, and the chamber was set such that the chamber temperature could be as much as 10°C below the setpoint, so as low

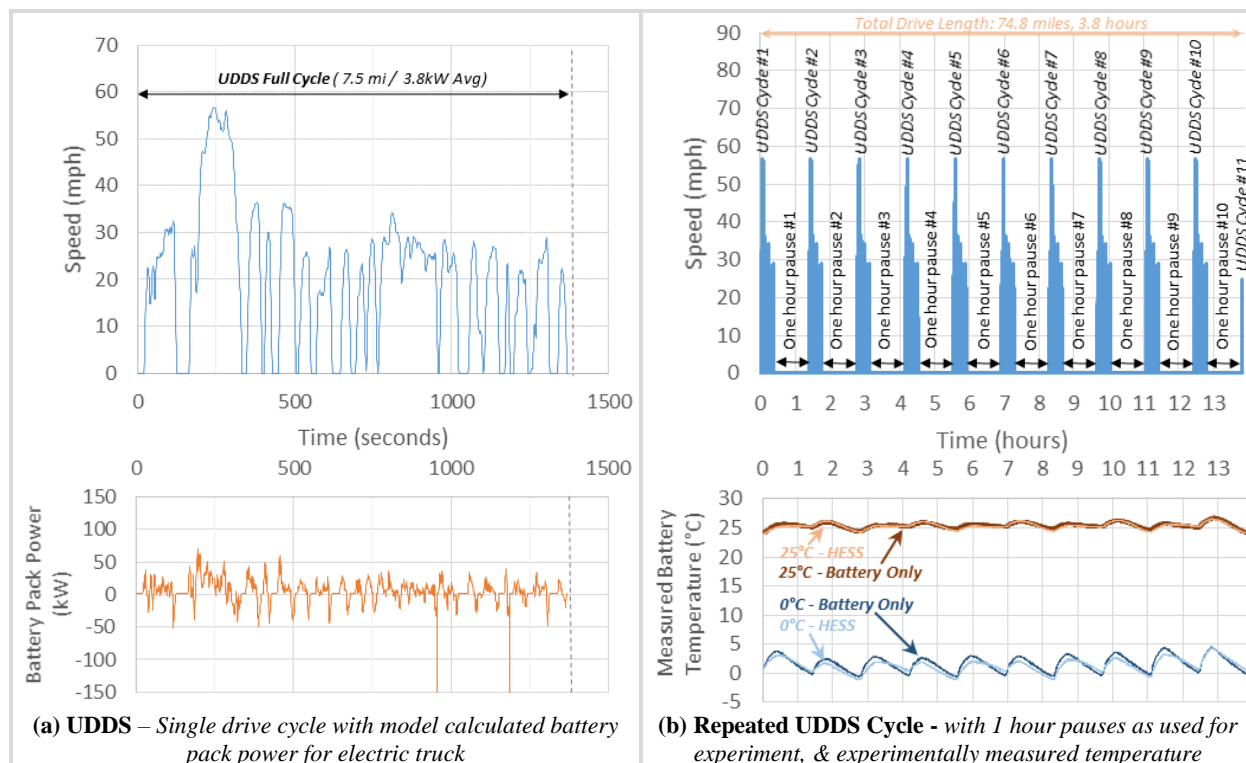


Figure 7.16 UDDS drive cycle speed profile, power calculated for electric truck, experimental testing profile with pauses, and experimentally measured temperature for profile with pauses

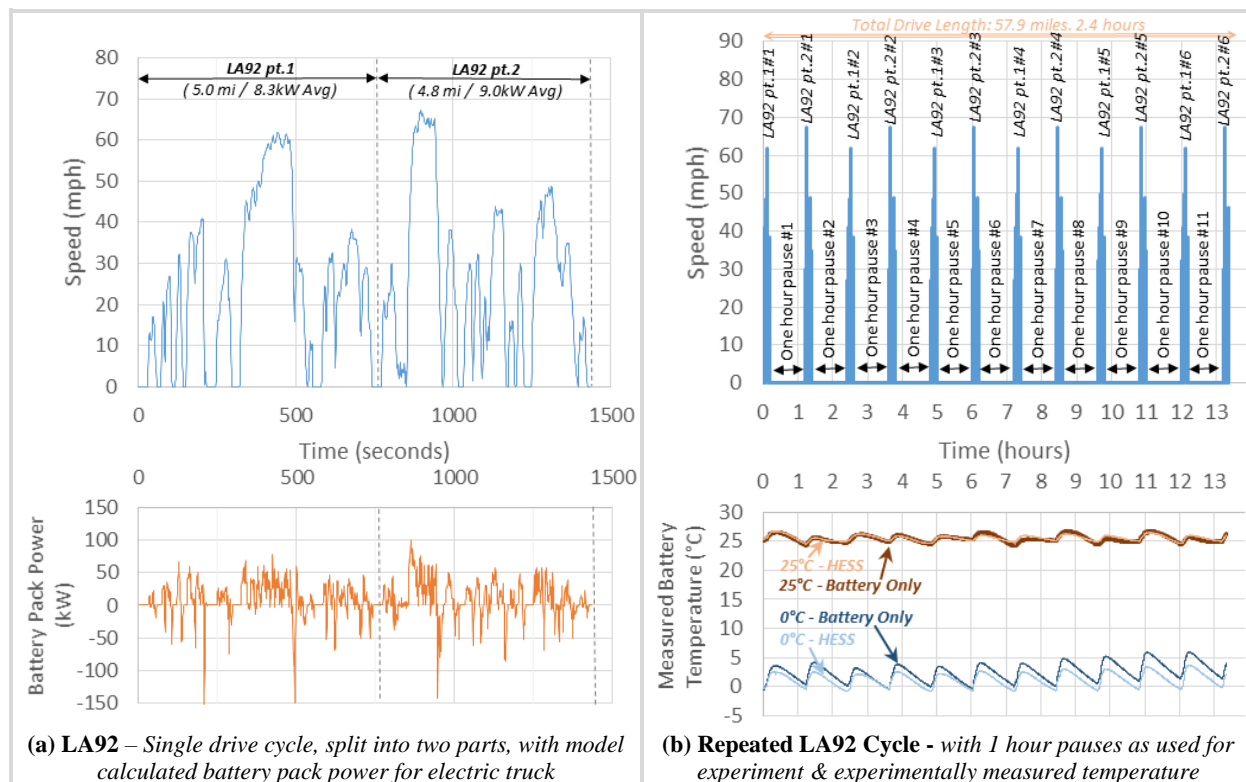


Figure 7.17 LA92 drive cycle speed profile, power calculated for electric truck, experimental testing profile with pauses, and experimentally measured temperature for profile with pauses

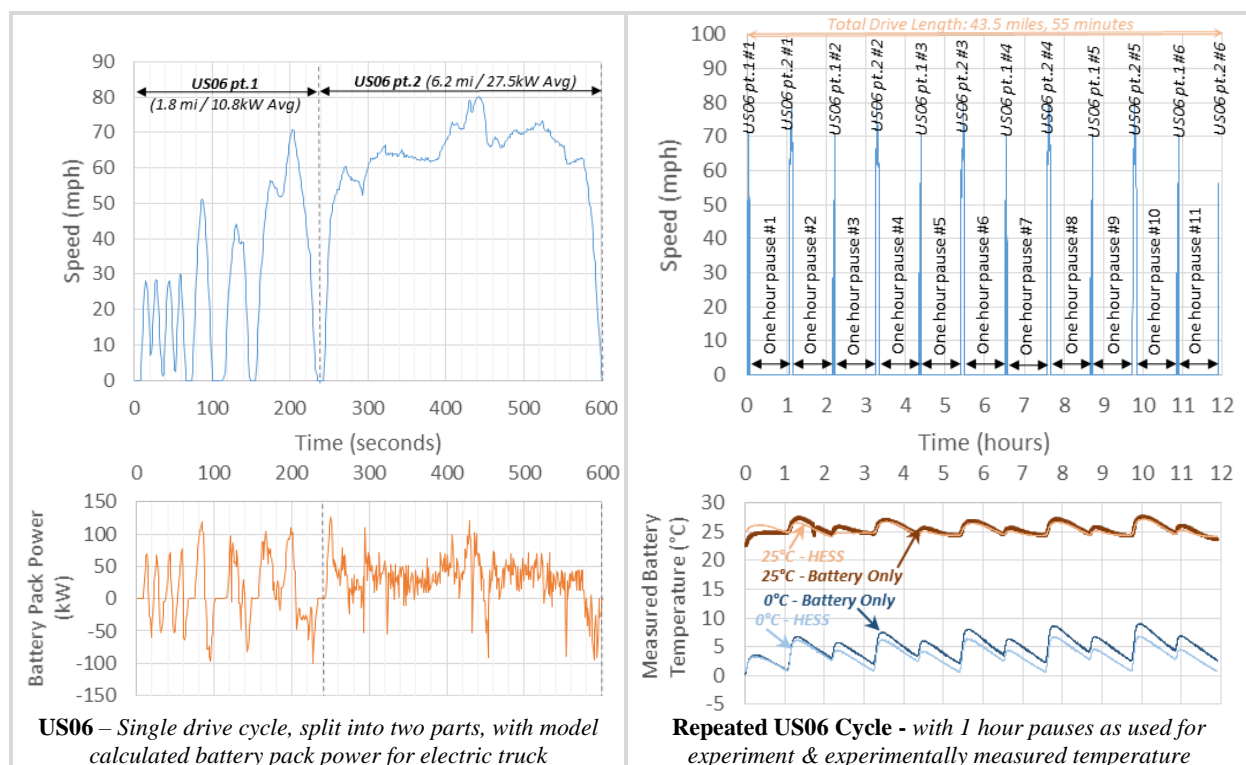


Figure 7.18 US06 drive cycle speed profile, power calculated for electric truck, experimental testing profile with pauses, and experimentally measured temperature for profile with pauses

as -10°C for the 0°C test and 15°C for 25°C test. This helped to both keep the battery temperature more constant during the test and to cool the battery more quickly during the one hour pauses. The measured temperature for each test is also shown in Figure 7.16 - Figure 7.18, showing that the changes to the test procedure resulted in relatively constant battery temperature as desired.

7.6 HESS Efficiency versus Power

The efficiency benefit's which can be achieved by the hybrid energy storage system are largely a function of the ultracapacitor pack resistance and the dc/dc converter efficiency. Because the dc/dc converter efficiency is so low for the scaled system tested, the hybrid energy storage system will not be as capable of improving the system efficiency as the full scale system. To illustrate the efficiency benefits achieved with the HESS, the battery only and HESS efficiency as a function of the system output power was calculated using the parameters in Table 7.10. The efficiency was

calculated for the nominal dc/dc converter efficiency of the experimental system, 89%, as well as for a 97% dc/dc converter efficiency. The results in Figure 7.20 show that the experimental system can only provide improved efficiency beyond an output power of about 12kW, while a system with a 97% efficient converter has improved efficiency beyond an output power of about 4kW.

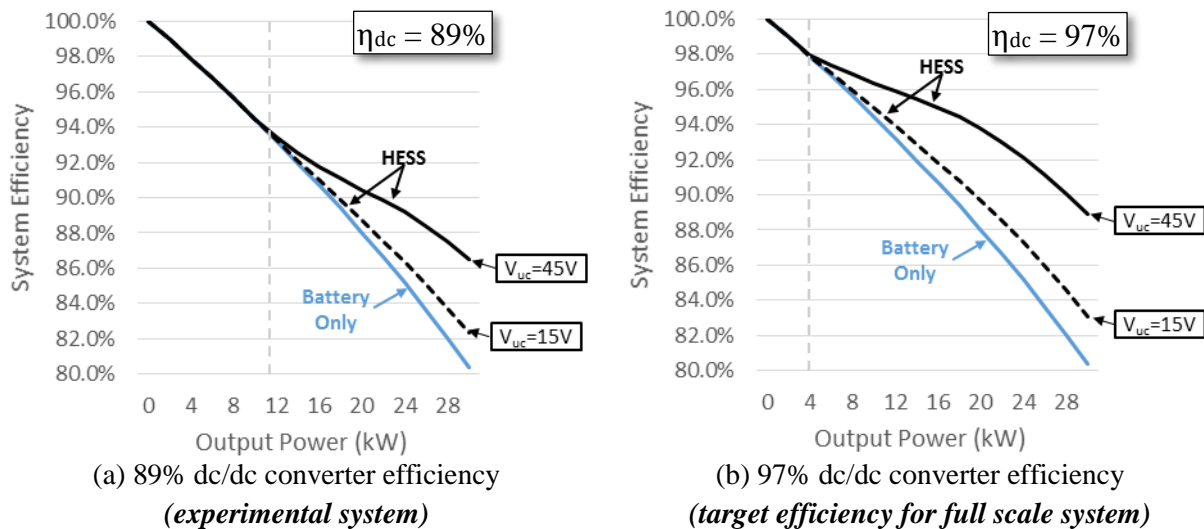


Figure 7.19 Battery only and HESS efficiency for scaled system at 25°C, calculated with scaled system parameters in Table 7.10

To further demonstrate how much the HESS may improve system efficiency, the battery only and HESS efficiency for 0°C and 25°C is overlaid with the time distribution of the power for each drive cycle in Figure 7.20 below. The full vehicle scale power and efficiency is shown in the figure, but these results scale directly for the experimental system. The figure shows that the UDDS drive cycle will benefit very little from the HESS because the power is almost entirely below the threshold of improved efficiency with the HESS, while the LA92 and US06 drive cycles will benefit substantially more because of their proportion of higher power points. Additionally the figure shows that because battery resistance is higher at lower temperatures, all of the drive cycles will benefit more from the HESS at lower temperatures.

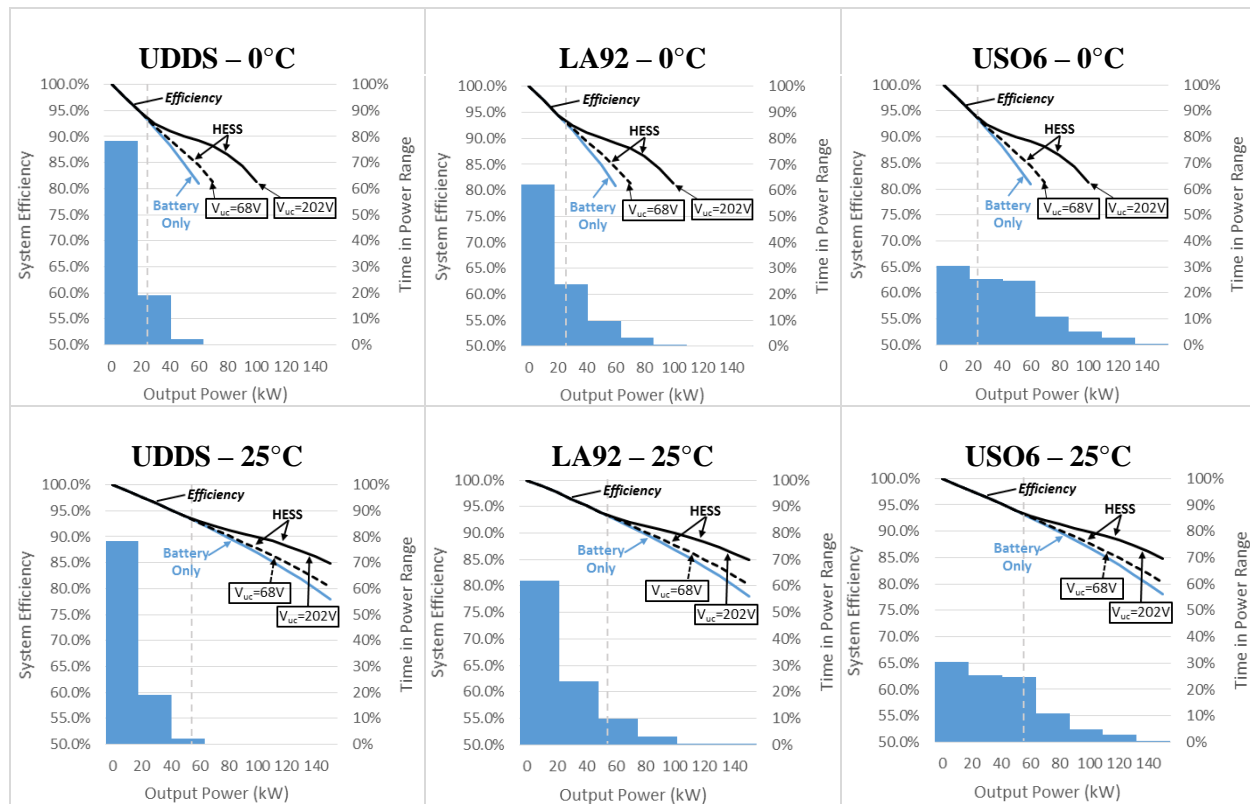


Figure 7.20 Drive cycle power distribution and battery only and HESS efficiency for full scale system, calculated with full scale system parameters in Table 7.10, including 89% dc/dc converter efficiency

7.7 Measured Results from Experimental Testing

The experimental test results for all of the test cases, including current, voltage, and temperature, were recorded at a rate of one hertz using the Digatron test equipment. For the HESS tests additional data was recorded using the dspace control system, including the ultracapacitor voltage and ultracapacitor, dc/dc converter output, and total system output current. These measured results are presented in the following subsections, first for a single drive cycle as an example, followed by a comparative summary of the results for all the test cases.

7.7.1 Overview of results for a single test case – LA92, 0°C, HESS & battery only

To provide insight into how the hybrid energy storage system performs, time series data for the first 0°C LA92 drive cycle of the battery only and HESS test cases is provided in this subsection.

Figure 7.21, which shows the battery, ultracapacitor, and total system power, illustrates how the ultracapacitor provides a significant amount of power during high power discharge pulses (positive power), while the ultracapacitor receives as much as 80% of the charging power as dictated by the rule based control. In Figure 7.22 it can be seen that the dc/dc converter ultracapacitor current limit of 200A_{dc} is regularly reached, limiting the benefit of the HESS, and additionally it can be seen that the ultracapacitor pack is cycled several times in this first 1400 seconds of the test. These results show that the rule based controller is functioning properly, and that the full current capability of the dc/dc converter and the full voltage range of the ultracapacitor pack is utilized.

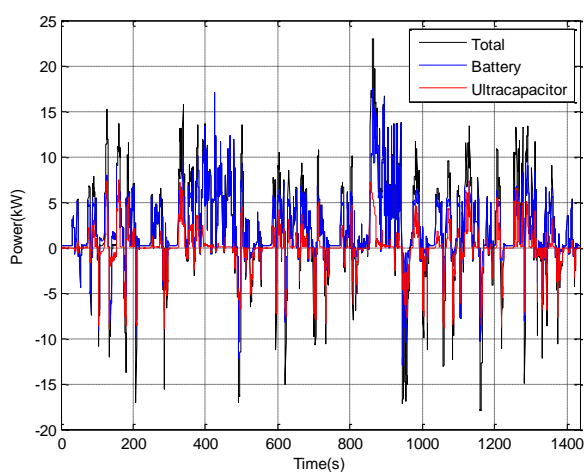


Figure 7.21 HESS battery, ultracapacitor, and total system power for first LA92 0°C drive cycle

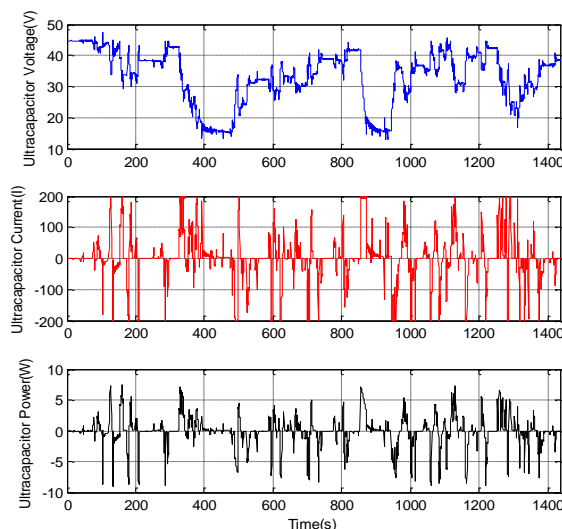


Figure 7.22 Ultracapacitor current, voltage, and power for first LA92 0°C drive cycle

The battery pack voltage for the battery only and HESS test cases is overlaid in Figure 7.23, showing that the battery voltage deviates less from the nominal open circuit value for the HESS test case. The lower voltage deviation, which is due to lower battery current, results in lower battery pack losses and hopefully lower system losses as well. An additional benefit of the HESS is also demonstrated in Figure 7.24, where it is observed that the HESS has a both a higher charge and discharge power capability, which will result in less power limiting during motoring and greater capture of regenerative braking energy.

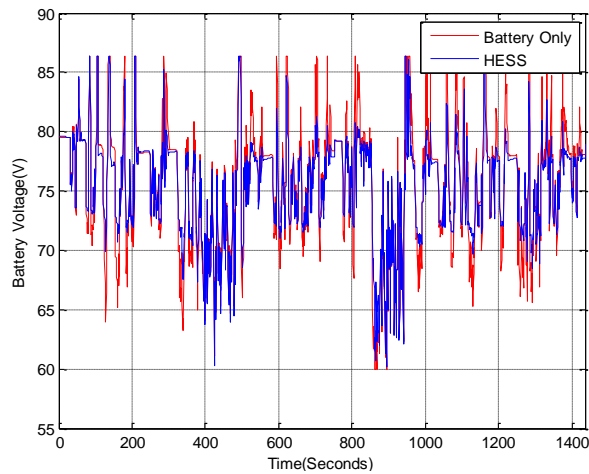


Figure 7.23 Battery voltage for battery only and HESS for first LA92 0°C drive cycle

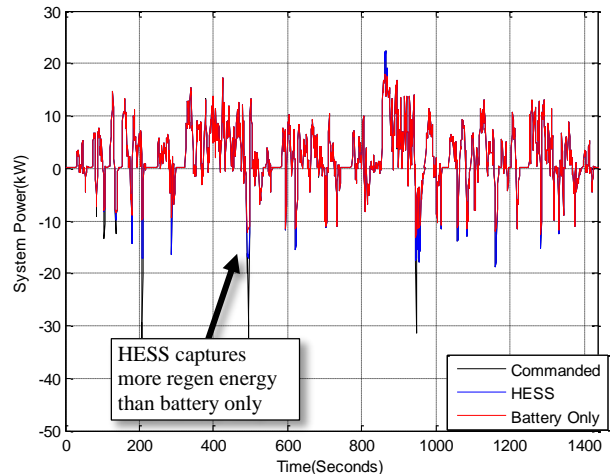


Figure 7.24 Commanded, HESS, and battery only power for first LA92 0°C drive cycle

7.7.2 Measured battery temperature for each test case

The battery temperature rise is an indicator of how much losses are being generated in the battery pack, providing a qualitative measure for comparing battery pack losses for different test cases. The battery pack temperature for each test case, with the temperature data removed for the one hour pauses, is shown below in Figure 7.25. There are several observations which can be made from these results, including: (1) temperature rise is greater for the battery only system because more of the system power is provided by the battery pack, (2) temperature rise is greater at low temperatures due to increased battery resistance resulting in greater battery losses, and (3) temperature rise is the greatest for the US06 cycle because it has the greatest average power and therefore the greatest average losses as well. These results confirm that the HESS does reduce battery pack losses and temperature, which will presumably reduce battery aging. With a more efficient dc/dc converter, as would be realized in a full scale system, the HESS would be able to further reduce battery pack losses, increasing the difference in temperature between the battery only and HESS test cases.

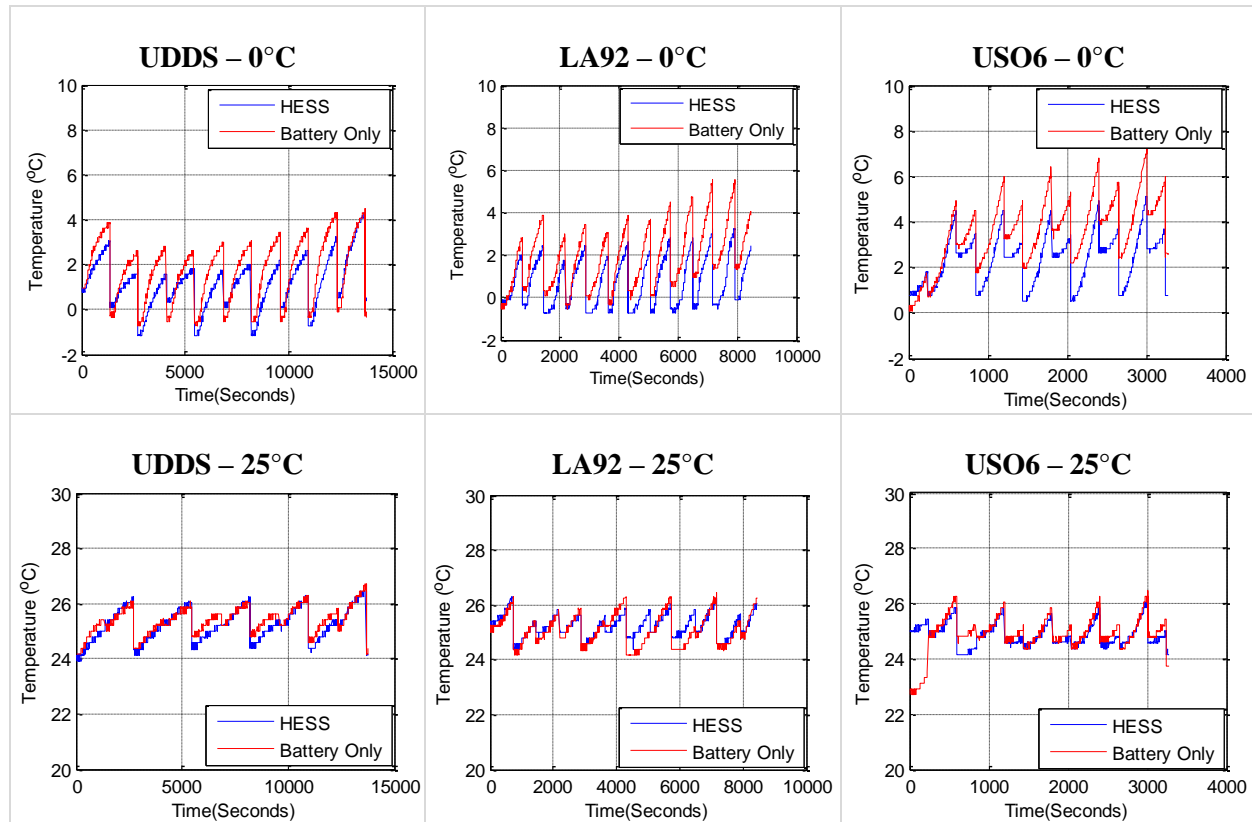


Figure 7.25 Measured battery temperature for each test case

7.7.3 Summary of Measured System Improvements Achieved with HESS

The primary goal of the HESS's rule based controller, as presented in 7.4, is to improve the system efficiency during discharging. To determine how successful the HESS is at improving system efficiency as well as other aspects of system performance, the experimental results for each drive cycle are analyzed and the HESS and battery only performance are compared in this subsection.

The energy storage system efficiency is indicated, albeit indirectly, by the amp-hours consumed from the battery for a given drive cycle. Each drive cycle requires a fixed amount of energy from the battery pack, if there are more battery losses, more amp-hours will be consumed from the battery pack because the battery must supply the drive energy plus the battery loss energy. The test length was chosen to be the amount of time it took to reach 65Ah discharged from the battery

for the 25°C battery only case, as can be observed in Figure 7.26. Considerably greater amp-hours are discharged from the battery for the 0°C cases due to increased battery losses and power limiting, and fewer amp-hours are consumed from the battery for the HESS cases due to a reduction of battery and overall energy storage system losses. Additionally to illustrate the limit of performance, the amp-hours consumed for an ideal battery only system with no battery losses is also included in Figure 7.26, showing that for a lossless system amp-hour consumption would be reduced a further 6 to 12%.

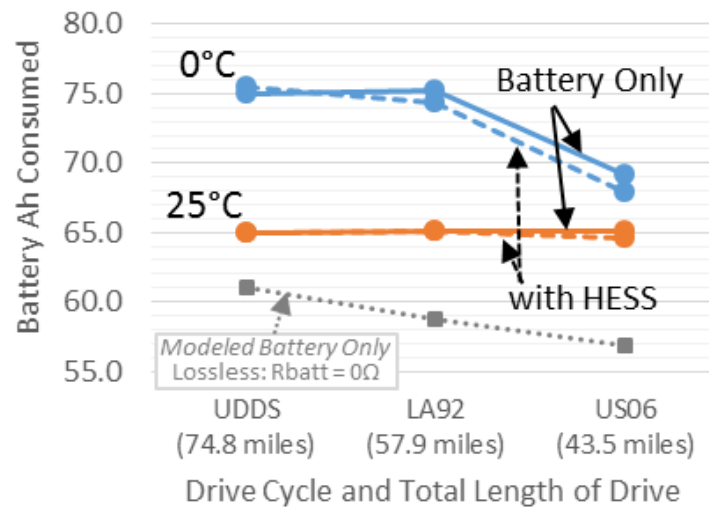


Figure 7.26 Experimentally measured amp-hours consumed from battery pack for each test case and model estimated amp-hours for lossless battery only case

To give a better understanding of just how much the HESS reduces the amp-hours drawn from the battery pack, the percentage reduction of amp-hours consumed from the battery pack is shown in Figure 7.27. The amp-hours consumed is reduced between 0.0 and 0.7% at 25°C and between -0.7 and 1.7% at 0°C. Considering the very low efficiency of the experimental dc/dc converter this a respectable improvement, with the exception of course of the UDDS 0°C case which performs worse with the HESS. More battery amp-hours are likely consumed for this case because the HESS does have the effect of keeping battery temperature lower, which has the downside of

keeping battery resistance and therefore losses higher. The reduction in amp-hours achieved for the other HESS cases translates directly to increased vehicle range, resulting in an increase of range of 0.75 miles for the US06 0°C case for example.

Several other performance improvements achieved with the HESS are also summarized in the graphs of Figure 7.27. The HESS is shown to reduce battery rms current by up to 25%, which helps to explain the lower battery temperatures observed in Figure 7.25 for the HESS cases. The HESS is also shown to increase the regenerative braking energy captured at 0°C, reducing the

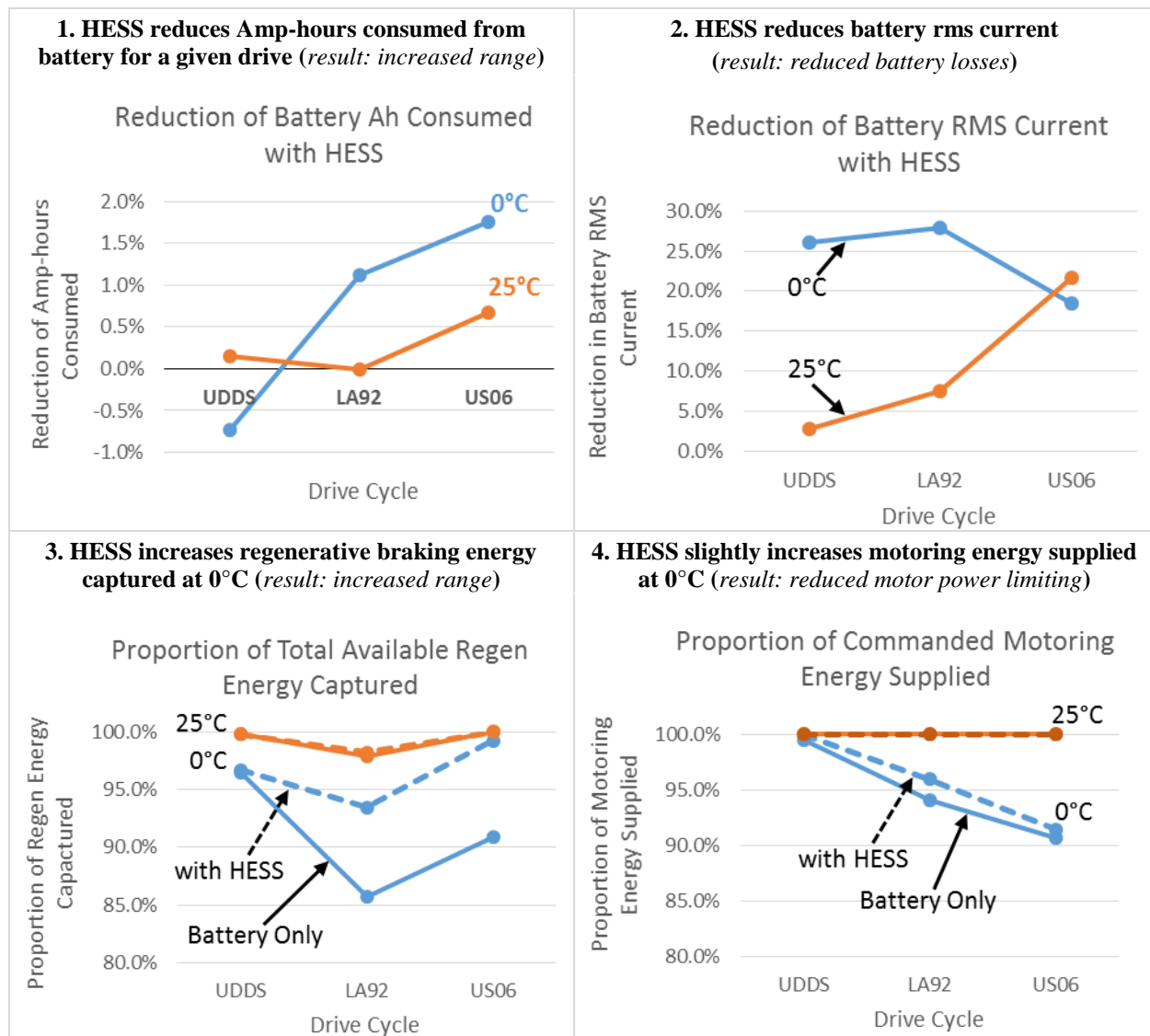


Figure 7.27 Summary of experimentally measured performance results for battery only and HESS tests

braking energy that would be dissipated as heat in the mechanical braking system and improving the range of the vehicle. Finally the HESS is also shown to slightly increase the motoring energy supplied at 0°C, meaning there is less power limiting due to the battery voltage hitting the minimum limit.

Figure 7.28 below shows the motoring energy, regenerative braking energy, and the total energy, which is the sum of the latter, for each test case. The energy storage system is shown to provide the most energy for the mild UDDS drive cycle, 4.8 to 4.9kWh, versus only 4.0 to 4.6kWh for the more aggressive LA92 and US06 cycles. More energy is output for the UDDS cycle because there are fewer energy storage system losses for this low power cycle, and therefore less of the battery energy goes to supply internal battery pack and HESS losses. Figure 7.28 also shows that the UDDS and LA92 cycles, which have a large number of starts and stops, have nearly double the regenerative braking energy of the US06 cycle, which has a long period of high speed driving but fewer starts and stops.

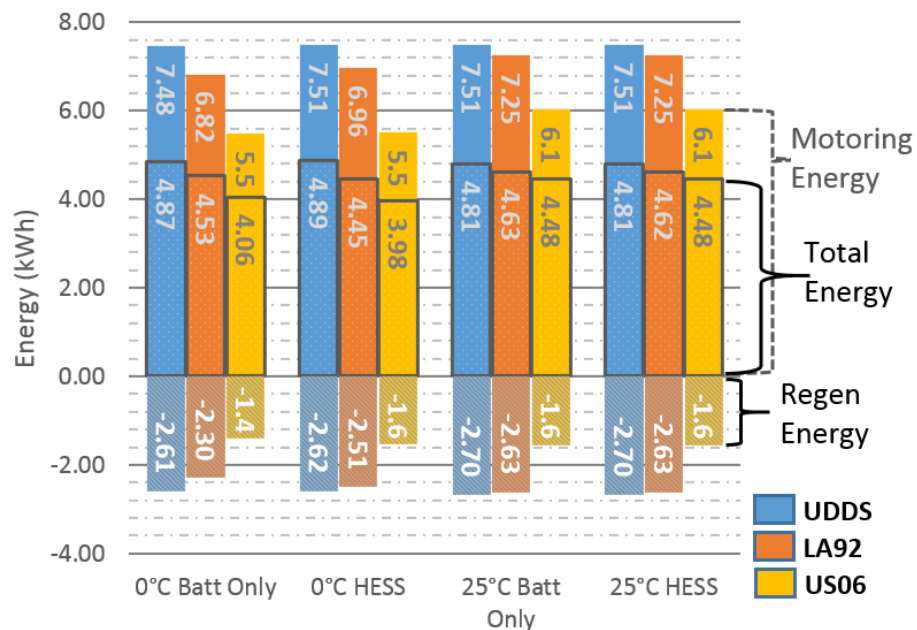


Figure 7.28 Experimentally measured motoring, regenerative braking, and total energy for all test cases

7.7.4 Ultracapacitor Pack Contribution to System Energy

To give insight into how much of the system energy is provided by the HESS, the distribution of battery and ultracapacitor motoring and regenerative braking energy is shown in Figure 7.29. The ultracapacitor is shown to provide a relatively small portion of the total energy for the UDDS and LA92 cycles at 25°C, while providing a significant portion of the energy for the US06 cycle and the lower temperature cases, ranging from 9 to 15% of the motoring energy and 37 to 62% of the regenerative braking energy. With a more efficient dc/dc converter and/or a controller which better manages ultracapacitor state of charge, even more of the drive energy could be provided by the ultracapacitor, resulting in additional system performance improvements.

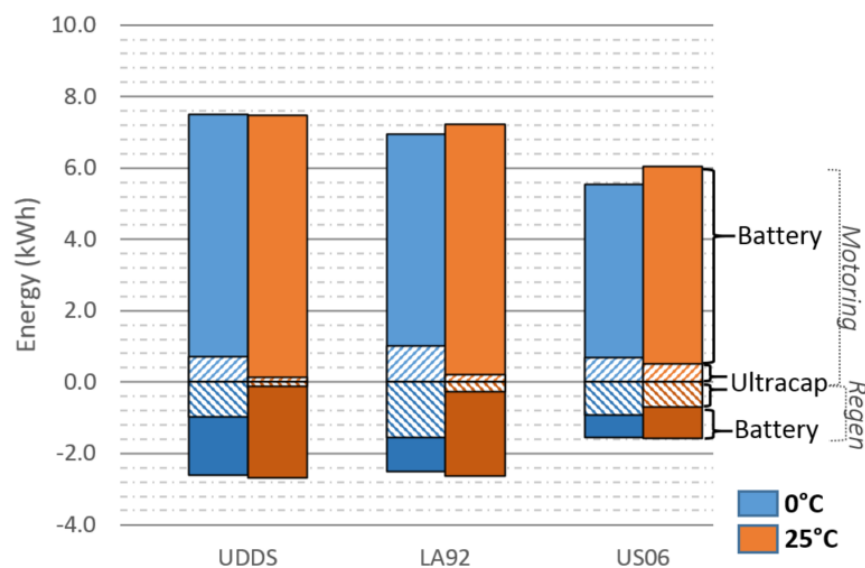


Figure 7.29 Experimentally measured distribution of battery and ultracapacitor motoring and regenerative braking energy for each HESS test case

7.8 Summary of Measured versus Modeled System Performance

The HESS model, which was developed for room temperature in Chapter 5 and for low temperatures in Chapter 6, is utilized in this section to predict the system performance for the various test cases. While the full system should perform similarly to the model, there are several reasons to expect that the experimental system performance will vary somewhat from the model,

including: (1) SOC imbalance and aging of the 24 cell battery pack, which was removed from the electric truck for this testing, (2) Self heating and temperature variation among cells in the battery pack, which is cooled by ambient air, (3) DC/DC converter output current delay, overshoot, and error due to the controls, and (4) battery amp-hour measurement error for the HESS, which is measured by the dspace system. Although many of these aspects could likely be captured in a more sophisticated model, they are expected to be minor enough that the existing system model will be sufficient to accurately capture many aspects of the system performance.

7.8.1 Measured and Modeled Ultracapacitor Voltage for Each Test Case

For each test case the ultracapacitor current command is determined by the rule based control as defined in section 7.4. The commanded current results in cycling of the ultracapacitor, as is shown in the measured and modeled ultracapacitor voltage traces in Figure 7.30 on the following page. The ultracapacitor pack is modeled using the same method as provided in Chapter 5, and the controller is set for a minimum voltage limit of 15V and a maximum voltage limit of 45V, as defined in Table 6.5. The measured and modeled voltages line up very well, showing that (1) the ultracapacitor model is accurate and (2) the rule based controller is correctly implemented in the dspace hardware.

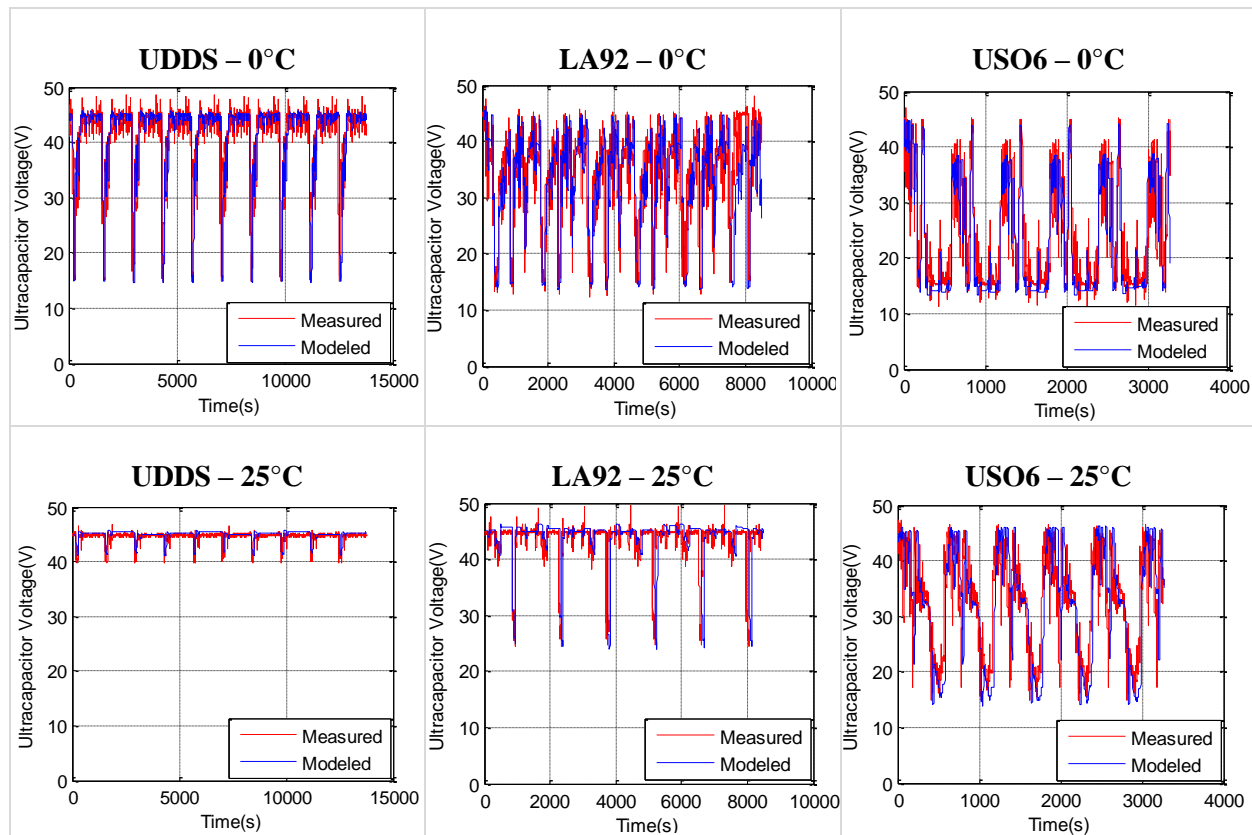


Figure 7.30 Measured versus modeled ultracapacitor voltage for each HESS test case

7.8.2 Measured versus Modeled Battery RMS Current

The HESS supplies a significant amount of the system power with the ultracapacitor pack, resulting in a reduction of the battery rms current, as was observed in Figure 7.27 above. The model predicted and measured battery rms current are overlaid in Figure 7.31 below, and are shown to be very similar for both the 0°C and 25°C cases. The similarity of the measured and model predicted results shows that the model is very good at capturing the reduction in rms current achieved with the HESS, and should therefore also be good at capturing the reduction in battery losses. Furthermore because the predicted battery rms current for the HESS is a function of not just the battery model but of the whole system model, the accuracy of the rms prediction indicates good performance of the full system model.

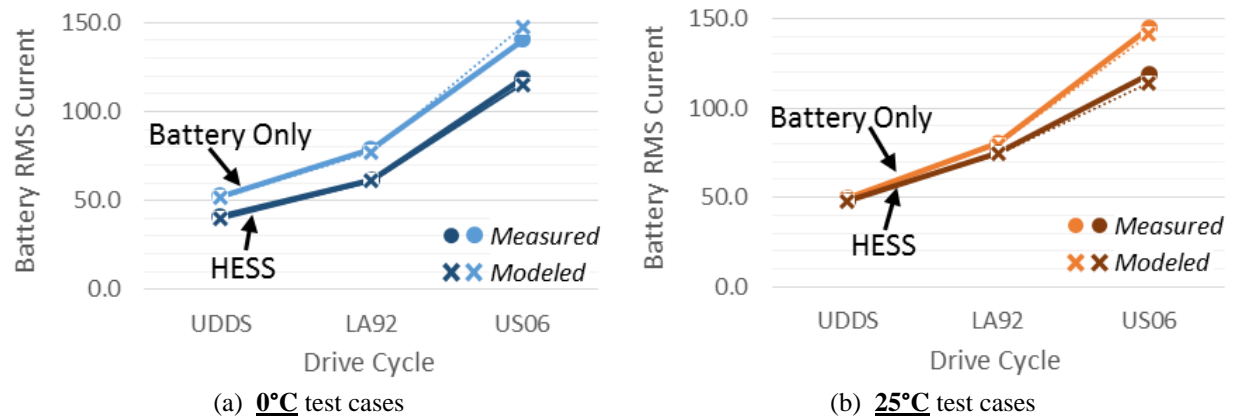


Figure 7.31 Measured versus modeled battery RMS current for each test case

7.8.3 Measured versus Modeled Battery Amp-hours for Each Test Case

One of the most important, but also challenging to predict parameters is the amp-hours consumed for each drive cycle. The amp-hours consumed is difficult to predict because it is a function of the battery's open circuit voltage as well as of the charge and discharge resistance, all of which are a function of state of charge, temperature, and age of the battery. The 24 cell battery pack under test was taken out of service from the electric truck and due to the inadequate accuracy of the truck's BMS the battery pack is quite imbalanced, as can be seen in the cell voltage plot of Figure 7.32.

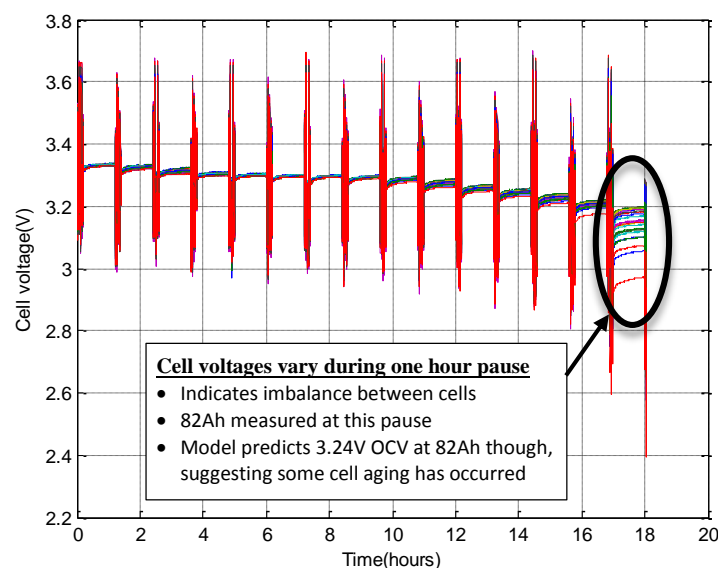


Figure 7.32 Experimentally measured cell voltage for LA92 25°C battery only test

Additionally the battery pack temperature varies significantly during each test case and the pack is aged – it is four years old and has been driven about 5000 miles. With all of these factors contributing to model error, the variance between the modeled and measured amp-hours, as shown in Figure 7.33 below, is actually quite reasonable. For the 25°C cases the model error ranges from 0 to 0.4Ah (0 to 0.6%), while for the 0°C cases the model error ranges from 0.7 to 3.0Ah (0.9 to 4.2%). For the 0°C case the error is likely larger because the Butler-Volmer effect's impact on the battery resistance makes the battery more difficult to accurately model.

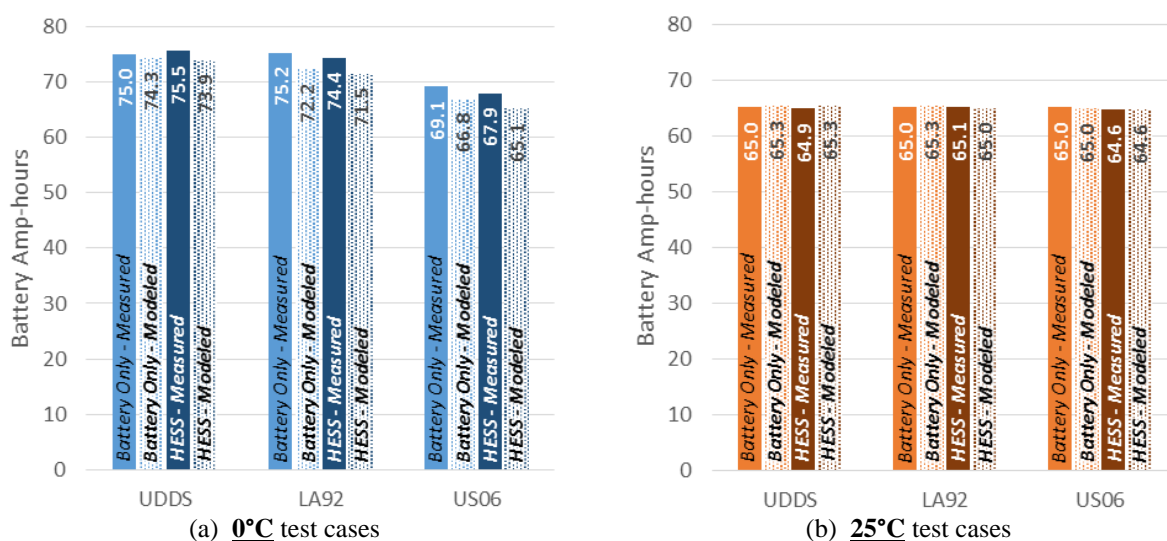


Figure 7.33 Measured versus modeled battery amp-hours consumed for each test case

One important use of the model is to predict how much the amp-hour consumption from the battery will be reduced by adding the HESS. Table 7.12 below provides the model predicted and measured reduction in amp-hours achieved with the HESS, and shows that the actual system tends to improve performance less than the model predicts. A reduction in amp-hours of 0 to 0.5% are predicted for the 25°C cases, while improvements of 0 to 0.7% are achieved, and reductions of 0.6 to 2.5% are predicted for the 0°C cases, while improvements of only -0.7 to 1.7% are achieved. The underperformance of the experimental system is likely due to a single cause – battery heating.

Even with the efforts made to keep battery temperature constant, the battery temperature is observed to be greater for the battery only case than the HESS case for all test cases. The greater battery temperature will result in lower battery resistance for the battery only test case, diminishing the comparative difference between the battery only and HESS case. This reduced performance compared to the model is therefore expected, and illustrates that due to battery heating an actual system will achieve less of a performance benefit than is predicted by a fixed temperature model.

Table 7.12 Modeled versus Measured Reduction in Amp-Hours Consumed for HESS versus Battery Only Case

	<i>0°C Reduction in Ah Consumed</i>			<i>25°C Reduction in Ah Consumed</i>		
	Modeled	Measured	Difference	Modeled	Measured	Difference
UDDS	0.6%	-0.7%	-1.3%	0.0%	0.1%	+0.1%
LA92	1.0%	1.1%	0.1%	0.4%	0.0%	-0.4%
US06	2.5%	1.7%	-0.8%	0.5%	0.7%	+0.2%

7.8.4 Modeled Reduction in Amp-hours for HESS with $\approx 97\%$ dc/dc converter efficiency

If the experimentally tested hybrid energy storage system had a $\approx 97\%$ efficient dc/dc converter, as would be utilized in the real application, the difference between the HESS and battery only system performance would be significantly more pronounced, as shown in the model results of Figure 7.34 below. The HESS with a $\approx 97\%$ efficient converter and rule based control is predicted to achieve a 1-2.5% reduction in amp-hours at 25°C and a 3.5-4.5% reduction at 0°C, about three times the performance improvement achieved with the 89% efficient converter. With a 350V dc bus, rather than the 80V dc bus used in the experiment, the experimental converter has efficiency in the range of 97%, and should achieve similar performance to that shown in Figure 7.34. With a higher voltage rated battery test system and more ultracapacitor modules, equipment which WEMPEC does not currently have, the system could be evaluated at it's a full voltage range and

the improvement in system performance would likely be much more significant than that achieved with the 80V system.

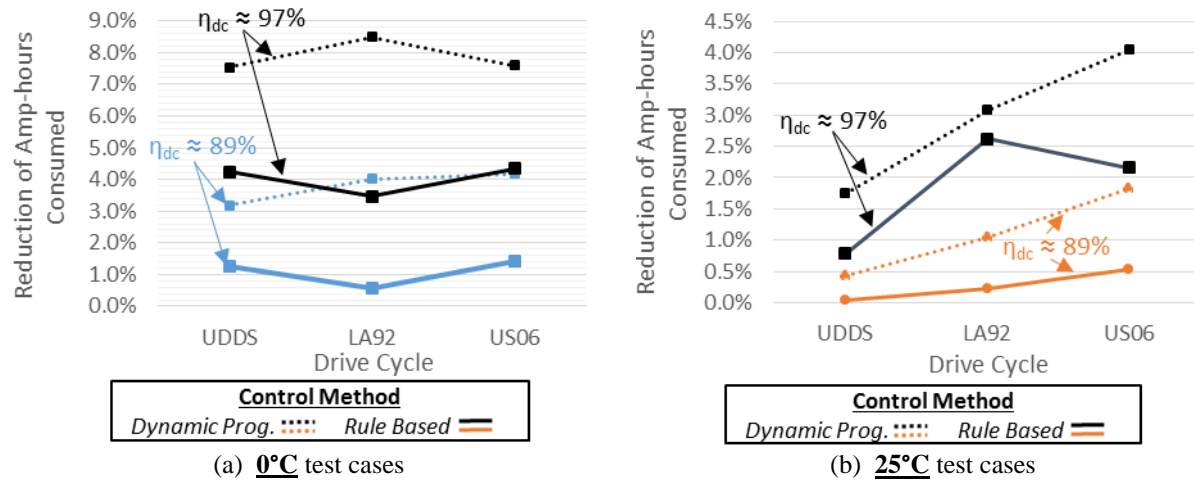


Figure 7.34 Modeled HESS versus battery only reduction in battery amp-hours consumed for experimental $\approx 89\%$ efficient dc/dc converter and for modeled $\approx 97\%$ efficient converter

For reference, Figure 7.34 also shows performance achieved with dynamic programming control. The dynamic programming algorithm is set to minimize the amp-hours consumed from the battery, and therefore results in the maximum reduction in amp-hours which could be achieved with the system. For the 97% controller case the rule based controller is shown to work quite well at 25°C, achieving a significant proportion of the reduction achieved with dynamic programming. For the 0°C case the performance is not quite as good, with the rule based controller only achieving about 1/2 of the possible reduction in amp-hours. This failing of the rule based controller is due to the ultracapacitor trending toward a discharged state, as can be seen for the experimental US06 cycle results in Figure 7.35 below. This tendency towards discharge can be combatted with additional control rules, such as the control rules implemented in Chapter 5 which were a function of vehicle speed. With the addition of a speed reference to the experimental system, which is not possible with the current Digatron based test system, these additional speed based control rules could be implemented.

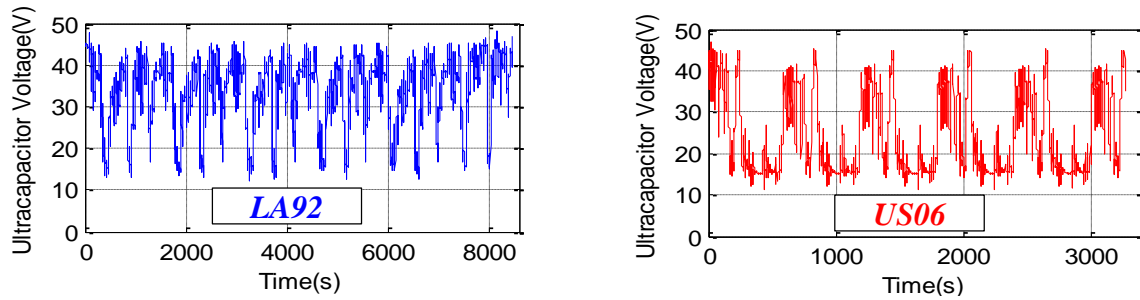


Figure 7.35 LA92 and US06 0°C experimentally measured ultracapacitor voltage

7.9 Conclusions

A scaled prototype hybrid energy storage system was designed, built, and experimentally tested in this chapter. The process began with the design and fabrication of a prototype 200A rated, bidirectional half-bridge dc/dc converter, utilizing components which were readily available in the lab. The converter loss was modeled, and the error between the modeled and measured loss was shown to be relatively small. The measured efficiency of the converter was found to be quite low for the 80V dc bus of the scaled HESS, ranging from 71% to 94%. A 400A dc/dc converter was then designed utilizing the latest generation of Semikron IGBTs, film capacitors, and a custom designed inductor, to demonstrate the size and performance of a higher power, more production oriented converter. The 400A dc/dc converter was modeled to have efficiency ranging from 97-99% with a 350Vdc bus, and to have a component mass of 13.5kg and volume of 3.3L. The converter was also paired, for the purposes of modeling, with a 375Wh pack of Skeleton ultracapacitors, creating a 50.5kg, 50L system.

The scaled hybrid energy storage system, which includes an 80V battery pack consisting of two of the truck's nine battery modules, a 48V / 165F ultracapacitor pack, and the prototype dc/dc converter, is then assembled. The scaled HESS is tested at two temperatures, 0°C and 25°C, for three drive cycles, and both for the battery only and HESS case. The rule based controller, which controls the dc/dc converter power, is shown to function properly, and the model is shown to

predict the amp-hours drawn from the battery to within a maximum error of 0.6% at 25°C and 4.2% at 0°C. The larger error at low temperatures is likely due mostly to battery heating. The model is also shown to predict the ultracapacitor current and the reduction in battery rms current very well. The HESS is also shown to result in a modest reduction in amp-hours drawn from the battery, as much as 0.7% at 25°C and 1.7% at 0°C, which would result in increased vehicle range. The increase in range is so small primarily because the converter efficiency is so low, with a nominal efficiency of 89%. With a converter with a nominal efficiency of 97%, as would be used in the full scale application, an increase in range as large as 4.5% would be expected.

Chapter 8

HESS Performance for Alternative Vehicle Configurations

8.1 Introduction

In the prior chapters of this dissertation the developed modeling methodology was only applied to a single vehicle and battery type. In this chapter three alternative vehicle configurations are modeled to demonstrate that the modeling can be easily applied to other vehicle and battery types, as well as to try and identify other promising applications of hybrid energy storage. For the first configuration, the prototype electric truck is modeled with an alternative battery pack consisting of Panasonic NCR18650PF cells, which are very similar to the cells used in the Tesla Model S electric vehicle. These LiNiCOMnO_2 batteries, which have very different characteristics than the LiFePO_4 cells used in the truck, including much higher energy density, lower resistance, higher minimum charging temperature, and lesser effect of temperature on resistance, are shown to still benefit significantly from the addition of an HESS.

For the second configuration, a 40 foot electric city transit bus is modeled with a 140kWh LiFePO_4 pack, and is modeled with and without an HESS for various transit bus drive cycles. Due to the very heavy mass of the bus, and the large numbers of starts and stops in a bus drive cycle, the energy storage system in the bus has to provide a much greater number of higher power pulses than a light duty vehicle and as a result is shown to be a very good candidate for an HESS. For the third configuration, an electric truck with 2015 model year performance specifications is modeled, which has roughly double the power, wheel torque, and towing capability of the 2002 model year specifications that the prototype electric truck design was based off of. The same LiFePO_4 battery pack is utilized in this modeled truck though, resulting in an interesting scenario:

the battery pack can only provide about 180kW peak and the drivetrain can draw more than 270kW, meaning the HESS is necessary to achieve the full power rating of the vehicle. The 2015 model year truck study examines this power limited scenario as well as performance over a range of towed mass.

8.2 HESS Performance for an Electric Truck with a Panasonic Battery Pack

One of the most significant ways the electric truck can be improved is to switch to a different, higher energy density, and hopefully lower resistance, battery pack, resulting in reduced vehicle mass and improved performance. To provide a significant contrast in performance compared to the truck's existing LiFePO_4 battery pack (103Wh/kg), a very high energy density (211Wh/kg) Panasonic NCR18650PF power cell with a LiNiCOMnO_2 chemistry is studied as a replacement, as shown in Figure 8.1. The Panasonic cell is similar to that utilized in the Tesla Model S, and only very basic specifications are available publicly, so several cells were purchased and one was tested to provide all the information needed to model its performance in the electric truck. The test parameters are provided, then a battery pack is designed with the cells, a drive cycle is applied to one cell to confirm the model accuracy, and lastly the performance of the electric truck with the Panasonic pack and an HESS is modeled for a range of temperatures.



Figure 8.1 Panasonic NCR18650PF LiNiCOMnO_2 Battery

8.2.1 Measured Panasonic NCR18650PF Parameters

The LA92 HPPC resistance and HPPC Butler-Volmer pulse resistance tests, as described in the low temperature modeling chapter, were performed on the Panasonic cells at 25°C, 10°C, 0°C,

-10°C, and -20°C, and the measured parameters are provided in Table 6.2, Table 6.1, and Table 8.3 below. The cells are rated to provide 2.7Ah nominal, but resistance more than doubles after 2.5Ah have been discharged, so the battery is considered to provide about 2.5Ah of useful charge and test data is not provided beyond that depth of discharge.

Table 8.1 LA92 HPPC Resistance and Open Circuit Voltage for Panasonic NCR18650PF Cell

25°C										
<i>Ah discharged</i>	0 Ah	0.29 Ah	0.58 Ah	0.87 Ah	1.16 Ah	1.45 Ah	1.74 Ah	2.03 Ah	2.32 Ah	2.51 Ah
<i>OCV</i>	4.179 V	4.048 V	3.935 V	3.836 V	3.752 V	3.662 V	3.590 V	3.525 V	3.443 V	3.353 V
<i>R_{batt-dis}</i>	60.7 mΩ	46.6 mΩ	43.1 mΩ	40.2 mΩ	39.5 mΩ	39.1 mΩ	39.1 mΩ	40.4 mΩ	45.9 mΩ	102 mΩ
<i>R_{batt-ch}</i>	39.0 mΩ	38.9 mΩ	36.0 mΩ	34.4 mΩ	32.7 mΩ	32.9 mΩ	33.8 mΩ	34.7 mΩ	37.8 mΩ	50.6 mΩ

10°C										
<i>Ah discharged</i>	0 Ah	0.29 Ah	0.58 Ah	0.87 Ah	1.16 Ah	1.45 Ah	1.74 Ah	2.03 Ah	2.32 Ah	2.51 Ah
<i>OCV</i>	4.188 V	4.034 V	3.919 V	3.820 V	3.74 V	3.653 V	3.578 V	3.506 V	3.425 V	3.362 V
<i>R_{batt-dis}</i>	90.0 mΩ	63.6 mΩ	56.9 mΩ	53.3 mΩ	52.6 mΩ	52.2 mΩ	52.6 mΩ	55.7 mΩ	72.8 mΩ	113 mΩ
<i>R_{batt-ch}</i>	56.0 mΩ	55.2 mΩ	49.0 mΩ	46.2 mΩ	43.8 mΩ	43.8 mΩ	44.8 mΩ	47.9 mΩ	54.8 mΩ	45.6 mΩ

0°C									
<i>Ah discharged</i>	0 Ah	0.29 Ah	0.58 Ah	0.87 Ah	1.16 Ah	1.45 Ah	1.74 Ah	2.03 Ah	2.32 Ah
<i>OCV</i>	4.127 V	3.975 V	3.877 V	3.816 V	3.701 V	3.620 V	3.558 V	3.489 V	3.407 V
<i>R_{batt-dis}</i>	120 mΩ	93.4 mΩ	81.9 mΩ	80.3 mΩ	74.0 mΩ	75.3 mΩ	76.0 mΩ	85.0 mΩ	128 mΩ

-10°C								
<i>Ah discharged</i>	0 Ah	0.29 Ah	0.58 Ah	0.87 Ah	1.16 Ah	1.45 Ah	1.74 Ah	2.03 Ah
<i>OCV</i>	4.110 V	3.930 V	3.840 V	3.796 V	3.671 V	3.590 V	3.532 V	3.467 V
<i>R_{batt-dis}</i>	157 mΩ	110 mΩ	107 mΩ	110 mΩ	101 mΩ	107 mΩ	108 mΩ	128 mΩ

-20°C								
<i>Ah discharged</i>	0 Ah	0.29 Ah	0.58 Ah	0.87 Ah	1.16 Ah	1.45 Ah	1.74 Ah	2.03 Ah
<i>OCV</i>	4.100 V	3.882 V	3.800 V	3.715 V	3.631 V	3.564 V	3.455 V	3.376 V
<i>R_{batt-dis}</i>	309 mΩ	179 mΩ	183 mΩ	163 mΩ	171 mΩ	187 mΩ	183 mΩ	238 mΩ

Table 8.2 Resistance versus HPPC pulse current magnitude for Panasonic NCR18650PF battery with 0.58Ah discharged at 10°C and 0°C

10°C			
<i>Battery Current</i>	2.9 A	5.8 A	8.7 A
<i>Resistance (R_{batt-BV})</i>	64.5 mΩ	61.6 mΩ	59.5 mΩ
<i>Resistance Normalized to 5.8 A (BV_{scale})</i>	1.05	1.00	0.967

0°C			
<i>Battery Current</i>	2.9 A	5.8 A	8.7 A
<i>Resistance (R_{batt-BV})</i>	92.8 mΩ	85.9 mΩ	80.8 mΩ
<i>Resistance Normalized to 5.8 A (BV_{scale})</i>	1.08	1.00	0.941

Table 8.3 Resistance versus HPPC pulse current magnitude for Panasonic NCR18650PF battery with 0.58Ah discharged at -10°C and -20°C

-10°C			
<i>Battery Current</i>	2.9 A	5.8 A	8.7 A
<i>Resistance ($R_{batt-BV}$)</i>	142 mΩ	124 mΩ	112 mΩ
<i>Resistance Normalized to 5.8 A (BV_{scale})</i>	1.15	1.00	0.907
-20°C			
<i>Battery Current</i>	2.9 A	5.8 A	8.7 A
<i>Resistance ($R_{batt-BV}$)</i>	223 mΩ	183 mΩ	161 mΩ
<i>Resistance Normalized to 2.9 A (BV_{scale})</i>	1.00	0.823	0.721

8.2.2 Panasonic Battery Pack Design and Specifications

To provide the same amp-hours as the electric truck's battery pack, 40 of the Panasonic cells must be connected in parallel, providing about 100Ah of useful charge. Also because the voltage characteristic of the Panasonic cells is different, with a peak voltage of 4.2V compared to 3.6V for the LiFePO₄, only 92 series connected cells are necessary to achieve a similar peak voltage. The resulting Panasonic pack will therefore consist of 40 parallel connected, 92 series connected cells, for a total of 3,680 cells. The cell and pack parameters for the Calb battery pack, which has

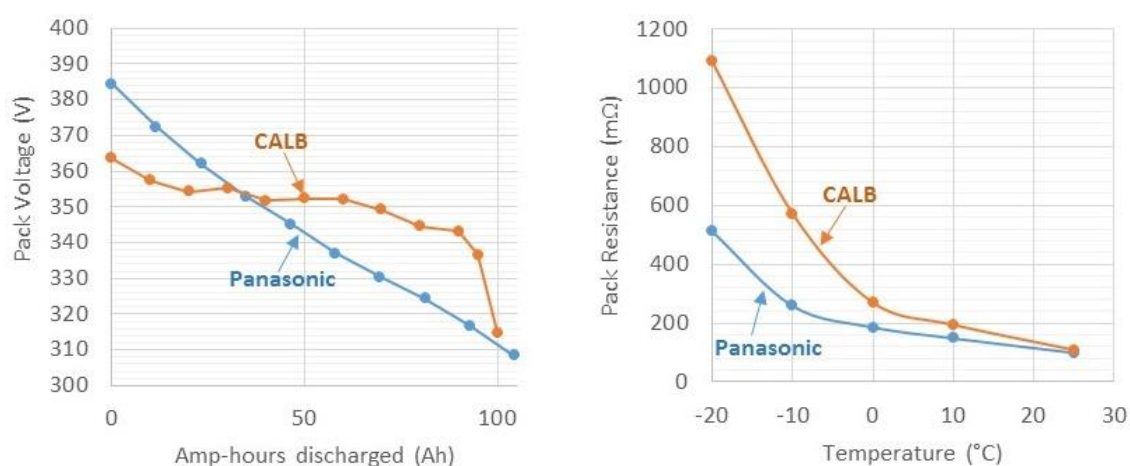
Table 8.4 Panasonic and Calb Battery Cell and Pack Specifications for Electric Truck

	Calb 100AHA LiFePO₄		Panasonic NCR18650PF	
	<i>Cell</i>	<i>Pack</i>	<i>Cell</i>	<i>Pack</i>
# of cells in series	-	108	-	92
# of cells in parallel	-	1	-	40
Open Circuit Voltage	3.3V	356.4V	3.6V	331.2V
Amp-hours	100Ah	100Ah	2.7Ah	108Ah
Nominal Resistance	1.1mΩ @ 25°C 2.5mΩ @ 0°C	119mΩ @ 25°C 270mΩ @ 0°C	43mΩ @ 25°C 80mΩ @ 0°C	99mΩ @ 25°C 184mΩ @ 0°C
Minimum Voltage	2.5V	270V	2.5V	230V
Maximum Voltage	3.6V	388.8V	4.2V	385.4V
Mass	3.2kg	345.6kg	0.0465kg	171.1kg
Volume	2.04L	221L	0.017L	62.8L
Energy Storage	330Wh	35.6kWh	9.72Wh	35.8kWh
Price (1 Pack Quantity)	\$139	\$15,012	\$4.88	\$17,940
Chemistry	LiFePO ₄		LiNiCOMnO ₂	
Minimum Charging Temperature	0°C		10°C	
Rated Cycles	3000 cycles at 70% DOD		More than 300 cycles	

been implemented in the electric truck, and for the modeled Panasonic battery pack, which is examined in this section, are provided above in Table 8.4. The packs provide a similar amount of energy and have a similar cost for a single battery pack, but the Panasonic pack is about half of the mass and $\frac{1}{4}$ the volume, and has 20% lower resistance at 25°C and 30% lower resistance at 0°C, all very desirable parameters compared to the LiFePO₄ pack. The two downsides of the Panasonic pack are a higher minimum charge temperature, 10°C versus 0°C, and presumably lower cycle life, which has only been roughly specified by the manufacturer to be greater than 300 cycles.

8.2.3 Temperature Dependence of Battery Pack Resistance and Power Capability

The open circuit voltage versus amp-hours discharged and pack resistance versus temperature are provided for both packs in Figure 8.2 below, providing further comparison between the two battery packs. The first significant difference between the two packs is that the CALB battery voltage is relatively constant, while the Panasonic voltage decreases linearly, which is a function of their respective chemistries. The second significant difference is that Panasonic pack is much less affected by low temperatures, especially at -10 and -20°C where the Panasonic resistance is shown in Figure 8.2 (b) to be less than half that of the CALB pack.



(a) Pack voltage versus amp-hours discharged

(b) Pack resistance versus temperature

Figure 8.2 Comparison of CALB LiFePO₄ and Panasonic LiNiCOMnO₂ Pack Voltage and Resistance

To better illustrate how the Panasonic pack will perform as a function of temperature, the discharge and charge power capability of the battery pack was calculated from the experimentally determined parameters and is shown in Figure 8.3 below. The Panasonic pack can provide more than 150kW, the peak power required by the truck's drivetrain, down to 0°C, and can still provide greater than 50kW down to -20°C, which is still enough power to drive the vehicle conservatively. This is very good performance compared to the LiFePO₄ pack, which is so power limited at -10°C that it is barely functional. The charging power capability is shown to be somewhat less desirable though, with lower charge acceptance until the pack is about 20% discharged.

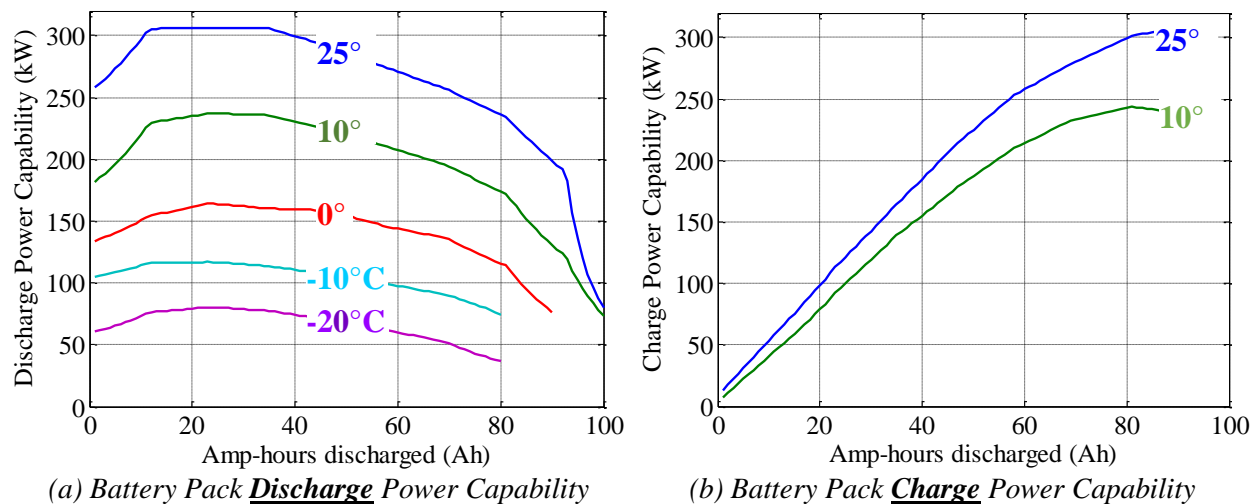


Figure 8.3 Truck Panasonic battery pack discharge and charge power capability calculated from Butler-Volmer model

8.2.4 Measured versus Modeled Battery Drive Cycle Performance at 0°C and 25°C

Because the Panasonic battery has such different characteristics from the CALB battery, it is necessary to again perform experimental tests to confirm that the developed model accurately captures the battery's performance for a drive cycle. An LA92 drive cycle power profile was scaled for a single NCR18650PF cell, and applied to the cell at 0°C and 25°C. The modeled and measured results for the 25°C case, as shown in Figure 8.4, align very well, with a model error of

less than 50mV and less than 100mA over most of the drive cycle, a very accurate result considering the wide swing in open circuit voltage over the drive cycle.

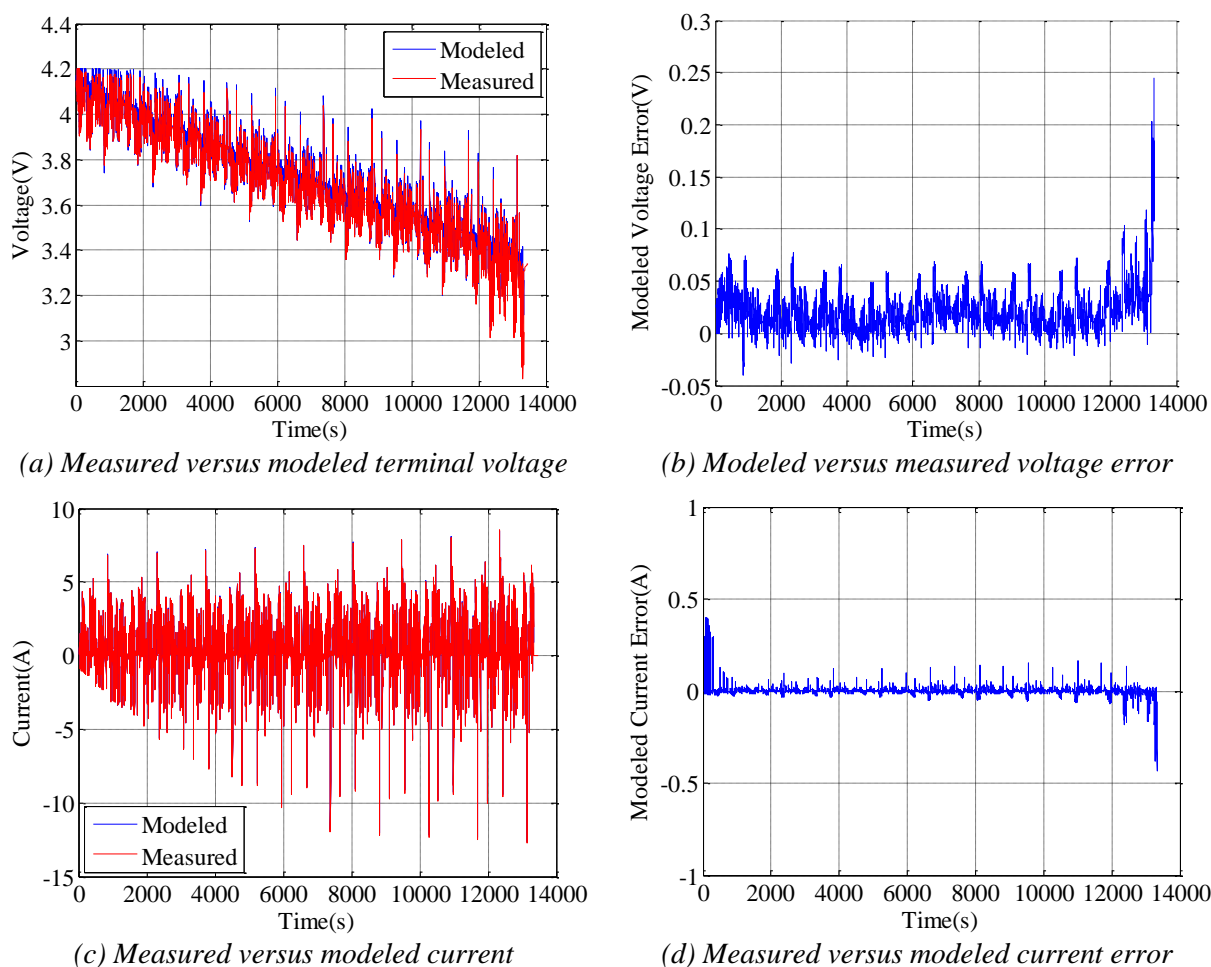


Figure 8.4 Measured versus modeled current and voltage for Panasonic NCR18650PF performing LA92 drive cycle power profile at 25°C

The exact same power profile is used for the 0°C case with one exception; the battery is not rated to charge below 0°C so the power is set to zero for all regenerative braking charging power points. The modeled and measured results for this 0°C test case are shown in Figure 8.5, and again the model error is very low, with error less than 100mV and less than 100mA except for the highest power points and near the end of the drive cycle. The measured versus modeled amp-hours drawn from the battery for both temperatures is additionally provided in Table 8.5, and the error is very small for both cases: +2.5% for 0°C and -0.08% for 25°C. This experimental testing clearly

demonstrates that the model accurately captures the battery's performance characteristics, giving confidence that an actual vehicle will perform similarly to the model prediction.

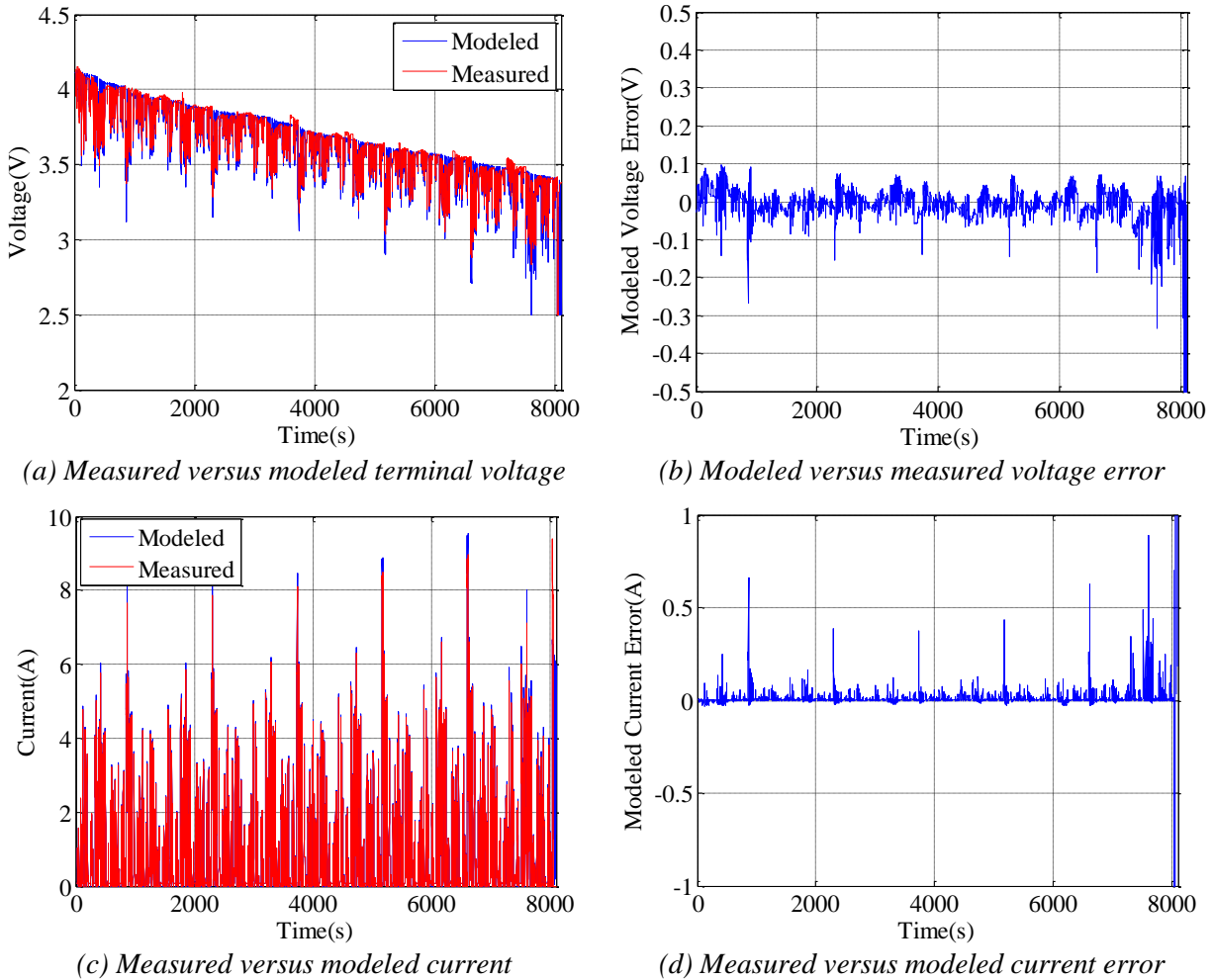


Figure 8.5 Measured versus modeled current and voltage for Panasonic NCR18650PF performing LA92 drive cycle power profile at **0°C**

Table 8.5 LA92 Drive Cycle Discharge Measured versus Modeled Amp-hours for Panasonic NCR18650PF Cell

Temperature	Modeled	Measured	Model Error
0°C	2.383 Ah	2.325 Ah	+2.5%
25°C	2.525 Ah	2.527 Ah	-0.08%

8.2.5 Electric Truck Performance with Panasonic Battery Pack and an HESS

The electric truck is modeled with just the Panasonic battery pack as well as with a hybrid energy storage system, consisting of the Panasonic battery pack with the 400A dc/dc converter and

the 375Wh Skeleton ultracapacitor pack designed in the prior chapter and controlled with dynamic programming. The modeled range results for four drive cycles and temperatures ranging from -20 to 25°C are shown in Figure 8.6. Range decreases substantially at lower temperatures for two reasons: (1) the battery discharge is limited to 80Ah at -20°C and -10°C and to 90Ah at 0°C, while it's limited to 100Ah at 10°C and 25°C, and (2) the battery pack is not rated to receive charging power below 10°C, so all regenerative braking energy is lost at temperatures below 10°C. With the addition of the HESS, as is shown in subfigure (b), the range at low temperatures increases substantially due to the capture of regenerative braking energy.

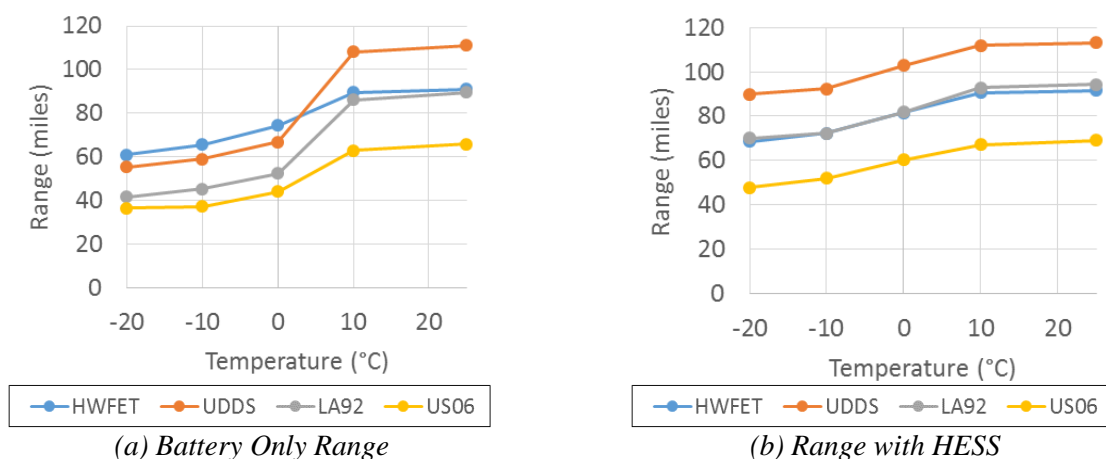


Figure 8.6 Battery only and HESS range for four drive cycles for electric truck with Panasonic battery pack

Many more characteristics of the battery only and HESS performance are detailed in Figure 8.7 below. Subfigure (a) shows that just the battery pack can supply almost all of the motoring energy for all of the drive cycles, even at very low temperatures, and that with the HESS there is no power limiting for any of the cases, a significant improvement over the CALB pack. Subfigure (b) shows that nearly all of the available regenerative braking energy is captured with the addition of the HESS, resulting in range improvements from 10 to 71% at low temperatures as shown in subfigure (c).

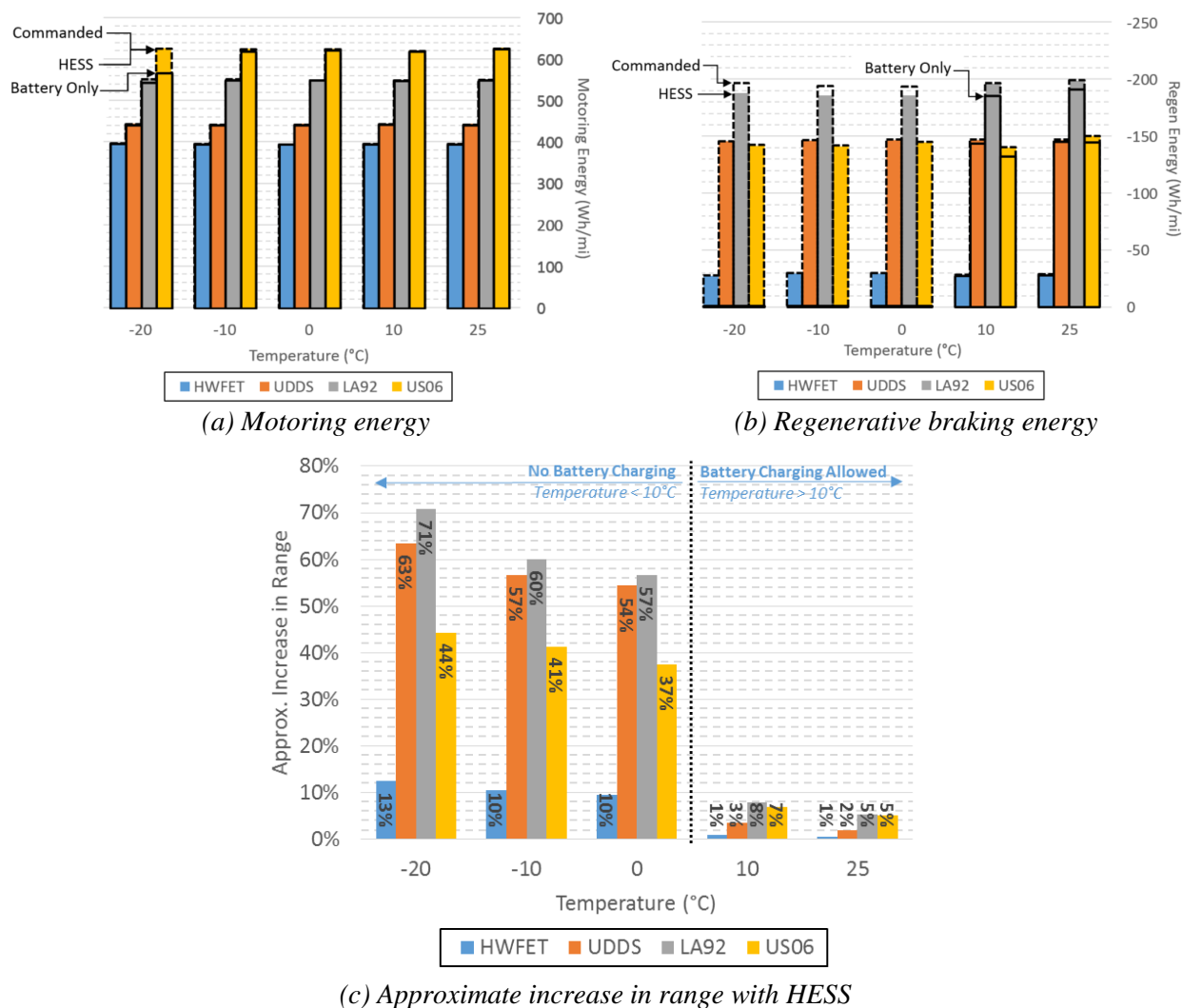


Figure 8.7 HESS versus battery performance for Panasonic Battery Pack and HESS with 375Wh ultracapacitor pack and 400A dc/dc converter rating

In addition to the range improvements, the HESS also helps to substantially reduce the battery and total energy storage system losses, as is shown in Figure 8.8 and subfigure (a) of Figure 8.9. Battery losses are reduced between 30 and 80%, reducing the cooling requirements for the battery pack as well as likely resulting in reduced battery aging due to reduced internal temperatures. Due to the ultracapacitor pack absorbing most of the regenerative braking energy the battery cycles are also reduced substantially, between 7 and 40% as shown in subfigure (b) of Figure 8.9.

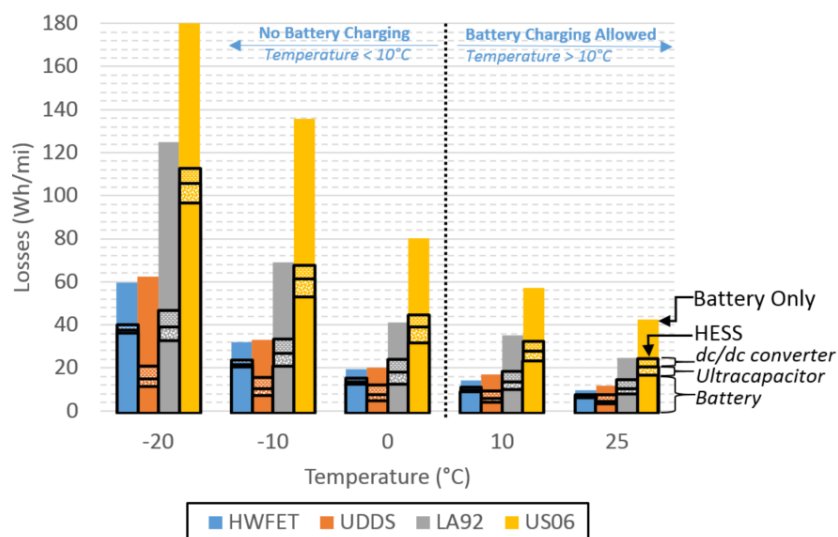


Figure 8.8 Battery only and HESS losses for Panasonic Battery Pack and HESS with 375Wh ultracapacitor pack and 400A dc/dc converter rating

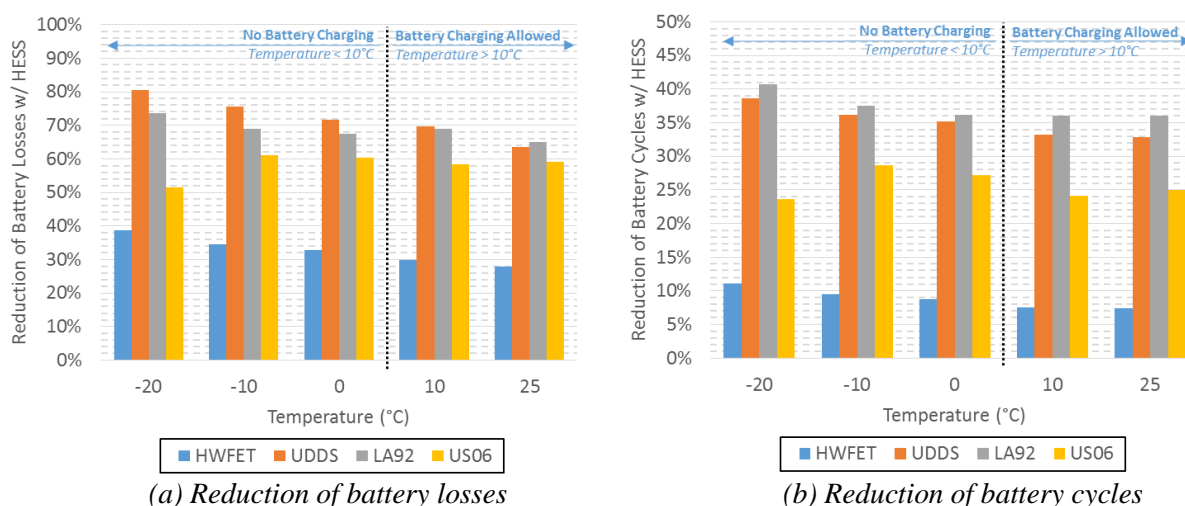


Figure 8.9 Performance improvements achieved for Panasonic Battery Pack and HESS with 375Wh ultracapacitor pack and 400A dc/dc converter rating

8.2.6 Comparison to Benefits Achieved with HESS with the CALB Pack

Overall the Panasonic pack, which has only slightly lower resistance at 25°C, is shown to have similar performance improvements as achieved with the CALB pack. There are several important differences between the two applications though. Because the Panasonic pack is only rated to charge down to 10°C, the HESS enables regenerative braking over a wider temperature range than for the CALB pack. Also because the Panasonic pack power capability is so much higher at low

temperatures, the vehicle is able to perform with its full rated power at very low temperatures, while with the CALB pack there was significant power limiting even with the HESS at lower temperatures. Another significant difference between the two packs is that the Panasonic pack is rated for much fewer cycles than the CALB pack, meaning that there is greater value for any battery cycle life improvements that are achieved by adding the HESS to the Panasonic system. Neglecting the cycle life limitation of the Panasonic pack, it has superior performance and characteristics compared to the CALB pack, and its performance is further improved with the addition of an HESS.

8.3 HESS Performance for a City Passenger Bus

The vast majority of city transit buses are currently diesel powered, but many transit bus manufacturers have begun to offer battery electric powered buses as well, such as the New Flyer Excelsior and Complete Coach Works electric buses shown in Figure 8.10 below. The New Flyer bus has a 200kWh pack providing 80 miles range while the Complete Coach Works bus has a 213kWh pack providing 85 miles range [137] [138]. Due to the very heavy mass of city transit buses, around 40,000lb fully loaded, and the frequent number of starts and stops, they are an



(a) New Flyer Excelsior 40' electric bus with overhead charging connection [137]



(b) Complete Coach Works 40' bus electric conversion [138]

Figure 8.10 Two examples of 40' electric buses in production

excellent candidate for hybridization, which will result in reduced battery pack losses and substantially reduced throughput energy due to the ultracapacitor capturing much of the regenerative braking energy. In this section an electric bus drivetrain configuration will first be developed and modeled, then the bus drive cycles and modeled power profiles will be presented, and finally the buses range and performance characteristics with and without a hybrid energy storage system will be modeled and presented.

8.3.1 Electric Bus Drivetrain Specifications

The electric bus is designed to have similar or better performance than a typical diesel powered bus, such as the New Flyer Excelsior 40' diesel powered bus whose specifications are provided in Table 8.6 below. The diesel bus is powered by a 209kW, 1220Nm Cummins diesel engine, which

Table 8.6 Specifications for New Flyer Excelsior 40' Diesel Bus

Engine	Cummins ISL 280 Diesel
Power	209 kW (280 hp)
Torque	1,220 Nm (900 ft-lb)
Engine Mass	764 kg (1,684 lb)
Transmission	Allison B400 (1 st 3.49:1 / 6 th gear 0.65:1)
Transmission Mass	243kg (535lb)
Rear differential	5.28:1 Gear Ratio
Max Wheel Torque	22,555 Nm (1 st gear)
Unloaded Vehicle Mass	11,793 kg (26,000 lb)
Fully Loaded Mass (83 160lb passengers)	17,816 kg (39,280 lb)

Table 8.7 Specifications for Modeled Electric Bus Utilizing Components from Electric Truck

Motor	Quantity 2 IPM Machines as used in Prototype Electric Truck
Motor Drive	Quantity 2 Rinehart PM150 Drives
Power	270 kW (362 hp)
Torque	920 Nm (678 ft-lb)
Motor and Drive Mass	564 kg (1,243 lb)
Transmission	IEdrives EVT Heavy Duty EV Gearbox (1 st gear 4.39:1 / 4 th gear 1:1)
Transmission Mass	40 kg (88 lb)
Rear differential	5.28:1 Gear Ratio
Max Wheel Torque	21,325 Nm (1 st gear)
Unloaded Vehicle Mass ¹	14,061 kg (31,000 lb)
Fully Loaded Mass (83 160lb passengers)	20,837 kg (44,280 lb)

1. Assumed mass of New Flyer Xcelsior 40' electric bus

is paired with an Allison B400 automatic transmission and a 5.28:1 ratio rear differential, providing 22,555 Nm of torque to the wheels in 1st gear. The bus drivetrain provides such a large wheel torque - more than four times that of electric truck – to quickly accelerate the massive 40,000lb fully loaded weight of the vehicle quickly at low speed.

To provide similar power and torque as the diesel bus, the modeled electric bus is outfitted with two of the prototype electric truck motors, for a total of 920Nm of torque and 270kW of power, paired with a gearbox with a 4.39:1 ratio 1st gear and a differential with a 5.28:1 ratio, providing 21,325Nm to the wheels, as is specified in Table 8.7 above. Additionally, as is also shown in Table 8.6, the electric bus is assumed to be 5,000lb heavier than its diesel counterpart due to mass of the energy storage system and related electrification equipment.

The diesel engine's torque-speed and power-speed curve are provided in Figure 8.11 below, providing further comparison between the diesel and electric drivetrain. The diesel engine is shown to operate over a narrow speed range, 1200-2200RPM, requiring frequent gear changes as speed increases. The diesel engine also only provides peak torque in a narrow region, meaning the electric drivetrain, which provides constant torque to 2600RPM, may result in quicker acceleration than is achieved with the diesel drivetrain even though the electric bus is heavier.

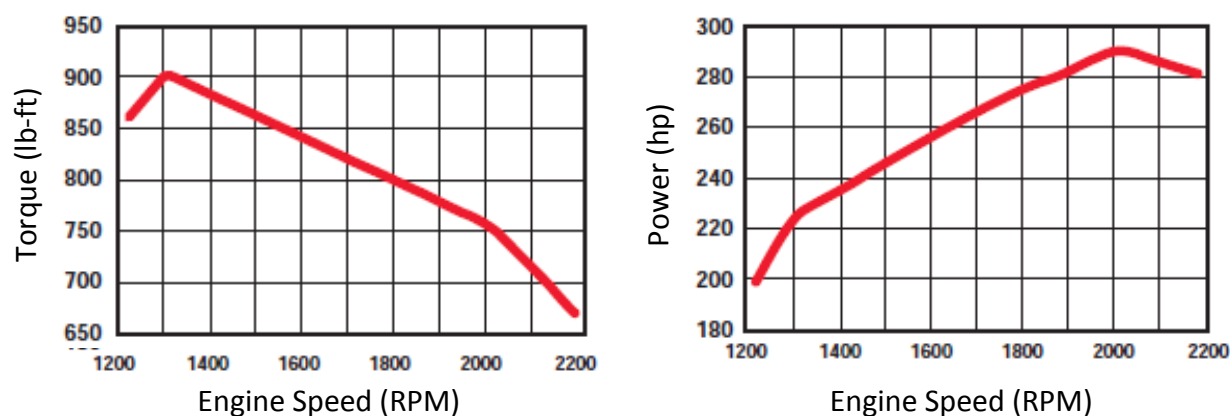


Figure 8.11 Torque and power versus engine speed for Cummins ISL 280 diesel engine [139]

The electric bus is modeled with a 140kWh battery pack - about 30% less energy storage than is in the two production electric buses shown prior – to highlight the performance benefits achieved with a hybrid energy storage system. The 140kWh pack consists of 108 series connected 400Ah CALB LiFePO₄ cells, which have about 40% the resistance of the 100Ah cells used in the truck. The battery pack is capable of providing more than enough power at 25°C, 380kW, and weighs a total of 1469kg and cost \$55,998 in quantity one pricing, as shown in Table 8.8. A 400Ah cell was not actually tested to obtain the parameters, so the measurements made on the 100Ah CALB cell were scaled by the datasheet resistance values for both cells to obtain the model parameters.

Table 8.8 Battery Pack Specifications for Modeled Electric Bus

	<i>Cell</i>	<i>Pack</i>
# of cells in series	-	108
# of cells in parallel	-	1
Open Circuit Voltage	3.3V	356.4V
Amp-hours	400Ah	400Ah
Nominal Resistance	0.5mΩ @ 25°C 1.1mΩ @ 0°C	52.9mΩ @ 25°C 120mΩ @ 0°C
Discharge Power Capability	3.5kW @ 25°C	380kW @ 25°C
Minimum Voltage	2.5V	270V
Maximum Voltage	3.6V	388.8V
Mass	13.6kg	1469kg
Volume	9L	970L
Energy Storage	1320Wh	143kWh
Price (1 Pack Quantity)	\$518.50	\$55,998
Manufacturer/Chemistry	Calb / LiFePO ₄	
Cell Part Number	CA400	
Min. Charging Temperature	0°C	

8.3.2 Mechanical Model of the Electric Bus

A somewhat different approach was taken to model the electric bus than was used for the electric truck because a bus was not available to perform coast down tests on. The transit bus mechanical drag parameters for the model, including the coefficient of aerodynamic drag, frontal area, and tire rolling friction coefficient for a transit bus, as shown in Table 8.9, were obtained in [140].

Table 8.9 Electric Bus Road Load Drag Parameters

Description	Parameter	Value
Coefficient of aerodynamic drag	C_d	0.62
Frontal Area of Vehicle	A_f	7 m ²
Density of Air	ρ	1.202 kg/m ³
Tire Rolling Friction Coefficient	μ_r	0.01

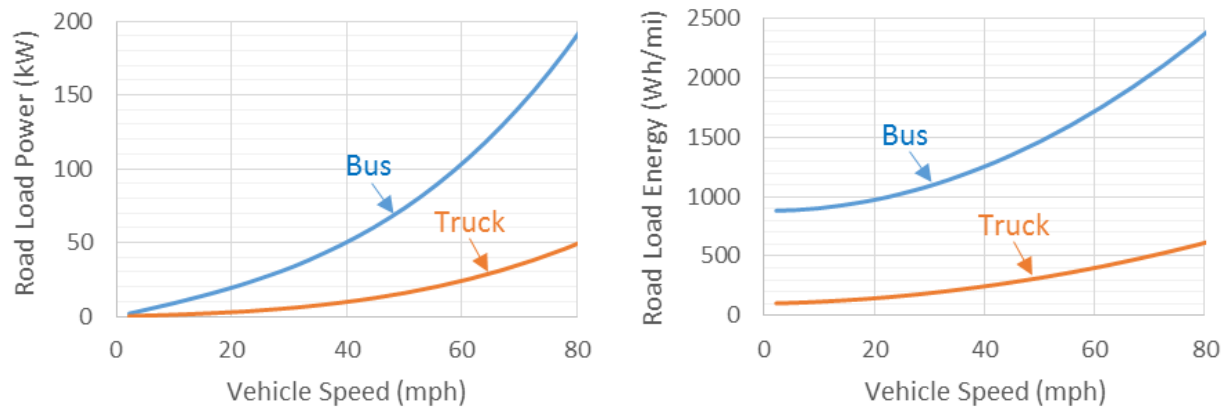
The drag power coefficients, as are used to calculate the road load power, are calculated from the parameters. The road load aerodynamic drag coefficient, A , is calculated in (6.5), and the tire friction road load coefficient C , is calculated in (4) from the tire rolling coefficient, gravity and the mass of the vehicle, which is taken to be the fully loaded vehicle mass in Table 8.7. The resulting calculated parameters which are used in the modeling are provided Table 8.10, and the road load power versus speed for the bus and the electric truck are shown in Figure 8.12, illustrating how much more power and energy is required to propel the transit bus at a constant speed.

$$A = 1/2 \rho C_d A_f \quad (37)$$

$$C = f_{rr} m_{veh} g \quad (4)$$

Table 8.10 Road Load Coefficients for Fully Loaded Electric Bus

Road Load Coefficient	A	B	C
Value	2.61 N/(m/s ²) (0.117 lbf/mph ²)	0 N/(m/s) (0 lbf/mph)	1970 N (443 lbf)

**Figure 8.12** Comparison of electric truck and electric bus road load power and energy

8.3.3 Bus Drive Cycles and Modeled Power Profiles

The bus's performance is modeled for three drive cycles: the low speed and frequent stopping NYC and Manhattan cycles, and the more suburban, higher speed Orange county cycle, whose speed profiles are shown in (a)-(c) of Figure 8.13 below. Even though speed is quite low, the acceleration for the NYC and Manhattan cycles is so great that the maximum drivetrain power limit is hit for both cases, as can be observed in the model calculated power profiles in (d)-(f) of Figure 8.13. The average speed, assumed accessory power, average energy, and other parameters are also given in Table 11, showing the bus consumes about five times more energy per mile than the electric truck.

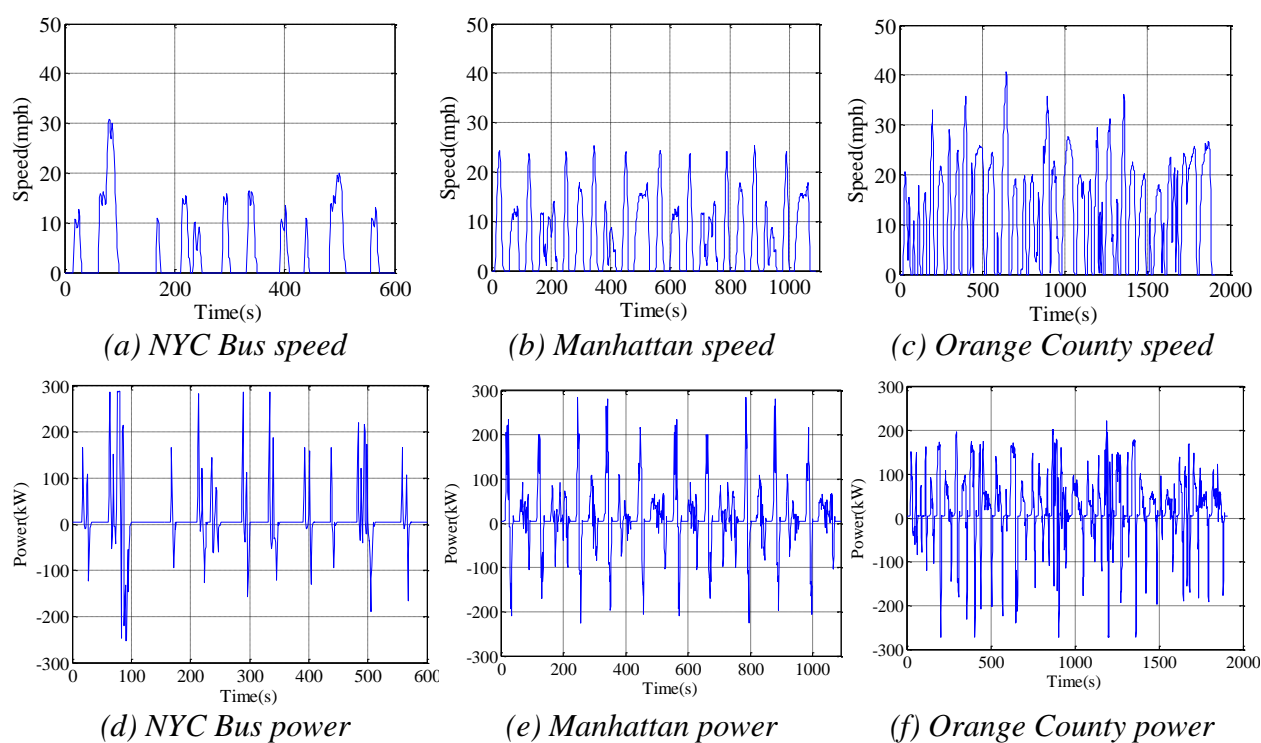


Figure 8.13 Speed and model calculated power profile for three bus drive cycles

Table 8.11 Selected Drive Cycle Parameters for Electric Bus

Drive Cycle	NYC Bus	Manhattan	Orange County
Stops per Mile	66	66	31
Average Speed	3.7 mph	6.8 mph	12.3 mph
Accessory Power	5 kW	5 kW	5 kW
Total Average Power	9.6 kW	13.9 kW	20.8 kW
Average Energy	2.6kWh/mi	2.0 kWh/mi	1.7 kWh/mi

8.3.4 Bus Driving Range and Performance Improvements Achieved with HESS

The electric bus is modeled for three drivetrain cases, including (1) Battery only, (2) Small HESS, with a single 375 Wh Skeleton ultracapacitor pack paired with a 400A dc/dc converter, and (3) Large HESS, with two of the systems used in the Small HESS system, totaling 750 Wh of ultracapacitor energy storage and 800A dc/dc converter current, as is shown in Table 8.12.

Table 8.12 Energy Storage System (ESS) Configurations Modeled for Electric Bus

Description	Battery Only	Small HESS	Large HESS
Ultracapacitor	-	375 Wh Skeleton Pack	750 Wh Skeleton Pack
DC/DC Converter	-	400 A	800 A
HESS Mass	-	60kg	120kg

The bus was modeled for all three bus drive cycles as well, and the model estimated range in miles and hours is shown in Figure 8.14 below. With the addition of the HESS, the range is increased quite significantly, between 10 and 18%, with the largest increase achieved for the drive cycle with the most aggressive accelerations, the NYC bus cycle. Going from the small, 375Wh HESS, to the large 750Wh HESS, only improves range a further 3-4%, but it has a very positive effect on battery and HESS losses, as is shown in Figure 8.15. For the small HESS, battery losses are reduced by about 60% and ESS losses are reduced by about half, and for the large HESS the losses are reduced by half again, greatly diminishing the battery losses and thereby reducing battery temperature and aging as well.

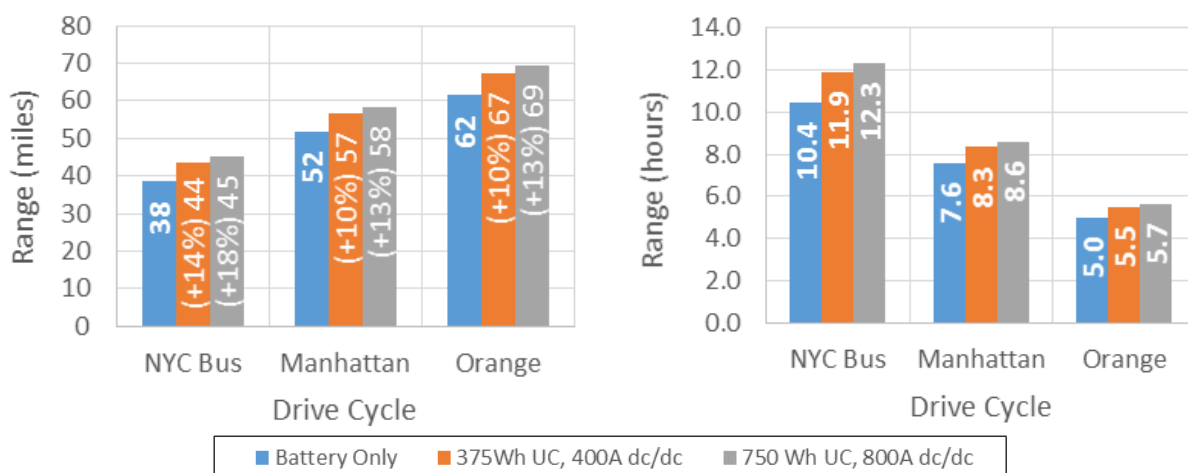


Figure 8.14 Electric bus range improvement achieved with HESS at 25°C

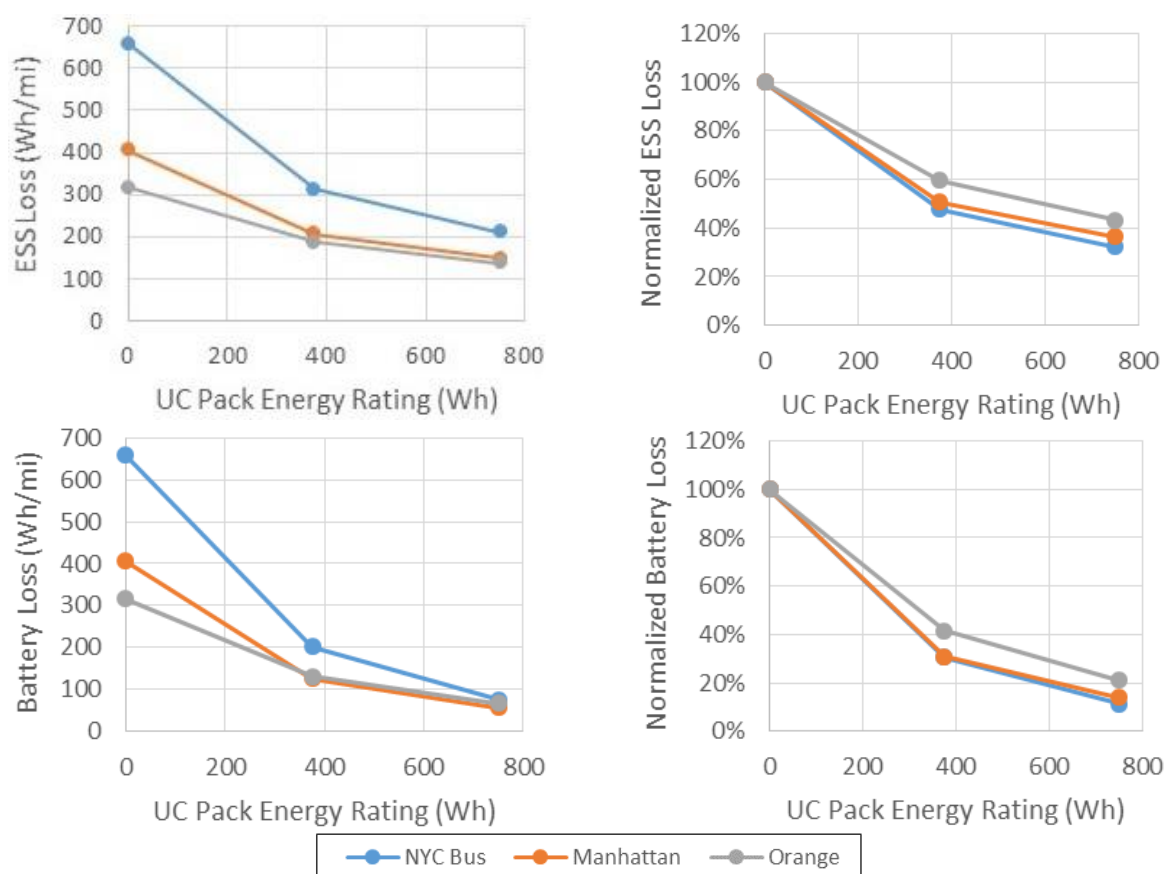


Figure 8.15 Electric bus ESS and battery loss reduction achieved with HESS

Another important performance improvement achieved with the HESS is a substantial reduction in regenerative braking energy supplied by the battery. Subfigure (a) of Figure 8.16 shows that regenerative braking energy supplied by the battery is reduced from about 2kWh mile for the

battery only case, to about 900Wh/mile with the 375Wh HESS and to less than 500Wh/mile with the 750Wh HESS. To provide an estimate of how many more miles the bus may be able to drive over the life of the battery pack, the miles driven per 3000 battery cycles is calculated and is shown in subfigure (b). The miles per 3000 cycles increases between 36 and 72%, suggesting that the HESS may be able to greatly increase the useful life of the battery pack in this application. This does however assume that all battery cycles are equal, including the regenerative braking microcycles, so the actual improvement due to cycling would likely be less. However any

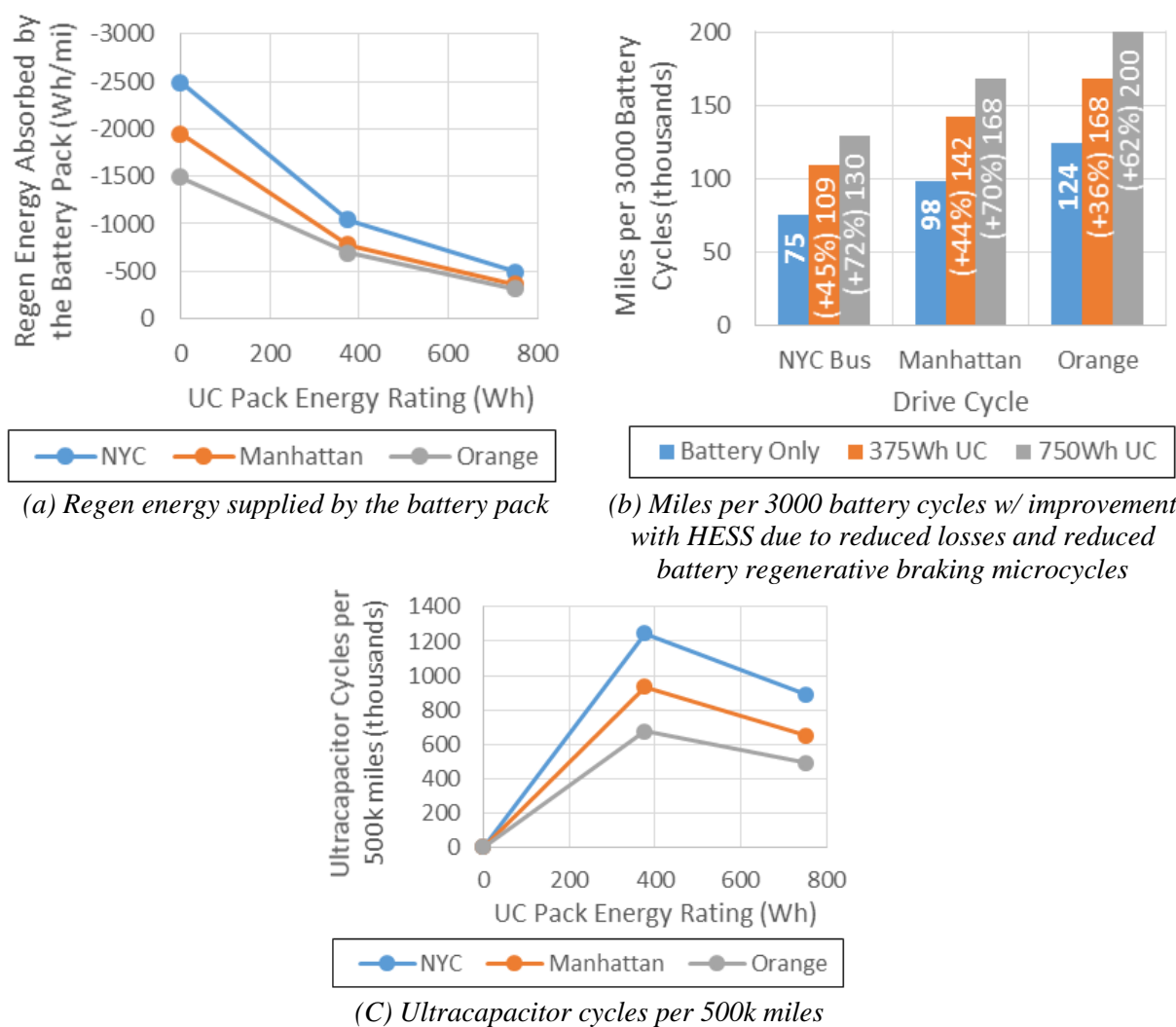


Figure 8.16 Electric bus improvements in miles driven over battery lifetime with HESS and ultracapacitor cycles over approximate vehicle lifetime of 500k miles

reduction in aging will be important since transit buses have an expected lifetime of 500 thousand miles, far longer than could be achieved with this battery pack. Finally one last important result, the ultracapacitor cycles per 500k miles, is shown in Figure 8.16 (c). For the small ultracapacitor pack there are between 700k and 1.2 million cycles, and for the large pack there are between 500k and 900k cycles. Ultracapacitors are typically rated for around 1 million cycles, so an ultracapacitor pack should last the service life of the vehicle.

8.3.5 Summary of Electric Bus Results

The addition of an HESS was shown to provide several important performance improvements to the modeled electric bus, including an increase in range of 10-18%, a 60-80% reduction of battery losses, and an increase in miles driven per battery cycle ranging from 36-72%. These very positive results suggest that electric transit buses may be a good application for hybrid energy storage systems. A tradeoff study, including comparative cycle life testing of battery packs, would be necessary to determine if a battery pack paired with an HESS would actually be a better solution than a battery pack designed to have low enough resistance and high enough cycle life to last 500k miles. Specifically the use of the HESS would need to contribute to an overall reduction in the price of the energy storage system, helping to reduce the very high price of electric buses.

8.4 HESS Performance for an Electric Truck with 2015 Model Year Ford F150 Truck Performance Capabilities

The prototype electric truck developed for this dissertation was designed to have similar power and wheel torque to the 2002 model year Ford F150 which was converted to electric, as shown in Figure 8.17 (a). The performance of light duty trucks has increased substantially since 2002 though, with the higher torque and power engines available in 2015 model year trucks, the crew cab version of which is shown Figure 8.17 (b), enabling a 49% increase in rated towing mass and

a 32% increase in the gross combined weight rating (GCWR) of the vehicle, as shown in Table 8.13. In this section an electric truck is modeled which has the same performance as the highest performance configuration of the 2015 model year Ford F150 crew cab truck. The goal of the modeling is to highlight how much an HESS can improve the performance of a truck with the more aggressive, modern specifications. The drivetrain and energy storage configuration is first defined, then drive cycle power profiles for the unloaded and max GCWR cases are given and the performance improvements achieved with the HESS are presented as a function of the total vehicle payload.



(a) 97-03 Model Year Ford F150



(b) 15- Model Year Ford F150

Figure 8.17 Ford F150 from 97-03 as used for the prototype electric truck and current model year truck

Table 8.13 Comparison of Specifications for 2002 and 2015 Model Year Ford F150 Crew Cab 2-wheel Drive Trucks Configured for Maximum Towing Capability

	2002 Model Year	2015 Model Year	Change
Engine	5.4L V8	3.5L V6	
Engine Power Available	260 hp	365 hp	+40%
Engine Torque	350 lb-ft	410 lb-ft	+17%
Max Payload	1,840 lb	2,900 lb	+58%
Max Trailer Weight	8,000 lb	11,900 lb	+49%
GCWR	13,000 lb	17,100 lb	+32%

8.4.1 2015 Model Year Electric Truck Performance Specifications

The 2015 model year Ford F150 truck configured for maximum towing capability has a 3.5L V6 gasoline engine rated to provide a peak of 272kW and 570Nm, and is paired with a six-speed gearbox and rear differential which provides 8,437 Nm of wheel torque in 1st gear, as is shown in

Table 8.14 below. To achieve the same power as the gas powered truck, two of the 460Nm, 135kW IPM machines which were utilized in the prototype electric truck are used in the electric truck modeled in this section, as is shown in Table 8.15. The two machines create a total of 270kW and 920Nm of torque, and provide 9,798Nm of torque in first gear, easily matching the capabilities of the gas engine version of the truck.

Table 8.14 Specifications for 2015 Model Year Ford F150 Crew Cab 2-wheel Drive Truck Configured for Maximum Towing Capability

Engine	3.5l EcoBoost V6
Power	272kW (365 hp)
Torque	570Nm (420 ft-lb)
Gearbox	6-speed Automatic (1 st 4.17:1 / 6 th gear 0.69:1)
Rear differential	3.55:1 Gear Ratio
Wheel Torque	8,437 Nm (1 st gear) 1,396 Nm (6 th gear)
Unloaded Vehicle Mass	2,125kg (4,685 lb) (‘02 MY, 4,655 lb)
Max Trailer Weight	5,398 kg (11,900 lb)
GCWR	7,756 kg (17,100 lb)

Table 8.15 Drivetrain Specifications for Electric Version of 2015 Model Year Ford F150 Truck

Motor	Quantity 2 IPM Machines as used in Prototype Electric Truck
Motor Drive	Quantity 2 Rinehart PM150 Drives
Power	270kW (362 hp)
Torque	920Nm (678 ft-lb)
Gearbox	1:1 and 3:1 Gear Ratio IE Drives Gear box
Rear differential	3.55:1 Gear Ratio
Wheel Torque	9,798 Nm (3:1 gear) 3,266 Nm (1:1 gear)
Unloaded Vehicle Mass	3,047 kg (6,717 lb)
Max Trailer Weight	4,491 kg (9,900 lbs)
GCWR	7,756 kg (17,100 lbs)

The downside of utilizing two of the prototype machines though is their very large mass, each weighing about 600lb, resulting in an estimated total vehicle mass of 6,717lb, as shown in Table 8.16. A much less massive liquid cooled machine could be designed as an alternative, but is not necessary for the purposes of the modeling performed in this section.

There are several other assumptions made for the modeling in this section, including: (1) same road load drag as 2002 model year prototype electric truck, (2) road load drag is not affected by

the addition of towed mass, and (3) the rotating inertia is the same as for the prototype truck, with additional inertia added to account for the second machine rotor. Additionally the same 35kWh LiFePO₄ battery pack is utilized, and it is paired with the Skeleton ultracapacitor pack and dc/dc converter designed in the prior chapter.

Table 8.16 Mass of 2015 Model Year F150 with Two Prototype IPM Machines and HESS

Prototype Electric Truck Mass	2,704 kg (5,960 lb)
2 nd Motor Mass	272 kg (600 lb)
2 nd Motor Drive Mass	11 kg (24 lb)
HESS Mass	60 kg (132 lb)
Total Mass of 2015 MY Equivalent Truck w/ HESS	3,047 kg (6,717 lb)

Table 8.17 Energy Storage System Configuration for 2015 Model Year F150

Battery Pack	Same as Prototype Electric Truck (35kWh, 356V, LiFePO ₄)
Ultracapacitor	95 series connected 3500F Skeleton Ultracapacitors (375Wh, 270V)
DC/DC Converter	400A

8.4.2 Modeled Drive Cycle Power Profiles for No Load and Max GCWR Load

The battery power profile required for the HWFET, UDDS, LA92, and US06 drive cycles, with no added vehicle load and for the maximum GCWR of 17,100lb is shown in Figure 8.18 and Figure 8.19 below. The power profiles show a rather surprising result, even at the max GCWR the peak power of the engine is rarely required, with only the very aggressive US06 drive cycle

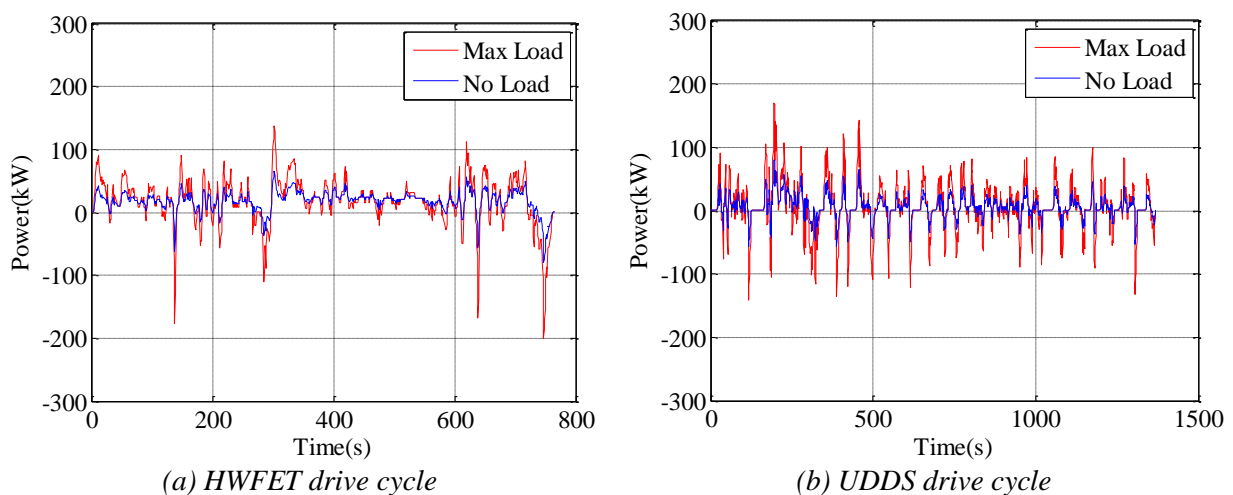


Figure 8.18 Model calculated power profile for HWFET and UDDS drive cycles for 2015 MY Ford F150 electric truck with no load and with max GCWR mass of 17,100lb (7,759kg)

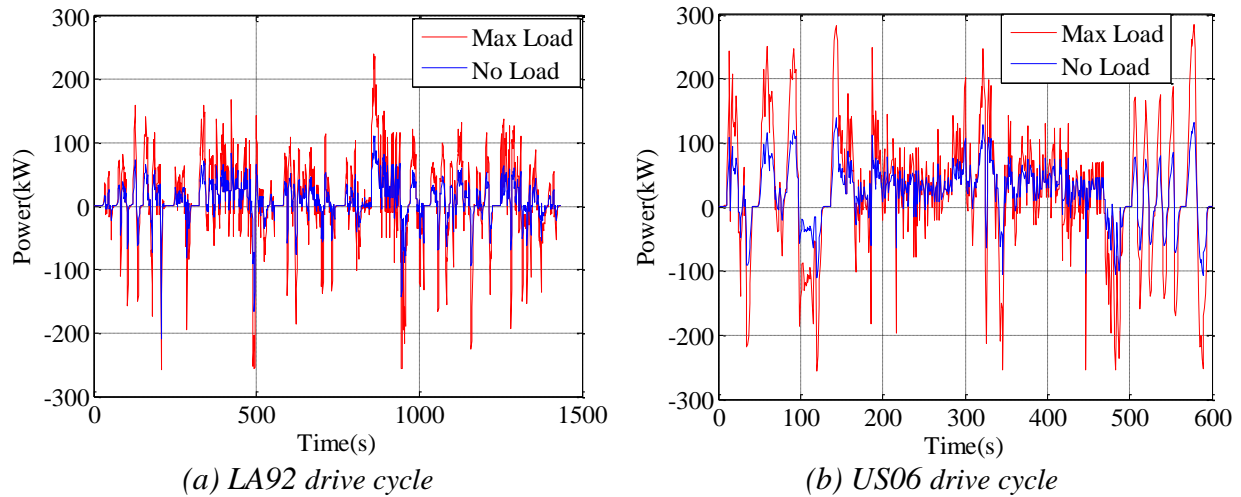


Figure 8.19 Model calculated power profile for LA92 and US06 drive cycles for 2015 MY Ford F150 electric truck with no load and with max GCWR mass of 17,100lb (7,759kg)

utilizing the full power capability of the vehicle. This shows that the 2015 Ford F150 is a very capable vehicle, and that the existing prototype electric truck could also follow most of the drive cycles when towing a large mass. Additionally when the vehicle is towing large loads, the HESS is likely to greatly improve the system performance due to the frequent, high power pulses.

8.4.3 Performance Improvement Achieved with HESS

In the prior sections of this dissertation, the HESS has been evaluated primarily as a tool to improve vehicle range, reduce battery losses, reduce battery throughput energy, and to enable low temperature operation without power limiting. This application, for the 2015 model year performance electric truck, is unique though because the battery pack utilized can only provide a maximum of about 180kW, while the drivetrain can draw more than 270kW from the energy storage system. In other words, for this application the battery pack cannot provide sufficient power, even at 25°C. Because power points above the battery power rating will typically only occur for a very short period, the HESS is able to supplement the system power such that the full power is provided, as is shown for the US06 drive cycle in Figure 8.20 below. The battery only

power, in red, is limited to the power limit of the battery pack, while with the HESS the ultracapacitor pack and dc/dc converter supplement the power and enable the majority of the regenerative braking power to be absorbed and all of the motoring power to be supplied.

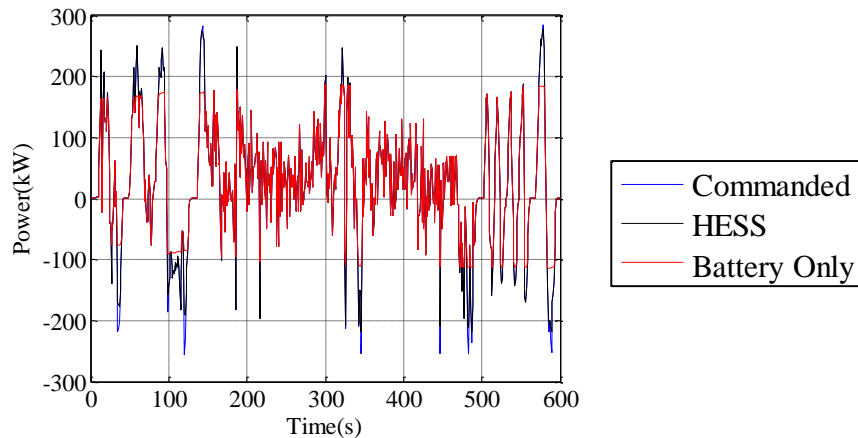


Figure 8.20 Battery only and HESS power for US06 drive cycle for 2015 MY Ford F150 electric truck with max GCWR mass of 17,100lb (7,759kg)

In addition to enabling the energy storage system to supply the full rated power of the drivetrain, the HESS also substantially reduces the battery losses, as is shown Figure 8.21 below. For the battery only case, which has some motoring power limiting, the battery losses increase substantially as the vehicle's towed mass is increased, tripling or more for the max towing mass. The HESS substantially reduces the battery losses, so much that the battery losses are less with heavy towing and the HESS than they are for no towing and no HESS. Additionally the total HESS losses, the sum of the battery, dc/dc converter, and ultracapacitor losses, as shown in the dashed grey line of Figure 8.21 are lower than the battery only losses for all cases.

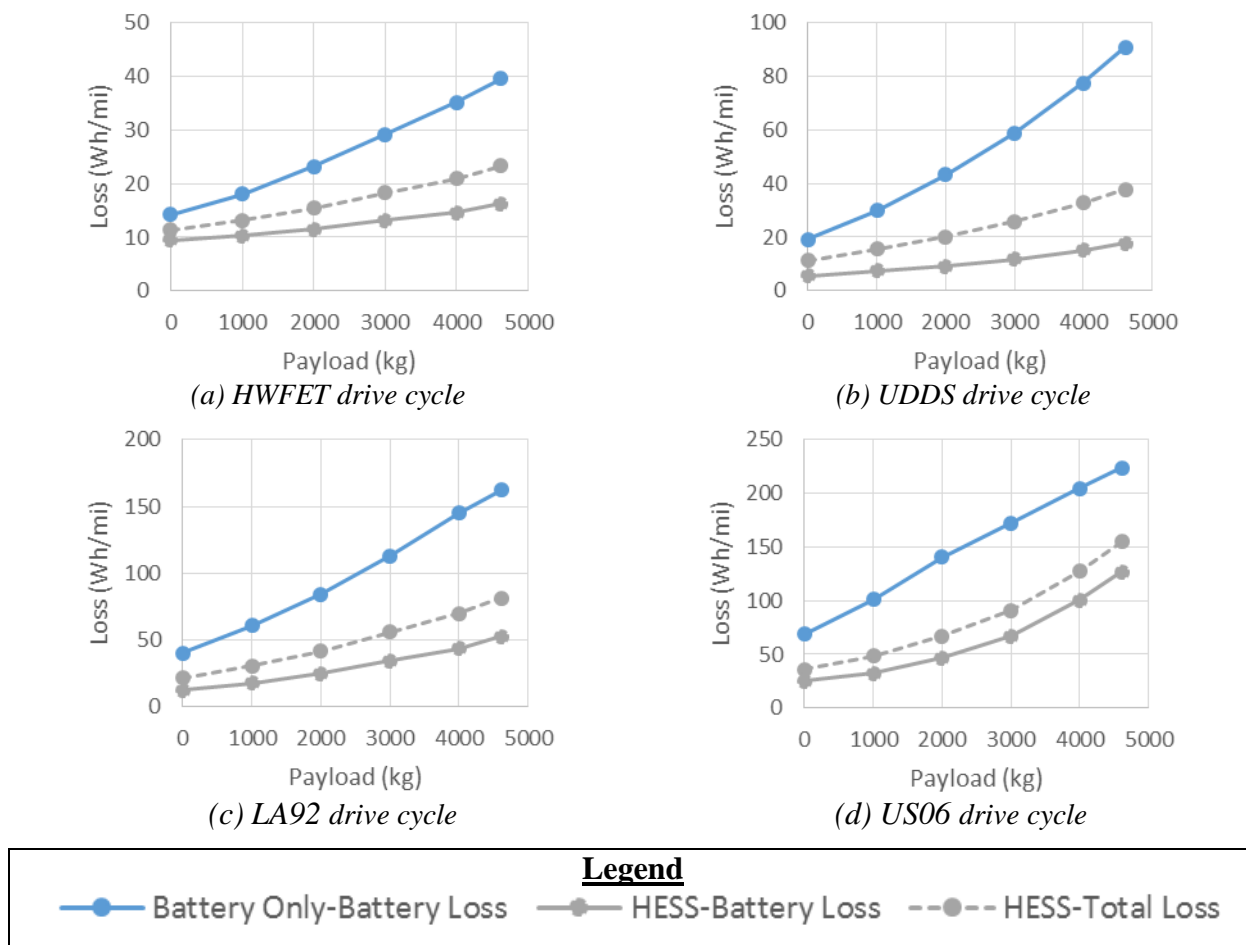


Figure 8.21 Battery only and HESS losses versus payload mass 2015 MY Ford F150 electric truck at 25°C

The reduction in losses achieved with the HESS, as well as a modest increase in captured regenerative braking energy, contribute to significant improvements in vehicle range, from 1 to 7% with no towed mass up to 7 to 29% when towing 4,500kg, as is shown in Figure 8.22. Even with the HESS though range does decrease for greater towed mass, reducing from 82 to 58 miles for the LA92 drive cycle when going from no towed mass to 4,500kg of towed mass, as is shown in Figure 8.23. While this does show the HESS provides very large improvements in range, it should be clear this is not the most realistic example. The losses with no HESS and a large towed mass are so high that the battery pack would likely quickly very quickly overheat, except for very

mild driving cases. The HESS therefore really enables this battery pack to be used for this application, and while it does increase range, the comparison is not entirely equal because not all of the driving cases could be completed without the HESS.

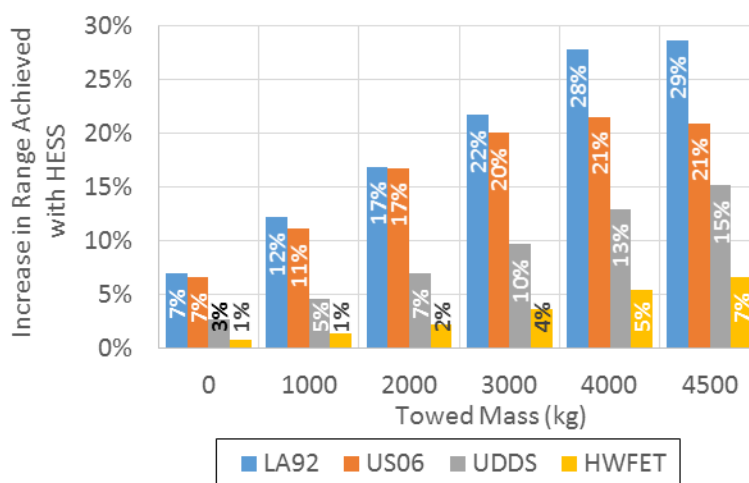


Figure 8.22 Range improvement achieved with HESS for 2015 MY Ford F150 electric truck at 25°C

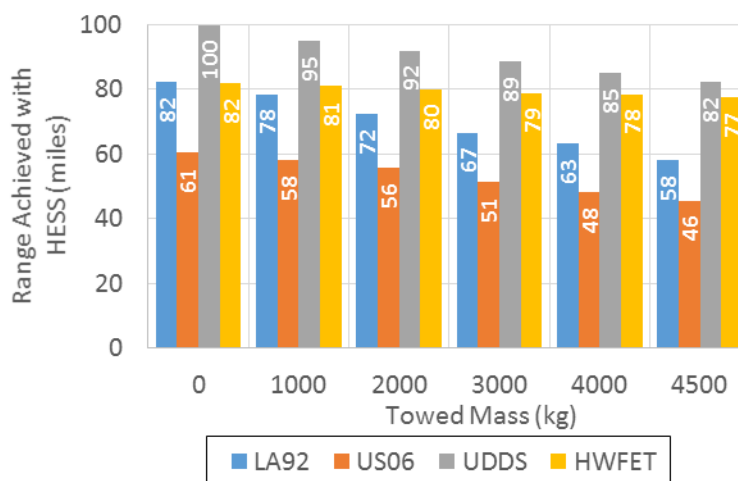


Figure 8.23 Range achieved with HESS for 2015 MY Ford F150 electric truck at 25°C

8.4.4 Summary of 2015 Model Year Performance Electric Truck Results

The much higher performance of the 2015 model year gas truck was equaled in the electric truck design by utilizing two of the IPM machines which were utilized in the prototype electric truck, providing a total of 270kW of power and 900Nm of torque. The HESS also enables the use of the same battery as was used in the prototype electric truck, which is only capable of providing

about 180kW, by providing the power for points beyond the power rating of battery pack. Furthermore the HESS was shown to reduce battery losses by about 2/3 and to increase range as much as 29% for high amounts of towed mass. In general, the HESS is really shown to enable the use of a power limited battery pack, and to allow the vehicle to tow large loads with less adverse effects on vehicle range and battery losses.

8.5 Conclusion

By investigating HESS performance for an electric truck with an alternative battery pack, an electric bus, and an electric truck rated to provide much greater power, this chapter demonstrated that the modeling methodology developed in prior chapters can successfully be applied for a variety of applications. The results also highlight how variants in vehicle design effect the performance benefits achieved with an HESS. For the first case examined, the electric truck with a Panasonic battery pack, there were several significant conclusions including: the LiNiCOMnO₂ chemistry Panasonic batteries have lower resistance and are much less effected by temperature than the CALB LiFePO₄ batteries, the developed battery modeling methodology very accurately captures the Panasonic battery's performance, and the HESS improves vehicle range as much as 8% for temperatures 10°C and above and as much as 71% for temperatures below 10°C, where the battery is not rated to charge. These results show overall that an HESS can still improve system performance significantly even when a different, higher performance, battery chemistry is utilized.

The second case, the electric bus, is also shown to benefit substantially from an HESS due to the frequent, high power starts and stops experienced by transit buses. At 25°C, the bus range is increased between 10 and 18% with an HESS, battery losses are reduced 60-80%, and the majority of the regenerative braking energy is diverted to the ultracapacitor pack, reducing and battery through energy and presumably reducing aging of the battery pack. With transit buses having an

expected lifetime of 500k miles, an HESS may be a very useful tool for increasing the life of the battery pack.

For the final case, the 2015 model year performance electric truck, the HESS is shown to enable the use of a battery pack which cannot provide the rated drivetrain power, even at 25°C. This is a very useful feature of an HESS, especially if an existing battery pack design is desired to be used for a higher power application. The HESS is also shown to reduce battery losses by about 2/3, even when the truck is towing the maximum rated trailer weight, enabling the electric truck to tow as much mass as the gasoline truck without excessive battery losses.

Chapter 9

Contributions & Future Work

This chapter presents the most important new conclusions and contributions made during the course of this research program, and recommends future work. The conclusions are presented first, consisting of a list of the most important overarching conclusions that have emerged from this research program. The contributions, which are presented next, fall into three major categories, as follows: 1) Electric truck powertrain design; 2) Electric truck powertrain modeling with on-the-road experimental verification; and 3) Hybrid Energy Storage System (HESS) investigation. Finally, a list of suggested future research topics that are inspired by the results of this investigation is presented and discussed.

9.1 Conclusions

Electric Vehicle Drivetrain Design & Instrumentation

- A simplified electric vehicle model using conservative component efficiency estimates can be used during the design phase of an electric vehicle to estimate vehicle range to within approximately 10 to 20% of the final result.
- A detailed electric vehicle model, combined with accurate road load parameters, battery loss modeling, and drivetrain efficiency maps, can be used to estimate vehicle range more accurately, within approximately 5% of the actual range.
- A Class 2a electric truck, such as the Ford F150 pickup truck investigated in this research program, consumes approx. 50% more energy per mile than a compact electric vehicle. As a result, approx. 50% more energy storage capacity will be needed to achieve the same range.

- An air-cooled permanent magnet synchronous machine was successfully designed to provide the power and torque required for this light-duty truck, but the resulting machine is very large (410mm diameter) and very massive (272kg) compared to PM traction machines with similar ratings that are more aggressively cooled. A liquid-cooled machine would be better suited for the light-duty truck application. However, the air-cooled machine developed during this research program could be an attractive candidate for an electric bus traction system that can better tolerate the larger size and mass.
- A battery pack for an electric vehicle should be designed with a capability of providing at least 50% more power than is required by the drivetrain when the battery is fully charged in order to be able to accommodate the loss of power capability at low temperatures and as the battery's state-of-charge decreases. The installed truck battery pack can only provide approx. 20% more power than required. As a result, experience with driving the electric truck has demonstrated that the vehicle is power-limited when the battery states-of-charge is low or when the battery temperature is even moderately cold (i.e., 0°C)
- Driving experience with the electric truck has confirmed that lithium batteries perform very poorly at low temperatures, suffering from the fact that the LiFePO_4 batteries used in the truck have nine times higher resistance at -20°C than at 25°C.
- The Panasonic NCR18650PF LiNiCOMnO_2 chemistry cells, which are similar to those used by Tesla in their production electric vehicles, perform much better than the LiFePO_4 cells at low temperature, with resistance only increased fourfold at -20°C compared to 25°C.

- Instrumentation of an electric vehicle can be used to accurately measure the efficiency of drivetrain components and energy consumption of subcomponents. Experience with the electric truck has shown this approach to be a cost-effective alternative to testing components individually in a lab environment.
- A torque sensor embedded in the vehicle's drivetrain has been demonstrated to be a very helpful and effective tool for measuring the traction machine's efficiency while driving. However, the changing temperature of the drivetrain resulted in offset drift appearing in the torque measurement signal. Replacement of this unit with a higher-accuracy, lower-drift (i.e., more expensive) torque sensor is a likely approach for solving this problem.
- Battery management systems are very difficult and time consuming to design, and this design task is complicated by their vulnerability to electrical noise in the vehicle. In retrospect, it would have been much more time- and cost-effective to purchase an off-the-shelf system for this project.
- A reliable, highly-sophisticated prototype electric vehicle can be designed and built with moderate resources within a period of approx. two years. The process of vehicle and traction drive calibration, as well as adjusting all of the software and hardware systems to work properly and reliably, is likely to require an additional year of part-time effort.

Hybrid Energy Storage System Design (General Conclusions for any Vehicle Type)

- For boost ratios of approx. 2:1 or less, efficiency values ranging from 97-99% can be achieved for a half-bridge bidirectional dc/dc converter in a

battery/ultracapacitor hybrid energy storage system with a 350V battery pack and 200A or 400A rated dc/dc converter.

- A properly-formed discrete-time ultracapacitor model is necessary for large simulation time steps such as the 1 second time step utilized in this work. If the discrete-time model is not correctly formulated, the law of conservation of energy will not be met and the ultracapacitor will create or absorb *extra* energy as an artifact of the model.
- Lithium batteries have non-linear resistance values at low temperatures, as described by the Butler-Volmer equation. The non-linear resistance must be included in the battery model to accurately predict the battery's power capability, amp-hours consumed for a discharge power profile, and other parameters.
- Hybridizing an existing battery pack by adding an ultracapacitor pack and dc/dc converter will be the most effective for:
 - More resistive or power-limited battery packs
 - Applications that benefit from increasing the cycle life of the battery
 - Applications that benefit from increasing the power capability of an existing battery pack design
 - Vehicles with frequent, high-power acceleration and deceleration
 - Heavy vehicles, or vehicles that tow or carry heavy payloads

- Operation at low temperatures using lithium-based batteries or other battery types that suffer from significant performance degradation at low operating temperatures.
- Highly-engineered systems, where the tradeoffs between a battery-only system and an HESS can be quantified during the development phase
- Applications such as start-stop or micro-hybrid vehicles that can benefit significantly from introduction of a small ultracapacitor pack
- Conclusions regarding battery / ultracapacitor HESS design for electric vehicle applications:
 - The majority of the available benefits from introducing an HESS in the categories of reduced battery losses, battery cycling reduction, and range extension can be achieved with a relatively small ultracapacitor pack.
 - A larger ultracapacitor pack is necessary to boost the power capability of the traction drive system beyond that achievable with the battery alone.
 - A dc/dc converter that is rated at 50% of the power rating of the complete HESS unit will provide the majority of the available battery and total ESS loss reduction benefits, while a higher converter power rating is necessary if the ultracapacitor is required to compensate for severe power limiting of the battery pack.
 - The majority of the regenerative braking energy from the traction drive can be diverted to the ultracapacitor pack, reducing the associated cycling and losses in the batteries.

- Battery losses can be reduced substantially by introducing the HESS, achieving reductions of 70% or more in some cases.
- For battery and HESS performance at low ambient temperatures:
 - Lithium ion batteries are often only rated to charge down to 10°C or 0°C, so regenerative braking energy cannot be captured in a battery-only system until the battery has been heated above the specified threshold temperature.
 - Ultracapacitors have excellent performance at low temperatures, with resistance increasing just 30% at -30°C, making them an excellent candidate for pairing with lithium ion battery packs.
 - When the battery is too cold to charge, the HESS can improve driving range by 50% or more compared to the battery-only system.
 - When the battery power is limited due to low temperature conditions, the HESS can be designed to supplement the drivetrain power, eliminating any reduction in vehicle performance.

Hybrid Energy Storage System Design (Conclusions for Class 2a Truck Applications)

- A 150Wh ultracapacitor pack and a 200A, 50kW peak rated dc/dc converter is sufficient to achieve most of the battery loss reduction and range increase benefits for a Class 2a truck.
- A larger 300Wh ultracapacitor pack and a 400A, 100kW peak rated dc/dc converter is necessary to provide enough energy and power to boost the power capability of the HESS beyond that of just the battery (important for low temperature cases, or

cases where the battery pack alone cannot provide the drivetrain's peak power rating).

- An HESS can provide a very large range increase, 50% or more, at low temperatures where the battery pack is not rated to accept charge power.
- An HESS can reduce battery losses 30-70%, likely resulting in reduced battery aging
- The ultracapacitor pack in an HESS can absorb a substantial amount of the regenerative braking energy, reducing battery cycling by 10-40%, and likely reducing battery aging
- An HESS can reduce total energy storage system losses by about half, resulting in increased range
- An HESS allows a Class 2a truck to tow very large loads without an excessive increase in battery or reduction in range. For a towed mass of 9,900lbs for example, range was 7% to 27% greater with an HESS, and battery loss was reduced by 50-80%.

9.2 Contributions

9.2.1 Electric Truck Powertrain Design

While there are many production electric vehicles available, there are not yet any full-size electric pick-up trucks on the market. Furthermore, even though many electric vehicles are available for purchase, automakers have not published detailed design papers that lay out the system design process, and academic works in which a vehicle drivetrain is designed, modeled,

fabricated, and experimentally verified are rarely published. As a result, completion and presentation of the full design process for an electric truck in this thesis represents a valuable contribution. More specifically, the key components of this powertrain design process contribution include the following:

- **Developed a powertrain design with 10% less power and comparable torque at the wheels as a stock Class 2a pickup truck with a 4.2L V6 internal combustion engine.**

An electric drivetrain system, which consists of the battery pack, motor drive, electric traction motor, two-speed gearbox, driveshaft, and rear differential, was designed to deliver 135kW of peak output power, approx. 10% less than that of the stock 4.2L V6 internal combustion engine system. The machine combined with the two-speed gearbox delivers 4900Nm (peak) to the wheels and can achieve a top speed of over 100mph, equaling the performance of the gasoline-powered truck.

- **Developed a vehicle model to size the battery pack to meet the desired range goal of 73 miles**

A preliminary mechanical model of the truck was developed using the vehicle mass and coast-down data, combined with conservative estimates of the motor, drive, and gearbox efficiencies. Various drive cycles were then run using this preliminary model, and it was predicted that a 35kWh, 100Ah battery pack would make it possible for the vehicle to travel approx. 62 miles for the highway cycle and 74 miles for the city cycle. After the electric truck was completed, the vehicle model was updated with much more accurate, experimentally-based parameters, and a range of 83 miles for the highway cycle and 92 miles for the city cycle was calculated, demonstrating that the range was estimated reasonably well using a simplified model early in the design process.

- **Worked with team from Orchid International and UW-Madison on prototype IPM traction motor design and control parameter calculation**

Worked with team consisting of Orchid International, an external consultant, and other UW-Madison researchers on the design process of the electric machine. The 135kW (peak), 460Nm, air-cooled IPM traction motor was designed by an external consultant to meet the torque and power requirements of the vehicle and to fit approximately in the space where the original transmission for the truck was located. The prototype machine was fabricated by Orchid International using glued laser-cut laminations, a machined rotor shaft and stator housing, a resolver, and stranded windings with vacuum impregnated resin and 11 embedded temperature sensors. The machine was modeled in FEA by another UW-Madison researcher, and the control parameters were derived from the FEA model results. The system-level design work, coordination of different project contributors, and some of the modeling was performed by the author. The design and fabrication of this machine demonstrates that an air-cooled IPM machine can be successfully used in an electric truck, but a significantly smaller and less massive liquid-cooled machine could be utilized as well.

- **Designed and constructed a lithium-ion battery pack w/ BMS, housing, and cooling**

A battery pack consisting of 108 series-connected CALB 100Ah LiFePO₄ cells was designed and built that is capable of delivering greater than 150kW (peak) when fully charged, the maximum power needed for the truck drivetrain over most of the battery's state-of-charge range. A custom battery management system (BMS) that measures cell voltages, temperatures at 80 points in the pack, pack current, and pack voltage was also designed and built for the

vehicle. The battery packs have performed well in service, with a temperature rise of only a few degrees Celsius for typical vehicle drives.

- **Demonstrated 50kW fast charging capability for battery pack**

The battery pack has been fast-charged successfully at a rate of 125A for 40 minutes, resulting in maximum cell temperatures of 43°C. This fast-charging experiment demonstrated that the implemented forced-air cooling system is sufficient to cool the battery under one of the worst-case conditions.

- **Designed and implemented electrified versions of engine-powered vehicle subsystems**

In a gasoline- or diesel-powered vehicle, many vehicle functions are performed by the gas engine, including mechanically powering a 12V alternator, power steering pump, and radiator fan, as well as providing hot coolant to heat the cabin and a low-pressure air vacuum for the brake booster. All of these subsystems were replaced with electrical counterparts, consisting of a 2.2kW dc/dc converter in place of the alternator, an electric power steering pump, electric radiator fan, electric coolant heater, and electric brake vacuum pump. The measured results show that all of the electrical subsystems, with the exception of the 4kW heater, draw an average combined power of less than 1kW. Furthermore, the power drawn by each subsystem is separately measured, providing valuable power consumption information that provides insights regarding how much vehicle efficiency can be improved by increasing the efficiency of any of these electrified functions, such as a more efficient power steering pump or cooling fan.

- **Incorporated instrument-grade sensing into the traction system**

One of the primary goals of the project that makes the truck stand out as a unique research vehicle was to incorporate many high-accuracy sensors to perform real-time measurements of subsystem efficiency and performance. The most ambitious and difficult measurement to implement is traction system efficiency. To measure traction system efficiency, a 0.5% accuracy HBM torque sensor was designed into the motor and gearbox housing to measure motor shaft torque. In addition, a set of three-phase 0.8% accurate LEM voltage and current sensors are used to measure motor input power, and a LEM voltage and current sensor are used to measure the motor drive input power. With these measurements, plus the motor speed determined by the motor drive and resolver, the motor drive and motor efficiency can be measured in real time, and collected data has been utilized to verify the accuracy of the modeled motor and drive losses.

9.2.2 Electric Truck Powertrain Modeling with On-the-Road Experimental Verification

For the design phase of the electric truck, the vehicle traction system efficiency and performance was estimated using a simplified model. With the completion of the truck, a much more accurate and detailed model was developed and verified using on-the-road test data. This model accuracy was then verified using several experimental data sets. Subsequently, the model has been used to calculate constant-speed performance, drive cycle performance, gradeability performance, and the difference in performance for either gear. Key components of this contribution are discussed as follows:

- **Calculated the rotating inertia and documented the mass removed from and added to the truck**

The rotating inertia values of all the rotating components in the truck were calculated. These calculations revealed, most importantly, that the rotor inertia in first gear adds an

effective mass of 345kg to the vehicle, illustrating how important it is to keep the rotor inertia low. The total mass of the electric drivetrain equipment added to the truck was measured to be 984kg, almost twice the mass of the 515kg of gas engine drivetrain equipment which was removed. The massive, 272kg (est.) air cooled IPM machine and the 356kg battery pack accounted for about 2/3 of the electric drivetrain mass.

- **Conducted coast-down testing of the electric truck**

The electric truck coast-down results were expected to be slightly different from the gas truck results due to the increased mass of the vehicle that increases tire losses, and the use of a different gearbox that has different no-load drag properties from the original automatic transmission. However, the electric truck road load results were, surprisingly, almost identical to the manufacturer's reported road load for the stock vehicle, likely due to a reduction in gearbox drag and tire drag (due to use of low rolling resistance tires). These drag reductions apparently offset the expected increase in tire drag attributable to the increased mass of a larger truck tire and an increase in aerodynamic drag due to the addition of a truck bed enclosure ("topper"). Coast-down data results have been collected both before and after the electric vehicle conversion, providing valuable test data that has not been available in the literature to date. These results demonstrate that the increased drag due to extra mass in an electric vehicle may be counteracted with design changes that reduce drag, such as introduction of low rolling resistance tires and a low-friction gearbox that were used in the electric truck.

- **Carried out motor and drive loss modeling combined with experimental verification**

Loss models of the motor and drive were developed and used to create efficiency maps of both components, showing that a combined efficiency of greater than 94% is achieved over much of the system operating range. The loss modeling predictions were then compared to experimental results, and errors of up to 1kW were observed for the highest power cases. For longer drives the model was also found to estimate the total motor and drive loss energy very accurately, delivering estimates that fall within approx. 5% of the measured loss energy. Periodic zeroing of the torque sensor to account for offset drift due to changing temperature was required to achieve this accuracy. This loss model with experimental verification is a significant contribution because full loss measurements have not yet been presented for *any* production electric vehicle (ORNL is working on Nissan Leaf measurements).

- **Calculated constant-speed vehicle range for both gears**

The constant-vehicle-speed combined motor and drive efficiency is shown to be substantially different for each gear. In 1st gear (3:1, lower machine torque, higher machine speed gear), the constant-vehicle-speed predicted efficiency was shown to not exceed 86% due to iron losses and semiconductor losses in the flux weakening region. In contrast, during operation in 2nd gear (1:1, higher machine torque, lower machine speed gear) for speeds above 25mph, the predicted efficiency is much higher, ranging from 90 to 96%. Driving in 2nd gear increases vehicle range as much as 8.8 miles or 9.9%, clearly illustrating a possible drawback of utilizing a single-speed gearbox paired with a higher-speed machine in an electric vehicle.

- **Calculated drive cycle range for both gears and determined optimal gear selection**

For the urban-oriented UDDS drive cycle, a range of 90 miles can be achieved in 1st gear, 5% more range than can be achieved in 2nd gear, and for the highway-oriented HWFET drive

cycle, a range of 83 miles can be achieved in 2nd gear, 7% higher range than can be achieved in 1st gear. For more aggressive drive cycles involving combinations of low- and high-speed operation, both gears are required in order to provide sufficient torque and power. To cope with this requirement, the model was configured to select the gear with the lowest losses at each operating point. As a result, a range of 74 miles is predicted for the LA92 drive cycle and 56 miles is predicted for the US06 drive cycle.

- **Calculated drive cycle combined motor and drive efficiency**

With optimal gear selection to minimize the losses at each operating condition, the combined motor and drive efficiency for the UDDS cycle was calculated to be 94%, and the corresponding calculated efficiency for the HWFET, LA92, and US06 drive cycles was 95%. Calculated efficiencies for these drive cycles dropped to values as low as 88% when “non-optimal” gears were purposely selected, demonstrating that a significant improvement in drive system efficiency can be achieved by adding a second gear and using it wisely.

- **Calculated gradeability for various vehicle loadings**

Calculations have shown that the electric truck is capable of accelerating from a stop on grades up to 45% with 250kg of load and on grades up to 20% with 3000kg of load. The truck’s ability to start on steep grades with heavy loads is due to the high available wheel torque of 4900Nm in 1st gear, which is considerably greater than the 2000Nm of wheel torque provided by the Nissan Leaf, 1700Nm provided by the Chevy Spark, or even 4290Nm provided by the Tesla Model S.

- **Calculated power for various grades and vehicle loadings**

The power required to maintain speed at grade has also been calculated, showing that to maintain 60mph on a 6% grade with a 250kg load, 70kW is required; for a 3000kg load, 114kW is required. The power required to maintain speed on a grade under load is especially important because it represents the continuous power rating that the motor, drive, and battery pack must be capable of providing for a Class 2a pickup truck.

9.2.3 Hybrid Energy Storage System (HESS) Investigation

Hybrid energy storage, which is typically the combination of energy-dense and power-dense energy storage components, has been investigated for many applications that have been reported in the literature, and it has been applied commercially in a few micro-hybrid applications. However, hybrid energy storage has not yet been applied to a commercial electric vehicle. Although its application to light-duty electric vehicles has been proposed in at least ten different projects [30-42], only one of these projects has gone as far as installing a HESS in an electric vehicle and experimentally verifying its performance benefits. While a HESS has not been installed in the vehicle for this project, an actual test vehicle has been built and a scaled HESS has been tested with that battery pack to make the modeled results as realistic and applicable as possible. The components of the HESS work contribution are discussed in more detail as follows:

- **Developed a lookup table-based low-temperature nonlinear battery model**

A battery model based on a lookup table has been developed that can be efficiently incorporated into the dynamic programming optimization code. The battery model has two unique aspects; it includes non-linear current-dependent resistance, which is important at low temperatures, and it utilizes a pseudo-open circuit voltage measured during a drive cycle to improve model accuracy. Model parameters are measured for temperature ranging from -

20°C to 25°C for a Calb LiFePO₄ battery and a Panasonic NCR18650PF battery, and the model has been experimentally verified for both.

- **Derived and verified a discrete-time ultracapacitor model**

A discrete-time ultracapacitor model has been derived that made it possible to use a large time step of one second during the simulations in this HESS study without any discretization effects. The model parameters are a function of the ultracapacitor open-circuit voltage, and include capacitance, charge resistance, and discharge resistance. The model parameters were measured for a Maxwell ultracapacitor pack for temperatures ranging from -30°C to 25°C, and the ultracapacitor pack was subsequently tested for a complete drive cycle to experimentally verify the discrete-time model.

- **Carried out an analytical calculation to determine the power split to achieve minimum losses in the HESS**

An analytical model of the HESS system, including battery and ultracapacitor resistance and open-circuit voltage and dc/dc converter efficiency has been presented, and an analytical solution for the minimum-loss power split was derived. An analytical solution for minimum-loss power split has been utilized in prior art [84], but the authors only state that the sum of the loss equations should be differentiated to determine the minimum loss point, and the actual analytical solution is not presented. The solution was likely not presented because the authors' models were too complex and resulted in a very large equation. A more simplified, but sufficiently accurate model has been developed during this research program so that an actual equation for minimum-loss power split could be presented in this dissertation.

- **Developed a vehicle model including hybrid energy storage system with dynamic programming algorithm to calculate optimal power split**

The battery and ultracapacitor models described above have been incorporated into the vehicle model, together with a dc/dc converter loss model. A dynamic programming algorithm has been utilized to calculate how the power should ideally be split between the battery and ultracapacitor pack to minimize the energy storage system losses under the non-causal assumption that the complete details for the studied drive cycle are known apriori.

- **Compared rule-based control & the optimal power split calculated with dynamic programming**

A rule-based heuristic control that utilizes the analytical minimum-loss power split calculation has been implemented, and its performance has been compared to that of the optimal, system-loss-minimizing dynamic programming control. The rule-based controller was demonstrated to perform almost as well as the dynamic programming control for larger ultracapacitor pack sizes. However, the rule-based control performs more poorly when a small ultracapacitor pack is utilized. This is a characteristic that most rule-based control methods are likely to share, although this result has not been discussed previously in the prior-art literature.

- **Evaluated HESS performance for a Class 2a electric truck using the computer model for a wide range of conditions and component ratings**

The system model was utilized to evaluate the predicted HESS performance for four different drive cycles in a Class 2a electric truck for temperatures ranging from -20°C to 25°C. The HESS was shown to reduce battery losses by as much as 80% and to improve vehicle range by 50% or more at low temperatures where the battery is not rated to accept charging

power. The HESS performance was also evaluated for a range of ultracapacitor pack sizes and dc/dc converter current ratings, and most of the system efficiency improvements were shown to be achieved with a small ultracapacitor pack and low dc/dc converter current rating. However, a larger ultracapacitor pack and dc/dc converter were shown to be necessary for the HESS to significantly boost the battery's power capability.

- **Built a scaled HESS and used it to experimentally verify the model-predicted results**

A scaled HESS, consisting of an 80V LiFeP0₄ battery pack made of cells from the electric truck, a 48V / 165F ultracapacitor pack, and a prototype 200A-rated dc/dc converter was built. A rule-based controller was implemented with the dc/dc converter controls, and the HESS and the battery-only system was tested for three drive cycles at two temperatures. The experimental and model-predicted results were compared, showing that the model predicted amp-hours drawn from the battery with a maximum error of 0.6% at 25°C and 4.2% at 0°C. Additionally, the model predicted that amp-hours drawn from the battery with the HESS would be reduced between 0% and 0.5% at 25°C and between 0.6% and 2.5% at 0°C, while the measured reduction ranged between 0.0 and 0.7% at 25°C and between -0.7% and 1.7% at 0°C. The error between the measured and modeled amp-hour reduction at 0°C was likely due to battery heating, which was not accounted for in the model.

- **Utilized developed modeling methodology to evaluate three alternative vehicle configurations**

An electric Class 2a truck with a different battery pack, an electric bus, and an electric Class 2a truck with a much higher power rating and towing capability were modeled. The truck with the Panasonic battery pack was shown to achieve similar performance benefits as

the truck with the CALB battery pack, and the battery model was shown to very accurately capture the performance of the Panasonic cell. An electric city transit bus, weighing over 40,000 pounds when fully loaded, was shown to have its range improved significantly by 10 to 18% with the HESS. For the electric truck with the much higher power rating, the HESS was shown to enable full drivetrain power capability with a power-limited battery pack and to enable towing of heavy loads without excessive battery pack losses.

9.3 Recommended Future Work

The following areas of research are recommended for future work, based on the work performed and conclusions from this dissertation:

i. Battery pack model including heating and cooling system design and thermal modeling

The conclusions presented in this dissertation assume constant battery temperature because a thermal model was not included in the modeling. To determine how a battery pack will perform as it heats up under load, or as it is heated up with a battery heating system, a thermal model of the battery pack and the heating and cooling. Production electric vehicles contain sophisticated cooling and heating systems, so to accurately predict how a hybrid energy storage system would benefit a more production oriented system, this more sophisticated modeling is a necessity.

ii. High performance liquid cooled machine design for light-duty trucks and medium- and heavy-duty commercial vehicles

The air cooled IPM machine developed for the truck was shown to perform very well for this prototype application, but a much more power dense liquid cooled machine design would

be preferred for a production vehicle. The continuous power and high torque requirements for light-duty trucks, as well as medium- and heavy-duty commercial vehicles are very different than passenger car requirements, so contributions could likely be made in this less studied area.

iii. Performance comparison of different machine types in electric vehicles

The electric truck's traction drive and IPM machine were shown to be very efficient, with a combined efficiency ranging from 94-95% for the simulated drive cycles. There are some downsides of the machine though, particularly in the flux weakening region where semiconductor drive losses and iron losses can be high. Wound-field synchronous machines and induction machines have often been proposed as a better alternative to IPM machines, but there is still relatively little research providing a full traction system design comparison between them. A comparison of the three machine types, including machine, drive, and gearbox losses, is recommended.

iv. Detailed multi-gear EV study

Having two gears was shown to both allow higher wheel-torque at low-speed and to substantially reduce drivetrain losses when the optimal efficiency gear was chosen, and there is a trend, albeit small, in the auto industry towards multi-gear drivetrains for electric vehicles. A preliminary study was performed by the author and published outside of this dissertation, and a more detailed study is recommended to determine the tradeoffs in mass, volume, cost, efficiency, etc. between single and multi-gear drivetrains.

v. Characterize batteries used in other production vehicles

This dissertation only studies two batteries, a LiFePO_4 cell whose commercial application is largely limited to Chinese built electric buses, and a Panasonic LiNiCOMnO_2 which is similar to that used by Tesla. These two batteries only cover a very narrow range of vehicle applications, so to better determine if an HESS could benefit existing production electric vehicles, batteries from those vehicles should be tested and the vehicles should be modeled with an HESS. This would help to identify other good applications of an HESS, and whether other battery technology is sufficient to possibly negate the need for an HESS.

vi. Study of hybrid energy storage application to start-stop and micro-hybrid vehicles

Most gasoline powered micro-hybrid and start-stop vehicles have two energy sources, a 12V lead acid battery and a small lithium battery pack or ultracapacitor pack. Because there are two energy sources, this is technically hybrid energy storage, although that terminology is not always used to describe these system. The market for start-stop and micro-hybrid vehicles is projected to be very large in the coming years as fuel economy standards increase, so any work in this area would be very valuable. One good focus area would be to study multiple systems, consisting of different pairings of energy sources, and evaluate their efficiency, power capability, mass, volume, cost and other performance factors over a wide range of temperatures.

vii. Cycle life testing to quantify HESS benefits

An HESS can substantially reduce battery microcycles due to regenerative braking and battery losses, potentially reducing battery aging significantly. No studies have been published which quantify these benefits through experimental testing, so any contributions in this area would be very valuable. A simple test could be performed, in which two production electric

vehicle battery cells, or preferably modules with the manufacturer's cooling system, and one battery could be cycled till end of life with a power profile for the vehicle without an HESS, and the other could be tested with the power profile for the vehicle with an HESS. This could provide a starting point for more work in this area.

viii. Heavy duty vehicle applications

Heavy duty vehicles are one of the best applications for hybrid energy storage because they experience frequent, high-power starts and stops, and because they are rated for a very long service life, 500,000 miles or more, and therefore may benefit from a reduction in battery aging achieved with an HESS. Electric buses would be one of the best applications to study, since the market for them is growing and current designs either utilize somewhat oversized battery pack to achieve long cycle life, or very expensive high cycle life rated batteries, such as the XALT batteries used in the New Flyer Excelsior electric bus. These vehicle are so expensive, \$500k or more, that they could likely tolerate the extra cost of the HESS if it enabled better service life, the use of a cheaper battery pack, or other benefits.

ix. Improved battery / ultracapacitor power split control for HESS, possibly utilizing model predictive control

The goal of this dissertation was primarily to determine how much an HESS could improve system performance with an ideal, optimal controller, which knows the entire drive cycle ahead of time. To implement an HESS in a vehicle though, a very good power split control, better than the rule based controller proposed here, will be necessary to achieve most of the potential performance benefits. Model predictive control (MPC) has been used in hybrid energy storage systems to determine the power split based on an optimal trajectory calculated for the next several seconds of driving. Other researchers have shown that similar performance to rule-

based control can be achieved with MPC, and a preliminary study on this topic which was not included in this dissertation confirms those results. However MPC is a good starting point for improved control, MPC combined with an estimate of what the speed trajectory for the next several minutes of driving is could result in improved control performance.

x. Evaluation of full scale HESS in the electric truck

In only one other case in the research has an HESS been tested in a full scale electric vehicle. This could relatively easily be done in the electric truck, using the existing prototype dc/dc converter, which has a very robust controller which ran for weeks straight without issue. Two 48V / 165F ultracapacitor packs are already available in the lab, if an additional two were purchased then a 196V pack could be assembled, which would be sufficient.

xi. Investigate controls for changing gears in electric vehicles with multi-speed gearboxes

One of the challenges associated with having a two-speed gearbox, as the developed electric truck does, is changing gears while driving. In the truck, the gears can currently only be changed while stopped when neither the wheels nor the machine are spinning. In order to change gears while the truck is moving, a control system must be implemented which proceeds through a sequence of events to execute the gear change. First, the gearbox must be changed to neutral and the electric machine's drive must be switched from torque mode (normal for the vehicle) to speed mode. Second, the drive speed must be adjusted to match the speed of the gears (from 1st (3:1) to 2nd (1:1) gear, the speed must be reduced by 2/3). Third, the clutch must be closed when the speed is matched, accompanied by returning the machine drive to torque mode.

This is difficult for several reasons, including: (1) the gearbox in the truck has a very fast acting clutch so that any difference in speed between the machine and the gearing when closing

the clutch will result in a large torque transient; (2) the drive is currently implemented as the vehicle controller, meaning the motor drive reads accelerator and brake pedal position and controls torque. As a result, the NI cRio would have to be used as the vehicle controller to switch between torque and speed modes, controlling the motor drive via CAN; and (3) since there is no speed sensor on the driveshaft side of the gearbox, the speed sensor built into the rear differential would have to be used to measure speed on the gear side of the gearbox.

An additional challenge is that adding the automated gear changing creates a significant risk to the electric traction system in the event of any malfunction. More specifically, if the gear-changing controller makes a mistake and closes the gear at the wrong machine speed, the rotor inertia is so high that the rear wheels can lock up. This is a dangerous condition that actually happened once before when attempting to implement a simple gear-changing controller. Therefore, if such a control is attempted, it should first be developed in simulation and then tested thoroughly at low speed.

Performing gear changing in the truck is an implementation issue that applies to any electric vehicle that utilizes a gearbox. A suggested first step would be to first perform a study that investigates candidate control algorithms for gear changing in more detail, including effects of rotor inertia, gear ratios, gearbox clutch type and design, and other physical design aspects on control performance. Very importantly, the controller and gearbox must be designed to execute very quick gear changes ($<100\text{ms}$) that are very smooth with no perceptible shudder. Furthermore, the design must be highly robust, never locking the clutch at an incorrect time that would result in damage to the gearbox.

xii. **Characterize accessory power loading in the electric truck, including HVAC power, and investigate methods for reducing the accessory power that is drawn during vehicle acceleration**

In the electric truck, the power delivered to all of the individual 12V and high-voltage accessory systems is measured and recorded in the driving log. In the modeling of the truck to date, the truck's accessory power has simply been assumed to be constant at 1kW, which is close to the average measured accessory power drawn when the truck heater is not being utilized. For this future work, the power drawn by each accessory system would be characterized, and efficiency benefits achievable with alternative systems would then be investigated. The power steering pump is one of the accessory systems that deserves special attention since approx. 3% of the drive energy is currently required to power that pump. Much better solutions than the truck's current add-on hydraulic power steering pump are available, and their effect on vehicle range could be studied. Additionally, HVAC system improvements, as well as improvements in cabin insulation could be investigated as well. Furthermore, methods of reducing the accessory power that is drawn during high-power acceleration conditions could be investigated as well, including opportunities to reduce the energy storage system losses and increase vehicle range.

xiii. **Develop a region-based control for hybrid energy storage systems – possibly utilize some of the following provided suggestions for regions**

Region-based control (sometimes known as fuzzy logic control) is also an excellent candidate for controlling hybrid energy storage systems, as has been studied in [64] and [68] and in many other publications. Region-based controls utilize a different control methodology based on the operating region of the vehicle, with the goal of achieving the best control outcomes. The rule-based control implemented in Chapter 7 of this dissertation is, in a sense, a region-based control because it utilizes different control rules for the charging and

discharging case. A study is recommended that implements a region-based control in simulation and compares the results to the optimal solution achieved with dynamic programming. Several candidate control regions, developed from insights into hybrid energy storage systems that have been gained while completing the research for this dissertation, are identified as follows together with suggested controller responses:

1. **Low-speed (<10mph), low acceleration:** Ensure that the ultracapacitors are full to allow the ultracapacitors to assist acceleration to higher speeds. Charge the ultracapacitors at a rate that is low enough to not have a significant negative impact on efficiency, but high enough that the ultracapacitors will soon be capable of providing substantial discharge energy.
2. **Mid-speed (10 to 50mph), low acceleration (<1mph/s):** Maintain ultracapacitor charge at approx. half full, such that the ultracapacitors can either collect regenerative braking energy when slowing or provide discharge power when accelerating. Consider having an acceptable charge band, perhaps 40-60% SOC or a band that scales with speed, and charge or discharge the ultracapacitors slowly to stay within that band.
3. **High-speed (>50mph), low acceleration (<1mph/s), with no further acceleration expected:** Maintain the ultracapacitors at a discharged state so that they can be utilized to capture regenerative braking energy when the vehicle decelerates. Implementing this operation mode requires the controller to predict whether or not the vehicle will accelerate in the near future. This could be accomplished using a predictive control utilizing mapping that includes speed limits and stop lights or stop signs.
4. **High-speed (>50mph), low acceleration (<1mph/s), further acceleration expected:** In this region, it is expected the vehicle will accelerate further. For example, the truck could be on the expressway where passing maneuvers are likely. Maintain the ultracapacitor voltages at a full state-of-charge so that the

ultracapacitors can assist the execution of high-power, high-speed passing maneuvers, and also to enable high power in the case of power limiting.

5. **Acceleration (>1mph/s):** Supply discharge power with the ultracapacitors utilizing the power split values that are calculated to achieve maximum efficiency as discussed in Chapter 5 of the dissertation. Consider splitting this into high- and low-power acceleration regions, so that the ultracapacitors are only utilized under conditions that can deliver reductions in losses that are greater than a certain minimum threshold.
6. **Deceleration (>1mph/s):** Calculate the kinetic energy of the vehicle and capture all of the regeneration energy with the ultracapacitors if the energy needed to fully charge the ultracapacitors is greater than the vehicle kinetic energy. If the energy needed to fully charge the ultracapacitors is less than the kinetic energy of the vehicle, then use the maximum efficiency power-split calculation to determine the ultracapacitor charging current.
7. **Battery power-limited (cold temperature) operation:** When battery power is limited, adjust the rules in the other regions to ensure that the HESS is available to both provide acceleration power above the battery power limit and to capture regenerative braking energy if the battery temperature is below the minimum threshold temperature for charging.

References

- [1] S. F. Tie and C. W. Tan, "A review of energy sources and energy management system in electric vehicles," *Renewable and Sustainable Energy Reviews*, vol. 20, pp. 82-102, 4// 2013.
- [2] Union of Concerned Scientists, "State of Charge: Electric Vehicles' Global Warming Emissions and Fuel-Cost Savings across the United States," 2012.
- [3] Electric Drive Transportation Association. *Cumulative U.S. Plug-In Vehicle Sales*. Available: <http://electricdrive.org/ht/d/sp/i/20952/pid/20952>
- [4] J. Y. Wong, *Theory of Ground Vehicles*, Second ed.: John Wiley & Sons, Inc., 1993.
- [5] P. J. Kollmeyer. (2011). *Electromechanical Modeling and Analysis of a Corbin Sparrow Electric Vehicle using On the Road Data*. Available: <http://www.wempec.wisc.edu/MS%20&%20PhD%20Theses.htm>
- [6] A. Ukaew, "Model Based System Design of Urban Fleet Electric Vehicle Conversion," presented at the SAE World Congress and Exposition, 2014.
- [7] M. De Gennaro, E. Paffumi, G. Martini, U. Manfredi, H. Scholz, H. Lacher, *et al.*, "Experimental Investigation of the Energy Efficiency of an Electric Vehicle in Different Driving Conditions," presented at the SAE World Congress and Exposition, 2014.
- [8] US Department of Energy. *2011 Nissan Leaf VIN 0356 - Advanced Vehicle Testing - Baseline Testing Results*. Available: <http://avt.inel.gov/fsev.shtml>
- [9] D. Lee, A. Rousseau, and E. Rask, "Development and Validation of the Ford Focus Battery Electric Vehicle Model," presented at the SAE World Congress and Exposition, 2014.
- [10] S. Hawkins, A. Holmes, D. Ames, K. Rahman, and R. Malone, "Design Optimization, Development and Manufacturing of General Motors New Battery Electric Vehicle Drive Unit (1ET35)," *SAE Int. J. Alt. Power.*, vol. 3, pp. 213-221, 2014.
- [11] T. Schieffer, M. A. Jeffers, S. Hawkins, A. Heisel, C. Leahy, E. Rapa, *et al.*, "Spark EV Propulsion System Integration," presented at the SAE World Congress and Exposition, 2014.
- [12] R. Palin, V. Johnston, S. Johnson, A. D'Hooge, B. Duncan, and J. I. Gargoloff, "The Aerodynamic Development of the Tesla Model S - Part 1: Overview," presented at the SAE World Congress and Exposition, 2012.
- [13] A. D'Hooge, R. B. Palin, S. Johnson, B. Duncan, and J. I. Gargoloff, "The Aerodynamic Development of the Tesla Model S - Part 2: Wheel Design Optimization," presented at the SAE World Congress and Exposition, 2012.

- [14] E. Samadani, R. Fraser, and M. Fowler, "Evaluation of Air Conditioning Impact on the Electric Vehicle Range and Li-Ion Battery Life," presented at the SAE World Congress and Exposition, 2014.
- [15] G. Gao, "Investigation of Climate Control Power Consumption in DTE Estimation for Electric Vehicles," presented at the SAE World Congress and Exposition, 2014.
- [16] J. Kendall. (21 Jun 2010, PSA's new stop/start system uses ultracaps for energy storage, extra power. *Automotive Engineering Magazine*. Available: <http://articles.sae.org/8412/>
- [17] Peugeot. (2014), e-HDI Micro Hybrid System Technology. Available: <http://www.peugeot.com/en/technology/engines/e-hdi-micro-hybrid>
- [18] P. Valdes-Dapena. (2014), Lamborghini Aventador: Insanity in the big city. *CNN Money*. Available: <http://money.cnn.com/gallery/autos/2013/11/04/lamborghini-aventador-review/>
- [19] M. LaMonica. (14 Apr 2014), Supercapacitor-Enhanced Hybrid Storage to Earn Cash for Subways. *IEEE Spectrum*. Available: <http://spectrum.ieee.org/energywise/energy/the-smarter-grid/supercapacitor-enhanced-hybrid-storage-could-earn-cash-for-subways/>
- [20] A. Khaligh and L. Zhihao, "Battery, Ultracapacitor, Fuel Cell, and Hybrid Energy Storage Systems for Electric, Hybrid Electric, Fuel Cell, and Plug-In Hybrid Electric Vehicles: State of the Art," *Vehicular Technology, IEEE Transactions on*, vol. 59, pp. 2806-2814, 2010.
- [21] A. Ostadi, M. Kazerani, and C. Shih-Ken, "Hybrid Energy Storage System (HESS) in vehicular applications: A review on interfacing battery and ultracapacitor units," in *Transportation Electrification Conference and Expo (ITEC), 2013 IEEE*, 2013, pp. 1-7.
- [22] S. Mariethoz and P. Barrade, "Design methodology of an electric vehicle hybrid energy storage unit for improved energy efficiency," in *Vehicle Power and Propulsion Conference (VPPC), 2010 IEEE*, 2010, pp. 1-6.
- [23] O. Laldin, M. Moshirvaziri, and O. Trescases, "Optimal power flow for hybrid ultracapacitor systems in light electric vehicles," in *Energy Conversion Congress and Exposition (ECCE), 2011 IEEE*, 2011, pp. 2916-2922.
- [24] O. Laldin, M. Moshirvaziri, and O. Trescases, "Predictive Algorithm for Optimizing Power Flow in Hybrid Ultracapacitor/Battery Storage Systems for Light Electric Vehicles," *Power Electronics, IEEE Transactions on*, vol. 28, pp. 3882-3895, 2013.

- [25] T. Chia-Hao and A. Emadi, "A novel series-parallel reconfigurable hybrid energy storage system for electrified vehicles," in *Transportation Electrification Conference and Expo (ITEC), 2012 IEEE*, 2012, pp. 1-4.
- [26] W. O. Avelino, F. S. Garcia, A. A. Ferreira, and J. A. Pomilio, "Electric go-kart with battery-ultracapacitor hybrid energy storage system," in *Transportation Electrification Conference and Expo (ITEC), 2013 IEEE*, 2013, pp. 1-6.
- [27] E. Ugur, S. Dusmez, B. Vural, and M. Uzunoglu, "Implementation of a reliable load sharing strategy between battery and ultra-capacitor on a prototype electric vehicle," in *Transportation Electrification Conference and Expo (ITEC), 2012 IEEE*, 2012, pp. 1-4.
- [28] N. Shaha and M. B. Uddin, "Hybrid energy assisted electric auto rickshaw three-wheeler," in *Electrical Information and Communication Technology (EICT), 2013 International Conference on*, 2014, pp. 1-6.
- [29] P. B. Bobba and K. R. Rajagopal, "Modeling and analysis of hybrid energy storage systems used in Electric vehicles," in *Power Electronics, Drives and Energy Systems (PEDES), 2012 IEEE International Conference on*, 2012, pp. 1-6.
- [30] N. Schofield, H. T. Yap, and C. M. Bingham, "Hybrid energy sources for electric and fuel cell vehicle propulsion," in *Vehicle Power and Propulsion, 2005 IEEE Conference*, 2005, pp. 522-529.
- [31] V. Shah, R. Chaudhari, P. Kundu, and R. Maheshwari, "Performance analysis of hybrid energy storage system using hybrid control algorithm with BLDC motor driving a vehicle," in *Power Electronics, Drives and Energy Systems (PEDES) & 2010 Power India, 2010 Joint International Conference on*, 2010, pp. 1-5.
- [32] W. Chien-Hsun, C. Yi-Hsien, S. Wu-Yang, L. Shih-Ming, K. Jia-Cheng, and H. Yi-Hsuan, "Optimal designs and experimental verification for a hybrid energy storage system," in *Computer Communication Control and Automation (3CA), 2010 International Symposium on*, 2010, pp. 158-161.
- [33] K. B. A. Mikkelsen and S. Lambert, "Evaluation of a Hybrid Energy Storage System for EV's," 2011.
- [34] M. Neenu and S. Muthukumaran, "A battery with ultra capacitor hybrid energy storage system in electric vehicles," in *Advances in Engineering, Science and Management (ICAESM), 2012 International Conference on*, 2012, pp. 731-735.
- [35] J. Cao and A. Emadi, "A new battery/ultra-capacitor hybrid energy storage system for electric, hybrid and plug-in hybrid electric vehicles," in *Vehicle*

- Power and Propulsion Conference, 2009. VPPC '09. IEEE, 2009, pp. 941-946.*
- [36] J. Cao and A. Emadi, "A New Battery/UltraCapacitor Hybrid Energy Storage System for Electric, Hybrid, and Plug-In Hybrid Electric Vehicles," *Power Electronics, IEEE Transactions on*, vol. 27, pp. 122-132, 2012.
 - [37] M. Michalczyk, L. M. Grzesiak, and B. Ufnalski, "A lithium battery and ultracapacitor hybrid energy source for an urban electric vehicle," *Electrical Review*, 2012.
 - [38] S. Rogers, A. Saul, S. Dusmez, and A. Khaligh, "Enhanced battery / ultracapacitor hybrid energy storage system and split powertrain for next generation performance vehicles," in *Transportation Electrification Conference and Expo (ITEC), 2013 IEEE*, 2013, pp. 1-3.
 - [39] S. Misal and B. Divakar, "Performance Evaluation of Ultra-Capacitor in Hybrid Energy Storage System for Electric Vehicles," in *Modelling Symposium (AMS), 2013 7th Asia*, 2013, pp. 212-217.
 - [40] J. Moreno, M. E. Ortuzar, and J. W. Dixon, "Energy-management system for a hybrid electric vehicle, using ultracapacitors and neural networks," *Industrial Electronics, IEEE Transactions on*, vol. 53, pp. 614-623, 2006.
 - [41] M. Ortuzar, J. Moreno, and J. Dixon, "Ultracapacitor-Based Auxiliary Energy System for an Electric Vehicle: Implementation and Evaluation," *Industrial Electronics, IEEE Transactions on*, vol. 54, pp. 2147-2156, 2007.
 - [42] J. Dixon, I. Nakashima, E. F. Arcos, and M. Ortuzar, "Electric Vehicle Using a Combination of Ultracapacitors and ZEBRA Battery," *Industrial Electronics, IEEE Transactions on*, vol. 57, pp. 943-949, 2010.
 - [43] R. Li, A. Pottharst, N. Frohliche, J. Bocker, K. Witting, M. Bellnitz, *et al.*, "Design and implementation of a hybrid energy supply system for railway vehicles," in *Applied Power Electronics Conference and Exposition, 2005. APEC 2005. Twentieth Annual IEEE*, 2005, pp. 474-480 Vol. 1.
 - [44] Y. Gao, H. Moghbelli, M. Ehsani, G. Frazier, J. Kajs, and S. Bayne, "Investigation of High-Energy and High-Power Hybrid Energy Storage Systems for Military Vehicle Application," 2003.
 - [45] S. Butterbach, B. Vulturescu, C. Forgez, G. Coquery, and G. Friedrich, "Lead-acid battery model for hybrid energy storage," in *Vehicle Power and Propulsion Conference (VPPC), 2011 IEEE*, 2011, pp. 1-5.
 - [46] L. Jeeho, J. Namju, and L. Hyeongcheol, "HIL simulation approach for feasibility study of a tram with an onboard hybrid energy storage system," in *ICCAS-SICE, 2009, 2009*, pp. 5305-5312.

- [47] I. Szenasy, "Energy management and hybrid energy storage in metro railcar," in *Renewable Energy Research and Applications (ICRERA), 2012 International Conference on*, 2012, pp. 1-6.
- [48] I. Szenasy, "Capacitive and Hybrid Energy Storages for Metro Railcars," in *Electric Vehicle Conference (IEVC), 2013 IEEE International*, 2013, pp. 1-5.
- [49] G. Nielson and A. Emadi, "Hybrid energy storage systems for high-performance hybrid electric vehicles," in *Vehicle Power and Propulsion Conference (VPPC), 2011 IEEE*, 2011, pp. 1-6.
- [50] V. Chheda and D. Y. Vernekar, "Hybrid Power Pack (Ultra Capacitor + Battery) for Two Wheelers Fitted with Starter Motor," 2009.
- [51] C. Bond, K. Boyle, N. Freeman, D. Orr, D. Brewin, R. Christenson, *et al.*, "Design and Development of the 2003 University of Alberta Hybrid Electric Vehicle," 2003.
- [52] N. Di, F. Crescimbeni, A. Lidozzi, L. Solero, M. Pasquali, A. Puccetti, *et al.*, "Design and Testing of a Fuel-Cell Powered Propulsion System Supported by a Hybrid UC-Battery Storage," 2004.
- [53] A. W. Stienecker, M. A. Flute, and T. A. Stuart, "Improved Battery Charging in an Ultracapacitor - Lead Acid Battery Hybrid Energy Storage System for Mild Hybrid Electric Vehicles," 2006.
- [54] J. Duan and M. Xu, "Simulation research on hybrid energy storage system of hybrid electric vehicle," in *Automation and Logistics (ICAL), 2010 IEEE International Conference on*, 2010, pp. 197-201.
- [55] J. Wang, K. Li, Q. Lv, H. Zhou, and L. Shang, "Hybrid energy storage system integration for vehicles," in *Low-Power Electronics and Design (ISLPED), 2010 ACM/IEEE International Symposium on*, 2010, pp. 369-374.
- [56] D. Shichuan, C. Ming, W. Zheng, K. T. Chau, W. Wei, and W. Yubing, "A hybrid energy source based double-stator permanent magnet brushless motor drive for hybrid electric vehicles," in *Electrical Machines and Systems (ICEMS), 2011 International Conference on*, 2011, pp. 1-5.
- [57] S. Gopalakrishnan, C. Namuduri, and M. Reynolds, "Ultracapacitor Based Active Energy Recovery Scheme for Fuel Economy Improvement in Conventional Vehicles," 2011.
- [58] B. Gao, K. Svancara, A. Walker, D. Kok, M. Conen, and D. Kees, "Development of a BISG Micro-Hybrid System," 2009.
- [59] K. El Kadri, A. Djerdir, and A. Berthon, "Hybrid Energy Sources for Heavy Truck: Simulation and Behavior," in *Power Electronics and Motion Control*

- Conference, 2006. EPE-PEMC 2006. 12th International*, 2006, pp. 1395-1400.
- [60] W. Tiecheng, Y. Haifang, and Z. Chunbo, "Hybrid energy sources for hybrid electric vehicle propulsion," in *Vehicle Power and Propulsion Conference, 2008. VPPC '08. IEEE*, 2008, pp. 1-4.
 - [61] Q. Xiaodong, W. Qingnian, and Y. YuanBin, "Power Demand Analysis and Performance Estimation for Active-Combination Energy Storage System Used in Hybrid Electric Vehicles," *Vehicular Technology, IEEE Transactions on*, vol. PP, pp. 1-1, 2014.
 - [62] M. M. Tehrani, M. R. Hairi-Yazdi, D. Bazargan, and M. Esfahanian, "Performance analysis of hybrid energy storage in different driving cycles," in *Power Electronics, Drive Systems and Technologies Conference (PEDSTC), 2011 2nd*, 2011, pp. 330-335.
 - [63] W. Hongmei, W. Qingfeng, H. Baozan, and F. Qiang, "The novel hybrid energy storing unit design for hybrid excavator by the effective integration of ultracapacitor and battery," in *Advanced Intelligent Mechatronics (AIM), 2013 IEEE/ASME International Conference on*, 2013, pp. 1585-1590.
 - [64] R. Felix, J. Economou, and K. Knowles, "Control System for a PEM Fuel Cell Powered Heavy Duty Tactical Mobility Truck with Auxiliary Power Generation Capabilities," *SAE Int. J. Alt. Power.*, vol. 2, pp. 413-427, 2013.
 - [65] J. Malaize and P. Tona, "Optimization-based control design for hybrid energy storage systems in electric vehicles," in *Vehicle Power and Propulsion Conference (VPPC), 2011 IEEE*, 2011, pp. 1-7.
 - [66] P. Sangyoung, K. Younghyun, and C. Naehyuck, "Hybrid energy storage systems and battery management for electric vehicles," in *Design Automation Conference (DAC), 2013 50th ACM / EDAC / IEEE*, 2013, pp. 1-6.
 - [67] R. Dhaouadi, Y. Hori, and H. Xiaoliang, "Robust control of an ultracapacitor-based hybrid energy storage system for electric vehicles," in *Advanced Motion Control (AMC), 2014 IEEE 13th International Workshop on*, 2014, pp. 161-166.
 - [68] M. Choi, J. Lee, and S. Seo, "Real-time Optimization for Power Management Systems of a Battery/Supercapacitor Hybrid Energy Storage System in Electric Vehicles," *Vehicular Technology, IEEE Transactions on*, vol. PP, pp. 1-1, 2014.
 - [69] F. S. Garcia, A. A. Ferreira, and J. A. Pomilio, "Control Strategy for Battery-Ultracapacitor Hybrid Energy Storage System," in *Applied Power Electronics Conference and Exposition, 2009. APEC 2009. Twenty-Fourth Annual IEEE*, 2009, pp. 826-832.

- [70] Alle, x, A. L. gre, R. Trigui, and A. Bouscayrol, "Different energy management strategies of Hybrid Energy Storage System (HESS) using batteries and supercapacitors for vehicular applications," in *Vehicle Power and Propulsion Conference (VPPC), 2010 IEEE*, 2010, pp. 1-6.
- [71] C. Mid-Eum and S. Seung-Woo, "Robust energy management of a battery/supercapacitor Hybrid Energy Storage System in an electric vehicle," in *Electric Vehicle Conference (IEVC), 2012 IEEE International*, 2012, pp. 1-5.
- [72] A. L. Allegre, A. Bouscayrol, and R. Trigui, "Influence of control strategies on battery/supercapacitor hybrid Energy Storage Systems for traction applications," in *Vehicle Power and Propulsion Conference, 2009. VPPC '09. IEEE*, 2009, pp. 213-220.
- [73] Alle, x, A. L. gre, A. Bouscayrol, and R. Trigui, "Flexible real-time control of a hybrid energy storage system for electric vehicles," *Electrical Systems in Transportation, IET*, vol. 3, pp. 79-85, 2013.
- [74] C. Romaus, J. Bocker, K. Witting, A. Seifried, and O. Znamenshchykov, "Optimal energy management for a hybrid energy storage system combining batteries and double layer capacitors," in *Energy Conversion Congress and Exposition, 2009. ECCE 2009. IEEE*, 2009, pp. 1640-1647.
- [75] C. Romaus, D. Wimmelbucker, K. S. Stille, and J. Bocker, "Self-optimization energy management considering stochastic influences for a hybrid energy storage of an electric road vehicle," in *Electric Machines & Drives Conference (IEMDC), 2013 IEEE International*, 2013, pp. 67-74.
- [76] W. Bin, Z. Fang, L. Fei, G. Weiwei, Q. Yang, and L. YanQin, "A management strategy for solar panel — battery — super capacitor hybrid energy system in solar car," in *Power Electronics and ECCE Asia (ICPE & ECCE), 2011 IEEE 8th International Conference on*, 2011, pp. 1682-1687.
- [77] L. Baek-Haeng, S. Dong-Hyun, K. Byeong-Woo, K. Hee-Jun, L. Byoung-kuk, W. Chung-Yuen, *et al.*, "A Study on Hybrid Energy Storage System for 42V Automotive Power-net," in *Vehicle Power and Propulsion Conference, 2006. VPPC '06. IEEE*, 2006, pp. 1-5.
- [78] L. Baek-Haeng, S. Dong-Hyun, S. Hyun-Sik, J. Jin-Beom, K. Hee-Jun, and K. Byeong-Woo, "The Dynamic Control of Hybrid Energy Storage Sysem for Mild HEV," in *Vehicle Power and Propulsion Conference, 2007. VPPC 2007. IEEE*, 2007, pp. 796-801.
- [79] S. Hyun-Sik, J. Jin-Beom, L. Baek Haeng, S. Dong-Hyun, K. Byoung-Hoon, P. Yu-Cheol, *et al.*, "A study on the dynamic SOC compensation of an ultracapacitor module for the hybrid energy storage system," in

- Telecommunications Energy Conference, 2009. INTELEC 2009. 31st International*, 2009, pp. 1-7.
- [80] S. S. Kulkarni, N. Gandhi, N. Chaithanya, and S. Govindarajan, "Ultra-Capacitor based Hybrid Energy Storage and Energy Management for Mild Hybrid Vehicles," *SAE Technical Pap*, 2014.
 - [81] S.-m. Cui, D.-w. Tian, and Q.-f. Zhang, "Study of hybrid energy control strategy for hybrid electric drive system in All Electric Combat Vehicles," in *Vehicle Power and Propulsion Conference, 2008. VPPC '08. IEEE*, 2008, pp. 1-5.
 - [82] M. Masih-Tehrani, M.-R. Ha'iri-Yazdi, V. Esfahanian, and A. Safaei, "Optimum sizing and optimum energy management of a hybrid energy storage system for lithium battery life improvement," *Journal of Power Sources*, vol. 244, pp. 2-10, 12/15/ 2013.
 - [83] Y. Haifang, L. Rengui, W. Tiecheng, and Z. Chunbo, "Energetic Macroscopic Representation based modeling and control for battery/ultra-capacitor hybrid energy storage system in HEV," in *Vehicle Power and Propulsion Conference, 2009. VPPC '09. IEEE*, 2009, pp. 1390-1394.
 - [84] T. P. Kohler, D. Buecherl, and H. Herzog, "Investigation of control strategies for hybrid energy storage systems in hybrid electric vehicles," in *Vehicle Power and Propulsion Conference, 2009. VPPC '09. IEEE*, 2009, pp. 1687-1693.
 - [85] W. Lei, L. Xiaohu, L. Hui, I. Won-Sang, and K. Jang-Mok, "Power electronics enabled energy management for energy storage with extended cycle life and improved fuel economy in a PHEV," in *Energy Conversion Congress and Exposition (ECCE), 2010 IEEE*, 2010, pp. 3917-3922.
 - [86] W. Lei, E. G. Collins, Jr., and L. Hui, "Optimal Design and Real-Time Control for Energy Management in Electric Vehicles," *Vehicular Technology, IEEE Transactions on*, vol. 60, pp. 1419-1429, 2011.
 - [87] E. Vinot and R. Trigui, "Optimal energy management of HEVs with hybrid storage system," *Energy Conversion and Management*, vol. 76, pp. 437-452, 12// 2013.
 - [88] S. M. Lukic, S. G. Wirasingha, F. Rodriguez, J. Cao, and A. Emadi, "Power Management of an Ultracapacitor/Battery Hybrid Energy Storage System in an HEV," in *Vehicle Power and Propulsion Conference, 2006. VPPC '06. IEEE*, 2006, pp. 1-6.
 - [89] A. Santucci, A. Sornioti, and C. Lekakou, "Power split strategies for hybrid energy storage systems for vehicular applications," *Journal of Power Sources*, vol. 258, pp. 395-407, 7/15/ 2014.

- [90] V. Larsson, L. Johannesson, and B. Egardt, "Analytic Solutions to the Dynamic Programming sub-problem in Hybrid Vehicle Energy Management," *Vehicular Technology, IEEE Transactions on*, vol. PP, pp. 1-1, 2014.
- [91] H. El Fadil, F. Giri, and J. Guerrero, "Lyapunov based control of hybrid energy storage system in electric vehicles," in *American Control Conference (ACC), 2012*, 2012, pp. 5005-5010.
- [92] H. El Fadil, F. Giri, J. Guerrero, and A. Tahri, "Modeling and Nonlinear Control of Fuel Cell / Supercapacitor Hybrid Energy Storage System for Electric Vehicles," *Vehicular Technology, IEEE Transactions on*, vol. PP, pp. 1-1, 2014.
- [93] X. Hu, L. Johannesson, N. Murgovski, and B. Egardt, "Longevity-conscious dimensioning and power management of the hybrid energy storage system in a fuel cell hybrid electric bus," *Applied Energy*.
- [94] J. M. Miller and G. Sartorelli, "Battery and ultracapacitor combinations — Where should the converter go?," in *Vehicle Power and Propulsion Conference (VPPC), 2010 IEEE*, 2010, pp. 1-7.
- [95] R. H. Staunton, C. W. Ayers, L. D. Marlino, J. N. Chiasson, and T. A. Burrell, "Evaluation of 2004 Toyota Prius Hybrid Electric Drive System," Oak Ridge National Labs, Oak Ridge, Tennessee, May 2006.
- [96] H. Al-Sheikh, O. Bennouna, G. Hoblos, and N. Moubayed, "Power electronics interface configurations for hybrid energy storage in hybrid electric vehicles," in *Mediterranean Electrotechnical Conference (MELECON), 2014 17th IEEE*, 2014, pp. 122-126.
- [97] R. M. Schupbach and J. C. Balda, "Comparing DC-DC converters for power management in hybrid electric vehicles," in *Electric Machines and Drives Conference, 2003. IEMDC'03. IEEE International*, 2003, pp. 1369-1374 vol.3.
- [98] Y. Ju-Seung, C. Jae-Yeon, Y. Min-Kwon, C. Hyoung-Sup, and C. Woo-Young, "High efficiency power conversion system for battery-ultracapacitor hybrid energy storages," in *Applied Power Electronics Conference and Exposition (APEC), 2013 Twenty-Eighth Annual IEEE*, 2013, pp. 2830-2835.
- [99] H. Di, J. Noppakunkajorn, and B. Sarlioglu, "Efficiency comparison of SiC and Si-based bidirectional DC-DC converters," in *Transportation Electrification Conference and Expo (ITEC), 2013 IEEE*, 2013, pp. 1-7.
- [100] D. Han, J. Noppakunkajorn, and B. Sarlioglu, "Comprehensive Efficiency, Weight, and Volume Comparison of SiC and Si-Based Bidirectional DC-DC

- Converters for Hybrid Electric Vehicles," *Vehicular Technology, IEEE Transactions on*, vol. PP, pp. 1-1, 2014.
- [101] S. Kumar and H. P. Ikkurti, "Design and control of novel power electronics interface for battery-ultracapacitor Hybrid Energy Storage System," in *Sustainable Energy and Intelligent Systems (SEISCON 2011), International Conference on*, 2011, pp. 236-241.
 - [102] L. Hui and L. Danwei, "Power Distribution Strategy of Fuel Cell Vehicle System with Hybrid Energy Storage Elements Using Triple Half Bridge (THB) Bidirectional DC-DC converter," in *Industry Applications Conference, 2007. 42nd IAS Annual Meeting. Conference Record of the 2007 IEEE*, 2007, pp. 636-642.
 - [103] R. Karimi, T. Koeneke, D. Kaczorowski, T. Werner, and A. Mertens, "Low voltage and high power DC-AC inverter topologies for electric vehicles," in *Energy Conversion Congress and Exposition (ECCE), 2013 IEEE*, 2013, pp. 2805-2812.
 - [104] H. Jung, H. Wang, and T. Hu, "Control design for robust tracking and smooth transition in power systems with battery/supercapacitor hybrid energy storage devices," *Journal of Power Sources*, vol. 267, pp. 566-575, 12/1/ 2014.
 - [105] J. Wang, P. Liu, J. Hicks-Garner, E. Sherman, S. Soukiazian, M. Verbrugge, *et al.*, "Cycle-life model for graphite-LiFePO₄ cells," *Journal of Power Sources*, vol. 196, pp. 3942-3948, 4/15/ 2011.
 - [106] M. Levine. (May 12, 2011). *Driven: Protean Ford F-150 All-Electric Pickup Truck*. Available: www.pickuptrucks.com
 - [107] Green Car Congress. (April 22, 2010). *Enova Expands Ze Electric Drive System to Ford F-150 and Chevrolet Express Cargo Van*. Available: <http://www.greencarcongress.com/2010/04/enova-20100422.html>
 - [108] Green Car Congress. (July 29, 2008). *HEVT Showcases Converted F-150 PHEV*. Available: <http://www.greencarcongress.com/2008/07/hevt-showcases.html>
 - [109] Green Car Congress. (March 12, 2010). *ALTe Reveals Converted Ford F-150 Range Extended Electric Vehicle Demonstrator at NTEA Show*. Available: <http://www.greencarcongress.com/2010/03/alte-f150-20100312.html>
 - [110] Green Car Congress. (May 6, 2011). *Quantum launches new line of converted plug-in hybrid F-150 pickup trucks for fleets*. Available: <http://www.greencarcongress.com/2011/05/qttw-20110506.html>

- [111] M. C. Algrain, W. H. Lane, and D. C. Orr, "A case study in the electrification of Class-8 trucks," in *Electric Machines and Drives Conference, 2003. IEMDC'03. IEEE International*, 2003, pp. 647-655 vol.2.
- [112] O. Tur, H. Ucarol, E. Ozsu, M. Demirci, Y. Solak, E. Elcik, *et al.*, "Sizing, Design and Prototyping of an Electric Drive System for a Split Drive Hybrid Electric Vehicle," in *Electric Machines & Drives Conference, 2007. IEMDC '07. IEEE International*, 2007, pp. 1745-1750.
- [113] H. Yoo, S. Seung-Ki, P. Yongho, and J. Jongchan, "System Integration and Power-Flow Management for a Series Hybrid Electric Vehicle Using Supercapacitors and Batteries," *Industry Applications, IEEE Transactions on*, vol. 44, pp. 108-114, 2008.
- [114] P. Mulhall, M. Naviwala, S. M. Lukic, J. Braband, and A. Emadi, "Entrepreneurial Projects Program at Illinois Institute of Technology: Solar/Battery Hybrid Three-Wheel Auto Rickshaw for India," in *Vehicle Power and Propulsion Conference, 2007. VPPC 2007. IEEE*, 2007, pp. 682-689.
- [115] J. P. Trovao, P. G. Pereirinha, and H. M. Jorge, "Simulation model and road tests comparative results of a small urban electric vehicle," in *Industrial Electronics, 2009. IECON '09. 35th Annual Conference of IEEE*, 2009, pp. 836-841.
- [116] P. J. Kollmeyer, L. W. Juang, and T. M. Jahns, "Development of an electromechanical model for a Corbin Sparrow electric vehicle," in *Vehicle Power and Propulsion Conference (VPPC), 2011 IEEE*, 2011, pp. 1-8.
- [117] P. J. Kollmeyer, L. W. Juang, and T. M. Jahns, "Evaluation of an electromechanical model for a Corbin Sparrow electric vehicle," in *Vehicle Power and Propulsion Conference (VPPC), 2011 IEEE*, 2011, pp. 1-6.
- [118] P. Mantravadi, I. Husain, and Y. Sozer, "Modeling, implementation and analysis of a Li-ion battery powered electric truck," in *Energy Conversion Congress and Exposition (ECCE), 2011 IEEE*, 2011, pp. 1428-1435.
- [119] Ford Motor Company. 2002 Ford F150 Specifications. Available: <http://www.fordf150.net/specs/02f150.php>
- [120] A. Harwood, "First Test: 2011 Ford F-150 Full Line," in *Motor Trend Magazine*, Oct. 2011.
- [121] Integrated Electric Drives Incorporated, "Heavy Duty EV3 Series 2 Speed Transmission Datasheet," 2011.
- [122] US DOE. *Fuel Economy Testing*. Available: www.fueleconomy.gov
- [123] EValbum. *Log of EV projects (see projects for Thunder Sky and Sky Energy (former CALB name))*. Available: <http://www.evalbum.com/battb>

- [124] U.S. Environmental Protection Agency. *Annual Certification Test Results & Data*. Available: <http://www.epa.gov/otaq/crttst.htm>
- [125] P. J. Kollmeyer, W. Lamb, L. W. Juang, J. D. McFarlan, T. M. Jahns, and B. Sarlioglu, "Design of an electric powertrain for a Ford F150 crew cab truck utilizing a lithium battery pack and an interior PM synchronous machine drive," in *Transportation Electrification Conference and Expo (ITEC), 2012 IEEE*, 2012, pp. 1-8.
- [126] J. M. Miller, "Electric Motor R&D Presentation, Oak Ridge National Laboratory," ed, 2013.
- [127] J. M. Miller, "Energy storage technology markets and application's: ultracapacitors in combination with lithium-ion," in *Power Electronics, 2007. ICPE '07. 7th International Conference on*, 2007, pp. 16-22.
- [128] D. Rotenberg, A. Vahidi, and I. Kolmanovsky, "Ultracapacitor assisted powertrains: Modeling, control, sizing, and the impact on fuel economy," in *American Control Conference, 2008*, 2008, pp. 981-987.
- [129] China Aviation Lithium Battery Co. Ltd. (2014). *SE100AHA LiFePO₄ Battery Datasheet*. Available: <http://en.calb.cn>
- [130] Maxwell Technologies Inc. *K2 Series High Capacity Ultracapacitor Datasheet*. Available: http://www.maxwell.com/products/ultracapacitors/docs/k2series_ds_1015370-4.pdf
- [131] O. Sundstrom and L. Guzzella, "A generic dynamic programming Matlab function," in *Control Applications, (CCA) & Intelligent Control, (ISIC), 2009 IEEE*, 2009, pp. 1625-1630.
- [132] O. Sundstrom and L. Guzzella. (2009), DPM-function. *Institute for Dynamic Systems, Department of Mechanical and Process Engineering, ETH Zurich*. Available: <http://www.idsc.ethz.ch/Downloads/DownloadFiles/dpm/index>
- [133] Digatron Firing Circuits. *Universal Battery Tester Specifications*. Available: <http://www.digatron.com/en/automotive-battery/universal-battery-tester/>
- [134] W. Waag, C. Fleischer, and D. U. Sauer, "On-line estimation of lithium-ion battery impedance parameters using a novel varied-parameters approach," *Journal of Power Sources*, vol. 237, pp. 260-269, 9/1/ 2013.
- [135] M. Allen. (2013). *Electric Range for the Nissan Leaf and Chevrolet Volt in Cold Weather*. Available: <http://www.fleetcarma.com/nissan-leaf-chevrolet-volt-cold-weather-range-loss-electric-vehicle/>
- [136] Skeleton Technologies. *SkelCap High Energy Series Ultracapacitor Datasheet*. Available: cdn2.hubspot.net/hubfs/1188159/SK_2015/Resources/skelcap-energy-en.pdf

- [137] New Flyer. *Excelsior Electric Bus Specifications*. Available:
<http://www.newflyer.com/index/electricbus>
- [138] Complete Coach Works. *ZEPS Electric Bus Specification*. Available:
<http://completecoach.com/electric-bus/>
- [139] Cummins Inc. *ISL Series Diesel Engine Specifications*. Available:
<http://cumminsengines.com/uploads/docs/4103683.pdf>
- [140] K. Holmberg, P. Andersson, N.-O. Nylund, K. Mäkelä, and A. Erdemir,
"Global energy consumption due to friction in trucks and buses," *Tribology International*, vol. 78, pp. 94-114, 10// 2014.

Appendix I – Modeling of Electric Truck Rotating Inertial Components (by Scott Tovsen)

UNIVERSITY OF WISCONSIN - MADISON

ECE-399
1-Credit

FALL 2012

**Inertial Modeling of
Fully Electric Ford F-150**

Submitted by:

Scott Tovsen

Advisor:
Professor Thomas Jahns

DECEMBER 22, 2012

TABLE OF CONTENTS

Executive Summary	3
Background	3
Methods	3
Modeling	3
Inertia Results	4
Derivation of Equivalent Mass	5
Equivalent Mass Results	7
Conclusion	8
References	9
Appendix 1. SolidWorks Screen Shots of Mass/Inertia Values	10

Executive Summary

This paper describes the inertial modeling of the fully electric drivetrain for the Ford F-150 developed at the University of Wisconsin - Madison. The inertia for each rotating piece was found through the manufacturer's specifications or through computer aided simulation. Once each component's inertia was determined, it was converted from its rotational inertia to an equivalent linear mass. All equivalent masses were summed to determine the following total equivalent mass for each gear ratio.

$$m_{eq,total,1st\ gear} = 392.7\ kg \quad m_{eq,total,2nd\ gear} = 81.75\ kg$$

These values highlight that the rotating components add observed linear mass to the vehicle. This is a critical step to properly understand the energy and power balance for the modeling of the electric vehicle.

Background

In order to accurately model the fully electric Ford F-150, the inertia of the drivetrain must be understood. Not only must the electric motor accelerate the mass in the linear direction, but also accelerate the inertia of each spinning component in the drivetrain. This added analysis provides a more clearly understood model of the energy and power flow from the energy source through the vehicle.

Methods

Modeling

If the manufacturer did not provide an inertia measurement, each part was modeled in the computer aided design program, SolidWorks. This process consisted of measuring the dimensions of, weighing, and modeling the part. SolidWorks combines the geometry of the part with a set of material properties to calculate the mass and inertia. An example of this is shown below in Figure 1. The parts' actual weight was compared to the modeled weight to ensure the accuracy of the simulated inertia. As these parts were hand measured and weighed, there is a dimensional tolerance of ± 0.05 inches.

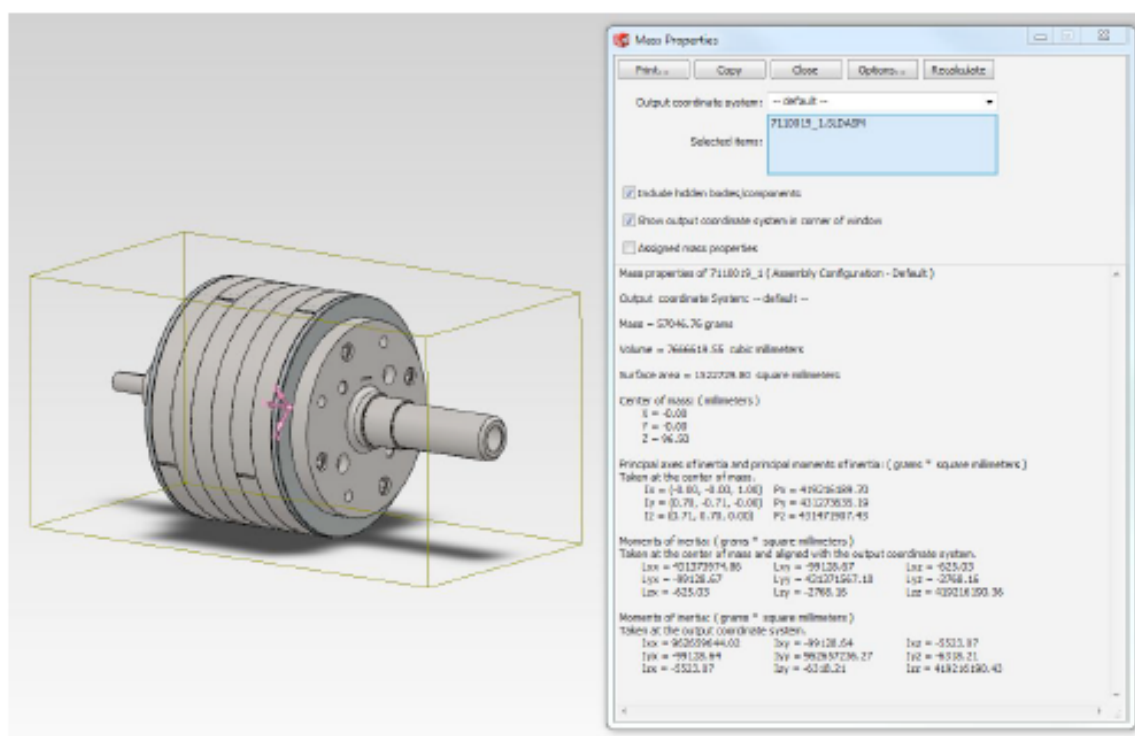


Figure 1. Screen shot of SolidWorks simulation used to determine part inertia*.

*The other SolidWorks screenshots can be found in Appendix 1.

Inertia Results

Part	Mass [kg]	Inertia [kg-m ²]	Source
Tire and Rim	30.21	1.219	SolidWorks Simulation
Front Disc	7.2	0.0846	SolidWorks Simulation
Rear Disc	9.84	0.139	SolidWorks Simulation
Drive Shaft	14.03	0.0291	SolidWorks Simulation
Torque Sensor	2	0.0003519	Manufacturer Provided Data
Rear Axle	22.69	0.0393	SolidWorks Simulation
Differential - Input	5	0.00345	SolidWorks Simulation
Differential - Output	5	0.00816	SolidWorks Simulation
Gear Box - Input	4.54	0.00576	Manufacturer Provided Data
Gear Box - Output	6.8	0.00621	Manufacturer Provided Data
Motor Rotor	57.04	0.4192	Manufacturer Provided Model / SolidWorks Simulation

Figure 2. Measured mass, inertia, and source of values

Derivation of Equivalent Mass

Newton's law of acceleration acts upon the linearly accelerating vehicle mass as well as the rotationally accelerating drivetrain inertias. The rotating inertias can be reflected in an equivalent mass to add to the total linear load of the vehicle. The force to accelerate a mass is the mass multiplied by the acceleration, given by

$$F = m a \quad (1)$$

The torque to accelerate the rotational inertia is the inertia of the part multiplied by the acceleration of the part, given by

$$T_{part} = J_{part} a_{part} \quad (2)$$

Converting from the rotational reference frame to the linear reference frame can be understood with Figure 3.

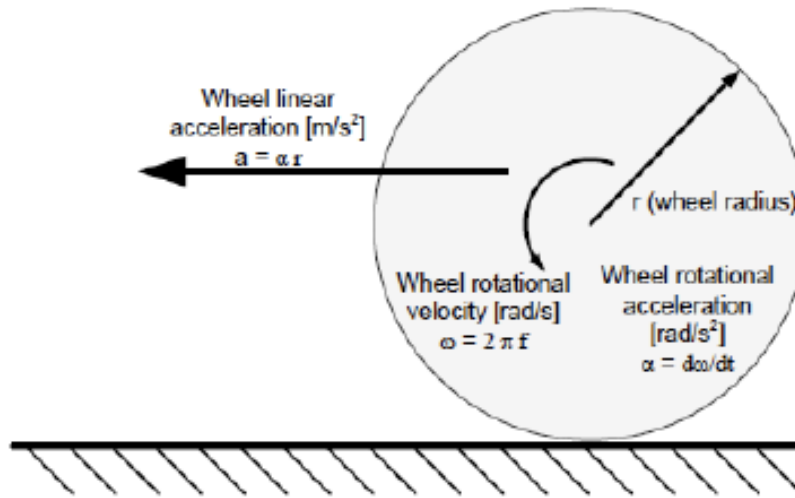


Figure 3. Converting linear reference frame to rotational reference frame [1].

Using the relation described in figure XX, the wheel rotational acceleration is given as a function of vehicle acceleration by

$$a_{wh} = \frac{a_{veh}}{r_{wh}} \quad (3)$$

Stepping through the various gear changes in the drivetrain results in changing rotational velocities and accelerations. For example, the rotational acceleration of the driveshaft is related to the rotational acceleration of the axle by

$$\begin{aligned} a_{axle} &= a_{driveshaft} * AxleRatio \\ AxleRatio &= 3.55 : 1 \end{aligned} \quad (4)$$

Equivalently, the rotational acceleration of the motor is related to the rotational acceleration of the driveshaft by

$$\begin{aligned} a_{motor} &= a_{driveshaft} * GearRatio \\ GearRatio &= 1 - or - 3 \end{aligned} \quad (5)$$

The power to accelerate mass and a single wheel is expressed as a function of a_{veh} and v_{veh} using the relation given in equation (3) below.

$$\begin{aligned} P_{mass,acc} &= F_{mass,acc} v_{veh} = m_{veh} a_{veh} v_{veh} \\ P_{wh,acc} &= T_{wh,acc} * \omega_{wh} = J_{wh} * a_{wh} * \omega_{wh} \end{aligned} \quad (6)$$

$$P_{wh,acc} = J_{wh} \frac{a_{veh}}{r_{wh}} \frac{v_{veh}}{r_{wh}} \quad (7)$$

By cancelling a_{veh} and v_{veh} , an equation for equivalent mass is described by

$$\begin{aligned} P_{wh,acc} &= \frac{J_{wh}}{r_{wh}^2} a_{veh} v_{veh} = m_{fwh-eq} a_{veh} v_{veh} \\ m_{fwh-eq} &= \frac{J_{wh}}{r_{wh}^2} \end{aligned} \quad (8)$$

The equivalent mass calculations for the components at the rotational speed of the driveshaft and motor are detailed by

$$m_{Jeq-drivetrain-speed} = J_{part} \left(\frac{AxleRatio}{r_{wh}} \right)^2$$

$$m_{Jeq-motor-speed} = J_{part} \left(\frac{AxleRatio * GearRatio}{r_{wh}} \right)^2$$

(9)

The total equivalent mass can be calculated by added each of the equivalent masses together.

$$m_{veh,eq} = 4 \cdot m_{eq,1} + 2 \cdot m_{eq,2} + 2 \cdot m_{eq,3} + m_{eq,4} + m_{eq,5} + m_{eq,6} + m_{eq,7} + m_{eq,8} + m_{eq,9} + m_{eq,10} + m_{eq,11}$$

(10)

Equivalent Mass Results

Part	Equivalent Mass [kg]	
	1st Gear	2nd Gear
Tire and Rim	8.84	8.84
Front Disc	0.6135	0.6135
Rear Disc	1.008	1.008
Drive Shaft	2.659	2.659
Torque Sensor	0.2894	0.03216
Rear Axle	0.285	0.285
Differential - Input	0.02502	0.02502
Differentia - Output	0.7457	0.7457
Gear Box - Input	4.738	0.5264
Gear Box - Output	0.5675	0.5675
Motor Rotor	344.8	38.31
Total	392.7	81.75

Figure X. Equivalent mass results (1st gear = 3:1, 2nd gear = 1:1)*.

*EES code used to generate the results are attached.

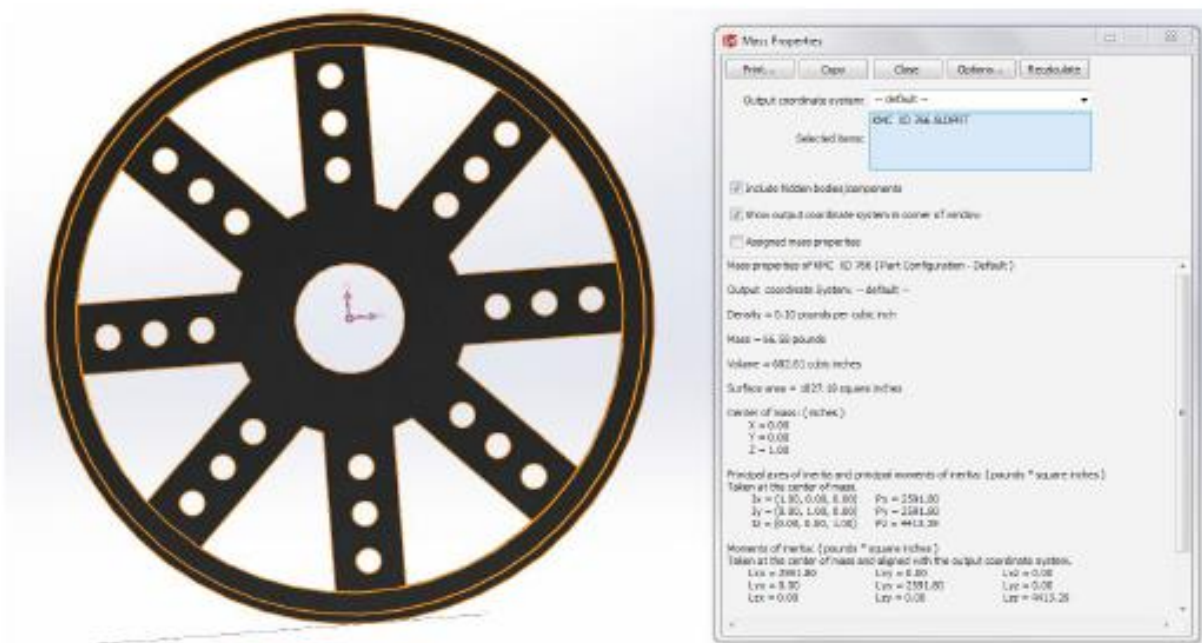
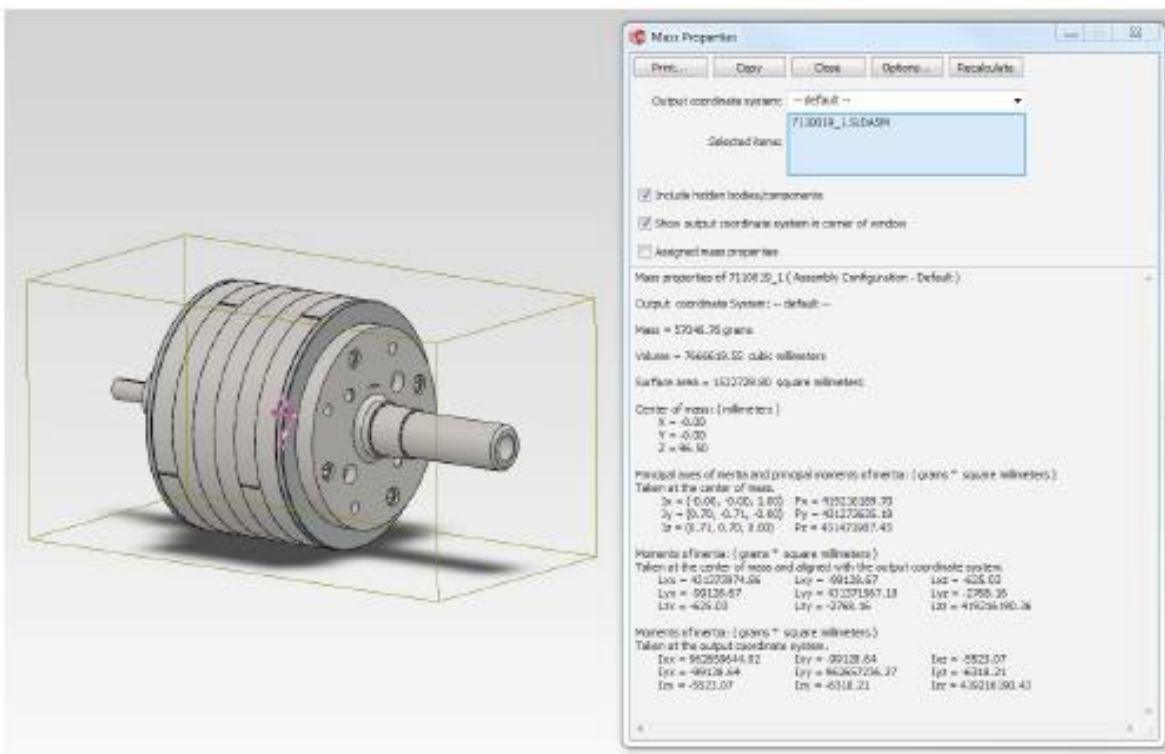
Conclusion

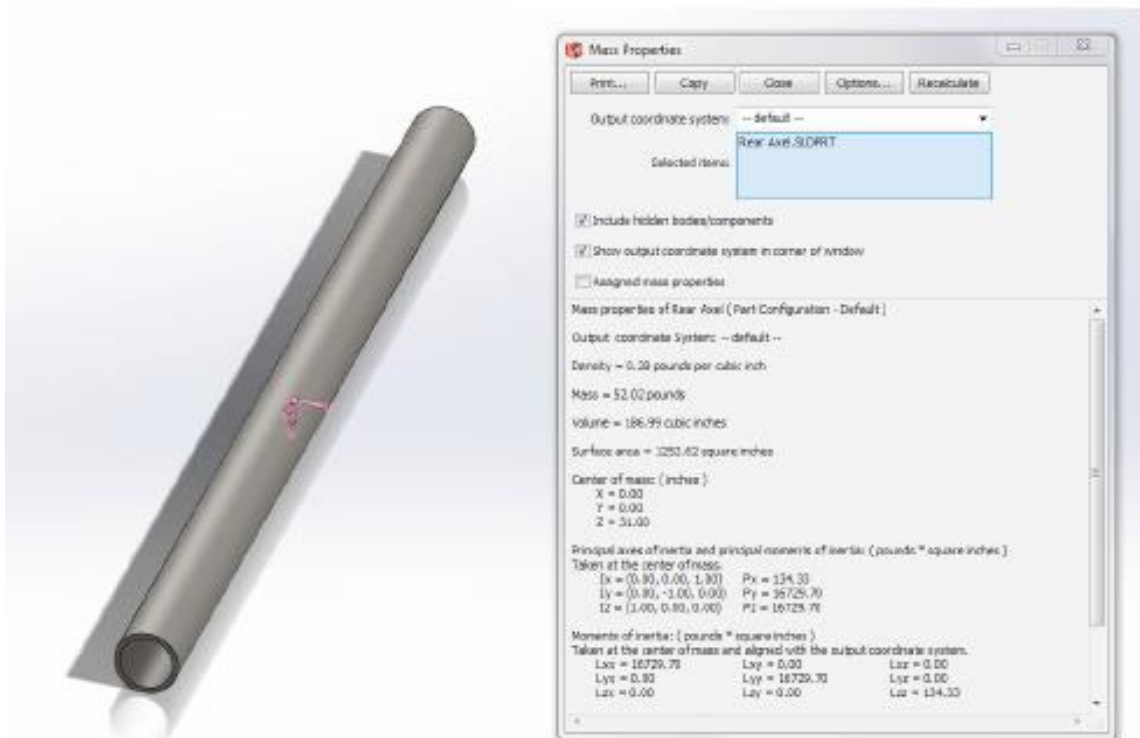
With the Ford F-150 weighing in at 5400 lbs (2449 kg), the equivalent mass of the inertia provides an additional 392.7 kg in 1st gear and 81.75 kg in 2nd gear. The total drivetrain inertia for 1st gear is 4.8 times the inertia of 2nd gear. Assuming an 80 kg driver, the drivetrain inertia accounts for 13.4% (1st) and 3.1% (2nd) of the total equivalent mass of the accelerating vehicle. The relatively high inertia values for first gear are caused by the two-part gear reduction of 3.55:1 in the differential and 3:1 in the gearbox – causing the rotational velocity of the rotor to spin at 10.65 times the speed of the wheels.

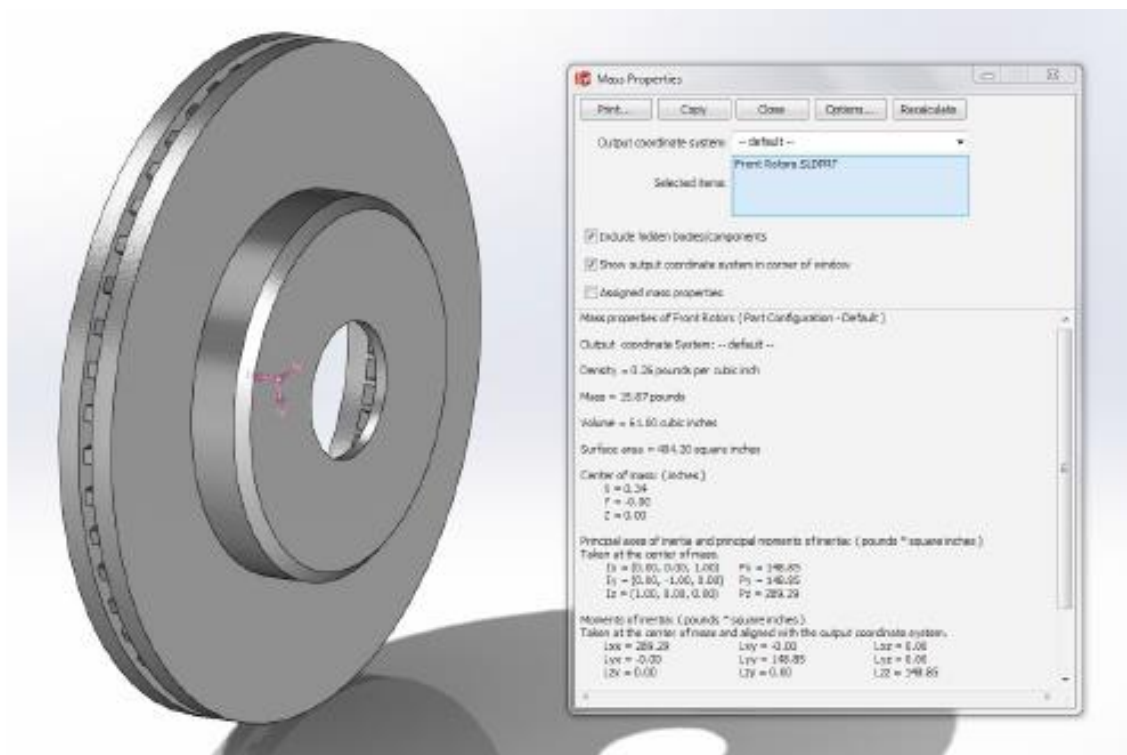
References

- [1] Kollmeyer, Phillip J. (2011) Electromechanical modeling and analysis of a Corbin Sparrow electric vehicle using on the road data. University of Wisconsin – Madison.

Appendix 1. SolidWorks Screen Shots of Mass/Inertia Values







Appendix II - Motor control operating tables for electric machine

Positive Torque I_d Programming Points for Drive

Torque(Nm)	0	20	40	60	80	100	120	140	160	180	200	220	240	260	280	300	320	340	360	390	420	450
Speed	I_d (rms)	I_d (rms)	I_d (rms)	I_d (rms)	I_d (rms)	I_d (rms)	I_d (rms)	I_d (rms)	I_d (rms)	I_d (rms)	I_d (rms)	I_d (rms)	I_d (rms)	I_d (rms)	I_d (rms)	I_d (rms)	I_d (rms)	I_d (rms)	I_d (rms)	I_d (rms)	I_d (rms)	I_d (rms)
100	0.0	-1.2	-4.6	-9.8	-16.1	-23.7	-31.4	-41.0	-52.0	-60.7	-72.7	-85.9	-98.7	-108.2	-124.5	-143.1	-155.2	-167.2	-188.2	-219.1	-237.8	-269.9
2500	0.0	-1.2	-4.6	-9.8	-16.1	-23.7	-31.4	-41.0	-52.0	-60.7	-72.7	-85.9	-98.7	-108.2	-124.5	-143.1	-155.2	-167.2	-188.2	-219.1	-237.8	-269.9
2750	0.0	-1.2	-4.6	-9.8	-16.1	-23.7	-31.4	-41.0	-52.0	-60.7	-72.7	-85.9	-98.7	-108.2	-124.5	-143.1	-161.8	-185.9	-211.0	-251.7	-296.5	
3000	0.0	-1.2	-4.6	-9.8	-16.1	-23.7	-31.4	-41.0	-52.0	-60.7	-77.7	-97.3	-118.0	-139.3	-161.8	-185.2	-210.1	-236.3	-264.5	-311.6		
3250	0.0	-1.2	-4.6	-9.8	-16.1	-23.7	-35.2	-53.3	-72.0	-91.3	-111.0	-131.7	-153.3	-175.9	-199.9	-225.5	-252.7	-282.7	-315.5	-375.6		
3500	0.0	-1.2	-4.6	-12.9	-27.3	-43.5	-61.0	-79.4	-98.6	-118.6	-139.4	-161.2	-184.2	-208.4	-234.7	-262.7	-294.0	-329.4	-372.5			
3750	-15.3	-17.9	-25.2	-36.2	-50.1	-66.1	-83.5	-102.2	-122.0	-142.8	-164.5	-187.6	-212.2	-238.5	-267.5	-299.5	-337.1	-385.1				
4000	-37.1	-39.5	-46.3	-56.9	-70.4	-86.2	-103.7	-122.7	-143.0	-164.6	-187.4	-211.8	-238.4	-267.2	-300.0	-338.8	-391.0					
4250	-56.3	-58.6	-65.1	-75.4	-88.7	-104.3	-122.0	-141.3	-162.1	-184.5	-208.6	-234.6	-263.4	-296.2	-334.8	-389.0						
4500	-73.4	-75.6	-82.0	-92.0	-105.1	-120.8	-138.6	-158.3	-179.7	-203.0	-228.5	-256.7	-288.4	-326.3	-378.3							
4750	-88.7	-90.9	-97.0	-107.0	-120.0	-135.8	-153.8	-173.9	-196.1	-220.5	-247.6	-278.1	-314.3	-362.1								
5000	-102.5	-104.6	-110.8	-120.6	-133.6	-149.5	-167.9	-188.5	-211.5	-237.2	-266.1	-300.1	-343.1									
5250	-114.9	-117.1	-123.1	-132.9	-146.1	-162.1	-180.9	-202.1	-226.0	-253.1	-284.6	-323.2	-381.6									
5500	-126.3	-128.5	-134.5	-144.4	-157.6	-173.9	-192.9	-214.8	-239.8	-268.8	-303.3	-349.6										
5750	-136.6	-138.8	-145.0	-154.8	-168.1	-184.7	-204.3	-227.0	-253.2	-284.2	-323.2	-388.4										
6000	-146.1	-148.3	-154.5	-164.4	-178.0	-194.8	-214.9	-238.5	-266.1	-299.8	-345.9											
6250	-154.9	-157.1	-163.3	-173.2	-187.1	-204.2	-225.0	-249.5	-278.8	-316.0	-376.1											
6500	-163.0	-165.1	-171.4	-181.6	-195.6	-213.2	-234.4	-260.0	-291.4	-333.6												
6750	-170.5	-172.6	-178.9	-189.4	-203.6	-221.6	-243.6	-270.3	-304.2	-354.4												
7000	-177.4	-179.6	-186.0	-196.6	-211.0	-229.5	-252.3	-280.5	-317.5	-389.9												

Positive Torque I_q Programming Points for Drive

Torque(Nm)	0	20	40	60	80	100	120	140	160	180	200	220	240	260	280	300	320	340	360	390	420	450
Speed	I _q (rms)	I _q (rms)	I _q (rms)	I _q (rms)	I _q (rms)	I _q (rms)	I _q (rms)	I _q (rms)	I _q (rms)	I _q (rms)	I _q (rms)	I _q (rms)	I _q (rms)	I _q (rms)	I _q (rms)	I _q (rms)	I _q (rms)	I _q (rms)	I _q (rms)	I _q (rms)	I _q (rms)	I _q (rms)
100	0.0	21.3	42.2	62.2	81.4	99.6	117.2	134.0	150.0	166.6	182.1	196.9	211.7	228.2	241.5	253.3	268.8	285.1	296.2	313.0	339.6	358.9
2500	0.0	21.3	42.2	62.2	81.4	99.6	117.2	134.0	150.0	166.6	182.1	196.9	211.7	228.2	241.5	253.3	268.8	285.1	296.2	313.0	339.6	358.9
2750	0.0	21.3	42.2	62.2	81.4	99.6	117.2	134.0	150.0	166.6	182.1	196.9	211.7	228.2	241.5	253.3	265.3	274.1	282.6	293.5	302.9	
3000	0.0	21.3	42.2	62.2	81.4	99.6	117.2	134.0	150.0	166.6	180.1	192.2	203.3	214.2	224.0	233.4	241.9	249.9	256.8	265.8		
3250	0.0	21.3	42.2	62.2	81.4	99.6	116.2	130.3	143.6	156.1	168.1	179.5	190.2	200.2	209.5	218.0	226.0	232.6	238.9	245.2		
3500	0.0	21.3	42.2	61.7	79.2	95.2	109.9	123.6	136.3	148.3	159.6	170.4	180.4	190.0	198.4	206.5	213.3	219.2	223.1			
3750	0.0	20.4	40.1	58.5	75.4	90.9	105.2	118.5	130.8	142.3	153.3	163.5	173.0	182.0	189.7	197.1	202.7	206.7				
4000	0.0	19.5	38.3	56.0	72.4	87.6	101.6	114.5	126.6	137.7	148.3	158.2	166.9	175.5	182.8	188.7	192.5					
4250	0.0	18.7	36.8	54.0	70.0	84.9	98.6	111.3	123.1	134.1	144.2	153.7	162.3	169.7	176.5	180.0						
4500	0.0	18.1	35.7	52.4	68.1	82.7	96.2	108.7	120.2	131.0	140.9	149.8	158.0	165.0	169.6							
4750	0.0	17.6	34.8	51.1	66.5	80.8	94.1	106.4	117.8	128.2	137.8	146.6	154.1	159.8								
5000	0.0	17.2	34.0	50.0	65.1	79.3	92.4	104.5	115.6	125.9	135.3	143.4	150.2									
5250	0.0	16.9	33.3	49.1	64.0	77.9	90.8	102.8	113.8	123.8	132.7	140.5	145.6									
5500	0.0	16.6	32.8	48.3	63.0	76.7	89.5	101.3	112.1	121.8	130.4	137.4										
5750	0.0	16.3	32.3	47.6	62.1	75.6	88.2	99.9	110.5	120.0	128.2	133.2										
6000	0.0	16.1	31.8	47.0	61.3	74.7	87.2	98.6	109.0	118.3	125.7											
6250	0.0	15.9	31.4	46.4	60.6	73.9	86.2	97.5	107.7	116.6	122.6											
6500	0.0	15.7	31.1	45.9	59.9	73.1	85.3	96.4	106.4	114.8												
6750	0.0	15.6	30.8	45.5	59.4	72.4	84.4	95.4	105.1	112.8												
7000	0.0	15.4	30.5	45.0	58.8	71.7	83.7	94.5	103.9	109.6												

Positive Torque Gamma Angle

Torque(Nm)	0	20	40	60	80	100	120	140	160	180	200	220	240	260	280	300	320	340	360	390	420	450
Speed	Gamma	Gamma	Gamma	Gamma	Gamma	Gamma	Gamma	Gamma	Gamma	Gamma	Gamma	Gamma	Gamma	Gamma	Gamma	Gamma	Gamma	Gamma	Gamma	Gamma	Gamma	Gamma
100	90.0	3.2	6.2	9.0	11.2	13.4	15.0	17.0	19.1	20.0	21.8	23.6	25.0	25.4	27.3	29.5	30.0	30.4	32.4	35.0	35.0	37.0
2500	90.0	3.2	6.2	9.0	11.2	13.4	15.0	17.0	19.1	20.0	21.8	23.6	25.0	25.4	27.3	29.5	30.0	30.4	32.4	35.0	35.0	37.0
2750	90.0	3.2	6.2	9.0	11.2	13.4	15.0	17.0	19.1	20.0	21.8	23.6	25.0	25.4	27.3	29.5	31.4	34.1	36.7	40.6	44.4	
3000	90.0	3.2	6.2	9.0	11.2	13.4	15.0	17.0	19.1	20.0	23.3	26.9	30.1	33.0	35.8	38.4	41.0	43.4	45.8	49.5		
3250	90.0	3.2	6.2	9.0	11.2	13.4	16.9	22.2	26.6	30.3	33.4	36.3	38.9	41.3	43.7	46.0	48.2	50.5	52.9	56.9		
3500	89.9	3.2	6.2	11.8	19.0	24.5	29.0	32.7	35.9	38.7	41.1	43.4	45.6	47.7	49.8	51.8	54.0	56.4	59.1			
3750	90.0	41.2	32.1	31.8	33.6	36.0	38.4	40.8	43.0	45.1	47.0	48.9	50.8	52.6	54.7	56.7	59.0	61.8				
4000	90.0	63.8	50.4	45.5	44.2	44.6	45.6	47.0	48.5	50.1	51.6	53.3	55.0	56.7	58.6	60.9	63.8					
4250	90.0	72.3	60.5	54.4	51.7	50.9	51.0	51.8	52.8	54.0	55.4	56.8	58.4	60.2	62.2	65.2						
4500	90.0	76.5	66.5	60.3	57.1	55.6	55.2	55.5	56.2	57.2	58.3	59.7	61.3	63.2	65.9							
4750	90.0	79.0	70.3	64.5	61.0	59.2	58.5	58.5	59.0	59.8	60.9	62.2	63.9	66.2								
5000	90.0	80.7	72.9	67.5	64.0	62.1	61.2	61.0	61.3	62.0	63.1	64.5	66.4									
5250	90.0	81.8	74.9	69.7	66.4	64.3	63.3	63.0	63.3	63.9	65.0	66.5	69.1									
5500	90.0	82.7	76.3	71.5	68.2	66.2	65.1	64.8	65.0	65.6	66.7	68.6										
5750	90.0	83.3	77.5	72.9	69.7	67.7	66.6	66.2	66.4	67.1	68.4	71.1										
6000	90.0	83.8	78.4	74.1	71.0	69.0	67.9	67.5	67.7	68.5	70.0											
6250	90.0	84.2	79.1	75.0	72.1	70.1	69.0	68.7	68.9	69.8	71.9											
6500	90.0	84.6	79.7	75.8	73.0	71.1	70.0	69.6	69.9	71.0												
6750	90.0	84.8	80.2	76.5	73.7	71.9	70.9	70.6	70.9	72.3												
7000	90.0	85.1	80.7	77.1	74.4	72.6	71.7	71.4	71.9	74.3												

Positive Torque Stator Current

Torque(Nm)	0	20	40	60	80	100	120	140	160	180	200	220	240	260	280	300	320	340	360	390	420	450
Speed	<i>Is</i> (rms)	<i>Is</i> (rms)	<i>Is</i> (rms)	<i>Is</i> (rms)	<i>Is</i> (rms)	<i>Is</i> (rms)	<i>Is</i> (rms)	<i>Is</i> (rms)	<i>Is</i> (rms)	<i>Is</i> (rms)	<i>Is</i> (rms)	<i>Is</i> (rms)	<i>Is</i> (rms)	<i>Is</i> (rms)	<i>Is</i> (rms)	<i>Is</i> (rms)	<i>Is</i> (rms)	<i>Is</i> (rms)	<i>Is</i> (rms)	<i>Is</i> (rms)	<i>Is</i> (rms)	<i>Is</i> (rms)
100	0.0	21.4	42.4	63.0	83.0	102.4	121.4	140.1	158.7	177.3	196.1	214.8	233.6	252.5	271.7	291.0	310.4	330.5	350.9	382.1	414.6	449.1
2500	0.0	21.4	42.4	63.0	83.0	102.4	121.4	140.1	158.7	177.3	196.1	214.8	233.6	252.5	271.7	291.0	310.4	330.5	350.9	382.1	414.6	449.1
2750	0.0	21.4	42.4	63.0	83.0	102.4	121.4	140.1	158.7	177.3	196.1	214.8	233.6	252.5	271.7	291.0	310.7	331.2	352.7	386.6	423.9	
3000	0.0	21.4	42.4	63.0	83.0	102.4	121.4	140.1	158.7	177.3	196.2	215.4	235.1	255.4	276.3	297.9	320.4	343.9	368.7	409.5		
3250	0.0	21.4	42.4	63.0	83.0	102.4	121.4	140.8	160.6	180.8	201.5	222.6	244.2	266.5	289.6	313.6	339.0	366.1	395.7	448.6		
3500	0.0	21.4	42.4	63.1	83.8	104.7	125.7	146.8	168.2	189.9	211.9	234.6	257.8	282.0	307.3	334.2	363.2	395.7	434.2			
3750	15.3	27.2	47.3	68.8	90.5	112.4	134.4	156.5	178.9	201.6	224.9	248.9	273.8	300.0	327.9	358.5	393.4	437.1				
4000	37.1	44.0	60.1	79.8	101.0	122.9	145.2	167.8	190.9	214.6	239.0	264.4	291.1	319.7	351.3	387.8	435.8					
4250	56.3	61.5	74.8	92.7	113.0	134.5	156.9	179.9	203.6	228.1	253.6	280.5	309.4	341.3	378.5	428.6						
4500	73.4	77.8	89.4	105.9	125.3	146.4	168.7	192.0	216.2	241.6	268.4	297.2	328.9	365.7	414.5							
4750	88.7	92.5	103.1	118.5	137.2	158.0	180.3	203.9	228.8	255.1	283.4	314.4	350.1	395.8								
5000	102.5	106.0	115.9	130.6	148.7	169.2	191.6	215.5	241.1	268.5	298.5	332.6	374.5									
5250	114.9	118.3	127.5	141.7	159.5	179.9	202.4	226.7	253.1	281.8	314.1	352.4	408.4									
5500	126.3	129.5	138.5	152.2	169.7	190.0	212.6	237.5	264.7	295.1	330.2	375.7										
5750	136.6	139.8	148.5	162.0	179.2	199.6	222.5	248.0	276.3	308.5	347.7	410.5										
6000	146.1	149.2	157.7	171.0	188.2	208.6	231.9	258.1	287.6	322.3	368.0											
6250	154.9	157.9	166.3	179.4	196.7	217.2	240.9	267.8	298.9	336.8	395.6											
6500	163.0	165.9	174.2	187.3	204.6	225.4	249.4	277.3	310.2	352.8												
6750	170.5	173.3	181.6	194.8	212.0	233.1	257.8	286.7	321.9	371.9												
7000	177.4	180.2	188.5	201.7	219.0	240.5	265.8	296.0	334.0	405.0												

Negative Torque I_d Programming Points for Drive

Torque(Nm)	-20	-40	-60	-80	-100	-120	-140	-160	-180	-200	-220	-240	-260	-280	-300	-320	-340	-360	-390	-420	-450
Speed	I _d (rms)	I _d (rms)	I _d (rms)	I _d (rms)	I _d (rms)	I _d (rms)	I _d (rms)	I _d (rms)	I _d (rms)	I _d (rms)	I _d (rms)	I _d (rms)	I _d (rms)	I _d (rms)	I _d (rms)	I _d (rms)	I _d (rms)	I _d (rms)	I _d (rms)	I _d (rms)	I _d (rms)
100	-1.2	-4.6	-9.8	-16.1	-23.8	-31.5	-40.9	-52.0	-60.7	-72.6	-85.6	-98.6	-107.5	-123.5	-141.8	-154.7	-165.3	-186.2	-218.1	-236.5	-267.6
2500	-1.2	-4.6	-9.8	-16.1	-23.8	-31.5	-40.9	-52.0	-60.7	-72.6	-85.6	-98.6	-107.5	-123.5	-141.8	-154.7	-165.3	-186.2	-218.1	-236.5	-268.4
2750	-1.2	-4.6	-9.8	-16.1	-23.8	-31.4	-40.9	-52.0	-60.7	-72.6	-85.6	-98.6	-107.5	-123.5	-141.8	-162.8	-187.0	-212.0	-252.5	-297.4	
3000	-1.2	-4.6	-9.8	-16.1	-23.8	-31.5	-40.9	-52.0	-60.7	-78.2	-97.8	-118.5	-139.8	-162.3	-185.8	-210.6	-236.8	-265.0	-312.0		
3250	-1.2	-4.6	-9.8	-16.1	-23.8	-35.4	-53.5	-72.2	-91.6	-111.4	-132.0	-153.6	-176.3	-200.3	-225.8	-253.1	-282.9	-315.7	-375.7		
3500	-1.2	-4.6	-13.0	-27.4	-43.6	-61.1	-79.5	-98.8	-118.8	-139.7	-161.4	-184.5	-208.7	-234.9	-262.9	-294.2	-329.6	-372.6			
3750	-17.9	-25.2	-36.3	-50.2	-66.1	-83.6	-102.4	-122.1	-142.9	-164.7	-187.8	-212.4	-238.6	-267.7	-299.6	-337.2	-385.2				
4000	-39.5	-46.3	-56.9	-70.5	-86.3	-103.8	-122.8	-143.1	-164.7	-187.5	-211.9	-238.6	-267.4	-300.1	-338.9	-391.1					
4250	-58.6	-65.1	-75.4	-88.7	-104.4	-122.0	-141.3	-162.2	-184.6	-208.7	-234.7	-263.5	-296.2	-334.9	-389.0						
4500	-75.6	-82.0	-92.0	-105.2	-120.8	-138.6	-158.3	-179.8	-203.1	-228.5	-256.7	-288.5	-326.4	-378.3							
4750	-90.9	-97.1	-107.0	-120.1	-135.8	-153.9	-174.0	-196.2	-220.6	-247.7	-278.2	-314.4	-362.1								
5000	-104.6	-110.8	-120.6	-133.7	-149.6	-167.9	-188.5	-211.5	-237.2	-266.2	-300.1	-343.1									
5250	-117.1	-123.1	-133.0	-146.2	-162.2	-180.9	-202.1	-226.1	-253.2	-284.7	-323.2	-381.6									
5500	-128.5	-134.5	-144.4	-157.6	-173.9	-192.9	-214.9	-239.9	-268.8	-303.4	-349.7										
5750	-138.8	-145.0	-154.9	-168.1	-184.8	-204.3	-227.0	-253.2	-284.2	-323.2	-388.4										
6000	-148.3	-154.5	-164.4	-178.0	-194.8	-215.0	-238.5	-266.2	-299.8	-345.9											
6250	-157.1	-163.3	-173.3	-187.1	-204.2	-225.0	-249.5	-278.8	-316.0	-376.1											
6500	-165.1	-171.4	-181.6	-195.7	-213.2	-234.4	-260.0	-291.4	-333.6												
6750	-172.6	-178.9	-189.4	-203.6	-221.6	-243.6	-270.4	-304.2	-354.4												
7000	-179.6	-186.0	-196.6	-211.0	-229.5	-252.3	-280.5	-317.5	-389.9												

Negative Torque I_q Programming Points for Drive

Torque(Nm)	-20	-40	-60	-80	-100	-120	-140	-160	-180	-200	-220	-240	-260	-280	-300	-320	-340	-360	-390	-420	-450
Speed	I _q (rms)	I _q (rms)	I _q (rms)	I _q (rms)	I _q (rms)	I _q (rms)	I _q (rms)	I _q (rms)	I _q (rms)	I _q (rms)	I _q (rms)	I _q (rms)	I _q (rms)	I _q (rms)	I _q (rms)	I _q (rms)	I _q (rms)	I _q (rms)	I _q (rms)	I _q (rms)	I _q (rms)
100	-21.3	-42.2	-62.2	-81.4	-99.6	-117.2	-133.9	-149.8	-166.5	-181.9	-196.7	-211.4	-228.0	-241.3	-253.2	-268.0	-284.8	-295.8	-311.5	-337.7	-357.0
2500	-21.3	-42.2	-62.2	-81.4	-99.6	-117.2	-133.9	-149.8	-166.5	-181.9	-196.7	-211.4	-228.0	-241.3	-253.2	-268.0	-284.8	-295.8	-311.5	-337.7	-356.4
2750	-21.3	-42.2	-62.2	-81.4	-99.6	-117.2	-133.9	-149.8	-166.5	-181.9	-196.7	-211.4	-228.0	-241.3	-253.2	-263.7	-272.2	-280.6	-291.3	-300.1	
3000	-21.3	-42.2	-62.2	-81.4	-99.6	-117.2	-133.9	-149.8	-166.5	-179.7	-191.7	-202.8	-213.5	-223.3	-232.5	-240.9	-248.8	-255.7	-264.3		
3250	-21.3	-42.2	-62.2	-81.4	-99.6	-116.1	-130.2	-143.4	-155.8	-167.8	-179.1	-189.7	-199.7	-208.9	-217.4	-225.2	-231.9	-238.1	-244.3		
3500	-21.3	-42.2	-61.7	-79.2	-95.2	-109.8	-123.4	-136.1	-148.1	-159.4	-170.1	-180.0	-189.5	-197.9	-206.0	-212.7	-218.6	-222.5			
3750	-20.4	-40.1	-58.4	-75.3	-90.9	-105.2	-118.4	-130.7	-142.2	-153.1	-163.2	-172.7	-181.6	-189.3	-196.7	-202.2	-206.2				
4000	-19.4	-38.2	-56.0	-72.4	-87.5	-101.5	-114.5	-126.5	-137.6	-148.2	-158.0	-166.7	-175.2	-182.5	-188.3	-192.1					
4250	-18.7	-36.8	-54.0	-70.0	-84.8	-98.6	-111.3	-123.0	-134.0	-144.1	-153.5	-162.1	-169.5	-176.2	-179.7						
4500	-18.1	-35.7	-52.4	-68.1	-82.6	-96.1	-108.6	-120.2	-130.9	-140.8	-149.7	-157.8	-164.8	-169.4							
4750	-17.6	-34.7	-51.1	-66.5	-80.8	-94.1	-106.4	-117.7	-128.1	-137.7	-146.5	-154.0	-159.6								
5000	-17.2	-34.0	-50.0	-65.1	-79.2	-92.3	-104.4	-115.6	-125.8	-135.2	-143.3	-150.0									
5250	-16.8	-33.3	-49.1	-63.9	-77.9	-90.8	-102.7	-113.7	-123.7	-132.7	-140.4	-145.5									
5500	-16.5	-32.7	-48.2	-62.9	-76.7	-89.4	-101.2	-112.0	-121.8	-130.4	-137.3										
5750	-16.3	-32.2	-47.5	-62.0	-75.6	-88.2	-99.8	-110.4	-119.9	-128.1	-133.1										
6000	-16.1	-31.8	-46.9	-61.2	-74.7	-87.1	-98.6	-109.0	-118.2	-125.6											
6250	-15.9	-31.4	-46.4	-60.5	-73.8	-86.1	-97.4	-107.6	-116.5	-122.6											
6500	-15.7	-31.1	-45.9	-59.9	-73.0	-85.2	-96.4	-106.4	-114.7												
6750	-15.5	-30.8	-45.4	-59.3	-72.3	-84.4	-95.4	-105.1	-112.7												
7000	-15.4	-30.5	-45.0	-58.8	-71.7	-83.6	-94.4	-103.8	-109.6												

Negative Torque Gamma Angle

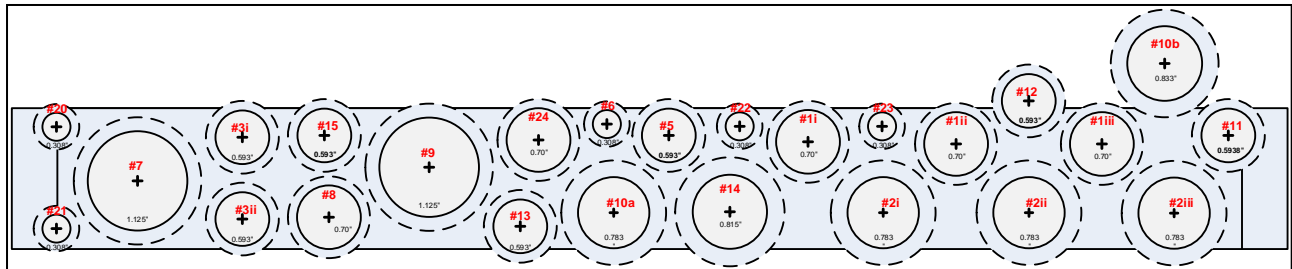
Torque(Nm)	-20	-40	-60	-80	-100	-120	-140	-160	-180	-200	-220	-240	-260	-280	-300	-320	-340	-360	-390	-420	-450
Speed	Gamma	Gamma	Gamma	Gamma	Gamma	Gamma	Gamma	Gamma	Gamma	Gamma	Gamma	Gamma	Gamma	Gamma	Gamma	Gamma	Gamma	Gamma	Gamma	Gamma	Gamma
100	90.0	-6.2	-9.0	-11.2	-13.4	-15.0	-17.0	-19.1	-20.0	-21.8	-23.5	-25.0	-25.2	-27.1	-29.2	-30.0	-30.1	-32.2	-35.0	-35.0	-36.8
2500	90.0	-6.2	-9.0	-11.2	-13.4	-15.0	-17.0	-19.1	-20.0	-21.8	-23.5	-25.0	-25.2	-27.1	-29.2	-30.0	-30.1	-32.2	-35.0	-35.0	-37.0
2750	90.0	-6.2	-9.0	-11.2	-13.4	-15.0	-17.0	-19.1	-20.0	-21.8	-23.5	-25.0	-25.2	-27.1	-29.2	-31.7	-34.5	-37.1	-40.9	-44.7	
3000	90.0	-6.2	-9.0	-11.2	-13.4	-15.0	-17.0	-19.1	-20.0	-23.5	-27.0	-30.3	-33.2	-36.0	-38.6	-41.2	-43.6	-46.0	-49.7		
3250	90.0	-6.2	-9.0	-11.2	-13.4	-17.0	-22.4	-26.7	-30.4	-33.6	-36.4	-39.0	-41.4	-43.8	-46.1	-48.3	-50.7	-53.0	-57.0		
3500	89.9	-6.2	-11.9	-19.1	-24.6	-29.1	-32.8	-36.0	-38.7	-41.2	-43.5	-45.7	-47.8	-49.9	-51.9	-54.1	-56.4	-59.2			
3750	90.0	-32.1	-31.8	-33.7	-36.0	-38.5	-40.8	-43.0	-45.2	-47.1	-49.0	-50.9	-52.7	-54.7	-56.7	-59.1	-61.8				
4000	90.0	-50.5	-45.5	-44.2	-44.6	-45.6	-47.0	-48.5	-50.1	-51.7	-53.3	-55.1	-56.8	-58.7	-60.9	-63.8					
4250	90.0	-60.5	-54.4	-51.7	-50.9	-51.1	-51.8	-52.8	-54.0	-55.4	-56.8	-58.4	-60.2	-62.3	-65.2						
4500	90.0	-66.5	-60.3	-57.1	-55.6	-55.3	-55.5	-56.2	-57.2	-58.4	-59.8	-61.3	-63.2	-65.9							
4750	90.0	-70.3	-64.5	-61.0	-59.2	-58.6	-58.6	-59.0	-59.8	-60.9	-62.2	-63.9	-66.2								
5000	90.0	-73.0	-67.5	-64.0	-62.1	-61.2	-61.0	-61.4	-62.1	-63.1	-64.5	-66.4									
5250	90.0	-74.9	-69.7	-66.4	-64.4	-63.4	-63.1	-63.3	-64.0	-65.0	-66.5	-69.1									
5500	90.0	-76.3	-71.5	-68.2	-66.2	-65.1	-64.8	-65.0	-65.6	-66.7	-68.6										
5750	90.0	-77.5	-72.9	-69.7	-67.7	-66.7	-66.3	-66.4	-67.1	-68.4	-71.1										
6000	90.0	-78.4	-74.1	-71.0	-69.0	-67.9	-67.5	-67.7	-68.5	-70.0											
6250	90.0	-79.1	-75.0	-72.1	-70.1	-69.0	-68.7	-68.9	-69.8	-72.0											
6500	90.0	-79.7	-75.8	-73.0	-71.1	-70.0	-69.7	-69.9	-71.0												
6750	90.0	-80.2	-76.5	-73.8	-71.9	-70.9	-70.6	-70.9	-72.4												
7000	90.0	-80.7	-77.1	-74.4	-72.7	-71.7	-71.4	-71.9	-74.3												

Negative Torque Stator Current

Torque(Nm)	-20	-40	-60	-80	-100	-120	-140	-160	-180	-200	-220	-240	-260	-280	-300	-320	-340	-360	-390	-420	-450
Speed	<i>Is</i> (rms)	<i>Is</i> (rms)	<i>Is</i> (rms)	<i>Is</i> (rms)	<i>Is</i> (rms)	<i>Is</i> (rms)	<i>Is</i> (rms)	<i>Is</i> (rms)	<i>Is</i> (rms)	<i>Is</i> (rms)	<i>Is</i> (rms)	<i>Is</i> (rms)	<i>Is</i> (rms)	<i>Is</i> (rms)	<i>Is</i> (rms)	<i>Is</i> (rms)	<i>Is</i> (rms)	<i>Is</i> (rms)	<i>Is</i> (rms)	<i>Is</i> (rms)	<i>Is</i> (rms)
100	21.4	42.4	63.0	83.0	102.4	121.3	140.0	158.6	177.2	195.9	214.5	233.2	252.0	271.1	290.2	309.5	329.3	349.5	380.2	412.3	446.2
2500	21.4	42.4	63.0	83.0	102.4	121.3	140.0	158.6	177.2	195.9	214.5	233.2	252.0	271.1	290.2	309.5	329.3	349.5	380.2	412.3	446.2
2750	21.4	42.4	63.0	83.0	102.4	121.3	140.0	158.6	177.2	195.9	214.5	233.2	252.0	271.1	290.2	309.9	330.2	351.7	385.5	422.5	
3000	21.4	42.4	63.0	83.0	102.4	121.3	140.0	158.6	177.2	196.0	215.2	234.9	255.2	276.0	297.6	320.0	343.5	368.2	408.9		
3250	21.4	42.4	63.0	83.0	102.4	121.4	140.8	160.6	180.8	201.4	222.5	244.1	266.4	289.4	313.4	338.8	365.8	395.4	448.2		
3500	21.4	42.4	63.1	83.8	104.7	125.7	146.8	168.2	189.8	211.9	234.5	257.8	281.9	307.2	334.0	363.0	395.5	434.0			
3750	27.2	47.3	68.8	90.5	112.4	134.4	156.5	178.9	201.6	224.9	248.8	273.7	299.9	327.8	358.4	393.2	436.9				
4000	44.0	60.1	79.8	101.0	122.9	145.2	167.9	190.9	214.6	239.0	264.3	291.0	319.7	351.2	387.7	435.7					
4250	61.5	74.8	92.7	113.0	134.5	156.9	179.9	203.6	228.1	253.6	280.5	309.4	341.3	378.4	428.5						
4500	77.8	89.4	105.9	125.3	146.4	168.7	192.0	216.3	241.6	268.4	297.2	328.9	365.6	414.5							
4750	92.5	103.1	118.5	137.2	158.0	180.3	203.9	228.8	255.1	283.4	314.4	350.1	395.7								
5000	106.0	115.9	130.6	148.7	169.2	191.6	215.5	241.1	268.5	298.5	332.6	374.5									
5250	118.3	127.5	141.7	159.5	179.9	202.4	226.7	253.1	281.8	314.0	352.4	408.4									
5500	129.5	138.5	152.2	169.7	190.0	212.6	237.5	264.7	295.1	330.2	375.7										
5750	139.8	148.5	162.0	179.2	199.6	222.5	248.0	276.3	308.5	347.6	410.5										
6000	149.2	157.7	171.0	188.2	208.6	231.9	258.1	287.6	322.3	368.0											
6250	157.9	166.3	179.4	196.7	217.2	240.9	267.8	298.9	336.8	395.6											
6500	165.9	174.2	187.3	204.6	225.4	249.4	277.3	310.2	352.8												
6750	173.3	181.6	194.8	212.0	233.1	257.8	286.7	321.9	371.9												
7000	180.2	188.5	201.7	219.0	240.5	265.8	296.0	334.0	405.0												

Appendix III – Pinouts for Electric Truck Cables and Sockets

Layout of connectors on back of control box:



Pinouts for control box connectors:

Connector Number	Connector goes to
1i	Battery box #1
1ii	Battery box #2
1iii	Battery box #3
2i	Battery Box #1
2ii	Battery Box #2
2iii	Battery Box #3
3i	Motor RTDs Conn 1
3ii	Motor RTDs Conn 2
5	Motor 3 ph VI Sense
6	Charger VI Sense
7	12V Distribution Box
8	Torque Sensor
9	Motor Controller
10a	12V Distribution Box
10b	Motor Cooling Fan
11	Ethernet to Router
12	Router & Touchscreen
13	GPS
14	Gear Box Solenoids HVDC Sense/Relay
15	Box

20 *DC DC/ Mot Cont.
Can*
 21 *Battery Charger Can*
 22 *J1772*
 23 *Brake Sensor
To other vehicle
signals*
 24 *Bender Isolation
Sensor*
 25

Connector #: **2i**
 Turck Part #: **CSFL 12-9-0.5**
 Connector
 Goes To: **Battery Box 1 (rear drivers side)**

<i>Turck Connector</i>			<i>Control Interface Board Connector</i>		
Pin	Color	Signal	Conn Name	Conn #	Pin
1	Brown	Gigavac Ground	GigRel	CON89	2
2	N/C				
3	Blue	Gigavac +12V	GigRel	CON89	1
4	White	Fan Ground	Box1Fan	CON10	3
5	N/C				
6	Green	Fan Ground	Box1Fan	CON10	3
7	Yellow	Fan +12V	Box1Fan	CON10	2
8	Gray	Fan +12V	Box1Fan	CON10	2
9	Pink	Heaters - future use			
10	Red	Heaters - future use			
11	N/C				
12	Green/Yellow	Heaters - future use			

Connector #: **2ii**
 Turck Part #: **CSFL 12-9-0.5**
 Connector
 Goes To: **Battery Box 1 (rear passenger side)**

<i>Turck Connector</i>			<i>Control Interface Board Connector</i>		
Pin	Color	Signal	Conn Name	Conn #	Pin
1	Brown	Gigavac Ground	GigRel	CON89	4
2	N/C				
3	Blue	Gigavac +12V	GigRel	CON89	3

4	White	Fan Ground	Box2Fan	CON10	3
5	N/C				
6	Green	Fan Ground	Box2Fan	CON10	3
7	Yellow	Fan +12V	Box2Fan	CON10	2
8	Gray	Fan +12V	Box2Fan	CON10	2
9	Pink	Heaters - future use			
10	Red	Heaters - future use			
11	N/C				
12	Green/Yellow	Heaters - future use			

Connector #: 2iii
Turck Part #: CSFL 12-9-0.5
Connector
Goes To: Battery Box 3 (Under hood)

<i>Turck Connector</i>			<i>Control Interface Board Connector</i>		
Pin	Color	Signal	Conn Name	Conn #	Pin
1	Brown	Gigavac Ground	GigRel	CON89	6
2	N/C				
3	Blue	Gigavac +12V	GigRel	CON89	5
4	White	Fan Ground	Box3Fan	CON10	2
5	N/C				
6	Green	Fan Ground	Box3Fan	CON10	2
7	Yellow	Fan +12V	Box3Fan	CON10	1
8	Gray	Fan +12V	Box3Fan	CON10	1
9	Pink	Heaters - future use			
10	Red	Heaters - future use			
11	N/C				
12	Green/Yellow	Heaters - future use			

Connector #: 3i
Turck Part #: FS 12-0.5
Connector
Goes To: Motor RTDs

<i>Turck Connector</i>			<i>Control Interface Board Connector</i>		
Pin	Color	Signal	Conn Name	Conn #	Pin
1	White	RTD #1 -	*Wire broken in motor		

2	Brown	RTD #1 +	*Wire broken in motor		
3	Green	RTD #2 -	RTDs#7-#11	CON173	4
4	Yellow	RTD #2 +	RTDs#7-#11	CON173	2
5	Gray	RTD #3 -	RTDs#7-#11	CON173	4
6	Pink	RTD #3 +	RTDs#7-#11	CON173	3
7	Blue	RTD #4 -	RTDs#7-#11	CON173	8
8	Red	RTD #4 +	RTDs#7-#11	CON173	6
9	Orange	RTD #5 -	*Wire broken in motor		
10	Tan	RTD #5 +	*Wire broken in motor		
11	Black	RTD #6 -	RTDs#1-#6	CON174	8
12	Violet	RTD #6 +	RTDs#1-#6	CON174	5

Connector #: **3ii**
Turck Part #: **FS 12-0.5**
Connector
Goes To: **Motor RTDs**

<i>Turck Connector</i>			<i>Control Interface Board Connector</i>		
Pin	Color	Signal	Conn Name	Conn #	Pin
1	White	RTD #7 -	RTDs#1-#6	CON174	8
2	Brown	RTD #7 +	RTDs#1-#6	CON174	6
3	Green	RTD #8 -	RTDs#1-#6	CON174	4
4	Yellow	RTD #8 +	RTDs#1-#6	CON174	3
5	Gray	RTD #9 -	RTDs#1-#6	CON174	4
6	Pink	RTD #9 +	RTDs#1-#6	CON174	1
7	Blue	RTD #10 -			
8	Red	RTD #10 +	1K RTD	**Connected to Motor Drive	
9	Orange	RTD #11 -			
10	Tan	RTD #11 +	1K RTD	**Connected to Motor Drive	
11	Black				
12	Violet				

Connector #: **5**
Turck Part #: **FK 12-0.5**

Connector
Goes To: Motor 3ph VI Sense

<i>Turck Connector</i>			<i>Control Interface Board Connector</i>		
Pin	Color	Signal	Conn Name	Conn #	Pin
1	White	GND	Ph1VI	CON22	4
2	Brown	GND	Ph2VI	CON23	4
3	Green	12V	Ph1VI	CON22	1
4	Yellow	12V	Ph2VI	CON23	1
5	Gray	Phase A Vsense signal	Ph1VI	CON22	2
6	Pink	Phase A Isense signal	Ph1VI	CON22	3
7	Blue	Phase B Vsense signal	Ph2VI	CON23	2
8	Red	Phase B Isense signal	Ph2VI	CON23	3
9	Orange	Phase C Isense signal	Ph3VI	CON38	3
10	Tan	Phase C Vsense signal	Ph3VI	CON38	2
11	Black	Thermistor -	RTDs#1-#6	CON174	8
12	Violet	Thermistor +	RTDs#1-#6	CON174	7

Connector #: 6
Turck Part #: MFS 6-0.5
Connector Charger AC V/I Sense
Goes To: Box

<i>Turck Connector</i>			<i>Control Interface Board Connector</i>		
Pin	Color	Signal	Conn Name	Conn #	Pin
1	Brown	GND	ChVIsns In	CON43	4
2	White	Isense Signal	ChVIsns In	CON43	3
3	Blue	Vsense Signal	ChVIsns In	CON43	2
4	Black	12V	ChVIsns In	CON43	1
5	Grey	Thermistor -	RTDs#1-#6	CON174	4
6	Pink	Thermistor +	RTDs#1-#6	CON174	2

Connector #: 7
Turck Part #: DSF 28-27-0.5
Connector
Goes To: 12V Distribution Box

Turck Connector		Control Interface Board Connector			
Pin	Color	Signal	Conn Name	Conn #	Pin
1	Brown	+12V Relays	Rel#5-#10	CON165	4
2	White/Grey	Coolant Pump Relay	Rel#5-#10	CON165	1
3	Blue/Grey	Radiator Fan Relay	Rel#5-#10	CON165	2
4	Brown/Grey	Air Compressor Relay	Rel#5-#10	CON165	3
5	Black/Yellow	Brake Vacuum Relay	Rel#5-#10	CON165	4
6	White/Yellow	Power Steering Relay	Rel#5-#10	CON165	5
7	Blue/Yellow	Spare Relay (not populated)	Rel#5-#10	CON165	6
8	Brown/Yellow	-15V_Current Sensors			
9	Black/Red	Gnd_Current Sensors			
10	White/Red	+15V_Current Sensors			
11	Blue/Red	Current Sensor #1			
12	Brown/Red	Current Sensor #2			
13	Black	Current Sensor #3			
14	White	Current Sensor #4			
15	Blue	Current Sensor #5			
16	Black/Grey	Current Sensor #6			
17	Brown/Orange	Current Sensor #7			
18	White/Orange	Current Sensor #8			
19	Black/Orange	Current Sensor #9			
20	Black/Green	Current Sensor #10			
21	White/Green	Current Sensor #11			
22	Blue/Green	12V_Sense			
23	Brown/Green				
24	Blue/Orange				
25	Green/Yellow				
26	Grey				
27	Orange				
28	NC	No Connection			

Connector #: 8
Turck Part #: BSF 12-12-0.5
Connector Goes To: Torque Sensor

Turck Connector

Control Interface Board Connector

Pin	Color	Signal	Conn Name	Conn #	Pin
A	Brown	No Function			
B	Blue	No Function			
C	White	Torque signal +/-5V			
D	Green	Ground (signal)	TorqSns	CON24	3
E	Yellow	Ground (supply)	TorqSns	CON24	3
F	Grey	12V supply voltage	TorqSns	CON24	1
G	Pink	No function			
H	Red	No function			
J	Black	No function			
K	Orange	No function			
L	Tan	Torque signal 10 +/- 8mA	TorqSns	CON24	2
M	Violet	Cable shield	TorqSns	CON24	3

Connector #: 9
Turck Part #: DKF 28-27-0.5
Connector
Goes To: Motor Controller

Turck Connector			Control Interface Board Connector		
Pin	Color	Signal	Conn Name	Conn #	Pin
1	Brown	*See motor controller worksheet			
2	White/Grey				
3	Blue/Grey				
4	Brown/Grey				
5	Black/Yellow				
6	White/Yellow				
7	Blue/Yellow				
8	Brown/Yellow				
9	Black/Red				
10	White/Red				
11	Blue/Red				
12	Brown/Red				
13	Black				
14	White				
15	Blue				
16	Black/Grey				
17	Brown/Orange				

18	White/Orange	-			
19	Black/Orange	-			
20	Black/Green	-			
21	White/Green	-			
22	Blue/Green	-			
23	Brown/Green	-			
24	Blue/Orange	-			
25	Green/Yellow	-			
26	Grey	-			
27	Orange	-			
28	NC	No Connection			

Connector #: 10a
Turck Part #: CSF 64-6-0.5
Connector
Goes To: 12V Distribution Box

<i>Turck Connector</i>			<i>Control Interface Board Connector</i>		
Pin	Color	Signal	Conn Name	Conn #	Pin
1	White	GND Rio Input Power	+12V Unreg	CON3	5
2	Red	12V Rio Input Power	+12V Unreg	CON3	1
3	Green	GND Fans	GND	CON14	1
4	Orange	12V Fans	+12V	CON13	1
5	Black	GND Fans	GND	CON14	2
6	Blue	12V Fans	+12V	CON13	2

Connector #: 13
Turck Part #: FK 8-0.5
Connector
Goes To: Garmin GPS 18x-5Hz

<i>Turck Connector</i>			<i>Control Interface Board Connector</i>		
Pin	Color	Signal	Conn Name	Conn #	Pin
1	White	Meas. Pulse Output			
2	Brown	Vin (5V)	GPS 18x	CON25	1
3	Green	Ground	GPS 18x	CON25	2
4	Yellow	Transmit Data (Tx)	GPS 18x	CON25	4
5	Gray	Ground	GPS 18x	CON25	3
6	Pink	Receive Data (Rx)	GPS 18x	CON25	5

7	Blue	No Connection			
8	Red	No Connection			

Connector #: **14**
Turck Part #: **RSF 511-0.5M**
Connector
Goes To: **Gear Box**

<i>Turck Connector</i>			<i>Control Interface Board Connector</i>		
Pin	Color	Signal	Conn Name	Conn #	Pin
1	Red/White (Black @ cable)	Gear 1 (3:1) Solenoid Ground	Rel#11-#16	CON166	3
2	Red/Blue (Blue @ cable)	Gear 1 (3:1) Solenoid +12V	Rel#11-#16	CON166	4
3	Green (Green/Yellow @ cable)	Gear 2 (3:1) Solenoid Ground	Rel#11-#16	CON166	5
4	Red/Orange (Brown @ cable)				
5	Red/Black (White @ cable)	Gear 2 (3:1) Solenoid +12V	Rel#11-#16	CON166	4

Connector #: **15**
Turck Part #: **FS 12-0.5** 2A per pin rated current
Connector **HVDC Distribution**
Goes To: **Box**

**Use DC DC on VI Sense Board to provide +/-15V for LEM Hal50s*

<i>Turck Connector</i>			<i>Control Interface Board Connector</i>		
Pin	Color	Signal	Conn Name	Conn #	Pin
1	White	Gig/PreCh Relay Ground	12VUnreg	CON3	3
2	Brown	Gigavac Relay	*to Motor Controller Main Contactor Driver - CON7 Pin 17 (Brown/Orange)		
3	Green	Battery Charger Relay	Rel#17-#20	CON17	5
4	Yellow	Mot Drive Precharge Relay	*to Motor Controller Precharge Relay Driver - CON7 Pin 16 (Black/Grey)		

5	Gray	Sensing Ground	MCinVI	CON33	4
6	Pink	+12V	MCinVI	CON33	1
7	Blue	Battery Pack Voltage	MCinVI	CON33	2
8	Red	Battery Pack Current	MCinVI	CON33	3
9	Orange	DC DC Conv. Input Current	DCDC_lin	CON48	3
10	Tan	Battery Charger Current	Ch&Heat_lin	CON37	2
11	Black	Heater Current	Ch&Heat_lin	CON37	3
12	Violet	Ambient Temp. Sensor	RTDs#7-#11	CON173	5

Connector #: 24
Turck Part #: BSF 14-14-0.5 3A per pin rated current
Connector Other Vehicle
Goes To: Signals

<i>Turck Connector</i>			<i>Control Interface Board Connector</i>		
Pin	Color	Signal	Conn Name	Conn #	Pin
1	Brown	E-stop line 1 (black dash #1 wire)			
2	Red/Blue	Compressor Pressure Switch -	Connect Switch in series with compressor relay (Con165 Pin3)		
3	Black	Motor Fan PWM Signals	MotFan	CON15	3
4	Pink	System Enable Switch P1 (black dash #2 wire)	SysEna	CON18	1
5	Green				
6	Blue	Forward Enable (green dash #1 cable)	DIO#3-#7	34	3
7	Orange	Reverse Enable (red dash #1 cable)	DIO#3-#7	34	4
8	Grey/Brown	E-stop line 2 (white dash #1 wire)			
9	Violet	System on Blue LED (white dash #2 wire)			
10	White	Heater Enable/Fluid Pump Power	SprRel#2	CON84	2
11	Red	Heater Fault Output	??	??	??

12	Grey	Red Charge LED + (red dash #2 wire)			
13	Yellow	Green Charge LED + (green dash #2 wire)			
14	Tan	Compressor Pressure Switch +	Connect Switch in series with compressor relay (Con165 Pin3)		

Connector #: **10b**
Turck Part #: **BSF 22-0.5/14.5/NPT**
Connector
Goes To: **Motor Fan**

<i>Turck Connector</i>			<i>Control Interface Board Connector</i>		
Pin	Color	Signal	Conn Name	Conn #	Pin
1	White	Fan +12V	MotFan	CON15	1
2	Black	Fan Ground	MotFan	CON15	2

Connector #: **12**
Turck Part #: **FKD 4.4-0.5**
Connector **Router &**
Goes To: **Touchscreen**

<i>Turck Connector</i>			<i>Control Interface Board Connector</i>		
Pin	Color	Signal	Conn Name	Conn #	Pin
1	Brown	Router Ground	DispPow	CON30	4
2	White	Router Positive (+12V)	DispPow	CON30	3
3	Blue	Touchscreen Black/Green (-15V)	DispPow	CON30	2
4	Black	Touchscreen Red/White (+15V)	DispPow	CON30	1

Connector #: **22**
Turck Part #: **MFSS 3-0.5**
Connector
Goes To: **J1772 Conn**

<i>Turck Connector</i>					
Pin	Color	Signal			

1	Brown	Pilot Signal	to J1772 Board		
2	Blue	Proximity Pin	to J1772 Board		
3	Black	Earth Ground Pin	to J1772 Board		

Connector #: 23
Turck Part #: MFKS 3-0.5
Connector
Goes To: Brake switch

Turck Connector			Control Interface Board Connector		
Pin	Color	Signal	Conn Name	Conn #	Pin
1	Brown	12V when Brake act.	DIO#3-#7	34	5
2	Blue	Broke Pot +5V (future)			
3	Black	Brake Pot Gnd (future)			

Connector #: 25
Turck Part #: MFKS 6-0.5
Connector HV DC Distribution Box - Bender
Goes To: Isometer

Turck Connector			Control Interface Board Connector		
Pin	Color	Signal	Conn Name	Conn #	Pin
1	Brown	Bender Pin 1: Chassis Ground			
2	White	Bender Pin 2: Supply Voltage (10-30Vdc)			
3	Blue	Bender Pin 5-Data Out PWM (high side)	Spare Relay #1	80	5
4	Black	Bender Pin 6 Dat Out PWM (low side) - not active for this part			
5	Grey	Bender Pin 8-Status Output (high side)	Spare Relay #2	84	5
6	Pink				

Motor Resolver cable wiring:

<i>Turck Connector</i>				<i>Motor Controller Connector</i>				
Pin	Color	Signal	Use Pin??	Conn Name	Pin #	Pin Name	Description	Notes
4	Black - at motor (Red/White - at motor drive)	Red/White (Exciter Windings R1)	Yes	J2-23p	17	EXC	Resolver excitation output	Used with PM Motors
8	Red - at motor (Yellow/White - at motor drive)	Yellow/White (Exciter Winding R2)	Yes	J2-23p	3	GND	Resolver excitation return	
7	Yellow - at motor (Red - at motor drive)	Red S1 (Cosine Output Winding S1)	Yes	J2-23p	4	COS	Resolver Cosine winding +	Cosine
3	Blue - at motor (Black - at motor drive)	Black (Cosine Output Winding S3)	Yes	J2-23p	12	/COS	Resolver Cosine winding -	Cosine
9	Red/White - at motor (Yellow - at motor drive)	Yellow (Sine Output Winding S2)	Yes	J2-23p	11	SIN	Resolver Sine winding +	Sine
5	Yellow/White - at motor (Blue - at motor drive)	Blue (Sine Output Winding S4)	Yes	J2-23p	18	/SIN	Resolver Sine winding -	Sine
2	Black/White							
6	Blue/White							
Braid		Cable Shield	Yes	J2-23p	19	GND		Resolver Shield GND

Motor controller serial cable in cab wiring:

		<i>Motor Controller Connector</i>				
	Use Pin??	Conn Name	Pin #	Pin Name	Description	Notes
Serial Cable Red	Yes	J1-35p	7	/PROG_ENA	Serial Boot Loader Enable	
Serial Cable Green	No	J1-35p	22	GND	Ground	
Serial Cable Black	Yes	J1-35p	12	TXD	RS-232 Transmit	
Serial Cable White	Yes	J1-35p	35	RXD	RS-232 Receive	
Dash #3 Red Wire	Maybe	J2-23p	22	RLY4	Lo-Side Relay Driver	Fault Indicator Drive

Motor controller connector wiring description:

Motor Controller Wiring Goes To:														
		Turck Connector		Turck Connector		Motor Controller Connector								
Con #	Goes to	Pin	Color	Signal	Pin	Color	Signal	Use Pin??	Conn Name	Pin #	Pin Name	Description	Notes	
22	Accelerator Pot	1	Brown	+5V	1	Brown		Yes	J1-35p	1	XDCR_PWR	+5V @ 80mA max	Accel Pedal Power	
22	Accelerator Pot	3	Black	0-5V Signal	2	White/Grey		Yes	J1-35p	13	AIN1	Analog Input 1 0-5Vfs	Accel Pedal Wiper	
22	Accelerator Pot	2	Blue	Ground	3	Blue/Grey		Yes	J1-35p	2	AGND	Analog Ground	Accel Pedal GND	
3ii	Motor RTDs II	7 & 9	Blue & Orange	RTD #10 - & RTD #11 -	4	Brown/Grey		Yes	J1-35p	15	AGND	Analog Ground		
3ii	Motor RTDs II	8	Red	RTD #10 +	5	Black/Yellow	*	Yes	J1-35p	5	RTD1	PT100 or PT1000 RTD		
3ii	Motor RTDs II	10	Tan	RTD #11 +	6	White/Yellow	*	Yes	J1-35p	6	RTD2	PT100 or PT1000 RTD		
					7	Blue/Yellow		Maybe	J1-35p	33	CANA_H	CAN Channel A Hi		
					8	Brown/Yellow		Maybe	J1-35p	11	CANA_L	CAN Channel A Low		
					9	Black/Red		Yes	J1-35p	19	AGND	Analog Ground		
					10	White/Red		yes	J1-35p	30	DIN1	Digital Input 1 - STG	Forward Enable Switch	
					11	Blue/Red		Yes	J1-35p	8	DIN2	Digital Input 1 - STG	Reverse Enable Switch	
					12	Brown/Red		Maybe	J1-35p	20	DIN3	Digital Input 1 - STG	Brake Switch	
					13	Black	*Splice with green wire of Dash #3 cable		J2-23p	15	RLY3	Lo-Side Relay Driver	OK Indicator Drive / 12V Power Relay Drive	
CON3	Ground	3	EV Int Bd	Ground	14	White		Yes	J2-23p	6	GND	Main 12V Return	Chassis GND	
					15	Blue	*Blue to Pin 10 was not intentional, so Encoder GND is unused	No	J2-23p	10	GND	GND	Encoder GND	
					16	Black/Grey		Yes	J2-23p	21	RLY1	Hi-Side Relay Driver	Pre-Charge Contactor Drive	
					17	Brown/Orange		Yes	J2-23p	7	RLY2	Hi Side Relay Driver	Main Relay Drive	
CON80	Spare Relay #1	3	EV Int Bd	Switched +12V	18	White/Orange		Yes	J2-23p	8	BATT+	Main 12V power source	12V Ignition Power	
CON34	DIO#3-#7	7	EV Int Bd	DIO #7	19	Black/Orange	*12V power enable signal for DC DC converter		J2-23p	23	BATT+	Main 12V Power source	12V Ignition Power	
CON80	Spare Relay #1	4	EV Int Bd	Switched +12V	20	Black/Green		Maybe	J1-35p	9	DIN5	Digital Input 1 - STB	Ignition Input (if used)	
					21	White/Green		Maybe	J1-35p	21	DIN6	Digital Input 1 - STB	Start Input (if used)	
					22	Blue/Green	*Splice with white wire of Dash #3 cable		J2-23p	14	GND	Main 12V Return	Chassis GND	
CON3	Ground	4	EV Int Bd	Ground	23	Brown/Green	Accel Pedal Ground (Blue Wire)		J2-23p	14	GND	Main 12V Return	Chassis GND	
					24	Blue/Orange	Accel Pedal +5V supply (White wire)							
					25	Green/Yellow	12V Ignition (Black wire of Dash #3 cable)							
					26	Grey	Accel Pedal 0.5V to 4.5V signal (Orange Wire)							
					27	Orange								
					28	NC								

*Tie to Pin 3 (Blue/Grey) - alternative, run to cRio/EV Interface Board Input

*Tie to Pin 1 (Brown) - alternative, run to cRio/EV Interface Board Input

*Tie to Pin 2 (White/Grey) - alternative, run to cRio/EV Interface Board Input

Appendix IV – DC/DC Converter Loss Modeling Report

University of Wisconsin-Madison

Independent Study Report

Analysis and Design of a Half-Bridge DC-DC converter for hybrid
energy storage system for electric vehicles

Renato Amorim Torres

May, 18th 2014

Contents

Introduction.....	402
Selection of DC-DC converter topology.....	402
Initial, derived parameters and components ratings.....	403
Important aspects of the components.....	404
Selection of components.....	413
Efficiency Calculation Method Used.....	415
Efficiency Results.....	418
Appendix.....	425
1- Calculation of derived parameters	425
2- Ratings of the components.....	427
3 Efficiency considering conduction losses	428
3- Useful Links:.....	431
Bibliography	432

List of figures

Figure 1 - Hybrid Energy Storage System.....	402
Figure 2 - Combination of Ultra-capacitor with Battery.....	402
Figure 3 – Boost/Buck Operation Maximum Power.....	404
Figure 4 - Buck Converter	405
Figure 5 - Diode Recovery time and power dissipation in the switching device.....	405
Figure 6- Selection of switching device.....	406
Figure 7 - Buck Converter	407
Figure 8 - Waveforms for IGBT turn-off transition for the buck converter	407
Figure 9 - Hysteresis loop of ferromagnetic material	408
Figure 10 – On the left, the continuous operation limit. On the right, the discontinuous operation mode.....	409
Figure 11 – Inductance vs Minimum Power Operation (Boost).....	410
Figure 12 - Inductance vs Minimum Power Operation (Buck).....	410
Figure 13 – Inductor Ratio Loss vs Ripple Current Ratio	411
Figure 14 – Waveform of current with ripple in the diode/switch.....	412
Figure 15 – Schematic of the IGBT (SKM 400GB066D) used in calculations.....	413
Figure 16 – Turn-on IGBT losses	416
Figure 17– Curve Fitting for IGBT.....	419
Figure 18 – Efficiency for different voltage ratios.....	419
Figure 19 – Efficiency $V_{IN} = 175V$, $V_{OUT} = 227V$	420
Figure 20 - Efficiency $V_{IN} = 175V$, $V_{OUT} = 280V$	420
Figure 21 Efficiency $V_{IN} = 175V$, $V_{OUT} = 350V$	421
Figure 22 Efficiency $V_{IN} = 200V$, $V_{OUT} = 260V$	421
Figure 23 Efficiency $V_{IN} = 200V$, $V_{OUT} = 320V$	422
Figure 24 Efficiency $V_{IN} = 200V$, $V_{OUT} = 380V$	422

Figure 25 Efficiency $V_{IN} = 250V$, $V_{OUT} = 280V$	423
Figure 26 Efficiency $V_{IN} = 250V$, $V_{OUT} = 280V$	423
Figure 27 Efficiency $V_{IN} = 250V$, $V_{OUT} = 380V$	424
Figure 28 – Boost Converter at on state (top) and at off state (bottom)	428
Figure 29 – Equivalent circuit for the equation $\langle V_L \rangle = 0$	428
Figure 30 - Equivalent circuit for the equation $\langle I_C \rangle = 0$	429
Figure 31 – Equivalent Circuit of the Boost Converter	429
Figure 32 – Equivalent Circuit for the average voltage in the inductor	430
Figure 33 - Equivalent Circuit for the average current in the capacitor	430
Figure 34 – Equivalent Circuit of the buck converter.....	431

List of tables

Table 1 - DC-DC converter parameters	403
Table 2 – K_{CRIT} values to avoid DCM.....	409
Table 3- Inductors model used in calculations.....	413
Table 4 - Information of Toyota Prius 2010	414
Table 5 - Comparison of switching loss results with the Semikron tool.....	417
Table 6 - Initial Parameters for a 30kW – 50kW DC-DC converter.....	425

Introduction

Hybrid energy storage in electric vehicles consists of combining different types of energy storage in order to provide not only high energy density, but also high power density that allows increase in the efficiency of the vehicle. One type of hybrid storage system consists in the utilization of an energy dense battery pack and a power dense ultra-capacitor connected through a DC-DC converter. This energy storage system is analyzed and evaluated in the digest [1]. The DC-DC converter connection for that system is shown in the figure below extracted from [1].

Since the DC-DC converter efficiency is an important prerequisite for the hybrid energy system, this report aims to design and analyze a potential DC-DC converter for the application, the half-H DC-DC converter. This report calculates analytically the variables associated with the electrical operation of the converter, the necessary ratings of the components and, after the selection of the components, the losses associated with the conduction losses, switching losses and inductor losses.

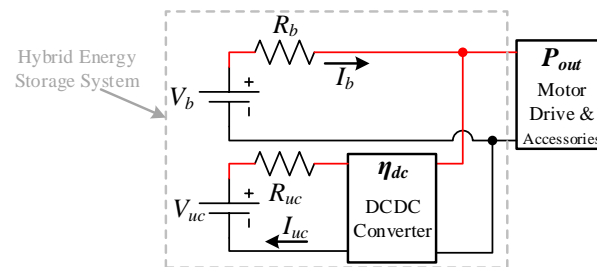


Figure 1 - Hybrid Energy Storage System

Selection of DC-DC converter topology

The first step taken was to define the DC-DC converter topology. In order to make a decision the literature was consulted and, based on the previous analysis of the articles [2], [3] and [4], the half-H topology was adopted. The article [3] also discuss the possibility of using multiple interleaved stages, where trade-offs between efficiency and stress in the elements, size and temperature are explored. The figure below represents the half-H converter connected to ultra-capacitor pack. The figure was extracted from [2].

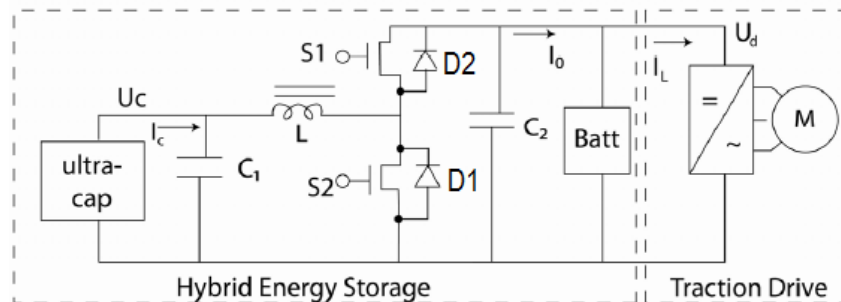


Figure 2 - Combination of Ultra-capacitor with Battery

The half-H converter is a bidirectional converter operating as a boost converter when power flows from the ultra-capacitor pack to the DC bus (S_2 and D_2 are active, and S_1 and D_1 are inactive), and as a buck converter when power flows from the DC bus to the pack (S_1 and D_1 are active, and S_2 and D_2 are inactive).

Initial, derived parameters and components ratings

In order to start the analysis, some initial parameters were defined and also the ones possible to be derived from those. In addition, the maximum ratings of the components were defined. The values are displayed in the tables below:

Table 1 - DC-DC converter parameters

Parameter	Value
Min Ultra capacitor voltage	135V
Max Ultra capacitor voltage	270V
Battery min voltage	270V
Battery max voltage	395V
Switching Frequency	15KHz
Max Inductor Average Current	300A
Inductor (90A ripple current)($R_L = 0.3$)	300uH
Diodes blocking voltage	395V
Diodes Maximum Current	390A
IGBTs blocking voltage	395V
IGBTs Maximum Current	390A
Duty cycle region (Boost Operation)	0 - 0.66
Duty cycle region (Buck Operation)	0.34 - 1

Obs.: The calculations done to achieve the values above are in the Appendix – 1 & 2

Although the calculations are just presented in the appendix, it is important to point out some of the considerations during the work:

The values R_L is the inductor ripple current ratio and it represents the ratio between the ripple current value and the average current value. The article [4], which is also related with hybrid electric vehicle says that values of R_L between 0.3 and 0.4 provide a good compromise between the allowed ripples. This aspect will be more explored in the section of important component aspects.

With the parameters defined above it is possible to define the maximum power region for the buck and for the boost operation. Neglecting the losses, the boost operation power is given by $P_{out} = V_{in} I_{in}$. As in the boost operation $I_{IN} = I_L$ and the maximum value for I_L is 300A, the output power is directly related with the input voltage, which corresponds to the ultra-capacitor voltage.

To calculate the buck operation maximum output power we can do similar approach. The buck operation power is given by $P_{out} = V_{out} I_{out}$. In the boost operation, $I_{OUT} = I_L$ and the maximum value for I_L is 300A, then the output power is proportional to the output voltage, which corresponds again to the ultra-capacitor voltage.

The graph below shows the operating region of the boost and buck operation that assures inductor average current lower than 300A.

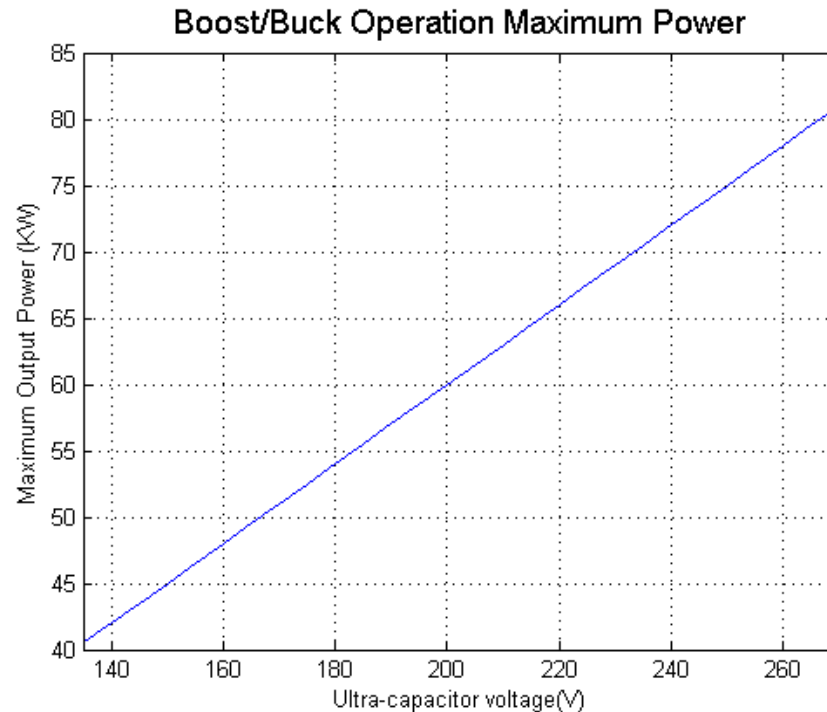


Figure 3 – Boost/Buck Operation Maximum Power

Important aspects of the components

Diodes

The first thing to pay attention when selecting the diodes is that its specification obeys the maximum blocking voltage and current (these values are calculated in the appendix-2). Once, these requisites are satisfied it is important to take into consideration the losses. The losses due to the diode operation can be divided in two types of loss: the conduction loss and the switching loss. The conduction loss is associated with the voltage drop across the diode when it is conducting current. In the other hand, the switching loss is related with recovery time and current, that is explained below. It is worthy pointing out that, although the loss is related with the diode recovery current, most part of the power related with this phenomenon is dissipated in the switching device.

As in converter applications, the switching frequency is too high the switching losses becomes significant even if the recovery time and current are low, therefore special attention is necessary. The diode has a capacitance associated with it that is intrinsic with its principle of operation. Due to that capacitance, when the diode is turned off a current in the opposite direction starts to flow. This current flows for a short period known as the recovery time. Moreover, the voltage across the diode does not change simultaneously neither. During this time, power is dissipated in the switching device, as we can verify that there is a period of positive current and voltage across the switch as shown in the figures below extracted from the book [5].

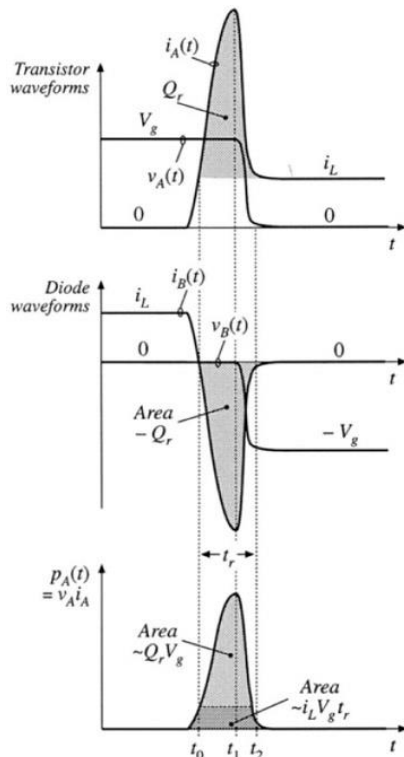


Figure 5 - Diode Recovery time and power dissipation in the switching device

The switching device reverse recovery time t_r is given by $(t_2 - t_0)$. The energy dissipated in the switching device due to the diode recovery current can be approximated by the formula below also extracted from the book [5]:

$$\text{Energy Dissipated} = W_{\text{recovery}} = V_g i_L t_r + V_g Q_r$$

Where V_g is the initial voltage across the diode, i_L is the current in the inductor, t_r the recovery time and Q_r the recovery charge. Generally, the t_r and Q_r are obtained in the diode datasheet. It is important to clarify that this formula is considered for switches with switching time much faster than the diode switching time.

It is important to pay attention in the trade-offs of the diode: increases in its conductivity by increasing the recovery charge, leads to a lower diode on-resistance, but on the other hand it takes time to insert and remove this charge leading to slower switching times that means more switching loss. For switching applications as converters it is expected to use fast or ultra-fast recovery time power diodes.

Switches (IGBT)

Similarly to the diode, the first thing to pay attention when selecting the switches is that its specification obeys the maximum blocking voltage and current (these values are calculated in the appendix-2). Once, these prerequisites are satisfied it is important to take into consideration the voltage drop across the switch, the series resistance and the switching time. In the same way, the losses associated with switching becomes large due to the high frequency and a special attention is necessary.

Considering converters applications the IGBT and the MOSFET are the most likely switching devices to be used. BJTs are inappropriate for the purpose, once these devices cannot handle high currents. Thyristors, although it can easily handle high voltages and currents, it has too long switching times that is impracticable

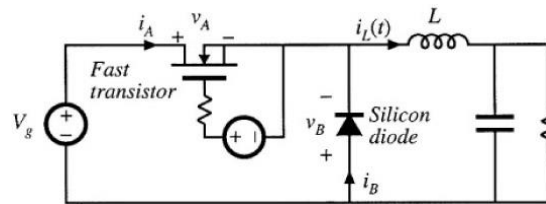


Figure 4 - Buck Converter

for high frequency and have uncontrolled turn off, which means that they can only be used for AC applications.

The MOSFET has the advantage of faster switching times, but its series resistance is high. The IGBT has almost the same structure of a MOSFET, the difference is the p region connected to the collector of the IGBT. The injection of this p region increases the minority charges, which is responsible for reducing the on-resistance of the device. The forward voltage drops of IGBTs devices are typically 1 to 2 V, much lower than would be obtained in equivalent MOSFETs of the same silicon area.

The figure below shows the usage of the MOSFET and IGBT for applications of different voltages and is helpful to pick the correct switching device for our DC-DC converter.

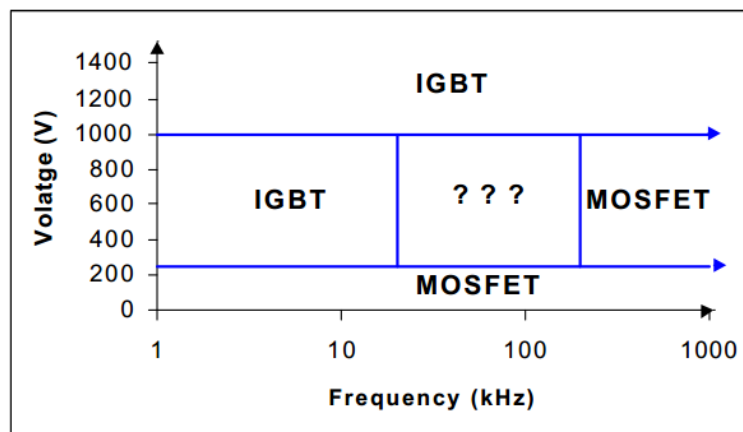


Figure 6- Selection of switching device

Looking at the figure above, we can verify that the IGBT is preferable until the switching frequency of 20 kHz. As the frequency of our device is 15 KHz and also checking previous works as shown in the articles [3] and [4], the IGBT has been selected in our application.

The figure below shows the turn-off transition of an IGBT for a buck converter. The figure was extracted from the book [5].

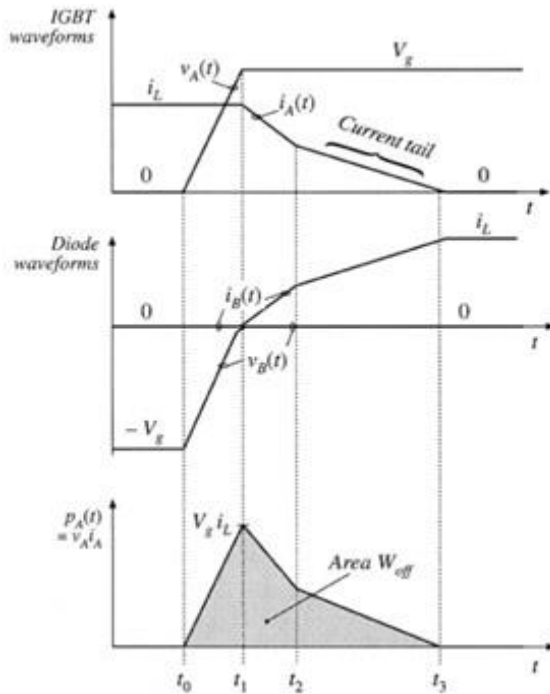


Figure 8 - Waveforms for IGBT turn-off transition for the buck converter

During the switching, it can be observed that the voltage across the IGBT does not change instantaneously; it is due to the time necessary to charge the gate capacitance of the IGBT.

The switching starts at t_0 . The current in the circuit cannot change instantaneously due to the inductor and when the switching starts the on-resistance of the switch increases as charge is removed from its junction. These two factors cause the voltage across the switch to increase and, consequently, the voltage across the diode. When the voltage across the diode achieves its necessary value to turn on, the current will start flowing through the diode. After the diode starts conducting, the current in the IGBT does not drop instantaneously due to the capacitance between the gate and the emitter and due to the phenomenon known as current tail where the minority charges are recombined.

From the curves above, we can verify that during the switching interval, power is dissipated in the IGBT, the total energy dissipated in the IGBT is given by the area W_{off} in the last chart. This area can be approximated by the following equation:

$$\text{Energy dissipated} = W_{IGBT} = \frac{V_g i_L (t_3 - t_0)}{2}$$

The turn on transition of the IGBT is essentially the same with the time axis reversed. In the boost operation, the waveforms are the same, but the value of V_G (V_{IN}) is swapped by the value of V_{OUT} .

Inductor

The inductor is a key element in the DC-DC converter application because it is the component responsible to store energy from one source and transfer to another. One aspect really important to observe when it comes to the inductor is the ripple current. The ripple current increases the conduction losses, influences in the voltage ripple during the buck operation, increase the amount of core loss in itself and provokes stress

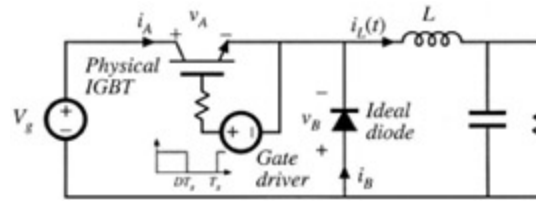


Figure 7 - Buck Converter

in the elements of the circuit. The ripple current is inversely proportional to the inductance and is given by the formula:

$$\Delta I_l = V_{out} (1 - D) \frac{T_s}{2L}$$

It is worthy pointing out that the ripple current is also associated with the switching frequency. On one hand, the increase of frequency decreases the conduction losses, but, in the other hand, it increases the switching losses.

The core loss resultant from the ripple current corresponds to the energy associated with the area of the hysteresis loop multiplied by the volume of the core. The higher the ripple current, the larger becomes the area of the hysteresis loop and consequently the core losses. It is worthy point out that DC components in the inductor current does not implies in hysteresis losses, as it does not provokes changes in the flux core.

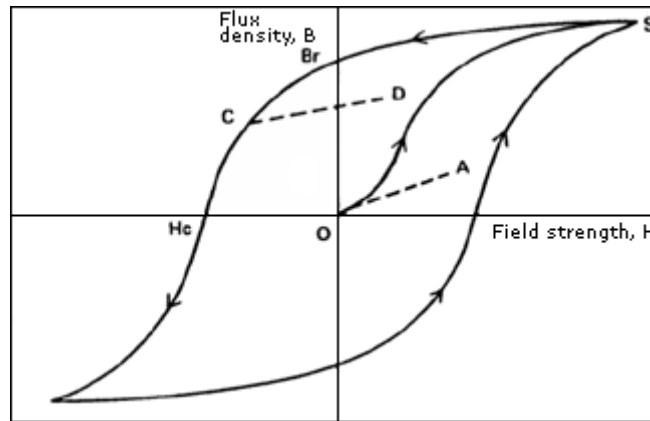


Figure 9 - Hysteresis loop of ferromagnetic material

During the operation of the DC-DC converter, if the ripple current in the inductor becomes higher than the inductor current average, the converter will start operating at the discontinuous mode of operation. The discontinuous mode of operation can be easily understood observing the figures below extracted from the book [5].

The first figure, in the right, shows the inductor current in the buck converter in the continuous mode operation and its respective diode current curve. It can be observed that, if the average current in the inductor reduces more than the actual value, the current ripple will achieve negative values and the diode will not be able to conduct the ripple current anymore. When it occurs the discontinuous mode operation starts, and it is characterized by a period of no current conduction in the inductor as shown in the figure in the left.

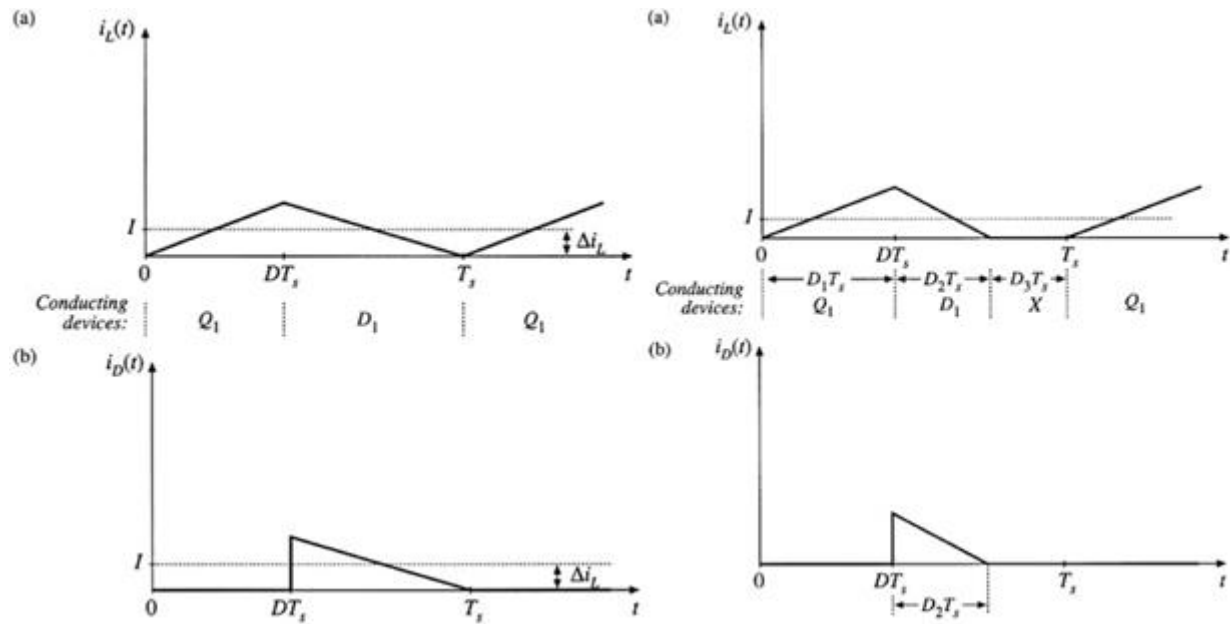


Figure 10 – On the left, the continuous operation limit. On the right, the discontinuous operation mode

The disadvantage of the discontinuous mode in the DC-DC converter is that it reduces its efficiency, as the ripple current is very expressive if compared to the average current. The ripple current increases the core losses and also the copper losses, as it will be explained later.

The discontinuous mode can be avoided during the buck and during the boost operation if the following condition is obeyed:

$$K > K_{crit}(D)$$

Where:

$$K = \frac{2L}{R_{load}T_s}$$

K_{CRIT} is defined for the buck and boost operation as shown in the table below, the table also shows the global maximum value that the K_{CRIT} can assume.

Table 2 – K_{CRIT} values to avoid DCM

Operation	$K_{CRIT}(D)$	Max(K_{CRIT})
Buck	1-D	1
Boost	$D(1-D)^2$	4/27

Obs.: this conditions are explained in chapter 5 of [5].

For different power operations the equivalent resistance R_{LOAD} changes and consequently the inductance must change to maintain the same value of K . The lower the power value can reaches, the bigger the inductance to avoid the discontinuous mode of operation. Considering the presented above the following graphs were generated.

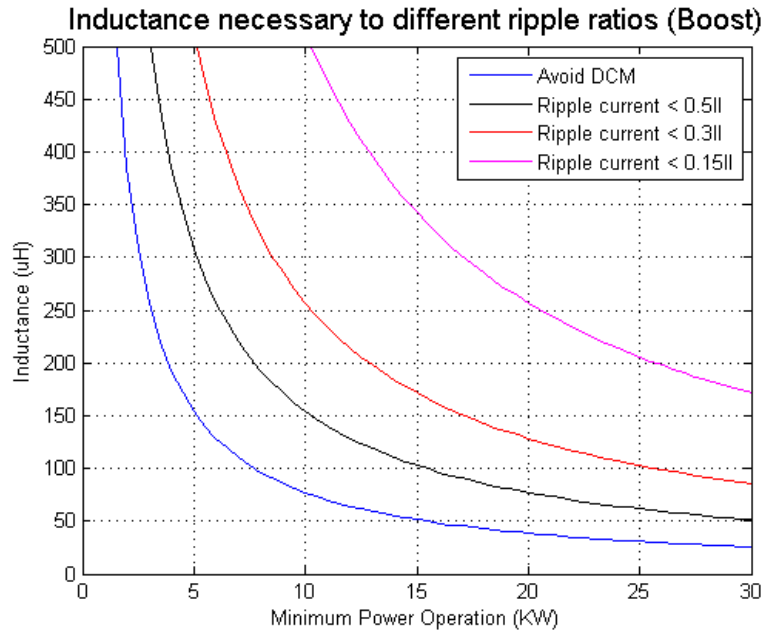


Figure 11 – Inductance vs Minimum Power Operation (Boost)

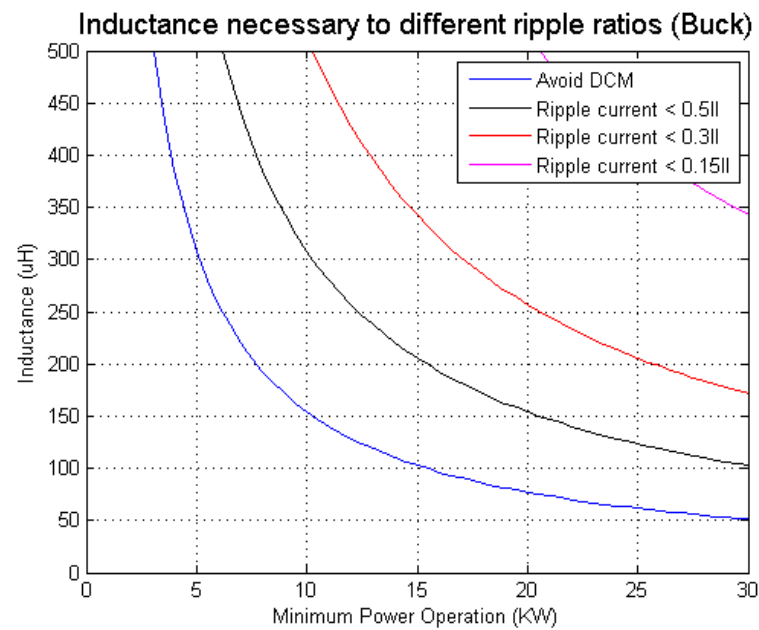


Figure 12 - Inductance vs Minimum Power Operation (Buck)

It is worthy pointing out that, in the boost operation for a given power condition and inductor value, the K critical situation occurs when the duty cycle is equal $1/3$, which means a voltage ratio of 1.5.

For the buck converter, this critical situation occurs when the duty cycle is zero, which means output voltage equals zero. As in our application there is no interest in a buck operation at that point, the K_{CRIT} considered in the graph of buck operation above was considered doing the following procedure:

$$K = \frac{2L}{R_{load}T_s} = \frac{2L}{\frac{V_{out}^2}{P_{out}}T_s}$$

As K for the buck operation is (1-D) we have that:

$$L = \frac{V_{out}^2}{P_{out}} \frac{1-D}{2}$$

Substituting $V_{OUT} = V_{IN}D$:

$$T_s = \frac{V_{in}^2 D^2}{2P_{out}} (1-D)T_s$$

We can verify that for a given output power and frequency the inductor size is the biggest when V_{IN} is maximum (395V) and $D^2 (1-D)$ is maximum, it occurs when $D = 2/3$.

As mentioned before the ripple current increases the conduction losses and reduces the efficiency. It happens because the RMS value of the current increases with the ripple current, while the average current maintain the same. It is well known that the loss in the resistances is associated with RMS value and therefore more power is lost in the resistances due to ripple current, for the same power delivered that is only proportional to the average current. The following graph shows the Conduction Loss Ratio vs Ripple Current Ratio ($\frac{\Delta I_L}{I_L}$). The Conduction loss ratio corresponds to a factor that defines how much more power is lost in the resistances due to ripple current when compared to the losses when there is no ripple current.

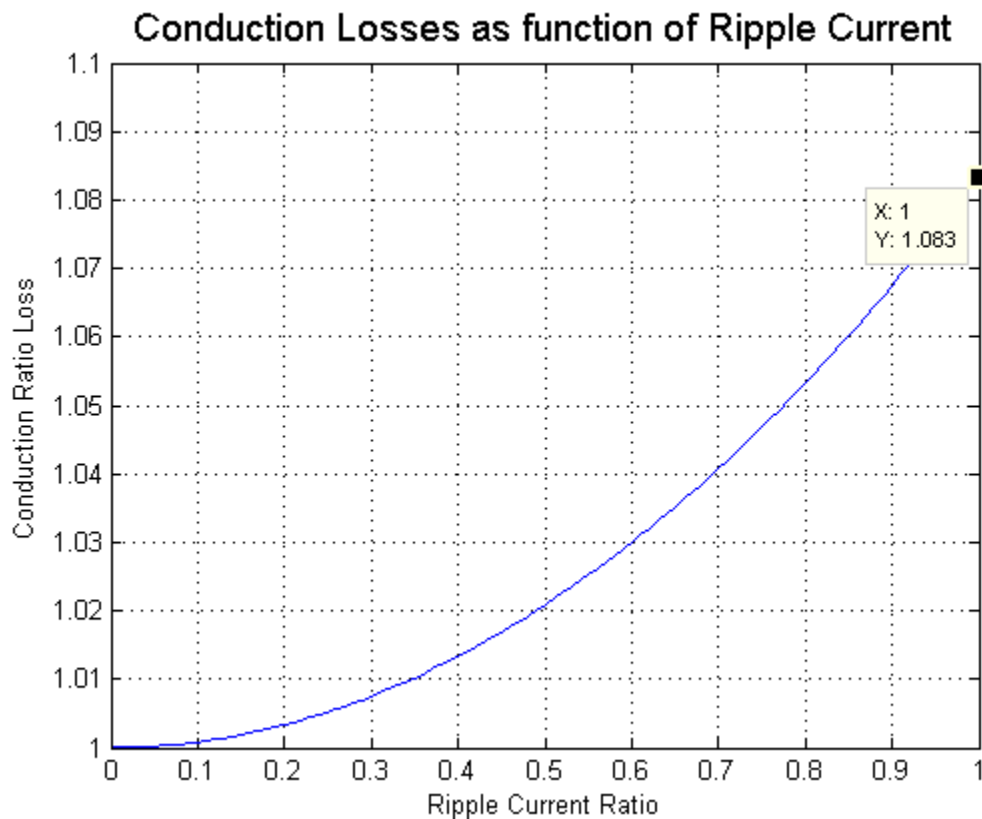


Figure 13 – Inductor Ratio Loss vs Ripple Current Ratio

The calculation done to obtain the graph above is in shown below:

Considering a waveform of $i(t)$ in a diode/switch and that the average current in the inductor is I as shown below the RMS value of $i(t)$ is calculated:

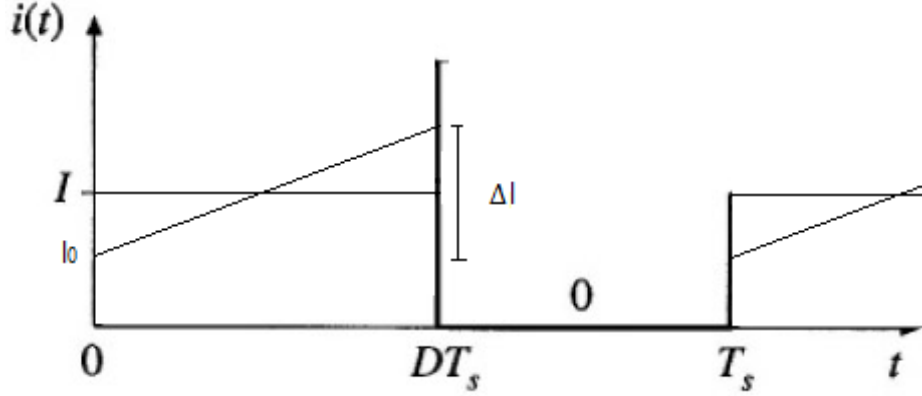


Figure 14 – Waveform of current with ripple in the diode/switch

$$RMS = \sqrt{\frac{1}{T_s} \int_0^{T_s} f(t)^2 dt} = \sqrt{\frac{1}{T_s} \int_0^{DT_s} i(t)^2 dt}, \text{ where } i(t) = \begin{cases} i_0 + \frac{\Delta i}{DT_s} t, & \text{if } t < DT_s \\ 0, & \text{if } t > DT_s \end{cases}$$

$$RMS = \sqrt{\frac{1}{T_s} \int_0^{DT_s} (i_0 + \frac{\Delta i}{DT_s} t)^2 dt} = \sqrt{\frac{1}{T_s} DT_s I^2 \left(\left(1 - \frac{r_L}{2}\right)^2 + r_L \left(1 - \frac{r_L}{2}\right) + \frac{r_L}{3} \right)}, \text{ where } r_L = \frac{\Delta I}{I} \text{ and } i_0 = I - \frac{\Delta I}{2}$$

$$RMS = \sqrt{D} I \sqrt{\left(\left(1 - \frac{r_L}{2}\right)^2 + r_L \left(1 - \frac{r_L}{2}\right) + \frac{r_L}{3} \right)}$$

$$RMS = \sqrt{D} I \text{ ConductionLossRatio}, \text{ for } \text{ConductionLossRatio} = \sqrt{\left(\left(1 - \frac{r_L}{2}\right)^2 + r_L \left(1 - \frac{r_L}{2}\right) + \frac{r_L}{3} \right)}$$

For the diode or for the IGBT the formula above can be used directly substituting the D for the duty cycle that the element is conducting.

For the inductor, as this element conducts during the whole period, we can think that the square of its RMS value must be equal to the sum of the squares of the RMS of the diode and of the switch. It leads to the following equation:

$$(RMS_L)^2 = (RMS_D)^2 + (RMS_{Sw})^2$$

$$RMS_L = I \sqrt{\left(\left(1 - \frac{r_L}{2}\right)^2 + r_L \left(1 - \frac{r_L}{2}\right) + \frac{r_L}{3} \right)} = I \text{ ConductionLossRatio}$$

Selection of components

Diode and IGBT

The diode and IGBT selected for the application and in which the following calculations are based is the device: SKM 400GB066D that consists in two pairs of an IGBT with a built-in diode.

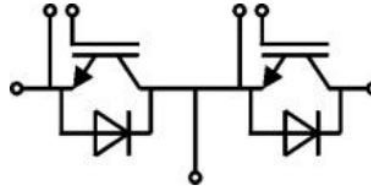


Figure 15 – Schematic of the IGBT (SKM 400GB066D) used in calculations

Inductor

Unfortunately, it was impossible to find inductors models that meets the prerequisites of current and inductance at the same time. In order to have an initial idea of the physical size of the inductor and its winding resistance before having to designing it, some attempts to try to define the inductors characteristics were done. The first attempt was trying to make combinations of inductors in series and in parallel, using the values of the inductors shown in the table below extracted from *West Coast Magnetics*:

Table 3- Inductors model used in calculations

Product Code	Inductance (μH)	DCR (mOhms)	I _{rms} (amps) INPUT	Weight (kg)
306-1	582	15.98	15.0	1.0
306-2	494	12.61	17.0	1.0
306-3	388	9.77	19.0	1.0
306-4	273	6.56	23.0	1.0
306-5	195	4.40	27.0	1.0
306-6	178	3.92	28.0	1.0
306-7	146	3.20	31.0	1.0
306-8	131	2.80	33.0	1.0
306-9	103	2.14	37.0	1.0
306-10	91	1.89	39.0	1.0
306-11	79	1.63	42.0	1.0
306-12	58	1.25	48.0	1.0
306-13	49	1.03	55.0	1.0
306-14	40	0.81	58.0	1.0
306-15	33	0.70	66.0	1.0
306-16	26	0.55	74.0	1.0

A code in *Matlab* was implemented to make series and parallel assemblies for each model in order to achieve the minimum inductance and current necessary. The best combination has used 24 inductors. The attempt has shown impracticable.

The second attempt was looking in the literature. The first characteristic estimated was the inductor series resistance that was extracted from the article [7]. This article analyses a DC-DC converter for the inverter in the vehicle Ford C-MAX 2013. Through the equation of the power loss and the graph of power loss vs current (both provided), it is possible to extract the value of the series resistance of the inductor, 15mOhms. Certainly, the value is an estimation, but, considering that the power of the DC-DC converter of the article is in the same magnitude of our application, the estimation is valid. Moreover, the value found consists in an initial value to start the efficiency calculations, but this value is subject to changes. It is worthy pointing out that the resistance of the inductor is related with the length and cross-sectional area of the wire, changes in its value may implies in the size and the mass of the inductor.

The next characteristics estimated from the literature were the inductance and the size of the inductor, the minimum inductance of the inductor was defined as the one necessary to maintain the current ripple ratio small than 0.3, as recommend in the article [4]. Therefore, the initial inductance for our application was defined to 300uH considering that the boost operation power will be higher than 8kW and the buck operation power higher than 17kW.

Looking at the article [5], it refers to an inductor used in Ford prototype fuel cell vehicle. This inductor is designed for 150 A dc current with 50 A current ripple and the power loss of the core is around 120 W. The inductor weights more than 2 kg and has an approximate dimension of 150x100x60 mm³ (LxWxH) (0.9L). The inductance changes almost linearly from 190 uH to 70 uH with the DC bias current changes from 0 to 300 ampere.

Also looking at the report ORNL Prius Report 2010 [8], the following information of the DC-DC converter was extracted:

Table 4 - Information of Toyota Prius 2010

Design Feature	2010 Prius
DC-dc converter power rating	27 kW
Battery voltage	201.6 V
Filter capacitor (LV side)	470 Vdc, 315 μ F
Inductor	225.6 μ H at 1 kHz
Small resistor (HV side)	53.8 k Ω
Small filter capacitor (HV side)	860 Vdc, 0.562 μ F 900 Vdc, 0.8 μ F 950 Vdc, 0.562 μ F
Smoothing capacitor (HV side)	750 Vdc, 888 μ F

Item	Mass (kg)	Volume (L)
Inductor (without housing)	3.67	2.59

Parameter	2010 Prius
Bi-directional dc-dc converter SP, kW/kg.	27/5.1 = 5.3
Bi-directional dc-dc converter PD, kW/L.	27/4.8 = 5.7

We can verify that the power of the DC-DC converter of the Prius (27kW) is almost the same to the one used so far in our calculations. The DC-DC converter of Prius has 5.1Kg and 4.8L. Looking at the picture of the DC-DC converter provided in the report, we can verify that the inductor occupies approximately half of the volume.

From the information of the inductor used in the Ford vehicle and from the information of the Prius converter, in the table above, we can expect that the inductor after the design will have a mass of around 2kg - 4kg and a volume between 1L-3L.

It is important to point out that the DC-DC converter in the Prius is used as an inverter and, once the DC converter in Prius is also a half bridge, the information in the table was used to estimate the current in its inductor. Using the same procedure used to calculate the maximum current in our design, the maximum current calculated for the Prius inductor was 133A.

Efficiency Calculation Method Used

Efficiency considering only conduction Losses

To calculate the conduction losses in the converter the following formulas were used:

Boost Operation

$$\eta = \frac{V_{in} - V_{on}D - V_D D'}{V_{in}} * \frac{1}{\frac{R_L + R_{on}D + R_D D'}{RD'^2} + 1}$$

Buck Operation

$$\eta = \frac{\left(1 - \frac{D'V_D}{DV_{in}}\right)R}{R_L + DR_{ON} + D'R_D + R}$$

Where R_D is the diode resistance, V_D is the diode drop voltage, V_{ON} is the IGBT drop voltage, R_{ON} is the IGBT resistance, R_L is the inductor resistance and R the equivalent output resistance.

It is important to pay attention that: while in the boost operation the V_{OUT} corresponds to the battery voltage, in the buck operation the V_{OUT} corresponds to the ultra-capacitor voltage.

Obs.: The calculation done to find this final formulas is long and therefore it is attached in the Appendix 3.

Switching Losses

The switching losses calculation consists in the sum of the energies lost in the transistor and diode due to the switching phenomenon. Although the explanations done before gives a good understanding of the causes of the switching losses, the formulas provided are very simple and does not provide accurate values for the switching losses. In order to achieve more accurate values the following attempt was done. The method was obtained in [9] and the figure related with the calculation is shown below:

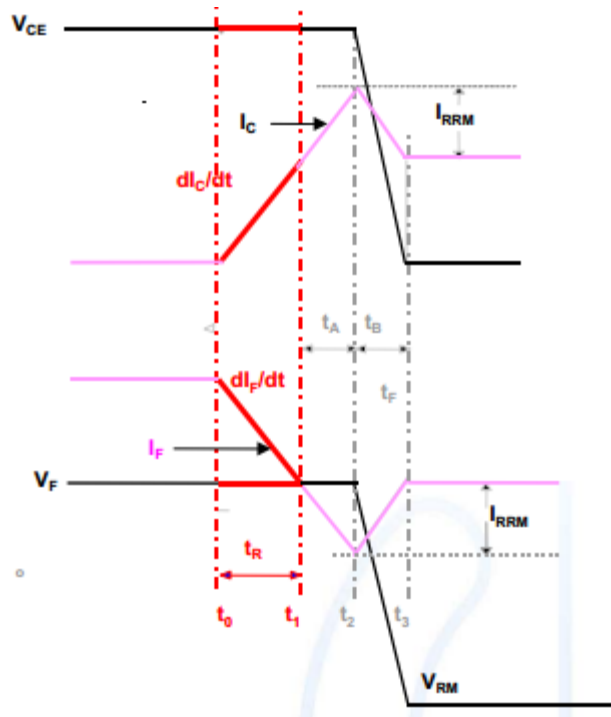


Figure 16 – Turn-on IGBT losses

The figure above shows in the top the waveforms related with the IGBT and in the bottom the waveforms related with the diode. The IGBT turn on process starts at t_0 and it will be divided in three subintervals: 1st subinterval: $t_0 < t < t_1$, 2nd subinterval: $t_1 < t < t_2$ and 3rd subinterval: $t_2 < t < t_3$. It is worthy pointing out that the recovery current in the diode was approximated by a triangular waveform. The formulas shown below corresponds to the boost operation and therefore the voltage across the switch at off state corresponds to the V_{OUT} .

Equations for energy lost in IGBT during turn on:

$$E_{on1} = \frac{V_{out} I_L t_R}{2}$$

$$E_{on2} = V_{out} \left(I_L + \frac{I_{RRM}}{2} \right) t_A$$

$$E_{on3} = V_{out} \left(\frac{I_L}{2} + \frac{I_{RRM}}{3} \right) t_B$$

Where:

$$\frac{dI_C}{dt} = \frac{I_L}{t_R} \quad t_A = \frac{I_{RRM}}{\frac{dI_C}{dt}}$$

The value I_L corresponds to the inductor current in the moment of switching; the value $\frac{dI_C}{dt}$ corresponds to the speed that the current decreases in the diode and increases in the switch, and it can be calculated using the I_L current and the period t_R , value provided in the datasheet. The value I_{RRM} was also extracted from the datasheet and corresponds to the diode maximum recovery current and this value proportion to collector

current and di/dt . Finally, the value t_b correspond to the fall time of the diode recovery current and it can be calculated using the formula shown below:

$$t_B = \sqrt{\frac{2Q_{RR}}{\frac{dI}{dt}}} - t_A$$

Where the value Q_{RR} corresponds to the total recovery charge of the diode also provided in the datasheet.

Equation for energy loss in Diode during IGBT turn on:

$$E_{Diode} = \frac{V_{out} I_{RRM} t_b}{6}$$

Equation for energy loss in IGBT during turn off:

For the IGBT turn off, as it does not involves the diode recovery current, the calculation is much simpler. The formula used is the same shown in the explanation of important aspects

$$E_{off} = \frac{V_{out} i_L (t_{off})}{2}, \text{ where } t_{off} = t_{d(off)} + t_f$$

$t_{d(off)}$ is the turn off delay time and t_f is the fall time provided in the datasheet.

The efficiency using the method above was also calculated for the Semikron device SKM 400GB066D. The Semikron website provides a tool that is possible to evaluate the losses in the components of a DC/DC converter providing some of the circuit variables. Therefore, the results obtained using the procedure showed above was compared to the results of the website tool. It was observed that the losses were in the same magnitude, although the errors were significant. The table below shows some examples of comparison:

Table 5 - Comparison of switching loss results with the Semikron tool

Input Parameters			Switching Loss (W)	
V_{IN} (V)	V_{OUT} (V)	I_{OUT} (A)	Calculated	Semikron Tool
150	300	150	501	636
200	250	100	145	232
250	380	175	577	716
250	380	200	692	816

Obs.: A Matlab file with the method implemented is attached with this report.

The difference in the results can rely in different factor: the model used, although it is more specific and take into account many variables, it still makes many assumptions as linear falling and rising current or triangular recovery current.

Researching for information from the Semikron supplier, the following formulas were provided in [10] for calculating switching losses in the boost operation:

IGBT loss:

$$P_{sw(T)} = f_{sw} \cdot E_{on+off} \cdot \left(\frac{I_{in}}{I_{ref}} \right)^{K_i} \cdot \left(\frac{V_{out}}{V_{ref}} \right)^{K_v} \cdot (1 + TC_{Esw} \cdot (T_j - T_{ref}))$$

Where E_{ON+OFF} is the value in the datasheet that represents the energy lost during the turn of and off of the IGBT for a given condition; I_{REF} , V_{REF} , T_{REF} are reference values of the switching loss measurements taken from the datasheet; $K_i \approx 1$ is an exponent for the current dependency of switching losses; $K_v \approx 1.3...1.4$ is an exponents for the voltage dependency of switching losses and $TC_{ESW} \approx 0.003/K$. is Temperature coefficients of the switching losses

Diode Loss:

$$P_{sw(D)} = f_{sw} \cdot E_{rr} \cdot \left(\frac{I_{in}}{I_{ref}} \right)^{K_i} \cdot \left(\frac{V_{out}}{V_{ref}} \right)^{K_v} \cdot (1 + TC_{Err} \cdot (T_j - T_{ref}))$$

Where $K_i \approx 0.6$, $K_v \approx 0.6$ and $TC_{ESW} \approx 0.006/K$.

Certainly, these formulas are an approximation and, differently from the method used before, it relates the total power loss more directly to the input variables, regardless of the intermediate losses calculations associate with each stage of the transition. Anyway, this formula must be more accurate for the device SKM 400GB066D than the calculation model in this report, because probably some experiments were done for different operations of the IGBT and a curve of losses that better fits these results was implemented. However, the model provided in this report can be a good switching loss approximation in case the supplier does not provide a specific formula for the losses.

Efficiency Results

The following efficiency results has used the conduction losses formulas shown before and the switching losses formulas of the Semikron Tool (without the temperature effects). This graphs below are based in the boost operation. In order to obtain more accurate results, the curves of voltage drop in the diode and in the IGBT provided in the datasheet was imported to the Matlab code making a curve fitting as shown below. It is worth pointing out that for the following graphs the value for the inductor resistance considered was 5mOhms.

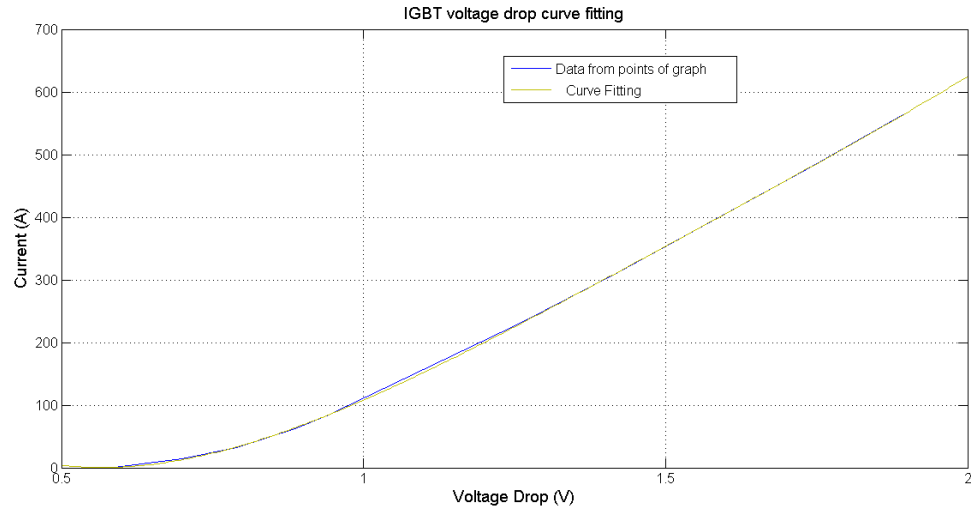


Figure 17– Curve Fitting for IGBT

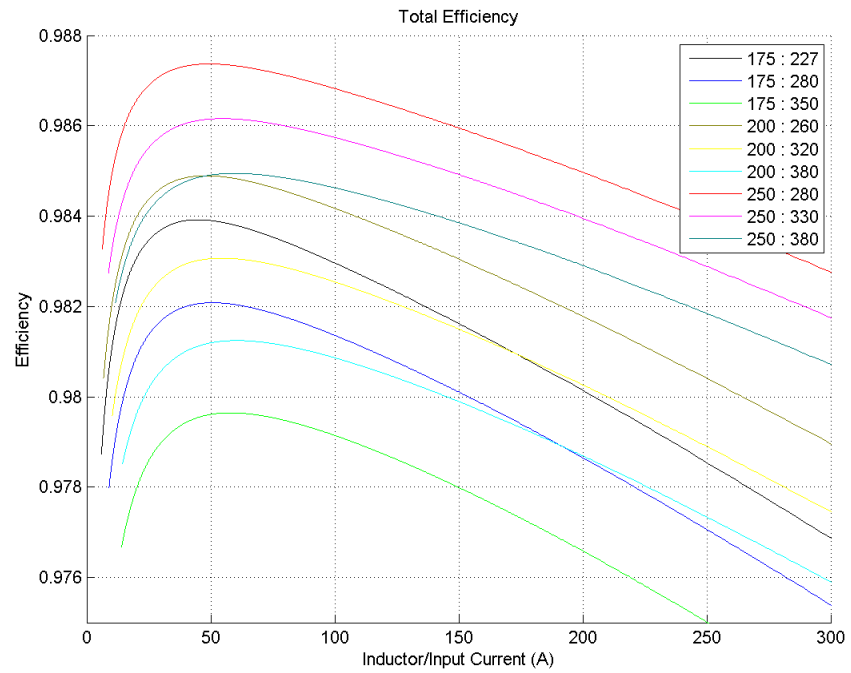


Figure 18 – Efficiency for different voltage ratios

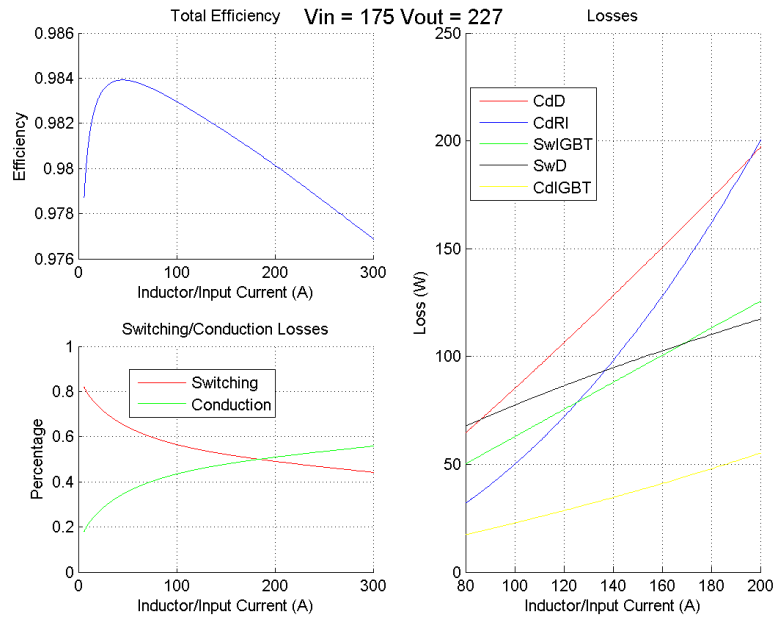


Figure 19 – Efficiency $V_{IN} = 175V$, $V_{OUT} = 227V$

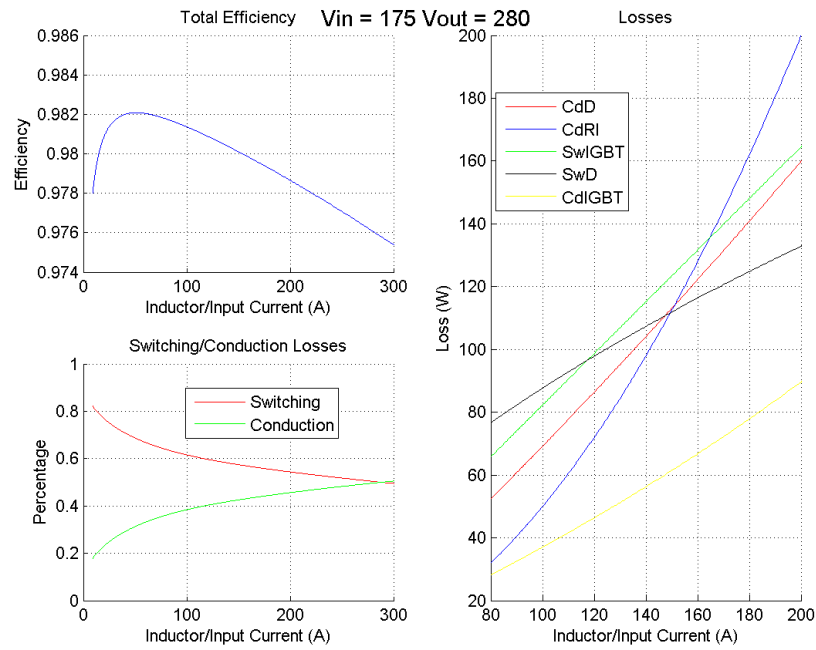


Figure 20 - Efficiency $V_{IN} = 175V$, $V_{OUT} = 280V$

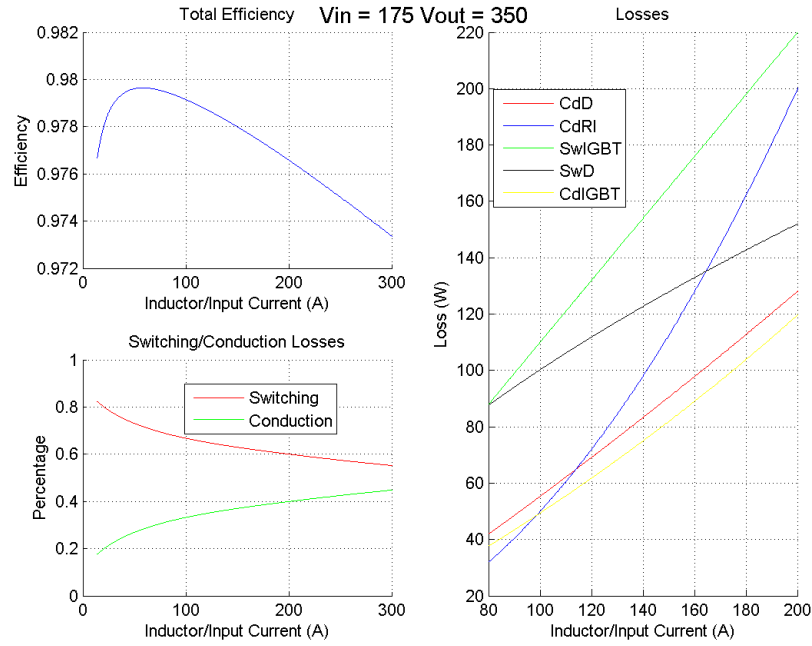


Figure 21 Efficiency $V_{IN} = 175V$, $V_{OUT} = 350V$

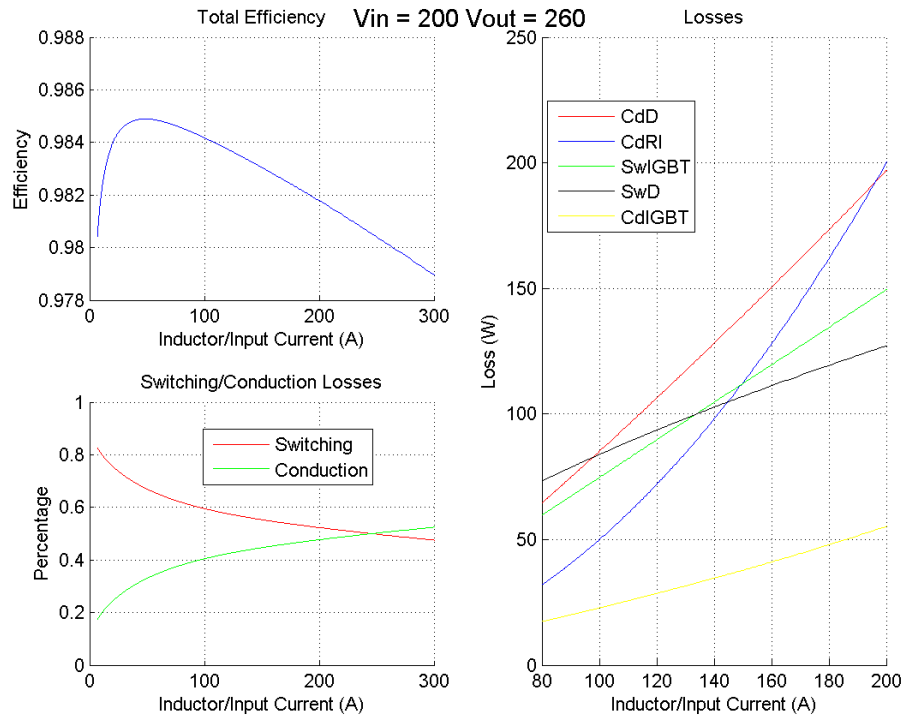


Figure 22 Efficiency $V_{IN} = 200V$, $V_{OUT} = 260V$

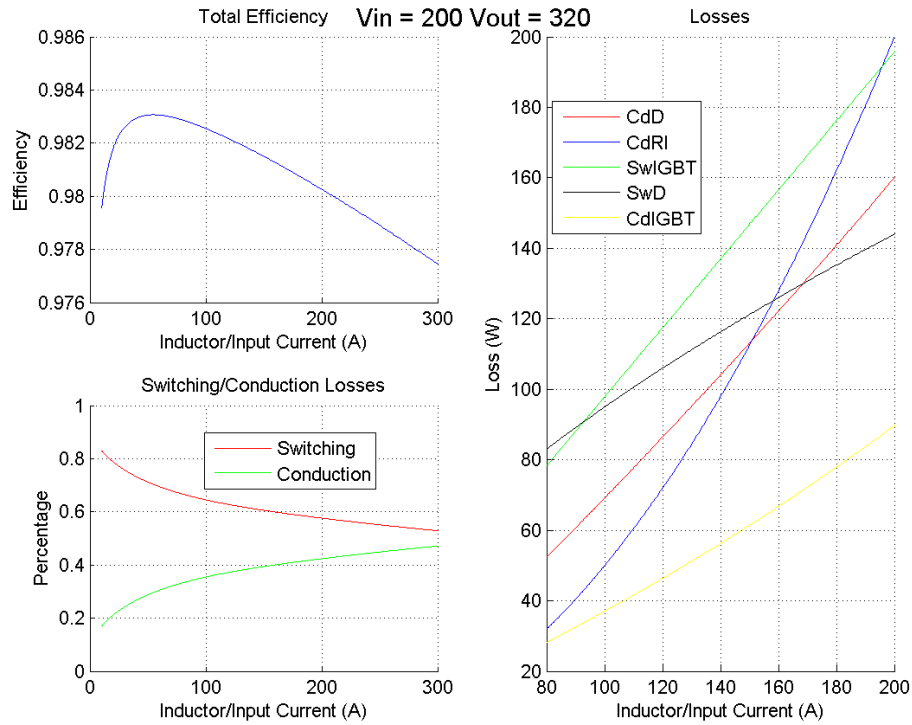


Figure 23 Efficiency $V_{IN} = 200V$, $V_{OUT} = 320V$

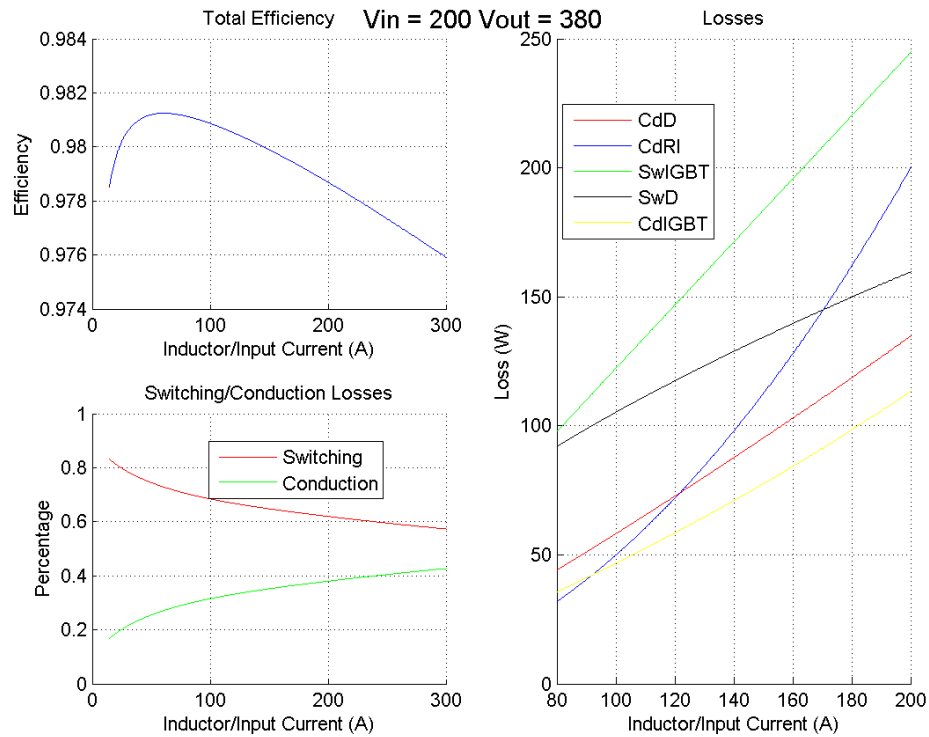


Figure 24 Efficiency $V_{IN} = 200V$, $V_{OUT} = 380V$

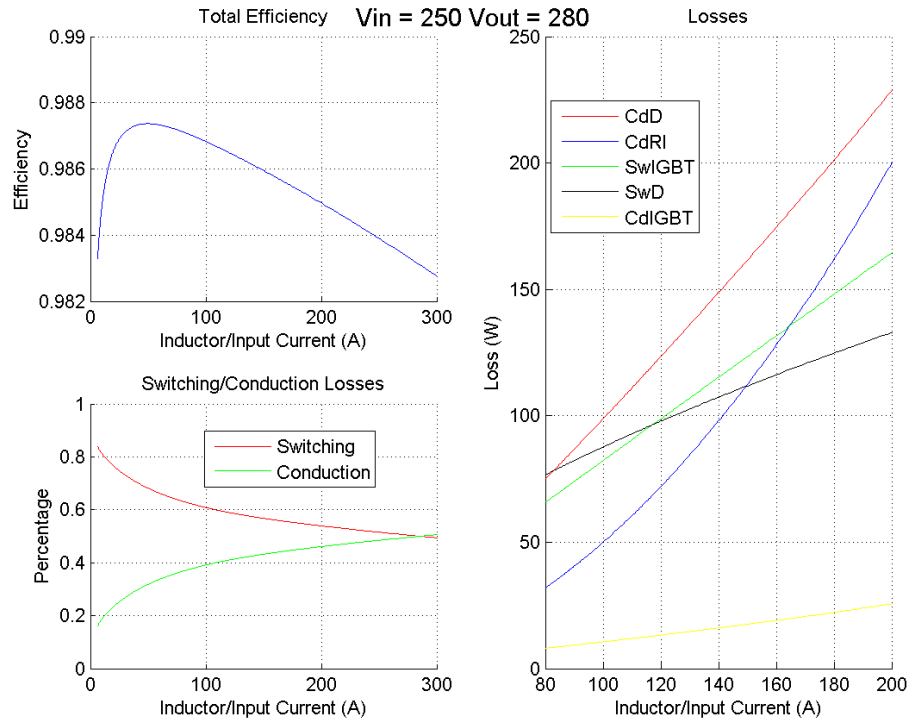


Figure 25 Efficiency $V_{IN} = 250V$, $V_{OUT} = 280V$

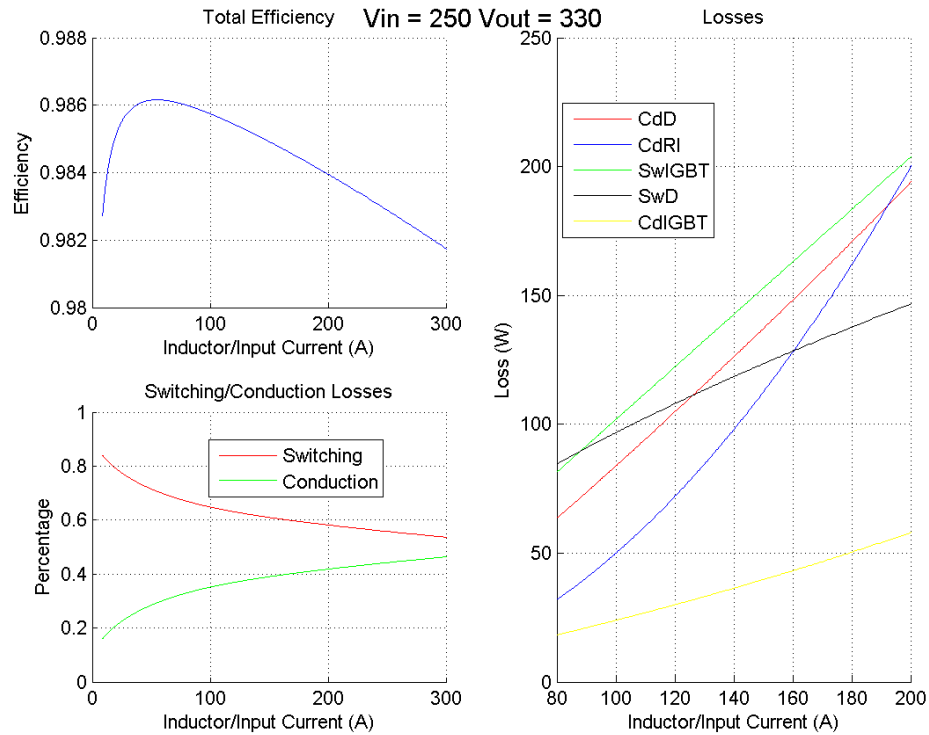


Figure 26 Efficiency $V_{IN} = 250V$, $V_{OUT} = 280V$

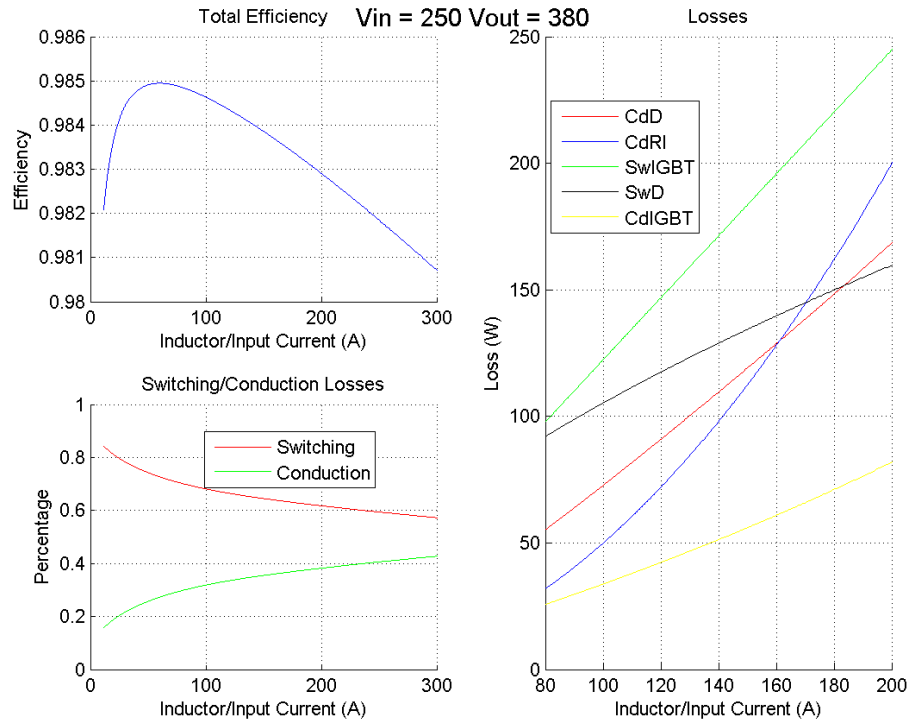


Figure 27 Efficiency $V_{IN} = 250V$, $V_{OUT} = 380V$

From the graphs above we can verify that all losses increase with the input current, and consequently with the power. Moreover, the power loss in the inductor is generally the smallest for low input currents, but it becomes the highest for high currents. In general, the power is well distributed between each power loss factor.

It is worthy pointing out that these graphs do not include the power loss due to the ripple current. However, if we implement the inductor of 300 μ H, the power due to ripple current would increase less than 1% the conduction losses. It can also affect the switching losses as the current in the switching devices will change and the input current in these devices influences its switching losses. This factor will be analyzed more precisely in the inductor design as it consists in a trade-off between inductor size and efficiency, the frequency of operation is also a factor plausible of change.

Appendix

1- Calculation of derived parameters

Boost Operation:

Table 6 - Initial Parameters for a 30kW – 50kW DC-DC converter

Min Ultra capacitor voltage	135V
Max Ultra capacitor voltage	270V
Battery min voltage	270V
Battery max voltage	395V
Switching Frequency	15KHz
Maximum Inductor Average Current	300A

Duty Cycle limits:

$$D = 1 - \frac{V_{in}}{V_{out}}$$

$$\text{Maximum duty cycle} = 1 - \frac{135}{395} = 0.66$$

$$\text{Minimum duty cycle} = 1 - \frac{270}{270} = 0 \text{ (the fraction } V_{in}/V_{out} \text{ can assume different values in the numerator and denominator)}$$

Input Current:

$$I_{in} = I_L = \frac{V_{in}}{R(1-D)^2} = \frac{V_{out}}{R(1-D)} = \frac{I_{out}}{1-D}$$

The maximum input current occurs when the inductor current is maximum.

$$\text{Max } (I_{in}) = 300A$$

Output Current:

$$I_{out} = \frac{I_{in}}{1-D} = \frac{I_L}{1-D}$$

The maximum output current occurs when the inductor current is maximum and D is maximum.

$$\text{Max } (I_{out}) = \frac{I_{in}}{1-D} = 882.32A \text{ (This current is too high for the components, it means that the control must limit the region of operation some voltage ratios)}$$

Inductor Ripple Current:

$$\Delta I_L = V_{in} D \frac{T_s}{2L} = \left(V_{in} - \frac{V_{in}^2}{V_{out}} \right) \frac{T_s}{2L}$$

Considering a constant value of switching frequency and a constant value of inductance, the maximum current ripple occurs when the value $\left(V_{in} - \frac{V_{in}^2}{V_{out}} \right)$ is the biggest. It happens when V_{OUT} is highest value, 395V, and to find the value of V_{IN} , it is only necessary to substitute the value of V_{OUT} and then find the peak of the one variable function. It occurs when $V_{IN} = 197.5V$ and $V_{OUT} = 395V$ and $D = 0.5$.

Another way of think is that $V_{IN} * D$ must be highest as possible and we know that:

$$V_{out} = \frac{V_{in}}{1 - D}$$

Therefore, if we increase the input current or the duty cycle the V_{OUT} is going to increase. Consequently, we want the highest value of V_{OUT} that means that neither V_{IN} nor D can be increased anymore. Once V_{OUT} must be the highest value as possible, this variable can be substitute for 395V, the duty cycle substitute by $1 - \frac{V_{in}}{V_{out}}$ and finally the equation can be solved for one variable.

Buck Operation:

Obs.: It is important to remind that in the buck operation, the Battery corresponds to V_{IN} and the ultra-capacitor corresponds to V_{OUT} . Moreover, it will be considered that the power that flows from the battery/inverter to the ultra-capacitor has the same rate of the power in the other direction (boost operation). Although, it is interesting to keep in mind that in most part of times the power from the ultra-capacitor to the battery/inverter is higher, as, generally the car accelerates with a higher module than it decelerates.

Duty Cycle limits:

$$D = \frac{V_{out}}{V_{in}}$$

$$V_{out} = V_{in} D$$

$$\text{Maximum duty cycle} = \frac{270}{270} = 1$$

$$\text{Minimum duty cycle} = \frac{135}{395} = 0.34$$

Input Current:

$$I_L = \frac{I_{in}}{D}$$

$Max(I_{in}) = 882.35A$ (This current is too high for the components, it means that the control must limit the region of operation some voltage ratios)

Output Current:

$$I_L = I_{out} = \frac{I_{in}}{D}$$

$$Max(I_{out}) = 300A$$

Inductor Ripple Current:

$$\Delta I_L = V_{out} (1 - D) \frac{T_s}{2L} = (V_{in} - V_{out}) D \frac{T_s}{2L} = (V_{out} - \frac{V_{out}^2}{V_{in}}) \frac{T_s}{2L}$$

Obs.: We can verify a similarity with the boost operation, comparing the equation above we can verify that it is the same of the calculated in the *Inductor Ripple Current* for the *Boost Operation* if the V_{OUT} is swapped with the V_{IN} . This interchange is exactly what occurs when analyzing the buck operation once the power flows in a reverse direction. In few words, it is only necessary to calculate the inductor ripple in one operation, as the result for both operations is the same.

2- Ratings of the components

Diodes: Analyzing the half-H circuit the following values for maximum blocking Voltage and maximum current for the diode are achieved:

In boost operation:

Diode₁ blocking voltage: $V_{OUT} (V_{BATTERY})$.

Diode₁ maximum current: maximum current in the inductor.

Diode₂ blocking voltage: $V_{OUT} (V_{BATTERY})$

In buck operation:

Diode₂ blocking voltage: $V_{IN} (V_{BATTERY})$.

Diode₂ maximum current: maximum current in the inductor.

Diode₁ blocking voltage: $V_{IN} (V_{BATTERY})$.

Switches (IGBT): Analyzing the half-H circuit the following values for maximum blocking voltage and maximum current for the IGBT are achieved

In boost operation:

IGBT₁ blocking voltage = Diode₂ blocking voltage: approximately $V_{OUT} (V_{BATTERY})$.

IGBT₁ maximum current: maximum current in the inductor.

IGBT₂ maximum current: maximum current in the inductor

In buck operation:

IGBT₂ blocking voltage = Diode₁ blocking voltage: approximately $V_{IN} (V_{BATTERY})$.

IGBT₂ maximum current: maximum current in the inductor.

IGBT₁ maximum current: maximum current in the inductor

3 Efficiency considering conduction losses

Boost Operation

We know that the average voltage in the inductor must be equal zero and that the average current in the capacitor must also be equal zero. Analyzing the on state and of state of the Boost converter as shown in the figure below, we can evaluate these average values by:

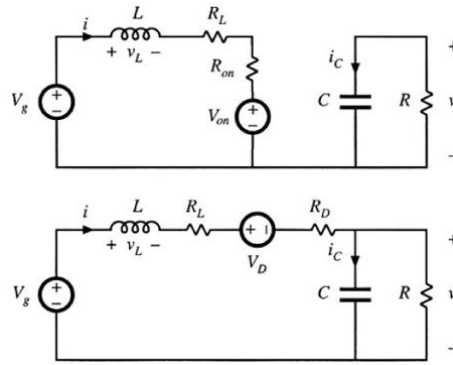


Figure 28 – Boost Converter at on state (top) and at off state (bottom)

$$\langle V_L \rangle = 0$$

$$(V_g - IR_L - IR_{on} - V_{on})D + (V_g - IR_L - V_D - IR_D - V)D' = 0$$

$$V_g - IR_L - IR_{on}D - V_{on}D - V_D D' - IR_D D' - VD' = 0$$

This equation can be represented by the following circuit:

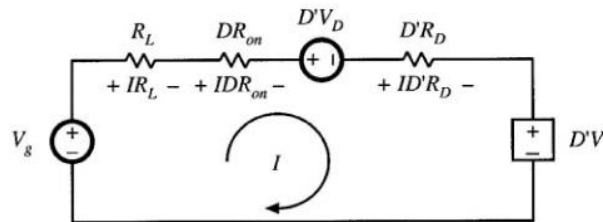


Figure 29 – Equivalent circuit for the equation $\langle V_L \rangle = 0$

$$\langle i_c \rangle = 0$$

$$-\frac{V}{R}D + \left(I - \frac{V}{R}\right)D' = 0$$

$$-\frac{V}{R} + D'I = 0$$

This equation can be represented by the following circuit:

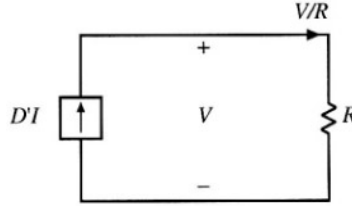


Figure 30 - Equivalent circuit for the equation $\langle I_C \rangle = 0$

These two circuits of figure 19 and figure 18 can be joined to an equivalent final equivalent circuit, that has an ideal transformer:

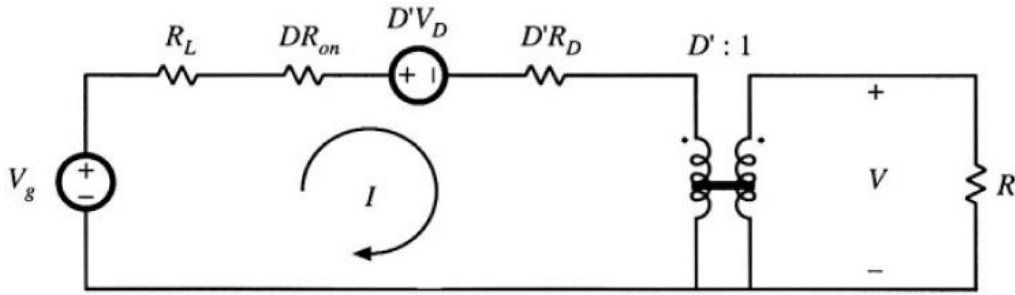


Figure 31 – Equivalent Circuit of the Boost Converter

With this equivalent circuit the efficiency can be easily calculated by:

$$V_g - I(R_L + R_{on}D + R_D D') - V_{on}D - V_D D' - D'V = 0$$

$$\frac{V}{V_g} = \frac{V_g - V_{on}D - V_D D'}{V_g} \frac{1}{D' + \frac{R_L + R_{on}D + R_D D'}{RD'^2}}$$

$$\eta = \frac{P_{out}}{P_{in}} = \frac{V_{out}D'I}{V_{in}I} = \frac{D'V_{out}}{V_{in}}$$

$$\eta = \frac{V_{in} - V_{on}D - V_D D'}{V_{in}} \frac{1}{1 + \frac{R_L + R_{on}D + R_D D'}{RD'^2}}$$

Buck Operation

In order to calculate the conduction losses an equivalent circuit model was used. As the average voltage in the inductor must be zero we have the following equation:

$$\langle V_L \rangle = D(V_G - IR_L - IR_{ON} - V) + D'(-V - V_D - IR_D - IR_L) = 0$$

$$DV_G - IR_L - DIR_{ON} - D' - D'IR_D = V$$

Where I is the output current, V_G is the input voltage. This equation can be represented by the following circuit:

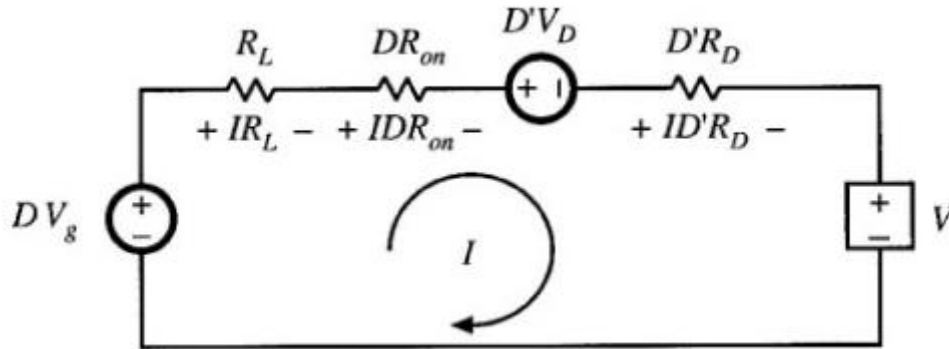


Figure 32 – Equivalent Circuit for the average voltage in the inductor

As the average current in the capacitor must be zero, we have the following equation:

$$\langle I_C \rangle = \left(I - \frac{V}{R}\right)D + D'\left(I - \frac{V}{R}\right) = 0$$

. This equation can be represented by the following circuit:

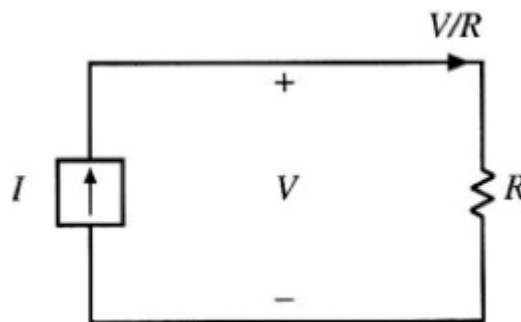


Figure 33 - Equivalent Circuit for the average current in the capacitor

These two circuits of figure 19 and figure 18 can be joined to an equivalent final equivalent circuit that has an ideal transformer:

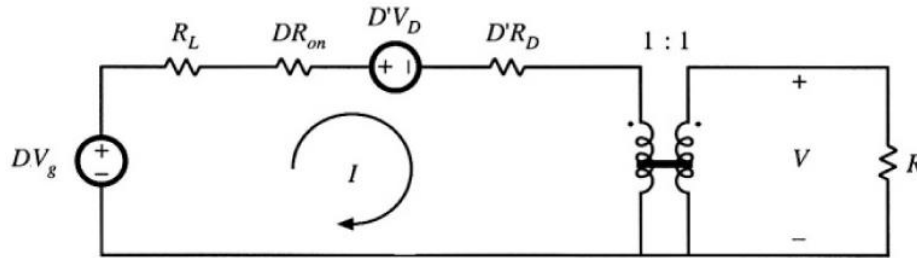


Figure 34 – Equivalent Circuit of the buck converter

Using the circuit model above the efficiency including the conduction losses is given by:

$$\eta = \frac{P_{out}}{P_{in}} = \frac{VI}{DV_G I} = \frac{V}{DV_G}$$

$$\eta = \frac{\left(1 - \frac{D'V_D}{DV_G}\right) R}{R_L + DR_{ON} + D'R_D + R}$$

3- Useful Links:

Video about diodes: <https://www.youtube.com/watch?v=JBtEckh3L9Q>

Video to understand MOSFET operation: <https://www.youtube.com/watch?v=zMAaZfh1yz8>

Terminology in datasheets:

<http://www.vishay.com/docs/84064/anphyexp.pdf>

http://www.allaboutcircuits.com/vol_3/chpt_3/3.html

http://www.infineon.com/dgdl/Infineon_Bipolar-AN20012_01_Technical_Information-AN-v1.0-en.pdf?folderId=db3a304412b407950112b408e8c90004&fileId=db3a304412b407950112b40ec42b126a

[http://www05.abb.com/global/scot/scot256.nsf/veritydisplay/f63a04e9734e7f0cc1257a590042f31c/\\$file/5SYA2053-04%20Applying%20IGBTs.pdf](http://www05.abb.com/global/scot/scot256.nsf/veritydisplay/f63a04e9734e7f0cc1257a590042f31c/$file/5SYA2053-04%20Applying%20IGBTs.pdf)

Bibliography

- [1] Phillip J. Kollmeyer, Larry W. Juang, T. M. Jahns, “Optimized Ultracapacitor Pack Sizing for Vehicles with Battery/Ultracapacitor Hybrid Energy Storage”, University of Wisconsin-Madison - Wisconsin Electric Machines and Power Electronics Consortium (WEMPEC)
- [2] Miller, J.M., Sartorelli, G., “Battery and Ultracapacitor Combinations – Where Should the Converter Go?”, Vehicle Power and Propulsion Conference, Sept. 2010, pp.1-7
- [3] R.M. Schupbach, J.C. Balda, “35kW Ultracapacitor unit for Power Management of Hybrid Electric Vehicles: Bi-directional dc-dc Converter Design,” The 35th IEEE Power Electronics Specialists Conference, PESC2004, Aachen, Germany
- [4] R.M. Schupbach, J.C. Balda, “Comparing dc-dc Converters for Power Management in Hybrid Electric Vehicles,” IEEE International Electric Machines and Drives Conference, IEMDC’03, Madison, WI, Vol.3,pgs 1369-1374, 1-4 June 2003
- [5] Robert W. Erickson, Dragan Maksimovic, “Fundamentals of Power Electronics, Second Edition”, University of Colorado Boulder: Kluwer Academic Publishers, 2004
- [6] Jin Wang, “Practical Design Considerations of Power Electronics in Hybrid and Fuel Cell Vehicles”, IEEE Vehicle Power and Propulsion Conference (VPPC), September 3-5, 2008, Harbin, China
- [7] Lihua Chen, “A Variable Voltage Converter with Direct Bypass for Traction Drive Inverters”, Energy Conversion Congress and Exposition (ECCE), 2013 IEEE
- [8] T. A. Burress, S. L. Campbell, C. L. Coomer, C. W. Ayers, A. A. Wereszczak, J. P. Cunningham, L. D. Marlino, L. E. Seiber, H. T. Lin, “EVALUATION OF THE 2010 TOYOTA PRIUS HYBRID SYNERGY DRIVE SYSTEM”, Oak Ridge National Laboratory, March 2011
- [9]http://www.micrus.ru/UPLOAD/fck/image/lines_pict/fchild/Understanding_Diode_Reverse_Recovery_And_Its_Effect_On_Switching_Losses_2007-09-10.pdf
- [10]http://www.semikron.com/skcompub/en/SEMIKRON_Application_Manual_Power_Semiconductors_.pdf

Appendix V – DC/DC Converter Control Design Report

Control of Power Transfer between an Ultracapacitor Pack and a Battery Pack using a Half-bridge DC-DC converter

Independent Study Report, Spring 2015

Anantharaghavan Sridhar
6/26/2015

This document summarizes the design and implementation methodology for a control system to regulate the current (and hence the power flow) between an ultracapacitor pack and a battery pack using a half-bridge DC-DC converter

Table of Contents

1. Introduction	437
1.1. Objective	437
1.2. Literature Review	438
2. Equipment.....	439
2.1. System Topology	439
2.2. System Parameter Specifications.....	439
3. Theoretical Model.....	440
3.1. Exact Continuous-Time Model with Sampling	440
3.2. Discrete-Time Averaged Model using Volt-seconds approximation	442
3.3.1. Discrete-time ultracapacitor voltage model	443
3.4.2. Discrete-time average current model.....	444
3.5.3. Discrete-time rate of change of average current model	445
3.6.4. Discrete-time rate of change of ultracapacitor voltage model	446
3.7.5. Discrete-time parsed relationships between states	446
4. Simulation Framework in MATLAB	448
4.1. Overview	448
4.2. PLECS simulation framework.....	448
4.3. Controller Implementation Topology	449
4.2.1. Disjoint buck-boost control topology	449
4.2.2. Drawback of disjoint buck-boost control topology.....	450
4.2.3. Smooth buck-boost control topology	450
5. Controller Design	451
5.1. Overview	451
5.1.1. Inner Control Loop – Current Mode Controller	451
5.1.2. Outer Control Loop – Voltage Mode Controller	452
5.2. Current-Mode Controller	452
5.2.1. Choice of sample frequency.....	452
5.2.2. General PID Overview	452
5.2.3. Controller Design	453
5.2.4. Practical considerations and controller tuning	455
5.3. Voltage-Mode Controller	456

5.3.1. Overview of topologies	456
5.3.2. Choice of sample frequency.....	457
5.3.3. Methodology used to choose the sample frequency	458
5.3.4. Controller Design	459
5.3.5. Practical considerations and controller tuning.....	462
5.4. Controller implementation	463
5.4.1. Over-current and over-temperature protection	463
5.4.2. Average current estimation	463
5.4.3. Ultracapacitor and Battery voltage limits enforcement	463
6. Experiments	465
6.1. Tests with DC Power Supply.....	465
6.1.1. Command Tracking Frequency Response Function (FRF).....	465
6.1.2. Dynamic Stiffness Frequency Response Function (FRF)	466
6.1.3. Sine Wave Tests	467
6.1.4. Square Wave Tests.....	468
6.2. Tests with Battery	469
6.2.1. State machine test for limit operation.....	469
6.2.2. Current profile test	471
7. Summary	474
8. Future Work	475
9. References	476

1. Introduction

1.1. Objective

Build a working, state-of-the-art controller to control power transfer between an ultracapacitor pack and a battery pack in a hybrid energy storage system using the existing half-bridge bidirectional dc-dc power converter and a dSpace embedded platform programmable using MATLAB/Simulink.

Specifically:

1. Design and validate the controller using MATLAB simulations
 - a. Develop a complete system model (DC-DC Converter, ultracapacitor pack, battery pack)
 - i. Generic, so that circuit specs can be modified
 - ii. Include battery and ultracapacitor model (voltage and resistance)
 - iii. Model motor drive as dc current sink/source
 - b. Design controller for ultracapacitor voltage and ultracapacitor current
 - i. Should be capable of charging ultracapacitor pack up from 0V
 - c. Analyse stability and determine operating range
 - d. Desired bandwidth $\sim 100\text{Hz}$ for the ultracapacitor current control
2. Implementation – using dSpace Hardware
 - a. Migrate Simulink (+MATLAB) design to dSpace
 - b. Develop a robust signal/measurement interface to the controller
 - c. Add protection and limit features to control design, including: ultracapacitor under and over voltage, battery pack under and over voltage, semiconductor instantaneous over current and input and output current limits
 - d. Demonstrate controller operation at limit conditions e.g. it can transition from hitting ultracapacitor under voltage limit while discharging, back to ultracapacitor charging with no delay
3. Evaluation and Testing
 - a. Comprehensive controls performance testing
 - b. Power conversion efficiency characteristics

1.2. Literature Review

[7] describes the development of a nonlinear system model and a Lyapunov-based control strategy for a supercapacitor-fuel cell hybrid energy system. Results are discussed only based on numerical simulations. The primary metrics discussed in the paper are command tracking and dynamic stiffness (the author refers to the dynamic stiffness as DC bus voltage regulation).

In contrast, this independent study presents a linear system model and demonstrates excellent command tracking and dynamic stiffness properties, with experimental results.

[8] describes the development of a “dynamic evolution control” technique to achieve the same objectives for an ultracapacitor-fuel cell hybrid energy system. The author mentions that the controller gains are variable and claims better performance, but has not offered any analysis on the system stability. Physical insight into the controller development is also missing.

In contrast, this independent study presents a system and controls model with physical insight and demonstrates stability on the basis of root-locus techniques and extensive time-domain tests on hardware.

[9] describes the development of a Model Predictive Controller (MPC) for a similar system, the difference being the use of a full-bridge DC-DC converter. The author demonstrates a complex model for the system and presents results only through simulation, and does not present a clear design and implementation methodology.

In contrast, this independent study presents a clear design and implementation method and outlines the important criteria used for the controller.

[10] describes the usage of a PI controller for the same type of system and shows experimental results for the same. However, the author has presented only the system architecture but not presented any design methodology used. Also, results have been demonstrated only using the DC power supply but not using a Fuel-cell (or) Battery, where the bus voltage fluctuations will be significant.

In contrast, this independent study presents results from using both the DC power supply and the battery, and demonstrates equivalent closed-loop system performance in both cases.

[11] describes the development of a sliding mode controller for a half-bridge DC-DC converter system for controlling energy flow between the ultracapacitor and a power source. No experimental results have been shown and the controls methodology presents by the author is mathematically intensive and a clear presentation of the model validity and impact on the parameter estimates is missing.

In contrast, this independent study presents a simple, traditional PI control structure and the technique to tune it appropriately, along with demonstrating that approximate parameter estimates are sufficient for the controller design, thereby signifying robustness to parameter estimation uncertainty and parameter variations.

2. Equipment

The hardware setup was created by a previous student, Renato Amorim Torres [1], the control structures have been developed for this setup, along with some minor changes in the hardware.

2.1. System Topology

The system topology is illustrated in Figure 2.1.

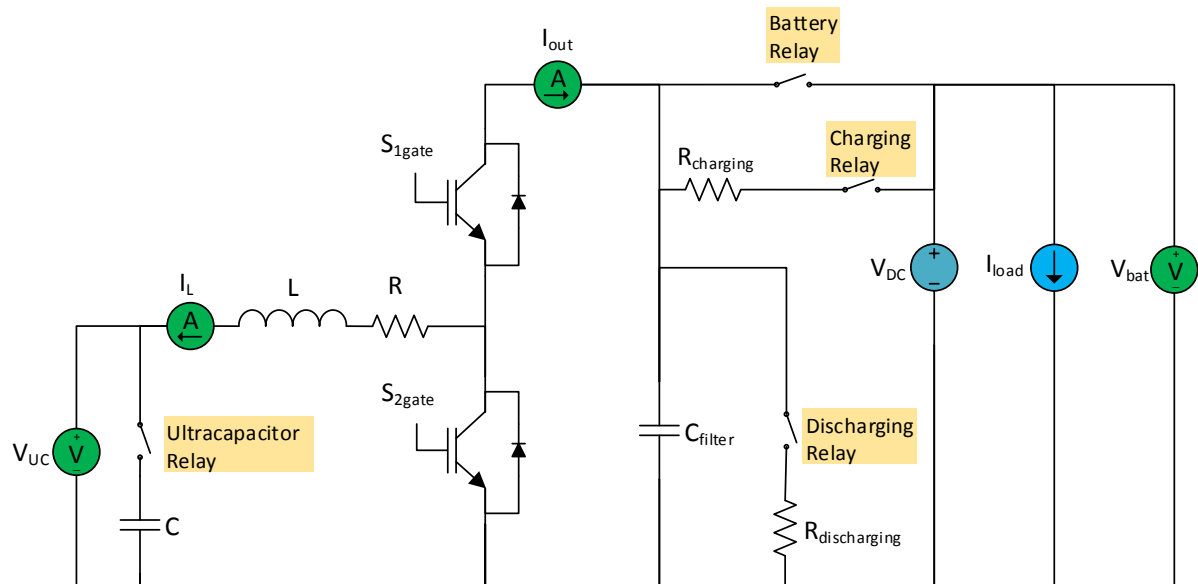


Fig 2.1 Hardware topology of the test setup

2.2. System Parameter Specifications

The parameter estimates from the system specifications are detailed below.

Component	Value	Description
Ultracapacitor	188 F	5.5 m Ω parasitic resistance
Inductor	195 μ H	3 x 65 μ H inductances in series, 1.2 m Ω parasitic resistance each
Parasitic Resistance	9.1 m Ω	Lumped parasitic resistance estimate
IGBT		Semikron SKiiP 402GD061-358CTV
Voltage Sensors	0-500V (rated)	LEM LV25-P
Current Sensors	0-300A (rated)	LEM LA205-S
Filter Capacitance	2400 μ F	
Table 2.1. Parameter estimates summary		

3. Theoretical Model

There are two different approaches that may be considered when building a theoretical model for this DC-DC converter system. Both modelling approaches were developed, and have been described in detail in the following subsections. The averaged model was finally chosen for further work since it offered the simplicity and abstraction needed to complete the controls development and implementation within the planned timeframe.

Model assumptions:

1. Constant DC Bus Voltage
2. Ideal Switches
IGBT switching delays and “on” resistance have been ignored.
3. Linear Inductance
Inductance is assumed to be constant. Parasitic resistance estimate of the inductance has been borrowed from the specifications.
4. Simple capacitance model for the ultracapacitor
The ultracapacitor has been modelled as a linear capacitance. Parasitic series resistance estimate borrowed from the specifications. Self-discharge of the ultracapacitor has not been modelled.
5. Simple drive model
Drive has been modelled as an ideal current source.

3.1. Exact Continuous-Time Model with Sampling

This model predicts the exact instantaneous current value in the system, accounting for the transients within every PWM cycle. The model developed is capable of accommodating predicted switching delays, but these delays have not been analysed or calculated for the current system. In other words, the simulations and validation done for this model assume zero switching delay. A note at the end of this section explains a method to incorporate the switching delays in this model.

Case 1: Top IGBT is ON, Bottom IGBT is OFF (Battery Connected)

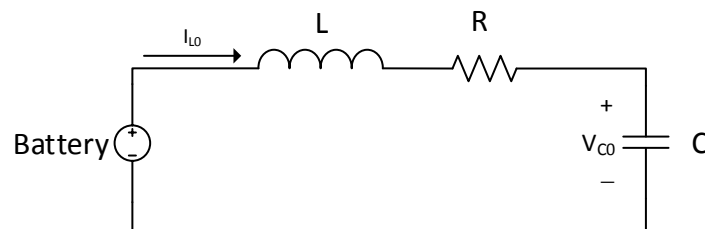


Fig 3.1. Circuit representation when the battery is connected to the system

Writing the s-domain equations for the circuit in Figure 3.1,

$$\frac{V_{bat}}{s} - \left(I_L(s) sL - I_L(0^-) L \right) - \left(I_L(s) \frac{1}{sC} + \frac{V_C(0^-)}{s} \right) - I_L(s) R = 0 \quad (1)$$

Using $I_{L0} = I_L(0^-)$, and $V_{C0} = V_C(0^-)$ henceforth, and rearranging,

$$I_L(s) = \frac{V_{bat} - V_{C0}}{L} \frac{1}{s^2 + s \frac{R}{L} + \frac{1}{LC}} + I_{L0} \frac{s}{s^2 + s \frac{R}{L} + \frac{1}{LC}} \quad (2)$$

$$\omega_r = \frac{1}{\sqrt{LC}} \quad (3)$$

ω_r is the resonant frequency of the system.

$$\delta = \frac{R}{2} \sqrt{\frac{C}{L}} \quad (4)$$

δ is the damping factor of the system.

$$I_L(s) = \frac{V_{bat} - V_{C0}}{L} \frac{1}{s^2 + s 2\delta\omega_r + \omega_r^2} + I_{L0} \frac{s}{s^2 + s 2\delta\omega_r + \omega_r^2} \quad (5)$$

Roots of the quadratic equation,

$$\text{roots}(s^2 + s 2\delta\omega_r + \omega_r^2) = \omega_r^2 \left(-RC + \sqrt{R^2 C^2 - 4LC} \right), \quad \omega_r^2 \left(-RC - \sqrt{R^2 C^2 - 4LC} \right) \quad (6)$$

$$p_1 = -\omega_r^2 \left(-RC + \sqrt{R^2 C^2 - 4LC} \right) \quad (7)$$

$$p_2 = -\omega_r^2 \left(-RC - \sqrt{R^2 C^2 - 4LC} \right) \quad (8)$$

For the purposes of this study, the roots will be assumed to be real values (i.e. the system is assumed to be overdamped in nature). This is indeed the case based on the parameter estimates of the test system, so this assumption is valid.

$$I_L(s) = \frac{V_{bat} - V_{C0}}{L} \frac{1}{(s + p_1)(s + p_2)} + I_{L0} \frac{s}{(s + p_1)(s + p_2)} \quad (9)$$

Resolving into partial fractions,

$$I_L(s) = \frac{V_{bat} - V_{C0}}{L} \left\{ \frac{1}{p_2 - p_1} \frac{1}{(s + p_1)} - \frac{1}{p_2 - p_1} \frac{1}{(s + p_2)} \right\} + I_{L0} \left\{ \frac{-p_1}{p_2 - p_1} \frac{1}{(s + p_1)} + \frac{p_2}{p_2 - p_1} \frac{1}{(s + p_2)} \right\} \quad (10)$$

Taking the inverse laplace transform

$$i_L(t) = \frac{V_{bat} - V_{C0}}{L} \left(\frac{1}{p_2 - p_1} \right) \left(e^{-p_1 t} - e^{-p_2 t} \right) + I_{L0} \left(\frac{1}{p_2 - p_1} \right) \left(-p_1 e^{-p_1 t} + p_2 e^{-p_2 t} \right) \quad (11)$$

This is the exact continuous time model for the system when the battery is connected. Since the measurements are sampled values, to estimate the samples we use $t = kT_s$, where k corresponds to the k^{th} sample, and T_s is the sampling frequency.

An important point to note that, for this model, k (or t) should be relative to when this mode was turned on. In other words, the sample instant (or time) used in the model is relative to the instant

when the battery was connected to the system (i.e. the instant when the top IGBT was turned on). The initial values of the inductor current and the ultracapacitor voltage should be used appropriately.

Case 2: Top IGBT is OFF, Bottom IGBT is ON (Battery Disconnected)

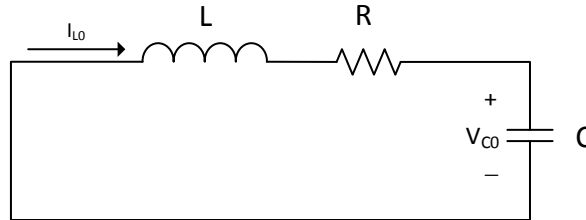


Fig 3.2. Circuit representation when the battery is disconnected from the system

This case is just equivalent the battery voltage being set to zero in the previously developed model for the battery connected scenario. Consequently,

$$i_L(t) = \frac{-V_{C0}}{L} \left(\frac{1}{p_2 - p_1} \right) \left(e^{-p_1 t} - e^{-p_2 t} \right) + I_{L0} \left(\frac{1}{p_2 - p_1} \right) \left(-p_1 e^{-p_1 t} + p_2 e^{-p_2 t} \right) \quad (12)$$

The initial values of the inductor current and the ultracapacitor voltage should be used appropriately.

3.2. Discrete-Time Averaged Model using Volt-seconds approximation

The “volt-seconds approximation” refers to the use of the average applied voltage in a PWM cycle as manipulated input to the system model. Figure 3.3 illustrates the volt-seconds approximation.

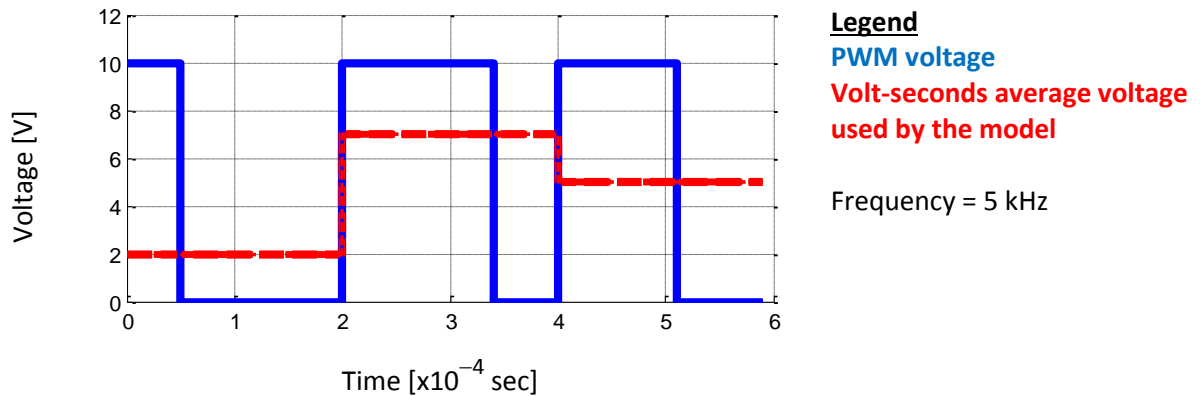


Fig. 3.3. Illustration of the volt-seconds approximation

Since the volt-seconds approximation just refers to the average voltage applied per PWM cycle, the model is described as a “discrete-time averaged model”.

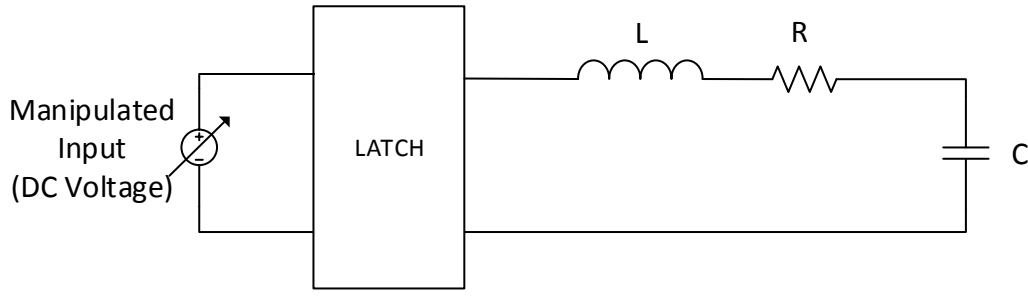


Fig. 3.4. System representation used for the discrete-time model with volt-seconds approximation

3.3.1. Discrete-time ultracapacitor voltage model

The s-domain system model (including the model of the latch interface) is described in equation (13).

$$\frac{V_{UC}(s)}{V(s)} = \left(\frac{1-e^{-sT}}{s} \right) \left(\frac{1}{R + sL + \frac{1}{sC}} \right) \frac{1}{sC} \quad (13)$$

$$\frac{V_{UC}(s)}{V(s)} = \left(\frac{1-e^{-sT}}{s} \right) \frac{1}{LC} \left(\frac{1}{s^2 + s \frac{R}{L} + \frac{1}{LC}} \right) \quad (14)$$

$$\omega_r = \frac{1}{\sqrt{LC}} \quad (15)$$

$$\delta = \frac{R}{2} \sqrt{\frac{C}{L}} \quad (16)$$

$$\frac{V_{UC}(s)}{V(s)} = \left(\frac{1-e^{-sT}}{s} \right) \omega_r^2 \left(\frac{1}{s^2 + s 2\delta\omega_r + \omega_r^2} \right) \quad (17)$$

Roots of the quadratic equation,

$$\text{roots}(s^2 + s 2\delta\omega_r + \omega_r^2) = \omega_r^2 \left(-RC + \sqrt{R^2C^2 - 4LC} \right), \quad \omega_r^2 \left(-RC - \sqrt{R^2C^2 - 4LC} \right) \quad (18)$$

$$p_1 = -\omega_r^2 \left(-RC + \sqrt{R^2C^2 - 4LC} \right) \quad (19)$$

$$p_2 = -\omega_r^2 \left(-RC - \sqrt{R^2C^2 - 4LC} \right) \quad (20)$$

For the purposes of this study, the roots will be assumed to be real values (i.e. the system is assumed to be overdamped in nature). This is indeed the case based on the parameter estimates of the test system, so this assumption is valid.

$$\frac{V_{UC}(s)}{V(s)} = \left(1-e^{-sT} \right) \omega_r^2 \frac{1}{s(s+p_1)(s+p_2)} \quad (21)$$

$$\frac{V_{UC}(s)}{V(s)} = \left(1-e^{-sT} \right) \omega_r^2 \left\{ \frac{\left(\frac{1}{p_1 p_2} \right)}{s} + \frac{\left(\frac{1}{p_1(p_1-p_2)} \right)}{s+p_1} + \frac{\left(\frac{1}{p_2(p_2-p_1)} \right)}{s+p_2} \right\} \quad (22)$$

Resolving partial fractions and converting to Z-transform

$$\frac{V_{UC}(z)}{V(z)} = (1-z^{-1}) \omega_r^2 \left\{ \frac{1}{p_1 p_2} \left(\frac{1}{1-z^{-1}} \right) + \frac{1}{p_1(p_1-p_2)} \left(\frac{1}{1-e^{-p_1 T} z^{-1}} \right) + \frac{1}{p_2(p_2-p_1)} \left(\frac{1}{1-e^{-p_2 T} z^{-1}} \right) \right\} \quad (23)$$

Cross-multiplying the expression inside the curly braces, the numerator simplifies to:

$$\text{numerator} = z^{-1} k_a [1 - \delta_z z^{-1}] \quad (24)$$

$$k_a = (p_1 - p_2) + p_2 e^{-p_1 T} - p_1 e^{-p_2 T} \quad (25)$$

$$\delta_z = -\frac{(p_1 - p_2) e^{-(p_1 + p_2)T} + p_2 e^{-p_2 T} - p_1 e^{-p_1 T}}{k_a} \quad (26)$$

$$\text{denominator} = p_1 p_2 (p_1 - p_2) (1-z^{-1}) (1-e^{-p_1 T} z^{-1}) (1-e^{-p_2 T} z^{-1}) \quad (27)$$

$$\delta_{p1} = e^{-p_1 T} \quad (28)$$

$$\delta_{p2} = e^{-p_2 T} \quad (29)$$

Using equations (24) – (29) in (23)

$$\frac{V_{UC}(z)}{V(z)} = \frac{k_a}{p_1 p_2 (p_1 - p_2)} \omega_r^2 \frac{z^{-1} [1 - \delta_z z^{-1}]}{(1 - \delta_{p1} z^{-1}) (1 - \delta_{p2} z^{-1})} \quad (30)$$

$$k_b = \frac{k_a}{p_1 p_2 (p_1 - p_2)} \quad (31)$$

$$\frac{V_{UC}(z)}{V(z)} = k_b \omega_r^2 \frac{z^{-1} [1 - \delta_z z^{-1}]}{(1 - \delta_{p1} z^{-1}) (1 - \delta_{p2} z^{-1})} \quad (32)$$

3.4.2. Discrete-time average current model

Using the system model with latch interface (as used before),

$$\frac{I_L(s)}{V(s)} = \left(\frac{1-e^{-sT}}{s} \right) \left(\frac{1}{R + sL + \frac{1}{sC}} \right) \quad (33)$$

$$\frac{I_L(s)}{V(s)} = (1-e^{-sT}) \frac{C}{LC} \left(\frac{1}{s^2 + s \frac{R}{L} + \frac{1}{LC}} \right) \quad (34)$$

$$\frac{I_L(s)}{V(s)} = (1-e^{-sT}) \omega_r^2 C \left(\frac{1}{s^2 + s \frac{R}{L} + \frac{1}{LC}} \right) \quad (35)$$

$$\frac{I_L(s)}{V(s)} = (1-e^{-sT}) \omega_r^2 C \frac{1}{(s + p_1)(s + p_2)} \quad (36)$$

$$\frac{I_L(s)}{V(s)} = (1 - e^{-sT}) \omega_r^2 C \left\{ \frac{1}{(p_2 - p_1)} \left(\frac{1}{s + p_1} \right) + \frac{1}{(p_1 - p_2)} \left(\frac{1}{s + p_2} \right) \right\} \quad (37)$$

Resolving partial fractions and converting to Z-transform

$$\frac{I_L(z)}{V(z)} = (1 - z^{-1}) \omega_r^2 C \left\{ \frac{1}{(p_2 - p_1)} \left(\frac{1}{1 - e^{-p_1 T} z^{-1}} \right) + \frac{1}{(p_1 - p_2)} \left(\frac{1}{1 - e^{-p_2 T} z^{-1}} \right) \right\} \quad (38)$$

$$\frac{I_L(z)}{V(z)} = (1 - z^{-1}) \omega_r^2 C \frac{1}{(p_1 - p_2)} \left\{ - \left(\frac{1}{1 - e^{-p_1 T} z^{-1}} \right) + \left(\frac{1}{1 - e^{-p_2 T} z^{-1}} \right) \right\} \quad (39)$$

$$\frac{I_L(z)}{V(z)} = (1 - z^{-1}) \omega_r^2 C \frac{1}{(p_1 - p_2)} \left\{ \frac{z^{-1} [e^{-p_2 T} - e^{-p_1 T}]}{(1 - e^{-p_1 T} z^{-1}) (1 - e^{-p_2 T} z^{-1})} \right\} \quad (40)$$

$$k_d = \frac{[e^{-p_2 T} - e^{-p_1 T}]}{(p_1 - p_2)} \quad (41)$$

$$\frac{I_L(z)}{V(z)} = k_d \omega_r^2 C \left\{ \frac{z^{-1} (1 - z^{-1})}{(1 - \delta_{p1} z^{-1}) (1 - \delta_{p2} z^{-1})} \right\} \quad (42)$$

3.5.3. Discrete-time rate of change of average current model

$$\frac{s I_L(s)}{V(s)} = (1 - e^{-sT}) \omega_r^2 C \frac{s}{(s + p_1) (s + p_2)} \quad (43)$$

$$\frac{I_L'(s)}{V(s)} = (1 - e^{-sT}) \omega_r^2 C \left\{ \frac{p_1}{p_1 - p_2} \left(\frac{1}{s + p_1} \right) - \frac{p_2}{p_1 - p_2} \left(\frac{1}{s + p_2} \right) \right\} \quad (44)$$

Resolving partial fractions and converting to Z-transform

$$\frac{I_L'(z)}{V(z)} = (1 - z^{-1}) \frac{\omega_r^2 C}{(p_1 - p_2)} \left\{ \frac{p_1}{(1 - \delta_{p1} z^{-1})} - \frac{p_2}{(1 - \delta_{p2} z^{-1})} \right\} \quad (45)$$

$$\frac{I_L'(z)}{V(z)} = (1 - z^{-1}) \frac{\omega_r^2 C}{(p_1 - p_2)} \left\{ \frac{[p_1 - p_2] - [p_1 \delta_{p2} - p_2 \delta_{p1}] z^{-1}}{(1 - \delta_{p1} z^{-1}) (1 - \delta_{p2} z^{-1})} \right\} \quad (46)$$

$$\frac{I_L'(z)}{V(z)} = (1 - z^{-1}) \frac{\omega_r^2 C}{(p_1 - p_2)} \left\{ \frac{[p_1 - p_2] - [p_1 \delta_{p2} - p_2 \delta_{p1}] z^{-1}}{(1 - \delta_{p1} z^{-1}) (1 - \delta_{p2} z^{-1})} \right\} \quad (47)$$

$$\delta_{z2} = \frac{p_1 \delta_{p2} - p_2 \delta_{p1}}{p_1 - p_2} \quad (48)$$

$$\frac{I_L'(z)}{V(z)} = \omega_r^2 C \left\{ \frac{(1 - z^{-1}) (1 - \delta_{z2} z^{-1})}{(1 - \delta_{p1} z^{-1}) (1 - \delta_{p2} z^{-1})} \right\} \quad (49)$$

3.6.4. Discrete-time rate of change of ultracapacitor voltage model

$$\frac{s V_{UC}(s)}{V(s)} = (1 - e^{-sT}) \omega_r^2 \frac{1}{(s + p_1)(s + p_2)} \quad (50)$$

This equation only differs from equation (42) for the average current model by scaling (in both the s and the z domains), and hence the previous result can be used to derive the relationship for the rate of change of ultracapacitor voltage.

$$\frac{V_{UC}'(z)}{V(z)} = k_d \omega_r^2 \left\{ \frac{z^{-1} (1 - z^{-1})}{(1 - \delta_{p1} z^{-1})(1 - \delta_{p2} z^{-1})} \right\} \quad (51)$$

$$\frac{V_{UC}'(z)}{V(z)} = \frac{1}{C} \frac{I_L(z)}{V(z)} \quad (52)$$

3.7.5. Discrete-time parsed relationships between states

By definition

$$\frac{I_L(z)}{\Delta I_L(z)} = \frac{1}{1 - z^{-1}} \quad (53)$$

From equations (42), (49) and (53)

$$\frac{\Delta I_L(z)}{I_L'(z)} = k_d z^{-1} \left(\frac{1 - z^{-1}}{1 - \delta_{z2} z^{-1}} \right) \quad (54)$$

From equations (32) and (52)

$$\frac{V_{UC}(z)}{V_{UC}'(z)} = \frac{k_b}{k_d} \left(\frac{1 - \delta_z z^{-1}}{1 - z^{-1}} \right) \quad (55)$$

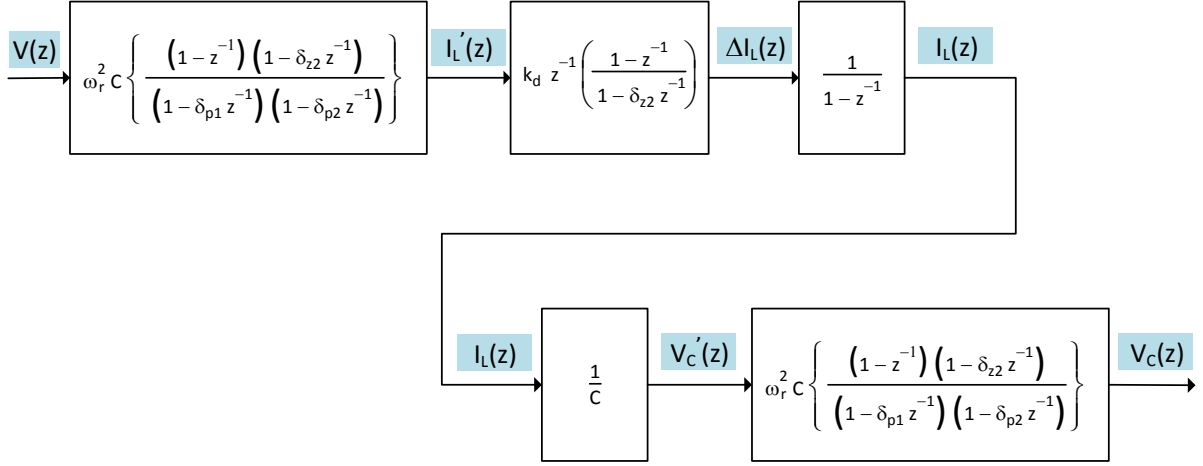


Fig. 3.5. Comprehensive discrete-time state block diagram of the complete system

The state sequence found in the block diagram above is described below:

1. $V(z)$ – The manipulated input, average voltage applied for one time period; in other words, the volt-seconds input
2. $l_L'(z)$ – Instantaneous rate of change of average current at every sample instant
3. $\Delta l_L(z)$ – Average current difference between subsequent samples
4. $l_L(z)$ – Instantaneous value of average current
5. $V_{UC}'(z)$ – Instantaneous rate of change of ultracapacitor voltage
6. $V_{UC}(z)$ – Instantaneous value of ultracapacitor voltage

The states listed above are in descending order in terms of how fast they change in the system, i.e. the manipulated input is the fastest changing quantity, the rate of change of average current is the second fastest changing quantity and so on.

Also, the current is intentionally referred to as the “average current” to represent the fact that in an actual PWM DC-DC converter system, the current waveform would have transients within the PWM cycle. The model however, assumes linearly controllable variable DC source (volt-sec approximation) and consequently the current model conforms to the average current within the PWM cycle.

4. Simulation Framework in MATLAB

4.1. Overview

The simulation framework has been built in MATLAB using three different methods:

1. Exact continuous-time model with sampling
2. Discrete-time averaged model using volt-seconds approximation
3. Plecs MATLAB blockset for power electronics modelling

Since Plecs is a known, well-received Power Electronics simulation tool, it was used for benchmarking the controller design in simulation.

The equations for #1 and #2 have already been discussed in Chapter 3, so this chapter will just focus on the Plecs simulation framework and some design aspects of the controller.

4.2. Plecs simulation framework

The Plecs simulation framework just implements the circuit design in Figure 4.1 using the Plecs libraries.

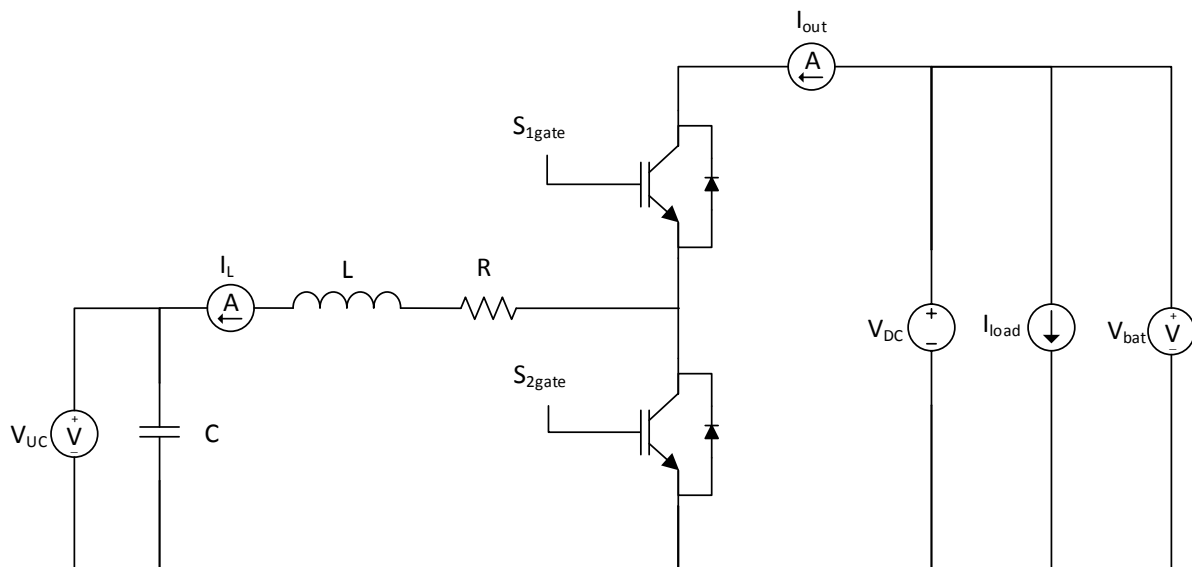


Fig. 4.1. Plecs simulation circuit

4.3. Controller Implementation Topology

Two possible controller implementation topologies are possible. Both are discussed below, with a proposed name for each of them.

4.2.1. Disjoint buck-boost control topology

When the ultracapacitor is being charged, the converter is operated in the buck mode, so that it can draw current from the power source. For this mode of operation only the top IGBT S_{1gate} will be controlled, with the bottom IGBT switched off for the buck operation $S_{2gate} = 0V$.

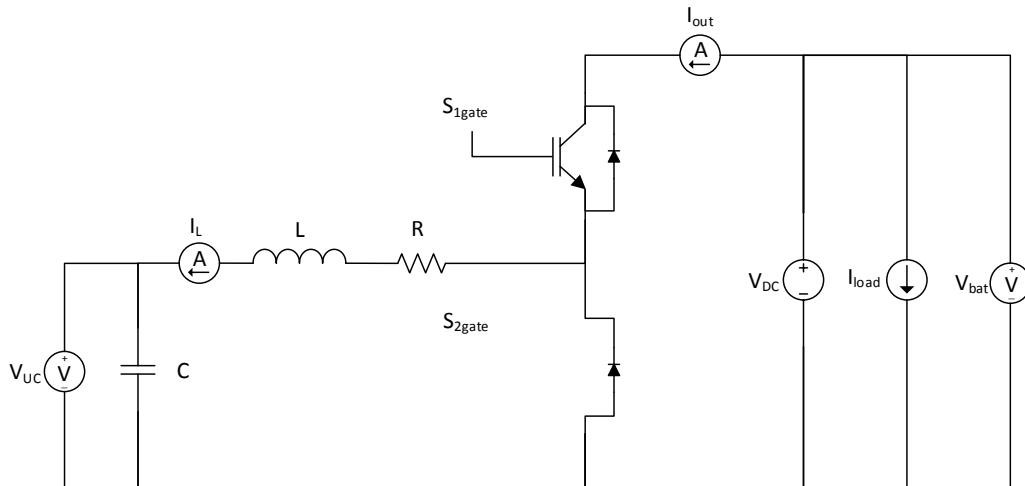


Fig. 4.2. Effective circuit structure for buck operation mode

When the ultracapacitor is being discharged, the converter is operated in the boost mode, so that it can supply current to the power source. For this mode of operation only the bottom IGBT S_{2gate} will be controlled, with the top IGBT switched off for the buck operation $S_{1gate} = 0V$.

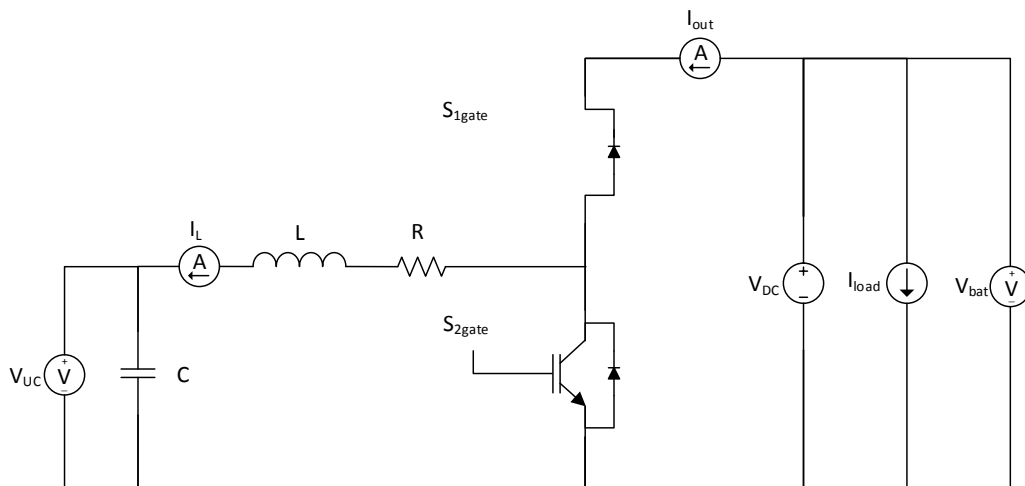


Fig. 4.3. Effective circuit structure for boost operation mode

4.2.2. Drawback of disjoint buck-boost control topology

When the current-command is low, the current becomes discontinuous i.e. the system operates in discontinuous conduction mode. The exact range referred as “low” depends on the system’s voltage rating; for a ~12V system (as in the test setup) discontinuous conduction mode is found to occur for current commands between (–1A, +1A). In this report, this is labelled as the no-zone. For a 350V system, this no-zone could be as high as (–25A, 25A).

This means that a true 0A average current flow can never be achieved with the disjoint-buck boost strategy. Consequently, when in the voltage control mode, since a true 0A average current can never be commanded, the system keeps oscillating between the buck and the boost mode, causing a minor voltage ripple in the ultracapacitor voltage.

4.2.3. Smooth buck-boost control topology

In the smooth buck-boost control topology, both the IGBTs are controlled simultaneously with a slight modification to the controller structure.

Considering the buck mode of operation, the reason behind the discontinuous conduction mode at low currents can be attributed to the flyback diode. For low currents, during the “off” time within the PWM cycle, the current quickly reaches zero, but is not able to reverse its polarity since the diode only conducts current in one direction. The case is similar for the boost mode at low currents.

To resolve this issue, both IGBTs are turned “on” and “off” complementary to each other (with a dead-time between successive switching). The dead-time is required to avoid shorting the DB bus through the IGBT module. The dead-time specification can be found in the Semikron IGBT module datasheet [5].

When this is done, the current can reverse polarity at low currents (zero-crossing is possible). In a switched power-electronic system, the current flow always has a ripple about its average value. To achieve an average current flow of 0A, zero-crossing needs to be possible for the current flow, which this proposed topology achieves.

5. Controller Design

5.1. Overview

As Illustrated in Chapter 3, the discrete-time averaged model with volt-seconds approximation will be used for the controller design. Figure 5.1 shows the system in view of this system modelling and controls design approach.

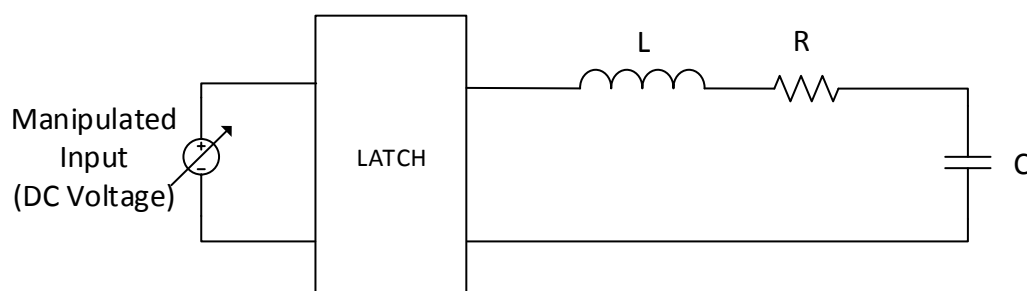


Fig. 5.1. System representation used for the discrete-time model with volt-seconds approximation

Consequently, the differences between this approach and the physical system need to be evaluated before translating the controller design to the hardware. These design aspects are designed in the context of tuning the controller and implementation details.

In review, the system states arranged in descending order from fastest to slowest are:

1. Manipulated Input (Voltage)	Fastest state
2. Rate of Change of Average Current	
3. Average Current	Primary interest for control
4. Rate of Change of Ultracapacitor Voltage	
5. Ultracapacitor Voltage	Slowest state – secondary interest for control To maintain operating voltage limits

Table 5.1. Review of system states and their characteristics

A cascaded controller topology has been chosen for the design.

5.1.1. Inner Control Loop – Current Mode Controller

The rationale for this is evident from Table 5.1. We have direct access to the current measurement and that can be used to build the first (innermost) control loop.

The only other meaningful control loop that can be nested within the current mode controller is a control loop for the rate of change of average current. Since the current measurement is noisy, calculating the rate of change from the measurement directly will result in poor performance. This necessitates the use of a state observer or a well-designed filter, with the observer being the better choice because of its frequency response properties. This hasn't been done to accommodate the project within the given time frame.

Most of the system operation will use the Current Mode Controller exclusively in order to control the power split between the ultracapacitor pack and the battery pack.

5.1.2. Outer Control Loop – Voltage Mode Controller

The voltage mode controller has been designed to control the system behaviour near the operating limits. During the course of operation, the controller is expected to contain the ultracapacitor voltage between pre-defined limits, which necessitates the use of an outer voltage control loop.

The voltage controller is built as the outer loop because it is a much slower state than the current. Consequently, the faster states of the system must be controlled with an appropriate command trajectory in order for the slower state to reach its commanded value, which is precisely what the voltage controller does. Additionally, the voltage mode controller will be designed to operate at a much lower sample frequency since the state itself is slow to change. This is an important design consideration and is explained in details in section 5.3 dealing with the voltage mode controller design.

5.2. Current-Mode Controller

5.2.1. Choice of sample frequency

For the current-mode controller, the sample frequency and the operating frequency of the current-control loop will be the same as the PWM frequency of the power electronic system (this is its maximum value). Although the model is not aware of the PWM interface (as explained section 3.2), the sample frequency is chosen in this manner since an atomic time step is equal to the PWM time period. In other words, since the system model conforms to the average current (which in effect, is the average current over every PWM cycle) the fastest meaningful sampling rate is the PWM frequency itself.

5.2.2. General PID Overview

The current mode controller is an independent operational mode in itself, so a PI controller is required to achieve good command tracking and dynamic stiffness properties.

Why an “integral” loop? The integral loop offers the following benefits:

1. When correctly tuned, the loop is not very sensitive the measurement noise (the integrator filters the noise)
2. Infinite static stiffness
3. Unity steady state command tracking

However, the integral control has a lagging property (slow to respond), which in this case is compensated by the proportional controller.

Why not a “differential” loop?

1. Implementing a differential loop directly from the measurement would be a terrible idea because of the noise it would inject into the system. A better way to implement the

controller would be to design an observer and use the rate of change of average current estimated from the observer as the feedback input. This is discussed briefly in section 8.

5.2.3. Controller Design

The mathematics behind the design of the current-mode controller has been outlined below.

From equation (42) in chapter 3

$$\frac{I_L(z)}{V(z)} = k_d \omega_r^2 C \left\{ \frac{z^{-1} (1 - z^{-1})}{(1 - \delta_{p1} z^{-1}) (1 - \delta_{p2} z^{-1})} \right\} \quad (56)$$

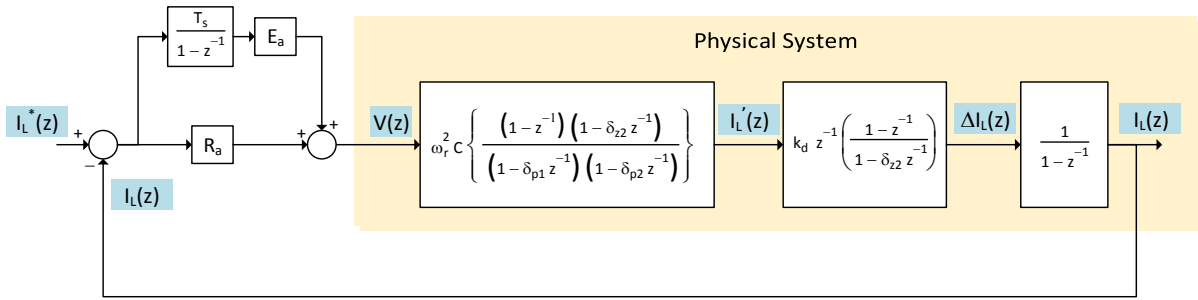


Fig. 5.2. State block diagram of system with current-mode controller

Using parameter values from Table 2.1 from chapter 2 for the system model in equation (56), the transfer function of the system is

$$\frac{I_L(z)}{V(z)} = 1.0209 \left\{ \frac{z^{-1} (1 - z^{-1})}{(1 - 0.999882 z^{-1}) (1 - 0.990827 z^{-1})} \right\} \quad (57)$$

Where,

$$\delta_{p1} = 0.999882 \quad (58)$$

$$\delta_{p2} = 0.990827 \quad (59)$$

$$G_{C-I_L}(z) = K_m \left(\frac{1 - \delta_{z5} z^{-1}}{1 - z^{-1}} \right) \quad (60)$$

$$K_m = R_a + E_a T_s \quad (61)$$

$$\delta_{z5} = \frac{1}{1 + \left(\frac{E_a}{R_a} \right) T_s} \quad (62)$$

The root-locus approach is used to tune the controller.

Step #1: Controller zero placement

The controller zero should be chosen to approximately cancel the dynamics of one of the system poles so that the resultant closed-loop dynamics are improved. Here the controller pole is chosen to approximately cancel δ_{p2} . The rationale behind this is not apparent from the root-locus design methodology. Considering the alternative, if the zero is placed to approximately cancel δ_{p1} ($= 1$ for all practical purposes), the zero would be located extremely close to 1. This in turn necessitates {from equation (62)} that the value of E_a be approximately zero, resulting in no benefit or impact from the integral loop (only the proportional controller is left). In other words, although the intuitive choice is to use the controller zero to cancel the slower system pole (which in this case is δ_{p1}), but doing so results in an incorrect design, as described above.

Also, the controller zero is made slightly faster than the system pole δ_{p2} whose dynamics the zero is trying to approximately cancel. In general, the zero should be slightly slower to avoid under-damped response, but this can be ascertained at the design level only if the parameters are known accurately. Since the parameter estimates are not known accurately, designing the controller zero to be slightly faster or slower is of equivalent uncertainty at design level, with the faster zero considered a more aggressive approach.

Step #2: Controller gain tuning

Once the pole is chosen, the controller is tuned to achieve the desired bandwidth. Since the controller zero is considered to approximately cancel the dynamics of δ_{p2} , the tuning is done to control the movement of δ_{p1} to the correct value that achieves the desired bandwidth.

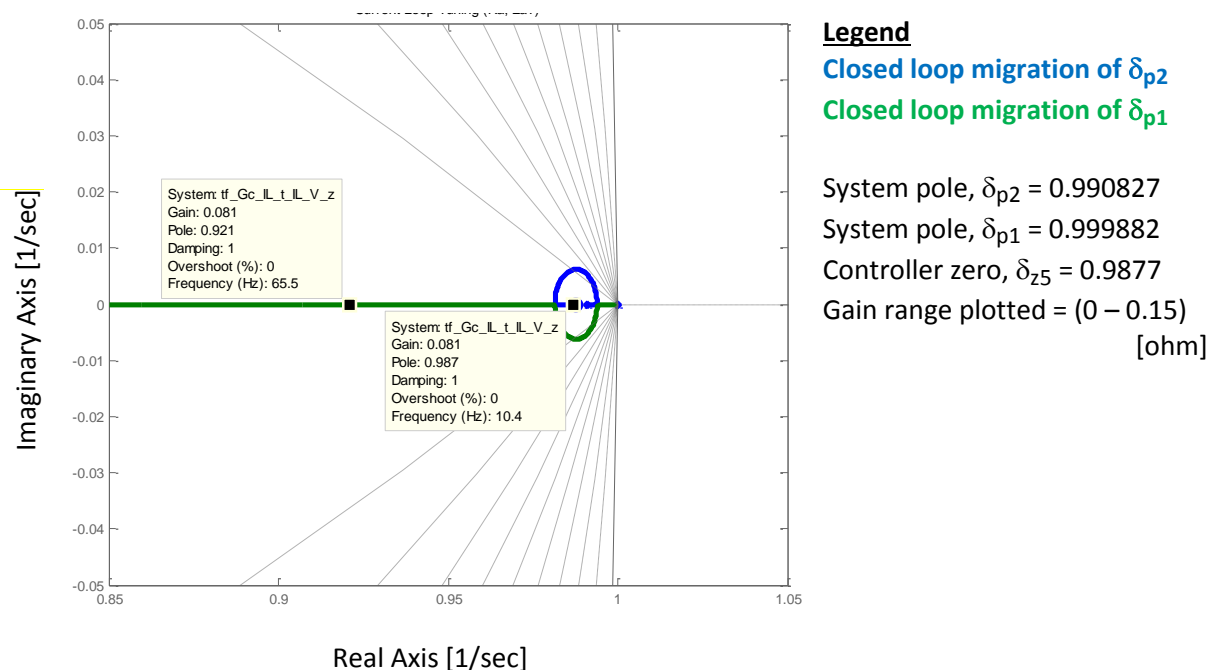


Fig. 5.3. Root locus for current-mode controller design

5.2.4. Practical considerations and controller tuning

An important aspect of a high frequency switched power electronic system is that the averaged models do not account for the transient dynamics within the switching period. This stems from the volt-seconds approximations illustrated in Figure 3.3. As far as the model is concerned the commanded voltage is directly applied to the system, which if it occurs, would result in a current transient that the model can predict correctly. However, since in a PWM-based switched system, a much higher voltage is applied for a short duration to get the equivalent volt-seconds within one time period. Consequently the current transient within the pulse width is directly proportional to the pulse width.

This fact has to be accounted for when tuning the controller. The impact of this observation is that the proportional gain cannot be made too high. A representative model for the limits can be derived using the accurate continuous-time model derived in Section 3.1, but this model development is not complete at this point. However, the controller tuning has been empirically cognizant of this fact. The dynamics of the system are already decided based on the controller zero positioning, so the only effect of the empirical tuning is to achieve the desired bandwidth. In other words, both R_a and E_a are modified simultaneously to maintain the controller zero at its design value. The final gains used for the current controller are

Controller Gain	Value
R_a	0.08 [ohm]
E_a	5 [1/farad]
Table 5.2. Current-controller gains – tuned values	

The final closed-loop command-tracking transfer function of the system with the current –mode controller is

$$\frac{I_L(z)}{I_L^*(z)} = 0.08269 \frac{z^{-1} (1 - 0.9877 z^{-1})}{(1 - 0.9871 z^{-1}) (1 - 0.9209 z^{-1})} \quad (63)$$

5.3. Voltage-Mode Controller

5.3.1. Overview of topologies

There are two different topologies that can be used to design the voltage-mode controller. A brief discussion of both topologies is presented, along with the reasons for choosing one over the other for this particular application.

Topology #1: “PI” voltage controller cascaded with “P” current controller

This is the straightforward approach to design a voltage controller since the Integral loop acts directly on the voltage error. However, in this case, since the design topology considers the ultracapacitor voltage to be the state of interest, the current loop is just a proportional controller. Consequently, this structure *may* result in wild transients in the current flow, since the proportional current controller does not have good command tracking (finite steady state error at a given frequency).

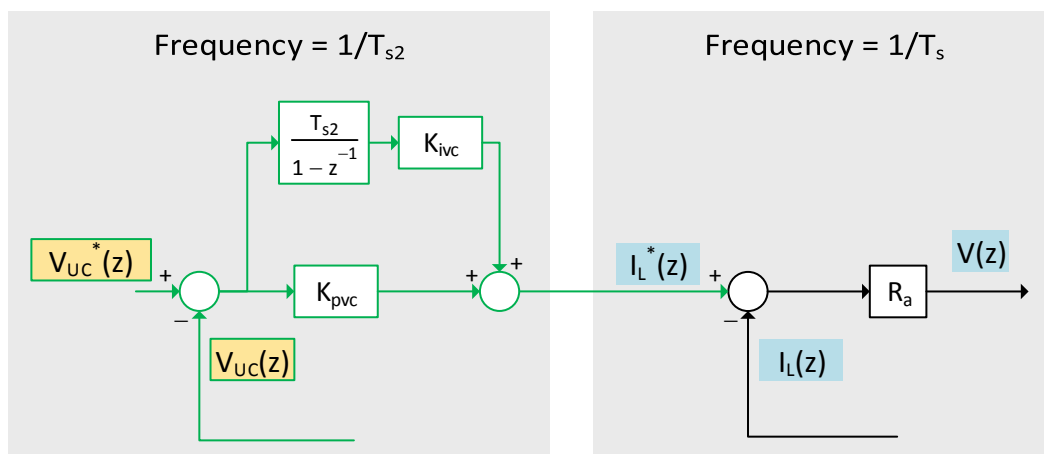


Fig. 5.4. State block diagram of voltage-mode controller, topology #1

Topology #2: “P” voltage controller cascaded with “PI” current controller

This approach is equivalent to topology 1, but the integral action on the voltage error is not directly observable and is buried within the current command. Even in this approach, the integral action exists on the voltage error, but since the current controller has excellent tracking properties, we can impose limits on the current command generated by the voltage control loop, thereby protecting the system from current transients that exceed safe operating levels.

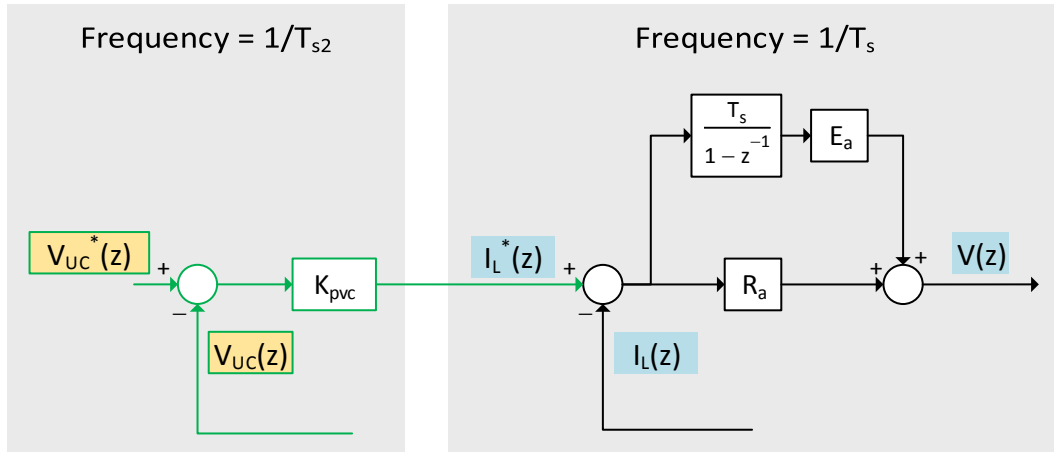


Fig. 5.5. State block diagram of voltage-mode controller, topology #2

Topology #3: “PI” voltage controller cascaded with “PI” current controller

A logical extension to topologies 1 and 2 above is topology 3. This does not make much sense from a design perspective because both the integral loops try to modify the same system eigenvalues. An extremely simple explanation of this conflict is presented in the Figure 5.6.

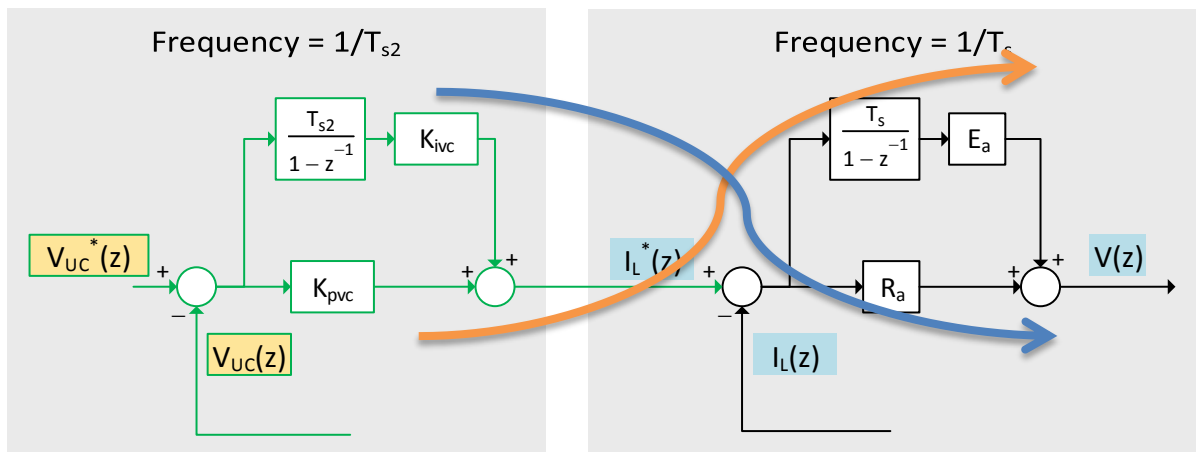


Fig. 5.6. State block diagram of voltage-mode controller, topology #3

5.3.2. Choice of sample frequency

The ultracapacitor voltage is an extremely slow state as compared to the current. Consequently, ultracapacitor voltage sampling frequency and the operating frequency of the voltage control loop need to be designed in a way such that subsequent samples will show a “reasonable” change in the

voltage value. This is done so that the effects of sensor quantization and sensor accuracy on the controller are minimized. Additionally, in design space, sampling much faster than the state changes will push the system poles towards the edge of the unit-circle in the Z-domain (which is the boundary of stability). This would make it tricky to tune the controller without causing any impact to system stability in general.

5.3.3. Methodology used to choose the sample frequency

The controller has been tested with the test setup connected to both the DC power supply and the Battery.

With DC Power Supply

The DC power supply module is only capable of sourcing ~20A, and cannot act as a sink at all. Consequently, for all tests with the DC power supply module, the peak current command has been restricted to $\pm 10A$, to be on the safer side and not damage the module. For the current sink, a DC load module is used, which draws a constant ~10A current from the system.

Since the current command is restricted to 10A peak in either direction, this directly determines the fastest rate of change possible for the ultracapacitor voltage. This understanding, along with some analysis of the sensor quality, is used to determine the sampling frequency for the ultracapacitor voltage.

The voltage sensors used initially, when the system was being tested with the DC power supply, had extremely noisy output for this low voltage system, since the sensors were rated for a 1200V system, and the test setup was operating at 10V. Looking at the impact of the noise on the scaled value, there was some noise in the first digit of precision after the decimal point, and significant noise in the second digit of precision after the decimal point, after the sensor output is scaled.

The change in ultracapacitor voltage at constant average current can be modelled as:

$$\Delta V = \frac{1}{C} I_L^* \cdot (time) \quad (64)$$

The model above can be used to estimate the time required for a “reasonable” change in the ultracapacitor voltage measurement when a 10A current limit is imposed on the system.

“Reasonable” change of a measurement: I define a “reasonable” change of a measurement as minimum change in the scaled measurement that cannot be attributed to sensor noise, but can be attributed to a real change in the system state.

In this case, based on observations of the measurement, the “reasonable” change for the voltage has been chosen as 0.05V. The time required for a 0.05V change in the ultracapacitor voltage measurement when operating at the current limit:

$$(time) = \frac{C (\Delta V)}{I_L^*} = \frac{188 (0.05)}{10} = 0.94s \approx 1s \quad (65)$$

Based on this calculation, the sampling frequency for the voltage control loop has been chosen to be 1Hz when the DC power supply is used and the current command is limited to a 10A peak value in either direction.

With Battery

In this case, the peak current commands are set to $\pm 200\text{A}$ since the battery is capable of sourcing, as well as sinking high current (of said magnitude).

Since with the battery, the DC bus voltage would not remain as stable as with the power supply in light of the battery's internal resistance, the existing voltage sensors were replaced with a set of sensors rated for 600V. Although this did reduce the measurement noise, the reduction was not considerable enough to warrant a change in the "reasonable" change estimate of 0.05V for the ultracapacitor voltage measurement. However, since the imposed current limits have been changed, time required for a reasonable change in the ultracapacitor voltage measurement operating at the current limit:

$$(time) = \frac{C (\Delta V)}{I_L^*} = \frac{188 (0.05)}{200} = 0.047\text{s} \approx 0.05\text{s} \quad (66)$$

Based on this calculation, the sampling frequency for the voltage control loop has been chosen to be 20Hz when the battery is used and the current command is limited to a 200A peak value in either direction.

5.3.4. Controller Design

The mathematics of the voltage controller design process is presented below. In order to simplify the design process but adequately capture the energy flow orchestrated by the current controller, an abstraction called the exponential power latch is created. The exponential power latch is a reduced-order representation of the inner loop controller in a cascaded structure that captures the essence of the dynamics of the inner loop. In this case, the current controller is reduced to a first-order system.

Exponential power latch model for closed-loop current controller system

This is done using MATLAB's system identification toolbox. The command tracking frequency response of the closed loop system model with the tuned current controller is generated and fed to the system identification toolbox. Following this, the toolbox is used to estimate a first-order continuous-time transfer function. The transfer function so generated will, in general, capture most of the dynamics of the closed loop system.

The first-order transfer function (reduced-order model) that is being identified has the following structure

$$(Reduced\ order\ model) = \frac{k_{el1}}{s + a_{el1}} \quad (67)$$

The estimates using the system identification toolbox have been tabulated below. These estimates will change when the current controller tuning is altered.

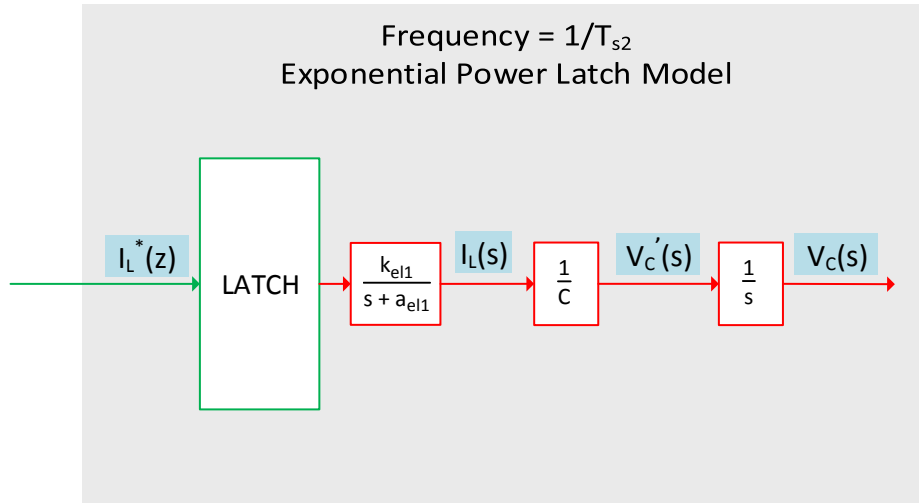


Fig. 5.7. System model with exponential power latch

Reduced-order Model		Current-controller tuning	
Model parameter	Estimated value	Gain	Design value
k_{el1}	448.7	R_a	0.08
a_{el1}	431.6	E_a	5

Table 5.3. Parameter estimates of first-order current regulator model for exponential power latch

Discrete-time system model with exponential power latch at lower sampling frequency

$$\frac{V_{UC}(s)}{I_L^*(s)} = \left(\frac{1-e^{-sT_2}}{s} \right) \left(\frac{k_{el1}}{s+a_{el1}} \right) \frac{1}{sC} \quad (68)$$

Converting to z-transform using a z-transform table, at sample frequency T_2 (or T_{s2}),

$$\frac{V_{UC}(z)}{I_L^*(z)} = \frac{(1-z^{-1})}{C} \left(\frac{k_{el1}}{a_{el1}} \right) \frac{z^{-1} \left[(a_{el1}T_2 - 1 + e^{-a_{el1}T_2}) + (1 - e^{-a_{el1}T_2} - a_{el1}T_2 e^{-a_{el1}T_2}) z^{-1} \right]}{a_{el1} (1-z^{-1})^2 (1 - e^{-a_{el1}T_2} z^{-1})} \quad (69)$$

For rearranging and simplifying this, we assign

$$k_f = \frac{(a_{el1}T_2 - 1 + e^{-a_{el1}T_2})}{a_{el1}} \quad (70)$$

$$\delta_{z3} = \frac{(1 - e^{-a_{el1}T_2} - a_{el1}T_2 e^{-a_{el1}T_2})}{(a_{el1}T_2 - 1 + e^{-a_{el1}T_2})} \quad (71)$$

$$\delta_{p3} = e^{-a_{el1}T_2} \quad (72)$$

$$\frac{V_{UC}(z)}{I_L^*(z)} = \left(\frac{k_f}{C} \right) \left(\frac{k_{el1}}{a_{el1}} \right) \frac{z^{-1} [1 + \delta_{z3} z^{-1}]}{a_{el1} (1 - z^{-1}) (1 - \delta_{p3} z^{-1})} \quad (73)$$

$$k_g = k_f \left(\frac{k_{el1}}{a_{el1}} \right) \quad (74)$$

$$\frac{V_{UC}(z)}{I_L^*(z)} = \left(\frac{k_g}{C} \right) \frac{z^{-1} [1 + \delta_{z3} z^{-1}]}{a_{el1} (1 - z^{-1}) (1 - \delta_{p3} z^{-1})} \quad (75)$$

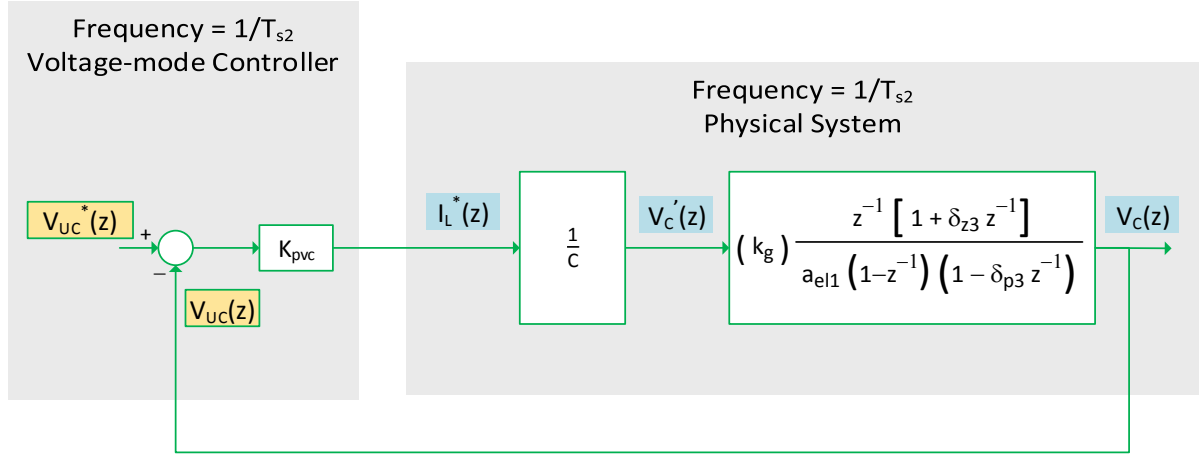


Fig. 5.8. State block diagram of system with voltage-mode controller and exponential power latch

Since just a proportional controller is just, there is no controller zero to be designed here. The only design element is the proportional gain (k_{pvc}), which should be tuned appropriately. The root locus of this system is given below.

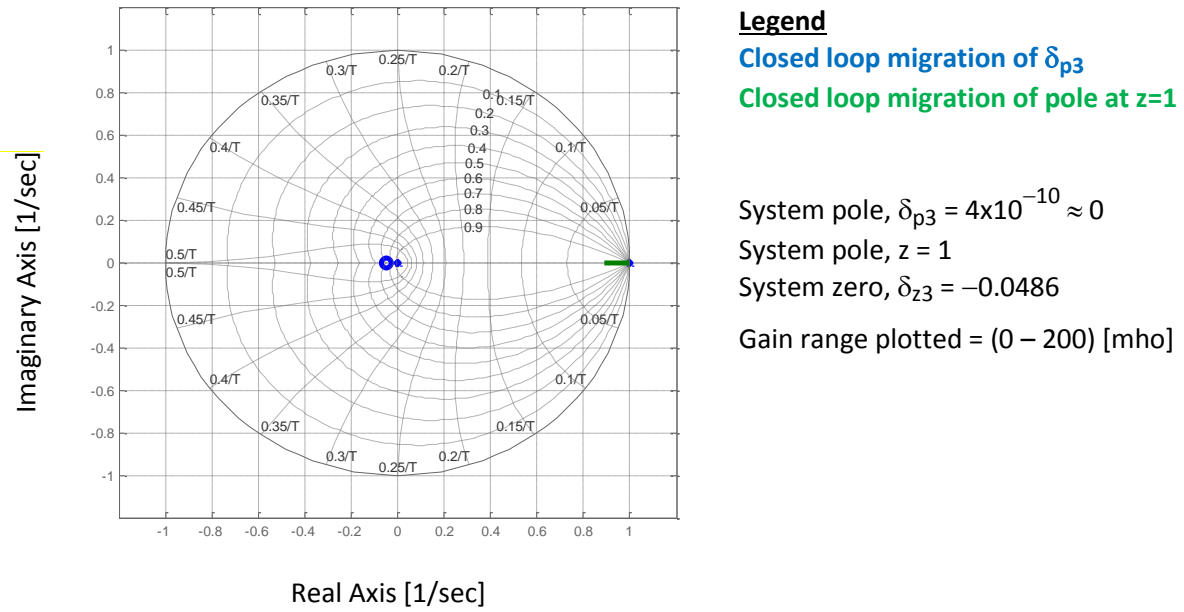


Fig. 5.7. Root locus for voltage-mode controller design

5.3.5. Practical considerations and controller tuning

The use of the voltage controller is to implement protection limits for the ultracapacitor voltage. In other words, when the ultracapacitor voltage hits either its upper or lower threshold, the voltage controller should step in and maintain the ultracapacitor voltage at either threshold. The voltage controller should also be able to charge the ultracapacitor from 0V and discharge it to 0V.

Also, the current command is limited based on whether the DC power supply or the battery is used. The tuning strategy used is based on the following property.

$$I_L^*(k) = K_{pvc} \left(V_{UC}^*(k-1) - V_{UC}(k-1) \right) \quad (76)$$

With DC Power Supply

The current command limit is 10A (peak). For a 1V voltage error, the current command is designed to be 10A. Consequently,

$$K_{pvc} = 10 \quad (77)$$

In this case, a feasible voltage command (which will not require the enforcement of limits on the current command) can be, at most, in steps of 1V.

With Battery

The current command limit is 200A (peak). For a 1V voltage error, the current command is designed to be 50A. Consequently,

$$K_{pvc} = 50 \quad (78)$$

In this case, a feasible voltage command (which will not require the enforcement of limits on the current command) can be, at most, in steps of 4V.

5.4. Controller implementation

While implementing the controller the following aspects need to be addressed:

5.4.1. Over-current and over-temperature protection

The circuit should trip when over-current or over-temperature is observed.

This was implemented by Renato [1] when the test setup was built. It reads the error signals from the Semikron IGBT module and trips the circuit if these signals go high.

5.4.2. Average current estimation

The measured value from the current sensor corresponds to the instantaneous current value and not the average current value. There are two possible ways of getting this estimate:

1. Designing an average current observer and estimating the average current based on the instantaneous current measurement
2. Oversampling the current measurement and using a low-pass filter to extract the DC component of the current, which will be equivalent to estimating the average current

Approach #2 is used for this study. Future work will present a comparison between both approaches, highlighting the strengths and weaknesses of either approach.

Since the PWM frequency is 5kHz, any FIR low-pass filter with a pass-band restricted below 2.5kHz would do the job. Being more conservative and using a smaller pass-band will result in a cleaner current measurement at the cost of some delay. For the purposes of this study, a very conservative filter is used (the filter parameters are presented in Table 5.4). Future work will involve experimenting with the filter design to improve the performance (bandwidth) of the closed-loop system.

Pass Frequency	10 Hz
Stop Frequency	50 Hz
Table 5.4. Low-pass FIR filter design parameters for average current estimation	

The same low-pass filter parameters are used for the voltage measurements, to minimize the noise in the feedback signal.

5.4.3. Ultracapacitor and Battery voltage limits enforcement

A new “supervisory control state machine” state machine is presented below to meet this requirement.

The desired behaviour is to have the current control mode enabled for most of the operation except in the cases when the ultracapacitor voltage could fall beyond either threshold or the battery

voltage could fall beyond either threshold. When the battery is used, the battery voltage fluctuates based on the the charged capacity of the battery. Consequently limits on the battery voltage are used to prevent over-charging or over-discharging the battery. The voltage controller needs to step in and regulate the ultracapacitor voltage until a feasible current command is received; one that will not push the ultracapacitor voltage or the battery voltage out of its legal range.

For smooth transitions between the control modes, a simplified open-loop observer for the ultracapacitor voltage is used to predict the voltage at the next instant. This estimate is used by the state machine to transition between the voltage and the current control modes. The state machine is illustrated in Figure 5.8.

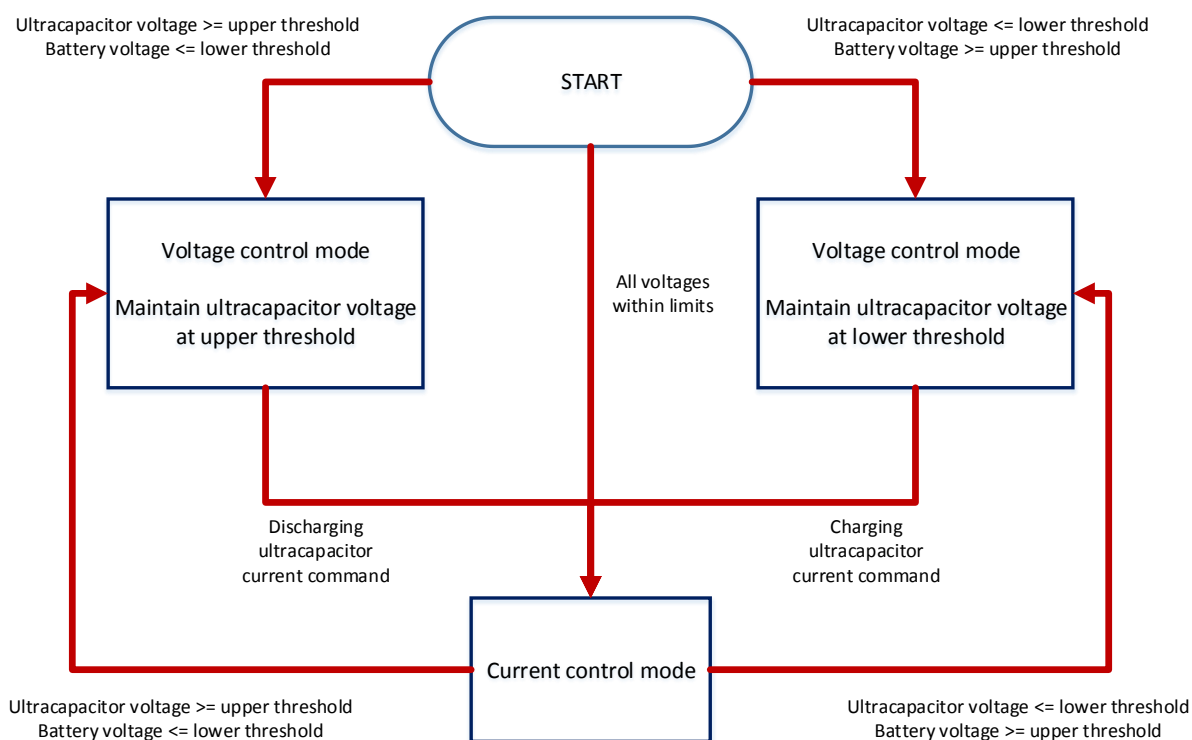


Fig. 5.8. State machine for ultracapacitor voltage limits enforcement

6. Experiments

The following experimental measurements illustrate the performance and operation of the controller, and illustrate the achievement of the design objectives.

6.1. Tests with DC Power Supply

6.1.1. Command Tracking Frequency Response Function (FRF)

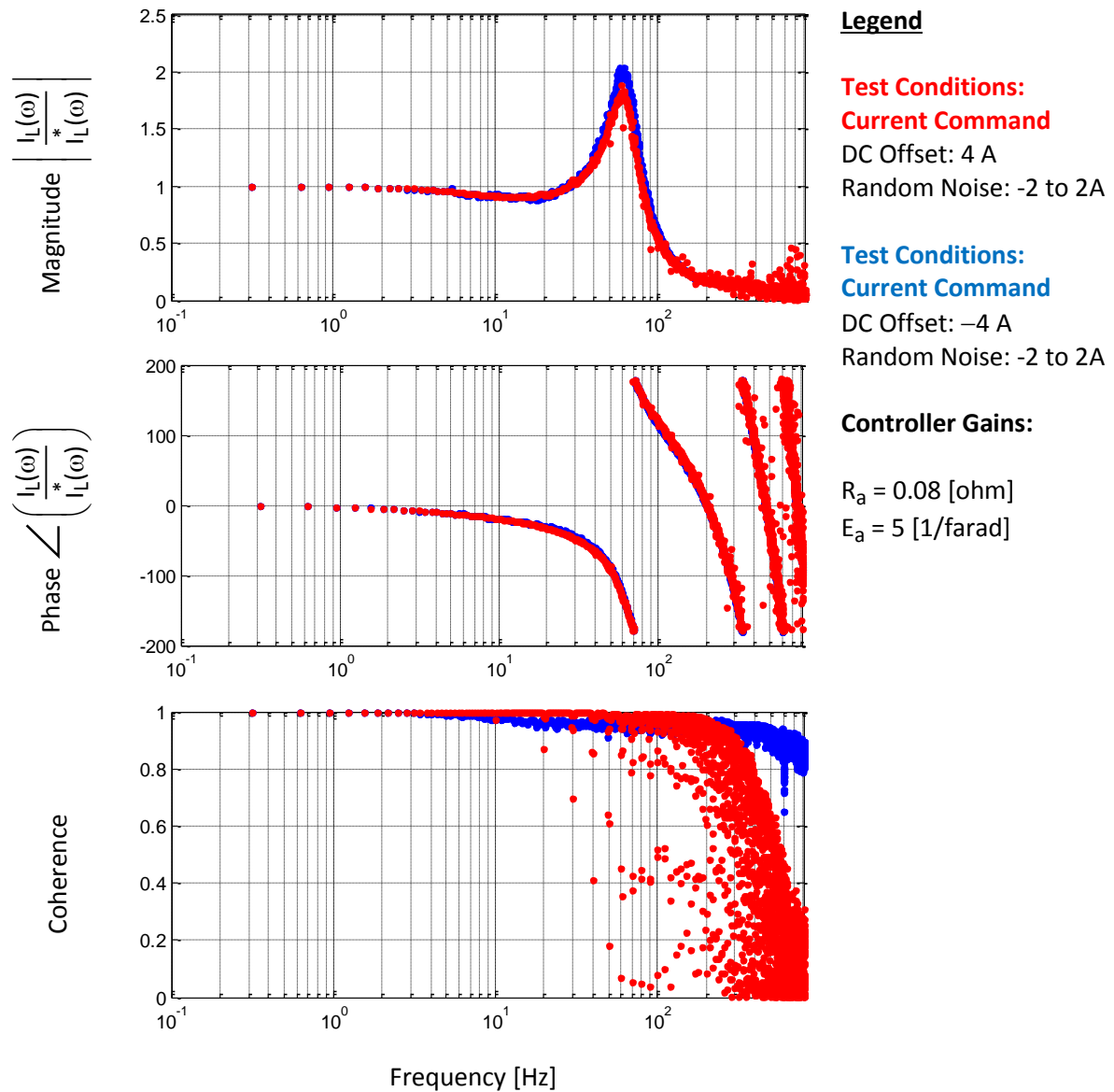


Fig. 6.1. Current Command Tracking FRF

Figure 6.1 illustrates the current command tracking frequency response. The bandwidth is observed to be 60Hz, based on the phase plot. This meets the target specifications, and can be tuned very easily to accommodate higher bandwidths (e.g. 100Hz), if required.

6.1.2. Dynamic Stiffness Frequency Response Function (FRF)

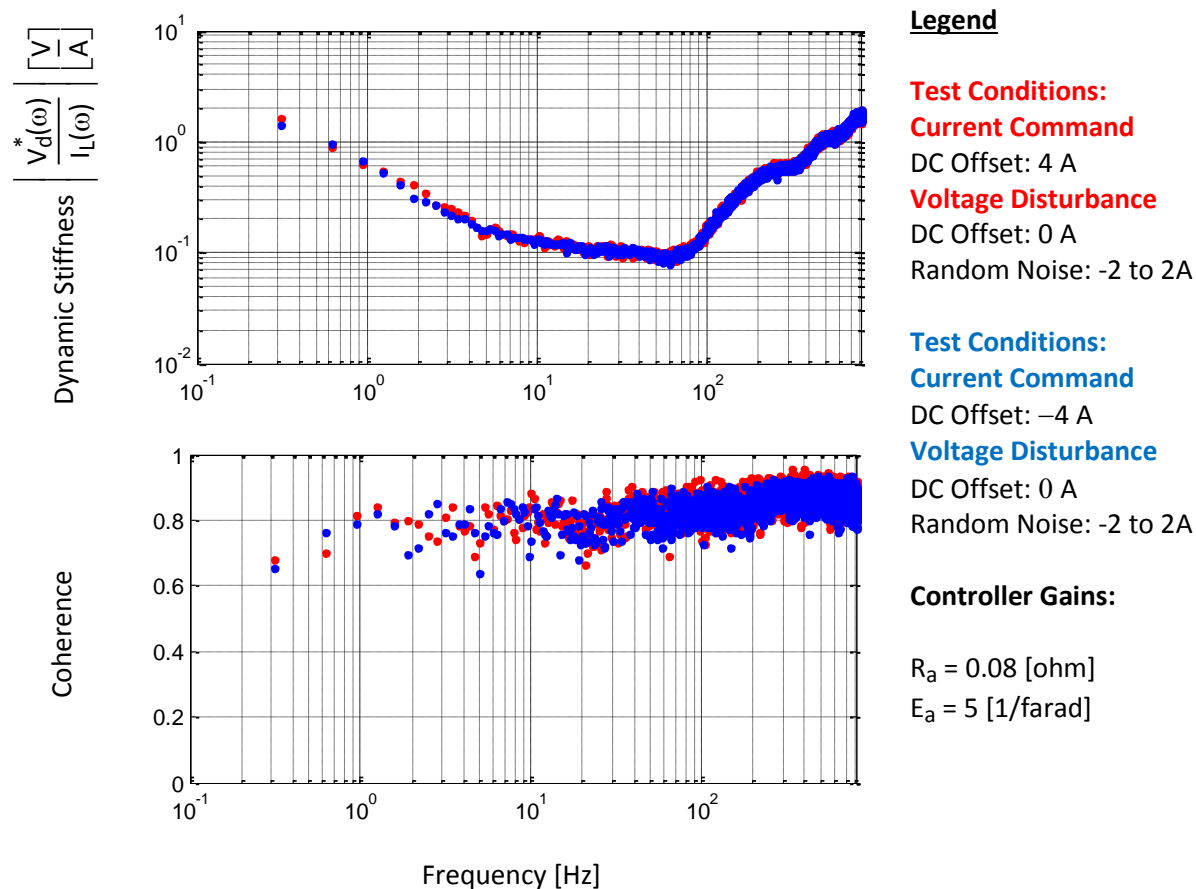


Fig. 6.2. Dynamic Stiffness FRF for current-mode controller

Figure 6.2 illustrates the dynamic stiffness of the current-mode controller system. Owing to the integral loop, we have infinite static stiffness, as validated by the measurements.

The lowest point on the curve is 0.1V/A, which translates to the property that a voltage rail disturbance of 0.1V at a frequency between 10Hz and 100Hz can cause a 1A disturbance in the current flow in the system. To overcome this, “disturbance input decoupling”, can be used, where the measurement of the bus voltage is used to compensate for the bus voltage disturbance.

For the system under test, with the power supply or the battery, the voltage disturbance was never in this problematic range (was always within the controller bandwidth), so disturbance input decoupling was never required. However, the feature is available in the controller, and can be enabled when desired.

6.1.3. Sine Wave Tests

The sine wave tests in Figure 6.3 validate the command tracking properties observed in Figure 6.1 (frequency response function).

The amplitude of the response decreases as the command frequency is increased beyond the bandwidth of the current regulator.

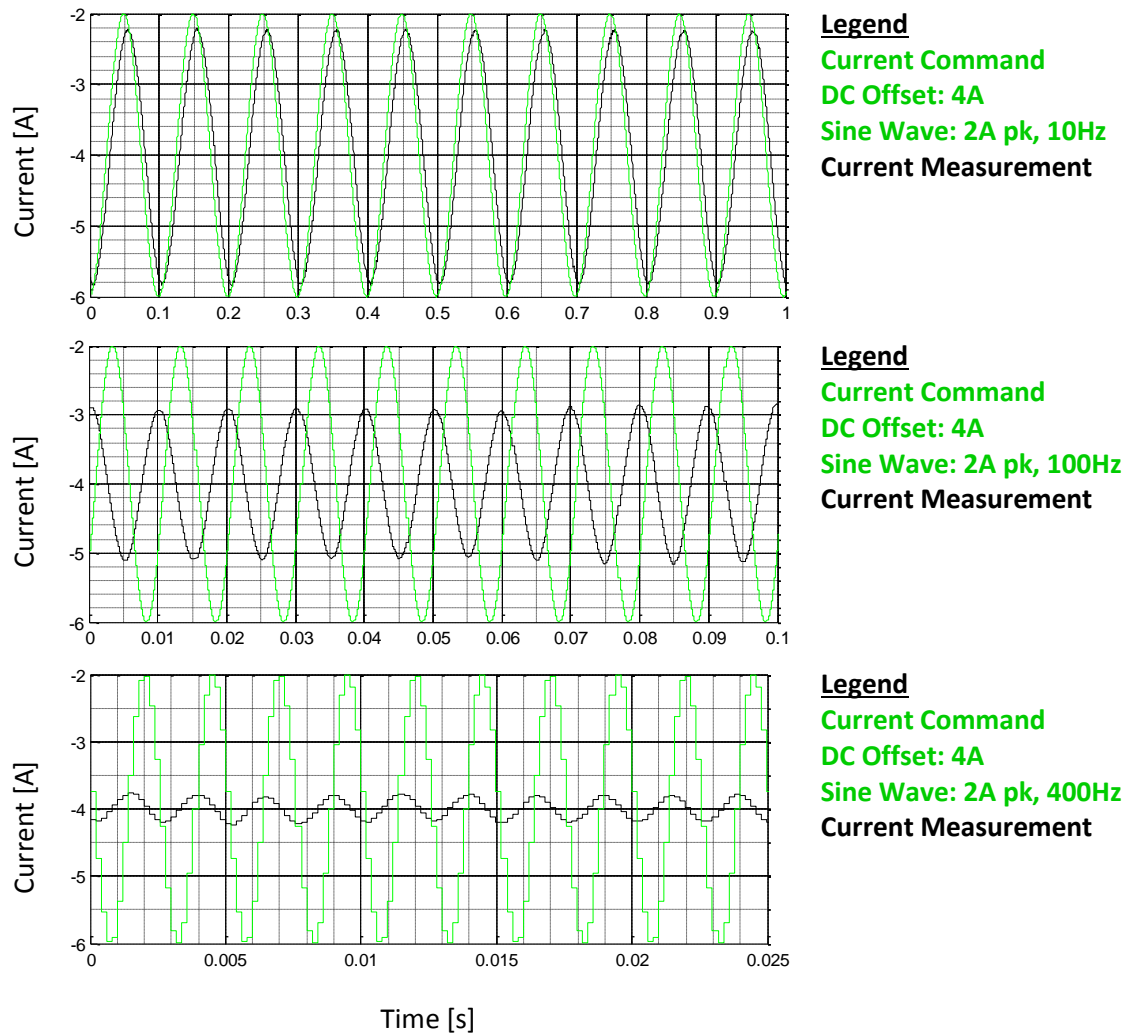


Fig. 6.3. Sine wave tests for current-mode controller

6.1.4. Square Wave Tests

The square wave tests are used to observe transient response to step commands. Here the irregularity caused by discontinuous conduction mode is clearly visible at low currents (-1A to 1A for this system).

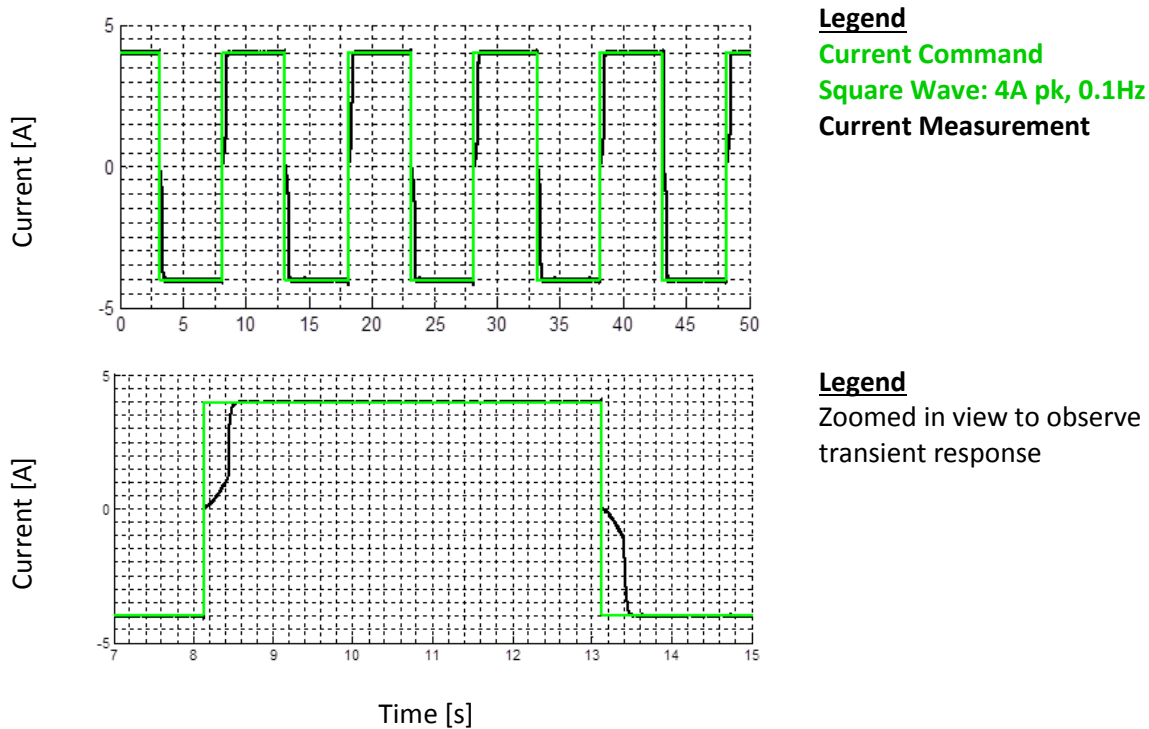


Fig. 6.4. Square wave test for current-mode controller (4A peak current command)

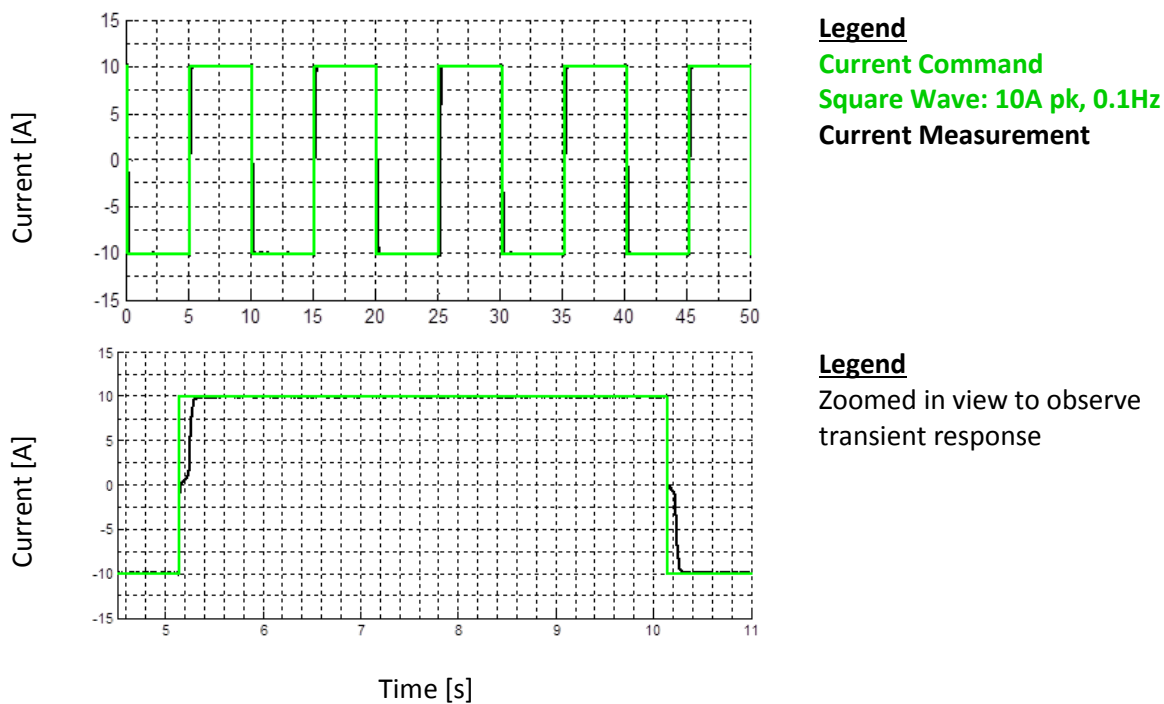


Fig. 6.5. Square wave test for current-mode controller (10A peak current command)

6.2. Tests with Battery

The following tests illustrate the controller operation with the battery connected to the system.

6.2.1. State machine test for limit operation

Figure 6.6 illustrates the state machine taking over from the current controller when the upper voltage limit of the ultracapacitor is reached.

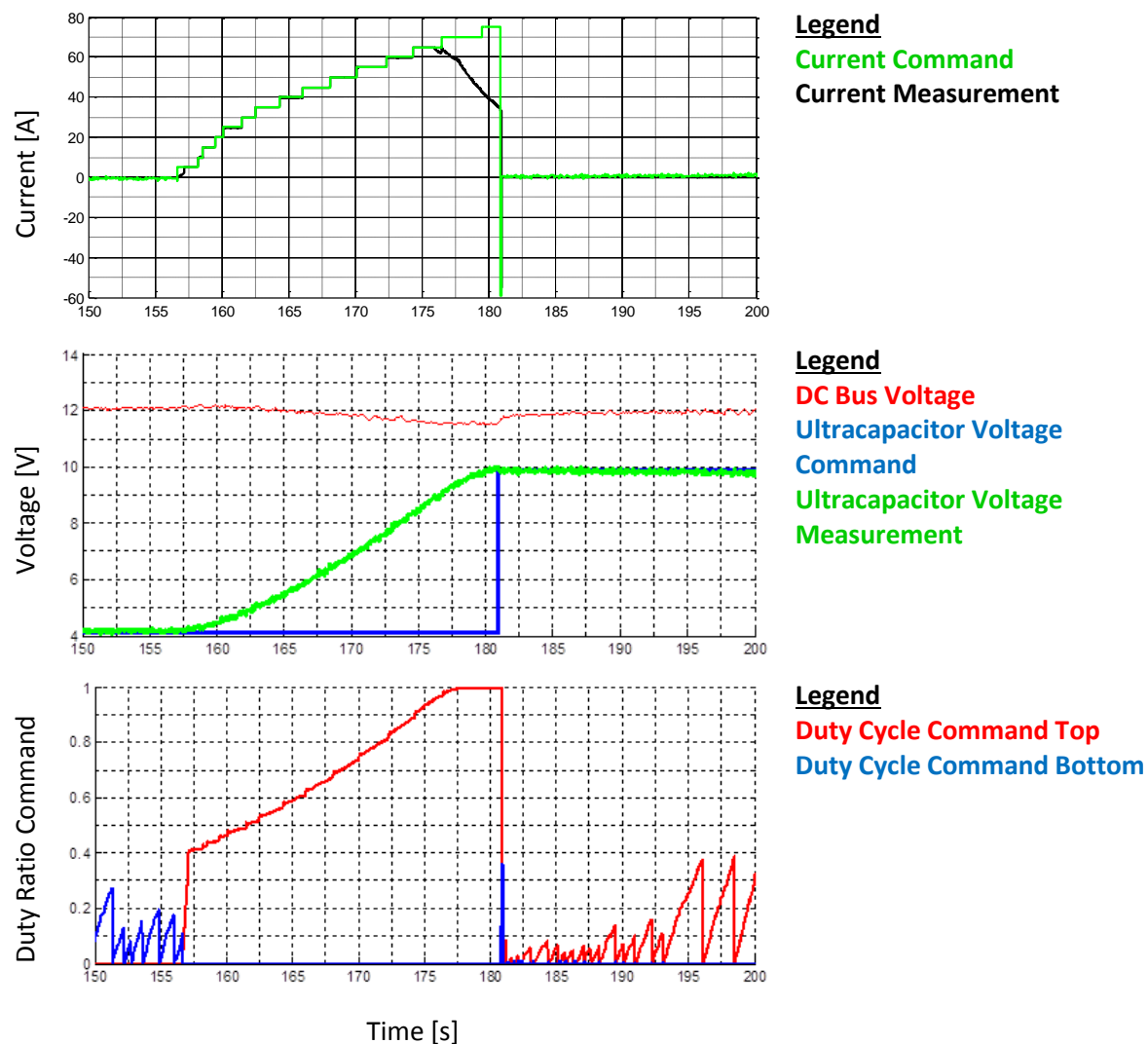


Fig. 6.6. State machine test for ultracapacitor upper voltage limit

Figure 6.6 illustrates the state machine taking over from the current controller when the lower voltage limit of the ultracapacitor is reached.

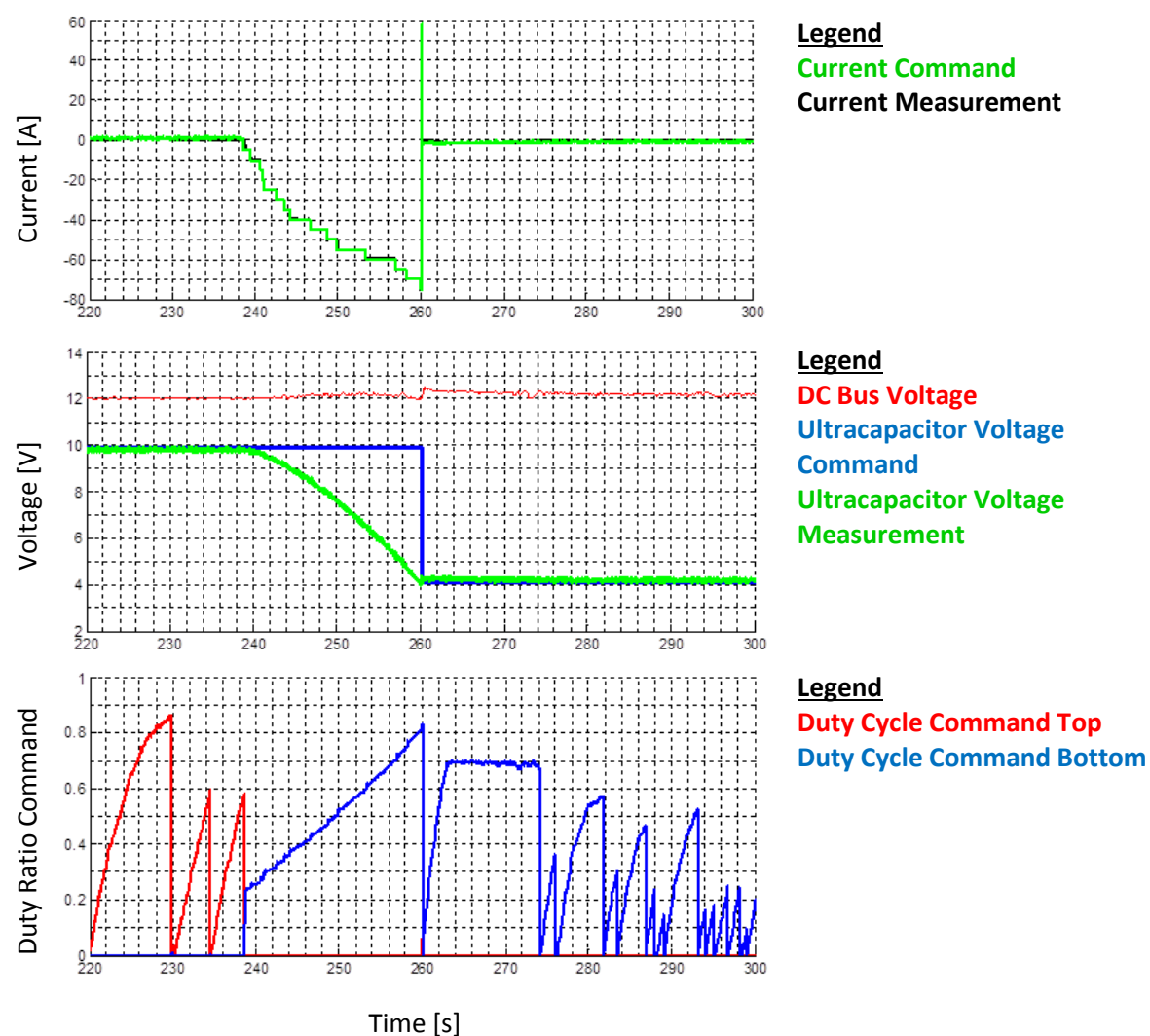


Fig. 6.7. State machine test for ultracapacitor lower voltage limit

6.2.2. Current profile test

The current profile was provided by Phil Kollmeyer as a representative use case of this controller. Figure 6.8 shows the command and the response for 20 minutes of the current profile command. Figures 6.9 and 6.10 zoom in on specific portions of the profile and response to illustrate properties of the controller.

Before testing this profile, the inductance in the circuit was changed to a 150 μH inductance, but the controller was not changed. In spite of this significant variation in the inductance in the circuit, the controller performance is still excellent, thereby highlighting the robustness to parameter variation provided by the PI controller.

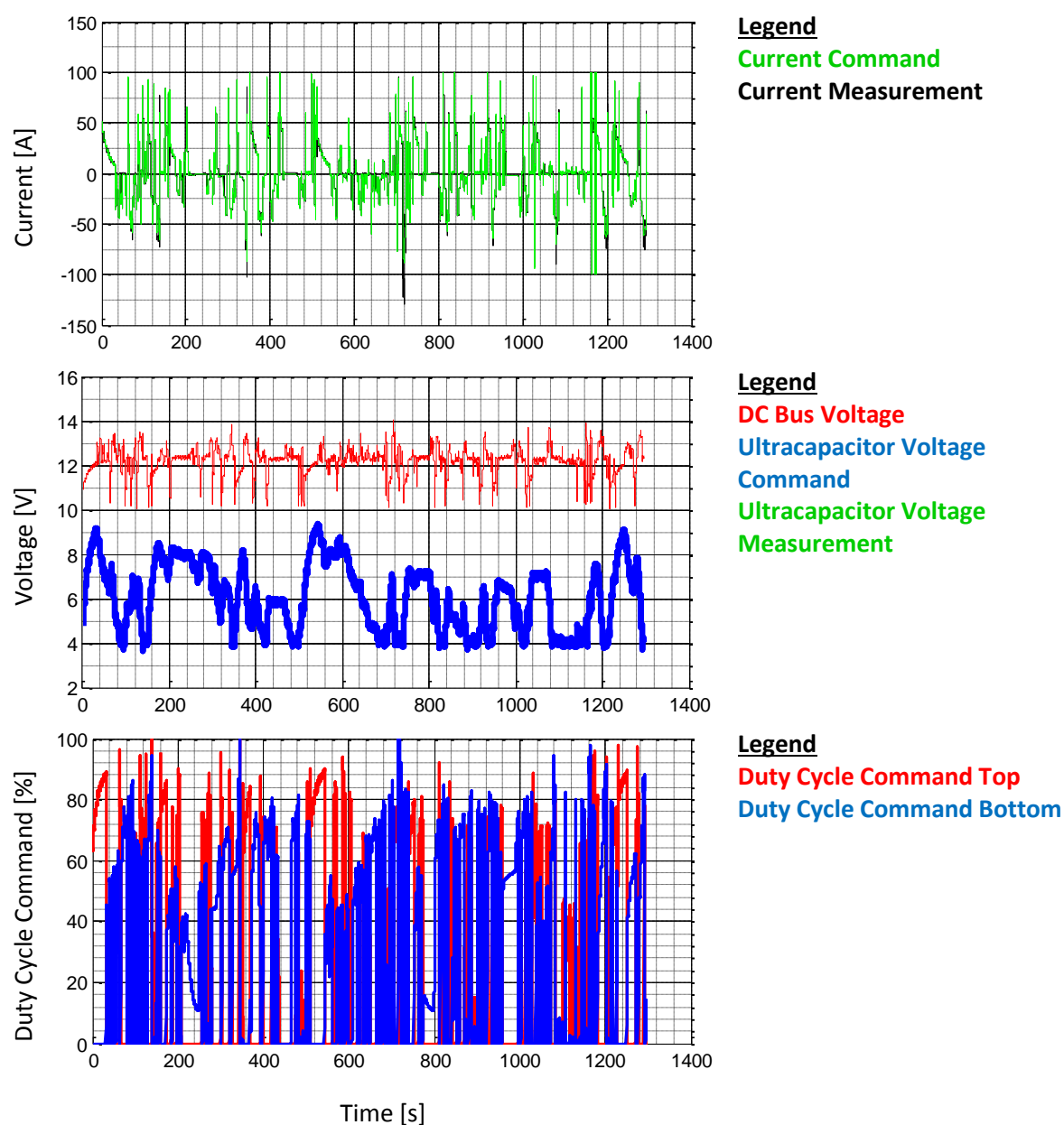


Fig. 6.8. Current profile test

Figure 6.9 illustrates the command tracking properties for the representative current profile. As can be observed, the tracking is excellent, validating that the design meets the target specifications.

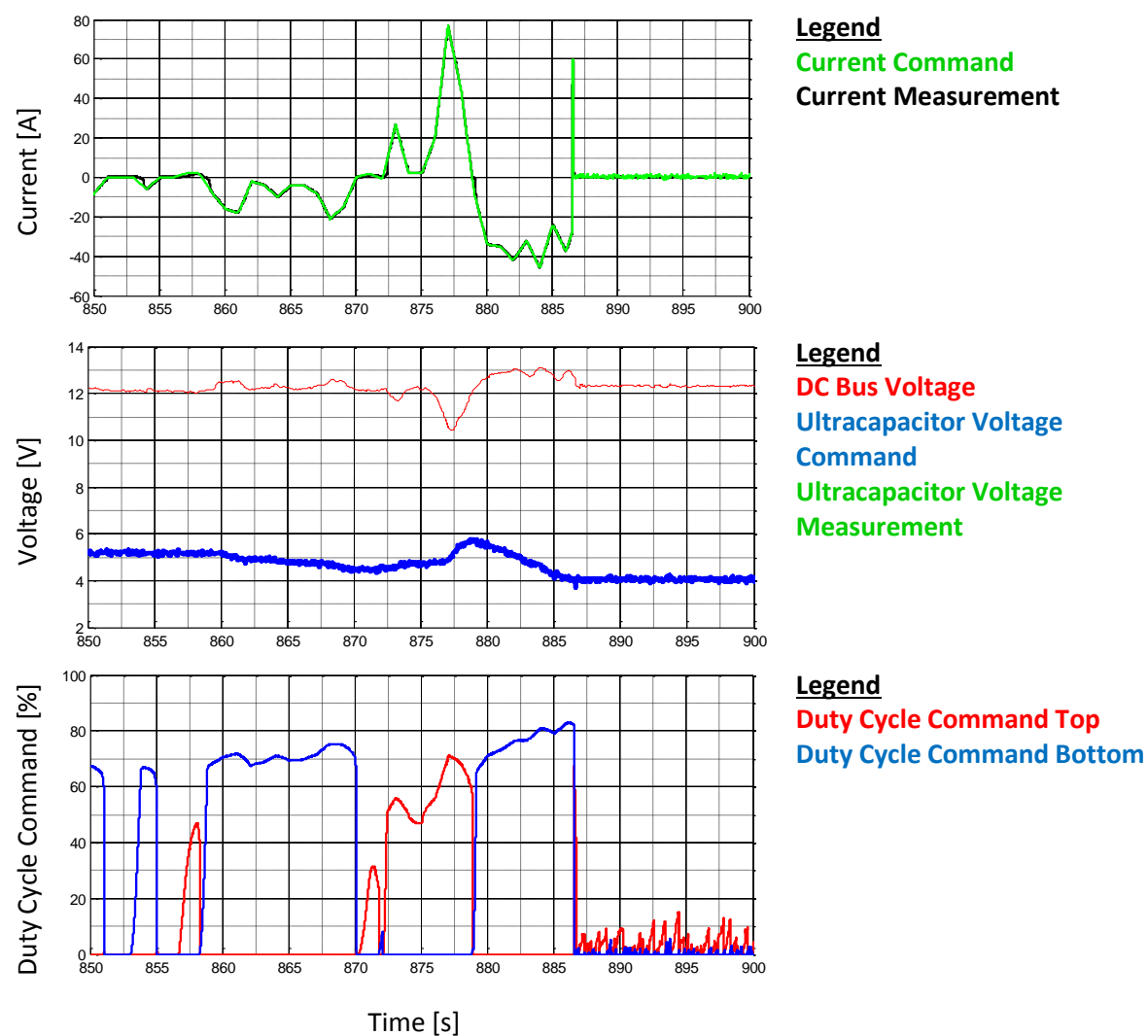


Fig. 6.9. Current profile test (zoomed in for command tracking illustration)

During this profile operation, two distinct protection triggers can be clearly observed:

1. Battery voltage lower limit protection
2. Ultracapacitor voltage lower limit protection

The battery voltage lower limit was set to 10V. It can be observed from Figure 6.10 that when the battery voltage approaches 10V the state machine takes over and prevents charging the ultracapacitor (in other words, prevents discharging the battery). Only for a negative current command (discharging the ultracapacitor, charging the battery), it permits the current controller to be enabled again.

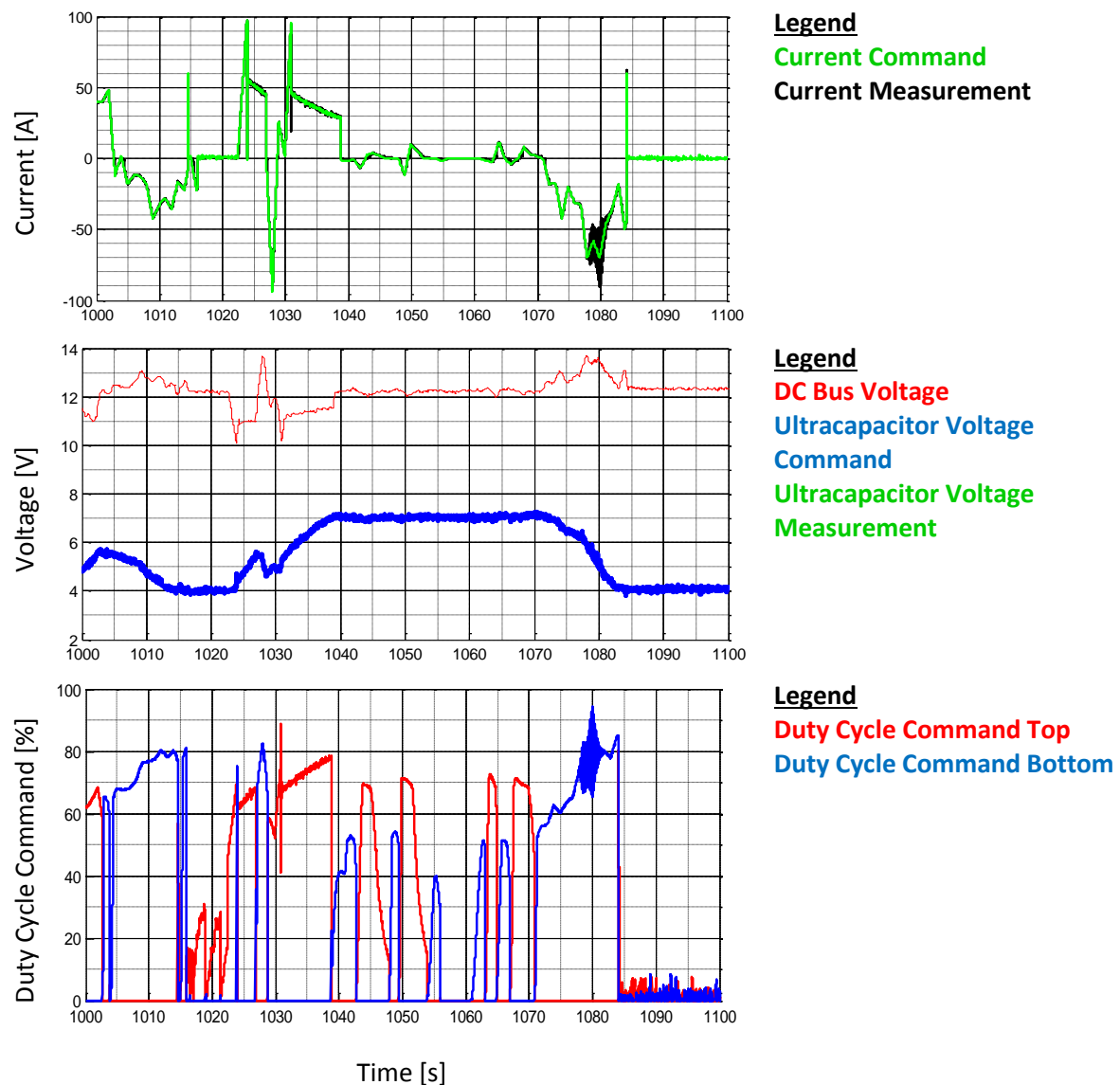


Fig. 6.10. Current profile test (zoomed in for limit protection illustration)

7. Summary

A controller for a DC-DC converter system to regulate energy flow between an ultracapacitor pack and battery pack has been modelled, developed and tested on a low-voltage representative system. The following objectives (as defined in the objectives section) have been achieved.

1. Ability to control the charging or discharging current through the Ultracapacitor pack with a bandwidth of 60 Hz
2. Self-regulation of Ultracapacitor pack voltage near voltage limits
3. Built-in protection algorithms for the system
4. Scalable modelling setup in MATLAB
5. Detailed controller design procedure and performance characterization

8. Future Work

The following sections describe different targets that may be used for future work

1. Scaling up the system to higher voltage that can be used in the vehicle directly
 - a. Redesign the system for a 350V rated battery
 - b. Construct the test-setup in accordance with the above design
2. Design a variable-frequency controller for the DC-DC converter system
 - a. Extend the developed continuous-time model for variable-frequency controller development by modelling the non-ideal characteristics of the system
 - b. Study the system performance at various frequencies and develop a model for variation of the power conversion efficiency with the current and the PWM frequency
 - c. Develop a variable-frequency control technique that will take advantage of the modelling and control the system given the current ripple limits as the command input
 - d. Develop optimization techniques that will optimize the PWM frequency used and compare efficiency improvements with fixed-frequency controllers
3. Adaptive Controller to account for saturating inductors
 - a. Characterize the magnetization characteristics of the inductance
 - b. Use the inductance characteristics to design an adaptive controller (nonlinear controller) for the system
 - c. Design an inductor which does not saturate in the operating regime and using a linear controller, compare with the performance of the adaptive controller
4. Model Reference Adaptive System
 - a. Design a model reference adaptive system for on-line estimation of system parameters
 - b. Use the estimates from the MRAS system to design an adaptive controller as described in the section 4
5. Control loop for rate of change of average current to increase command tracking bandwidth
 - a. Directly calculating from measurement results in poor performance because of noise in the current measurement → prove with data
 - b. Design an observer and build the control loop
 - c. Design a filter and design the same control loop
 - d. Examine differences between using an observer and filter

9. References

- [1] Independent Study Report (Analysis of a Half-Bridge DC-DC converter for a hybrid energy storage system for Electric Vehicles), Renato Amorim Torres, 2014
- [2] Course ME547 Physics-Based Modeling for Computer Control, Prof. Lorenz, 2014
- [3] Course ME746 Dynamics of Controlled Systems, Prof. Lorenz, 2014
- [4] Course ME746 Dynamics of Controlled Systems, Prof. Lorenz, 2014
- [5] Datasheet Semikron SKiiP 402GD061-358CTV (IGBT Module)
- [6] Datasheet LEM LV25-P (Voltage Sensor)
- [7] Modeling and Nonlinear Control of a Fuel Cell/Supercapacitor Hybrid Energy Storage System for Electric Vehicles, Fafil et.al., IEEE Transactions on Vehicular Technology, 2014
- [8] Implementation of Dynamic Evolution Control of Bidirectional DC-DC Converter for Interfacing Ultracapacitor Energy Storage to Fuel-Cell System, Samosir et.al., IEEE Transactions on Industrial Electronics, 2010
- [9] A Low Complexity Control System for a Hybrid Battery-Ultracapacitor Power Source, Demetriades et.al., ECCE Asia, 2013
- [10] A Parallel Energy-Sharing Control for Fuel cell-Battery-Ultracapacitor Hybrid Vehicle, Wong et.al., ECCE, 2011
- [11] Robust Control of an Ultracapacitor-based Hybrid Energy Storage System for Electric Vehicles, Wong et.al., Advanced Motion Control Workshop, 2014